

University of Nebraska - Lincoln

DigitalCommons@University of Nebraska - Lincoln

---

Theses, Dissertations, and Student Research:  
Department of Physics and Astronomy

Physics and Astronomy, Department of

---

8-2013

## Ferroelectric and Dielectric Properties of Electroactive Oligomers and Nanocomposites

Kristin Leigh Kraemer

University of Nebraska-Lincoln, [kkraemer@huskers.unl.edu](mailto:kkraemer@huskers.unl.edu)

Follow this and additional works at: <https://digitalcommons.unl.edu/physicsdiss>

 Part of the [Condensed Matter Physics Commons](#)

---

Kraemer, Kristin Leigh, "Ferroelectric and Dielectric Properties of Electroactive Oligomers and Nanocomposites" (2013). *Theses, Dissertations, and Student Research: Department of Physics and Astronomy*. 28.

<https://digitalcommons.unl.edu/physicsdiss/28>

This Article is brought to you for free and open access by the Physics and Astronomy, Department of at DigitalCommons@University of Nebraska - Lincoln. It has been accepted for inclusion in Theses, Dissertations, and Student Research: Department of Physics and Astronomy by an authorized administrator of DigitalCommons@University of Nebraska - Lincoln.

FERROELECTRIC AND DIELECTRIC PROPERTIES OF ELECTROACTIVE  
OLIGOMERS AND NANOCOMPOSITES

By

Kristin L. Kraemer

A DISSERTATION

Presented to the Faculty of

The Graduate College at the University of Nebraska

In Partial Fulfillment of Requirements

For the Degree of Doctor of Philosophy

Major: Physics and Astronomy

Under the Supervision of Professor Stephen Ducharme

Lincoln, Nebraska

August, 2013

# FERROELECTRIC AND DIELECTRIC PROPERTIES OF ELECTROACTIVE OLIGOMERS AND NANOCOMPOSITES

Kristin L. Kraemer, Ph.D.

University of Nebraska, 2013

Advisor: Stephen Ducharme

Polyvinylidene fluoride (PVDF) and its copolymers have been well established as ferroelectric polymers. The dielectric and ferroelectric properties for vinylidene fluoride (VDF) oligomer thin films were investigated. By synthesizing oligomers instead of long polymer chains, films with higher crystallinity can be formed and the locations of oligomers can be controlled for applications such as molecular electronics.

Evidence of ferroelectricity was observed in oligomer thin films evaporated onto room temperature substrates and by Langmuir-Blodgett (LB) deposition. Voltage and frequency dependence of the capacitance was measured. Oligomers functionalized with phosphonic acid formed self-assembled monolayers (SAM) on aluminum and mica substrates. Film thickness was measured by ellipsometry and atomic force microscopy (AFM). The time dependence on film growth was measured for SAMs on mica substrates by AFM. The islands had already formed by 1 minute, and by 1 hour film was continuous.

Additionally, studies were performed on composite dielectric systems with the goal of fabricating high energy density dielectrics containing nanoparticles with an organic shell. The first two types of samples had barium titanate nanoparticles coated with

functionalized alkanes or VDF oligomers. The first sample type consisted of coated nanoparticles embedded in a PVDF copolymer or terpolymer spin-coated film. At low particle concentrations, the matrix properties dominated the electrical measurements while at high concentrations, the samples were electrically fragile. The second sample type consisted of alternating layers of LB terpolymer and LB nanoparticles. These samples allowed for high particle concentrations while maintaining the high breakdown strength of the polymer layers. The final type of sample was titanium dioxide nanoparticles formed by cluster deposition and coated with an evaporated paraffin or VDF oligomer. These samples tended to have low breakdown strengths and poor repeatability from sample to sample.

The final study was on the effect of humidity in poly(vinylidene fluoride-trifluoroethylene) 70:30. Water vapor could enter the film, reside in the lattice, and affect the dielectric measurements. Based on dielectric measurements, the amount of water in the film at 80% relative humidity was 0.046%. With 50 nm aluminum electrodes, the vapor entered the film quickly, although it took five to six hours to leave at room temperature.

**Copyright 2013 Kristin Kraemer**

## ACKNOWLEDGEMENTS

I would like to express my extreme thanks to my advisor, Dr. Stephen Ducharme, for his guidance while pursuing a Ph. D. degree at UNL and for all of the opportunities he has provided me. His insight and support has been invaluable over the years.

I would also like to express my deep gratitude to Dr. Barry Cheung, Dr. James Takacs, and Dr. Christian Binek for serving on my doctoral committee and for providing many enlightening discussions over difficulties that have arisen. I would further like to thank Dr. Takacs for his support with the synthesis of the oligomers.

I would like to thank all of my collaborators for their support on the dielectric project. I would like to thank Dr. Balamurugan Balasubramanian for his help with the cluster deposition nanoparticles and with his help characterizing the particles by x-ray diffraction, transmission electron microscopy, and scanning electron microscopy. I would also like to thank Dr. Zhongxin Ge, Dr. Rajesh Krishnan, and Dr. Lesya Korbryn for all of their help synthesizing VDF oligomers.

I would also like to especially thank my past and present research group mates including Miss Susan Cooper, Dr. Rafal Korlacki, Mr. Shashi Poddar, Mr. Jingfeng Song, Mr. Steven Wignall, Mr. Nicholas Reding, Dr. Mengjun Bai, Dr. Christina Othon, Dr. Jihee Kim, Dr. Matthew Poulsen, Dr. Timothy Reece, Mr. Ben Hage, Mr. Ben Plowman, Mr. Travis Johnson, Mr. Mitch Schmidt, Mr. Ben Wotruba, Mr. Andy He, and Mr. Brad Peterson for all support and discussions. I would especially like to express my gratitude to Miss Susan Cooper for all of her assistance on the dielectric study project including making atomic force microscopy and energy density measurements. I would like to thank Mr. Steve Wignall for all of his assistance coating

nanoparticles and Mr. Nicholas Reding for his assistance with dielectric measurements. I would like to thank Mr. Ben Hage for his assistance with the x-ray diffraction measurements on the composite films.

Finally, I would like to thank my family. Without their love and support, this would have not been possible. I would like to thank my brother, John, for all of his support through the years of studies and my grandmother, Eleanor, for all of her love. I would especially like to thank my husband, Steve, for encouraging me when things were difficult. Finally, I would like to thank my parents, Karen and David Kraemer. They have always been the ones who encouraged me with everything I wanted to do.

## TABLE OF CONTENTS

Abstract	ii
Copyright	iv
Acknowledgements	v
Table of contents	vii
List of Tables	xvii
List of Figures	xix
<b>1. Chapter 1- Introduction to Thesis</b>	<b>1</b>
<b>1.1. Ferroelectric and Relaxor Polymers</b>	<b>1</b>
1.1.A. Organic Materials	1
1.1.B. Ferroelectric Theory	2
1.1.B.a. Effect of Temperature on Polarization and Phase Transition	3
1.1.B.b. Hysterisis of Polarization in an Electric Field	5
1.1.C. Relaxor Ferroelectric Theory	5
1.1.D. Poly(vinylidene fluoride) Polymer	7
<b>1.2. Energy Storage</b>	<b>9</b>
1.2.A. Energy Storage Devices	9
1.2.A.a. Electrochemical Capacitors	10
1.2.A.b. Electrolytic Capacitors	16
1.2.A.c. Capacitors and Dielectrics	17
1.2.B. Types of Capacitors in Current Use	19
1.2.B.a. Paper	20
1.2.B.b. Polymer	20
1.2.B.b.i. Polypropylene	22
1.2.B.b.ii. Poly(vinylidene fluoride) as a Dielectric	22
1.2.B.b.iii. Other Polymers Dielectrics	23
1.2.B.c. Ceramic	23
1.2.B.d. Mica	24
1.2.C. Current Research	24
1.2.C.a. Matrix Selection for Nanocomposites	25
1.2.C.b. Functionalized Barium Titanate Nanoparticles	26
1.2.D. Proposed Research	27

<b>1.3.</b>	<b>Overview of Organization of Dissertation</b>	<b>27</b>
<b>1.4.</b>	<b>References</b>	<b>29</b>
<b>1.5.</b>	<b>Tables</b>	<b>36</b>
<b>1.6.</b>	<b>Figures</b>	<b>41</b>
<b>2.</b>	<b>Chapter 2- Sample Preparation and Measurement Methods</b>	<b>74</b>
<b>2.1.</b>	<b>Introduction</b>	<b>74</b>
<b>2.2.</b>	<b>Sample Preparation</b>	<b>75</b>
2.2.A.	Spin Coating	75
2.2.A.a.	Background	75
2.2.A.b.	Experimental Method	78
2.2.B.	Langmuir Blodgett	78
2.2.B.a.	Background	78
2.2.B.b.	Experimental Method	80
2.2.C.	Solutions for Making Samples	84
2.2.D.	Substrate Choices and Preparation for Samples used in Electrical and Nonelectrical Measurements	85
2.2.D.a.	Cleaning Silicon Substrates	86
2.2.D.b.	Cleaning Glass Substrates	86
2.2.E.	Basic Capacitor Construction	87
2.2.E.a.	Thermal Evaporation of Electrodes	88
2.2.E.b.	Indium Tin Oxide Etched Electrodes	90
2.2.E.c.	Attaching leads	91
<b>2.3.</b>	<b>Dielectric Measurement</b>	<b>92</b>
2.3.A.	Quality Control	92
2.3.B.	Thermal Treatment and Temperature Dependence of Capacitance	93
2.3.C.	Voltage Dependence of Capacitance	94
2.3.C.a.	Background	94
2.3.C.b.	Experimental Details	95
2.3.D.	Capacitance as a Function of Frequency	96
2.3.D.a.	Background	96
2.3.D.b.	Experimental Details	97

<b>2.4.</b>	<b>Pyroelectric Measurements</b>	<b>97</b>
2.4.A.	Background	97
2.4.B.	Experimental Details	98
2.4.B.a.	Instrumentation	98
2.4.B.b.	Computer Virtual Instrument	99
<b>2.5.</b>	<b>Film Quality, Morphology, and Thickness Measurements</b>	<b>101</b>
2.5.A.	X-Ray Diffraction of Thin Films	101
2.5.A.a.	Background	101
2.5.A.b.	Experimental Details	102
2.5.B.	Atomic Force Microscopy	102
2.5.B.a.	Background	102
2.5.B.b.	Experimental Details	103
2.5.C.	Scanning Electron Microscopy	104
2.5.C.a.	Background	104
2.5.C.b.	Experimental Details	105
2.5.D.	Ellipsometry	106
2.5.D.a.	Background	106
2.5.D.b.	Experimental Details	109
<b>2.6.</b>	<b>Material Analysis</b>	<b>109</b>
2.6.A.	Nuclear Magnetic Resonance	109
2.6.A.a.	Background	109
2.6.A.b.	Experimental Details	112
2.6.B.	Thermal Gravimetric Analysis	112
2.6.B.a.	Background	112
2.6.B.b.	Experimental Details	113
<b>2.7.</b>	<b>References</b>	<b>115</b>
<b>2.8.</b>	<b>Tables</b>	<b>119</b>
<b>2.9.</b>	<b>Figures</b>	<b>121</b>
<b>3.</b>	<b>Chapter 3- Vinylidene Fluoride Oligomers</b>	<b>143</b>
<b>3.1.</b>	<b>Introduction to Oligomers</b>	<b>143</b>
<b>3.2.</b>	<b>Basic Properties of Oligomers</b>	<b>144</b>

3.2.A.	Melting Temperature of the VDF Oligomers	144
<b>3.3.</b>	<b>Oligomer Langmuir-Blodgett Films</b>	<b>145</b>
3.3.A.	Langmuir Isotherms of VDF Oligomers	145
3.3.B.	Deposition of Langmuir-Blodgett Oligomer Films	147
3.3.C.	Dielectric Results of Oligomer Langmuir Blodgett Films	148
<b>3.4.</b>	<b>Capillary Cells</b>	<b>149</b>
3.4.A.	Sample Fabrication of Capillary Cells	149
3.4.B.	Capillary Cell Dielectric Results	150
<b>3.5.</b>	<b>Evaporated VDF Samples</b>	<b>151</b>
<b>3.6.</b>	<b>Conclusions</b>	<b>152</b>
<b>3.7.</b>	<b>References</b>	<b>154</b>
<b>3.8.</b>	<b>Figures</b>	<b>156</b>
<b>4.</b>	<b>Chapter 4- Self-Assembled Monolayer Thin Films</b>	<b>177</b>
<b>4.1.</b>	<b>Introduction</b>	<b>177</b>
<b>4.2.</b>	<b>Overview of Materials</b>	<b>179</b>
4.2.A.	Organic Materials	180
4.2.A.a.	Octadecylphosphonic Acid	180
4.2.A.b.	Poly(vinylidene fluoride) Oligomer	181
4.2.B.	Substrates for Self-Assembled Monolayers	181
<b>4.3.</b>	<b>Procedure for Growing Self-Assembled Monolayers</b>	<b>182</b>
<b>4.4.</b>	<b>Octadecylphosphonic Acid Self-Assembled Monolayer Films</b>	<b>183</b>
4.4.A.	Ellipsometry Thickness Measurements	183
4.4.B.	Atomic Force Microscopy Thickness Measurements	183
<b>4.5.</b>	<b>Vinylidene Fluoride Oligomer Self-Assembled Monolayer Measurements</b>	<b>184</b>
4.5.A.	Ellipsometry Thickness Measurements of Vinylidene Fluoride Self-Assembled Monolayers	184
4.5.B.	Time Dependent Atomic Force Microscopy Measurements	184
<b>4.6.</b>	<b>Conclusion</b>	<b>187</b>
<b>4.7.</b>	<b>References</b>	<b>188</b>
<b>4.8.</b>	<b>Tables</b>	<b>191</b>

<b>4.9.</b>	<b>Figures</b>	<b>194</b>
<b>5.</b>	<b>Chapter 5- Chemical Coating of Barium Titanate Nanoparticles</b>	<b>212</b>
<b>5.1.</b>	<b>Introduction</b>	<b>212</b>
<b>5.2.</b>	<b>Choice of Particles</b>	<b>213</b>
<b>5.3.</b>	<b>Choice of Coatings</b>	<b>215</b>
<b>5.4.</b>	<b>Detailed Particle Coating Procedure</b>	<b>216</b>
5.4.A.	Cleaning the Particle Surface	216
5.4.B.	Coating Barium Titanate Nanoparticles with Alkane-Phosphonic Acids	218
5.4.C.	Coating Barium Titanate Nanoparticles with VDF Oligomer	221
<b>5.5.</b>	<b>Verification of Particle Coatings</b>	<b>223</b>
5.5.A.	Nuclear Magnetic Resonance of Particles and Coatings	223
5.5.B.	Thermal Gravitational Analysis of Particles and Surfactants	226
5.5.B.a.	Thermal Gravitational Analysis of Alkane Coated Nanoparticles	227
5.5.B.b.	TGA of VDFO coated particles	228
5.5.C.	Transmission Electron Microscopy of Coated Nanoparticles	229
<b>5.6.</b>	<b>Solubility Testing</b>	<b>230</b>
<b>5.7.</b>	<b>Conclusions</b>	<b>232</b>
<b>5.8.</b>	<b>References</b>	<b>233</b>
<b>5.9.</b>	<b>Tables</b>	<b>237</b>
<b>5.10.</b>	<b>Figures</b>	<b>242</b>
<b>6.</b>	<b>Chapter 6-Construction and Structural Measurements of Nanocomposite Dielectric Materials</b>	<b>262</b>
<b>6.1.</b>	<b>Introduction to Overall Project</b>	<b>262</b>
<b>6.2.</b>	<b>Spin-coated Nanocomposite Films</b>	<b>263</b>
6.2.A.	Solutions for Making Samples	264
6.2.B.	Sample Construction for Spin-coated Films	265
6.2.B.a.	Uncoated Barium Titanate in Copolymer P(VDF-TrFe)	265
6.2.B.b.	Octadecylphosphonic Acid Coated Barium Titanate Nanoparticles in 50/50 P(VDF-TrFe) Matrix	266

6.2.B.c.	Octadecylphosphonic Acid Coated Barium Titanate Nanoparticles in a Terpolymer Spin-coated Matrix	267
6.2.B.d.	Vinylidene Fluoride Oligomer Coated Barium Titanate Nanoparticles in a Polyvinylidene Fluoride Terpolymer	268
6.2.C.	Analyzing Film Properties of Spin-coated Samples	268
6.2.C.a.	Surface Morphology of Spin-coated Samples imaged with Scanning Electron Microscopy	269
6.2.C.b.	Cross-Sectional Scanning Electron Microscopy of Spin-coated Samples	270
6.2.C.c.	X-Ray Diffraction of Composite Spin-Coated Samples	271
6.2.C.d.	Thickness Measurements of Spin-Coated Composite Films	272
<b>6.3.</b>	<b>Langmuir-Blodgett Capacitor Samples</b>	<b>272</b>
6.3.A.	Langmuir-Blodgett Layers of Terpolymer	273
6.3.A.a.	Making Langmuir-Blodgett Layers	274
6.3.A.b.	Thickness Measurements of a Terpolymer Monolayer	275
6.3.A.c.	Terpolymer Capacitor Samples	276
6.3.B.	Langmuir-Blodgett Layers of Particles	276
6.3.B.a.	Langmuir Layers of Octadecylphosphonic Acid-coated Barium Titanate Nanoparticles	277
6.3.B.a.i.	Deposition of Langmuir Layer on Water and Isotherms of Particle Films	277
6.3.B.a.ii.	Nanoparticle Film Deposition onto Substrates	278
6.3.B.b.	Scanning Electron Microscopy of Multilayer Thin Films	279
6.3.B.c.	Ellipsometry	280
6.3.B.d.	Particle Coverage of a Langmuir-Blodgett Layer	281
6.3.B.e.	Pressure Dependent SEM Study on Langmuir-Blodgett nanoparticle Films	282
6.3.B.f.	Capacitor Samples of ODPA Coated BTO	286
6.3.B.g.	LB Layers of VDFO Coated BTO	286
6.3.C.	Composite Capacitor Samples	286
6.3.C.a.	Trough Setup of Langmuir-Blodgett Layers	286

6.3.C.b.	Design of Sample Structures	287
6.3.C.c.	Surface Morphology of Particles on Terpolymer Films	288
6.3.C.d.	Cross-Section Samples	289
6.3.C.e.	Thickness of Multilayer Composite Films	292
<b>6.4.</b>	<b>Cluster Deposition Nanoparticle Capacitor Samples</b>	<b>294</b>
6.4.A.	Methods for Production of Particles by Sputtering in a Vacuum	295
6.4.A.a.	Uncoated Titanium Dioxide Particles	296
6.4.A.a.i.	X-Ray Diffraction of Uncoated Titanium Dioxide Nanoparticles	296
6.4.A.a.ii.	Transmission Electron Microscopy Results of Uncoated Titanium Dioxide Nanoparticles	297
6.4.A.b.	Paraffin Coated Titanium Dioxide Nanoparticles	297
6.4.A.b.i.	Coating Thickness of Paraffin Coated Nanoparticles	298
6.4.A.b.ii.	X-ray Diffraction of Paraffin Coated Nanoparticles	299
6.4.A.b.iii.	Volume Ratios of Coated Titanium Dioxide Nanoparticles	300
6.4.A.c.	VDF Oligomer Coated Titanium Dioxide Nanoparticles	301
6.4.A.c.i.	Titanium Dioxide Particle Properties for the Particles to be Coated in VDFO	301
6.4.A.c.ii.	X-Ray Diffraction of VDFO Coated Titanium Dioxide nanoparticles	301
6.4.A.c.iii.	Volume Ratio Estimations of Particles to Coatings	302
6.4.B.	Measurement Methods for Determining Sample Thicknesses	305
6.4.B.a.	Optical Interference	305
6.4.C.	Capacitor Sample Properties	308
6.4.C.a.	Uncoated Titanium Dioxide Particles	308
6.4.C.a.i.	Scanning Electron Microscopy of the Surface of the Film	308
6.4.C.a.ii.	Cross-sectional Scanning Electron Microscope Imaging of Uncoated Titanium Dioxide Nanoparticle Thin Films	308
6.4.C.a.iii.	Sample Thickness Measurements of Uncoated Titanium Dioxide Nanoparticle Films	309
6.4.C.b.	Titanium Dioxide Nanoparticles with a Paraffin Shell as a Thin Film	310
6.4.C.b.i.	Scanning Electron Microscopy Studies of the Surface of Paraffin Coated Titanium Dioxide Nanoparticle Thin Films	310

6.4.C.b.ii.	Atomic Force Microscopy Studies of the Surface of Paraffin Coated Titanium Dioxide Nanoparticle Thin Films	311
6.4.C.b.iii.	Sample Thickness of Paraffin Coated Titanium Dioxide nanoparticles	312
6.4.C.c.	Titanium Dioxide Nanoparticle with a VDFO Shell as a Thin Film	313
6.4.C.c.i.	Scanning Electron Microscope Studies of the Surface of VDFO Coated Titanium Dioxide Nanoparticle Thin Films	313
6.4.C.c.ii.	Atomic Force Microscopy Studies of the Surface of VDFO Coated Titanium Dioxide Nanoparticle Thin Films	314
6.4.C.c.iii.	Sample Thickness of VDFO Coated Titanium Dioxide Nanoparticles	314
<b>6.5.</b>	<b>Conclusion</b>	<b>315</b>
<b>6.6.</b>	<b>References</b>	<b>317</b>
<b>6.7.</b>	<b>Tables</b>	<b>319</b>
<b>6.8.</b>	<b>Figures</b>	<b>327</b>
<b>7.</b>	<b>Chapter 7- Dielectric Studies of Composite Capacitors</b>	<b>375</b>
<b>7.1.</b>	<b>Introduction</b>	<b>375</b>
<b>7.2.</b>	<b>Electrical Measurement Results for Nanocomposite Samples Fabricated by Spin-coating</b>	<b>375</b>
7.2.A.	Uncoated Barium Titanate in Copolymer P(VDF-TrFe)	375
7.2.A.a.	Dielectric Measurements	376
7.2.B.	Octadecylphosphonic Acid Coated Barium Titanate in 50/50P(VDF-TrFe)	377
7.2.B.a.	Dielectric Measurements	377
7.2.B.b.	Energy Density Measurements	378
7.2.C.	Langmuir-Blodgett Layers of Terpolymer	378
7.2.C.a.	Dielectric Measurements	379
7.2.C.b.	Energy Density Measurements	380
7.2.D.	Octadecylphosphonic Acid Coated Barium Titanate in Terpolymer Matrix	380
7.2.D.a.	Dielectric Measurements	381
7.2.D.b.	Energy Density Measurements	381

7.2.E.	Spin-Coated Octadecylphosphonic Acid Coated Nanoparticles with No Matrix	382
<b>7.3.</b>	<b>Electrical Measurement Results for Nanocomposite Samples Fabricated by Langmuir-Blodgett Deposition</b>	<b>382</b>
7.3.A.	Langmuir-Blodgett Layers of Particles	382
7.3.A.a.	Dielectric Measurements of Langmuir-Blodgett Particle Films	383
7.3.A.b.	Energy Density Measurements	383
7.3.B.	Multilayer Composite Capacitor Samples	384
7.3.B.a.	Dielectric Measurements	384
7.3.B.b.	Energy Density Measurements	384
<b>7.4.</b>	<b>Electrical Measurement Results for Nanocomposite Samples Fabricated by Cluster Deposition</b>	<b>385</b>
7.4.A.	Uncoated Titanium Dioxide Particles	385
7.4.A.a.	Dielectric Measurements	385
7.4.B.	Paraffin Coated Particles	386
7.4.B.a.	Dielectric Measurements	386
7.4.C.	Oligomer Coated Particles	387
7.4.C.a.	Dielectric Measurements	387
7.4.C.b.	Energy Density Measurements	388
<b>7.5.</b>	<b>Conclusions</b>	<b>389</b>
<b>7.6.</b>	<b>References</b>	<b>390</b>
<b>7.7.</b>	<b>Figures</b>	<b>391</b>
<b>8.</b>	<b>The Effects of Humidity on the Dielectric and Ferroelectric Properties of PVDF</b>	<b>408</b>
<b>8.1.</b>	<b>Introduction</b>	<b>408</b>
<b>8.2.</b>	<b>Sample Preparation</b>	<b>409</b>
<b>8.3.</b>	<b>Experimental Setup</b>	<b>410</b>
8.3.A.	Temperature Dependence of the Capacitance at Low, Medium, and High Humidity Levels	414
8.3.B.	Dependence of Capacitance on Relative Humidity at a Constant Temperature	415

8.3.C.	Enthalpy and Activation Energy of Humidity in PVDF	415
8.3.D.	Dependence of Capacitance on Applied Bias at a Constant Relative Humidity	416
8.3.E.	The Effect of Relative Humidity on the Pyroelectric Hysteresis of PVDF	417
<b>8.4.</b>	<b>Results</b>	<b>418</b>
8.4.A.	Temperature Dependence of the Capacitance at Low, Medium, and High Humidity Levels	418
8.4.B.	Dependence of Capacitance on relative Humidity at a Constant Temperature	420
8.4.C.	X-Ray Diffraction of Swelled Films	421
8.4.D.	Enthalpy and Activation Energy of Humidity in PVDF	422
8.4.E.	Dependence of Capacitance on Applied Bias at a Constant Relative Humidity	426
8.4.F.	The Effect of Relative Humidity on the Pyroelectric Hysteresis of PVDF	428
<b>8.5.</b>	<b>Conclusions</b>	<b>431</b>
<b>8.6.</b>	<b>References</b>	<b>432</b>
<b>8.7.</b>	<b>Figures</b>	<b>434</b>

## LIST OF TABLES

Table 1-1. Further comparison of normal and relaxor ferroelectric properties.	36
Table 1-2. Properties of several electrolytes.	37
Table 1-3. Trends in Capacitor Applications.	38
Table 1-4. Performance requirements of capacitors.	39
Table 1-5. General characteristics of polymer dielectrics.	40
Table 2-1. Table of commonly used solvent properties.	119
Table 2-2. Table of metal melting points and densities.	120
Table 4-1. Common functional groups to attach to nanoparticles and substrates. Based on table from Love et al.	191
Table 4-2. Film thickness for VDF oligomer SAMs grown on aluminum oxide.	192
Table 4-3. AFM height and roughness for VDF oligomer SAMs at different deposition times.	193
Table 5-1. Table of high dielectric bulk materials. The bulk dielectric constants are from the CRC handbook unless stated otherwise.	237
Table 5-2. Table of molecular weights for the alkanes.	238
Table 5-3. The oligomers have the form of X-R, where X is the tail group and R is the functional group. The molecular weights of the VDFO are calculated by adding the tail weight to the functional group weight.	239
Table 5-4. Relative mass calculations for the VDF oligomers and BTO nanoparticles.	240
Table 5-5. Relative mass calculations for VDFO and BTO nanoparticles. Note that the bulk calculation has less oligomer than the double bilayer.	241
Table 6-1. Example of stock solutions used to make a series of samples.	319
Table 6-2. Sample configurations for uncoated, 65 nm diameter barium titanate particles in a copolymer matrix.	320
Table 6-3. Concentration ratios for ODPA coated 56 nm BTO particles in VDF copolymer or terpolymer.	321
Table 6-4. Volume percentages of barium titanate for different sample configurations.	322

Table 6-5. Ellipsometry thickness measurements of terpolymer Langmuir Blodgett films	323
Table 6-6. Ellipsometry results for ODPA coated BTO Langmuir-Blodgett films.	324
Table 6-7. Ellipsometry results for composite samples.	325
Table 6-8. Estimated film thickness for constructive interference of red light.	326

## LIST OF FIGURES

Figure 1-1. New demands on electronics require the use of new materials such as organics.	41
Figure 1-2. Organic molecules used in electronics range from simple monomers to complex biological inspired molecules such as proteins.	42
Figure 1-3. Schematic of the symmetry groups of crystals for piezoelectric, pyroelectric, and ferroelectric crystals.	43
Figure 1-4. Piezoelectric effect in a crystal. The application of strain produces a charge and the application of a charge creates a strain in the crystal.	44
Figure 1-5. The pyroelectric effect produces a charge that is proportional to the temperature change.	45
Figure 1-6. (A) Perovskite unit cell with the $ABO_3$ structure. The dipole is created by the displacement of the center atom towards an oxygen atom. (B) Sodium nitrite is an example of an order-disorder ferroelectric.	46
Figure 1-7. Dipoles for displacement and order-disorder ferroelectrics. The top row is paraelectric dipoles and the bottom row is ferroelectric dipoles. The left column is displacement dipoles compared to the right column of order-disorder dipoles. (A) Displacement dipoles in the paraelectric phase. (B) Order-disorder dipoles in the paraelectric phase. (C) Displacement dipoles in the ferroelectric phase. (D) Order-disorder dipoles in the ferroelectric phase.	47
Figure 1-8. (A) Temperature dependence of the relative polarization for (a) second-order LGD ferroelectrics and (b) first order LGD ferroelectrics. (B) Plot of the free energy density given in Equation 1-1 for the (a) second order transition and (b) first order transition.	48
Figure 1-9. (A) Theoretical polarization curve from the derivative of the Gibbs free energy equation shown in blue and the black curves represent the metastable polarization. (B) Example of a typical dielectric curve.	49
Figure 1-10. Comparison between regular ferroelectrics and relaxor ferroelectrics properties.	50
Figure 1-11. Decrease in the dielectric hysteresis as a function of temperature in PMN.	51
Figure 1-12. Plot of Gibbs free energy for ferroelectric as it goes from pure P(VDF-TrFe) to P(VDF-TrFe-CFE) with no sign of ferroelectricity remaining.	52
Figure 1-13. (A) PVDF in the ferroelectric all trans form. (B) PVDF in the paraelectric trans-gauche form. (C) The ferroelectric dipole goes from the	

fluorine atoms to the hydrogen atoms. (D) VDF oligomers were synthesized with an iodine or functional group on the end.	53
Figure 1-14. Phase diagram for P(VDF-TrFe) copolymers.	54
Figure 1-15. Comparison of the hysteresis loops of a regular ferroelectric and relaxor ferroelectric at room temperature.	55
Figure 1-16. Comparison of ferroelectric P(VDF-TrFe) polymer properties to relaxor ferroelectric P(VDF-TrFe-CFE). (A) Temperature dependence of the capacitance. (B) FTIR absorbance spectrum. (C) X-ray diffraction of the (110, 200) reflection region. (D) DSC over the phase transition temperatures.	56
Figure 1-17. Examples of a parallel plate capacitor, an electrolytic capacitor, and a electrochemical double layer super capacitor.	57
Figure 1-18. A Ragone plot showing the relationship between specific power and specific energy of various types of energy storage devices. The dashed lines represent the energy transfer times for a device.	58
Figure 1-19. A schematic of a charged electrochemical double layer capacitor showing the current collecting plates, electrodes, electrolyte and the separator.	59
Figure 1-20. a) Helmholtz layer with the thickness $d$ . b) Gouy-Champman model of the diffusion layer. c) Stern's model showing both the Helmholtz layer and the diffusion layer.	60
Figure 1-21. (A) The specific capacitance decrease with pore size until it reaches a critical value, where there is a sudden increase. The amount of solvent surrounding the ions decreases as the pore size decreases and the ions are located closer to the surface of the electrode. (B) Schematic of a negatively charged a) mesopore and b) micropore in an electrolyte solution.	61
Figure 1-22. Electrolytic capacitors. (A) Aluminum electrolytic capacitor and (B) a tanalum electrolytic capacitor. (C) Cut away of a tantalum capacitor.	62
Figure 1-23. A parallel plate capacitor with the area $A$ and thickness $d$ .	63
Figure 1-24. The shaded region is the energy densities for various types of polarizations. (A) Linear dielectric (B) Regular ferroelectric (C) Relaxor Ferroelectric (D) Antiferroelectric.	64
Figure 1-25. (A) and (B) Examples of commercial construction for energy discharge capacitors. (C) Metalized polymer capacitor. (D) Multilayer polymer film block capacitor.	65
Figure 1-26. Graceful failure in a polymer film. (A) A defect forms in the film. (B) The film and electrode burn away, leaving the rest of the capacitor functioning.	66

- Figure 1-27. Dielectric strength of biaxially oriented, single oriented, and unoriented polypropylene films. 67
- Figure 1-28. Temperature dependence of the breakdown strength for perovskites. 68
- Figure 1-29. Energy density considerations for dielectric materials. (A) The energy discharged in a capacitor is the area above the curve. (B) A material that quickly reaches saturation will not store as much energy as one that reaches saturation more slowly. (C) A relaxor ferroelectric will store more energy than a regular ferroelectric due to having little or no remnant polarization. 69
- Figure 1-30. (A) FTIR spectra for the barium titanate nanoparticles coated with functionalized alkanes. The dotted line at the bottom is the uncoated particles. The solid lines are OPA-BTO, OSA-BTO, OTMOS-BTO, and OCA-BTO from the top down. Only the octaphosphonic acid attached well.[50] request permission (B) FTIR for uncoated BTO, OPA, and OPA coated BTO in the region of the P-O stretching. 70
- Figure 1-31. Functionalized barium titanate were mixed with P(VDF-HFP) to create thin films. 71
- Figure 1-32. (A) Top view of composite films with different concentrations. (B) Cross sections of the composite films. As the concentration increased past 50%, the film started to crumble instead of being continuous and having a smooth appearance. The scale bars are 1  $\mu\text{m}$ . 72
- Figure 1-33. (A) Dielectric spectroscopy for different sample concentrations. (B) Dielectric loss for different sample concentrations. (C) The breakdown field as a function of various concentrations of particles. (D) The calculated energy density (grey) compared to the measured energy density (black) for each film concentration. 73
- Figure 2-1. Films were deposited by spin-coating. (A) A few drops of solution was dripped onto a slowly spinning substrate. The rate of rotation was then increased to create a thin film. (B) Numerous parameters affect the film thickness and quality as the film forms. Angular velocity and flow properties such as viscosity of the solution will affect the sample thickness. Also, enviromental changes such as the temperature and humidity of the air flow around the sample will affect the thinning rate and how the film dries during deposition. 121
- Figure 2-2. Sketch of a Langmuir-Blodgett trough. A dilute solution is dispersed on the surface of the water. The barriers of the trough compress the film to make a dense monolayer . 122
- Figure 2-3. (A) Typical pressure-area curve for an ideal Langmuir film, such as stearic acid. The solution on the trough starts as a gas phase. As the film is compressed, it becomes denser, entering a liquid and then a solid phase. The start of each phase is represented by a change in slope on the pressure area curve. (B)

A pressure area curve for PVDF-TrFe (70-30). PVDF shows gradual slope changes instead of sharp changes like stearic acid.

123

Figure 2-4. Langmuir-Blodgett deposition techniques. (A) There are three common vertical deposition techniques. X type deposition pushes the substrate into the water to deposit a layer. Z type deposition pulls the substrate from the water. Y type dipping deposits a layer onto the substrate as the substrate is pushed into and pulled from the water. (B) In some cases, the horizontal Schaefer method worked better to make films since it did not involve submerging the substrate in the water. (C) Depending on the deposition method, the molecules have different orientations on the substrate. X type deposition has the tails of each layer pointing towards the substrate. Z type dipping has the heads of each layer pointing towards the substrate. Y type deposition builds up layers that are head to tail. (D) Films deposited by Schaefer method have a structure similar to X type deposition with each layer's tails pointing towards the substrate.

124

Figure 2-5. A sketch of a typical sample construction showing the various layers in a sample. (A) The overhead view of a sample consisting of a thin film sandwiched between two aluminum electrodes on a glass substrate. Where the two electrodes cross is a capacitor sample. (B) A cross section of a typical sample. The film is made to the desired thickness by depositing the predetermined number of layers by Langmuir-Blodgett technique. (C) An actual sample with 9 parallel plate capacitors.

125

Figure 2-6. (A) The evaporator metal source is below the sample and mask. The metal is heated to a vapor which passes through the shadow mask to deposit electrodes on the substrate. (B) Examples of typical shadow masks. The masks can be configured into nearly any shape, with stripes being the most common for ease of use with parallel plate capacitors. (C) One metal source for the evaporator consists of a piece of tungsten metal bent into a "u" or "v" shape and wrapped with the metal wire for evaporation. (D) An alternative metal source is the preformed tungsten baskets which use a piece of metal as a source.

126

Figure 2-7. ITO Etching. (A) Scotch tape is applied to the ITO film. (B) The pattern to be etched is cut into the tape. All tape is removed from any area where the ITO should be etched. (C) The substrate is soaked in the etchant. The tape protects the electrode areas. (D) The substrate is rinsed first with water to remove any remaining etchant. (E) The tape is then removed and any tape residue is washed from the substrate. The dry substrate is then ready for a film.

127

Figure 2-8. Sample Leads (A) The leads on most samples were attached with indium metal. The indium would stick better to the glass than to the aluminum electrodes, so it was necessary to make the indium span the electrode catching on either side on the glass before it would stick to the aluminum. (B) Sketch of the cross section of the indium attachment of leads. The copper wires stuck to the

indium better if they were tinned with lead solder before being attached to the electrode. 128

Figure 2-9. Sketch of the cross section of the sample stage. The temperature is controlled through the heaters and coolers. Dry gas is brought into the chamber to flush any moisture from the samples and environment. Sample leads are attached to the solder pads, and 4 wire connections lead to instruments. 129

Figure 2-10. Sketch of temperature control feedback loops. The temperature is controlled by a microprocessor in the temperature controller. The output goes to transformer which reduces the voltage being applied to the heater. The heater will heat up the sample stage, and the temperature is measured by a RTD or thermocouple connected to the temperature controller. A second thermocouple measures the sample temperature. This current is amplified, and then recorded by a computer. 130

Figure 2-11. (A) Sketch of typical temperature profile versus time. (B) Example CT data for a 30 ML 70/30 PVDF-TrFe film. The peaks occur in heating and cooling at the phase transition between ferroelectric and paraelectric phases. 131

Figure 2-12. (A) Typical capacitance as a function of voltage curve (CV curve). Peaks appear in the capacitance when the polarization reverses. (B) A typical applied bias curve for CV scans. The bias is applied in a step-wise fashion, typically increasing by 0.1volts increments. 132

Figure 2-13. (A) Sketch of computerized pyroelectric apparatus. The sample is rapidly heated and cooled using a laser that is modulated with a chopper. The relay switch connects the sample first to a voltage source and then to the lockin amplifier to measure the pyroelectric current. (B) A voltage divider to reduce the signal to a safe level to be measured by the analog in on the computer. 133

Figure 2-14. Front panel of the Labview VI to control the computerized pyroelectric experiment. This VI was originally written for the humidity project and was used for all of the other pyroelectric measurements. 134

Figure 2-15. (A) Bragg scattering between planes of atoms or molecules. Constructive interference occurs when the difference in path length is an integer number of wave lengths. 135

Figure 2-16. AFM setup. Detector system for an AFM. 136

Figure 2-17. Sketch of SEM. 137

Figure 2-18. Ellipsometry Theory (A) Sketch of the interaction of linearly polarized light reflecting off of a sample. (B) The polarization axis in terms of  $\Psi$  and  $\Delta$ . The light propagates down the Z axis, which is pointing out of the page. 138

Figure 2-19. (A) Sketch of a rotating angle spectroscopic ellipsometer. The linearly polarized light reflects off of the sample and passes through a rotating

polarizer before it enters the detector. (B) Flowmap of the procedure to model ellipsometry data.	139
Figure 2-20. (A) Nucleus with different spins are at the same energy level in the absence of a magnetic field. When in a magnetic field, the energy splits into two levels. (B) The applied magnetic field causes the nucleus to start to precess.	140
Figure 2-21. NMR Typical Data. Block diagram of typical NMR system.	141
Figure 2-22. TGA Applications (A) Different compositions of polymers will give different shaped curves. This allows one to compare the characteristic decomposition curves.[34] (request permission) (B) TGA allows one to compare ratio of composite materials based on different decomposition temperatures. In this example, the composite is 75% polyethylene and 25% carbon black.[34] (request permission) (C) One can also look at the decomposition curve of a single material. In the case of $\text{CaC}_2\text{O}_4 \cdot \text{H}_2\text{O}$ , each time part of the molecule decomposes, there is a decrease in mass.	142
Figure 3-1. Poly(vinylidene fluoride) (A) polymers and (B) oligomers. The oligomers have a VDF tail and a head group such as iodine or phosphonic acid.	156
Figure 3-2. Sketch of the oligomer melting point experiment setup. The heater plate was placed on a microscope stage to observe the onset of melting of the oligomers.	157
Figure 3-3. Melting point of VDF oligomers.	158
Figure 3-4. Isotherms for 17 unit VDF oligomer from Kunshan Hisense Company in (A) DMSO at low trough loading, (B) DMSO at higher trough loading, (C) in DMF, and (D) in acetone. All sample concentrations were 0.4 mM and 225 $\mu\text{L}$ of solution was loaded onto the trough each time, except for (B) where 500 $\mu\text{L}$ was used.	159
Figure 3-5. Isotherms for several VDF oligomers including (A) 18 unit VDF with an iodine head group in DMSO, (B) 25 unit VDF with an iodine head group in DMSO, and (C) 20 unit of VDF with a phosphonic acid head group in butanone.	160
Figure 3-6. Multi-cycle isotherm for 18 unit VDF with an iodine head group with the first two cycles shown in (A) and the next two cycles shown in (B).	161
Figure 3-7. Y-type deposition of oligomer films.	162
Figure 3-8. Area transfer for iodine oligomers at 10 mN/m pressure to a 6 $\text{cm}^2$ substrate.	163
Figure 3-9. Dielectric results for an 18 unit VDF oligomer film compressed to a surface pressure of 10 mN/m. (A) Temperature dependence and (B) frequency dependence of the capacitance.	164

- Figure 3-10. Dielectric results for another typical 18 unit VDF oligomer sample. The (A) temperature dependence, (B) voltage dependence, (C) frequency dependence, and (D) Cole-Cole plot for the sample. 165
- Figure 3-11. Temperature dependence for a 25 unit VDF oligomer. 166
- Figure 3-12. Typical samples with 25 units of VDF. (A) Voltage dependence and (B) Frequency dependence for films deposited at 20 mN/m. (C) Voltage dependence and (D) frequency dependence for films deposited at 25 mN/m. 167
- Figure 3-13. Sketch of capillary cell setup. (A) Side view of two ITO coated plates with a Mylar spacer. (B) The top view of a capillary cell where one plate had patterned electrodes. 168
- Figure 3-14. The oligomers were melted on a strip heater. (A) Top and (B) side view of the heater stage for heating the capillary cells. (C) The unmelted oligomer was placed at the opening of the capillary cell. (D) When the oligomer melted, capillary forces drew it into the cell. 169
- Figure 3-15. Pictures of capillary cells with oligomers between the two plates. (A) Top view and (B) side view of a filled cell. 170
- Figure 3-16. (A) Temperature results for a 12 unit VDF oligomer with a 12  $\mu\text{m}$  Mylar spacer. (B) Voltage dependence for a 6 unit VDF oligomer in a capillary cell with a 12  $\mu\text{m}$  Mylar spacer. 171
- Figure 3-17. The cluster deposition system. Evaporated oligomer samples were made in the evaporation chamber with the substrate located at Substrate 1 location. 172
- Figure 3-18. Evaporated film (A) before and (B) after annealing. 173
- Figure 3-19. Temperature dependence of the capacitance for the evaporated oligomer film. 174
- Figure 3-20. Voltage dependence of an evaporated film (A) before and (B) after annealing. 175
- Figure 3-21. Pyroelectric hysteresis loop for the evaporated thin film after annealing. 176
- Figure 4-1. Parts of a Self-Assembled Monolayer. 194
- Figure 4-2. (A) At low temperatures, the SAM growth starts in the vapor phase. (B) At higher temperatures, the SAM has an additional laying down phase and a disordered phase as it grows into islands. 195
- Figure 4-3. (A) Common functional groups containing phosphorus. (B) Phosphonic acid attachments onto oxide surfaces. Phosphonic acid can attach to

an oxide with one, two, or three of its oxygens. This allows for a stronger attachment than many of the other functional groups. 196

Figure 4-4. The dielectric tail used for coating the oxide nanoparticles. (A) Alkanes were the prototype material since they were commercially available. (B) VDFO was synthesized by our collaborators. R is the functional group, in this case phosphonic acid used to attach the surfactant to the particles. 197

Figure 4-5. AFM of substrate surfaces, (A) Aluminum Oxide and (B) Mica. The left image is the amplitude and the right image is the phase. 198

Figure 4-6. Schematic of some of the defects found in SAMs grown on polycrystalline surfaces. 199

Figure 4-7. Basic procedure for making a self-assembled monolayer. (A) Prepare a clean substrate of the desired surface. (B) Make a solution of 0.01 to 1 mM in a suitable solvent. (C) Submerge the substrate in the solution and allow it to soak for several days. (D) Rinse off the surplus surfactant. Any surfactant that has chemically attached to the substrate should stay on the substrate. (E) Allow the remaining solvent to evaporate. Then, the SAM is ready for use. 200

Figure 4-8. Ellipsometry measurements and fit for an ODPA film grown on aluminum dioxide substrate. The orange curve was the measurement of the substrate and the green curve was the measurement of the film. With an index of 1.6, the film was calculated to be 2 nm thick. 201

Figure 4-9. AFM measurement of an ODPA SAM grown on aluminum oxide. (A) Amplitude and phase images for the film. (B) Section analysis of the film. Most islands were 4 nm tall, although some were 10-15 nm in height. 202

Figure 4-10. SAMs of VDF oligomers grown on aluminum oxide. (A) The film (8 units of VDF) was approximately 0.8 nm with an index of refraction of 1.4. (B) The film (7 units of VDF) was approximately 1.8 nm thick with an index of refraction of 1.4. Both films had good fits with the data, and the MSE values were between 0.75 and 0.85. 203

Figure 4-11. Time dependent growth of the VDF oligomer SAMs on mica. The left image is the amplitude and the right image is the phase. (A) 1 minute growth time. (B) 2 minutes growth time. (C) 3 minutes growth time. (D) 5 minutes growth time. (E) 20 minutes growth time. (F) 1 hour growth time. (G) 24 hours of growth time. 204

Figure 4-12. Section analysis for 1 minute deposition of the VDF oligomer SAM on mica. 205

Figure 4-13. Section analysis for 2 minute deposition of the VDF oligomer SAM on mica. 206

Figure 4-14. Section analysis for 3 minute deposition of the VDF oligomer SAM on mica.	207
Figure 4-15. Section analysis for 5 minute deposition of the VDF oligomer SAM on mica.	208
Figure 4-16. Section analysis for 20 minute deposition of the VDF oligomer SAM on mica.	209
Figure 4-17. Section analysis for 1 hour deposition of the VDF oligomer SAM on mica.	210
Figure 4-18. Section analysis for 24 hour deposition of the VDF oligomer SAM on mica.	211
Figure 5-1. SEM images of deagglomerated BTO nanoparticles. (A) A sample at 50k magnification showing that the particles are mostly the same size. (B) The same sample at 150k magnification. This image was used in Figure 5 2 to determine the size distribution of the particles.	242
Figure 5-2. Size distribution of the particles was determined by measuring each particle in the image and using the scale based on 300 nm= 65 mm, the particles were assigned to a color-coded bin size. After all of the particles were color-coded, the number of particles of each color was counted and the size distribution was plotted in Figure 5-3.	243
Figure 5-3. Distribution of sizes of barium titanate nanoparticles in Figure 5-2. The histogram was fitted with a Gaussian curve. The average particle size was 56 nm with a half width of 13 nm.	244
Figure 5-4. The dielectric tail used for coating the oxide nanoparticles. (A) Alkanes were the prototype material since they were commercially available. (B) VDFO was synthesized by our collaborators. R is the functional group, in this case phosphonic acid used to attach the surfactant to the particles.	245
Figure 5-5. Water bath setup for sonicating nanoparticles. It is important to use a large enough bath so the heat can be effectively transferred away from the solution. In this case, a 2L beaker was used with room temperature water. A smaller bath could also be used, if it was filled with ice.	246
Figure 5-6. Sketch of the stirrer for coating the particles with (A) alkanes and (B) oligomers. When coating with alkanes, the temperature of the solution was raised to about 65°C. The oligomers were stirred at room temperature.	247
Figure 5-7. 1D <sup>1</sup> H NMR spectrum of VDF oligomers in deuterated acetone.	248
Figure 5-8. 1D <sup>19</sup> F NMR spectrum of VDF oligomers in deuterated acetone.	249

Figure 5-9. 1D $^{31}\text{P}$ NMR spectrum of VDF oligomers in deuterated acetone.	250
Figure 5-10. 2D HMBC NMR spectrum of VDF oligomers in deuterated acetone.	251
Figure 5-11. Various configurations of oligomers used in the NMR studies. (A) In this case, we used liquid NMR to determine if the functional group was physically attached to the particles. (B) Since the particles are not in solution, anything directly attached to them will not give off a signal. In comparison, the tails are in solution, and we will pick up a NMR Signal from them. (C) If the oligomers were physically surrounding the particles as in Figure C, the head groups would also be in solution. By not seeing a phosphorus signal in the NMR data, we can infer that there were no free phosphorus or very few that are not attached to the particle. We were able to determine that the oligomers and alkanes were present by looking for the NMR signatures of the tail groups and not seeing a phosphorus signal.	252
Figure 5-12. TGA of cleaned and dried BTO nanoparticles. The change in the weight is likely caused by moisture leaving the particles.	253
Figure 5-13. TGA of octadecyl phosphonic acid ( $\text{C}_{18}\text{H}_{37}\text{P}(\text{O})(\text{OH})_2$ ). The sharp drop at $454^\circ\text{C}$ is from the thermal decomposition of the alkanes.	254
Figure 5-14. The TGA curve of the coated particles is shown in blue. The decrease in mass corresponds well with the decrease shown in the TGA curve of the pure alkanes, shown in red. There is a total mass reduction of about 17% at $1000^\circ\text{C}$ . 3.47% of this change is from the particles losing weight when they dry. The remainder of the loss belongs to the loss of the coatings on the particles. In this case, the coating account for about 14.8% of the mass. The remainder of the mass belongs to the particles.	255
Figure 5-15. TGA of several VDF oligomers. Decomposition temperature is lower than expected when compared to bulk PVDF which is around $380^\circ\text{C}$ in air.	256
Figure 5-16. TGA of oligomer coated nanoparticles (blue) compared to TGA data of uncoated particles (black) and pure oligomers (red).	257
Figure 5-17. TEM image of Alkane coated nanoparticles.	258
Figure 5-18. Solvent testing of the dodecylphosphonic acid coated BTO nanoparticles in various solvents. A small amount of the coated particles was added to a milliliter of various solvents and monitored over a few days to see which solvents allowed the particles to stay suspended the best.	259
Figure 5-19. Solvent testing of the dodecylphosphonic acid coated BTO nanoparticles in various solvents. After several days, the particles had settled from all of the solvents.	260
Figure 5-20. Solvent testing of the dodecylphosphonic acid coated BTO nanoparticles in various solvents.	261

Figure 6-1. Sketches of different sample configuration used for the dielectric study. Composite samples were made by spin coating a polymer matrix and (A) uncoated nanoparticles or (B) particles coated with an organic shell. (C) With Langmuir-Blodgett deposition, particles and polymers were deposited in alternating layers. (D) Particles created by sputtering metal oxides were coated with an organic shell and deposited directly onto the substrate without a matrix. 327

Figure 6-2. The discharged energy density of in capacitor is the blue shaded area. A ferroelectric loses a large amount of energy due to the permanent dipoles compared to the relaxor. 328

Figure 6-3. ODPA coated BTO nanoparticles were mixed with 50/50 copolymer and spin-coated into thin films. (A) Six percent of the samples volume was occupied by BTO particles. At this concentration, the particles were well dispersed in the polymer film. (B) With 14% of volume occupied by BTO, the particles were distributed on the surface and embedded in the film. (C) When the concentration of particles was increased to 24% of the volume, more particles are starting to appear at the surface of the film. (D) At a higher particle concentration of 40% particles, the film had started to form aggregates of polymer and particles. 329

Figure 6-4. ODPA coated BTO in 50/50 P(VDF-TrFe) with a volume ratio of 40% particles. This sample showed the segregation of polymer and particles, along with the structure of the polymer film. 330

Figure 6-5. (A) Sketch of sample holder for imaging cross sectional samples. (B) Diagram of the composition of the composite sample used for imaging the cross section. (C) FESEM image of the cross section of a 14% by volume ODPA coated BTO sample in 50/50 copolymer. The dielectric layer was in focus. 331

Figure 6-6. X-ray diffraction data for ODPA coated BTO in a 50/50 P(VDF-TrFe) matrix. As the volume concentration of particles increased, the BTO peaks increased while the polymer peak decreased. 332

Figure 6-7. Ratio of polymer and particle peaks as a function of the BTO volume concentration in composite spin-coated films. As the concentration of particles increased, the polymer peak area decreased. 333

Figure 6-8. Breakdown path of percolated sample compared to the LB samples. (A) In a spin-coated sample, there was no control of where the particles were located in the sample. This means that the probability of having spots in the sample where the particles create a path of lower breakdown strength increased as the particle concentration increased. (B) In the ideal LB multilayer sample, particles and polymer made alternating rows. (C) Even in a less ideal and more realistic sample, there is still little chance for particles to create a path from one electrode through the sample to the other. Since the film is flexible, it can conform to irregularities in the particle layers. By capping each layer with a thin

layer of particles, a much higher particle concentration can be created than with spin-coating. 334

Figure 6-9. Pressure area isotherm for a pure terpolymer film showing no evidence of collapse up to 18 mN/m. 335

Figure 6-10. Deposition of terpolymer films at 5 mN/m using 0.01% by weight terpolymer in DMF. (A) Typical PA curve on our trough. (B) PA curve from Wang's Paper. (C) The first 35 ML's transferred onto 8 substrates from our trough. For each sample, the first 5 ML were typically wetter than the later layers. The sample coverage was about 49% on average for all layers transferred. 336

Figure 6-11. Thickness of the terpolymer Langmuir-Blodgett films deposited at 5 mN/m. The uncertainty in the thickness came from the uncertainty in the index of refraction in the fittings of the data from ellipsometry. 337

Figure 6-12. Pressure area curve for ODPA coated BTO nanoparticles. The particles were compressed to the minimum area on the trough without any sign of major buckling or collapse, although minor collapse may have occurred at the slope change around 46 mN/m. 338

Figure 6-13. Three isotherm cycles for ODPA coated BTO nanoparticles. The particles behavior on the trough was nearly reversible up to pressures as high as 22 mN/m. 339

Figure 6-14. Deposition of ODPA coated BTO nanoparticle Langmuir-Blodgett layers onto substrates. The early cycles had a larger loss of area than the later cycles did. The inset shows the first few deposition cycles. The layers deposited with the horizontal method show a larger area loss per deposition than the cycles made with the vertical z-type deposition technique. 340

Figure 6-15. (A) Five monolayer of ODPA coated BTO nanoparticles deposited onto a silicon substrate using the Schaefer method of deposition at 7 mN/m. (B) Five bilayers of ODPA coated BTO nanoparticles deposited onto a silicon substrate using the Z-type deposition at 7 mN/m. 341

Figure 6-16. Particle coverage calculations for a sample deposited at 10 mN/m. (A) Low magnification image of sample. (B) The particles were masked off using the software Gyddion. The total area and masked area was measured. (C) The high magnification image of a typical cluster of particles. (D) The area of the cluster and (E) the area of the particles were measured using the masking procedure. 342

Figure 6-17. Particle coverage calculations for a sample deposited at 7 mN/m. (A) A low magnification image of sample showing clusters of particles. (B) The particle areas were masked off and measured using the software Gyddion. (C) A high magnification image of a typical cluster of particles. (D) The area of the

cluster and (E) the area of the particles of particles within a cluster were measured using the software. 343

Figure 6-18. Pressure-Area Isotherm for ODPA coated BTO nanoparticles. Samples were made at each of the deposition points. SEM images of the samples are shown in Figure 6-19 and Figure 6-20. 344

Figure 6-19. (A) Low magnification image of sample deposited at 7 mN/m. (B) High magnification image of sample deposited at 7 mN/m. (C) Low magnification image of sample deposited at 10 mN/m. (D) High magnification image deposited at 10 mN/m. (E) Low magnification image deposited at 12 mN/m. (F) High magnification image deposited at 12 mN/m. 345

Figure 6-20. (A) Low magnification image of a sample deposited at 15 mN/m. (B) High magnification image of a sample deposited at 15 mN/m. (C) Low magnification image of a sample deposited at 18 mN/m. (D) High magnification image of a sample deposited at 18 mN/m. (E) Low magnification image of a sample deposited at 21 mN/m. (F) High magnification image of a sample deposited at 21 mN/m. 346

Figure 6-21. (A) Multilayer samples were made by dividing the trough into two parts. Each side of the trough had its own movable barrier and a surface pressure sensor. This allowed for deposition of two materials. (B) Multilayer capacitor samples started with 5 to 20 ML of polymer on a glass or silicon substrate with aluminum electrodes. (C) Particle Langmuir-Blodgett layers were deposited onto the initial polymer layers. (D) The sample was built up alternating layers of polymer and particles until the desired composition was constructed. 347

Figure 6-22. Samples were constructed by building multilayers of particles. Each ML of terpolymer was on average 2 nm thick. The nanoparticles had an average diameter of 65 nm, and 19% coverage for deposition at 10 mN/m. (A) The most common sample composition was 5, 10, or 20 ML of terpolymer, and then a few layers of particles, capped with another polymer layer. (B) More complex samples were made by making many layers of polymer and particles. This allowed for a higher volume concentration of particles. 348

Figure 6-23. FESEM images of 1 ML of ODPA coated BTO on terpolymer films. (A) The particles had good adhesion over large sections of the film. While there are voids in the low magnification film, most of the sample was covered with particles. (B) At 10k magnification, there was some space between clusters of particles. (C) Most of the particles were in a single layer. Some particles were stacked on neighbors. (D) The high magnification 50k image showed that the particles were starting to pack together. 349

Figure 6-24. (A) Sketch of the multilayer sample used for cross sectional imaging. The sample consisted of a silicon substrate, aluminum bottom electrode, 20 ML of terpolymer, 3 ML of ODPA coated BTO, 20 ML of terpolymer, and aluminum top electrode. (B) FESEM image of the cross section of a composite

sample. The polymer layers were not clearly visible and the sample contracted upon initial contact with the beam, signifying damage from the electron beam to the polymer. 350

Figure 6-25. Sketches of the pattern milled by the FIB. (A) Each step was milled 60  $\mu\text{m}$  deeper than the previous step. (B) A cross section of the steps being milled into the sample. (C) The sample was rotated so the flat edge of the sample could be viewed. (D) The sample was mounted on a triangle wedge, and then the sample stage was rotated, so the surface to be imaged made a  $75^\circ$  angle with the electron beam. 351

Figure 6-26. FESEM images of cross section composite sample milled using a FIB. (A) Horizontal view of the sample showing the steps cut into the sample. (B) Low magnification image of the sample tilted at  $75^\circ$ . (C) Medium magnification image showing the layers of the film. (D) High magnification image with no evidence that nanoparticles were present. 352

Figure 6-27. Schematic of plasma condensation chamber. By sputtering on a titanium target in a mixed atmosphere of oxygen and inert gases, nanoparticles were created. The particles then passed into the evaporation chamber where they were coated with an organic shell. Finally, the particles entered the deposition chamber where they were deposited onto a substrate. 353

Figure 6-28. XRD results of uncoated Titanium oxide nanoparticles. (a) As the oxygen flow rate increased, the particles changed from Ti (curve i) to  $\text{TiO}$  (curve ii) to  $\text{TiO}_2$  (curve iii). (b) As the oxygen content increased, the nanoparticles went from a mixed rutile and anatase phase to a nearly pure anatase state. 354

Figure 6-29. (A) TEM image of  $\text{TiO}$  nanoparticles (B) The particle size distribution histogram. The average particle size,  $d$ , is 17.7 nm with a standard deviation,  $\sigma$ , of 1.1 nm. (C) TEM image showing well dispersed of  $\text{TiO}_2$  nanoparticles. The inset shows smooth, spherical particles. (D) The average size distribution is 13 nm with a narrow distribution of sizes. 355

Figure 6-30. Evaporation rate organic shells (A) Coating rates for paraffin shell. (B) TEM of paraffin coated  $\text{TiO}_2$  nanoparticles. The coating is the thin ring surrounding the dark particle in the center. 356

Figure 6-31. XRD of coated nanoparticles. (A) XRD results of  $\text{TiO}_2$ -Paraffin coated nanoparticles prepared under different evaporation temperatures. At low temperature, there was no evidence of any paraffin coating. The paraffin peaks increased as the evaporation temperature increased. (B) A slow scan of the region where the paraffin peaks were expected. 357

Figure 6-32. Uncoated titanium dioxide nanoparticles created with the process used for the VDFO coated particles. (A) SEM image of the uncoated particles. (B) The average particle size was 14.4 nm. (C) XRD data for particles made at different DC power. 358

Figure 6-33. X-ray diffraction of VDFO coated titanium dioxide nanoparticle films.	359
Figure 6-34. SEM image of VDFO coated Titanium Dioxide Particles.	360
Figure 6-35. Histogram of the VDFO coated titanium dioxide nanoparticles measured from Figure 6-34. The particles had an average width of 53 nm, and the half width was 18 nm.	361
Figure 6-36. A typical sample with different thicknesses. The contrast of the photo was increased to make it easier to see each of the color bands. In this sample, six red bands can be clearly seen.	362
Figure 6-37. The light reflecting from the top and bottom surfaces of the film created interference patterns such as the ones shown in Figure 6-36.	363
Figure 6-38. Scanning electron microscope image of an uncoated titanium dioxide nanoparticle film.	364
Figure 6-39. Cross sectional FESEM of a capacitor made on Si with TiO <sub>2</sub> nanoparticle. The dielectric layer was approx. 1 $\mu$ m thick, while the top electrodes were approx. 100 nm, the bottom electrodes were 60 nm, and it was on a thin SiO <sub>2</sub> covered Si substrate.	365
Figure 6-40. Plot of sample thickness with respect to distance from center of beam spot for the sample shown in Figure 6-36. The distribution of thickness fit a Gaussian distribution well.	366
Figure 6-41. Thin film of uncoated titanium dioxide nanoparticles with a distribution of thicknesses over the sample. (A) The desired sample spot was the one in the lower left corner with the faint green band. (B) Table of values used to calculate the sample thickness of 213 nm.	367
Figure 6-42. Two images from the same paraffin coated titanium dioxide nanoparticle thin film. (A) Scanning electron microscope image of the sample. (B) Atomic force microscopy images of the amplitude of deflection and the phase for the sample.	368
Figure 6-43. Section analysis for the paraffin coated titanium dioxide sample shown in Figure 6-42. (A) Line scan measuring the width of the bright center of a cluster. (B) Line scan measuring the darker soft region of a cluster.	369
Figure 6-44. A thin film of titanium dioxide nanoparticles with a paraffin shell deposited at 170°C. Index of refraction was the volume average of the coating and the particle.	370
Figure 6-45. Thin film of titanium dioxide nanoparticles coated with a paraffin shell deposited at 110 °C. The index of refraction was a composite value based	

off of the volume ratios of paraffin and nanoparticles. The sample thickness for this sample ranged from 248 nm to 310 nm, with an average value of 279 nm. 371

Figure 6-46. Scanning electron microscope image of a thin film consisting of VDFO coated titanium dioxide nanoparticles. 372

Figure 6-47. Titanium dioxide nanoparticles with a VFDO shell. (A) The SEM image shows a soft material, with no evidence of any particles. (B) The AFM also did not show any evidence of nanoparticles. 373

Figure 6-48. Psi and delta data for two sample spots on a sample of titanium dioxide with a VDFO shell. (A) The psi data and fits for spot B1. (B) The delta data and fits for spot B1. The sample thickness was 240 nm. (C) The psi data and fits for spot A3. (D) The delta data and fits for spot A3. The sample thickness was calculated to be 214 nm. (E) A sketch of the sample with each electrode labeled. (F) Table of thickness values for each spot on the sample. 375

Figure 7-1. Pure P(VDF-TrFE) 75:25 film and composite film with uncoated barium titanate nanoparticles spin-coated as a thin film. (A) Temperature dependence of the capacitance of a pure copolymer film. (B) Temperature dependence of the capacitance for a composite film. (C) Voltage dependence on the capacitance for a pure copolymer film. (D) Voltage dependence on the capacitance for a composite film. 391

Figure 7-2. Temperature dependence of the capacitance for samples with (A) 0%, (B) 6%, (C) 14%, (D) 24%, and (E) 40% by volume of ODPA-coated BTO nanoparticles in a 50:50 P(VDF-TrFE). (F) Peak location of the heating and cooling peaks for the series of data in the Figure 7 2 A-E. 392

Figure 7-3. Comparison of the frequency dependence of the capacitance for a (A) pure 50:50 P(VDF-TrFE) copolymer film and (B) a copolymer film with a 65% by volume ODPA-coated barium titanate nanoparticles. (C) The dielectric constant increased as the concentration of nanoparticles increased. 393

Figure 7-4. Energy results for ODPA coated BTO nanoparticles in 50/50 P(VDF-TrFE) matrix series. (A) Energy density results for the series of samples. (B) Energy efficiency results for the series of samples. 394

Figure 7-5. Terpolymer dielectric results for LB and spin-coated films. (A) The annealing cycle plus two more temperature cycles for a 35 mL sample. (B) The annealing cycle plus two more temperature cycles for a spin-coated terpolymer film. (C) Frequency dependency of the capacitance for a LB terpolymer film. (D) “Butterfly” curve for a 35 mL terpolymer sample. 395

Figure 7-6. (A) Absolute energy density for a terpolymer film. (B) Energy efficiency for a pure terpolymer film. 396

Figure 7-7. Dielectric results for octadecylphosphonic acid coated barium titanate in a PVDF terpolymer. (A) Temperature dependence on capacitance for a sample

with 13% BTO. (B) Temperature dependence on capacitance for a sample with 54% BTO. (C) Frequency dependence on capacitance for a sample with 13% BTO. (D) Frequency dependence on capacitance for a sample with 54% BTO. 397

Figure 7-8. Energy for terpolymer composite samples as a function of temperature, including (A) pure terpolymer, (B) 13% BTO composite, and (C) 33% BTO composite films. 398

Figure 7-9. Dielectric data for LB films made of ODPA-coated BTO. (A) Temperature dependence of the capacitance and (B) frequency dependence of the capacitance for a film containing no terpolymer layers. 399

Figure 7-10. Energy density results for a LB film constructed with 20 depositions of ODPA-coated BTO nanoparticles. (A) Energy density for two typical samples. (B) Energy efficiency for two typical samples. 400

Figure 7-11. Multilayer composite films. (A) Sketch of a typical sample with two layers of polymer and a layer of particles. (B) Temperature dependence of a sample with 20 ML of terpolymer, 3 layers of ODPA-coated BTO nanoparticles, and 20 more ML of terpolymer. (C) Comparison of a sample with VDF oligomer coated particle film with an ODPA-coated particle film. Both samples had 20 ML of terpolymer above and below the 3 particle layers. 401

Figure 7-12. Comparison of energy results for samples made with 3 layers of ODPA-coated particles and VDF oligomer coated particles. (A) Energy density comparison for the two films. (B) Energy efficiency for the two films. 402

Figure 7-13. Comparison for the series of multilayer samples, of configuration A/B/A where A is the number of terpolymer layers and B is the number of particle layers. (A) Energy density for the multilayer films. (B) Energy efficiency for the multilayer films. 403

Figure 7-14. Dielectric results for uncoated titanium dioxide particle samples made by cluster deposition. (A) Temperature dependency of the capacitance for three temperature cycles. (B) Frequency dependence of the capacitance. 404

Figure 7-15. Frequency dependence for titanium dioxide nanoparticles coated in paraffin at (A) 110 °C and (B) 170 °C with the cluster deposition system. 405

Figure 7-16. Comparison of two films of VDF oligomer coated titanium dioxide nanoparticles. The temperature dependence results are shown for (A) Sample 1 and (B) Sample 2. The frequency dependence on the capacitance for (C) Sample 1 and (D) Sample 2. The two samples were supposed to be of the same composition. 406

Figure 7-17. Energy measurements for VDF oligomer coated titanium dioxide nanoparticles. The energy densities are compared for (A) Sample 1 and (B) Sample 2. The energy efficiency for (C) Sample 1 and (D) Sample 2 also show a different trend for the same type of sample. 407

Figure 8-1. Typical temperatures scan of a PVDF copolymer thin film. The peak at 35° was originally attributed to the secondary phase transition seen in XRD data. It was the further investigation of this peak that led to this project. 434

Figure 8-2. Sketch and photos of the humidity sample chamber. (A) Moist air was brought into the side of the chamber and the level was monitored by the humidity sensor in the top of the box. (B) Photo of the chamber with the sensor in the top of the lid. (C) Photo of the inside of the chamber. The sample wires are soldered onto the pins inside of the chamber. 435

Figure 8-3. Sketch of the feedback loop to control the humidity levels in the chamber. The humidity sensor would measure the humidity and the controller would determine if the level was too high or too low. The controller would output a voltage which was passed to the analog in on the computer, and it would determine which of the two gas valves needed to be opened or closed to reach the desired humidity level. 436

Figure 8-4. The humidity production chambers. (A) When the sample chamber was at or above room temperature, the water used to produce humidity was warmed to a few degrees higher than the sample chamber with the use of a hotplate connected to a temperature controller. The dry nitrogen gas was bubbled into the chamber to force the moist air into the sample chamber. (B) When the sample chamber was cooled below room temperature, it was necessary to cool the water used to produce humidity. This was to prevent condensation in the chamber. The flask sat on a blanket heater in a small bucket that was sitting in an ice bath. The dry gas line ran through the copper tubing that was submerged in the ice bath, so it would not heat the sample chamber. 437

Figure 8-5. Sketch of setup for using the function generator to provide the voltage sweep for a capacitance versus voltage sweep with the Quadtech Digibridge. The voltage sweep was provided by a function generator while the capacitance was measured with the digibridge. 438

Figure 8-6. Peaks in the temperature data caused by the humidity. The shape and location of the peak is dependent on the conditions in the chamber. (A) The red curve shows the bumps in the curve from the humidity on heating and cooling. When the same experiment is reproduced in a dry nitrogen atmosphere, the bumps have nearly disappeared due to there being little or no condensation present (black curve). (B) This series of runs was one of the original sets of data demonstrating the effect of humidity on the thin films. The setup was primitive with very little control of the flow rates and a large environmental humidity sensor to monitor the humidity levels. The data is divided into three groups with low, medium, and high humidity levels. 439

Figure 8-7. Ramping of the humidity while holding the sample at a constant temperature. The increase in the capacitance is nearly linear with very little

hysteresis. At 80% relative humidity, there is 0.046% water volume in the sample based on dielectric calculations, assuming a constant thickness. 440

Figure 8-8. XRD results showing that the water vapor is in the crystal lattice causing the crystal spacing to increase. (A) As the concentration of water increases, the  $2\theta$  XRD peak shifts to smaller angles. (B) The lattice spacing increase when it is saturated, but when it is re-annealed, it returns to its original spacing. 441

Figure 8-9. A. A typical capacitance (black) and humidity (blue) plot. Some of the important events that occur in the data are 1. Drying out sample so there is no initial humidity present. 2. Heat the sample to the desired temperature. For this run, the sample was heated to 80C. 3. Load the humidity to 60%. 4. Turn on the dry nitrogen gas and flush the chamber. 5. The drying tail that is later analyzed to determine the time constants.( B) Loading the humidity into the chamber. The capacitance follows the same trend as the humidity. 442

Figure 8-10. The chamber takes about 45 seconds to flush out the humidity. After that, the humidity level stays nearly constant. 443

Figure 8-11. An example of typical drying curves. (A) The curve is fit with a two term exponential decay. (B) The  $y_0$  term from part A is subtracted from the data. This will allow us to linearize the data in Figure 8 9. 444

Figure 8-12. The natural log of the capacitance of the data in Figure 8-11. By fitting each linear portion of the data, the time constants can be determined. The time constants are the negative inverse of the slope. (A) The short time constant is found in the first linear section of each plot. (B) The long time constant is the straight section in the middle of the data. 445

Figure 8-13. (A) Short time constant plot. This time constant is believed to represent the time it takes the chamber to completely flush out and for the water to leave the surface of the sample. (B) The long time constant plot. This is believed to be the time it takes for the water to leave the bulk of the sample. The lack of a downward trend in the data means there is very little temperature dependence. 446

Figure 8-14. Martin's, et al. measurements of the desorption properties of a 50 ML film. The transient behavior of the current with the rapid change in humidity from near 100% to 0%. The desorption time,  $\tau_{des}$ , is marked by the red arrow and is around 100 seconds. 447

Figure 8-15. Capacitance vs voltage curves over the range of humidity levels from 0% relative humidity to 80% relative humidity. The data is continued in Figure 8-16. 448

Figure 8-16. Continuation of the humidity data from Figure 8-15. At higher humidity levels, the overall capacitance decreases while the peak shifts to much

larger voltages. At lower humidity levels, the switching peak moves to smaller voltages.	449
Figure 8-17. Peak switching voltages of samples under humidity. The largest uncertainty in the peak positions is due to the broadening and flattening of the peaks.	450
Figure 8-18. Offset of Bias at point where the increasing capacitance crosses itself. There was a shift to smaller and more negative bias at the crossing point in the capacitance data as the humidity was increased.	451
Figure 8-19. The overall capacitance measured at the point where the increasing capacitance of the butterfly loops cross each other. The capacitance remains relatively constant until it reaches 40%, and then it starts to decrease.	452
Figure 8-20. Pyroelectric scans of a 30 ML sample over range of humidity levels from 20% to 80% relative humidity. As the humidity level increases, the coercive voltage increases, the saturated pyroelectric current decreases, and the loop is no longer symmetric. See Figure 8-18, Figure 8-19, and Figure 8-20 for further analysis of this data.	453
Figure 8-21. For this spot, the 0% RH cycle was ran first, followed by the 80% RH cycle. After the 80% RH cycle, the sample had irreversible damage done to it, and the following runs showed no hysteresis.	454
Figure 8-22. The half-height remnant polarization for the data shown in Figure 8-20. With the increase in humidity and cycling, there is a decrease in the remnant polarization.	455
Figure 8-23. The vertical shift of the middle of the data shown in Figure 8-20. Overall, the data shifts downward as the humidity level increases. At 80% RH, the shift of the midpoint was less than at lower levels of humidity.	456
Figure 8-24. The coercive voltage for the series of runs in Figure 8 16. Each humidity level was cycled twice, except for the 80% relative humidity. There was very little change from cycle to cycle at a given humidity level, but there was an increase with humidity levels.	457
Figure 8-25. The figures in the first column are for a 50 ML sample. The figures in the second column are for a 30 ML sample.	458

## CHAPTER 1

### INTRODUCTION TO THESIS

#### 1.1 Ferroelectric and Relaxor Polymers

##### *1.1.A Organic Materials*

It would be difficult to imagine the world today without cell phones and flat screen televisions. As technology continues to improve, so must the electronics used to make the devices. As we move towards miniaturized and flexible technology, such as shown in Figure 1-1, we must be able to make electronics flexible. One way to do this is with organic electronics.

Organic electronics have been around since the mid 1900's, but it wasn't until the late 1970's and early 1980's when conducting polymer [1] and organic light emitting diodes (OLED) [2] were discovered that interest in the field increased. Since this time, OLED's have been commercially produced in high resolution displays [3]. Organic electronics are now found in a variety of applications including transistors [4], solar cells [1, 4], high performance LEDs [3, 5], liquid crystals [6], and memory devices[1].

The molecules used in organic electronics range from simple monomers to specialized polymers to biologically inspired materials such as proteins or DNA [4], as shown in Figure 1-2. These materials are ideal for a variety of low cost deposition methods using solvents or thermal techniques such as ink jet printing, spin-coating, stamping, lithography, thermal evaporation, and screen printing [4]. The materials and deposition techniques allow for inexpensive electronics to be made on a variety of

surfaces that were not previously available for applications such as electronic paper or radio frequency identification tags [6, 7].

### *1.1.B Ferroelectric Theory*

Ferroelectrics are a class of materials that have two permanent dipole states, which can be reversed with the application of an external electric field [8]. Ferroelectric crystals are a subset of pyroelectric and piezoelectric crystals. As shown in Figure 1-3, there are 32 point crystal symmetries [8-10]. Of the 32 crystal groups, 20 configurations are piezoelectric. Piezoelectric crystals produce a net charge when strain is produced in the crystal. As shown in the cartoon in Figure 1-4 [9], a charge is produced when there is mechanical pressure applied to the crystal. When an electric field is applied to the crystal, the reverse effect occurs and strain is created in the crystal.

Of the 20 crystal groups that are piezoelectric, 10 groups are also pyroelectric. Pyroelectric materials produce a current by changing the polarization as a function of temperature. As the pyroelectric crystal is heated or cooled, a current is produced proportional to the rate of temperature change, as shown in Figure 1-5. Of the crystals that are pyroelectric, a subset of these crystals are also ferroelectric. Ferroelectric materials are divided into two main categories based on the method of forming a dipole. It should be noted that there are ferroelectrics which belong to neither category or are a hybrid of both [11, 12]. The first category is displacive ferroelectrics. Ferroelectrics in this category have a dipole when an atom shifts within the unit cell to produce a net polarization. Examples of this type of ferroelectric are perovskites such as barium titanate. As shown in Figure 1-6A, perovskites with the  $ABO_3$  structure have an oxygen

in the center of each face of the unit cell and an ion such as barium or lead occupies the corners of the crystal structure. The center atom in the unit cell, often  $\text{Ti}^{+4}$  or  $\text{Zr}^{+4}$  shift slightly closer to one of the oxygen atoms, producing a net polarization when exposed to an electric field [8-10].

Order-disorder ferroelectric crystals, alternatively, are materials with a permanent molecular dipole which are randomly aligned resulting in no net dipole before the application of an electric field. An example is shown in Figure 1-6B [12] of sodium nitrite. Before the application of an electric field, the dipoles are aligned in random directions with no net polarization. With the application of a field, the dipoles caused by the nitrite ion align in the same direction producing a net polarization in the crystal [11, 12].

#### *1.1.B.a Effect of Temperature on Polarization and Phase Transitions*

When a ferroelectric crystal is heated above a specific temperature, the spontaneous net polarization disappears [8, 10, 11]. The temperature at which the polarization goes to zero is defined as the Curie point,  $T_c$ . The polarization may decrease continuously or discontinuously, depending on the material. Above the Curie point, when there is no net polarization, a displacive ferroelectric has no dipole (Figure 1-7A) while an order-disorder material has dipoles that point in random directions resulting in no net polarization (Figure 1-7B). Below the Curie temperature, both the displacive and the order-disorder crystals have a net polarization (Figure 1-7C & D).

The free energy of a ferroelectric is given by the Landau-Ginzburg-Devonshire (LGD) formalization of the Gibbs free energy[8, 11]. For uniaxial crystal symmetry, it is given by

$$G = G_0 + \frac{\alpha}{2}P^2 + \frac{\beta}{4}P^4 + \frac{\gamma}{6}P^6 - PE, \quad \text{Equation 1-1}$$

where  $G_0$  is the free energy density of the paraelectric phase at zero field;  $P$  is the polarization; and  $\alpha$ ,  $\beta$ , and  $\gamma$  are parameters that describe the LGD formalization. A graphical representation of the Gibbs free energy and the behavior of the polarization as a function of temperature are shown in Figure 1-8. The phase transition between ferroelectric and paraelectric phases is classified as a first or second order transition depending on the behavior of the polarization as it approaches the Curie temperature. In a first order transition (Figure 1-8Aa), the polarization is discontinuous as it approaches the Curie temperature. In a second order transition (Figure 1-8Aa), the polarization decrease continuously to zero polarization [8, 10, 11]. From LGD theory,  $\alpha$  vanishes at the Curie temperature. For a second order phase transition,  $\beta$  is greater than zero and  $\gamma$  is zero. As shown in Figure 1-8Ba, the second order transition shows a clear change in energy from ferroelectric with two minima to the paraelectric phase with just one minimum. The constants for a first order transition have  $\beta$  less than zero and  $\gamma$  greater than zero in the Gibbs free energy. The first order transition still has a minimum at zero polarization at  $T_c$ , as shown in Figure 1-8Bb. The zero net polarization occurs at  $T_1$ , which is above the Curie temperature [8].

### 1.1.B.b Hysteresis of Polarization in an Electric Field

The relationship between the polarization and the electric field [8, 11] can be found by calculating the minimum with respect to polarization of the Gibbs free energy, which is given by

$$E = \alpha P + \beta P^3 + \gamma P^5. \quad \text{Equation 1-2}$$

By inverting the relationship and plotting the polarization as a function of the electric field, the theoretical curve is shown in Figure 1-9A. In this plot, the curved blue line is the unstable minima from the Gibbs free energy. The black lines are the metastable polarization. In experimental data, the shape of the hysteresis loop is similar to the curve in Figure 1-9B. Point A is the zero net polarization state. With the application of an electric field, the polarization reaches a saturated value. Depending on the material, the curve between points B and C maybe horizontal or have a slight upward slope. As the electric field decreases, most of the polarization remains until after a critical voltage in the opposite direction, labeled as pint R on the plot. This switching voltage is called the coercive voltage. The polarization continues to increase in magnitude until it reaches the maximum negative voltage. The remanent polarization,  $P_r$ , may be less than the spontaneous polarization,  $P_s$ , due to some domains relaxing to an unaligned state at zero electric field.

### 1.1.C Relaxor Ferroelectric Theory

Relaxor ferroelectrics are a class of materials with broad phase transitions and an anomalously large dielectric maxima [13]. Relaxors are found in both perovskites with the general formula of  $\text{Pb}(\text{B}', \text{B}'')\text{O}_3$ , where B' is a low valence cation such as  $\text{Mg}^{+2}$  or

$\text{Zn}^{+2}$  and  $\text{B}^{++}$  is a high valence cation such as  $\text{Nb}^{+5}$  or  $\text{Ta}^{+5}$  [13] and polymers such as P(VDF-TrFe) copolymerized with either chlorofluoroethylene (CFE) [14] or chlorotrifluoroethylene (CTFE) [15]. This behavior is also seen in irradiated P(VDF-TrFe) films [16, 17].

Relaxors differ from regular ferroelectrics in a number of ways. Figure 1-10 [18] compares several of the characteristic properties of regular ferroelectrics and relaxor ferroelectrics. First, a ferroelectric has an open polarization loop with a remnant net polarization at zero electric field. A relaxor hysteresis loop is narrow with almost no remnant polarization at zero field. Figure 1-11 shows the temperature-dependent hysteresis curve for  $\text{Pb}(\text{Mg}_{1/3}\text{Nb}_{2/3})\text{O}_3$  (PMN) over a range of temperatures. As can be seen in the figure, the hysteresis does not completely disappear until well past the phase transition [13, 19]. Figure 1-10B shows the comparison of the temperature-dependent polarization values for a regular ferroelectric and a relaxor. As discussed in the previous section, the polarization of a regular ferroelectric goes to zero polarization above the Curie temperature. For a relaxor, the temperature,  $T_m$ , is defined as the temperature where the dielectric constant reaches a maximum and is frequency dependent. This trend is also seen in the dielectric data. In a ferroelectric such as BTO the dielectric anomaly at the phase transition is sharp, with little to no frequency dispersion. A relaxor has a very broad temperature-dependent peak and strong frequency dispersion. Further properties of the two types of material are compared in Table 1-1.

Figure 1-12 shows the LGD free energy curve for PVDF-TrFe as chlorofluoroethylene (CFE) monomers are added to the polymer. Curve A is the regular

ferroelectric curve. As CFE is added, the ferroelectric phase is destabilized (Curve B). By Curve E, the ferroelectric phase has been removed completely. Between Curves B and E, the paraelectric and ferroelectric phases can coexist, as shown in Curves C and D [20].

#### *1.1.D Poly(vinylidene fluoride) Polymer*

One of the organic ferroelectric polymers is poly(vinylidene fluoride) or PVDF. This polymer has the structure of  $(\text{CH}_2\text{-CF}_2)_x$ , with the dipole pointing from the fluorine atoms to the hydrogen atoms. Figure 1-13 is a sketch of the polymer structure in the all-trans ferroelectric phase (Figure 1-13A) and the trans-gauche paraelectric phase (Figure 1-13B). Since the PVDF phase transition between the ferroelectric and paraelectric phases is above the melting temperature, as shown in Figure 1-14, PVDF is copolymerized with trifluoroethylene (TrFe) to lower the phase transition temperature of the ferroelectric to paraelectric transition without greatly changing the melting point. The P(VDF-TrFe) polymer has the structure of  $(\text{CH}_2\text{-CF}_2)_x\text{-(CHF-CF}_2\text{)}_{1-x}$  where  $x$  is typically between 0.5-0.8. As  $x$  approaches values smaller than 0.5, the polymer starts to behave more relaxor-like. In addition to long chain polymers, oligomers of VDF are synthesized. These are short chains consisting of 6-25 units of VDF, capped on one end with either iodine or a functional group such as phosphonic acid and either  $\text{CF}_3$  or  $\text{CH}_3$  on the other end.

For some of the dielectric studies, it was desirable to change from a ferroelectric polymer to a relaxor polymer to improve energy storage properties [21].

Chlorofluoroethene (CFE) was copolymerized with P(VDF-TrFe) to create local defects

in the polymer and convert the polymer to a mixed phase with ferroelectric relaxor behavior [21]. Figure 1-15 compares the hysteresis of the copolymer (dashed lines) to the terpolymer (solid line). At room temperature, the polarization was nearly disappeared in the relaxor. Figure 1-16 compared several other properties of a 68/32 P(VDF-TrFe) polymer to a similar terpolymer with 63/37/7.5 composition [21]. While the P(VDF-TrFe) film in Figure 1-16A shows a sharp transition that was not frequency dependent, the P(VDF-TrFe-CFE) terpolymer has a broad, frequency dependent peak located near room temperature [21]. The changes in the polymer films also showed up in the FTIR spectra at room temperature. The all-trans bands at  $1210\text{ cm}^{-1}$  and the  $850\text{ cm}^{-1}$  are strongly present in the copolymer, but are significantly less in the terpolymer. The absorbance at  $612\text{ cm}^{-1}$  corresponds to the TGTG' conformation found only in the terpolymer [21].

The addition of the CFE to the polymer causes an expansion of the crystal lattice, as shown in the x-ray diffraction results in Figure 1-16C. The P(VDF-TrFe) has a (100, 200) peak at  $20.1^\circ$ , which gives a lattice spacing of  $4.417\text{ \AA}$ , and the P(VDF-TrFe-CFE) has a similar peak occurring at  $18.3^\circ$ , which corresponds to the  $4.848\text{ \AA}$  lattice spacing [21]. One final piece of evidence that the terpolymer is indeed a relaxor comes from the DSC data in Figure 1-16D. The copolymer shows a ferroelectric to paraelectric phase transition along with the melting transition, while the terpolymer only shows a melting phase transition [21].

## 1.2 Energy Storage

As the world strives to become ecologically friendly, there is a demand for better ways to store and release energy [22]. In many applications, batteries fill this role, but batteries are unable to charge and discharge quickly. When a device requires the ability to quickly charge and discharge, capacitors are often used. The issue with most regular capacitors is that they are unable to hold large amounts of charge in a compact space [23]. Supercapacitors are a hybrid between regular capacitors and batteries both in performance and construction.

Capacitors fall into three major categories, as shown in Figure 1-17. The first are regular capacitors. This is the category that the research in this thesis covers. Regular capacitors are bipolar and contain a pair of electrodes with some insulator between them. Electrolytic capacitors use an electrolyte solution as one of the electrodes and an oxide layer as the dielectric [24]. Electrochemical double-layer capacitors are the third type of capacitors. They contain a pair of electrodes, a separator, and an electrolytic solution. A capacitor is formed at each of the electrodes. In general, a double-layer capacitor will have a greater power density than batteries, but will have a lower specific energy.

### 1.2.A Energy Storage Devices

Ragone plots are used to compare properties of various types of energy storage devices. The horizontal axis is the specific power and the vertical axis is the specific energy (how much energy can be stored per mass). Both axis are plotted on a log scale and the diagonal lines show time of equal discharge. As can be seen in Figure 1-18, batteries tend to have high specific energy, but lower specific power compared to other

devices. Regular capacitors, though, are found in the lower right corner and have very high specific powers, but very low specific energies. Electrochemical capacitors tend to be in the middle between the two [25-27] .

#### *1.2.A.a Electrochemical Capacitors*

Electrochemical double-layer capacitors (ECDL) were first made in 1957 by Becker using high-surface-area carbon deposited onto a conducting metal and submerged in a sulfuric acid solution [26, 28]. It took many years, though, for supercapacitors to make into consumer products. NEC, in Japan, was one of the first companies to make commercial supercapacitors in 1971 [26] and they were used as backup power sources in cameras and VCRs. By the 1980's, small supercapacitors were found in solar-power wrist watches. It was not until the 1990's that they started being more commonly used as backup power sources for toys, electronic appliances and in home equipment [24]. In recent years, there has been a large push to use supercapacitors in electric vehicle systems and as power storage for renewable energy sources [24]. The next generation of supercapacitors is being designed for use in hybrid vehicles such as electric cars, trains, and tramways. Applications with hybrid vehicles will likely contain a battery or fuel cell being used in conjunction with a super capacitor to store energy from braking [26, 29]. Another application already in use is the supercapacitors which are integrated directly into the emergency exit doors of Airbus A380 airplanes [26, 29]. Some of the more recent applications for supercapacitors include using them in short use, rechargeable devices such as cordless screwdrivers and electric cutters since they have a very quick charging time [26].

Supercapacitors are known by number of names. Most commonly, they are referred to in scientific literature as electrochemical capacitors (EC), electrochemical double capacitors (EDLC), or ultracapacitors. They are also called double layer capacitors, power capacitors, gold capacitors, and power cache in some sources of literature and on the commercial market [24, 28].

Electric double layer capacitors span the energy and power performance between regular capacitors and batteries. The supercapacitors have a double layer of capacitance at the surface between the electrodes and the ions in the electrolyte [24]. They are similar to batteries in that they have two electrodes, a separator, and an electrolyte. In batteries, the electrodes expand and contract with the reactions which limit its lifetime. The cycle life of supercapacitors is longer than batteries because there are little to no permanent changes in the electrodes due to chemical reactions [28]. In theory, the lifetime of a ECDL capacitor should be infinite [30], while in practice it has been demonstrated to be millions of cycles [26].

Supercapacitors are typically divided into two categories, depending on the way they store charge [31]. Each type has a different physical process taking place, but gives similar outputs, which is why they are both called supercapacitors. Normal double layer capacitors usually contain carbon electrodes in an organic or aqueous electrolyte. These capacitors store charge based on a double layer capacitance where charge is adsorbed onto the surface of the electrodes. Pseudocapacitors are often made with either a metal oxide or polymer electrodes and work on the principle of redox reactions. Hybrid supercapacitors use both carbon and an oxide or polymer in the composition of the

electrodes and will often have double capacitance at one electrode and a redox reaction at the other [26, 30].

In pseudocapacitors, the charge is stored by fast, reversible redox reactions with metal oxide or conducting polymers electrodes [29, 30, 32]. This class of capacitors are often referred to as pseudocapacitors since the storage mechanism is not purely electrostatic charge accumulation [30]. Instead, the charging of the capacitor causes the surface of the electrodes to go from one oxidation state to another.

The best results for pseudocapacitors have been obtained with ruthenium oxide electrodes. Very high specific capacitances have been measured, as high as 750 F/g [28]. The major drawback to  $\text{RuO}_2$  as a material for capacitors is that it is extremely expensive and is only practical to use for very special purpose capacitors. Also,  $\text{RuO}_2$  is only suitable for use in aqueous solutions, which limits the applied voltage to 1 V [28]. Besides  $\text{RuO}_2$ , other oxide materials are being explored, including  $\text{Fe}_3\text{O}_4$ , and  $\text{MnO}_2$ , and electrically conducting polymers [33]. Manganese dioxide is a promising alternative to  $\text{RuO}_2$ . It has shown specific capacitances up to 300 F/g.[33] While the pseudocapacitors can produce higher capacitances than the double layer capacitors, their stability while cycling is not nearly as reliable due to the redox reactions [26].

Electrochemical double layer capacitors (EDLC) are the other major category of supercapacitors. An EDLC capacitor consists of two electrodes submerged in an electrolyte and connected to current collecting plates. In the center of the capacitor is a separator that the ions can pass through, as shown in Figure 1-19 [31]. Traditionally, carbon is used for EDLC since it is low cost, is easily available, has a high surface area,

and the industrial technology to work with it is already well established. In addition, it has good electrical conductivity and is electrochemically stable [26, 28]. There are many different types of carbon structures used in the capacitor electrodes including powders, felts, woven cloths, fibers, aerogels, nanotubes, nanofibers, nano-onions, and nanohairs [26, 28, 30]. Carbon can have a specific surface area up to  $2500 \text{ m}^2/\text{g}$ , depending on the structure [28]. By having a large surface area, more charge can be stored, which leads to a larger capacitance.

Electrolyte solutions are typically a salt in either an organic solvent or water. Aqueous solutions have the advantage that they tend to be cheaper and safer than organic solutions. A drawback is that they are limited to about 1 V across the device before the water breaks down [28, 34]. Many salts are more soluble in water than in an organic solvent, which leads to a higher capacitance due to more charge being available to form a double layer [28]. Also, the conditions needed to make capacitors with aqueous electrolytes do not require the same purification and drying processes as is needed with organic solvents [28].

Organic electrolyte solutions are an alternative to aqueous solutions. With organic solvents, a higher voltage can be applied to the cell, which leads to a higher energy density [28, 34]. The drawback for many of the organic solvents is that they have a higher resistance than aqueous solutions, which means more energy will be lost internally [26, 28, 34]. Table 1-2 [34] lists several different types of electrolytes along with some basic properties. Propylene carbonate and acetonitrile are two electrolytes that are commonly used with organic solvents.

In an electrochemical double layer (ECDL) supercapacitor, the energy is stored at the electrochemical double layer, also known as a Helmholtz layer, as shown in Figure 1-20. This is a double layer of charge that forms at the interface between the solid electrode and the liquid electrolyte [26, 31]. There are no redox reactions occurring in this class of supercapacitors. This means they have a longer cycle life compared to the pseudocapacitors with redox reactions.

There are three different models explaining the potentials and charge distribution at the interface between the electrodes and electrolytes, as shown in Figure 1-20 [29]. The first model is the Helmholtz layer model. This model states that two layers of opposite charge form at the boundary between the electrode and electrolyte interface. The distance between the layers is defined as the distance  $d$  [29]. The model of the surfaces was further refined by Gouy and Chapman to contain a diffusion layer. This is a continuous distribution of electrolyte ions, both anions and cations. By itself, this model will lead to an over estimation of the capacitance [29]. Stern then created the Stern layer model, which combines the first two models and explicitly recognizes both regions- the compact inner layer which is made of the Helmholtz layer, and the outer diffuse region. The inner region has charges that are strongly adsorbed to the surface, as shown in Figure 1-20 [29].

The capacitance per area of an electrochemical double layer is defined as

$$\frac{C}{A} = \frac{\epsilon_0 \epsilon_r}{d}, \quad \text{Equation 1-3}$$

where  $\epsilon_r$  is the dielectric constant,  $\epsilon_0$  is the permittivity of free space, and  $d$  is the thickness of the double layer [26, 28, 31]. The thickness of a layer is typically on the

order of angstroms, depending on the solvent and the geometry of the electrode. The area included in this calculation is the area that is accessible to the electrolyte [35]. The capacitance of the entire cell is defined as

$$\frac{1}{C_{cell}} = \frac{1}{C_1} + \frac{1}{C_2}, \quad \text{Equation 1-4}$$

where  $C_1$  and  $C_2$  are the capacitance of each capacitor in the double layer capacitor [26, 28, 31]. The easiest way to increase the overall capacitance is to increase the surface area,  $A$ . This is often done by creating electrodes made of nanotubes, nanoparticles, or other porous structures. By using high surface area carbon, which can be as high as  $1500 \text{ m}^2/\text{g}$ , the capacitance can go as high as  $300 \text{ F/g}$  [26, 28, 31].

The maximum energy stored in a capacitor is

$$E = \frac{1}{2} C V^2. \quad \text{Equation 1-5}$$

The  $C$  is the capacitance of the double layer, and the  $V$  is the voltage applied to the device [26]. The maximum power is

$$P_{max} = \frac{V^2}{4R}, \quad \text{Equation 1-6}$$

where  $R$  is the internal resistance of the device [26]. This means that the energy stored in the capacitor and maximum power both depend on the square of the voltage. Capacitors with an aqueous electrolyte solution are limited to about 1 volt applied due to the breakdown strength of water. When organic electrolyte solutions are used, the maximum voltage is increased to 2-3 volts. A drawback to organic electrolytes is that the resistance is higher than aqueous solutions, by as much as 20 to 50 times.

Unfortunately, the capacitance does not increase linearly as the surface area increases. As the pore size decreases, the capacitance also decreases until the pore size reaches a critical size less than 2 nm. Once the pore size reaches about 2 nm, there is a sudden and rapid increase in capacitance, as shown in Figure 1-21A [35]. Pores in the electrodes are typically divided into 3 classifications- macropores (> 50nm), mesopores (2-50 nm), and micropores (< 2nm), as shown in Figure 1-21B [26, 29]. As the pore changes size, so does the environment around the charges, especially the number of solvent molecules. The capacitance of the mesopore is defined as

$$\frac{C}{A} = \frac{\epsilon_0 \epsilon_r}{b \ln\left(\frac{b}{b-d}\right)}, \quad \text{Equation 1-7}$$

where b is the radius of the pore and d is the distance between the ion and the edge of the pore. When the micropore is less than 1 nm, the ions make an electric wire inside of the cylinder pore. This capacitance is defined as

$$\frac{C}{A} = \frac{\epsilon_0 \epsilon_r}{b \ln\left(\frac{b}{a_0}\right)}, \quad \text{Equation 1-8}$$

where  $a_0$  is the effective size of the ion and b is the radius of the pore [26, 29].

#### 1.2.A.b Electrolytic Capacitors

Electrolytic capacitors have the advantage that they are cheap to make, as shown in Figure 1-22. A drawback is that they are unipolar, and reversing the polarity may damage them. Aluminum electrolytic capacitors have a foil anode and cathode. The foils are impregnated with an electrolyte to enlarge the surface area. The thickness of the working layer will determine the working voltage of the capacitor. The capacitors are made into laminates of foil with a spacer. They are then wound into a coil and then

dipped into a liquid electrolyte [24]. These capacitors are often used in power supplies. Some issues with electrolytic capacitors are that they tend to have current spike noise, nonlinear temperature and frequency characteristics. The energy density tends to be in the range of  $0.1 \text{ J/cm}^3$  [36].

Solid Tantalum electrolytic capacitors have the advantage of having a high dielectric constant ( $K=28$ ), can handle high temperatures, highly reliable, and a long service life, as shown in Figure 1-22B & C. The tantalum pentoxide is the dielectric. It is applied to the electrodes by an electrolytic process and allows for the thickness of the layers to be controlled. The capacitors have either a liquid or solid electrolyte. For solid electrolytes, magnesium dioxide is often used as the cathodes as shown in Figure 1-22C [37].

#### *1.2.A.c Capacitors and Dielectrics*

Capacitors were first invented in 1745 with the development of the Leyden jar by Petrus Van Musschenbroek. The earliest capacitor consisted of a jar partially filled with water and a metal wire partially submerged in the liquid. The wire was then attached to an electrical source to charge the capacitor. The Leyden jar was used as a way to store electricity [38].

Modern capacitors no longer use a jar of water to store electrical charge. Instead, a typical configuration consists of a parallel plate capacitor, either rolled together into a coil or multilayers laminated together. A simple parallel plate capacitor consists of two pieces of metal electrodes with a space between them, as shown in Figure 1-23. The

space is often filled with an insulator material such as polymers, paper, mica, or a ceramic, called the dielectric layer.

Capacitance relates the charge stored,  $Q$ , to the applied voltage,  $V$ , by the equation

$$C = \frac{Q}{V}. \quad \text{Equation 1-9}$$

For actual devices, it is desirable to calculate the capacitance in terms of the properties of the capacitor. In this case,

$$C = \frac{\kappa \epsilon_0 A}{d}, \quad \text{Equation 1-10}$$

for a parallel plate capacitor where  $A$  is the area of the electrode,  $d$  is the thickness of the dielectric layer,  $\epsilon_0$  is the permittivity of free space, and  $\kappa$  is the dielectric constant. This implies that the amount of stored charge can be increased by increasing the area, decreasing the thickness of the dielectric layer, or by increasing the dielectric constant of the dielectric layer. For commercial applications, the area is determined by the user specifications and the thickness depends on the power requirements. This leaves only the dielectric constant which can be easily adjusted [27].

In addition to the amount of charge stored on a capacitor, it is also desirable to increase the stored energy in a device. The stored energy,  $U_{Store}$ , can be expressed in terms of the applied voltage and the capacitance,

$$U_{Store} = \frac{1}{2} CV^2. \quad \text{Equation 1-11}$$

When comparing bulk materials, the energy density,  $U$ , allows comparison regardless of the size of the capacitor. The energy density of a dielectric is given by the stored energy divided by the volume of the dielectric. When the polarization is plotted versus the

electric field, the energy density is the area above the curve, as shown in Figure 1-24.

For a dielectric with linear polarization, the energy density is given by

$$U = \frac{1}{2} \kappa \epsilon_0 E^2, \quad \text{Equation 1-12}$$

as shown in Figure 1-24A. For nonlinear dielectrics, the energy density is given by

$$U = \int_0^{D_{max}} E \, dD, \quad \text{Equation 1-13}$$

where  $D_{max}$  is the maximum polarization, and  $E$  is the electric field. Figure 1-24(B-D) show examples of nonlinear polarization, such as the case of the ferroelectric, the relaxor ferroelectric, and the antiferroelectric. Of the three, the ferroelectric will usually have the smallest energy density for a given dielectric due to having a nonzero polarization at zero electric field.

When designing capacitors, it is important to tailor the properties of the capacitor to the operating conditions needed for the role being performed. Table 1-3 shows a variety of power, voltage, and time requirements for different applications.[27] A capacitor that is used in a cell phone, for example, would be much different in size and voltage requirements compared to one used in a pulse power weapon.

### *1.2.B Types of Capacitors in Current Use*

There are currently a large variety of materials used in commercial capacitors. In addition to physical size and power, one of the key features is the material used in the dielectric layers, including paper, polymers, ceramics, and mica. Table 1-4 [27] has a summary of some of the features of the different dielectric materials, and individual ones are discussed in more detail in the following sections.

### *1.2.B.a Paper*

Paper dielectrics were common in the early capacitors. They are still manufactured for some high energy density pulse capacitors. These capacitors are suitable for single shot, low repetition rate applications such as electromagnetic rail guns and high energy physics. The dielectric layer is made of high density Kraft paper that can be impregnated with oil such as castor oil to help increase the dielectric constant and break down strengths [27, 39]. These capacitors are used with voltages around 100 kV and high peak currents in the range of 1 MA. The energy density of such films is in the range of 0.66 J/cc and they have a lifetime of a few thousand cycles.

### *1.2.B.b Polymer*

Polymer capacitors are popular due to being inexpensive, high quality performance, and easily scaled in size [40]. There are a variety of polymers used in a dielectric layer. These include polypropylene, polyester, polycarbonate, and PVDF [24, 36, 41]. Some of the characteristic properties are listed in Table 1-5 [41], and are discussed further below.

The capacitors made with polymer dielectrics are often constructed by winding together layers of polymer and metal, as shown in Figure 1-25A-C. Examples of capacitors made with two layers of dielectric materials and two foil electrodes are shown in Figure 1-25A and B [27]. The difference between the two methods is the way that the electrodes attach to the rest of the circuit. In Figure 1-25A, tabs are connected to the dielectric layer. In this case, all tabs to be connected to one electrode will be gathered and connected to a common source. This is an inexpensive way to design a capacitor, and

allows for flexible designs such as having several capacitors on the same winding.

Figure 1-25B shows a capacitor made with extended foil construction. In this type of capacitor, the foils extend past the dielectric layer, and molten metal is used to cap the capacitor on each end [27]. This construction is common in applications requiring high currents such as pulse power applications.

Figure 1-25C is an example of a metalized film capacitor [27]. While this fabrication technique is common with polymer dielectrics, it is also used with other materials such as mica [36]. For this configuration, a thin layer of metal is deposited directly onto one side of the dielectric layer. Each capacitor contains two sheets of dielectrics rolled together and capped with a metal spray. This method is advantageous since it allows for the graceful failure of the capacitor. Graceful failure allows for sections of the capacitor to burn out due to defects such as pin holes or micro flaws without compromising the entire capacitor [27]. Figure 1-26 shows a sketch of graceful failure in polymer layers. In Figure 1-26A, a defect is formed in the middle of the second polymer layer. When the defect burns out, shown in Figure 1-26B, the electrode also burns away, preventing catastrophic failure of the device. Once the damaged part has been removed, the capacitor will function as normal, with a slight reduction in capacitance.

A final method to construct polymer capacitors is with a multilayer film, as shown in Figure 1-25D. This construction is advantageous since the polymer films can withstand the high temperatures needed to solder leads to the capacitor for several minutes without damaging the polymer film [27].

### *1.2.B.b.i Polypropylene*

Most commercial capacitors are made with polypropylene. Polypropylene has a low dielectric constant of just 2.2, but due to the lack of polar groups, it has a low dissipation factor. Compared to the other polymer films, polypropylene has one of the higher breakdown voltages and performs graceful failure well. In addition, it is an inexpensive film to make which is a highly desirable trait for making large scale capacitors [27, 40]. The polypropylene used in capacitors is biaxially oriented to improve the mechanical and the electrical strengths of the film. Figure 1-27 shows the dielectric breakdown probability for film that were biaxially oriented, single oriented, and unoriented [40]. It was found that the films with biaxial orientation were able to withstand much higher breakdown voltages compared to single oriented and the unoriented films.

Future progress is being made by improving the purity of the films. By decreasing the ash content to less than 30 ppm, and reducing the thermal shrinkage, the electrical properties were improved. It is expected that the energy density will be doubled from  $1.2 \text{ J/cm}^3$  to close to  $2.5 \text{ J/cm}^3$  [41].

### *1.2.B.b.ii Poly(vinylidene fluoride) as a Dielectric*

Traditionally, PVDF has not been used in commercial capacitors due to its high dielectric loss caused by the dipoles in the film, and its high cost [41, 42]. While PVDF does contain a high dielectric constant, around 8-12, and higher energy densities compared to other polymers, the loss makes it unattractive for applications such as pulse

power [41]. It does show promise in the research and design phases of new technologies, which is discussed in Section 1.2.C.

#### *1.2.B.b.iii Other Polymers Dielectrics*

There are several other polymers used as dielectrics. Polyester is an inexpensive dielectric, with a dielectric constant higher than polypropylene along with a higher operating temperature. The disadvantage of polyester as a dielectric is that it has a high dissipation factor at high temperatures and frequencies [41], in addition to a 10% decrease in the capacitance over the operating temperature range [40].

Polycarbonate is used in specialty capacitors due to its stability over a large temperature range. The dielectric constant and operating temperatures are slightly higher than the values of polypropylene, 2.8 and 125 °C respectively. The drawback to polycarbonate, besides the cost, is that its dissipation factor is slightly higher than polypropylene [40, 41].

#### *1.2.B.c Ceramic*

Ceramic capacitors have been in use since the 1940's [27]. The primary material in the dielectric layer has been barium titanate, although other ferroelectric perovskites such as  $\text{Pb}(\text{Zr,Ti})\text{O}_3$  are used in recent capacitors [27]. The ceramic dielectric is advantageous over polymer dielectrics due to the much higher dielectric constants, ranging from 250-500 for barium titanate to over 1500 for  $\text{Pb}(\text{Mg,Nb})\text{O}_3$  [43]. The drawback to the perovskites is the lower break-down strengths. While the polymers can

withstand 5000 kV/cm, as shown in Table 1-5, ceramics are approximately an order of magnitude lower in break down strength, as shown in Figure 1-28 [27, 43].

#### *1.2.B.d Mica*

Mica is used as a dielectric in situations where very robust and high performance is required such as aerospace and military applications. Mica capacitors are suitable for high temperature applications up to 300 °C and environments where the capacitors are exposed to harsh conditions such as radiation or corona discharge [44]. The drawback to mica capacitors is the expense of making them as most are custom made.

#### *1.2.C Current Research*

There is a large range of configurations being attempted to obtain a higher energy densities and breakdown strengths in dielectric materials using organic polymers and composite materials. This includes blending oxide nanoparticles to polar polymers matrixes such PVDF copolymers and terpolymers [45-51] or to epoxy matrixes [52-55]. In some cases, the oxide particles are replaced with higher aspect ratio materials such as nanowires [49, 56]. Another approach is to use metallic nanoparticles such as gold or silver embedded into a PVDF polymer matrix [57-59]. In some cases, carbon multilayer nanotubes or nanowires are added to polymer films [60-62]. Other research groups are using all-organic composites consisting of a PVDF terpolymer and polyaniline conductive particles [63-65]. In some cases, coated oxide nanoparticles were made into films without a matrix [66-71]. A final method involves extrude multilayer polymer samples [72, 73].

Two different configurations that are directly related to the research discussed in this thesis are discussed in the following sections in more detail. The first, by the Zhang group at Penn State, discusses matrix selections [74]. The second discusses nanoparticle coating by the Perry group at Georgia Tech [50, 75].

#### *1.2.C.a Matrix Selection for Nanocomposites*

As shown in the previous section, there are many ideas of how to make composite materials for use as a dielectric. One paper that deserves further attention is by the Zhang [74] research group at Pennsylvania State University, in which they discuss the properties of a matrix that will help improve energy storage. Since the discharge energy was the area above the curve in the D-E diagram as shown in Figure 1-29A and the goal was to have the high energy storage, the area above the curve should be maximized. Another consideration was that the high dielectric constant material does not necessarily mean more energy stored (Figure 1-29B, curve I) if it saturates sooner than a low dielectric constant material (curve II). In this example, the area above the curve was greater for curve II even with the lower dielectric constant. This means that pushing for the highest dielectric constant may not result in the highest energy density.

The practical application of this was taken one step further. PVDF was a commonly used material as a matrix for composite samples due to its relatively high dielectric constant and high breakdown strength. The drawback to using a ferroelectric material was that most of the energy was lost due to the high remnant polarization, as shown in Figure 1-29C. By using a ferroelectric relaxor with a small remnant polarization, the energy density of the relaxor was much greater.

### *1.2.C.b Functionalized Barium Titanate Nanoparticles*

The next set of work that heavily influenced the work done in this dissertation is by the Perry research group at Georgia Tech. They started by examining a variety of functional groups to see which would best attach to barium titanate, including phosphonic acid, carbonic acid, trialkoxysilane, and sulfonic acid [50]. Of the functional groups that they examined, only phosphonic acid remained attached to the nanoparticles during the washing stage and was present in the FTIR measurements, as shown in Figure 1-30. When a closer examination was made to compare the coated particles to the uncoated particles and the pure surfactant, there was a shift in the P-O stretch and a disappearance of the PO-H stretch band, signifying that the ligands were attached to the nanoparticles.

The barium titanate particles were then coated with a fluorinated organophosphonic acid ligand, as shown in Figure 1-31 [75]. A number of different characterizations of the coated particles were examined, and are further discussed in the paper. The coated particles were ball milled with the polymer poly(vinylidene fluoride-co-hexafluoropropylene), P(VDF-HFP), to create a uniform mixture and then thin films were made by spin-coating. Some of the films were used for scanning electron microscopy, as shown in Figure 1-32. The low particle concentration films had a very smooth and uniform appearance. As the concentration increased past 50% volume concentration of particles, the film was no longer as uniform and started to crumble when cold fractured for cross sectional analysis.

Figure 1-33 shows the dielectric spectroscopy for the composite samples with volume concentrations ranging from 0% to 80% by volume of nanoparticles. The

dielectric constant increased in value until it reached 60% volume of particle concentration (Figure 1-33A). After that, the value started dropping. The dielectric loss started at its highest value with the pure polymer sample and dropped as the particle concentration was increased, implying that most of the loss came from the polymer (Figure 1-33B). The breakdown probability of the film was analyzed using Weibull analysis. It was found that there was a large decrease in the breakdown strength of the film when the particle volume concentration was increased past 20% by volume (Figure 1-33C). The final figure in Figure 1-33 shows the calculated and measured energy densities for the composite films. For all samples, the calculated energy density was much higher than the measured energy density the films breaking down.

#### *1.2.D Proposed Research*

The goal of this project is to develop dielectrics with high energy densities using two different configurations. Since the energy density depends on both the dielectric constant and the breakdown strength, the ideal situation will be to use the high breakdown strength of the polymer combined with the dielectric constant of the oxide nanoparticles. By choosing proper coating surfactants for the nanoparticles, the aim is to do reduce the defects at the interface between the particles and the matrix thus increasing the breakdown strength. The other section of this project was to make and coat particles in situ, preparing high quality films that did not contain a polymer matrix filler.

### **1.3 Overview of Organization of Dissertation**

The research in this dissertation ties together basic research and applications of PVDF copolymers and oligomers along with the pursuit of high energy density storage

devices using insight learned from the other projects. Chapter 2 is an overview of commonly used techniques and the theoretical backgrounds. Chapter 3 is a brief discussion of some of the properties of VDF oligomers. Chapter 4 is the development of self-assembled monolayers using VDF oligomers. Chapter 5 discusses the coating of barium titanate nanoparticles with oligomers and alkanes to be used in the composite systems. Chapter 6 uses those particles to create capacitor samples and discusses measurements related to the structure of capacitors. Chapter 7 discusses the electrical measurements of the composite samples. Finally, Chapter 8 changes topics slightly to examine the effect of humidity on Langmuir-Blodgett films composed of P(VDF-TrFe).

## 1.4 References

1. Yang, Y. and F. Wudl, *Organic Electronics: From Materials to Devices*. Advanced Materials, 2009. 21(14-15): p. 1401-1403.
2. Forrest, S.R. and M.E. Thompson, *Introduction: Organic electronics and optoelectronics*. Chemical Reviews, 2007. 107(4): p. 923-925.
3. Malliaras, G. and R. Friend, *An organic electronics primer*. Physics Today, 2005. 58: p. 53.
4. Forrest, S.R., *The path to ubiquitous and low-cost organic electronic appliances on plastic*. Nature, 2004. 428(6986): p. 911-918.
5. Loo, Y.-L. and I. McCulloch, *Progress and Challenges in Commercialization of Organic Electronics*. MRS Bulletin, 2008. 33(07): p. 653-662.
6. Dodabalapur, A., *Organic and polymer transistors for electronics*. Materials Today, 2006. 9(4): p. 24-30.
7. Gundlach, D.J., *Organic electronics: Low power, high impact*. Nat Mater, 2007. 6(3): p. 173-174.
8. Lines, M.E. and A.M. Glass, *Principles and applications of ferroelectrics and related materials*. 1977: Oxford University Press.
9. Haertling, G.H., *Ferroelectric ceramics: history and technology*. Journal of the American Ceramic Society, 1999. 82(4): p. 797-818.
10. Devonshire, A., *Theory of ferroelectrics*. Advances in Physics, 1954. 3(10): p. 85-130.
11. Ducharme, S., S.P. Palto, and V.M. Fridkin, *Ferroelectric Polymer Langmuir-Blodgett Films*, in *Handbook of Thin Film Materials*, H.S. Nalwa, Editor. 2002, Academic Press: San Diego.
12. Horiuchi, S. and Y. Tokura, *Organic ferroelectrics*. Nat Mater, 2008. 7(5): p. 357-366.
13. Shrout, T.R. and J. Fielding, Jr. *Relaxor ferroelectric materials*. in *Ultrasonics Symposium, 1990. Proceedings., IEEE 1990*. 1990.
14. Chu, B., et al., *Poly(Vinylidene Fluoride-Trifluoroethylene-Chlorofluoroethylene) Terpolymer as High-energy-density Capacitor Materials*. MRS Online Proceedings Library, 2005. 889: p. null-null.

15. Zhang, Z. and T.C.M. Chung, *Study of VDF/TrFE/CTFE Terpolymers for High Pulsed Capacitor with High Energy Density and Low Energy Loss*. Macromolecules, 2007. 40(4): p. 783-785.
16. Othon, C.M., F.B. Bateman, and S. Ducharme, *Effects of electron irradiation on the ferroelectric properties of Langmuir-Blodgett copolymer films*. Journal of Applied Physics, 2005. 98(1): p. 014106-014106-6.
17. Zhang, Q., V. Bharti, and X. Zhao, *Giant electrostriction and relaxor ferroelectric behavior in electron-irradiated poly (vinylidene fluoride-trifluoroethylene) copolymer*. Science, 1998. 280(5372): p. 2101-2104.
18. Samara, G.A., *The relaxational properties of compositionally disordered ABO<sub>3</sub> perovskites*. Journal of Physics: Condensed Matter, 2003. 15(9): p. R367.
19. Cross, L.E., *Relaxor ferroelectrics*. Ferroelectrics, 1987. 76(1): p. 241-267.
20. Bao, H.-M., et al., *Phase Transitions and Ferroelectric Relaxor Behavior in P(VDF TrFE CFE) Terpolymers*. Macromolecules, 2007. 40(7): p. 2371-2379.
21. Lang, S.B., et al., *Normal ferroelectric to ferroelectric relaxor conversion in fluorinated polymers and the relaxor dynamics*, in *Frontiers of Ferroelectricity*. 2007, Springer US. p. 271-280.
22. Gogotsi, Y. and M.S. Wittingham, *Materials for Electrical Energy Storage*. Journal of materials research, 2010. 25(8): p. 1411-1412.
23. Emmenegger, C., et al., *Investigation of electrochemical double layer (ECDL) capacitor electrodes based on carbon nanotubes and activated carbon materials*. Journal of Power Sources, 2003. 124: p. 321-329.
24. Jayalakshmi, M. and K. Balasubramanian, *Simple Capacitors to Supercapacitors-An Overview*. International Journal of Electrochemical Science, 2008. 3: p. 1196-1217.
25. Winter, M. and R.J. Brodd, *What Are Batteries, Fuel Cells, and Supercapacitors?* Chemical Reviews, 2004. 104(10): p. 4245-4270.
26. Simon, P. and Y. Gogotsi, *Materials for electrochemical capacitors*. Nat Mater, 2008. 7(11): p. 845-854.
27. Sarjeant, W.J., J. Zirnheld, and F.W. MacDougall, *Capacitors*. Plasma Science, IEEE Transactions on, 1998. 26(5): p. 1368-1392.
28. Kötz, R. and M. Carlen, *Principles and applications of electrochemical capacitors*. Electrochimica Acta, 2000. 45(15-16): p. 2483-2498.

29. Zhang, L.L. and X.S. Zhao, *Carbon-based materials as supercapacitor electrodes*. Chemical Society Reviews, 2009. 38(9): p. 2520-2531.
30. Arico, A.S., et al., *Nanostructured materials for advanced energy conversion and storage devices*. Nat Mater, 2005. 4(5): p. 366-377.
31. Pandolfo, A.G. and A.F. Hollenkamp, *Carbon Properties and their role in supercapacitors*. Journal of Power Sources, 2006. 157: p. 11-27.
32. Miller, J.R. and P. Simon, *MATERIALS SCIENCE: Electrochemical Capacitors for Energy Management*. Science, 2008. 321(5889): p. 651-652.
33. Xu, C., et al., *REVIEW: Recent progress on manganese dioxide based supercapacitors*. Journal of Materials Research, 2010. 124(8): p. 1421-1432.
34. Simon, P. and A. Burke, *Nanostructured Carbons: Double-Layer Capacitance*. The Electrochemical Society Interface, 2008. 17: p. 38-43.
35. Chmiola, J., et al., *Anomalous Increase in Carbon Capacitance at Pore Sizes Less Than 1 Nanometer*. Science, 2006. 313(5794): p. 1760-1763.
36. Harden, P., *The Handyman's Guide to Capacitors*. Homebrewer.
37. Sprague, V. (2005) *Tantalum Capacitors*. 2.
38. Heilbron, J.L., *GM Bose: The Prime Mover in the Invention of the Leyden Jar?* Isis, 1966. 57(2): p. 264-267.
39. Bulletin, G.A.E.P.E., *High Energy Capacitor Overview*. 2002, General Atomics Energy: San Diego, Ca.
40. Nash, J.L., *Biaxially oriented polypropylene film in power capacitors*. Polymer Engineering & Science, 1988. 28(13): p. 862-870.
41. Picci, G. and M. Rabuffi, *Status Quo and Future Prospects for Metallized Polypropylene Energy Storage Capacitors*. IEEE TRANSACTIONS ON PLASMA SCIENCE, 2002. 30(5): p. 1939-1942.
42. MacDougall, F., et al. *Energy Density of Film Capacitors for ETC Gun Applications*. in *18th Meeting of the Electric Launcher Association, San Diego, California*. 2001.
43. Dimos, D. and C. Mueller, *Perovskite Thin Films for High-Frequency Capacitor Applications I*. Annual Review of Materials Science, 1998. 28(1): p. 397-419.

44. MacDougall, F., et al., eds. *CAPACITORS-PAST, PRESENT, AND FUTURE*. Handbook of Low and High Dielectric Constant Materials and Their Applications, Two-Volume Set. 1999. 423.
45. Thomas, P., et al., *Dielectric properties of Poly (vinylidene fluoride)/CaCu<sub>3</sub>Ti<sub>4</sub>O<sub>12</sub> composites*. composites Science and Technology, 2010. 70(3): p. 539-545.
46. Zhou, T., et al., *Improving Dielectric Properties of BaTiO<sub>3</sub>/Ferroelectric Polymer Composites by Employing Surface Hydroxylated BaTiO<sub>3</sub> Nanoparticles*. ACS Applied Materials & Interfaces, 2011. 3(7): p. 2184-2188.
47. Bhadra, D., et al., *Low loss high dielectric permittivity of polyvinylidene fluoride and KTiNiO (x= 0.05, y= 0.02) composites*. Journal of Applied Physics, 2010. 107: p. 124115.
48. Dang, Z.M., Y.H. Lin, and C.W. Nan, *Novel Ferroelectric Polymer Composites with High Dielectric Constants*. Advanced Materials, 2003. 15(19): p. 1625-1629.
49. Li, J., et al., *Nanocomposites of ferroelectric polymers with TiO<sub>2</sub> nanoparticles exhibiting significantly enhanced electrical energy density*. Advanced Materials, 2009. 21(2): p. 217-221.
50. Kim, P., et al., *Phosphonic Acid-Modified Barium Titanate Polymer Nanocomposites with High Permittivity and Dielectric Strength*. Advanced Materials, 2007. 19(7): p. 1001-1005.
51. Zak, A., et al., *Experimental and theoretical dielectric studies of PVDF/PZT nanocomposite thin films*. Ceramics International, 2011. 37(5): p. 1653-1660.
52. Rao, Y., et al., *Novel Polymer-Ceramic Nanocomposite Based on High Dielectric Constant Epoxy Formula for Embedded Capacitor Application Published online 28 November 2001*. Journal of applied polymer science, 2002. 83(5): p. 7.
53. Liang, S., S.R. Chong, and E.P. Giannelis. *Barium titanate/epoxy composite dielectric materials for integrated thin film capacitors*. in *Electronic Components & Technology Conference, 1998. 48th IEEE*. 1998: IEEE.
54. Singha, S. and M.J. Thomas, *Dielectric properties of epoxy nanocomposites*. Dielectrics and Electrical Insulation, IEEE Transactions on, 2008. 15(1): p. 12-23.
55. Popielarz, R. and C. Chiang, *Polymer composites with the dielectric constant comparable to that of barium titanate ceramics*. Materials Science and Engineering: B, 2007. 139(1): p. 48-54.
56. Tang, H., et al., *Nanocomposites with increased energy density through high aspect ratio PZT nanowires*. Nanotechnology, 2011. 22(1): p. 015702.

57. Lu, J., et al., *Synthesis and dielectric properties of novel high-K polymer composites containing in-situ formed silver nanoparticles for embedded capacitor applications*. Journal of Materials Chemistry, 2006. 16(16): p. 1543-1548.
58. Huang, X., P. Jiang, and L. Xie, *Ferroelectric polymer/silver nanocomposites with high dielectric constant and high thermal conductivity*. Applied Physics Letters, 2009. 95(24): p. 242901-242901-3.
59. Ginzburg, V.V., et al., *High-dielectric-constant self-assembled nodular structures in polymer/gold nanoparticle films*. Macromolecules, 2006. 39(11): p. 3901-3906.
60. Li, Q., et al., *Temperature dependence of the electrical properties of the carbon nanotubes/polymer composites*. Express Polymer Lett, 2009. 3: p. 769-777.
61. Yuan, J.-K., et al., *Giant dielectric permittivity nanocomposites: realizing true potential of pristine carbon nanotubes in polyvinylidene fluoride matrix through an enhanced interfacial interaction*. The Journal of Physical Chemistry C, 2011. 115(13): p. 5515-5521.
62. Zhou, T., et al., *Surface-functionalized MWNTs with emeraldine base: Preparation and improving dielectric properties of polymer nanocomposites*. ACS Applied Materials & Interfaces, 2011. 3(12): p. 4557-4560.
63. Li, J.Y., C. Huang, and Q. Zhang, *Enhanced electromechanical properties in all-polymer percolative composites*. Applied Physics Letters, 2004. 84(16): p. 3124-3126.
64. Huang, C. and Q. Zhang, *Enhanced Dielectric and Electromechanical Responses in High Dielectric Constant All-Polymer Percolative Composites*. Advanced Functional Materials, 2004. 14(5): p. 501-506.
65. Yuan, J.-K., et al., *Fabrication and dielectric properties of advanced high permittivity polyaniline/poly (vinylidene fluoride) nanohybrid films with high energy storage density*. Journal of Materials Chemistry, 2010. 20(12): p. 2441-2447.
66. Jung, H.M., et al., *Barium titanate nanoparticles with diblock copolymer shielding layers for high-energy density nanocomposites*. Chemistry of Materials, 2009. 22(2): p. 450-456.
67. Balasubramanian, B., et al., *Synthesis of Monodisperse TiO<sub>2</sub>-Paraffin Core-Shell Nanoparticles for Improved Dielectric Properties*. ACS Nano, 2010. 4(4): p. 1893-1900.

68. Balasubramanian, B., et al., *Cluster synthesis of monodisperse rutile-TiO<sub>2</sub> nanoparticles and dielectric TiO<sub>2</sub>-vinylidene fluoride oligomer nanocomposites*. Nanotechnology, 2011. 22(40): p. 405605.
69. Rao, Y., A. Takahashi, and C.P. Wong, *Di-block copolymer surfactant study to optimize filler dispersion in high dielectric constant polymer-ceramic composite*. Composites Part A: applied science and manufacturing, 2003. 34: p. 1113-1116.
70. Cai, Q.J., et al., *Solution-processable organic-capped titanium oxide nanoparticle dielectrics for organic thin-film transistors*. Applied Physics Letters, 2008. 93(11): p. 113304-113304-3.
71. Maliakal, A., et al., *Inorganic Oxide Core, Polymer Shell Nanocomposite as a High K Gate Dielectric for Flexible Electronics Applications*. Journal of the American Chemical Society, 2005. 127(42): p. 14655-14662.
72. Wolak, M.A., et al., *Dielectric response of structured multilayered polymer films fabricated by forced assembly*. Applied Physics Letters, 2008. 92(11): p. 113301-3.
73. Wolak, M.A., et al., *Electromechanical Response of Multilayered Polymer Films for High Energy Density Capacitors*. MRS Online Proceedings Library, 2011. 1312: p. null-null.
74. Chu, B., et al., *A Dielectric Polymer with High Electric Energy Density and Fast Discharge Speed*. Science, 2006. 313(5785): p. 3.
75. Kim, P., et al., *High energy density nanocomposites based on surface-modified BaTiO<sub>3</sub> and a ferroelectric polymer*. ACS Nano, 2009. 3(9): p. 2581-2592.
76. Bune, A.V. and C. Zhu, *Piezoelectric and pyroelectric properties of ferroelectric Langmuir-Blodgett polymer films*. Journal of Applied Physics, 1999. 85(11): p. 7869.
77. Poulsen, M., *Investigation of ferroelectric behavior in electroactive polymer systems*. 2007.
78. Kao, K.C., *Dielectric phenomena in solids*. 2004: Access Online via Elsevier.
79. Blinov, L.M., et al., *Two-dimensional ferroelectrics*. Physics-Uspekhi, 2000. 43(3): p. 243.
80. Bauer, F., E. Fousson, and Q.M. Zhang, *Recent advances in highly electrostrictive P(VDF-TrFE-CFE) terpolymers*. Dielectrics and Electrical Insulation, IEEE Transactions on, 2006. 13(5): p. 1149-1154.

81. Burn, I. and D.M. Smyth, *Energy storage in ceramic dielectrics*. Journal of Materials Science, 1972. 7(3): p. 339-343.

## 1.5 Tables

Table 1-1. Further comparison of normal and relaxor ferroelectric properties. [13] © 1 IEEE

Property	Normal	Relaxor
Dielectric temperature dependence $K = K(T)$	Sharp 1st or 2nd order transition about Curie temperature ( $T_c$ )	Broad-diffuse phase transition about Curie maxima ( $T_{max}$ )
Dielectric temperature and frequency dependence $K = K(T, \omega)$	Weak frequency dependence	Strong frequency dependence
Dielectric behavior in paraelectric range ( $> T_c$ )	Follow Curie-Weiss law Equation: $1/K = C/(T - T_c)$	Follow Curie-Weiss square law Equation: $1/K = 1/K_{max} + (T - T_{max})^2/2K_{max}\delta^2$
Remanent polarization, ( $P_R$ )	Strong remanent polarization, ( $P_R$ )	Weak remanent polarization
Scattering of light	Strong anisotropy (birefringent, $\Delta n$ )	Very weak anisotropy to light (pseudo-cubic)
Diffraction of x-rays	Line splitting owing to spontaneous deformation from paraelectric→ferroelectric phase	No x-ray line splitting giving a pseudo-cubic structure

$\delta$  = diffuse coefficient describing breadth of statistical distribution of Curie temperatures.

Table 1-2. Properties of several electrolytes.[34] © 2008 The Electrochemical Society

Properties of various electrolytes.			
Electrolyte	Density (gm/ cm <sup>3</sup> )	Resistivity (Ohm-cm)	Cell Voltage
KOH	1.29	1.9	1.0
Sulfuric acid	1.2	1.35	1.0
Propylene carbonate	1.2	52	2.5-3.0
acetonitrile	.78	18	2.5-3.0
Ionic liquid	1.3-1.5	125 (25°C) 28 (100°C)	4.0 3.25

Table 1-3. Trends in Capacitor Applications. [27] © 1998 IEEE

TRENDS IN CAPACITOR APPLICATIONS AND OPERATING CONDITIONS			
Power	Voltage	Run-Time <sup>1</sup>	Application
kW (average)	kV (peak)	s	
<1	<50	>1000	* Electronic Counter-Measures * LADAR * Communications * Computers * Uninterruptible Power Supplies (UPS)
1-10	<100	>10	* LADAR * RADAR * Workstation Computers * Telecommunications * Power Quality * UPS
10-1000	<500	>100	* High Power Microwaves * RADAR * Power Quality * Distributed Power Systems
>1000	>100	single-pulse to continuous	* Directed Energy Weapons * Anti-Mine * Power Stabilization/Quality * Power Factor Control * Industrial Processing

1. Run-time refers to one operational cycle-time. For some applications, such as power factor control, systems run continuously for the entire life of the system.

Table 1-4. Performance requirements of capacitors.[27] © 1998 IEEE

<b>PERFORMANCE OF STATE-OF-THE-ART AND ADVANCED CAPACITOR SYSTEMS</b>				
Capacitor System	kJ/kg Now / Future	kW/kg (average power) Now / Future	Rep- Rate Hz	Main Issues
Polymer Film	0.4 / 20	5 / 20 k	> 100 k	* New Polymer Films * Impregnants * Foils and Conductors * > 200 °C * >> 1 kJ/unit * Voltage Reversal * Pulse Duration * Repetition Rate
Ceramic	0.01 / 5	10 / 10 k	> 1000 k	* Ceramic Formulations * Electrodes * > 300 °C * 1 kJ/unit * Voltage Scaling * Fusing
Electrolytic	0.2 / 2	2 / 10 k	> 10 k	* Electrolytes * Separators * > 200 °C * 1 KJ/unit * Gassing * Hermetic Sealing * Voltage Reversal * Pulse Repetition Rate
Mica	0.005 / 0.05	5 / 50 k	> 100 MHz	* Electrodes * > 400 °C * 1 kJ/unit * Voltage Scaling/Reversal * Materials * Impregnants

Table 1-5. General characteristics of polymer dielectrics. [41] © 2002 IEEE

Plastic film	$\epsilon$	Maximum operating temperature [°C]	Voltage Breakdown [V/ $\mu$ m]	Dissipat. Factor % 1kHz	Energy density [J/cc]
Polypropylene (PP)	2.2	105	640	<0.02	1-1.2
Polyester (PET)	3.3	125	570	<0.5	1-1.5
Polycarbonate (PC)	2.8	125	528	<0.15	0.5-1
Polyvinylidene- fluoride (PVDF)	12	125	590	<1.8	2.4
Polyethylene- naphlate (PEN)	3.2	125	550	<0.15	1-1.5
Polyphenylene- sulfide (PPS)	3.0	200	550	<0.03	1-1.5

## 1.6 Figures



Figure 1-1. New demands on electronics require the use of new materials such as organics. [4] (Taken from *Forrest, S.R., Nature, 428 (911-918)* with permission)

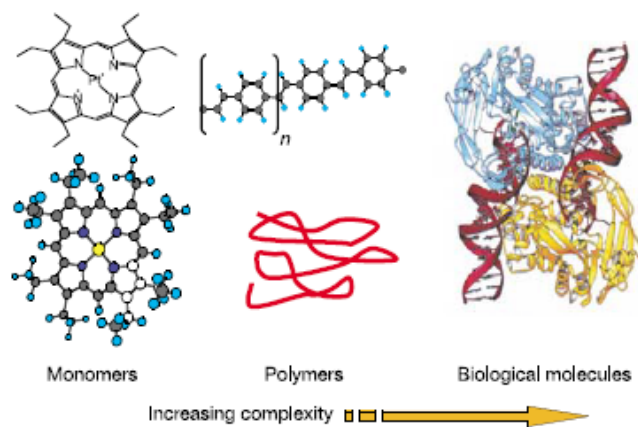


Figure 1-2. Organic molecules used in electronics range from simple monomers to complex biological inspired molecules such as proteins. [4] (Taken from *Forrest, S.R., Nature, 428 (911)* with permission)

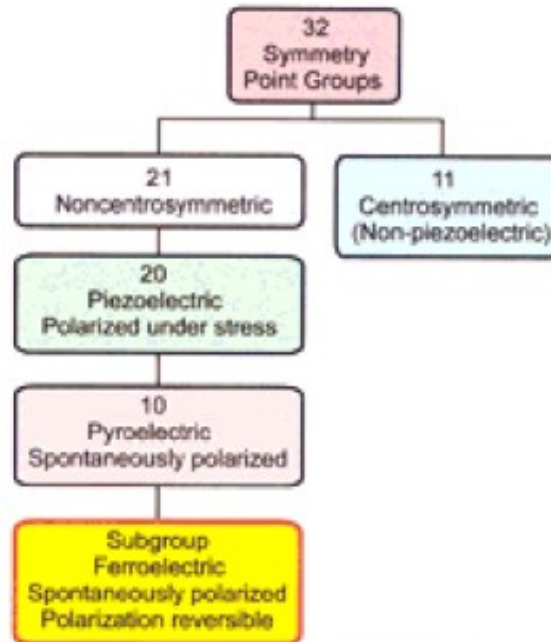


Figure 1-3. Schematic of the symmetry groups of crystals for piezoelectric, pyroelectric, and ferroelectric crystals. [9] (Taken from *Haertling, G.H., Journal of the American Ceramic Society, 1999. 82 (797)* with permission)

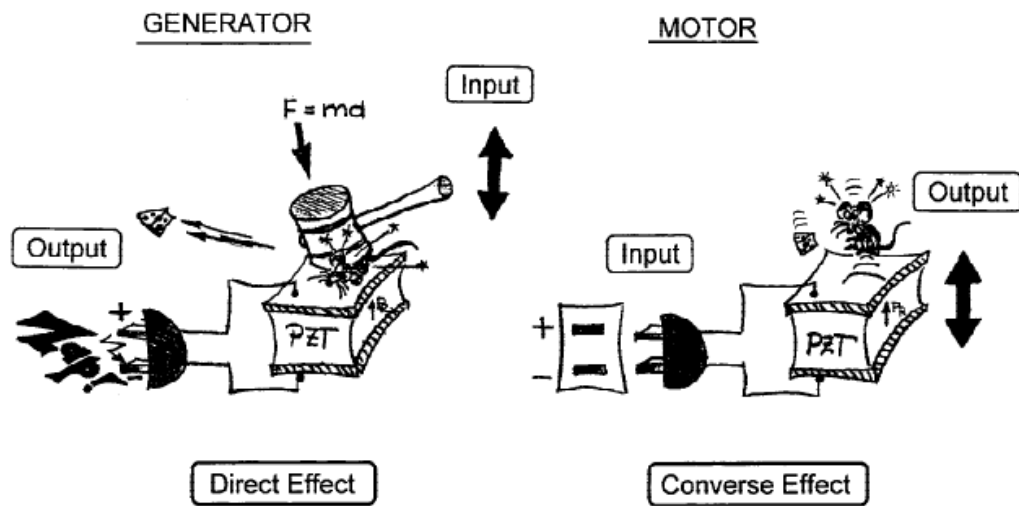


Figure 1-4. Piezoelectric effect in a crystal. The application of strain produces a charge and the application of a charge creates a strain in the crystal. [9] (Taken from *Haertling, G.H., Journal of the American Ceramic Society, 1999. 82 (797-818)* with permission)

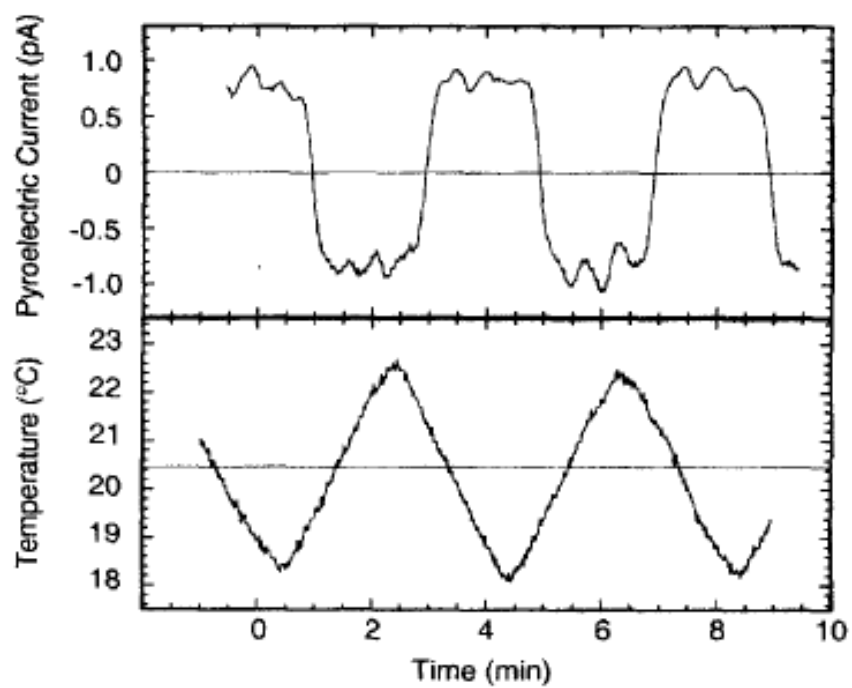


Figure 1-5. The pyroelectric effect produces a charge that is proportional to the temperature change.[76] (Taken from *Bune, A.V. and C. Zhu, Journal of Applied Physics, 1999. 85 (7869)* with permission)

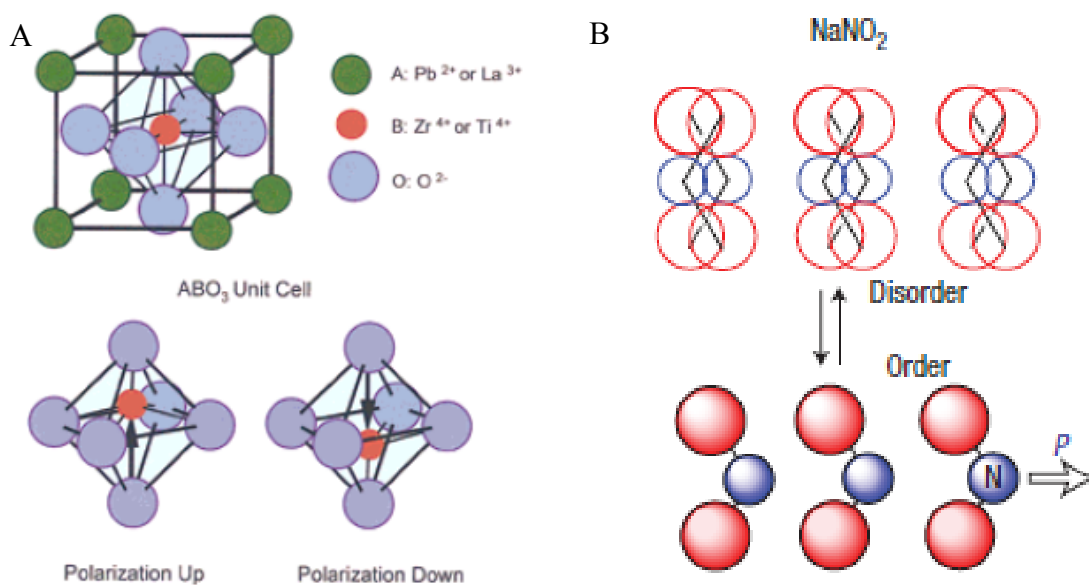


Figure 1-6. (A) Perovskite unit cell with the ABO<sub>3</sub> structure. The dipole is created by the displacement of the center atom towards an oxygen atom. [9] (Taken from Haertling, G.H., *Journal of the American Ceramic Society*, 1999. **82** (797) with permission) (B) Sodium nitrite is an example of an order-disorder ferroelectric. [12] (Taken from Horiuchi, S. and Y. Tokura, *Nat Mater*, 2008. **7** (357) with permission)

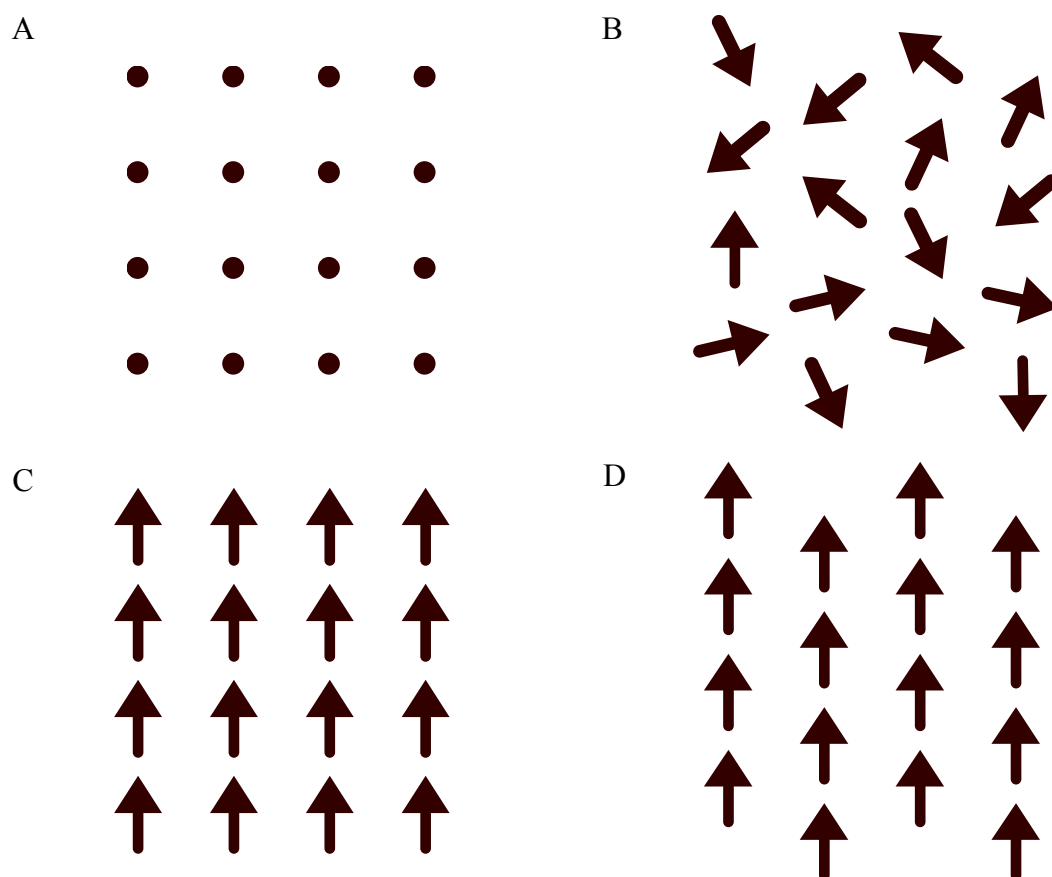


Figure 1-7. Dipoles for displacement and order-disorder ferroelectrics. The top row is paraelectric dipoles and the bottom row is ferroelectric dipoles. The left column is displacement dipoles compared to the right column of order-disorder dipoles. (A) Displacement dipoles in the paraelectric phase. (B) Order-disorder dipoles in the paraelectric phase. (C) Displacement dipoles in the ferroelectric phase. (D) Order-disorder dipoles in the ferroelectric phase.

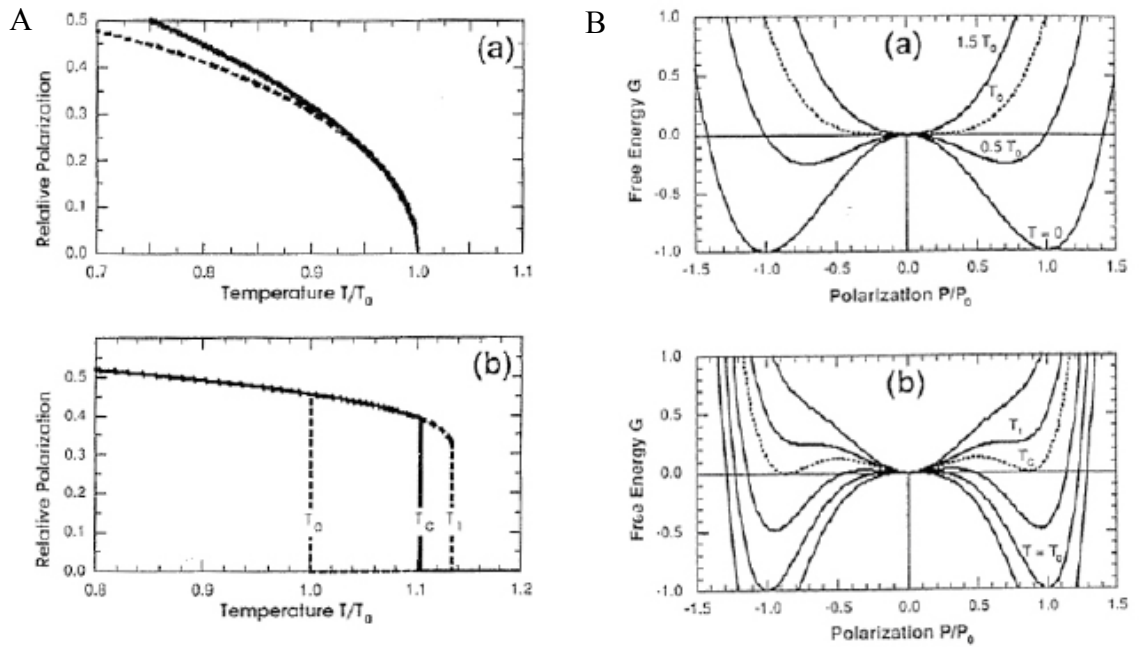


Figure 1-8. (A) Temperature dependence of the relative polarization for (a) second-order LGD ferroelectrics and (b) first order LGD ferroelectrics. (B) Plot of the free energy density given in Equation 1-1 for the (a) second order and (b) first order transition. [11] This figure was published in *Handbook of Thin Film Materials*, Vol 3, Nalwa, *Ferroelectric Polymer Langmuir-Blodgett Films*, Copyright Elsevier (2002).

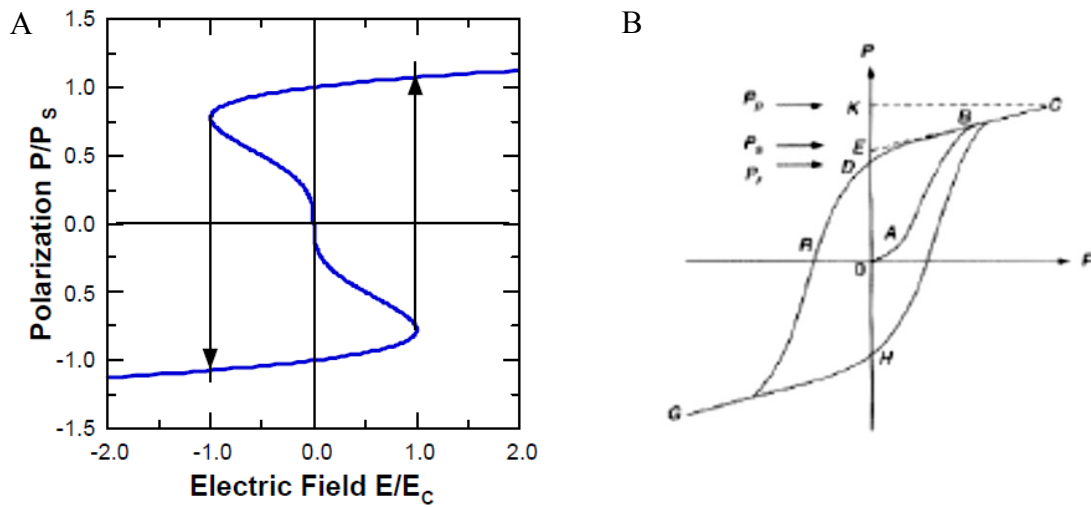


Figure 1-9. (A) Theoretical polarization curve from the derivative of the Gibbs free energy equation shown in blue and the black curves represent the metastable polarization.[77] (B) Example of a typical dielectric curve. [78] This figure was published in *Dielectric phenomena in solids*, Kao, K.C., Copyright Elsevier (2004).

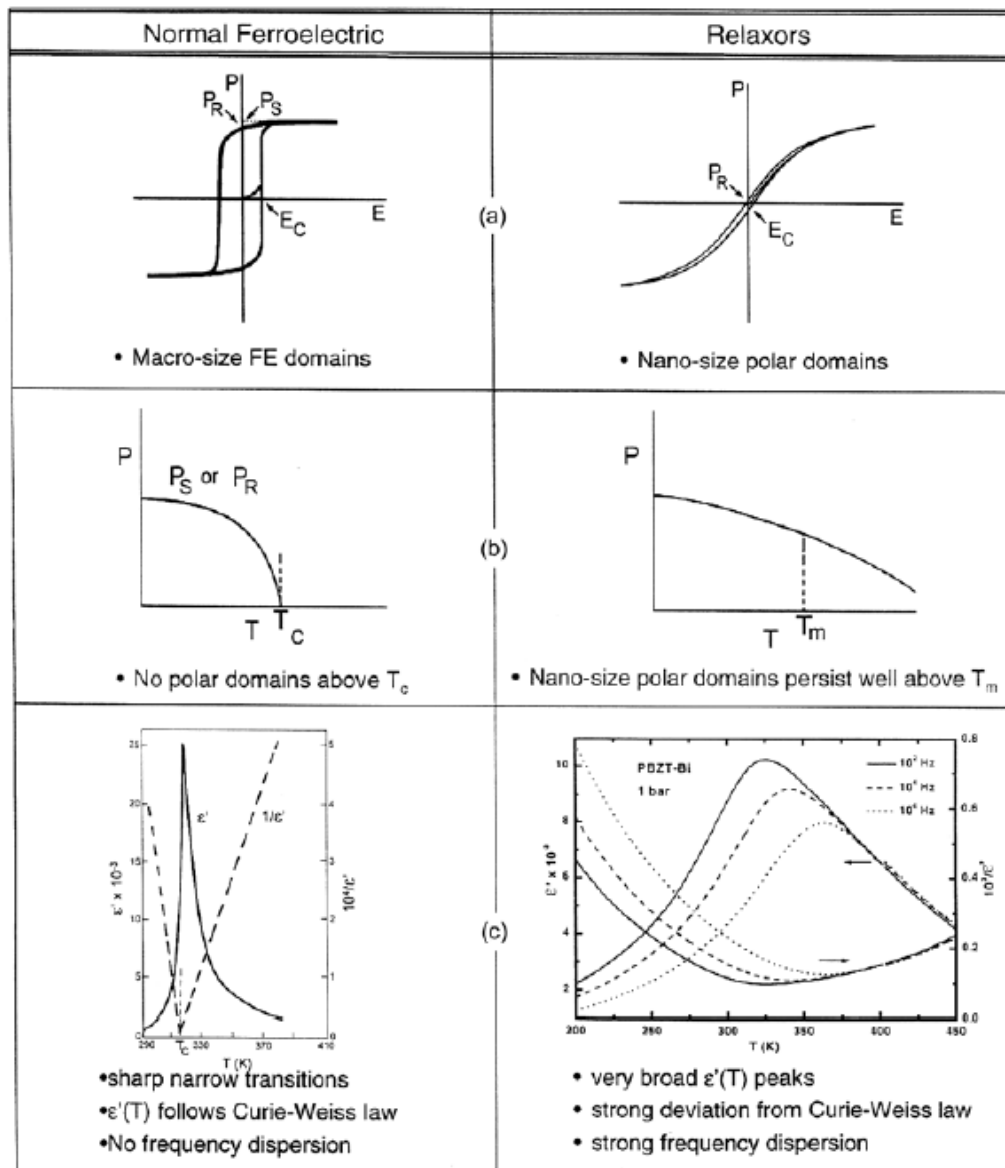


Figure 1-10. Comparison between regular ferroelectrics and relaxor ferroelectrics properties. [18] This figure was published in *Journal of Physics: Condensed Matter*, Samara, G.A., Copyright IOP (2003).

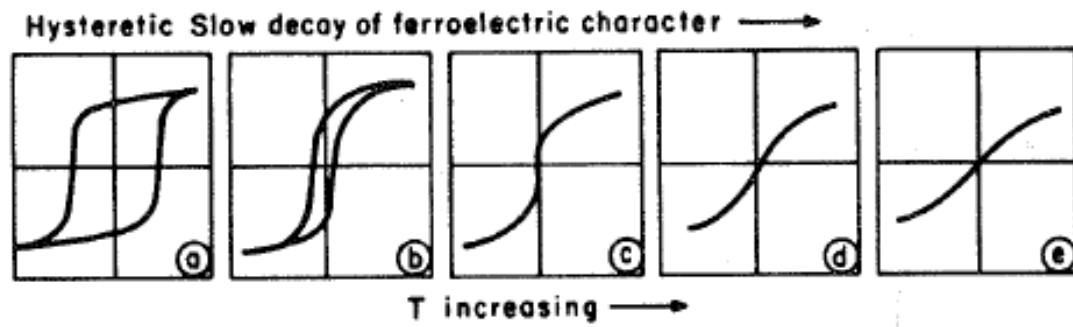


Figure 1-11. Decrease in the dielectric hysteresis as a function of temperature in PMN.  
 [19] (Taken from Cross, L.E., *Relaxor ferroelectrics*. *Ferroelectrics*, 1987. **76** (241) with permission.)

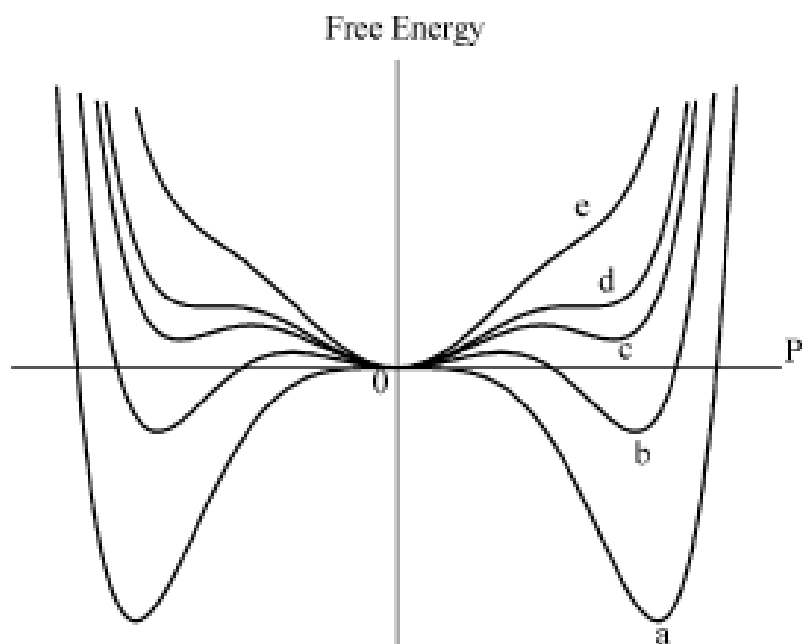


Figure 1-12. Plot of Gibbs free energy for ferroelectric as it goes from pure P(VDF-TrFe) to P(VDF-TrFe-CFE) with no sign of ferroelectricity remaining. [20] Reprinted with permission from (Bao, H.-M., et al., *Macromolecules*, 2007. 40(7): p. 2371-2379.). Copyright (2007) American Chemical Society.

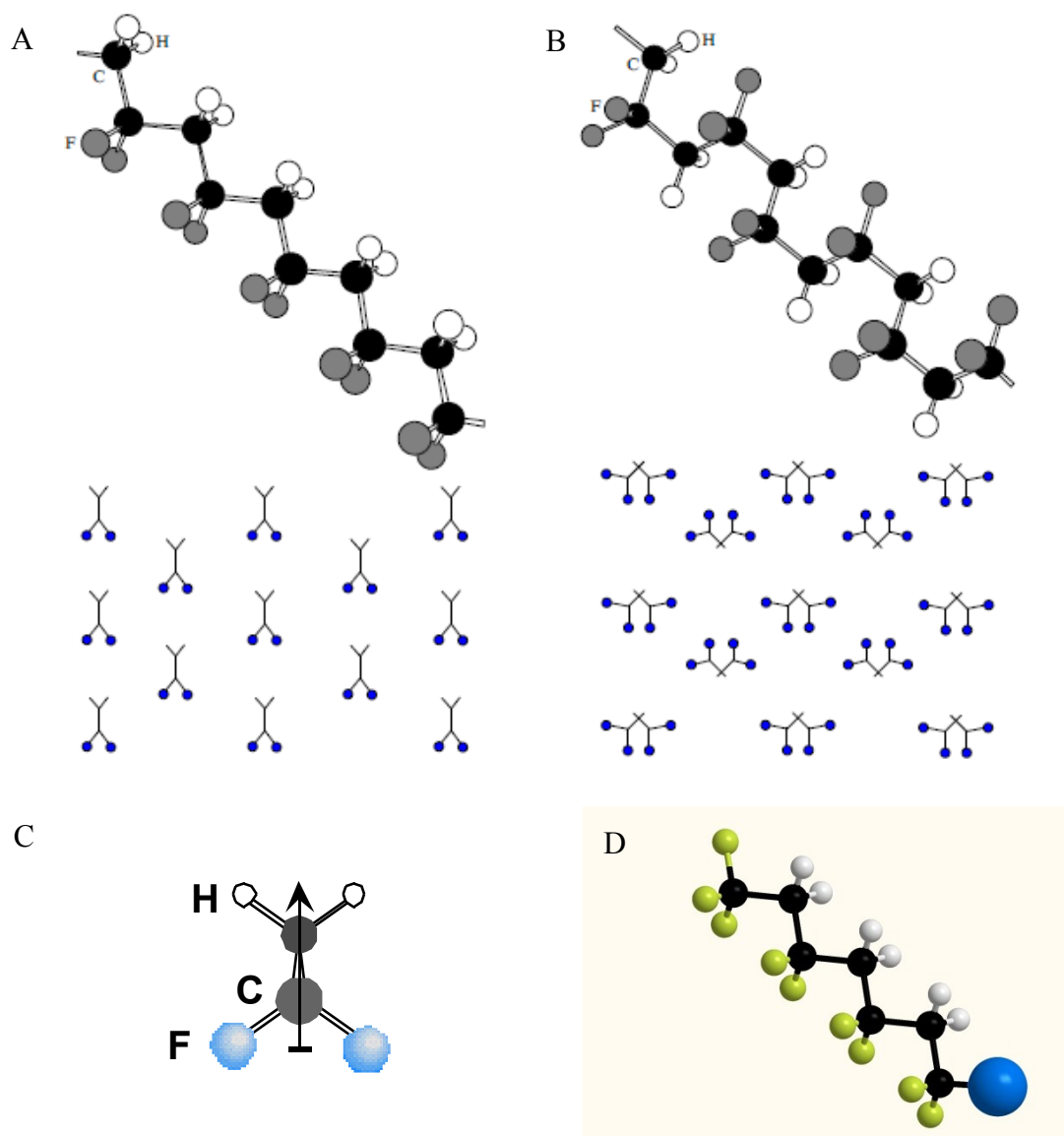


Figure 1-13. (A) PVDF in the ferroelectric all trans form. (B) PVDF in the paraelectric trans-gauche form. [79] Taken from *Blinov, L.M., et al., Physics-Uspekhi, 2000. 43 (243)* with permission. (C) The ferroelectric dipole goes from the fluorine atoms to the hydrogen atoms. (D) VDF oligomers were synthesized with an iodine or functional group on the end.

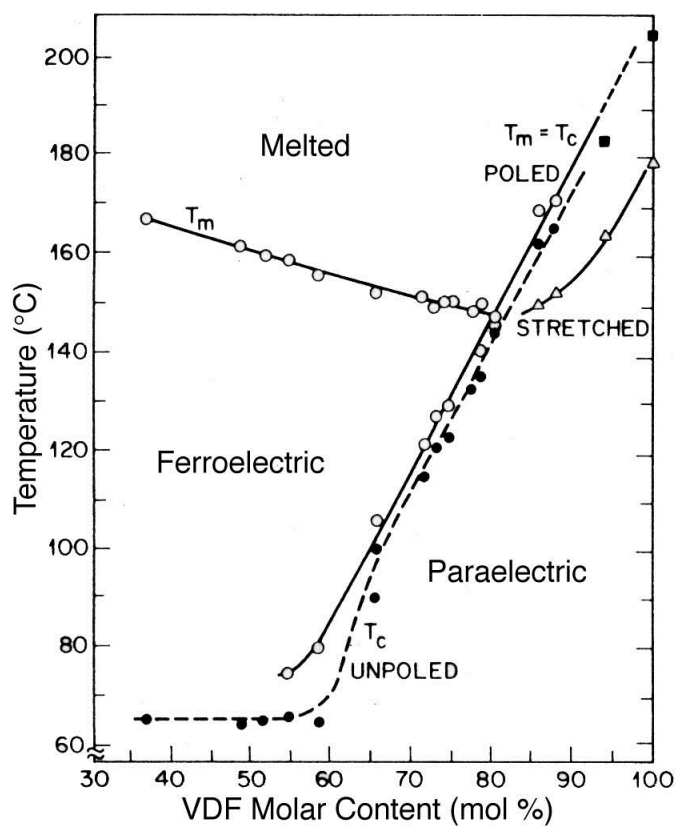


Figure 1-14. Phase diagram for P(VDF-TrFe) copolymers. [11] This figure was published in *Handbook of Thin Film Materials*, Vol 3, Nalwa, *Ferroelectric Polymer Langmuir-Blodgett Films*, Copyright Elsevier (2002).

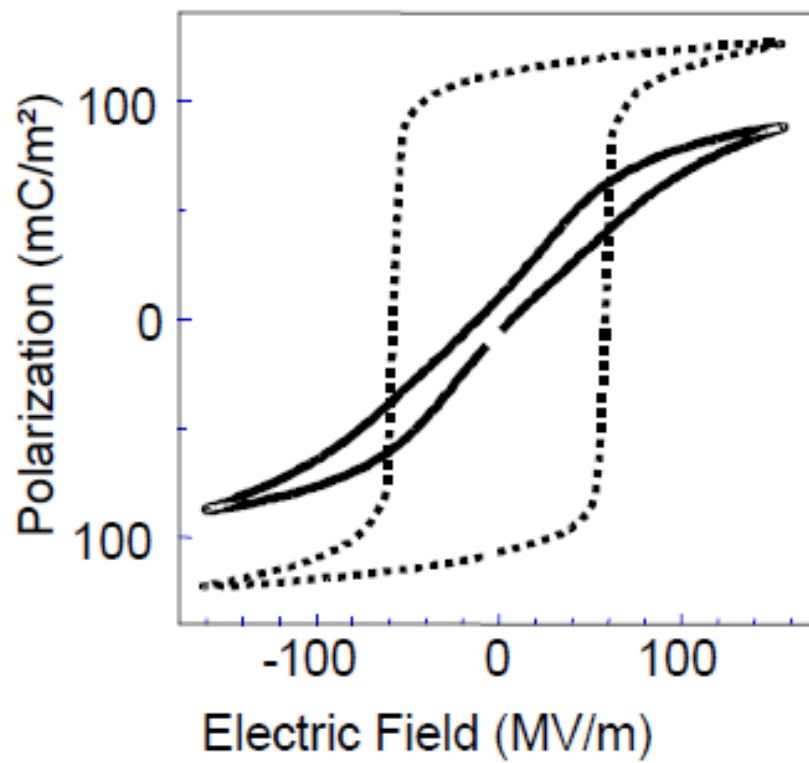


Figure 1-15. Comparison of the hysteresis loops of a regular ferroelectric and relaxor ferroelectric at room temperature. [80] This figure was published in *IEEE Transactions on Dielectrics and Electrical Insulation*, © 2006 IEEE.

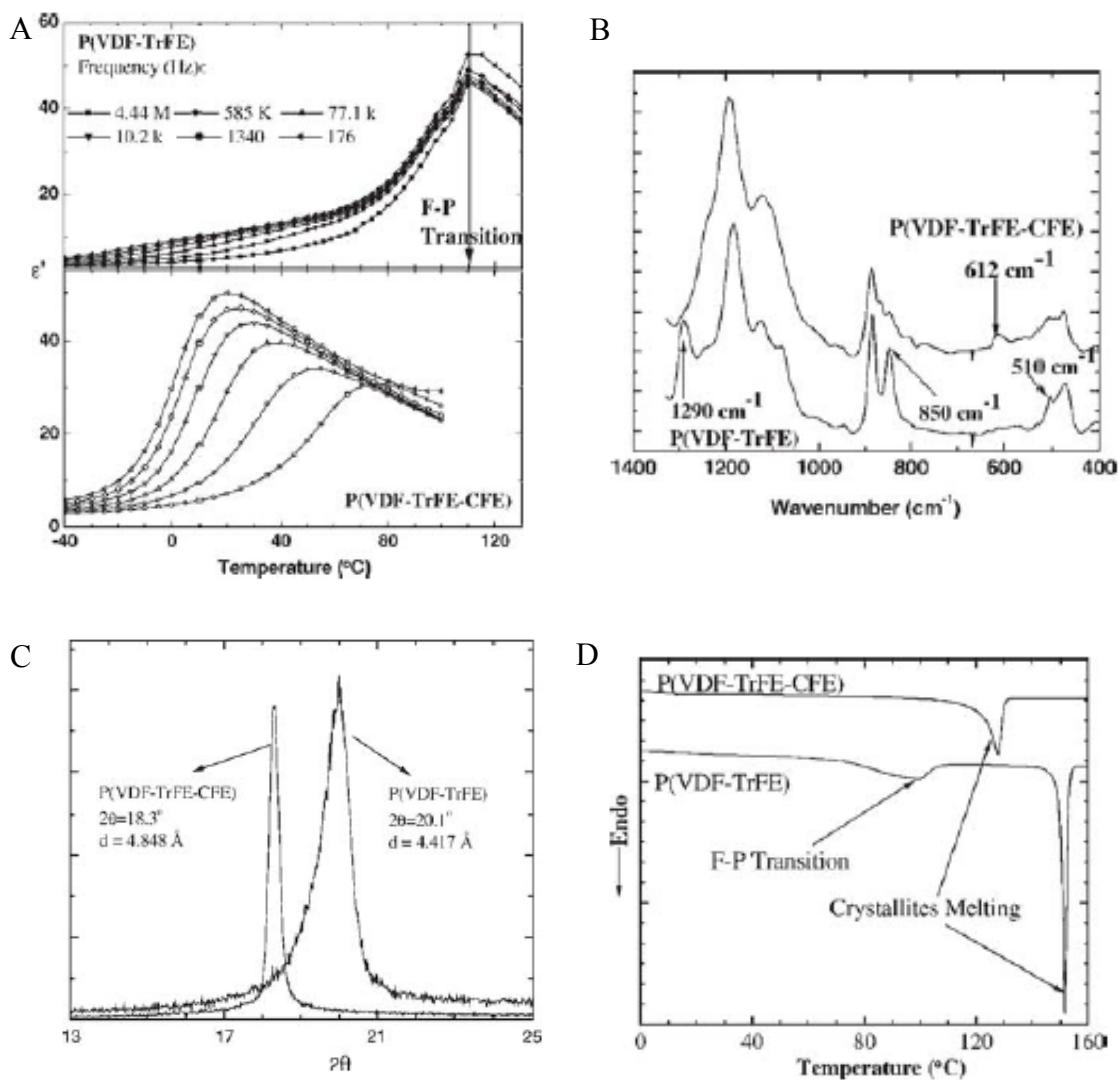


Figure 1-16. Comparison of ferroelectric P(VDF-TrFe) polymer properties to relaxor ferroelectric P(VDF-TrFe-CFE). (A) Temperature dependence of the capacitance. (B) FTIR absorbance spectrum. (C) X-ray diffraction of the (110, 200) reflection region. (D) DSC over the phase transition temperatures. [21] This figure was published in *Frontiers of Ferroelectricity*. Copyright Springer US (2007).

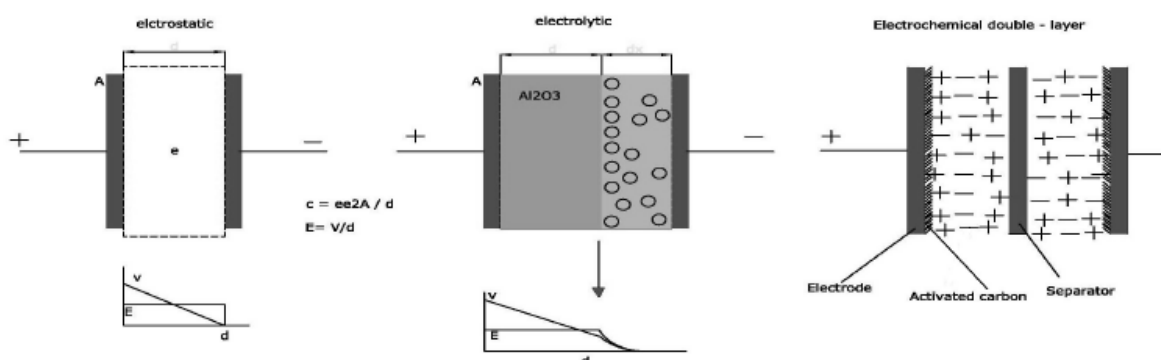


Figure 1-17. Examples of a parallel plate capacitor, an electrolytic capacitor, and a electrochemical double layer super capacitor. [24] This figure was published in *International Journal of Electrochemical Science*. Copyright ESG (2008)

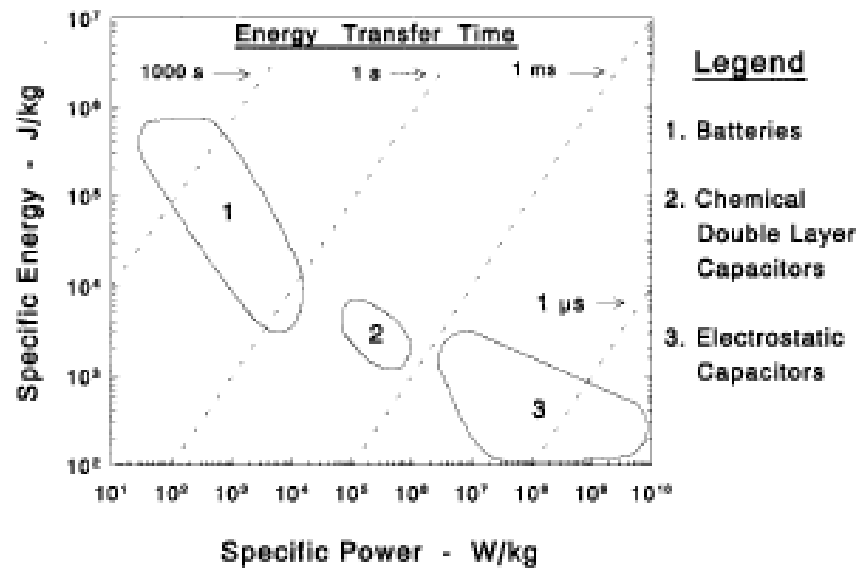


Figure 1-18. A Ragone plot showing the relationship between specific power and specific energy of various types of energy storage devices. The dashed lines represent the energy transfer times for a device. [27] Figure used with permission © 1998 IEEE.

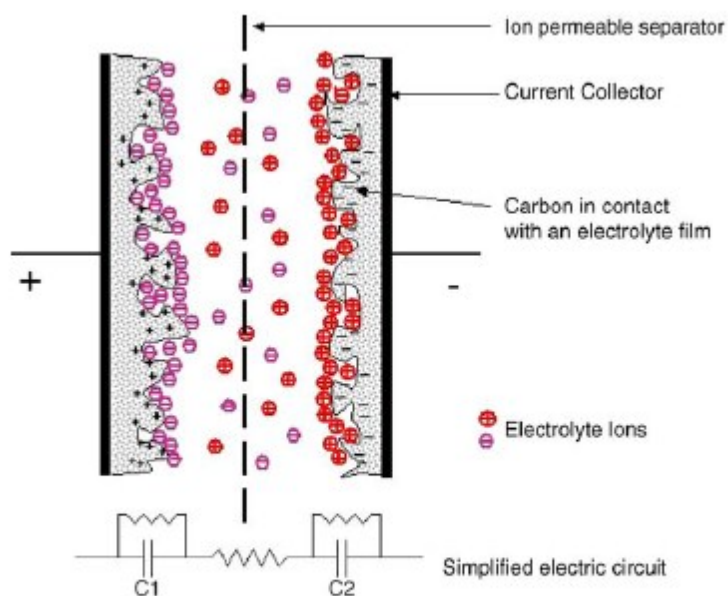


Figure 1-19. A schematic of a charged electrochemical double layer capacitor showing the current collecting plates, electrodes, electrolyte and the separator. [31] This figure was published in *Journal of Power Sources*, © 2006 Elsevier.

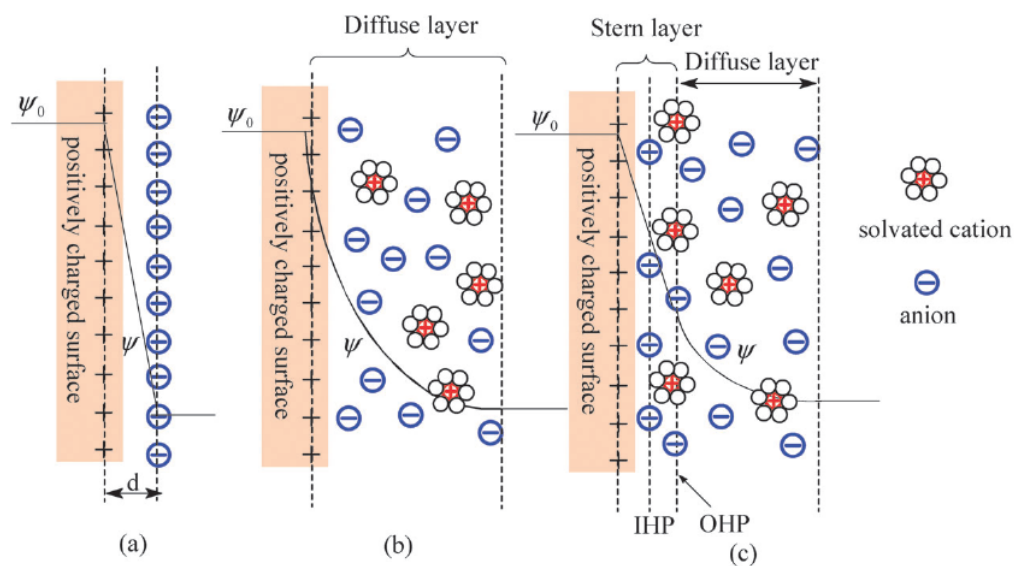


Figure 1-20. a) Helmholtz layer with the thickness  $d$ . b) Gouy-Champman model of the diffusion layer. c) Stern's model showing both the Helmholtz layer and the diffusion layer. [29] (Taken from Zhang, L.L. and X.S. Zhao, *Chemical Society Reviews*, 2009. **38** (2520-2531) with permission.)

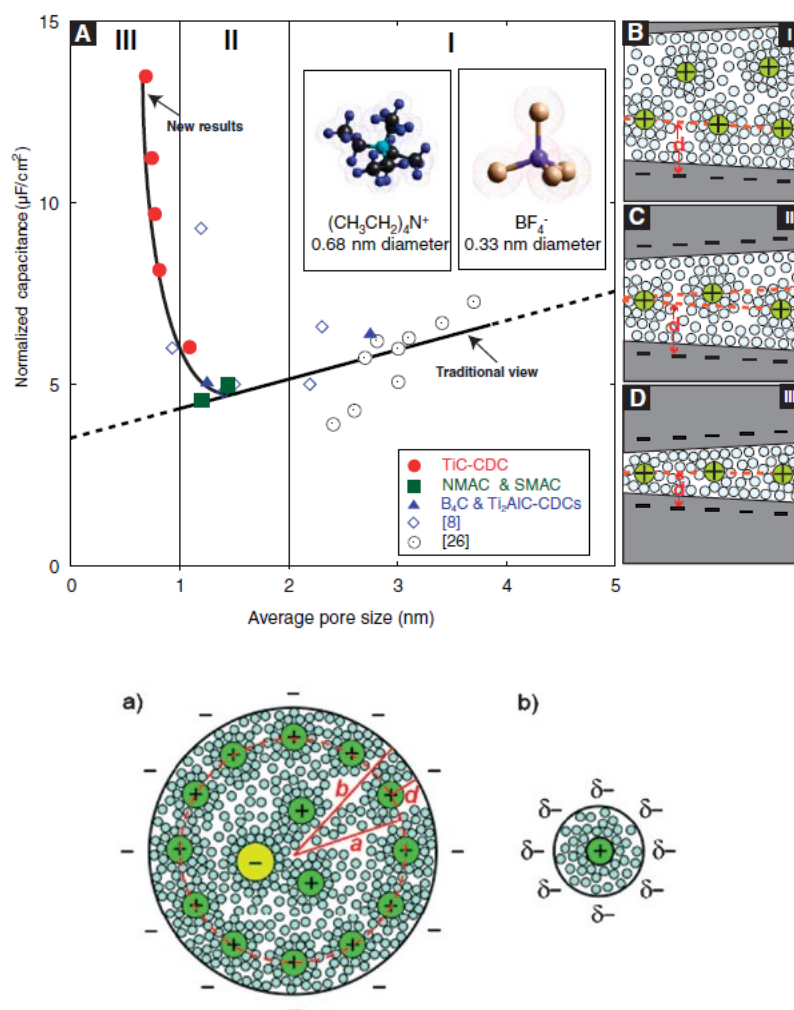


Figure 1-21. (A) The specific capacitance decrease with pore size until it reaches a critical value, where there is a sudden increase. The amount of solvent surrounding the ions decreases as the pore size decreases and the ions are located closer to the surface of the electrode. [35] Figure used with permission. © 2006 The American Association for the Advancement of Science (B) Schematic of a negatively charged a) mesopore and b) micropore in an electrolyte solution. [26] Figure used with permission. © 2008 Nature Materials.

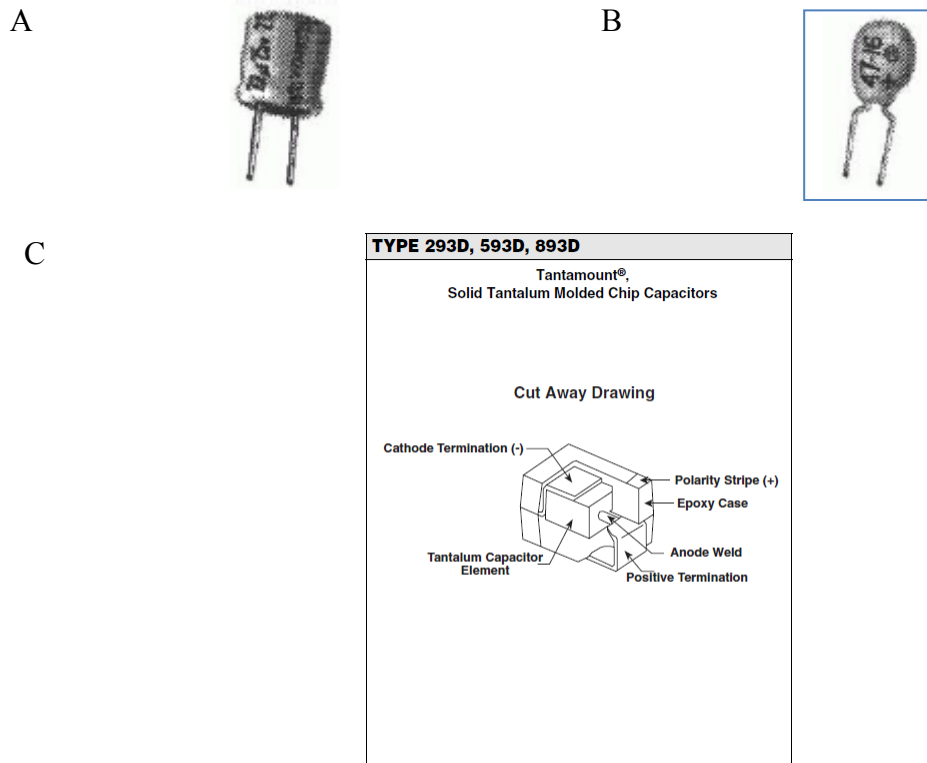


Figure 1-22. Electrolytic capacitors. (A) Aluminum electrolytic capacitor and (B) a tantalum electrolytic capacitor. (C) Cut away of a tantalum capacitor. [36, 37]

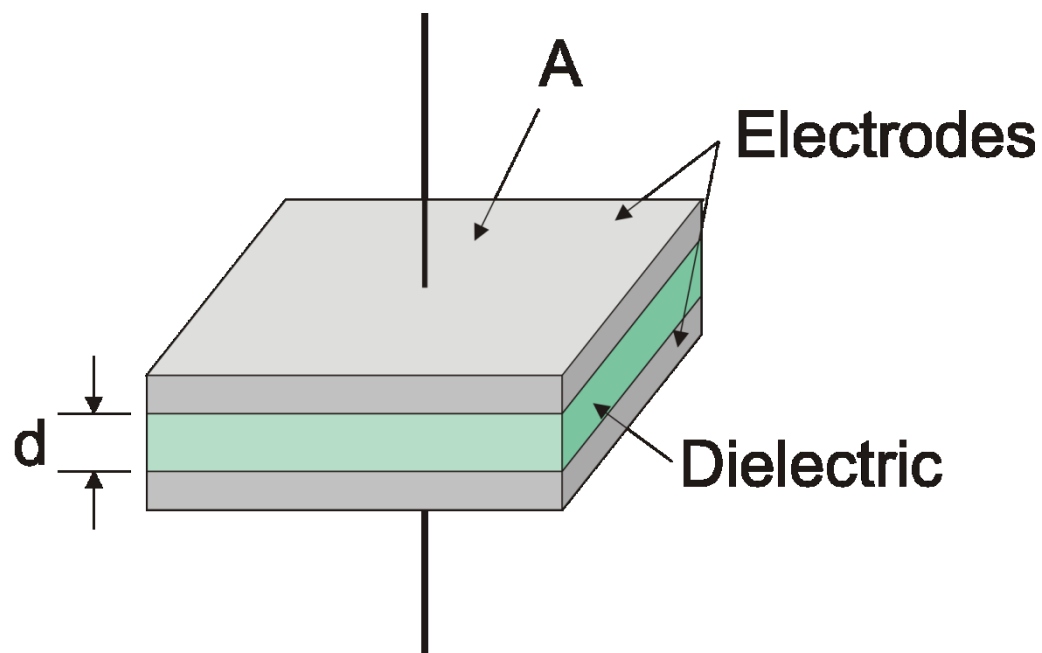


Figure 1-23. A parallel plate capacitor with the area  $A$  and thickness  $d$ .

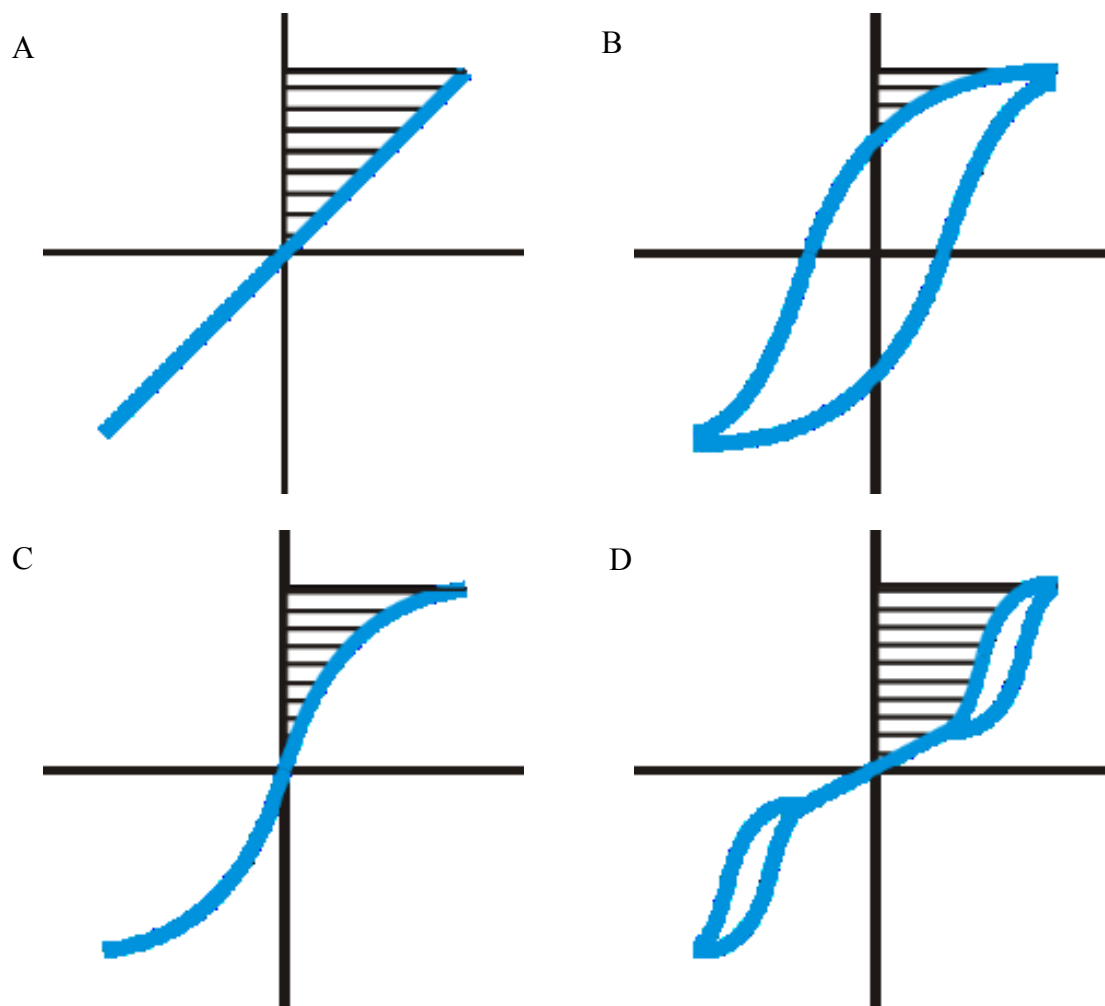


Figure 1-24. The shaded region is the energy densities for various types of polarizations.[81] (A) Linear dielectric (B) Regular ferroelectric (C) Relaxor Ferroelectric (D) Antiferroelectric

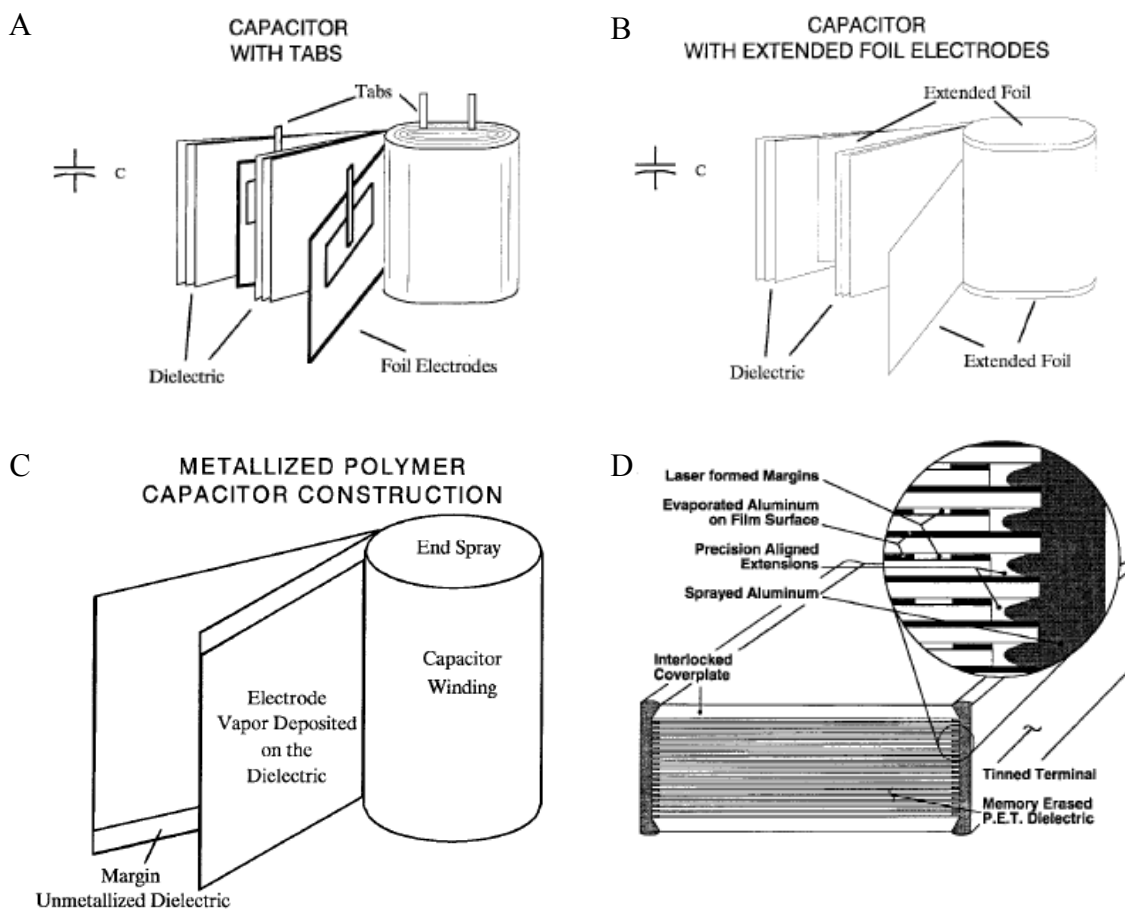
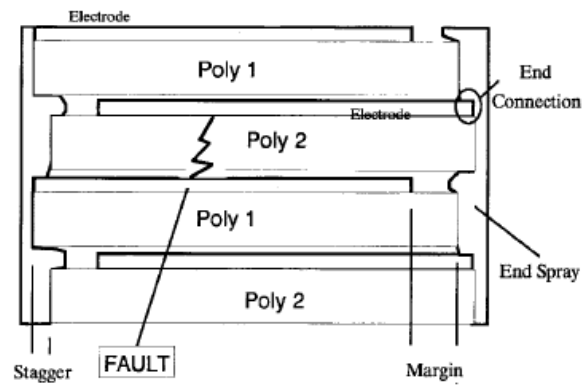


Figure 1-25. (A) and (B) Examples of commercial construction for energy discharge capacitors. [27] (C) Metallized polymer capacitor. (D) Multilayer polymer film block capacitor. [27] Figures used with permission © 1998 IEEE.

A



B

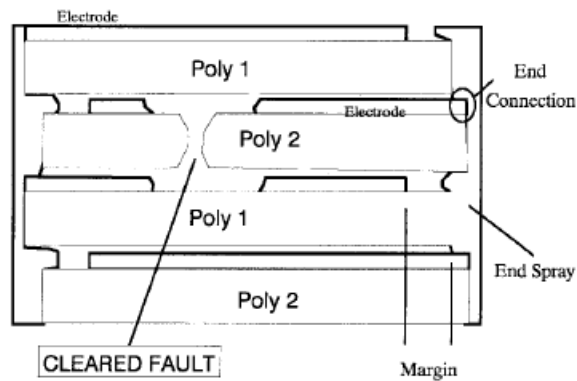


Figure 1-26. Graceful failure in a polymer film. (A) A defect forms in the film. (B) The film and electrode burn away, leaving the rest of the capacitor functioning. [27] Figures used with permission © 1998 IEEE.

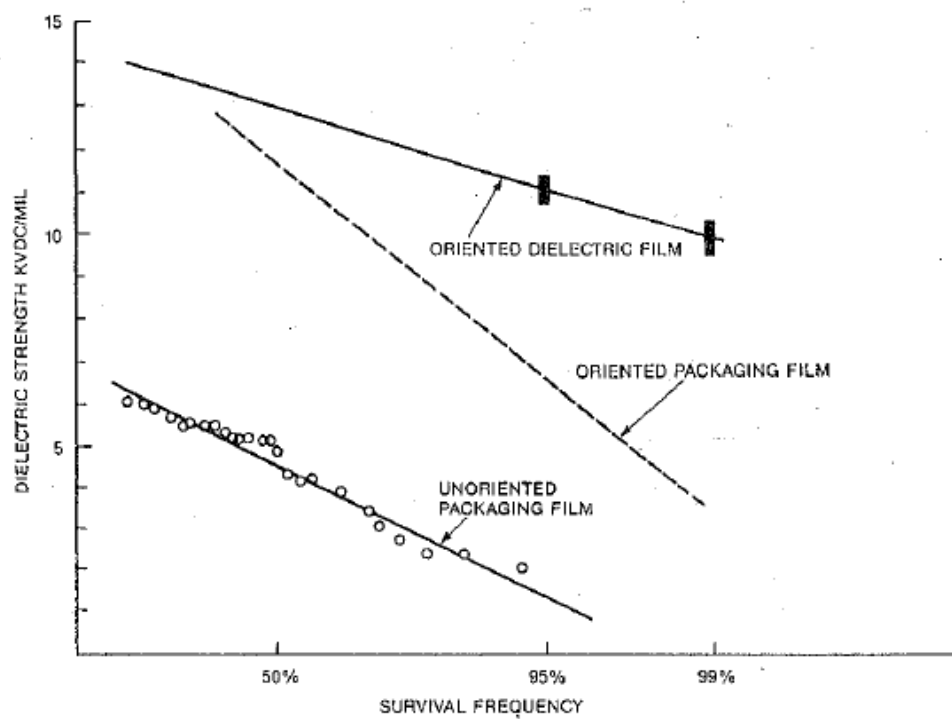


Figure 1-27. Dielectric strength of biaxially oriented, single oriented, and unoriented polypropylene films. [40] Figure used with permission. Copyright © 1988 Society of Plastics Engineers.

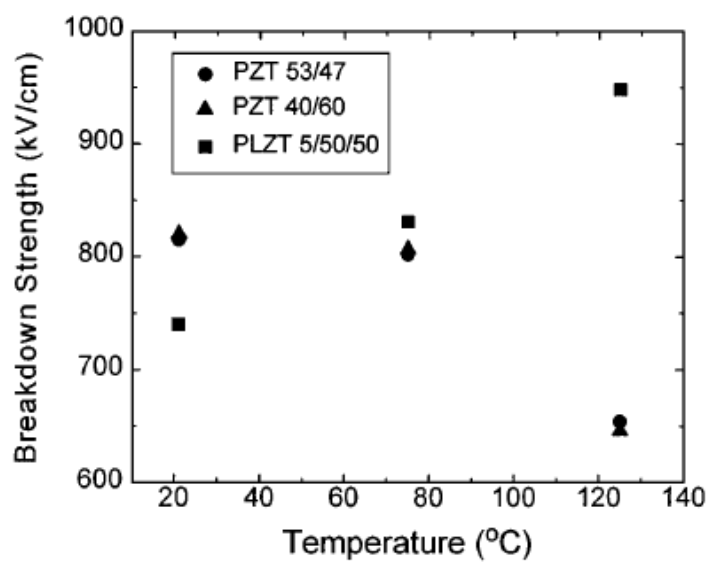


Figure 1-28. Temperature dependence of the breakdown strength for perovskites. [43]  
Figures used with permission. Copyright © 1998 ANNUAL REVIEWS, INC.

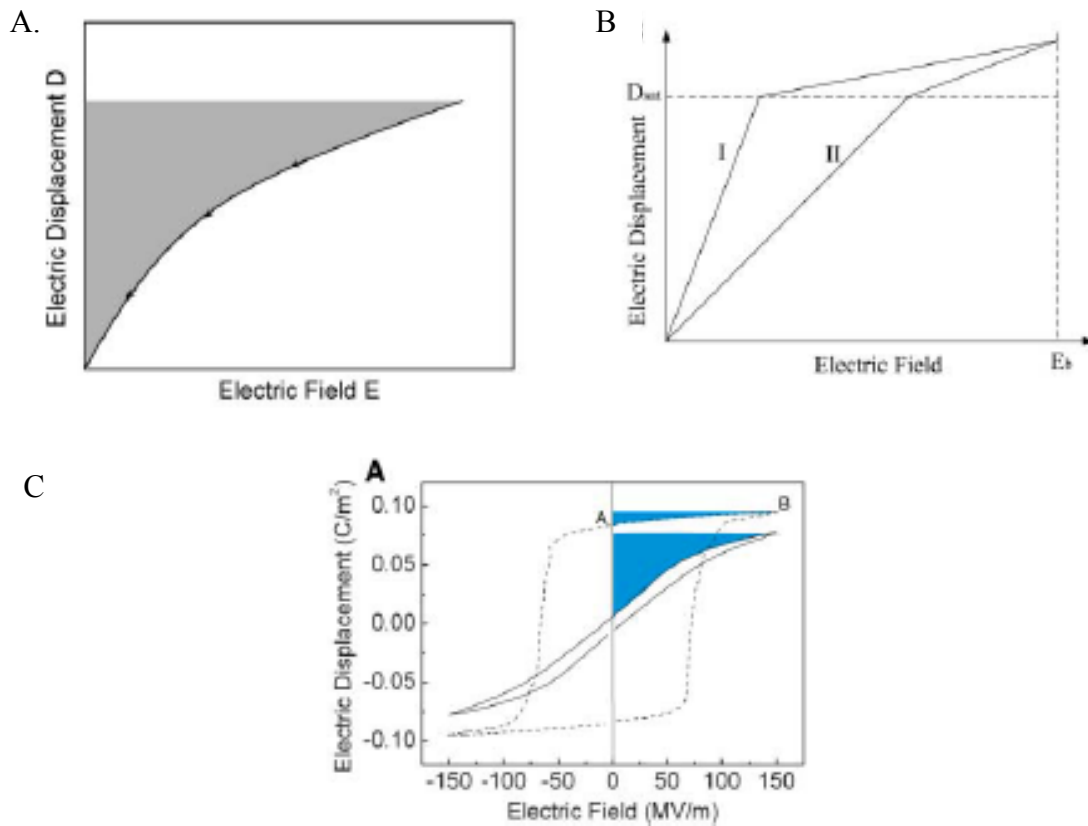


Figure 1-29. Energy density considerations for dielectric materials. (A) The energy discharged in a capacitor is the area above the curve. (B) A material that quickly reaches saturation will not store as much energy as one that reaches saturation more slowly. (C) A relaxor ferroelectric will store more energy than a regular ferroelectric due to having little or no remnant polarization. [74] Figures used with permission. Copyright © 2006 The American Association for the Advancement of Science.

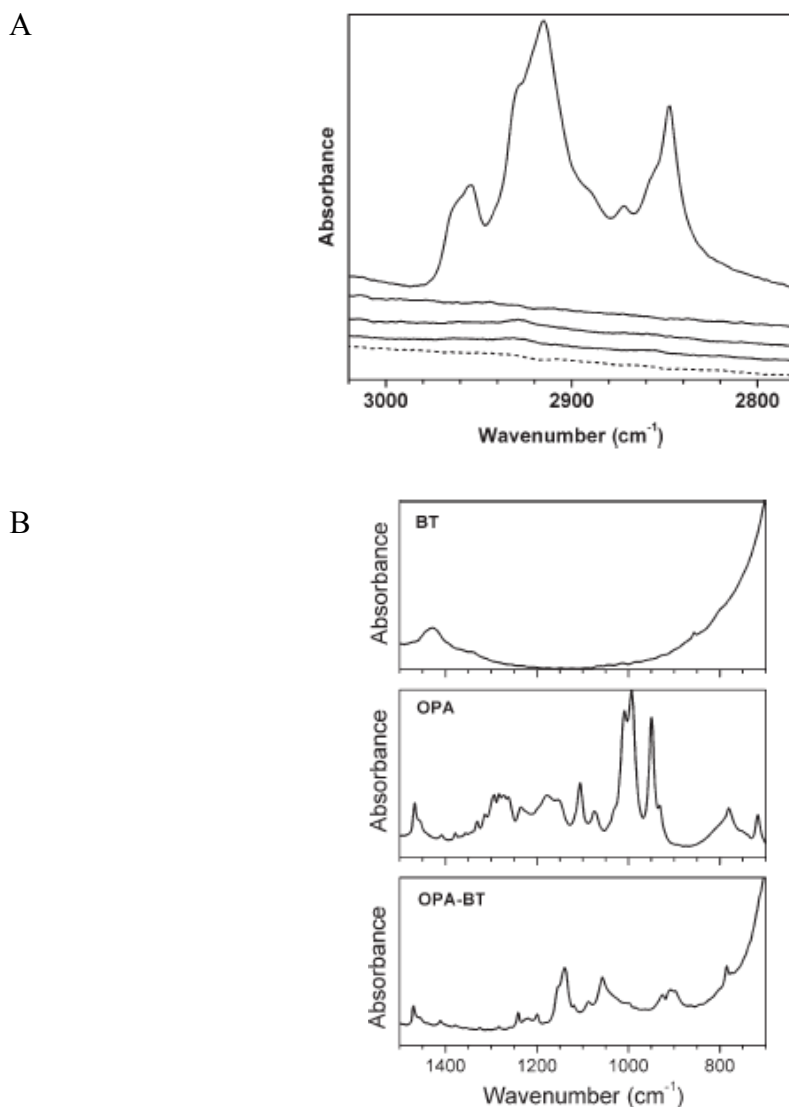


Figure 1-30. (A) FTIR spectra for the barium titanate nanoparticles coated with functionalized alkanes. The dotted line at the bottom is the uncoated particles. The solid lines are OPA-BTO, OSA-BTO, OTMOS-BTO, and OCA-BTO from the top down. Only the octaphosphonic acid attached well.[50] (B) FTIR for uncoated BTO, OPA, and OPA coated BTO in the region of the P-O stretching. [50] Figures used with permission. Copyright © 2007 WILEY-VCH Verlag GmbH & Co. KGaA, Weinheim.

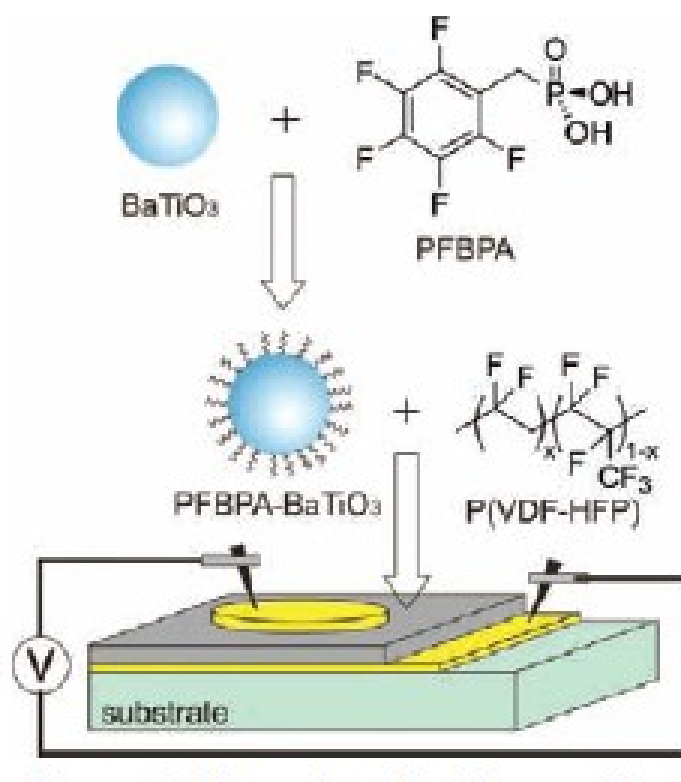


Figure 1-31. Functionalized barium titanate were mixed with P(VDF-HFP) to create thin films. [75] Reprinted with permission from (Kim, P., et al., *High energy density nanocomposites based on surface-modified BaTiO<sub>3</sub> and a ferroelectric polymer*. ACS Nano, 2009. 3(9): p. 2581-2592). Copyright (2009) American Chemical Society.

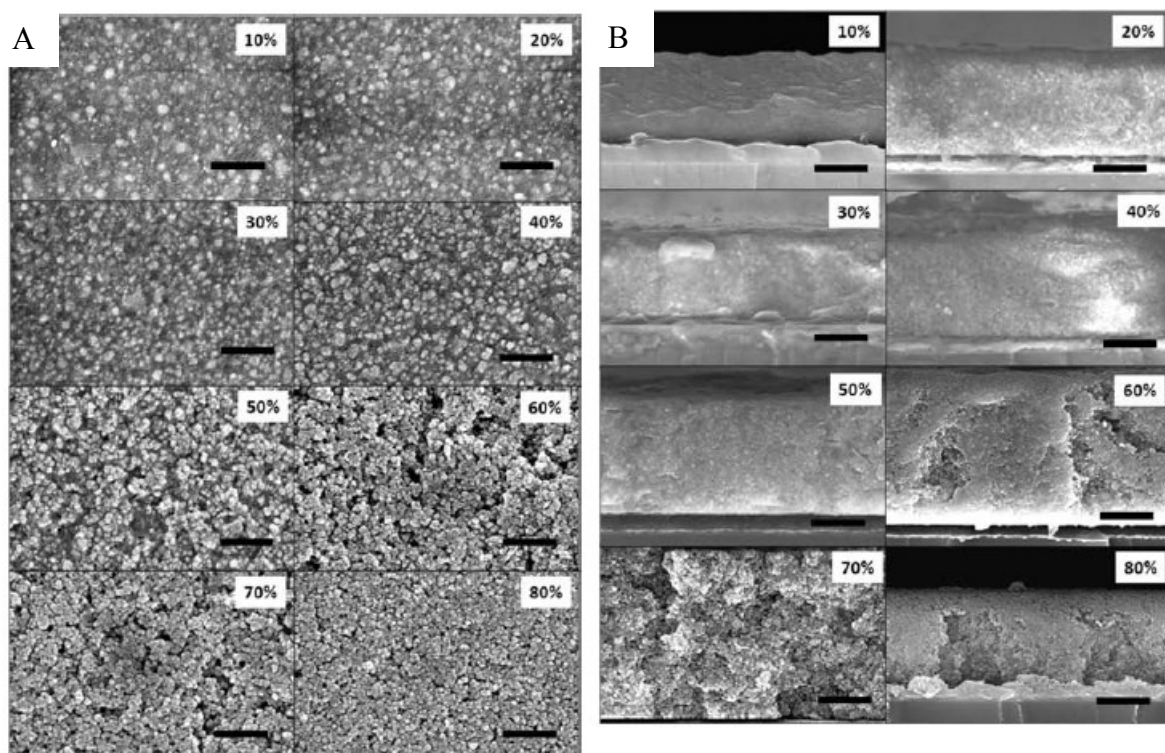


Figure 1-32. (A) Top view of composite films with different concentrations. (B) Cross sections of the composite films. As the concentration increased past 50%, the film started to crumble instead of being continuous and having a smooth appearance. The scale bars are 1  $\mu\text{m}$ . [75] Reprinted with permission from (Kim, P., et al., *High energy density nanocomposites based on surface-modified BaTiO<sub>3</sub> and a ferroelectric polymer*. ACS Nano, 2009. 3(9): p. 2581-2592). Copyright (2009) American Chemical Society.

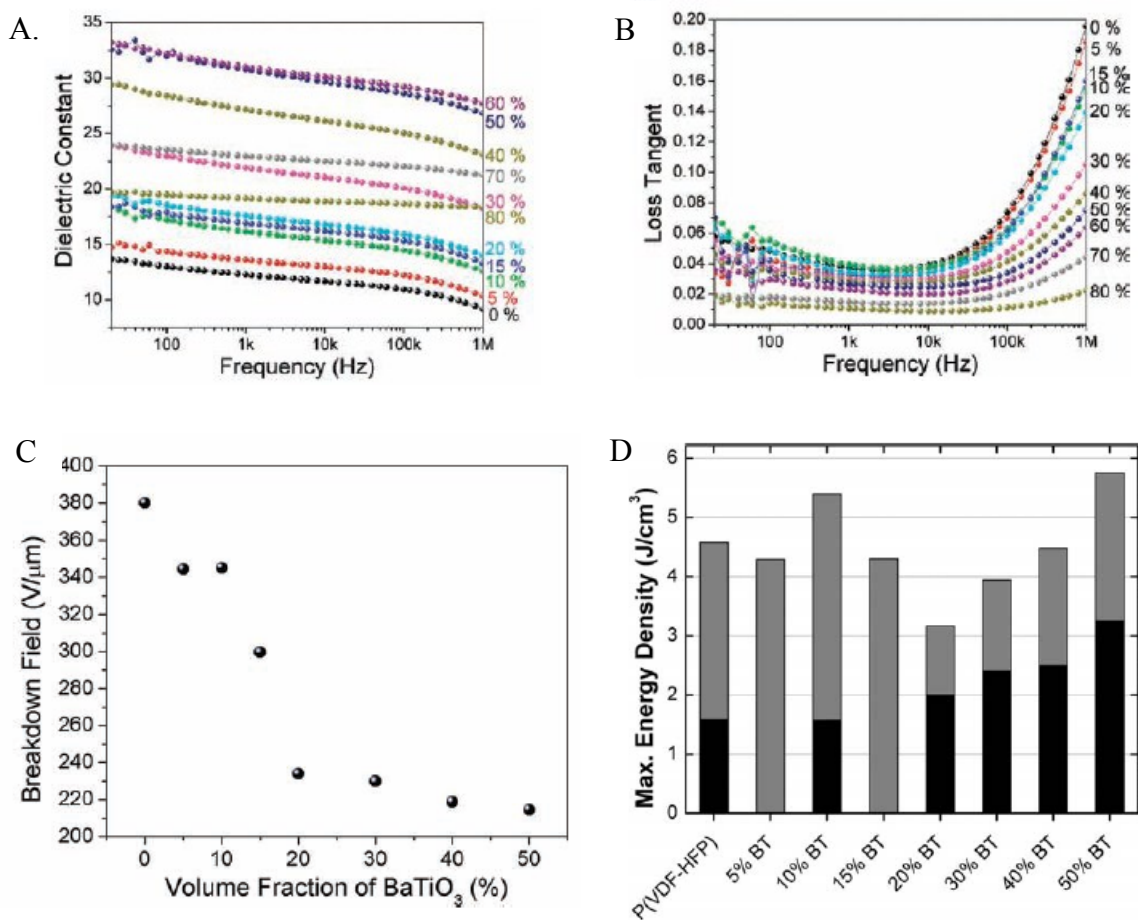


Figure 1-33. (A) Dielectric spectroscopy for different sample concentrations. (B) Dielectric loss for different sample concentrations. (C) The breakdown field as a function of various concentrations of particles. (D) The calculated energy density (grey) compared to the measured energy density (black) for each film concentration. [75] Reprinted with permission from (Kim, P., et al., *High energy density nanocomposites based on surface-modified BaTiO<sub>3</sub> and a ferroelectric polymer*. ACS Nano, 2009. 3(9): p. 2581-2592). Copyright (2009) American Chemical Society.

## CHAPTER 2

### SAMPLE PREPARATION AND MEASUREMENT METHODS

#### 2.1 Introduction

This chapter describes the basic methods for sample fabrication and measurements, along with the theory behind many of the measurements. Examples are discussed for typical results where applicable. Specific details, such as sample thickness, are discussed in individual chapters where the experimental outcomes are described. Also, modified or unique techniques used only for one set of experiments are discussed in the chapter where the technique is used.

This chapter is divided into several sections. Section 2.2 is sample preparation, with discussions of the methods and theory for making spin coated and Langmuir-Blodgett films. Also, in this section are the details for preparing substrates, electrodes, and fabricating capacitor samples. The next section (2.3) covers many typical measurements made on capacitor samples, starting with the basic quality control; annealing and examining temperature dependence of the dielectric; and examining how the frequency and applied bias affect the dielectric properties of the film. The final measurement discussed in Section 2.4 was the pyroelectric measurement.

In the next section, Section 2.5, measurements used to determine film morphology, structure, quality, and thickness are discussed. This includes x-ray diffraction (XRD), atomic force microscopy (AFM), scanning electron microscopy (SEM), tunneling electron microscopy (TEM), and ellipsometry. X-ray diffraction gives insight to the crystal structure. The surface profile and the relative stiffness of the surface

of the film are given by AFM. Images of the surface of the sample on the micron and nanometer scale were collected with SEM and TEM, and ellipsometry allows the determination of the sample thickness based on the optical properties of the thin film.

The final sets of measurements in Section 2.6 are used to characterize the materials used to create the samples discussed in this thesis. Nuclear magnetic resonance (NMR) and Infrared (IR) Spectroscopy are used to look for key signatures of bond types to verify the materials are of the proper composition and attached to the substrates. Thermal gravimetric analysis (TGA) is used to determine the weight ratios of composite samples. All of these measurement techniques and fabrication methods together allowed for insight into the properties of the organic and composite thin films studied in this thesis.

## **2.2 Sample Preparation**

There are several different methods used to make films. The two most common methods, spin coating and Langmuir-Blodgett are listed below. Other methods such as vapor deposition (Chapter 4), sputtered particles (Chapter 6) and capillary cells (Chapter 4) are discussed in their respected chapters.

### *2.2.A Spin Coating*

#### *2.2.A.a Background*

Spin coating is a deposition technique used to make thin films. This method is advantageous since it can easily be scaled up for industrial use to substrates over 30 cm in diameter.[1] It is used in applications such as electronics, photolithograph, sensors, and

protective coatings.[1, 2] Spin coating deposits a thin film by spreading drops of solution over a smooth substrate. Centripetal acceleration spreads the material to create a thin film ranging in thickness from a few nanometers of nanometers to microns thick.[1]

There are several different methods for depositing the material onto the substrate when spin coating. The first is to apply several drops of the solution onto a stationary substrate, and then increase the spin speeds. This works well if you have a more viscous solution that will stay on the substrate during the initial acceleration. The second method is to coat the entire substrate with the solution, and then start spinning it. This works with more volatile solutions and in situations where there are issues with wetting the surface. A third method is to start the spin coater rotating the substrate slowly and then to deposit the material onto the substrate. The third method was the one used for most samples in this study, as shown in Figure 2-1A [1].

There are several factors that affect the properties and quality of samples being produced. The first was the viscosity of the solution [1]. This property depends on both the solvent and the material in the solution. Typical polymer solutions for spin coating range from 0.5-20% by weight. [3-7] The thickness of the film,  $h$ , depends on several parameters including the angular velocity,  $\omega$ , and is given by the empirical equation

$$h = k_2 \eta_0^\beta \omega^\alpha, \quad \text{Equation 2-1}$$

where  $k_2$  is a constant, and  $\eta_0$  is the initial viscosity of the solution. The constant,  $\alpha$ , depends on the properties of the solvent, polymer, and the interactions between the solution and the substrate. For most polymer solutions, it has a value of approximately

-0.5.  $\beta$  is also a fit value, and it has values in the range of 0.29-0.39 for most polymer solutions.[1]

Another factor for spin coating is the volatility of the solvent.[1] If the solvent is too volatile, it evaporates too quickly and does not create uniform films. This can be controlled to some extent by controlling the temperature of the spin-coating chamber. Also, one can use a solvent with a higher boiling point, but similar chemical properties, to obtain higher evaporation rates (going from acetone to butanone to pentanone). By picking the proper solvent, one can control the evaporation conditions, film thicknesses and sample quality. A list of typical solvents and some properties such as viscosity and boiling points are shown in Table 2-1. This means one can obtain films with similar thicknesses by changing the rotational speed, the viscosity of the solution, or the evaporation rate of the solvent. The thickness of the film is related to the evaporation by expanding the  $k_2$  term in Equation 2-1, to include the average evaporation rate,  $E$ ; the latent heat of evaporation,  $\lambda$ ; and the heat capacity of the solvent,  $C_p$ .

$$h = k_3 \left( E\lambda / C_p \right)^\gamma \eta_0^\beta \omega^\alpha \quad \text{Equation 2-2}$$

The constants  $k_3$  and  $\gamma$  are empirically determined by fitting experimental data.[1]

Figure 2-1B shows a variety of parameters that can affect the quality and thickness of films produced by spin-coating. In addition to parameters like angular velocity, conditions of the air flow such the temperature, vapor pressure, and relative humidity of the surrounding environment in the spin-coating chamber will impact the evaporation rates.[1] With some solvents and materials, higher quality films were produced by raising the temperature of the chamber several degrees.

### *2.2.A.b Experimental Method*

The third deposition method was used to create films in the range of 100-150 nm thick. Typical deposition speeds were 400 revolutions per minute (RPM) for 10 drops of solution using a glass pipet, and then increasing the rotational speed to 1000 RPM for a total of 180 seconds. Most solutions were in the range of 1-5% of polymer by weight, to create films on the order of 100 nm thick. For PVDF films and related materials, butanone and DMF were the most commonly used solvents. The temperature of the sample chamber was raised to 40°C to improve the sample quality.

### *2.2.B Langmuir-Blodgett*

#### *2.2.B.a Background*

Langmuir-Blodgett films are made by spreading a solution over the surface of the water-filled trough. It was first observed by Benjamin Franklin in the 1800's that a tablespoon of oil could cover a half acre surface of a pond.[8] Lord Rayleigh[9] suggested that the maximum thickness of oil on water was one molecule thick. The transfer of films onto a rigid substrate was not reported until the 1900's when Langmuir transferred a layer of fatty acid salts onto a rigid substrate.[10] This study has led to an entire field of examining the properties of monolayers of material floating on the surface of water and the thin films created by the transfer of layers from the surface onto a rigid substrate.[11]

Most Langmuir layers are made with an amphiphilic material that contains a hydrophobic tail such as the alkane in stearic acid, which keeps the amphiphile floating on the surface of the water. With the addition of a hydrophilic acid head group, the

amphiphile tries to sit on the surface with the acid in the water and the alkane out of the water.[11] The Langmuir trough is a shallow tub with moveable arms used to compress the surface of the liquid. Once the material has been dispersed onto the surface of the trough as shown in Figure 2-2, the barriers close to compress the ampiphiles into a dense film.[12] This creates an ordered, tightly packed film, ideally one monolayer thick.[12, 13] As shown in Figure 2-3A, when an ideal amphiphile, such as stearic acid, is deposited on to the surface of the water, molecules start in the gas phase. This means that they have a random orientation relative to neighboring molecules and are far from each other [14]. As the pressure increases, the molecules are condensed into the liquid phase, signified by the change in slope in Figure 2-3A. The liquid phase has molecules that are still free to rotate [14], but are close enough to have interactions between molecules. At this point, the material is starting to stiffen, as shown by an increase in the surface pressure. With enough pressure, an ideal material will show a second change in slope on the pressure-area graph, signifying the transition into a solid phase. In this phase, the molecules have aligned themselves into a rigid packing, with little or no motion between them [14]. If the pressure continued to increase, the films would likely buckle. Not all molecules used to make Langmuir films behave like ideal amphiphiles. In the case of PVDF and its copolymers, there is not a sharp change in slope as it transitions from gas to liquid, and from liquid to solid phases, as shown in Figure 2-3B.

Langmuir films are floated on the surface of a liquid substrate. The substrate is typically ultra-pure water, although liquids such as glycerol, alcohols[11], or mercury [15] can be used. In some cases, it can be desirable to alter the PH of the water to change how the molecules behave on the surface [16]. The film is transferred to the surface of a

substrate through a variety of techniques. When a layer is transferred to a substrate, it is referred to as a Langmuir-Blodgett (LB) layer.[11, 12]. Monolayers (ML) can be transferred to a substrate with the use of vertical or horizontal dipping methods, as shown in Figure 2-4A and B.

There are three ways to transfer films by vertical dipping: x-type, y-type, and z-type as shown in Figure 2-4A.[11, 12] The dipping methods control which part of the molecule attaches to the substrate and the future layers, as shown in Figure 2-4C. In x-type dipping, the hydrophobic tails face the surface as the substrate is pushed into the water and each layer tends to have the tails pointing towards the substrate. Z-type dipping pulls the substrate out of the water, so the hydrophilic head groups attach to the surface of the substrate. Each of the following layers also has the head groups pointing towards the substrate. Y-type dipping deposits a layer of molecules as the substrate enters and leaves the water, creating bilayers of the film with head to tail arrangements. In some cases, the materials do not attach or stay attached to substrates being submerged in water, often due to a lack of a surface chemistry between the substrate and the film. Langmuir and Shaefer developed a horizontal technique [17] to deposit films where the substrate is touched flat to the surface of the water, transferring one layer of films as in Figure 2-4B. This tends to produce a film with the hydrophobic tails pointing towards the substrate, as shown in Figure 2-4D.

#### *2.2.B.b Experimental Method*

Before the trough can have a film deposited onto it, it was cleaned to remove contaminants. The trough was vacuumed dry of any remaining water. All surfaces that

would touch the water, including the trough, barriers, and the Teflon filler blocks, were wiped down with chloroform. All surfaces coming in contact with the water were then rinsed with ultra-pure water (18 MΩ). All water from the rinse cycle was vacuumed, so the surface of the trough would be free of any contaminants. Once the trough was cleaned, it was filled with ultra-pure water. The water level was filled to be slightly above the edge of the trough so the surface tension of the water holds water in the trough. A water cooling system brought the trough to the desired temperature, typically 25 °C.

A Wilhelmy plate was used to monitor the surface pressure of the trough. The plate was cut from filter paper (Whatman, grade 1) with an area of 2 cm by 1 cm. Once the paper was suspended in the trough, it must be allowed to soak up water and reach equilibrium. This step typically took 15-30 minutes, and equilibrium was required to ensure no drift due to the sensor absorbing additional later in the experiment, causing the surface pressure to not remain constant. Once the sensor had stabilized, the surface of the water was checked to be free of any contaminants. This was done by closing the barriers of the trough and monitoring the pressure. If the pressure increased, there were contaminants on the surface that were vacuumed off with a clean pipet. This was repeated as many times as necessary until there was no increase in pressure when the barriers were closed. Once the pressure was no longer increasing, the computer software set the surface pressure to zero, and all changes in pressure were measured relative to the clean surface of the water.

Once the trough was clean, the solution was dispersed onto the surface of the water with either the glass ramps or the micro-syringe technique. The amount of material

dispersed onto the trough depended on the loading efficiency and the final area desired for making samples. The loading efficiency depended on how much of the material stayed on the surface and how much went into the water. Care had to be taken to prevent overloading the trough, which would cause the film to start in the liquid phase instead of the gas phase and perhaps already be partially collapsed.

Langmuir films were created by spreading 500-2000  $\mu\text{L}$  of 0.001- 0.1% by weight solution on the surface of the trough. More details for making solutions are discussed in the following section. The solution was loaded onto the trough with one of two techniques. The first was to make ramps with clean microscope slides and allow the solution to slide from the ramps onto the surface of the water. This works well with some solvents such as DMSO and DMF. If the solvent was highly volatile, highly soluble, or much denser than water, it was difficult to obtain a high loading efficiency on the surface of the trough. The second method was to use a micro-syringe and place droplets of solution directly onto the surface of the water. This method was much more time consuming, but afforded a better loading efficiency.

Once the solution was deposited onto the surface of the trough, it was allowed time to disperse across the surface of the water and to allow the solvent to evaporate or disperse into the water. The surface pressure at this point was close to zero as long as the trough was not overloaded with solution. The bars of the trough were then slowly closed, at the rate of  $20 \text{ cm}^2/\text{min}$ . This allowed the trough to stay in quasi-equilibrium during the compression. For most PVDF samples, the pressure on the trough was increased to  $5 \text{ mN/m}$  for deposition of polymer films. Some films such as the oligomer

and nanoparticle samples were deposited at higher pressures. Once the film on the trough had reached the appropriate pressure and had stabilized, films were ready for deposition onto a substrate.

Unless stated otherwise, all films were deposited onto a substrate with the Schaefer method of horizontal deposition, as shown in Figure 2-4B. Early samples used modeling clay to attach the back of the substrate to the holder for dipping. Later substrates were held with either a vacuum pen (Pen-Vac, Virtual Industries, inc) or suction cups with the vacuum system to hold the substrate for deposition. The later methods had the advantage over the clay as it did not leave residue on the substrate and decreased the chance of contamination of the trough.

The barriers of the trough were controlled by the computer interface with a feedback loop with the Wilhelmy plate as the sensor. Each time a layer was dipped off of the surface of the trough, the barriers would close a small amount to ensure constant pressure on the surface of the film. Each sample was constructed by repeatedly touching the surface of the water with the substrate until the film was the desired thickness. Between dips, the substrate was allowed to dry to remove any remnant water and to also allow the pressure of the trough stabilized. Samples would range in thickness from one to several hundred monolayers (ML), depending on the desired thickness for the study. A monolayer for Langmuir-Blodgett films in this thesis is defined as one transfer of film from the trough, which does not necessarily correspond to one molecular layer.

### 2.2.C Solutions for Making Samples

The solutions were typically made by weight concentration. Since polymers contain a distribution of long chains lengths, it is difficult to discuss solutions in terms of moles. Solutions used for the self-assembled monolayers (SAMs) used a molar concentration, as described in Chapter 4.

The Langmuir solutions were very dilute, typically in the range of 0.001-0.1% by weight. The spin-coated solutions were more concentrated, ranging from 0.5-20% by weight, although most for the studies in this thesis were not above 5% by weight. To determine the amount of solution made at one time, it depended on 1) the concentration of the solution, 2) the size of the pellets that were unable to be easily broken down, and 3) the accurate measuring of very small quantities of polymers. Once an approximate volume had been determined, the mass of the solvent using the density of the solvent and the desire volume was calculated. With the mass of the solvent calculated, the amount of polymer used to create the desired concentration was calculated. Due to the pellet nature of some of the polymers, it was necessary to recalculate the final volume of solvent needed to obtain the desired concentration of the solution.

Once the polymer had been weighed out, it was carefully poured into a small glass vial or flask (5mL-200mL) with a stopper. The solvent was then poured into the polymer using a graduated cylinder or digital pipet (Eppendorf) to measure the solvent. The solution was then sonicated until the polymer had completely dissolved.

The choice of solvents had to be carefully matched to both the polymer and to the deposition technique. Polymers which were polar, such as PVDF and its copolymers,

required more polar solvents, such as DMF, DMSO, acetone, and butanone. Less polar solvents such as benzene, chloroform, and ethanol were used with materials like stearic acid, polyethylene, and alkanes. Additional consideration was the deposition technique. Solvents with very low or very high viscosities could be more difficult to produce high quality films by spin-coating. Since the solvent choices were limited by polymer properties, the organic solvents that were highly soluble in water required the use of more solution for Langmuir-Blodgett films due to a lower loading efficiency.

#### *2.2.D Substrate Choices and Preparation for Samples used in Electrical and Nonelectrical Measurements*

Substrates form the foundation to fabricate samples for analysis. There are several considerations when picking a substrate. When making capacitor samples, it was important to have an insulating substrate so the electrodes would not couple with the each other in electrical measurements. Microscope slides cut into one inch squares (2.54 cm) were the typical choice due to ease of use and inexpensive of material. The 1 inch size was ideal for use in the spin-coater and with the Langmuir-Blodgett trough. This size also allowed for multiple capacitor samples to be made on the same substrate.

For samples where the structure or morphology was being studied, it was desirable to use a substrate that was flatter than the glass. The typical substrate used was silicon with a native oxide. These substrates were ideal for XRD since they gave sharp peaks that did not overlap with peaks from the polymers being studied. Mica was used for some of the self-assembled monolayer (SAM) studies, because it was atomically flat and the preferential bonding between the head groups on the SAM and the mica. More

details of the SAM study are discussed in Chapter 4. For non-electrical measurements, smaller substrates could be made for SEM measurements. If the films were made with the Langmuir-Blodgett technique, the substrate area could be as small as a half centimeter in area. The substrates were cleaned after being cut into the desired size with a scoring technique, but prior to the application of film or electrodes. The method for cleaning substrates is similar for both glass and silicon as described in the following two sections.

#### *2.2.D.a Cleaning Silicon Substrates*

To clean silicon, any dust or other debris was first rinsed from the substrate with purified water or blown off with compressed gas. Then, the substrate was soaked first in acetone and then isopropanol to remove any organic contaminants. Finally, the substrate was rinsed with ultra-pure water. If the water is in a squeeze bottle, by starting at the top corner and carefully move the water down the substrate, one could have no water droplets left behind on most of the substrate. With patience, it was possible to get a single small droplet at the bottom corner and have the rest of the substrate be droplet free.

#### *2.2.D.b Cleaning Glass Substrates*

The procedure for cleaning the glass substrates used similar procedures as cleaning the silicon substrates. Depending on the brand of glass microscope slides, the level of cleaning needed changed greatly. Some slides had a thin film on them, even though they were labeled as pre-cleaned. To clean the cut slides, the slides were first sonicated in a labtone mixture (one scoop in 500 ml of warm water) for at least one hour. Then, the slides were rinsed with water to remove any soap residue. Next, the slides were soaked in acetone. If there was a thin coating on the slides, as was common with

the slides from companies such as Corning and VWR, it was necessary to soak the sliders for a longer time. Slides from Fisher Finest appeared to be coating free, and were the preferred slides to use as substrates. The time needed to remove the film and other contaminants from the slides varied from an hour to overnight. Once the slides were well cleaned and all films were removed, they looked clear and were relatively hydrophobic. When they had not been soaked long enough, water would stick to the slides. After the substrates had soaked in acetone, they were rinsed with either isopropanol or methanol. As needed, the slides were rinsed again with purified water to remove any remaining dust particles. The use of anti-capillary, reverse tweezers made it much easier to clean substrates and to prevent the solvent from re-depositing on the substrate from the tweezers.

### *2.2.E Basic Capacitor Construction*

Parallel plate capacitors were used for electrical measurements. As shown in Figure 2-5A and B, the capacitor was supported on a glass substrate. The bottom electrodes were deposited by thermal vapor deposition (Section 2.2.E.a). In most cases, it was desirable to have metal electrodes, although in some situations, transparent or smooth electrodes were required. In this situation, electrodes were made by etching pre-coated indium tin oxide (ITO) films (Section 2.2.E.b).

Once the bottom electrodes were prepared, the dielectric film was deposited by spin-coating or LB deposition. Another set of electrodes was deposited on top of the film to create parallel plate capacitors at locations where the top and bottom electrode crossed each other. The electrodes were strategically sliced to prevent coupling of neighboring

capacitors. The final step before measurements was to attach leads so the sample can be connected to instrumentation, as discussed in Section 2.2.E.c. Figure 2-5C shows a picture of an actual sample. The film was thin enough to be transparent, and the area measured was where the top and bottom electrodes crossed.

#### *2.2.E.a Thermal Evaporation of Electrodes*

Metal electrodes were deposited onto both the bare substrate and over the dielectric layer. A variety of metals can be used, limited by the melting points of the metal as shown in Table 2-2. The most commonly used metal was aluminum due to the high adhesion between the films and metal, its lower melting point. Thermal evaporation had the advantage over sputtering since the molecules are less energetic, therefore less likely to create shorts in the sample by embedding themselves past the surface. In some cases, sputtering must be used due to the high melting point of the metal, in cases such as platinum.

Metallic electrodes were deposited with a Bal-Tech thermal evaporator. The patterned electrodes were made by evaporation of metal onto the substrate through the shadow mask, as shown in Figure 2-6A. The shadow mask were milled out of thin metal into various patterns, as shown in Figure 2-6B. The electrode width varied from 1 mm to several centimeters. Typical capacitor electrodes were either 1 mm or 4 mm wide. The substrate and mask are mounted into the vacuum chamber above the metal source, as shown in Figure 2-6A. The chamber was pumped down to at least  $5 \times 10^{-5}$  mbar. Once the desired base pressure was obtained, the electrodes were deposited as follows. The source metal to be evaporated was mounted in the evaporator using one of two

techniques, as described in Figure 2-6C and D. In part C, a piece of straight tungsten wire is bent into a “v” or “u” shape. Gentler curves tended to create less stress in the metal wire when heated and allowed the metal source to be used for more deposition cycles without breaking. Once the wire was bent, it was heated until red hot to remove any surface contaminants. Then, the wire was removed from the evaporator, and approximately a third to half meter of fine gauge wire was wound around the bent part of the tungsten. The second method was to use the pre-formed metal baskets and place a small piece of metal or coiled wire into the basket, as shown in Figure 2-6D. With either method of mounting the metal source, the tungsten was then clamped onto the electrode posts below the sample.

Once the desired vacuum pressure was reached, the current was slowly increased with the shutter closed. When the tungsten was glowing brightly and the metal had melted completely, the shutter was opened and the metal was allowed to deposit onto the substrate. For the metal basket, a typical deposition current for aluminum was approximately 14 amps, and with the bent wire, the necessary current started at 9 amps. The current level varied slightly depending on the age of the basket and the amount of metal being melted. Also, if a metal with a higher melting point, such as gold, was used, higher currents were needed. Once the metal electrode was the desired thickness, as measured by either the quartz thickness monitor or by monitoring the transparency of the electrode, the substrate was removed from the evaporator. It was now ready for films to be deposited on the bottom electrode or to have leads attached in the case of top electrode. It is also worth mentioning that metals such as aluminum and silver will form a native oxide upon exposure to air after being removed from vacuum.[18] The oxide

layer provided a thin insulating layer [19] for capacitor samples and, in the case of SAMs with a phosphonic acid functional group, the proper surface for functionalization [20-22].

#### *2.2.E.b Indium Tin Oxide Etched Electrodes*

For some samples, it was desirable to etch indium tin oxide (ITO) instead of depositing metal electrodes. This could be for optical studies where transparent films and electrodes were needed. Other times, it was desirable to have smoother electrodes than could be obtained by vapor deposition or to have very thin electrodes, as in the case of capillary cells (Chapter 3).

The substrates used for ITO electrodes start as large sheets of glass with a commercially coated ITO film on one side. The glass was cut to the desired size. Then the electrode patterns were masked using Scotch tape. It was found that the Scotch brand had better adhesion and made sharper edges than the generic brands of tape when used as electrode masks. The tape was carefully applied to the ITO surface, and all of the air bubbles were pushed out from under the tape, as shown in Figure 2-7A. Once the tape was smooth, the electrode patterns were cut in the tape using an x-acto craft knife. While any straight edge would work, a shadow mask was often used as a template to keep the cuts evenly spaced and parallel with each other. Once the pattern was cut into the tape, the tape was removed from all of areas of the substrate where it was desirable to remove the ITO as shown in Figure 2-7B. The ITO substrate was then submerged into the etchant, which consisted of 50% ultra-pure water, 37% nitric acid, and 13% hydrochloric acid. The substrates were allowed to soak, as shown in Figure 2-7C, in the etchant for approximately 20 minutes (enough time to remove all of the exposed ITO, but not to start

soaking the tape off), and were then removed from the solution using plastic acid proof tweezers. The substrate was then rinsed with deionized water to remove any remaining etchant. At that point, the tape was removed from the substrate, and the substrate was washed with acetone and an alcohol until all remaining tape residue was removed, as shown in Figure 2-7D and E. If needed, the procedure for cleaning glass slides was used if the tape adhesive was sticking to the substrate. Once the substrate was clean and dry, it was ready for the application of films. The ITO coating could only be used for the bottom electrodes since it requires annealing temperatures of 180 °C or higher [23] to create clear electrodes, and this temperature would damage the polymer films.

#### *2.2.E.c Attaching leads*

Once the parallel plate capacitor had been fabricated, it was necessary to attach leads to the sample for electrical measurements. The leads were made of fine copper wire, either magnetic wire or unbraided copper solder wick. The wire was cut to two to five centimeters in length and attached to the electrode. For most samples, the wires were attached to the electrodes with a silver colloidal paint (Electron Microscopy Science).

In some cases, where the sample was being exposed to more extreme conditions, such as repeated freezing or high humidity, it was necessary to attach leads with indium metal to prevent the delamination of the leads from the electrodes, as shown in Figure 2-8. Indium has a melting point of 157°C [24]. To attach leads to the aluminum electrodes, the leads were first tinned with aluminum solder to increase the adhesion between the indium and copper. Then the soldering iron tip was carefully cleaned of lead

solder before turning down the temperature, to prevent scratching of the aluminum electrodes. Two small pieces of indium were cut from the sheet or wire. Slicing the wire was much more efficient than trying to use the wire as typical solder, since it consumed less material. The first small piece of indium was used to create a puddle on the aluminum electrode, and spanned from one side to the other side of the electrode. The indium attached better to the edges of the electrode and glass substrate than it did to the center of the aluminum pad. Then the second piece of metal was used to attach the lead to the indium that was already on the glass. As long as the time duration of the soldering iron in contact with the electrode was short, there was no evidence of the heat damaging the samples.

## **2.3 Dielectric Measurements**

### *2.3.A Quality Control*

After the top electrode was deposited on a sample, it was necessary to check the quality of the capacitors to verify there were no short circuits. This was done by measuring the DC resistance of the sample with the Keithley 2400 source meter. It was important to use the source meter and not one of ordinary multimeters, since the current could be limited with the source meter and this reduced the chance of shorting out a potentially good sample. A good sample had a DC resistance of a mega-ohm or higher. Ideally, the resistance was 10's of megaohms, although samples with just a few megaohms typically worked fine. If the resistance was less than a mega-ohm, the sample was often leaky and would either quickly burn out the bad spots or the capacitance meter would have trouble resolving the measurements. Samples with a DC resistance less than

half a mega ohm were not worth attempting to make electrical measurements on the spot due to leakiness. After the high resistance capacitors had been determined on a substrate, it was useful to measure the capacitance and D value. In general, if the DC resistance was good, the dielectric properties were also in a reasonable range.

### *2.3.B Thermal Treatment and Temperature Dependence of Capacitance*

Samples were annealed in a homemade copper temperature chamber, as the sketch of the cross section shown in Figure 2-9. The box was milled from a copper block. In the side of the box, there were feed-throughs for various electrical and gas connections. A soldering pad connected the samples to 4-wire connectors for electrical measurements. Thermocouple wires entered the chamber through additional openings. One thermocouple connected to the computer interface, as shown in Figure 2-10. A second thermocouple or RTD monitoring the temperature of the chamber was connected to the temperature controller. This controller heated the stage through a Minco heater located below the sample stage, as shown in Figure 2-9. Below the heater was a thermoelectric cooler which allowed the stage to cool below room temperature. The excess heat from the cooler and stage was removed by the water cooling system. Dry gas was brought into the chamber to prevent condensation and to decrease any effect of humidity, as further discussed in Chapter 8.

Samples were annealed to improve the overall crystallinity. The annealing temperature was above the Curie temperature, so to be in the paraelectric phase, if the materials were ferroelectric, but below the melting point. By heating the materials into the paraelectric phase, the lattice expanded, and allowed for short order rearrangement of

the crystal lattice. In some cases, materials were annealed at a lower temperature (but still above the Curie point), if they were annealed for a longer time.

Fresh films were typically annealed before any further measurements were made. A typical annealing and temperature dependent profile is shown in Figure 2-11A. Depending on the type of polymer, the sample was heated or cooled from room temperature at the rate of one degree per minute. Some samples were first cooled to -15 °C before being heated to the annealing temperature, typically samples with a lower phase transition temperature. PVDF copolymers were heated to 120°C and terpolymers were heated to 95°C, and held at temperature for three hours. The samples were cooled to either room temperature or as low as the sample stage could be practically cooled, in the range of -20°C. The sample was then heated and cooled two more times to verify that steady state in the sample had been reached. The soak times for samples after the initial annealing cycle were typically between 15 and 20 minutes.

The dielectric response of the capacitor was measured during temperature cycles with the Quad Tech 1689M RLC Digibridge. A typical set of data is shown in Figure 2-11B. Further discussions of experimental results are contained in later chapters.

### *2.3.C Voltage Dependence of Capacitance*

#### *2.3.C.a Background*

One of the ways to demonstrate switching in a ferroelectric film is through the use of capacitance-voltage measurements, commonly referred to as “butterfly curves” or C-V curves. At the switching voltage, there is a large increase in the dielectric constant. The source of this dielectric anomaly is heavily debated. The first perspective is that the

increase in the dielectric constant,  $\epsilon$ , is caused by the reversal of the dipoles at the coercive voltage. The second theory is that the domain switching would produce an insignificant contribution to the dielectric constant, and that other polar elements play a larger role. Brennan and others proposed that the increase in the dielectric contributor is from the capacitance of two Schottky space charge regions which formed at the interface of the film and electrodes [25]. In either case, there is a large dielectric constant in the region of switching, as shown in Figure 2-12A. The C-V curves show a dielectric anomaly at the coercive voltage, and long tails that pinch off when saturated at high voltages.

In addition to demonstrating the switching of the ferroelectric film, one can gather other details about the film from this measurement. Information can be obtained about space charge and electrode effects on the film [25].

### *2.3.C.b Experimental Details*

With the exception of the humidity experiments in Chapter 8, all C-V curves were measured with the HP 4192A impedance analyzer. This is a 4-lead measurement which analyzes the current and voltage, and the phase between them for the low and high side of the capacitor. PVDF films are measured with a 1 kHz frequency and a 0.1 volt oscillation level. The data is averaged through the instruments interface at the time of the measurement to help reduce noise. The C-V curves were measured in 0.1 volt increments at the rate of 2 seconds per step (0.05 volts per second). A sketch of the voltage cycle is shown in Figure 2-12B. The sample was allowed to remain at a given voltage for a short period before being stepped to the next one. The voltage started at zero volts, increased

to the maximum voltage, decreased through zero to the maximum negative voltage, and then returned to zero volts. In most cases, three cycles were recorded so the stable configuration could be observed. The first cycle was often observed a different shape, and three cycles was the minimum number of cycles to determine if the remaining cycles were stable or if the capacitance was decaying. The cycle was controlled a Labview VI, and resulting data was recorded by computer.

### 2.3.D Capacitance as a Function of Frequency

#### 2.3.D.a Background

By examining the capacitance as a function of the frequency, one can determine the behavior of the dielectric constant. The real part of the dielectric constant is related to the capacitance by

$$\varepsilon = \frac{Cd}{\varepsilon_0 A}, \quad \text{Equation 2-3}$$

where  $C$  is the capacitance,  $d$  is the sample thickness,  $A$  is the area of the parallel plate capacitor and  $\varepsilon_0$  is the permittivity of free space. When capacitance as a function of frequency (C-F) measurements are made, the capacitance and dissipation factor  $D$  are measured. The dissipation factor is also related to the dielectric loss tangent factor by  $D = \tan \delta$ . The imaginary part of the dielectric constant is

$$\varepsilon'' = D\varepsilon' \quad \text{Equation 2-4}$$

for a parallel plate capacitor. The complex permittivity relates the real and imaginary parts of the dielectric constant by [26]

$$\varepsilon^* = \varepsilon' - i\varepsilon''. \quad \text{Equation 2-5}$$

### 2.3.D.b Experimental Details

The measurements of capacitance as a function of frequency were made with a Hewlett-Packard 4192A Impedance Analyzer over the frequency range of 10 Hz to 13 MHz. The measurement bias oscillation level was 0.1 volts, which was small enough to leave the polarization state undisturbed. The temperature was controlled through the feedback loop described in Section 2.3.B. The impedance analyzer measured the capacitance and dissipation factor as a function of frequency. The frequency was increased logarithmically to allow for a large range of frequencies to be studied in a reasonable amount of time.

## 2.4 Pyroelectric Measurements

### 2.4.A Background

The pyroelectric current,  $I$ , is given by:[12, 27-30]

$$I = Ap_{eff} \frac{dT}{dt} \quad \text{Equation 2-6}$$

where  $A$  is the capacitor area, and  $\frac{dT}{dt}$  is the rate of change for the temperature. Since the capacitor samples are only free to expand in one direction, which is perpendicular to the substrate, the effective pyroelectric coefficient,  $p_{eff}$ , depends on two terms, the direct contribution and the indirect contribution due to the constraints, through the piezoelectric and stress tensors. This is given by:

$$p_{eff} = \left( \frac{\partial P_s}{\partial T} \right)_s + \frac{d_{33}^T \alpha_3^s}{s_{33}^s}, \quad \text{Equation 2-7}$$

where  $P_s$  is the spontaneous polarization,  $S$  is the strain,  $d_{33}^T$  is the stress-free polarization coefficient,  $\alpha_3^S$  is the thermal expansion coefficient, and  $s_{33}^S$  is the elastic compliance coefficient. By measuring the pyroelectric current, one can determine the relative polarization of the sample at different biases.

## 2.4.B *Experimental Details*

### 2.4.B.a *Instrumentation*

A helium-neon (HeNe) laser with a wavelength of 632 nm was directed onto the capacitor sample. The light passed through a chopper blade that modulated the power at 1 kHz by rapidly blocking and unblocking the light, causing the sample to heat and cool by a small amount. This created the temperature gradient which produced the pyroelectric current. The laser light was normally reflected by one or more mirrors to direct it to the sample inside of a sample chamber. A sketch of the apparatus is shown in Figure 2-13A.

The samples are of typical planar capacitor construction. The bottom electrode was connected to the ground. The top electrode was wired to the center pin of a two way digital switch. The switch was controlled by a solid state relay (see Figure 2-13A), which was controlled by a 5 volt signal from the DAQ board. The switch allowed the sample to be connected to either a voltage source, which applied a bias to the sample, or to the lock-in amplifier (Stanford Research Systems model SR830), which was referenced to the chopper frequency and measured the pyroelectric current from the sample.

Once the voltage was applied to the sample for the desired amount of time, the relay switch reversed and the sample was connected to the lock-in amplifier. The lock-in

amplifier used the chopper as an external trigger. The X and Y channels of the lock-in were recorded through the use of the analog outputs on the lock-in and analog inputs on the DAQ board. By recording both the X and Y channels, the magnitude of the signal could be calculated, even if the phase drifted while taking measurements.

The bias was applied to the sample with the analog output on the DAQ board. If the desired applied voltages were larger than 10 volts, an amplifier was added to the circuit. Although the typical amplifier was around 3 time amplification, the virtual Labview instrument was designed to be used with any of the amplifiers. The voltage applied to the sample was directly measured by the computer interface. Since the interface had a maximum input of 10 volts, if an amplifier was used to increase the voltage applied to the sample, it was necessary to reduce the maximum voltage below 10 volts before it was recorded by the computer. The voltage was reduced with the use of a voltage divider, and a typical one is shown in Figure 2-13B with a ratio of 1:9 between the two resistors to create a 1/10 voltage divider.

#### *2.4.B.b Computer Virtual Instrument*

The Labview Virtual Instrument (VI) (front panel shown in Figure 2-14) was designed specifically for the pyroelectric humidity experiment discussed in Chapter 8. The virtual instrument was also used for all other pyroelectric experiments. The VI was designed to allow for multiple cycles of measurements and for variable delays between each segment. The initial delay allowed for other functions to be started with another VI such as temperature ramps or bias sweeps, or to allow for temperature and humidity to fully stabilize before starting applying the bias. Since several different amplifiers were

shared between several experiments, the front panel for the voltage parameters and the amplifier factor to be entered. The VI then calculated the outputs needed based on these parameters. The number of steps between volts was calculated by the instrument when the user entered the desired step size. The typical step sizes were 0.1 volts, allowing experiments to be performed with several hundred data points easily. The VI also had a built in delay between cycles, to allow for other operations to execute, as needed.

The Labview VI read and wrote to the data acquisition (DAQ) board. In addition to recording analog signals such as the temperature and humidity sent from the respected sensors, it also recorded the pyroelectric signal from the analog output of the lock-in amplifier. Since the signal measured by lock-in amplifiers took a few time constants to stabilize, the VI allowed for measurements of both channels to be recorded at four different times. The first measurement was often made after a few time constants and the final one would be after 50-100 time constants. The other measurements were spaced in the middle of the two times. A typical measurement series might occur at 1, 2, 3, and 4 minutes. Once the polarization current has reached a steady value, all remaining measurements were the same value, within a noise range of 1% to 5%. In most cases, by the second set of measurements, the pyroelectric current had stabilized and therefore the last sets of measurements were redundant checks. If the lock-in phase was drifting or was the signal was mostly instrument noise, this was apparent by the multiple sets of measurements.

## 2.5 Film Quality, Morphology, and Thickness Measurements

### 2.5.A X-Ray Diffraction of Thin Films

#### 2.5.A.a Background

X-ray diffraction (XRD) uses high energy photons to probe structural properties of crystals and thin films. One can determine the crystal structure and orientation by examining the x-ray diffraction pattern. X-ray diffraction can also be used to determine properties of the film such as sample thickness and roughness using rocking curves[31].

X-ray diffraction patterns are produced by the constructive interference of photons being elastically scattered off of atoms or molecules. The diffraction peak locations are determined by the spacing between planes of atoms in a solid as shown in Figure 2-15. This relationship is given by Bragg's Law-

$$2d\sin\theta = n\lambda, \quad \text{Equation 2-8}$$

where  $d$  is the spacing between planes of atoms,  $\theta$  is the angle between the beam and the crystal surface,  $\lambda$  is the wavelength of the monochromatic x-ray source, and  $n$  is an integer.[32] By measuring the angles where maximum constructive interference occurs, one can calculate the characteristic spacing of the crystal lattice, and with a sufficiently detailed set of data, the position of all of the atoms. Since the basic crystal structure of our materials were already known, we focused on a few features such as the ratio of peak areas between barium titanate and the polymer in composite samples.

### *2.5.A.b Experimental Details*

X-ray diffraction was used to examine composite samples consisting of polymer and nanoparticles. Measurements were made with the Rigaku D/MaxB diffractometer with a cobalt k-alpha wavelength of 1.7903 Å. An aluminum or glass holder smeared with vacuum grease was used to position the sample in the beam. The peak width and area were calculated using the EVA diffraction software from the Bruker company.

Data for the samples were collected before and after annealing. The before annealing data was measured at the rate of 1-3 degrees per minute from 15° 2θ to 60° 2θ. After annealing, the samples were scanned from 15° 2θ to 25° 2θ at the rate of 1-2 degrees per minute. The areas of the polymer and particle peaks were calculated, and their relative ratios were determined.

### *2.5.B Atomic Force Microscopy*

#### *2.5.B.a Background*

Atomic force microscopy (AFM) uses a cantilever with a fine tip to interact with the surface of a film.[33] Since the AFM cantilever is probing the forces between the tip and the sample, it can be used with a large variety of conducting and insulating materials.[34] Information about the sample surface is gathered by monitoring the resonance frequency, amplitude, and deflection of the cantilever. A typical configuration is shown in Figure 2-16A.

There are several different modes of measurement that can be used with an AFM. The first is contact mode where the tip is scraped across the surface of the sample. This

measurement method uses the Van der Waal's repulsion forces between the surface atoms and the cantilever tip to produce an image. Thus, the resolution is limited, in part, by the area of contact between the sample and the tip.[33] While this method works well with hard materials, softer materials such as polymers are easily damaged by the force of the tip and require the use of a low force cantilever.

For softer materials, noncontact AFM can be used. In this method, a stiff cantilever is held above the sample and oscillates near the resonance frequency. As the tip is moved closer to the sample, the resonance frequency changed as the force constant of the cantilever is affected by the intermolecular forces between the tip and the sample.[33] The changes in the oscillations are then recorded with a detection system. The drawback to this method is that there is a loss of resolution due to the separation between the sample and the tip.

A third method for making measurements with an AFM is a hybrid of the contact and noncontact modes, commonly referred to as tapping mode.[33] This method will oscillate the cantilever near the surface of the sample. When the tip touches the sample, the oscillations are dampened out. This gives a higher resolution image than the noncontact mode while not damaging soft samples as much as the contact mode does with continuous pressure from dragging the tip.

#### *2.5.B.b Experimental Details*

Atomic force microscopy measurements were made in tapping mode with a Dimensions 3100 system. Data on both the height and phase was collected. Analysis

included line scans of the height profile and analysis of the roughness of the samples and substrates.

### *2.5.C Scanning Electron Microscopy*

#### *2.5.C.a Background*

Resolution of any microscope is limited by the wavelength of light. Since visible light has a wavelength of several hundred nanometers, it is impossible to obtain nanometer resolution with an optical microscope. Electrons with the energy of 0.5 -40 keV, though, can have wavelengths of an angstrom or less which allows images to be obtained of sample surfaces with the resolution as small as a few nanometers.[32]

A scanning electron microscope (SEM) uses a beam of electrons to image the surface of a sample. An electron gun shoots a beam of electrons through a pair of magnetic objective lenses, as shown in Figure 2-17. The objective lens steers and focuses the beam, similar to an optical lens focusing light. The electron beam then collides with the surface of the sample, interacting with the surface layers. The electrons that interact with the surface produce a number of interactions including backscattered electrons, secondary electrons, and x-ray emission.[34]

When an electron enters the sample and scatters off of the atoms elastically, the electron has a chance to leave the sample. These electrons are called back-scattered electrons. The back scattered electrons are focused on a screen to produce an image. Since the backscattered beam is typically much larger than the initial beam of electrons, this limits the resolution of the SEM images.[34] The electron beam will also cause some electrons in the atoms to be excited. These excited electrons will emit characteristic x-

rays which can be collected by an x-ray detector. This allows for elemental analysis of heavy atoms.[34]

### *2.5.C.b Experimental Details*

Most samples were imaged using a field emission SEM (FESEM), Hitachi S4700 FE-SEM. This SEM has the ability to image samples with a magnification from 20 times to 500,000 times, with a resolution down to 1 nm. The electron accelerating voltage was 10 kilovolts for the polymer samples and as high as 15 kilovolts for the pure particle samples. Typical resolution for the polymer samples ranged from a few microns to a few nanometers.

Before the sample could be viewed with an SEM, it was necessary to remove any water vapor in the film. This was done by placing the sample in a vacuum chamber or vacuum oven for at least 12 hours prior to measurements. The samples were then transported in a portable desiccator (Desi-Vac, Fisher Scientific) to reduce the amount of moisture that re-entered the samples. High levels of moisture caused charge to build on the surface and reduced resolution of the images.

One of the difficulties with the measurements was due to the fact that the samples were composed partially or completely of polymers which were insulating. Normally, samples would be coated with a thin film of metal such as chromium to reduce the electron charging of the surface. In the case of our samples, the metal coating was undesirable since the coating thickness was on the same size scale (20 nm) as the features that were being imaged. The conductive layer caused the sample features to be blurred together. The electron charging problem was partially resolved by covering the substrate

with a conductive layer such as aluminum before the film was deposited. This provided a place for the electrons to drain to and a way to dissipate the heat. It also helped provide contrast between the polymer film and the background. This did not resolve all of the issues with imaging the polymer and composite films, though. The electron beam energy had to be reduced to 10 kilovolts to prevent the polymer from being immediately burned away. Even with the lower energy beam, a single area of the sample could only be exposed to the beam for a limited amount of time before the beam significantly and irreversibly damaged the film. For some samples, this was a few seconds time. For other samples, it was several minutes. For the shortest duration samples, one had to focus the beam, move the sample and then capture an image. In other areas, the sample could be focused and zoomed in on an interesting feature, and that image could be captured without significantly distorting the surface.

#### *2.5.D Ellipsometry*

##### *2.5.D.a Background*

Ellipsometry is the study of the change in light properties as it reflects from or passes through thin films. Ellipsometry can measure thin film thickness, surface and interface roughness, optical constants, and properties of multilayer films.[35]

Ellipsometry is a noninvasive measurement that is performed by reflecting from or transmitting light through a sample and then measuring the changes in relative phase and amplitude of the light.

The theory of ellipsometry is based on Fresnel reflection and transmission. Linearly polarized light can be broken into two components, the one with the electric

field vibrating parallel to the surface plane of incidence is the p polarization and the one with the electric field perpendicular to the plane of incidence is the s polarization, as shown in Figure 2-18A. These two components are independent of each other and each part can be analyzed separately[36].

The electric field of the reflected light,  $E_r$ , is related to the initial electric field,  $E_i$ , and the reflection coefficient,  $R$ , by the following equations:

$$E_{rp} = R_p E_{ip} \quad \text{Equation 2-9}$$

$$E_{rs} = R_s E_{is}. \quad \text{Equation 2-10}$$

The complex reflection ratio,  $\rho$ , is the ratio of the p and s polarization reflection coefficients. This is given by

$$\rho = \frac{R_p}{R_s} = \tan\Psi e^{i\Delta}. \quad \text{Equation 2-11}$$

This complex number is typically written in polar form for use in ellipsometry.

The value  $\tan\Psi = \frac{|R_p|}{|R_s|}$  represents the relative amplitude attenuation and the value

$\Delta = \arg(R_p) - \arg(R_s)$  is the phase shift between the s and p polarized light after reflection as the sketch of phases shown in Figure 2-18B [36, 37].

Another way to describe  $\rho$  is as a function of the incident angle,  $\phi$ , and the wavelength of light,  $\lambda$ ,

$$\rho = f(\phi, \lambda). \quad \text{Equation 2-12}$$

In multi-angle spectroscopy, the angle of incidence is changed over a range of angles and the data is collected. For spectroscopic ellipsometry, the wavelength is varied over a

range such as the visible spectrum or uv spectrum of light. For variable-angle spectroscopic ellipsometry (VASE), both the angle and the wavelength are recorded.

There are a number of different configurations for ellipsometers. All measurements for this study were made on instruments in the class of rotating analyzer spectrometers. A sketch of a typical system is shown in Figure 2-19A. For this setup, linearly polarized light is reflected off of the sample. The reflected light then passes through a rotating polarizer (analyzer) before entering the detector [35].

Once the data has been collected, the film thickness and optical constants must be calculated from the  $\Psi$  and  $\Delta$  data. Figure 2-19B shows a flow map of the basic steps to fitting ellipsometry data. A model of the sample must first be constructed. For films, this was typically a substrate or electrode surface with a layer on top. From the Cauchy fit model, optical constants such as  $n$  and  $k$  are calculated using thin film Fresnel equations. Once a model has been constructed, it is compared to the data, and the data is further refined until the model represents the data reasonably well. The Levenburg-Marquardt non-linear regression algorithm was used to fit the data [35].

The Cauchy dispersion relationship is used to fit materials that are transparent or nearly transparent in the visible wavelength range, such as optical coating materials and organic films. The model presumes that all of the resonances in the material are well above the measurement frequency. The index of refraction for the Cauchy dispersion relation is given by

$$n(\lambda) = A + \frac{B}{\lambda^2} + \frac{C}{\lambda^4} \quad \text{Equation 2-13}$$

where  $A$  is the approximate index of refraction, while  $B$  and  $C$  allow for nonlinearity in the index [38].

### *2.5.D.b Experimental Details*

Ellipsometry measurements for this dissertation were made on two instruments. The first instrument was a Woollam VASE ellipsometer. Measurements were made at seven angles, ranging from 45° to 75°. The second instrument was a Woollam Alpha-SE ellipsometer which measures at three angles (65°, 70°, and 75°) in reflection mode over a range of wavelengths from 380 nm to 990 nm. Measurements were made at the standard data acquisition rate. The data was fit with the software provided by the Woollam Company. The typical model was an aluminum substrate and a layer of thin film.

## **2.6 Material Analysis**

### *2.6.A Nuclear Magnetic Resonance*

#### *2.6.A.a Background*

Just as electrons have spin, so do the protons and neutrons in the nucleus. The total nuclear spin is quantized, with a value given by  $I$  in multiples of 1/2. In the absence of an external magnetic field, the energy levels of all values of  $I$  for a given nucleus are the same. For the atoms used in nuclear magnetic resonance (NMR) studies such as  $^1\text{H}$ ,  $^{13}\text{C}$ ,  $^{19}\text{F}$ , and  $^{31}\text{P}$ ,  $I$  has values of 1/2.[34] The magnetic moment of the nucleus,  $\mu$ , is defined by

$$\mu = \gamma p, \quad \text{Equation 2-14}$$

where  $\gamma$  is the magnetogyric ratio and  $p$  is the angular momentum. The observable magnetic quantum states are  $m = I, I-1, I-2, \dots, -I$ . For the elements used in this study,  $I = 1/2$  and  $m = \pm 1/2$ . When a magnetic field is applied to the nucleus, the energy levels split into two levels as shown in Figure 2-20A. The potential energy is given by

$$E = \frac{-\gamma m \hbar}{2\pi} B_0. \quad \text{Equation 2-15}$$

This gives the change in energy between two consecutive  $m$  values as

$$\Delta E = \frac{\gamma \hbar}{2\pi} B_0. \quad \text{Equation 2-16}$$

This change in energy is the same as the energy a photon must possess to switch it from one state to another is given by

$$\Delta E = \frac{\gamma \hbar}{2\pi} B_0 = h\nu_0 \rightarrow \nu_0 = \frac{\gamma B_0}{2\pi}. \quad \text{Equation 2-17}$$

When no magnetic field is present, there are an equal number of atoms in each spin state. With the application of a magnetic field, there is a slight increase towards the lower energy level ( $m = +1/2$ ), allowing for measurements to be made.

When a spinning magnet has an external field applied to it, it will precess around the vector of the applied field with an angular frequency of  $\omega_0 = \gamma B_0$ , as shown in Figure 2-20B. This frequency is the Larmor frequency, which is the same frequency found in Equation 2-17 from the quantum mechanical arguments. This frequency is given by

$$\nu_0 = \frac{\gamma B_0}{2\pi}. \quad \text{Equation 2-18}$$

Atoms of the same type, but in slightly different environments such as having different neighbors, will produce different chemical shifts. This is due to the screening of

the atom by the environment. The shift will either reinforce or oppose the magnetic field, causing the shift to be at higher or lower than the single atom. This value is small, and is measured in parts per million (ppm). Since NMRs that operate at different frequencies will produce different shifts, the chemical shift parameter,  $\delta$ , is often used [34].

By knowing the chemical shifts, one can use NMR for a variety of applications. This includes determining structural arrangements and functional groups. Quantitative information can also be determined such as the number of hydrogen atoms in a molecule by comparing peak areas.[34] In some cases, it is desirable to know how one element is positioned relative to one of a different type, such as carbons and hydrogens. This can be done using two-dimensional Fourier transform NMR studies. The one used in this study was HMBC (heteronuclear multiple bond correlation), which gives correlation between the hydrogen and phosphorus atoms that are two, three, or four bonds away.[39]

The block diagram of a typical NMR system is shown in Figure 2-21. The sample is placed in a large magnet at the top of the diagram. The sample is surrounded by a transmitter/receiver coil which both applies the signal and captures the affect. The frequency synthesizer creates a radio pulse which is passed to the RF transmitter. The coil picks up the signal and applies it to the sample. The same coil then sends the received signal to the computer where Fourier transforms are performed on the data. In most cases, the magnet is a super conducting magnet, cooled by liquid helium. This will allows the magnetic field to reach values as large as 21T, permitting high resolution measurements.[34]

### *2.6.A.b Experimental Details*

The polymer and oligomer solutions were prepared by diluting the material in deuterated acetone. The alkane solutions were diluted with deuterated chloroform. Both solutions were placed in a 5 ml NMR tube for measurements.

The NMR measurements were made on the Bruker 600 MHz Avance Spectrometer unless otherwise specified. The  $^1\text{H}$  measurements were collected with a spectrum width of 12,376.237 Hz and 65536 data points. The  $^{31}\text{P}$  measurements were collected with a spectrum width of 97087.375 Hz and 65536 data points. The  $^{19}\text{F}$  measurements were collected with a spectrum width of 75187.969 Hz and 131072 data points. All measurements had two dummy scans, 16 scans, and a relaxation delay of 1 second. (Dummy scans are the scans before data is being recorded to ensure the sample is in steady state. The scans are the measurement cycles for actually collecting data. Relaxation delay is the time between scans.) The 2D  $^1\text{H}$ - $^{31}\text{P}$  HMBC data was measured using a hmbcgpndqf pulse sequence. All measurements had 16 dummy scans, 8 scans, and a relaxation delay of 1.5 seconds.

### *2.6.B Thermal Gravimetric Analysis*

#### *2.6.B.a Background*

Thermal gravimetric analysis (TGA) is a method used to determine mass ratios of materials and composites. A small amount of the sample material is placed in a balance, inside of a furnace. The furnace has a controlled atmosphere, typically either  $\text{N}_2$  or  $\text{O}_2$  gas, depending if an inert or oxidizing atmosphere is preferred. The balance typically ranges from 1 mg to 100g. The temperature is increased linearly and the mass is

recorded as a function of temperature or time. Then, the mass or percent weight is plotted as a function of time or temperature. This plot is called a thermogram or a thermal decomposition curve [34].

TGA measurements can give insight to decomposition and oxidation reactions, along with vaporization, sublimation, and desorption studies. TGA is especially useful for the study of carbon based materials, such as polymers. Each type of polymer will give a different type of signature, depending on the composition and bond types. Figure 2-22A shows the decomposition curves for five common polymers. Each polymer had a different shaped curve [34].

Another application of TGA is to examine the relative concentrations of a composite material. Figure 2-22B shows the thermogram for carbon black in polyethylene. There was a sharp drop when polyethylene decomposes and then a second one at a higher temperature when the carbon black decomposes. This gave the weight ratios of 75% to 25% for the materials in this example [34]. A third application of TGA is to examine the molecular makeup of a material. In Figure 2-22C,  $\text{CaC}_2\text{O}_4 \cdot \text{H}_2\text{O}$  was heated in an inert atmosphere. There was a drop in mass each time part of the material decomposed [34]. Through TGA, it was possible to gain insight into the properties of composite materials.

#### *2.6.B.b Experimental Details*

The TGA data was collected on a Perkin Elmer STA6000 instrument. The temperature was linearly increased from 25°C to 1000°C at the rate of 5°C per minute. The temperature was then held at 1000°C for 20 minutes before being cooled back to

room temperature at the rate of 20°C per minute. The samples were heated in a nitrogen atmosphere. Typical sample sizes were between 18 mg and 20 mg. Once the initial data was collected, the thermograms were plotted with the percent weight as a function of the temperature.

## 2.7 References

1. Norrman, K., A. Ghanbari-Siahkali, and N.B. Larsen, *6 Studies of spin-coated polymer films*. Annual Reports Section "C" (Physical Chemistry), 2005. 101(0): p. 174-201.
2. Sahu, N., B. Parija, and S. Panigrahi, *Fundamental understanding and modeling of spin coating process: A review*. Indian Journal of Physics, 2009. 83(4): p. 493-502.
3. Hall, D.B., P. Underhill, and J.M. Torkelson, *Spin Coating of Thin and Ultrathin Polymer Films*. Polymer Engineering and Science, 1998. 38(12): p. 2039-45.
4. Manuelli, A., et al. *Applicability of coating techniques for the production of organic field effect transistors*. in *Polymers and Adhesives in Microelectronics and Photonics, 2002. POLYTRONIC 2002. 2nd International IEEE Conference on*. 2002: IEEE.
5. Xia, F., et al., *Dependence of threshold thickness of crystallization and film morphology on film processing conditions in poly (vinylidene fluoride–trifluoroethylene) copolymer thin films*. Journal of Applied Physics, 2002. 92(6): p. 3111-3115.
6. Urayama, K., M. Tsuji, and D. Neher, *Layer-thinning effects on ferroelectricity and the ferroelectric-to-paraelectric phase transition of vinylidene fluoride-trifluoroethylene copolymer layers*. Macromolecules, 2000. 33(22): p. 8269-8279.
7. Zhang, Q., et al., *Critical thickness of crystallization and discontinuous change in ferroelectric behavior with thickness in ferroelectric polymer thin films*. Journal of Applied Physics, 2001. 89(5): p. 2613-2616.
8. Franklin, B., W. Brownrigg, and M. Farish, *Of the Stilling of Waves by means of Oil. Extracted from Sundry Letters between Benjamin Franklin, LL. D. F. R. S. William Brownrigg, M. D. F. R. S. and the Reverend Mr. Farish*. Philosophical Transactions, 1774. 64: p. 445-460.
9. Rayleigh, L., *Measurements of the Amount of Oil Necessary in Order to Check the Motions of Camphor upon Water*. Proceedings of the Royal Society of London, 1889. 47(286-291): p. 364-367.
10. Langmuir, I., *The mechanism of the surface phenomena of flotation*. Transactions of the Faraday Society, 1920. 15(June): p. 62-74.
11. Roberts, G.G., *An applied science perspective of Langmuir-Blodgett films*. Advances in Physics, 1985. 34(4): p. 475-512.

12. Ducharme, S., S.P. Palto, and V.M. Fridkin, *Ferroelectric Polymer Langmuir-Blodgett Films*, in *Handbook of Thin Film Materials*, H.S. Nalwa, Editor. 2002, Academic Press: San Diego.
13. Palto, S., et al., *Ferroelectric Langmuir-Blodgett films showing bistable switching*. EPL (Europhysics Letters), 1996. 34(6): p. 465.
14. Ulman, A., *Langmuir-Blodgett Films*. The Handbook of Surface Imaging and Visualization, 1995: p. 277.
15. Yamaki, M., K. Matsubara, and K. Nagayama, *A thin liquid layer on the surface of mercury as a matrix of a flow-mediated two-dimensional assembly of proteins*. Langmuir, 1993. 9(11): p. 3154-3158.
16. Langmuir, I. and V.J. Schaefer, *The effect of dissolved salts on insoluble monolayers*. Journal of the American Chemical Society, 1937. 59(11): p. 2400-2414.
17. Roberts, G., *An applied science perspective of Langmuir-Blodgett films*. Advances in Physics, 1985. 34(4): p. 475-512.
18. Love, J.C., et al., *Self-Assembled Monolayers of Thiolates on Metals as a Form of Nanotechnology*. Chemical Reviews, 2005. 105(4): p. 1103-1170.
19. Fisher, J. and I. Giaever, *Tunneling through thin insulating layers*. Journal of Applied Physics, 1961. 32(2): p. 172-177.
20. Koutsioubas, A.G., et al., *Formation of alkane-phosphonic acid self-assembled monolayers on alumina: an in situ SPR study*. Surface and Interface Analysis, 2009. 41(11): p. 897-903.
21. Hauffman, T., et al., *Study of the Self-Assembling of n-Octylphosphonic Acid Layers on Aluminum Oxide*. Langmuir, 2008. 24(23): p. 13450-13456.
22. Lushtinetz, R., et al. *Infrared spectra of alkylphosphonic acid bound to aluminium surfaces*. in *Macromolecular Symposia*. 2007: Wiley Online Library.
23. Paine, D.C., et al., *A study of low temperature crystallization of amorphous thin film indium--tin--oxide*. Journal of Applied Physics, 1999. 85(12): p. 8445-8450.
24. *CRC Handbook of Chemistry and Physics*. 92 ed, ed. W.M. Haynes. 2011: Taylor and Francis Group, LLC.
25. Brennan, C., *Landau theory of thin ferroelectric films*. Integrated Ferroelectrics, 1995. 9(4): p. 335-346.

26. Ducharme, S. and M. Jogad, *Dielectric properties of a ferroelectric copolymer Langmuir-Blodgett film*. Current Science, 2002. 83(4): p. 5.
27. Bune, A.V., et al., *Piezoelectric and pyroelectric properties of ferroelectric Langmuir-Blodgett polymer films*. Journal of Applied Physics, 1999. 85(11): p. 7869-7873.
28. Sorokin, A.V., V.M. Fridkin, and S. Ducharme, *Pyroelectric study of polarization switching in Langmuir-Blodgett films of poly(vinylidene fluoride trifluoroethylene)*. Journal of Applied Physics, 2005. 98(4): p. 044107-10.
29. Nye, F., *Physical properties of crystals*. 1964: Clarendon Press Oxford.
30. Lines, M.E. and A.M. Glass, *Principles and applications of ferroelectrics and related materials*. 1977: Oxford University Press.
31. Fewster, P.F., *X-ray diffraction from low-dimensional structures*. Semiconductor Science and Technology, 1993. 8(11): p. 1915.
32. Blakemore, J.S., *Solid state physics*. 1969, Philadelphia: W.B. Saunders Co.
33. Louder, D.R. and B.A. Parkinson, *An Update on Scanning Force Microscopies*. Analytical Chemistry, 1995. 67(9): p. 297A-303A.
34. Skoog, D.A., F.J. Holler, and T.A. Nieman, *Principles of Instrumental Analysis*. 5 ed. 1998: Saunders College Publishing.
35. Woollam, J.A., et al., *Overview of Variable Angle Spectroscopic Ellipsometry (VASE), Part I: Basic Theory and Typical Applications*, in *Optical metrology : proceedings of a conference held 18-19 July, 1999, Denver, Colorado*, G.A. Al-Jumaily and E. Society of Photo-optical Instrumentation, Editors. 1999, SPIE Optical Engineering Press: Bellingham, WA.
36. Azzam, R.M.A., *Ellipsometry*, in *Handbook of Optics, Third Edition Volume I: Geometrical and Physical Optics, Polarized Light, Components and Instruments*, M. Bass, et al., Editors. 2010, Mc Graw-Hills Companies, Inc.
37. Tompkins, H.G. and E.A. Irene, *Handbook of ellipsometry*. 2005, Norwich, NY, Heidelberg, Germany: William Andrew Pub. ; Springer. xvi, 870 p.
38. J. A. Woollam Co, I., *Complete Ease Data Analysis Manual*. 2011, Lincoln, Ne.
39. Vasavi, Y., et al., *Heteronuclear Multiple Bond Correlation Spectroscopy- An Overview*. International Journal of PharmTech Research, 2011. 3(3): p. 1410-1422.

40. Blinov, L.M., et al., *Two-dimensional ferroelectrics*. Physics-Uspekhi, 2000. 43(3): p. 243.

## 2.8 Tables

Table 2-1. Table of commonly used solvent properties. [24]

Solvent	Boiling Point (°C)	Viscosity (mPa s)	Dipole Moment $\mu/D$	Density (g/mL)	Deposition Technique
Acetone	56.05	0.036	2.88	0.7845	LB
Benzene	80.08	2.2825	0	0.8765	LB
Butanone	79.59	0.405	2.78	0.7999	Spin-coat, LB
Chloroform	61.7	0.537	1.04	1.4788	Spin-coat, LB
DMF	153	0.794	3.82	0.9445	Spin-coat, LB
DMSO	189	1.987	3.96	1.1010	LB
Ethanol	78.29	1.074	1.69	0.7893	Spin-coat, LB
THF	65	0.456	1.75	0.8833	Spin-coat
Water	100		1.86	1.000	-

\*When making samples, it is important to match the properties of the solvent with the polymer and the technique being used to make films. Polymers such as PVDF are polar, so choosing a solvent with a higher dipole moment will increase the solubility. Materials such as the alkanes which are nonpolar, dissolve better in a solvent with a low polarity. When trying to make composites containing both polar and nonpolar materials, a solvent must be picked that has a low enough polarity to dissolve the alkanes while high enough to dissolve the polymers. Also one must consider the type of samples to be made. Solvents that are very low viscosity do not spin coat well, and solvents that are very minuscule with water are more difficult to obtain high loading efficiencies for Langmuir Blodgett films.

Table 2-2. Table of metal melting points and densities. [24]

Metal or Oxides	Symbols	Melting Point (°C)	Density (g/cm <sup>-3</sup> )
Aluminum	Al	660	2.70
Chromium	Cr	1907	7.15
Cobalt	Co	1495	8.86
Copper	Cu	1085	8.96
Gold	Au	1064	19.3
Indium	In	157	7.31
Indium Tin Oxide	ITO	1800–2200	7.12–7.16
Platinum	Pt	1768	21.5
Silver	Ag	962	10.5
Tin	Sn	232	7.265
Zinc	Zn	419	7.14

\*When using thermal vapor deposition, it is ideal to have a material with a melting point well below the melting point of the tungsten wire (3414 °C). As the temperature increases, the tungsten wire becomes more brittle.

## 2.9 Figures

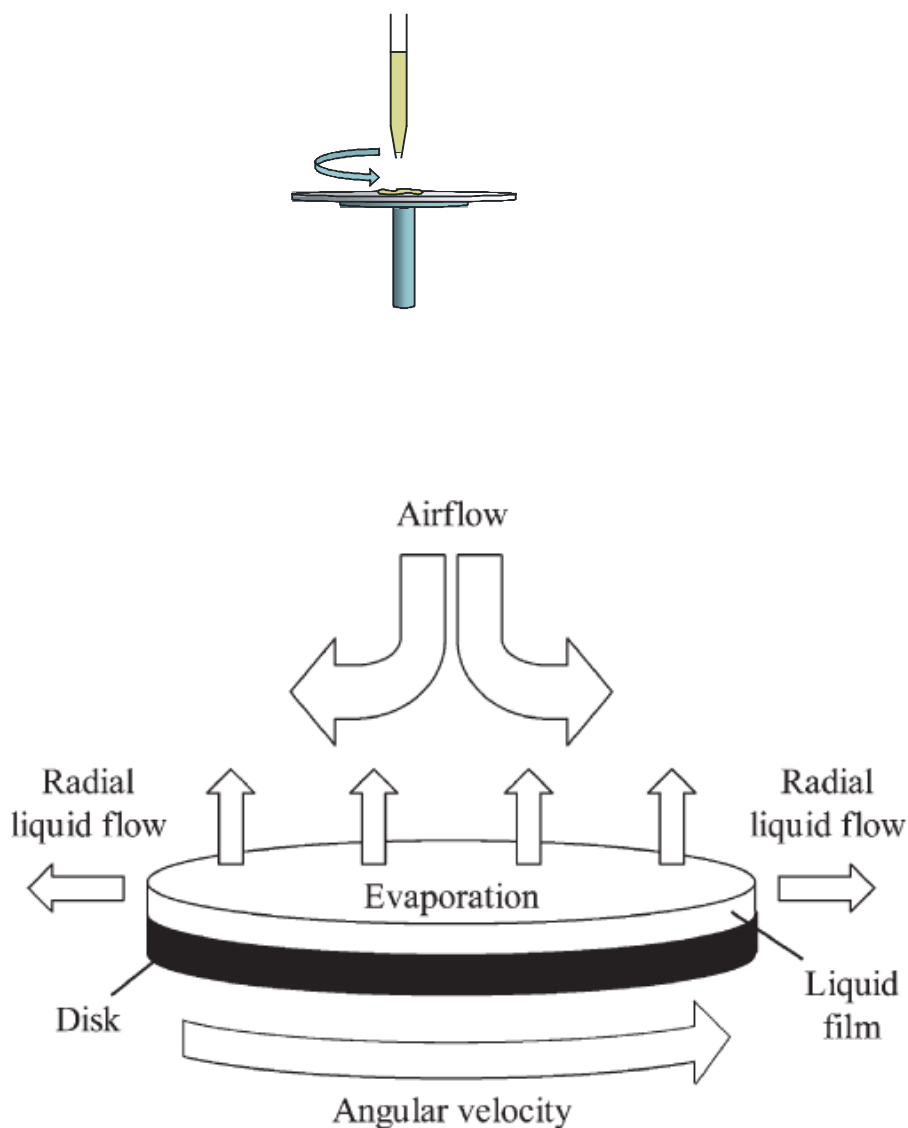


Figure 2-1. Films were deposited by spincoating. (A) A few drops of solution was dripped onto a slowly spinning substrate. The rate of rotation was then increased to create a thin film. (B) Numerous parameters affect the film thickness and quality as the film forms. Angular velocity and flow properties such as viscosity of the solution will affect the sample thickness. Also, enviromental changes such as the temperature and humidity of the air flow around the sample will affect the thinning rate and how the film dries during deposition. [1] Reproduced from Ref. (Norrman, K., *et al.*, *Annual Reports Section "C" (Physical Chemistry)*, 2005. **101**(174)) with permission from the Centre National de la Recherche Scientifique (CNRS) and The Royal Society of Chemistry.

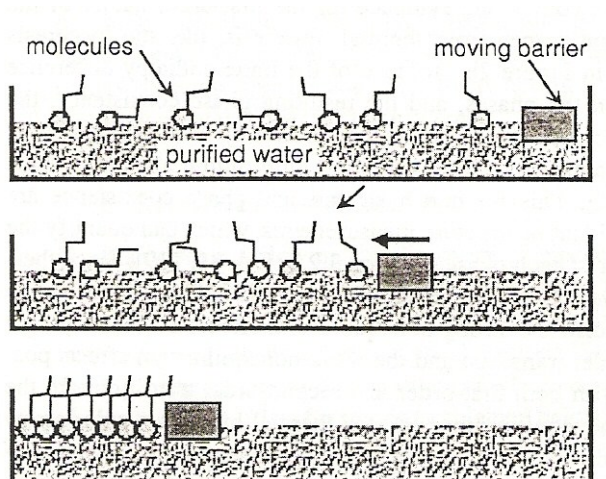


Figure 2-2. Sketch of a Langmuir-Blodgett trough. A dilute solution is dispersed on the surface of the water. The barriers of the trough compress the film to make a dense monolayer [12]. This figure was published in *Handbook of Thin Film Materials*, Vol 3, Nalwa, *Ferroelectric Polymer Langmuir-Blodgett Films*, Copyright Elsevier (2002).

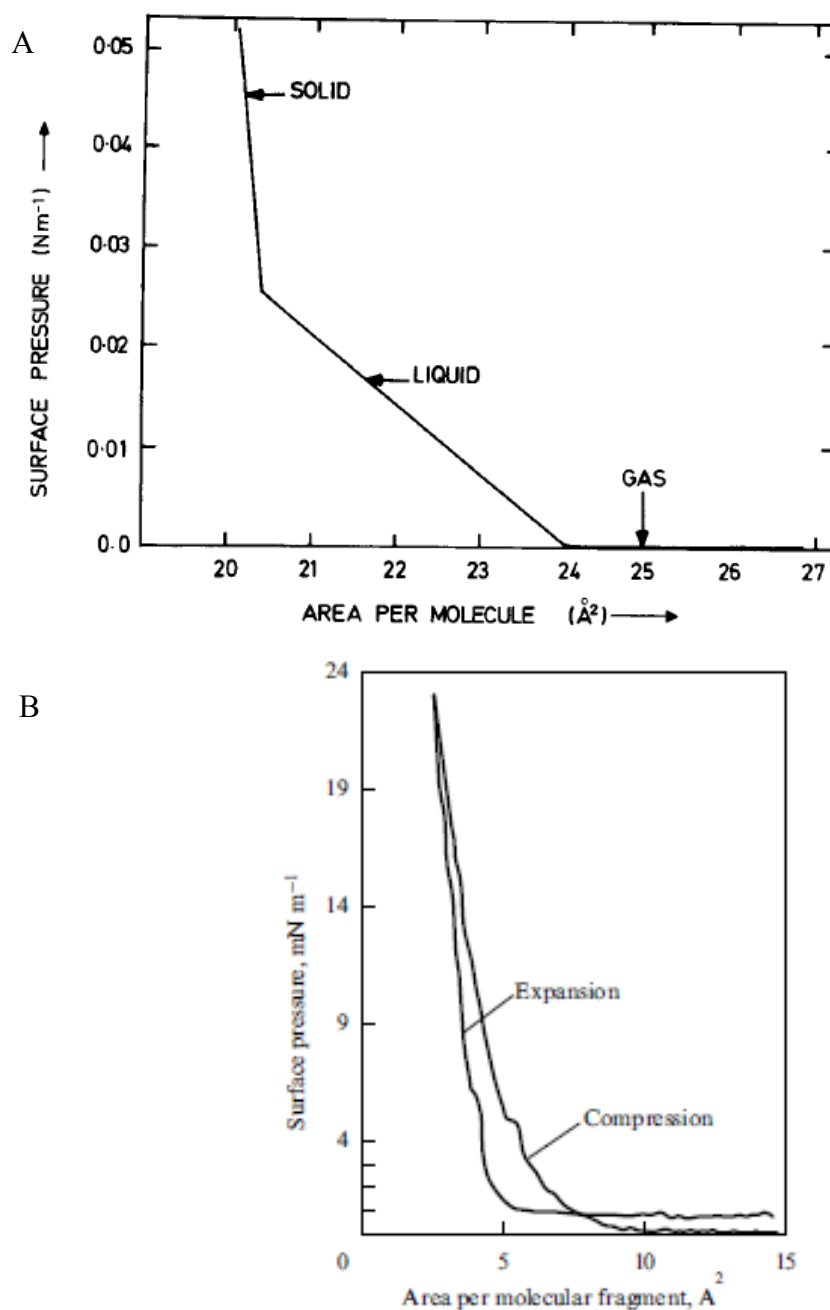


Figure 2-3. (A) Typical pressure-area curve for an ideal Langmuir film, such as stearic acid. [11] The solution on the trough starts as a gas phase. As the film is compressed, it becomes denser, entering a liquid and then a solid phase. The start of each phase is represented by a change in slope on the pressure area curve. Taken from *Roberts, G.G., Advances in Physics, 1985. 34(475)* with permission. (B) A pressure area curve for PVDF-TrFe (70-30) [40] PVDF does shows gradual slope changes instead of sharp changes like stearic acid. Taken from *Blinov, L.M., et al., Physics-Uspekhi, 2000. 43 (243)* with permission.

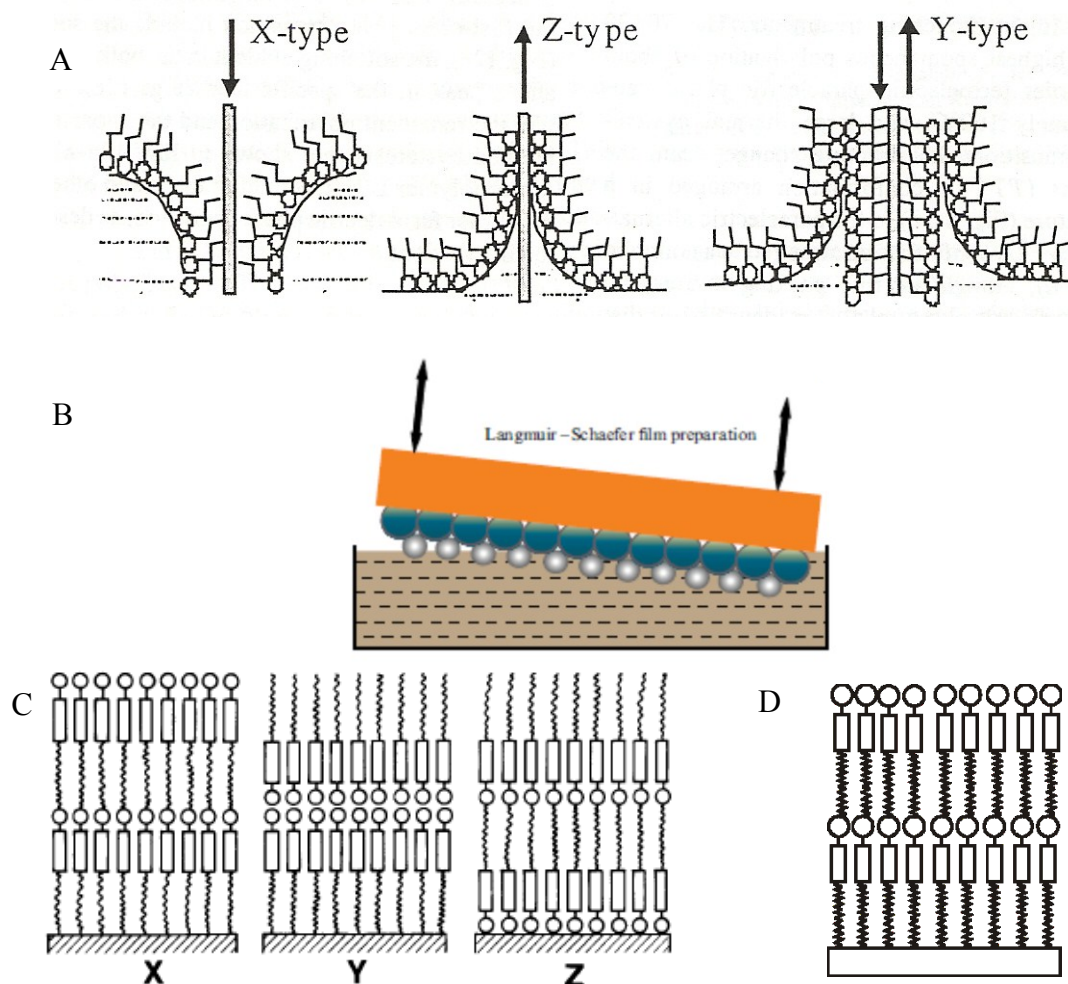


Figure 2-4. Langmuir-Blodgett deposition techniques. (A) There are three common vertical deposition techniques. X type deposition pushes the substrate into the water to deposit a layer. Z type deposition pulls the substrate from the water. Y type dipping deposits a layer onto the substrate as the substrate is pushed into and pulled from the water.[11, 12] This figure was published in *Handbook of Thin Film Materials*, Vol 3, Nalwa, *Ferroelectric Polymer Langmuir-Blodgett Films*, Copyright Elsevier (2002). (B) In some cases, the horizontal Schaefer method worked better to make films since it did not involve submerging the substrate in the water [40]. Taken from *Blinov, L.M., et al., Physics-USpekhi, 2000. 43 (243)* with permission. (C) Depending on the deposition method, the molecules have different orientations on the substrate. X type deposition has the tails of each layer pointing towards the substrate. Z type dipping has the heads of each layer pointing towards the substrate. Y type deposition builds up layers that are head to tail.[11] Taken from *Roberts, G.G., Advances in Physics, 1985. 34(475)* with permission. (D) Films deposited by Schaefer method have a structure similar to X type deposition with each layer's tails pointing towards the substrate.

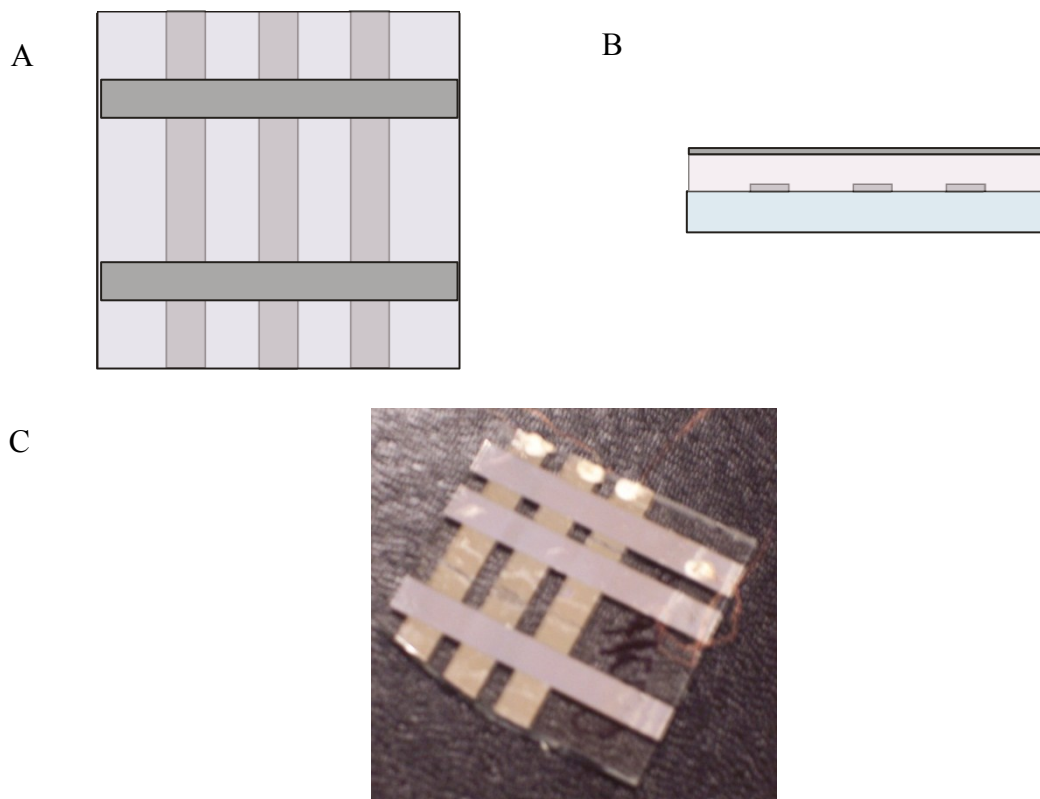


Figure 2-5. A sketch of a typical sample construction showing the various layers in a sample. (A) The overhead view of a sample consisting of a thin film sandwiched between two aluminum electrodes on a glass substrate. Where the two electrodes cross is a capacitor sample. (B) A cross section of a typical sample. The film is made to the desired thickness by depositing the predetermined number of layers by Langmuir-Blodgett technique. (C) An actual sample with 9 parallel plate capacitors.

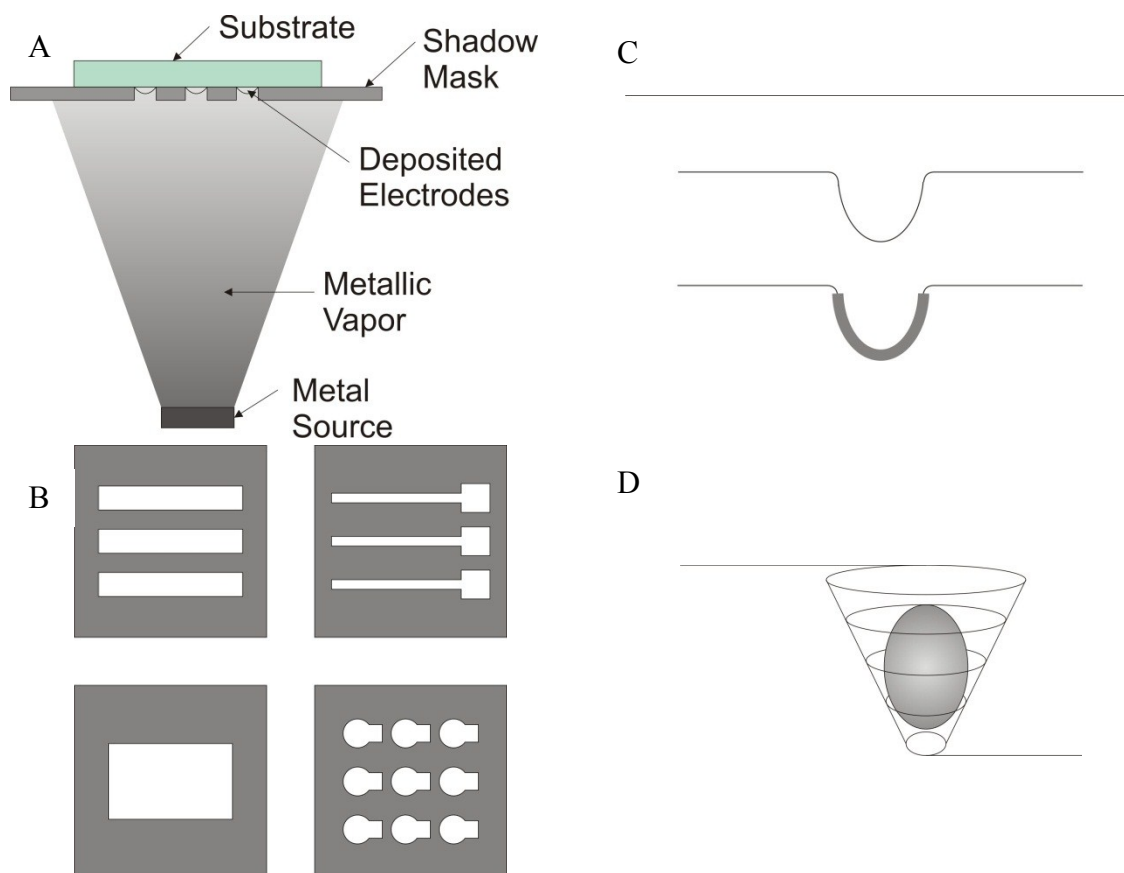


Figure 2-6. (A) The evaporator metal source is below the sample and mask. The metal is heated to a vapor which passes through the shadow mask to deposit electrodes on the substrate. (B) Examples of typical shadow masks. The masks can be configured into nearly any shape, with stripes being the most common for ease of use with parallel plate capacitors. (C) One metal source for the evaporator consists of a piece of tungsten metal bent into a “u” or “v” shape and wrapped with the metal wire for evaporation. (D) An alternative metal source is the preformed tungsten baskets which use a piece of metal as a source.

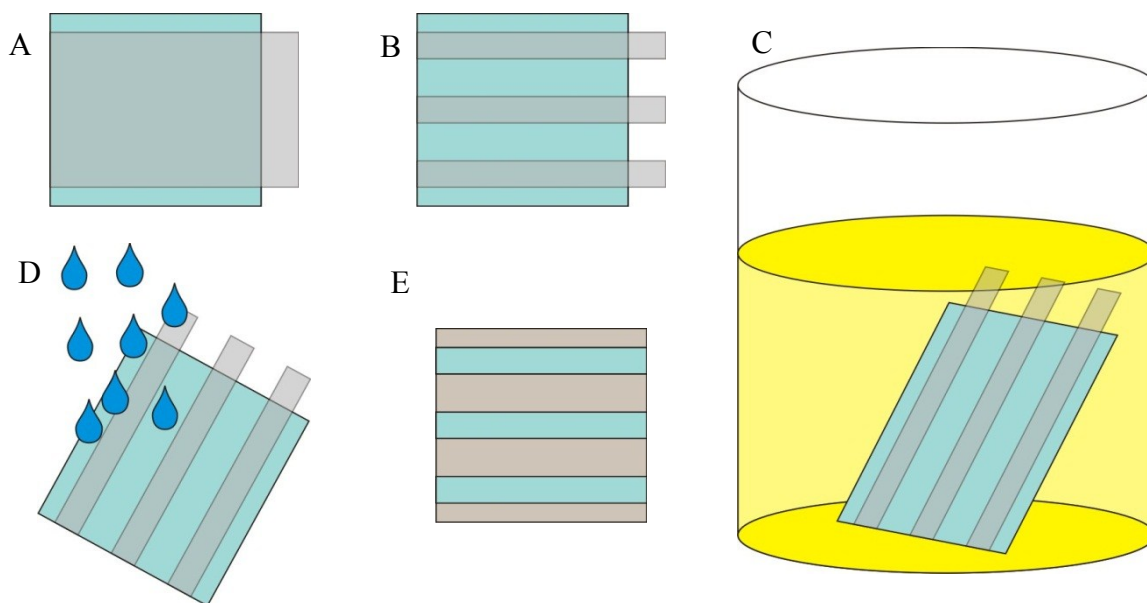


Figure 2-7. ITO Etching. (A) Scotch tape is applied to the ITO film. (B) The pattern to be etched is cut into the tape. All tape is removed from any area where the ITO should be etched. (C) The substrate is soaked in the etchant. The tape protects the electrode areas. (D) The substrate is rinsed first with water to remove any remaining etchant. (E) The tape is then removed and any tape residue is washed from the substrate. The dry substrate is then ready for a film.

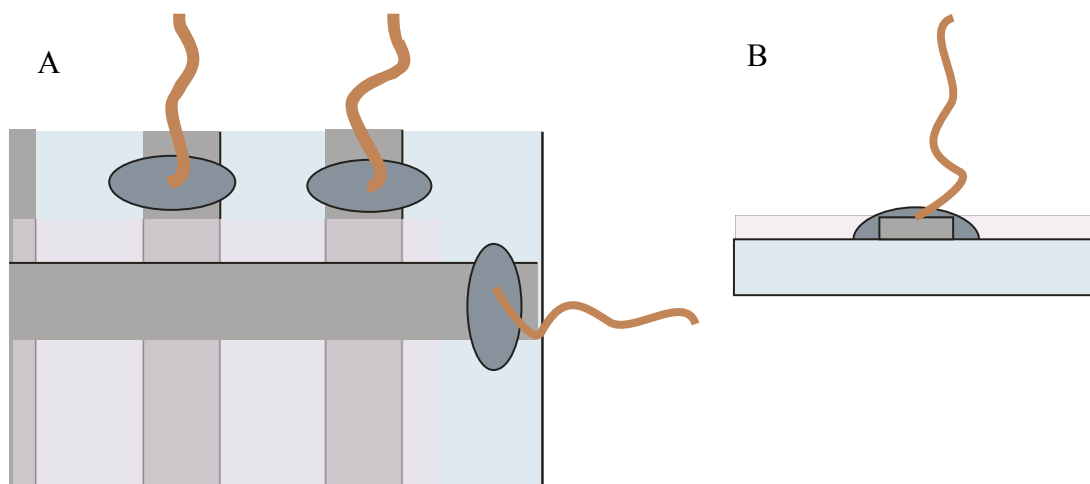


Figure 2-8. Sample Leads (A) The leads on most samples were attached with indium metal. The indium would stick better to the glass than to the aluminum electrodes, so it was necessary to make the indium span the electrode catching on either side on the glass before it would stick to the aluminum. (B) Sketch of the cross section of the indium attachment of leads. The copper wires stuck to the indium better if they were tinned with lead solder before being attached to the electrode.

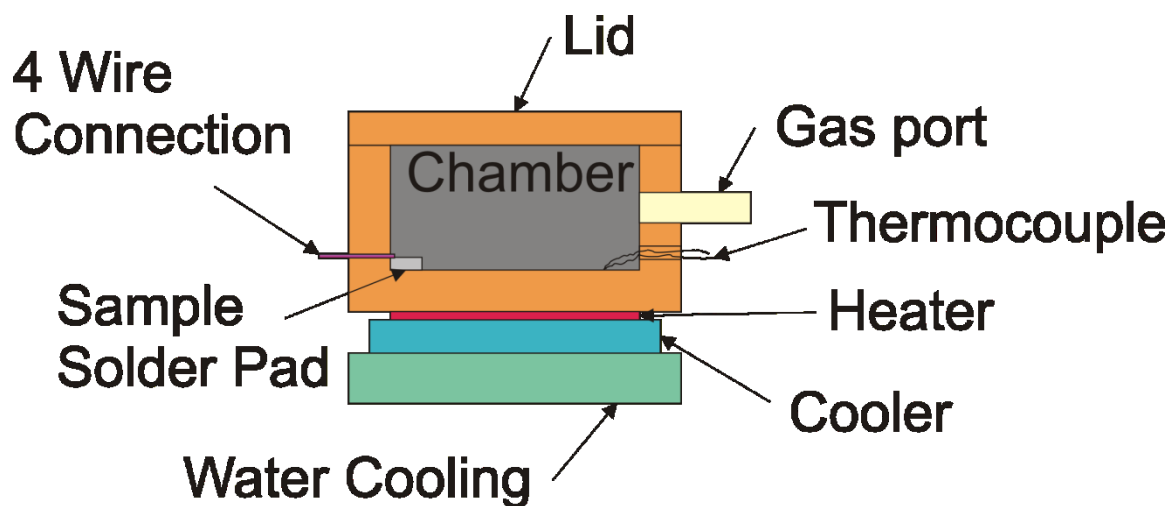


Figure 2-9. Sketch of the cross section of the sample stage. The temperature is controlled through the heaters and coolers. Dry gas is brought into the chamber to flush any moisture from the samples and environment. Sample leads are attached to the solder pads, and 4 wire connections lead to instruments.

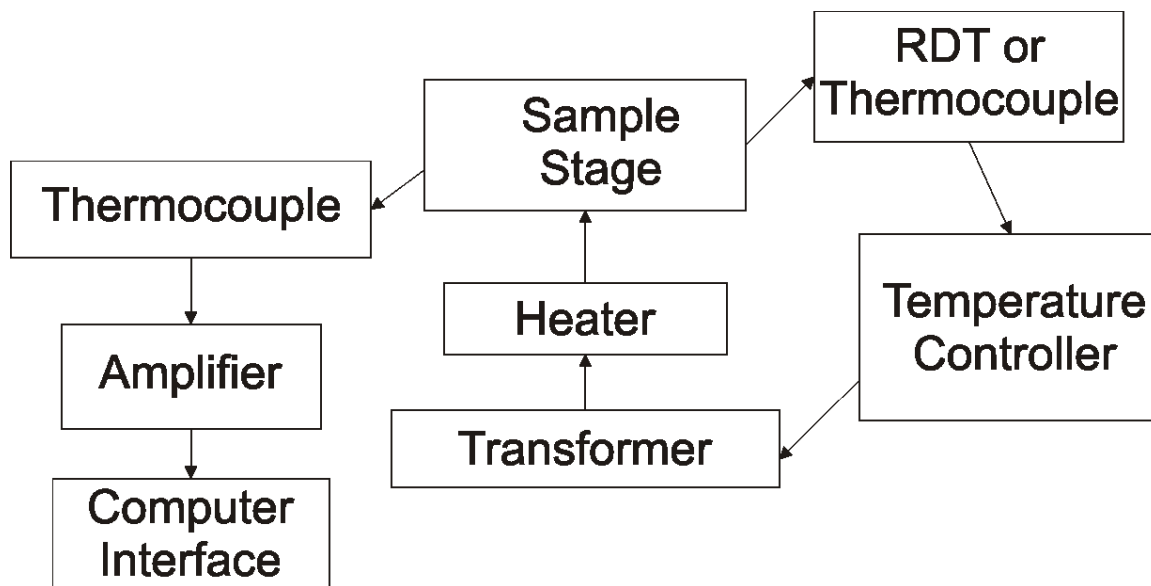


Figure 2-10. Sketch of temperature control feedback loops. The temperature is controlled by a microprocessor in the temperature controller. The output goes to transformer which reduces the voltage being applied to the heater. The heater will heat up the sample stage, and the temperature is measured by a RTD or thermocouple connected to the temperature controller. A second thermocouple measures the sample temperature. This current is amplified, and then recorded by a computer.

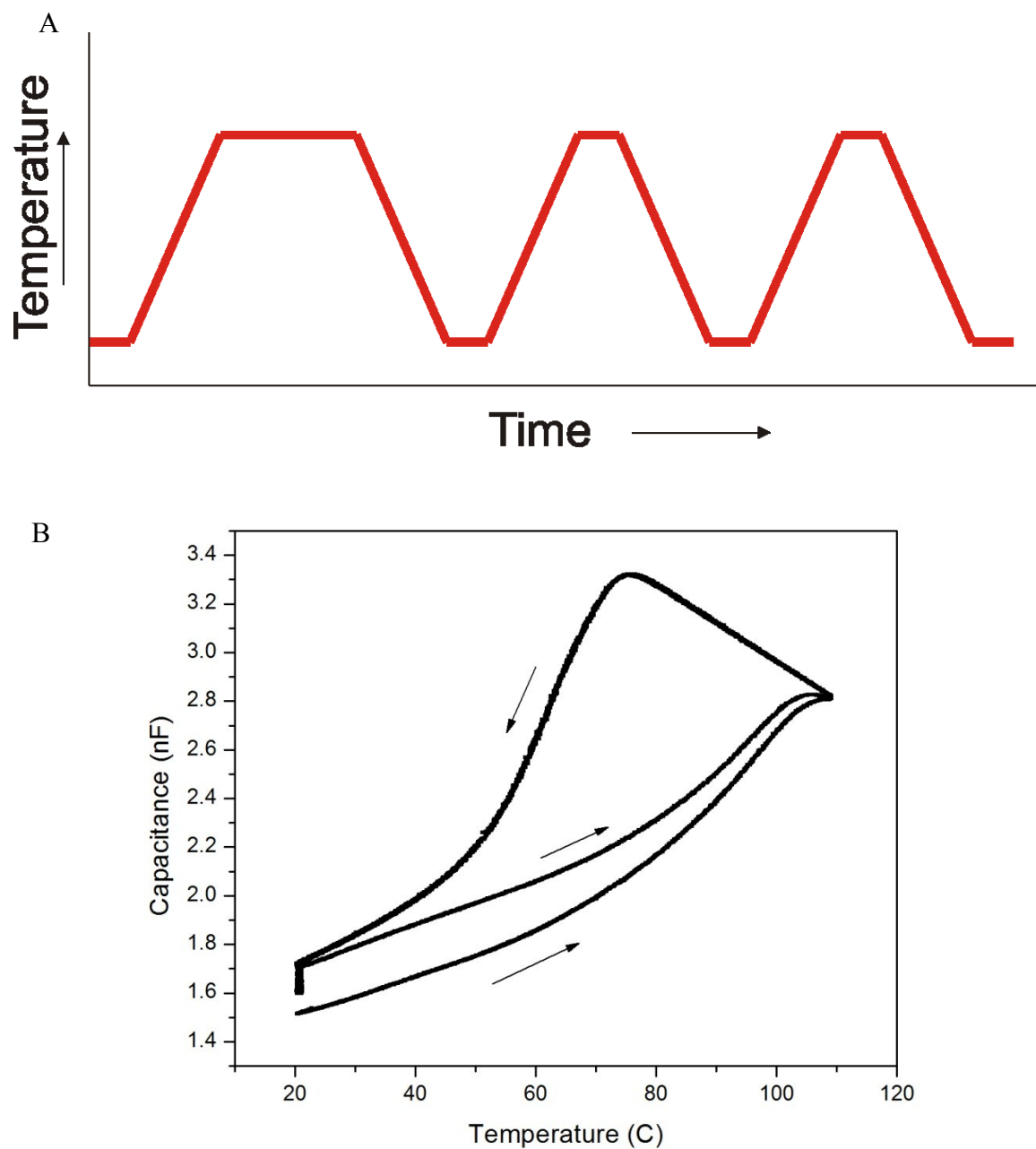


Figure 2-11. (A) Sketch of typical temperature profile versus time. (B) Example CT data for a 30 ML 70/30 PVDF-TrFe film. The peaks occur in heating and cooling at the phase transition between ferroelectric and paraelectric phases.

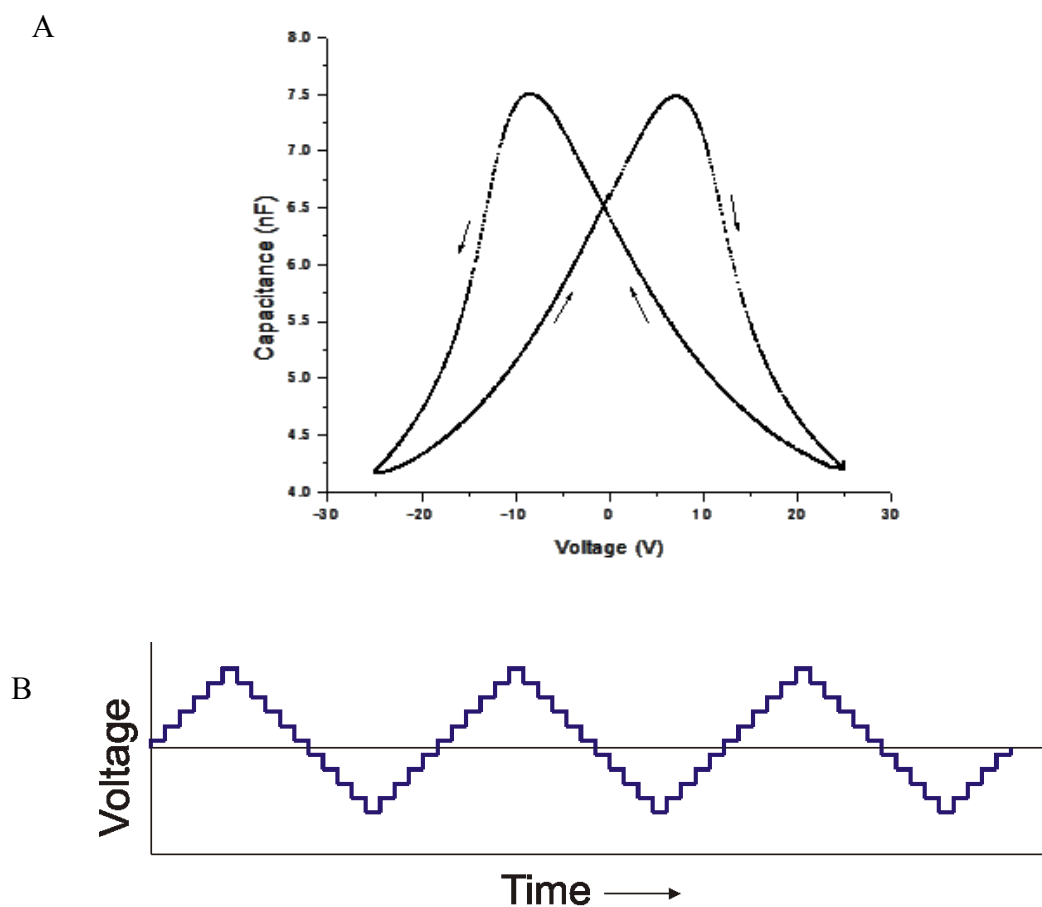


Figure 2-12. (A) Typical capacitance as a function of voltage curve (CV curve). Peaks appear in the capacitance when the polarization reverses. (B) A typical applied bias curve for CV scans. The bias is applied in a step-wise fashion, typically increasing by 0.1volts increments.

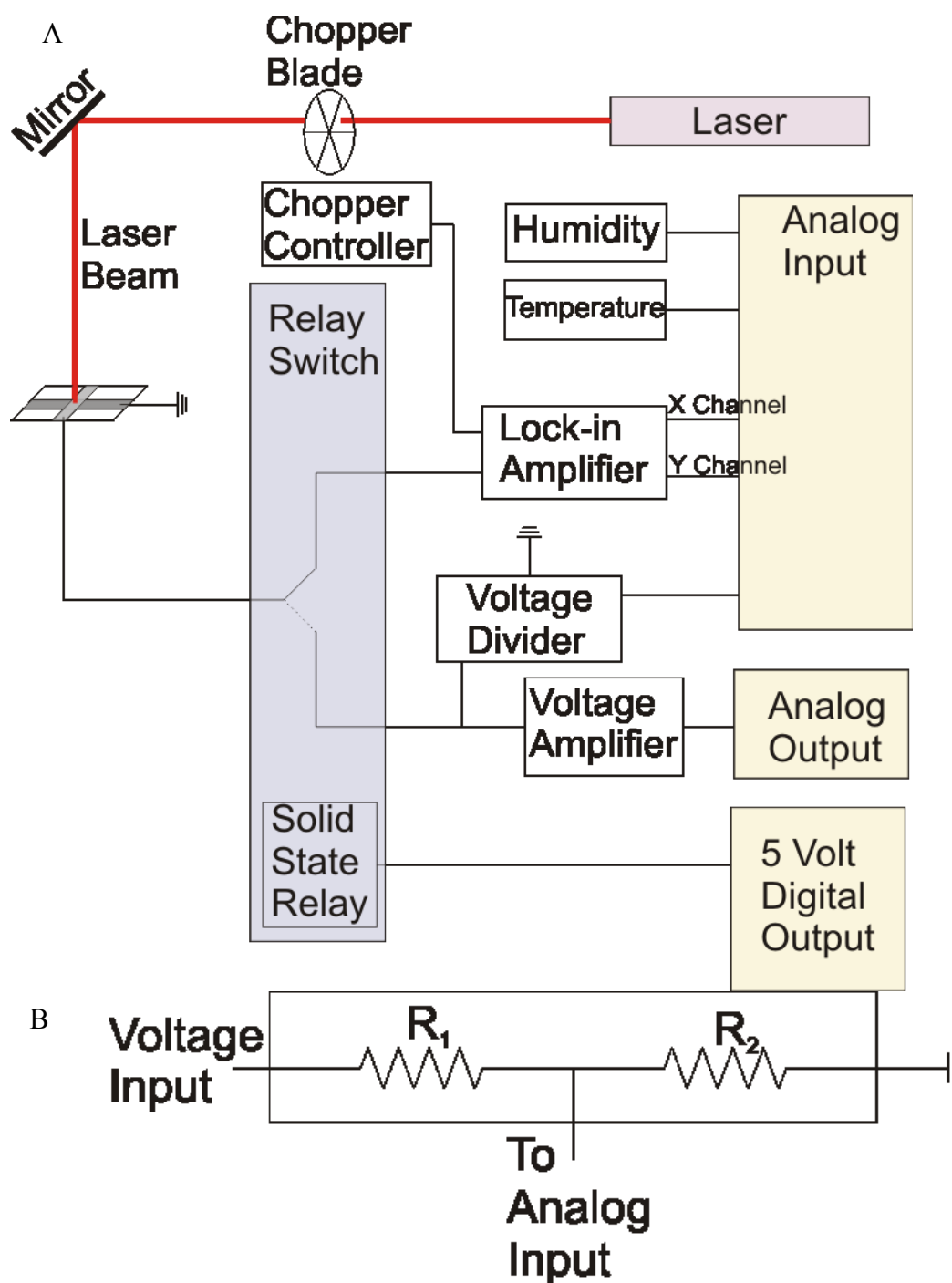


Figure 2-13. (A) Sketch of computerized pyroelectric apparatus. The sample is rapidly heated and cooled using a laser that is modulated with a chopper. The relay switch connects the sample first to a voltage source and then to the lockin amplifier to measure the pyroelectric current. (B) A voltage divider to reduce the signal to a safe level to be measured by the analog in on the computer.

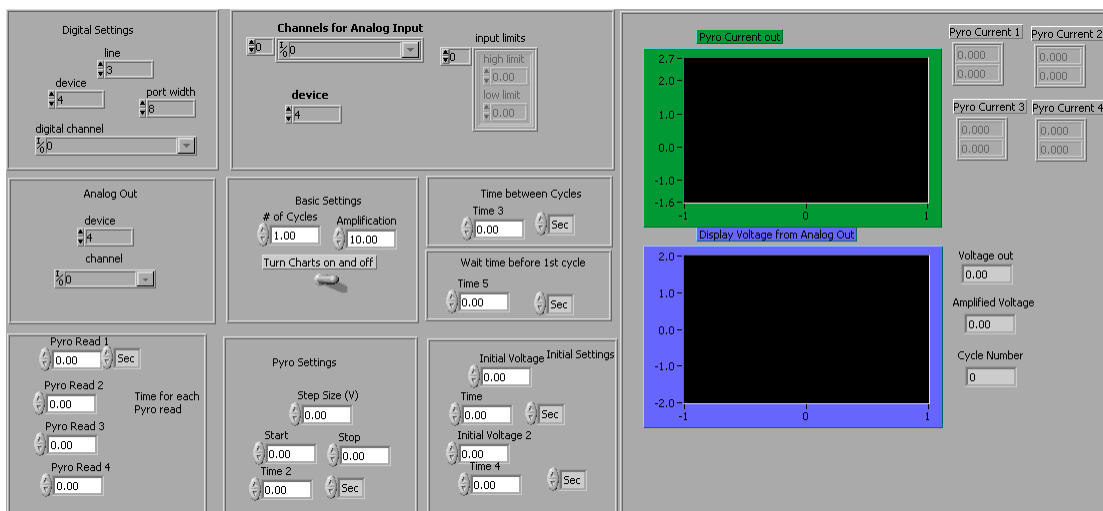


Figure 2-14. Front panel of the Labview VI to control the computerized pyroelectric experiment. This VI was originally written for the humidity project and was used for all of the other pyroelectric measurements.

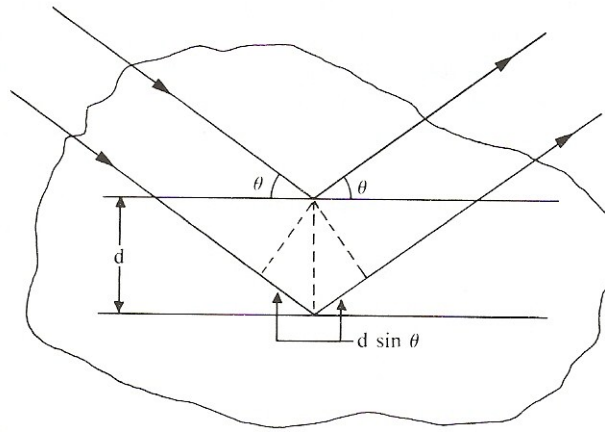


Figure 2-15. (A) Bragg scattering between planes of atoms or molecules. Constructive interference occurs when the difference in path length is an integer number of wave lengths.[32] This figure was published in *Solid state physics*, Blakemore, J.S., Copyright W.B. Saunders Co. (1985).

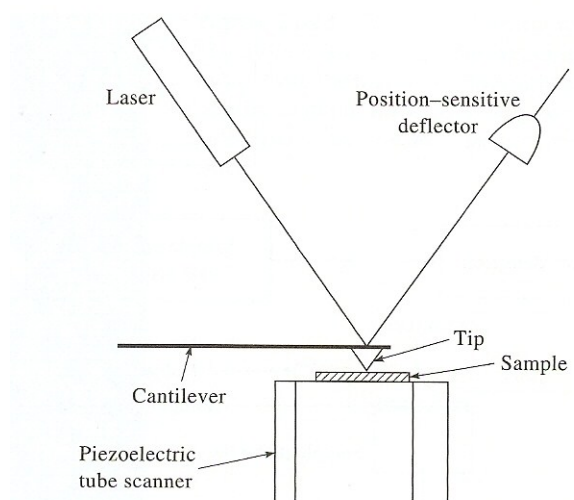


Figure 2-16. AFM setup. Detector system for an AFM.[34] This figure was published in *Principles of Instrumental Analysis*. 5 ed., Skoog, D.A., et al., Copyright Saunders College Publishing (1998).

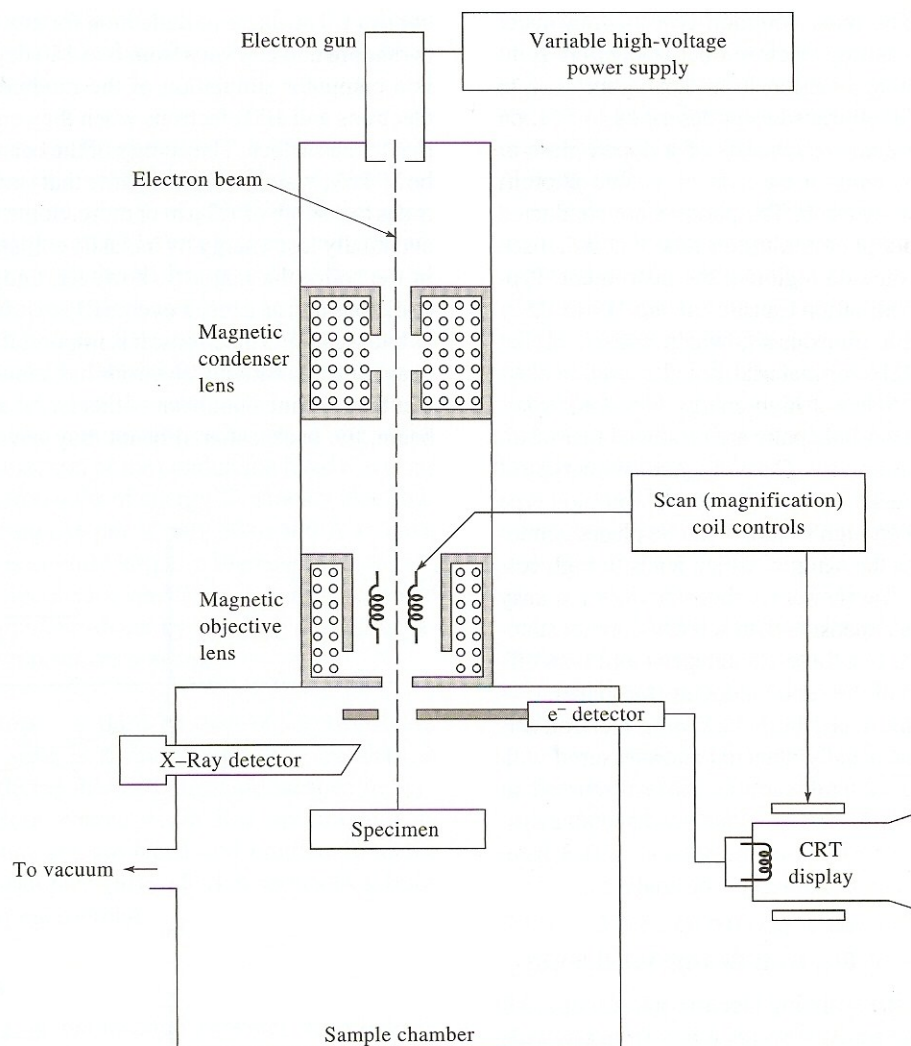


Figure 2-17. Sketch of SEM. [34] This figure was published in *Principles of Instrumental Analysis*. 5 ed., Skoog, D.A., et al., Copyright Saunders College Publishing (1998).

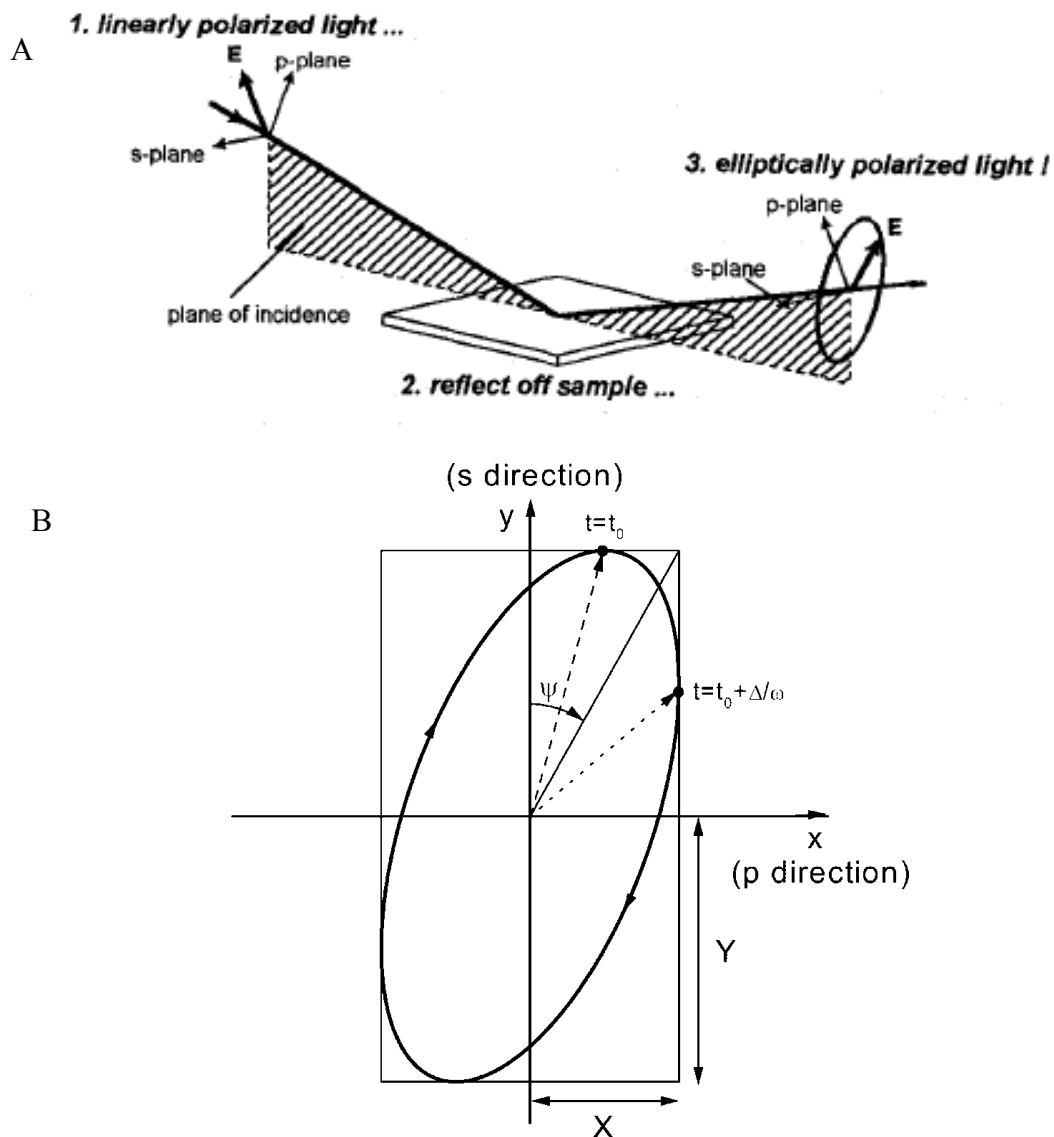


Figure 2-18. Ellipsometry Theory (A) Sketch of the interaction of linearly polarized light reflecting off of a sample. [35] This figure was published in *Overview of Variable Angle Spectroscopic Ellipsometry (VASE), Part I: Basic Theory and Typical Applications*, in *Optical metrology : proceedings of a conference held 18-19 July, 1999, Denver, Colorado*, Society of Photo-optical Instrumentation, Editors., Copyright SPIE Optical Engineering Press (1999). (B) The polarization axis in terms of  $\Psi$  and  $\Delta$ . The light propagates down the Z axis, which is pointing out of the page. [37] This figure was published in *Handbook of ellipsometry*. Copyright William Andrew Pub.; Springer (2005).

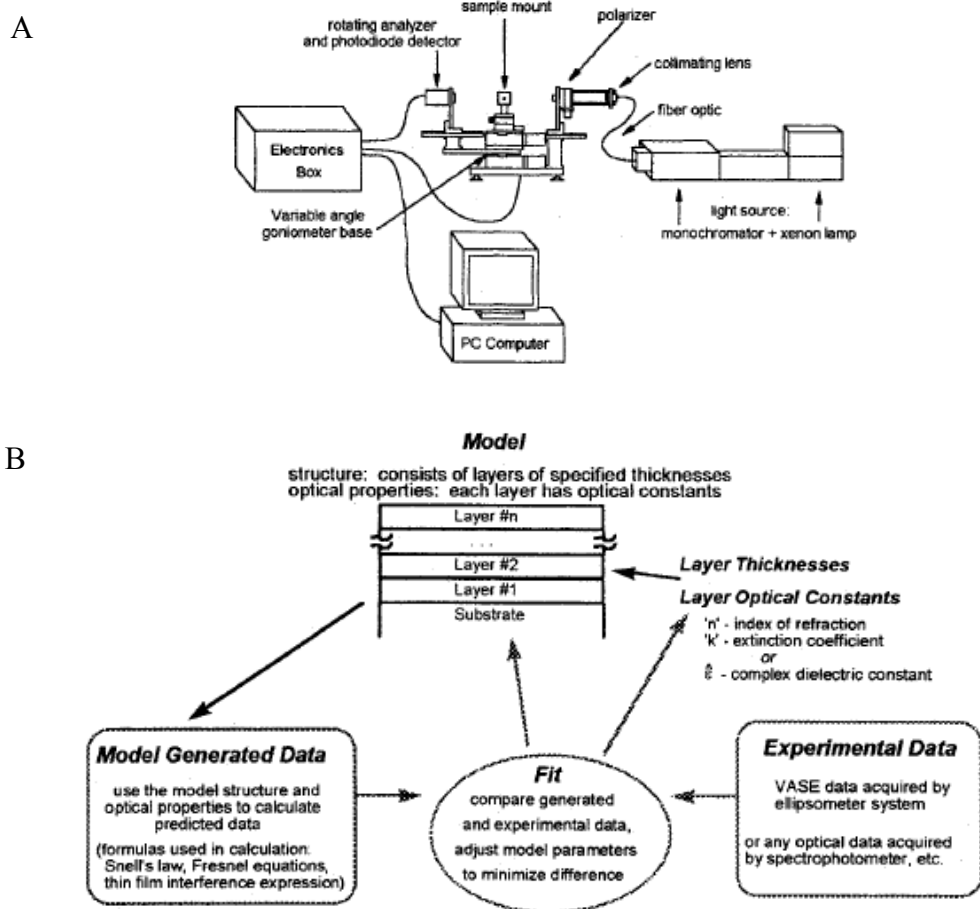


Figure 2-19. (A) Sketch of a rotating angle spectroscopic ellipsometer. The linearly polarized light reflects off of the sample and passes through a rotating polarizer before it enters the detector. (B) Flowmap of the procedure to model ellipsometry data.[35] This figure was published in *Overview of Variable Angle Spectroscopic Ellipsometry (VASE), Part I: Basic Theory and Typical Applications*, in *Optical metrology : proceedings of a conference held 18-19 July, 1999, Denver, Colorado*, Society of Photo-optical Instrumentation, Editors., Copyright SPIE Optical Engineering Press (1999).

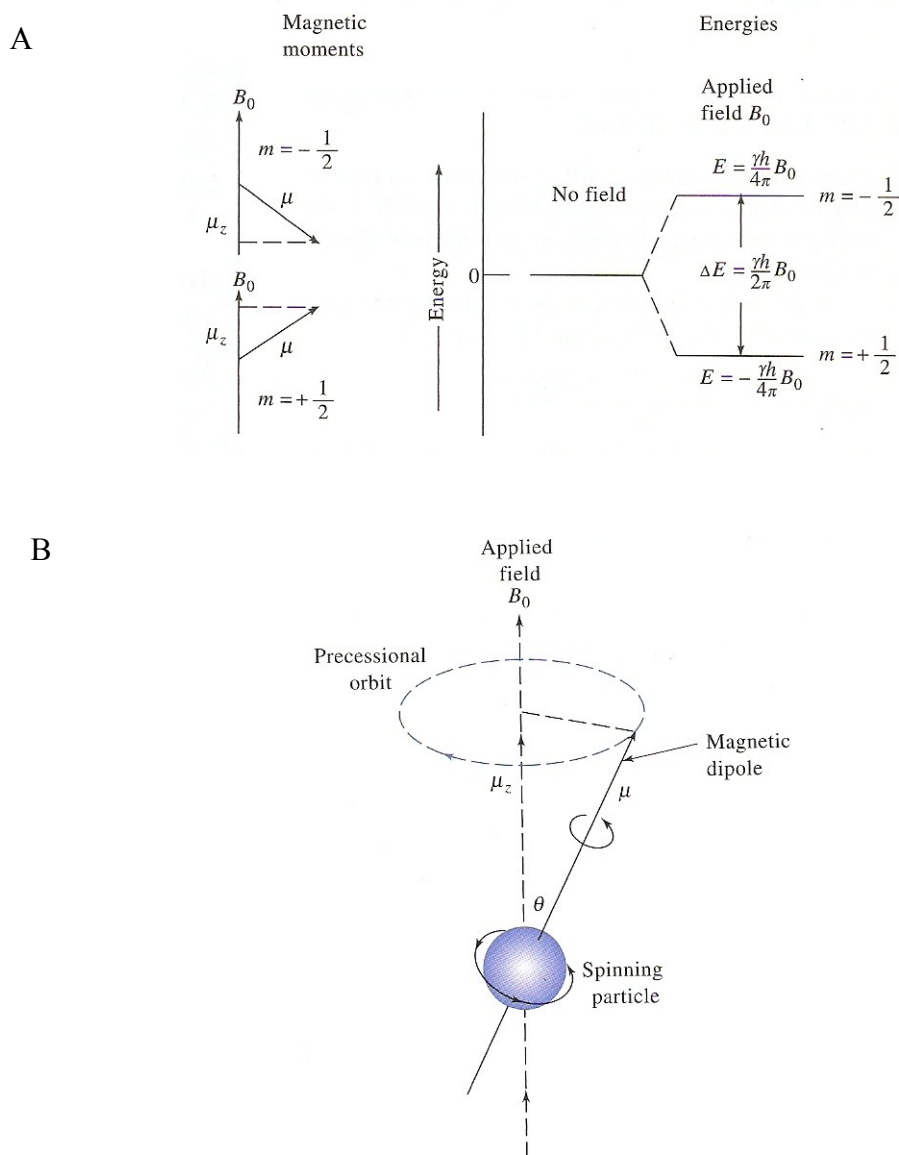


Figure 2-20. (A) Nucleus with different spins are at the same energy level in the absence of a magnetic field. When in a magnetic field, the energy splits into two levels. (B) The applied magnetic field causes the nucleus to start to precess.[34] This figure was published in *Principles of Instrumental Analysis*. 5 ed., Skoog, D.A., et al., Copyright Saunders College Publishing (1998).

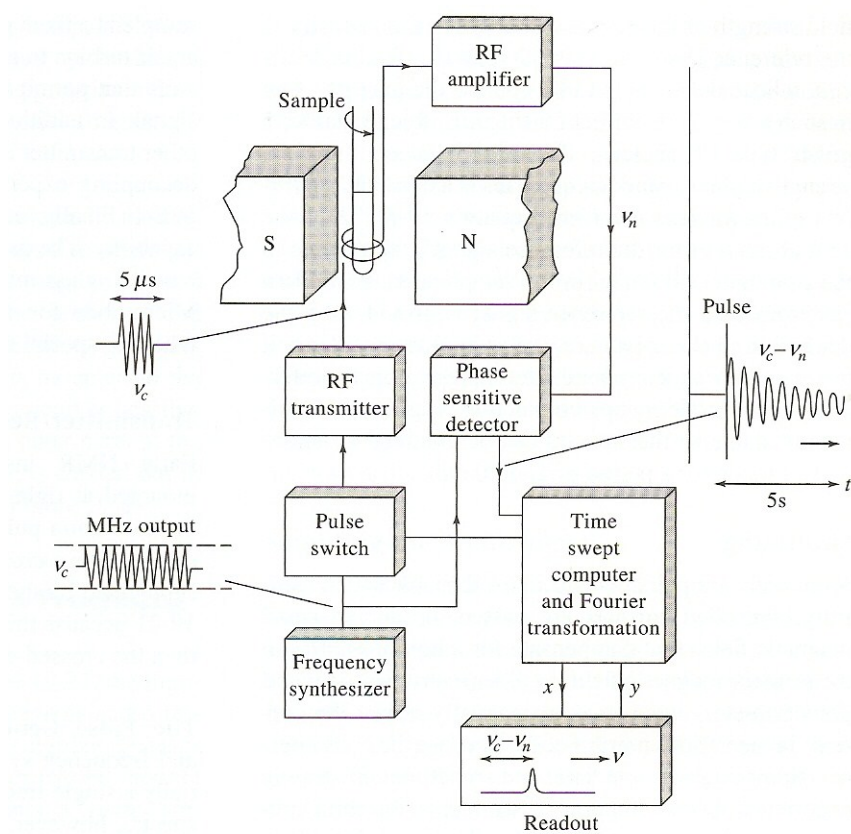


Figure 2-21. NMR Typical Data. Block diagram of typical NMR system.[34] This figure was published in *Principles of Instrumental Analysis*. 5 ed., Skoog, D.A., et al., Copyright Saunders College Publishing (1998).

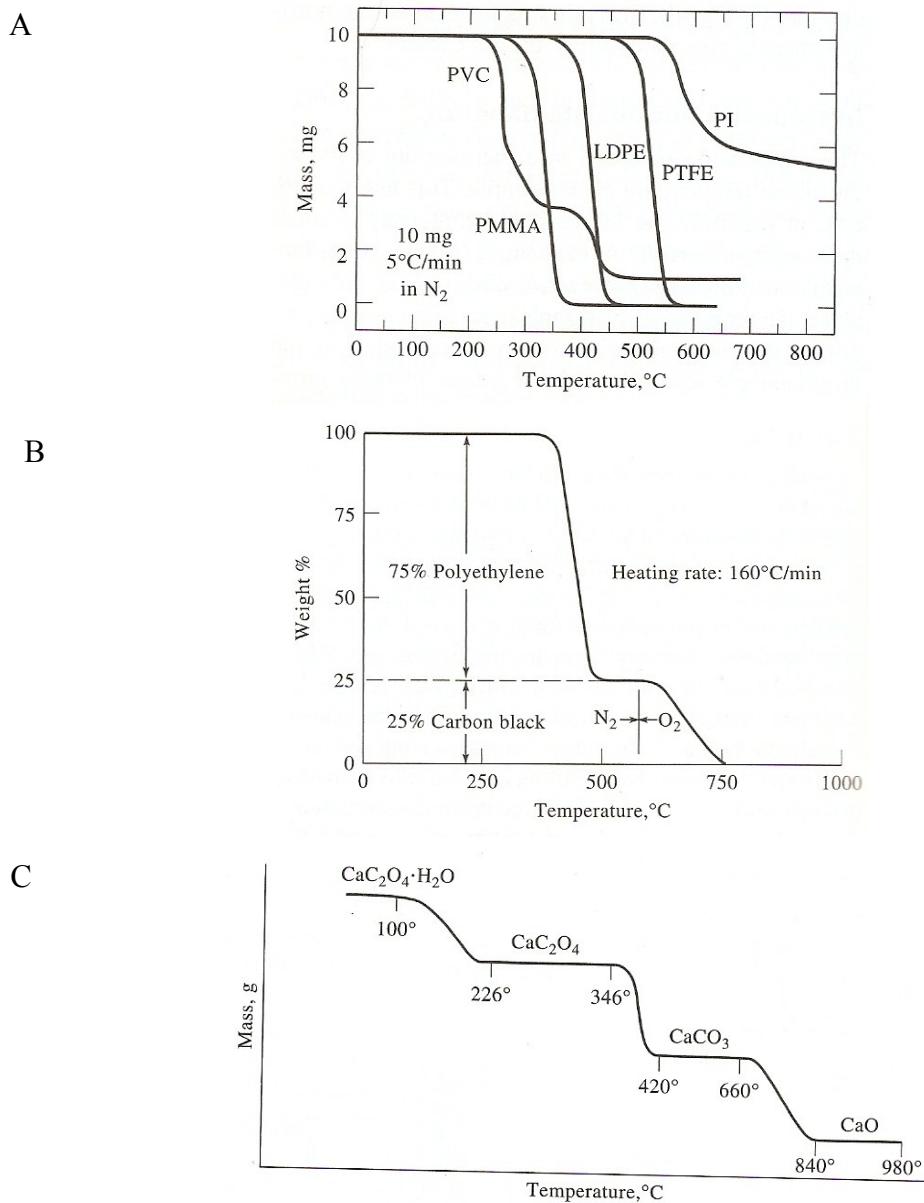


Figure 2-22. TGA Applications (A) Different compositions of polymers will give different shaped curves. This allows one to compare the characteristic decomposition curves.[34] (B) TGA allows one to compare ratio of composite materials based on different decomposition temperatures. In this example, the composite is 75% polyethylene and 25% carbon black.[34] (C) One can also look at the decomposition curve of a single material. In the case of  $\text{CaC}_2\text{O}_4 \cdot \text{H}_2\text{O}$ , each time part of the molecule decomposes, there is a decrease in mass.[34] These figures were published in *Principles of Instrumental Analysis*. 5 ed., Skoog, D.A., et al., Copyright Saunders College Publishing (1998).

## CHAPTER 3

### VINYLIDINE FLUORIDE OLIGOMERS

#### 3.1 Introduction to Oligomers

Poly(vinylidene fluoride) or PVDF polymers and copolymers are used in many different applications. One of the difficulties in large scale use of PVDF is obtaining highly crystalline films over large areas. By using VDF oligomers instead of polymers, it has been shown to obtain high crystallinity films through processes such as thermal evaporation [1-4]. The VDF monomer is one unit of  $(\text{CH}_2\text{CF}_2)$ . Polymer chain contains many thousand such monomers. This makes it difficult to control the exact placement of the polymer and to obtain high levels of crystallinity. Figure 3-1A shows a small section of PVDF polymer. An oligomer contains several up to a few dozen monomer units, such as shown Figure 3-1B. The structure of an oligomer can be divided into two parts. The section with the VDF units is the tail. At one end of the oligomer is the head or end group. For the VDF oligomers, iodine is the typical end group, although it can be removed and other functional groups such as thiols or phosphoric acid can be added [5].

Previously, ferroelectricity has been shown in oligomers deposited by vacuum evaporation on substrates close to liquid nitrogen temperatures [1, 3, 4]. In the studies in this chapter, films were deposited at or above room temperature and measurements were made on the dielectric and ferroelectric properties. Three types of samples were made: Langmuir-Blodgett films, capillary cell films, and evaporated thin films. In addition, other properties such as melting point of the oligomers were measured.

### 3.2 Basic Properties of Oligomers

Several basic properties of the VDF oligomers used in this thesis were investigated. The first was the melting point of the oligomers. The second was to verify the structure and to confirm the functional groups using NMR. The NMR results are discussed in Chapter 5 along with the coating of nanoparticles with functionalized coatings.

#### 3.2.A *Melting Temperature of the VDF Oligomers*

It was desirable to know the melting point of the oligomers for several applications such as making capillary cells, evaporating films, and being able to anneal the films without melting. The melting point was measured by heating the oligomers under a microscope and observing the onset of melting. A circular Mylar heater with a hole in the center was mounted between two glass plates, as shown in Figure 3-2. To protect the microscope stage from the heat, a Teflon block was placed under the heater plate. In the center of the block, was another hole to allow the transmission of light. The heater was connected to a variable transformer which provided the power for the heater. A thermocouple was mounted onto the top plate near the oligomer to be melted and the thermocouple's current was read with a Keithley digital multimeter.

The transformer's voltage was slowly increased and the stage was allowed to reach a steady temperature before the voltage was increased again. As the temperature increased, the oligomer was observed through the microscope of signs of melting, usually first occurring along the edge of a cluster or flake of oligomer, or in an isolated portion of powder. The temperature where the melting was first observed was recorded.

The results of the melting experiments for oligomers containing 6 to 18 VDF units with an iodine end group are shown in Figure 3-3. The resulting data was surprisingly linear for this length of oligomers and had a slope of 5.33 °C per VDF unit. As the oligomers increase in length, the melting point should eventually reach the temperature of bulk PVDF which is 177 °C [6].

### **3.3 Oligomer Langmuir-Blodgett Films**

While P(VDF-TrFe) copolymers are not traditional Langmuir materials with a hydrophobic and hydrophilic region of the polymer, there has been a substantial amount of work done on Langmuir-Blodgett films with the copolymer [7-9]. It was desirable to understand how the VDF oligomers would behave on the trough and to make samples with the Langmuir layers. Basic dielectric properties such as the effect of temperature and applied voltage on the capacitance were also measured.

#### *3.3.A Langmuir Isotherms of VDF Oligomers*

Studies were made of several different compositions of VDF oligomers. The first isotherm study was of VDF oligomers purchased from Kunshan Hisense Company with 17 units of VDF and an iodine end group. The oligomers were dissolved in three solvents: DMSO, acetone, and DMF. Since the solvents had different densities, the standard concentration for DMSO (0.05% by weight) was converted to molarity (0.4 mM). This concentration was used for measurements so there would be the same amount of oligomer deposited onto the trough each time. Figure 3-4 shows the results of the isotherms. Figure 3-4A & B were the oligomer in DMSO. The first figure had 250  $\mu$ L dispersed on the trough and the second had 500  $\mu$ L of solution dispersed. Figure 3-4C

had 250  $\mu\text{L}$  of solution with DMF as the solvent dispersed, while Figure 3-4D was 250  $\mu\text{L}$  of oligomer solution in acetone. All of the isotherms show the same general shaped curves, regardless of solvents. Each one starts with a horizontal gas phase until approximately 1 mN/m. Then, the slope increases and the pressure increases linearly until about 10 mN/m, where the slope rapidly increases. For some of the isotherm, this final phase was barely reached before running out area to compress on the trough.

The next series of samples contains two oligomers with iodine end groups and one oligomer with a phosphonic acid end group. The oligomers were chosen for studies due to the potential ferroelectric phase being found in the iodine ended oligomers in differential scanning calorimetry [10] and IR spectroscopy calculations and measurements [11]. Two oligomers had an iodine end group and a tail of 18 VDF units, or 25 units. The third oligomer was 20 VDF units long and had a phosphonic acid functional group. All of the oligomers were in a 0.05% by weight solution. The iodine functionalized oligomers were made with DMSO as the solvent; the oligomer with the phosphonic acid functional group used butanone for the solvent. The solvent for the phosphonic acid functionalized oligomer solution was different than the other two since the isotherm was being measured to compare it to coated nanoparticle isotherms. As shown in Figure 3-4, the solvent did not change the shape of the isotherms. The two isotherms of the iodine ended oligomers (Figure 3-5A & B) showed a gradual increase in the pressure as the area decreased. It did not show the sharp changes in slope at 10 mN/m that were present in the first series of isotherms. The third oligomer with the phosphonic acid functional group had an isotherm which did not increase in pressure for most of the compression, and then abruptly increased in pressure without having the

gradual increase in pressure as was typical with PVDF polymers and iodine functionalized oligomers(Figure 3-5C).

The Langmuir film was further studied by examining the several isotherm cycles, as shown in Figure 3-6. This isotherm was for an 18 unit VDF oligomer with an iodine end group that was in Figure 3-5A. The first isotherm cycle showed the gradual increment in pressure that was seen in Figure 3-5. Each expansion cycle showed only a slight increase in area at zero pressure. By the third and fourth cycles, the area at 30 mN/m was the same, although it expanded less on decompression each time.

### *3.3.B Deposition of Langmuir-Blodgett Oligomer Films*

Oligomer LB films were deposited onto substrates for dielectric measurements with two techniques: Y-dipping and Schaefer technique. Y-dipping was when the substrate was dipped vertically into the trough and removed on the same side with the surface film. In an ideal amphiphile, this will create a bilayer. As can be seen in Figure 3-7, the oligomer did not attach well to the substrate. The total area decrease for the surface of the trough for a 20 mL should have been 250 cm<sup>2</sup>. Instead, 15 cm<sup>2</sup> of area was lost.

Next, samples were deposited using Schaefer deposition. With this deposition, the substrate touches the surface of the water horizontally and picks up one layer of materials. Figure 3-8 shows the area lost from the surface of the trough each time a layer was transferred. The substrate had an area of 6.2 cm<sup>2</sup>. Each transfer had an average area of 5.7 cm<sup>2</sup>. Several trends can be observed in the data. First, the original five transfers resulted in little area lost. This was further corroborated by the observation that it took 5

or 6 depositions before layers transferred to the substrate without leaving large water droplets behind. The second observation was that later layers either lost much more than the 6 cm<sup>2</sup> or they lost very little area. This may have been caused by the film not fully compressing after layer, causing some compressions to lose the area of several previous depositions.

### *3.3.C Dielectric Results of Oligomer Langmuir Blodgett Films*

Langmuir-Blodgett films were made with 18 and 25 unit VDF oligomers with iodine end groups. Figure 3-9 and Figure 3-10 show results from two typical 18 unit VDF oligomers samples with 20 ML deposited at 10 mN/m. Figure 3-9A and Figure 3-10A show the temperature dependence of on capacitance which both films show an initial increase in capacitance. None of the oligomer films showed the dielectric maximum typical of PVDF and its copolymers as it switches phases from ferroelectric to paraelectric. After the first temperature cycle, there was no hysteresis present although the capacitance increased by about 20% from the lowest temperature to the highest temperature.

The voltage dependence on the capacitance showed “butterfly” curves with open loops and switching voltages between 3-4 volts. The tail of the curve was close to saturated in Figure 3-9B. In Figure 3-10B, the butterfly loop was open and repeatable with clear signs of switching but was not as close to saturated. Figure 3-10C shows the frequency dependence of the capacitance. The capacitance was horizontal until it read almost 100 kHz, then it started to decrease as was typical at higher frequencies. Figure 3-10D shows a Cole-Cole plot for this sample. In a Cole-Cole plot, the imaginary part of

the dielectric is plotted against the real part of the dielectric. When a single relaxation time is present in the material, the data would make half circle centered on the real dielectric constant axis [12]. In Figure 3-10D, the Cole-Cole plot a semi-circle with the center shifted below the x-axis. This signified a distribution of relaxation times, similar to measurements on a 70:30 copolymer [12].

The temperature dependence of the capacitance for the 25 unit VDF oligomers is shown in Figure 3-11. Similar to the 18 unit VDF oligomer, there was no sign of a phase transition between the ferroelectric and paraelectric phase. After the first annealing cycle there was no temperature hysteresis with further cycling.

Figure 3-12 shows a series of samples made at increasing surface pressure on the trough. Figure 3-12A & B were deposited at 20 mV/m, and Figure 3-12C & D were deposited at 25 mN/m. As the surface pressure increased, the butterfly curves showed a decreased in polarization. By 25 mN/m (Figure 3-12C), after the initial positive increase in voltage, the loops were nearly flat with no evidence of switching. The frequency dependence on the capacitance for films made over the range of pressures were all very similar. The capacitance stayed nearly horizontal until well after 100 kHz.

### **3.4 Capillary Cells**

#### *3.4.A Sample Fabrication of Capillary Cells*

Capillary cells were made with two pieces of indium tin oxide (ITO) coated glass. The coated surfaces of the glass face towards each with a thin spacer to keep the pieces of glass from touching (Figure 3-13). One piece of ITO glass was etched using the procedure described in Chapter 2. The pattern etched depended on the configuration of

the spacers, so only the oligomers dielectric was measured and not the contribution from the spacers. The spacers were made of either Mylar sheets (typically 12  $\mu\text{M}$  thick) or coverslip glass. The cell was first assembled with binder clips holding it together until the adhesive could dry. Typical adhesives used were JB Weld, Amazine E-6000, and Power Poxy- Proseries. The important parts of the adhesive selection were that they were rated to temperatures of at least 200  $^{\circ}\text{C}$  and that the adhesive was rigid when it dried.

Once the adhesive had dried, the capillary cells were ready to be filled with oligomers. The substrates were placed on a strip heater (Figure 3-14A). The heater regulated by an Omega temperature controller with a resistive temperature device (RTD) measuring the temperature. The heater stood on ceramic legs to insulate it from the ground (Figure 3-14B). Depending on the melting point of the oligomer, it was necessary to insulate the heater from the surrounding air with foil in some cases.

A small amount of oligomer was placed at one opening of the capillary cell. (Figure 3-14C). As the oligomer melted, the capillary forces drew the oligomer between the two ITO plates (Figure 3-14D). It was important that the cells were constructed in a way that the air could exit the cell, as trapped air created defects in the film. Ideally, future cells would be filled in a vacuum oven, preventing many complications from air. Figure 3-15 shows several actual filled cells. Air bubbles are visible in the sample shown in Figure 3-15A.

### *3.4.B Capillary Cell Dielectric Results*

Results for the capillary cells are shown in Figure 3-16. The temperature dependence of the capacitance is shown in Figure 3-16A. The melting point for the 12

VDF unit oligomers was around 83 °C. The temperature scan went past the melting point as can be seen by the large increase in capacitance. The inset shows the low temperature data. There was very slight hysteresis below the melting point with no evidence of the typical dielectric maxima that correspond to the phase changes.

The voltage dependence of the capacitance for a 6 unit VDF oligomer sample is shown in Figure 3-16B. The general shape of the curve was typical for all of the capillary cell samples. Samples showed decay in the capacitance value each cycle. While most samples showed dielectric maxima with increasing voltage, the samples were unable to withstand the needed voltages to saturate the polarization.

### **3.5 Evaporated VDF Samples**

The evaporated thin films were deposited in the vacuum cluster deposition system, as describe in [13]. A crucible containing 17 unit VDF from Kunshan Hisense Company was resistively heated and evaporated onto a substrate. The substrate was mounted above the oligomer source, in substrate location 1, shown in Figure 3-17. Images of the sample before and after annealing are shown in Figure 3-18. The pre-anneal image (Figure 3-18A) shows a thick film with the center of the deposition at the lower right corner. Annealing the film caused the film to spread and re-arrange over the entire substrate. The post-anneal film was about 100 nm thick, approximately 5 times thinner than the original film.

The temperature dependence of the capacitance is shown in Figure 3-19. The initial temperature cycle is shown in red, while the next two are shown in black. During the first anneal, the oligomers softened enough to rearrange on the surface of the

substrate. The increase in capacitance at low temperatures between the first and second heating cycle was likely the result of a thinner film, as supported by the photographs in Figure 3-18. At approximately 75 °C, there was a sharp increase in the capacitance. This was well below the expected melting point of 100 °C for a 17 unit VDF oligomer, and we were unable to resolve why this oligomer had a much lower melting point than the other VDF oligomers with an iodine end group which were synthesized locally.

The voltage dependence of the capacitance is shown in Figure 3-20. Before annealing, there was no evidence of ferroelectricity with applied voltages up to 32 V. After annealing, there were maxima in the dielectric peaks as the voltage was cycled to positive and negative values. The drawback to this sample was that the capacitance decayed with each cycle. The final set of data for the evaporated thin film was a pyroelectric hysteresis curve, shown in Figure 3-21. The hysteresis loop showed stable polarization as the pyroelectric current remained constant from saturation until 8 volts was applied in the opposite direction. There was very little decrease in current until switching occurred.

### **3.6 Conclusion**

VDF oligomers have many applications in thin films. The oligomer melting point increased by 5 °C per VDF unit, up to 18 VDF units, for oligomers with iodine functional groups. The oligomers can be melted into capillary cells for dielectric measurements. These cells had difficulties with stability, and we believe that fabricating the films in a vacuum oven would resolve many of the issues.

The VDF oligomers were also used in Langmuir-Blodgett thin films. The oligomer isotherms behaved similarly for solutions containing acetone, DMF, and DMSO, but did not always show the same characteristics on the trough for oligomers from different synthesis batches and lengths. Capacitor samples with 18 units of VDF deposited at 10 mN/m had butterfly curves with evidence of switching. The 25 unit VDF oligomers deposited at higher pressures showed little or no switching and the cycles were not stable. Finally, oligomer films were evaporated at room temperature. After annealing, the sample showed a degrading butterfly curve with evidence of switching, and a stable pyroelectric hysteresis loop.

### 3.7 References

1. Noda, K., et al., *Remanent polarization of evaporated films of vinylidene fluoride oligomers*. Journal of applied physics, 2003. **93**(5): p. 5.
2. Uno, T., et al., *Effect of molecular weight and chain end groups on crystal forms of poly (vinylidene fluoride) oligomers*. Polymer, 1997. **38**(7): p. 1677-1683.
3. Xu, H., et al., *The preparation and ferroelectric properties of defect-free ultrathin films of vinylidene fluoride oligomer*. Journal of Applied Physics, 2010. **107**(3): p. 034101-034101-5.
4. Kuwajima, S., et al., *Crystal and Layer Structures of Ferroelectric Oligomer Thin Films*. Macromolecules, 2009. **42**(9): p. 3353-3357.
5. Ameduri, B., *From Vinylidene Fluoride (VDF) to the Applications of VDF-Containing Polymers and Copolymers: Recent Developments and Future Trends* Chemical Reviews, 2009. **109**(12): p. 6632-6686.
6. Koga, K. and H. Ohigashi, *Piezoelectricity and related properties of vinylidene fluoride and trifluoroethylene copolymers*. Journal of Applied Physics, 1986. **59**(6): p. 2142-2150.
7. Bune, A.V. and C. Zhu, *Piezoelectric and pyroelectric properties of ferroelectric Langmuir-Blodgett polymer films*. Journal of Applied Physics, 1999. **85**(11): p. 7869.
8. Palto, S., et al., *Ferroelectric Langmuir-Blodgett films*. Ferroelectrics Letters Section, 1995. **19**(3-4): p. 65-68.
9. Tadros-Morgane, R. and H. Kliem, *Polarization curves of Langmuir-Blodgett PVDF-copolymer films*. Journal of Physics D: Applied Physics, 2006. **39**(22): p. 4872.
10. Korlacki, R., et al., *Oligo (vinylidene fluoride) Langmuir-Blodgett films studied by spectroscopic ellipsometry and the density functional theory*. The Journal of Chemical Physics, 2008. **129**: p. 064704.
11. Nakhmanson, S.M., et al., *Vibrational properties of ferroelectric  $\beta$ -vinylidene fluoride polymers and oligomers*. Physical Review B, 2010. **81**(17): p. 174120.
12. Ducharme, S. and M. Jogad, *Dielectric properties of a ferroelectric copolymer Langmuir-Blodgett film*. Current Science, 2002. **83**(4): p. 5.

13. Balasubramanian, B., et al., *Cluster synthesis of monodisperse rutile-TiO<sub>2</sub> nanoparticles and dielectric TiO<sub>2</sub>-vinylidene fluoride oligomer nanocomposites*. Nanotechnology, 2011. **22**(40): p. 405605.

### 3.8 Figures

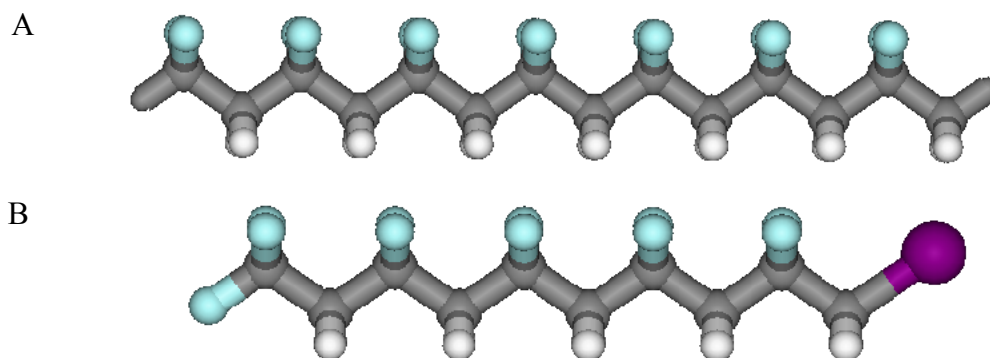


Figure 3-1. Poly(vinylidene fluoride) (A) polymers and (B) oligomers. The oligomers have a VDF tail and a head group such as iodine or phosphonic acid.

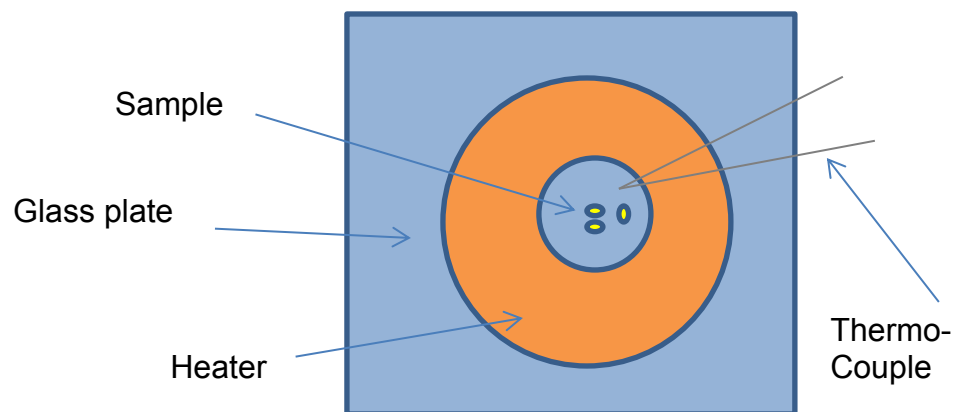


Figure 3-2. Sketch of the oligomer melting point experiment setup. The heater plate was placed on a microscope stage to observe the onset of melting of the oligomers.

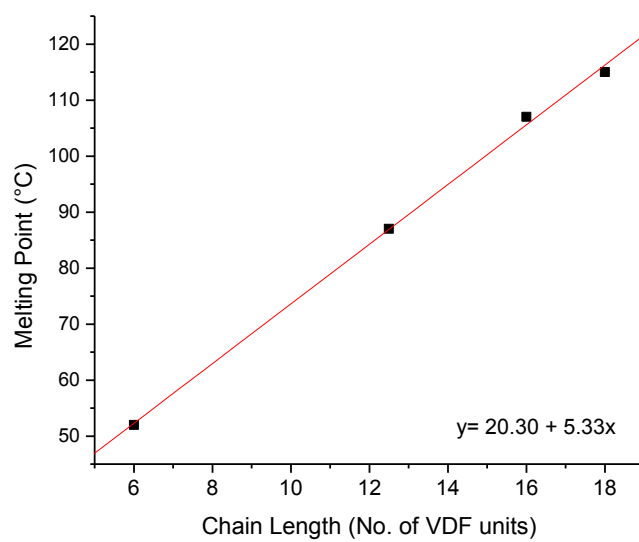


Figure 3-3. Melting point of VDF oligomers.

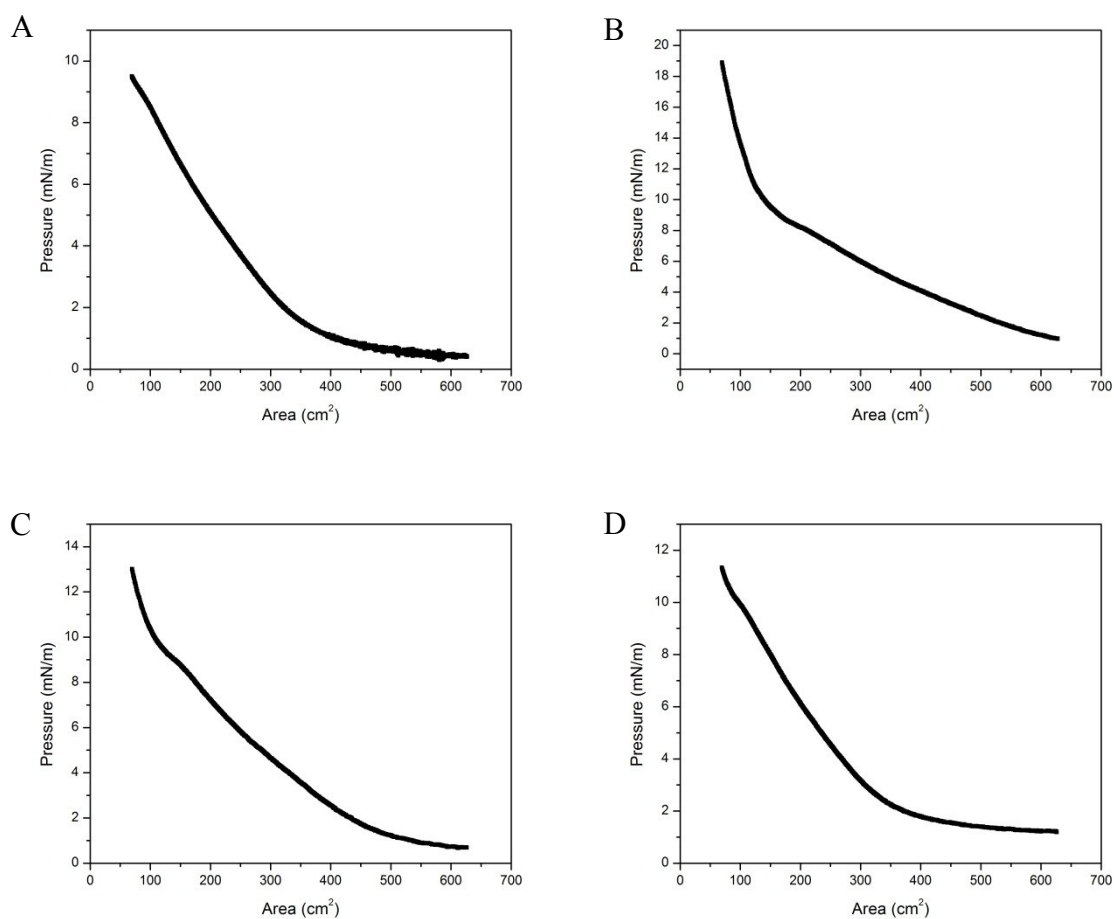


Figure 3-4. Isotherms for 17 unit VDF oligomer from Kunshan Hisense Company in (A) DMSO at low trough loading, (B) DMSO at higher trough loading, (C) in DMF, and (D) in acetone. All sample concentrations were 0.4 mM and 225  $\mu$ L of solution was loaded onto the trough each time, except for (B) where 500  $\mu$ L was used.

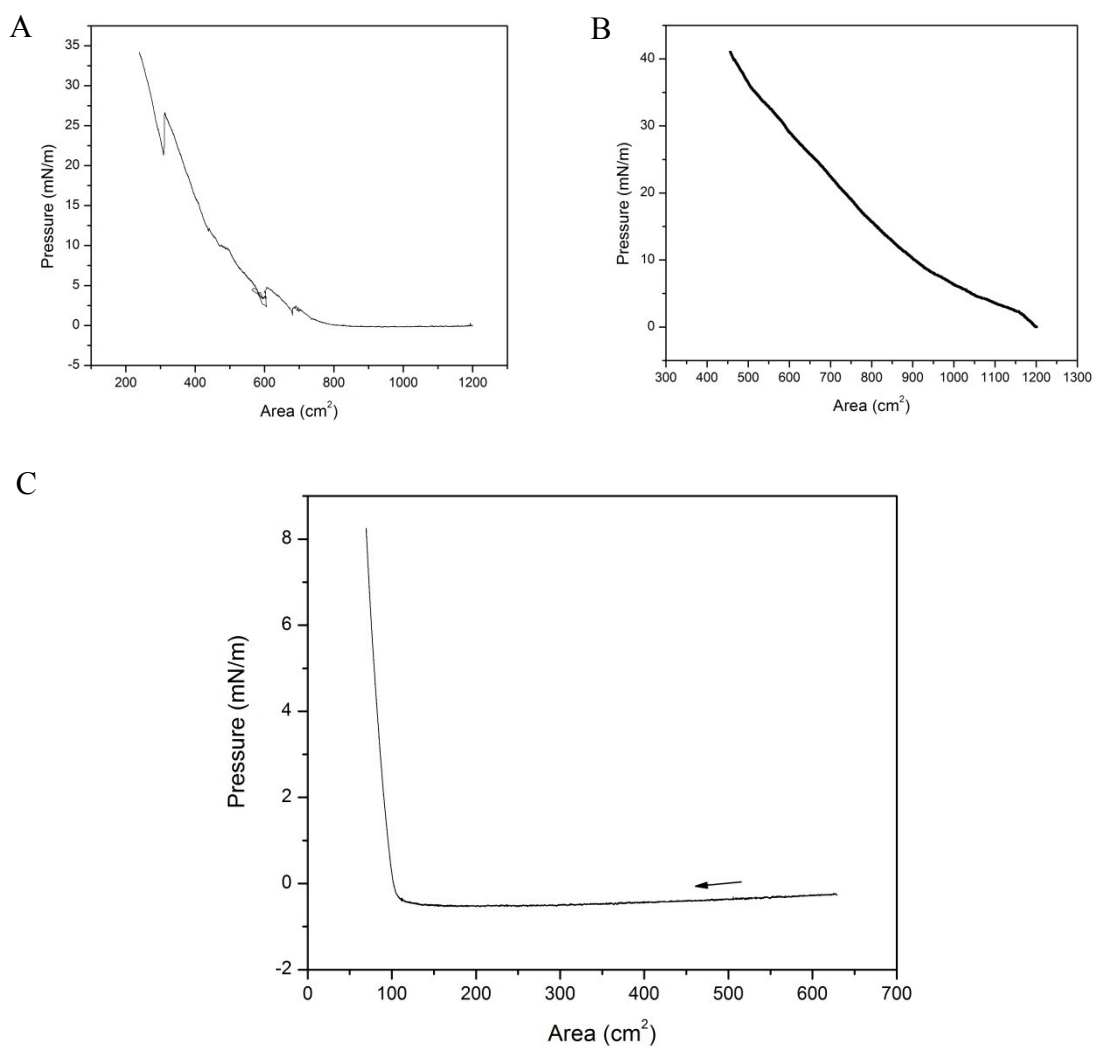
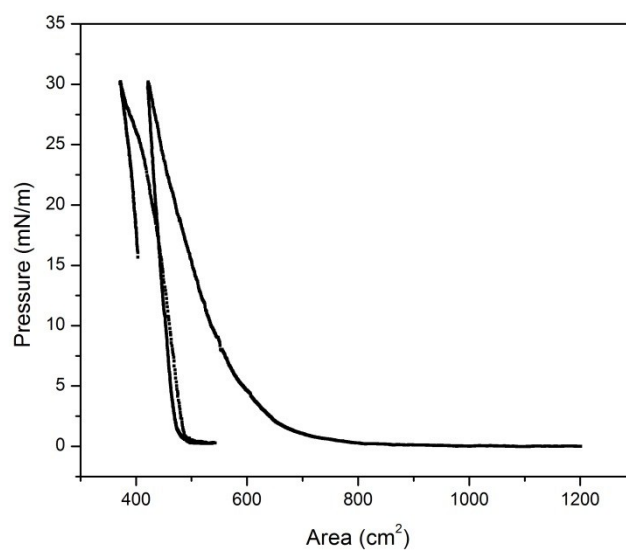


Figure 3-5. Isotherms for several VDF oligomers including (A) 18 unit VDF with an iodine head group in DMSO, (B) 25 unit VDF with an iodine head group in DMSO, and (C) 20 unit of VDF with a phosphonic acid head group in butanone.

A



B

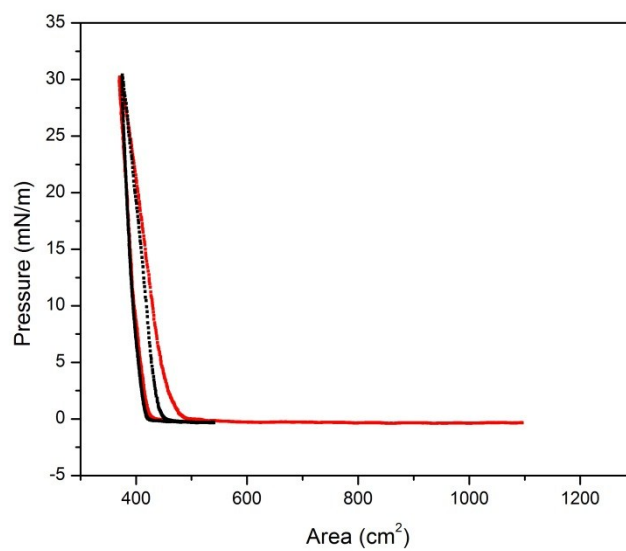


Figure 3-6. Multi-cycle isotherm for 18 unit VDF with an iodine head group with the first two cycles shown in (A) and the next two cycles shown in (B).

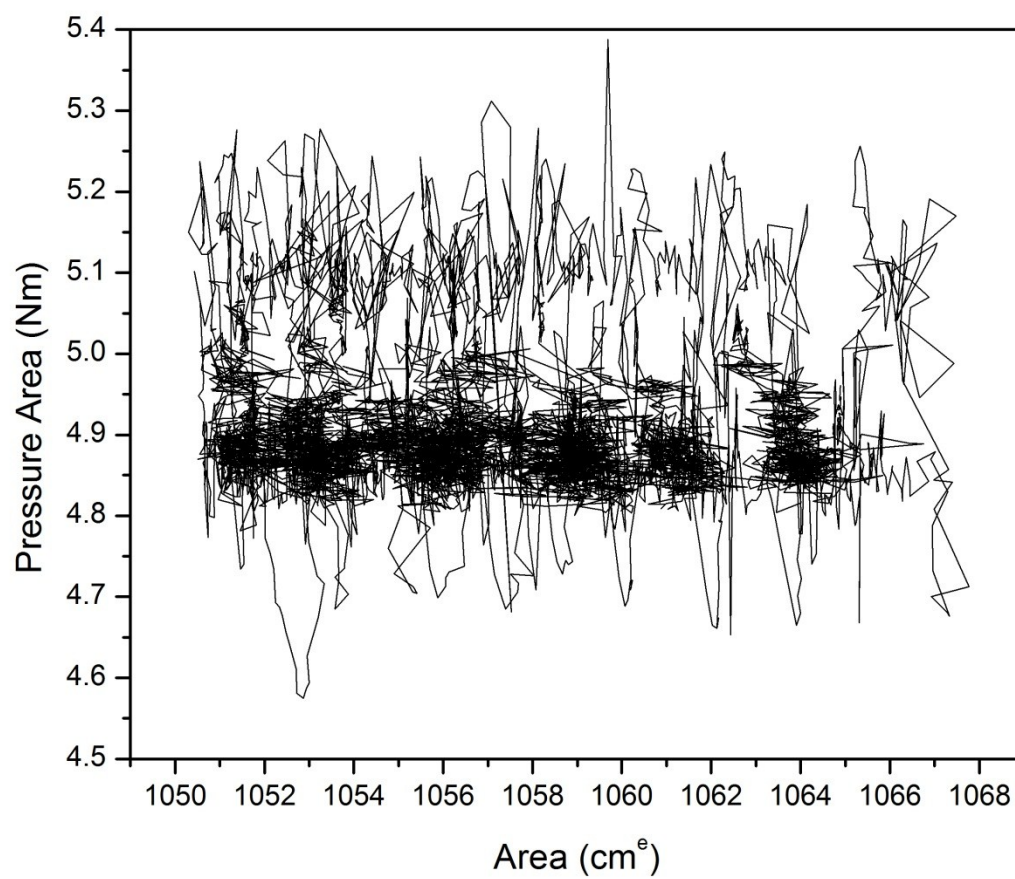


Figure 3-7. Y-type deposition of oligomer films.

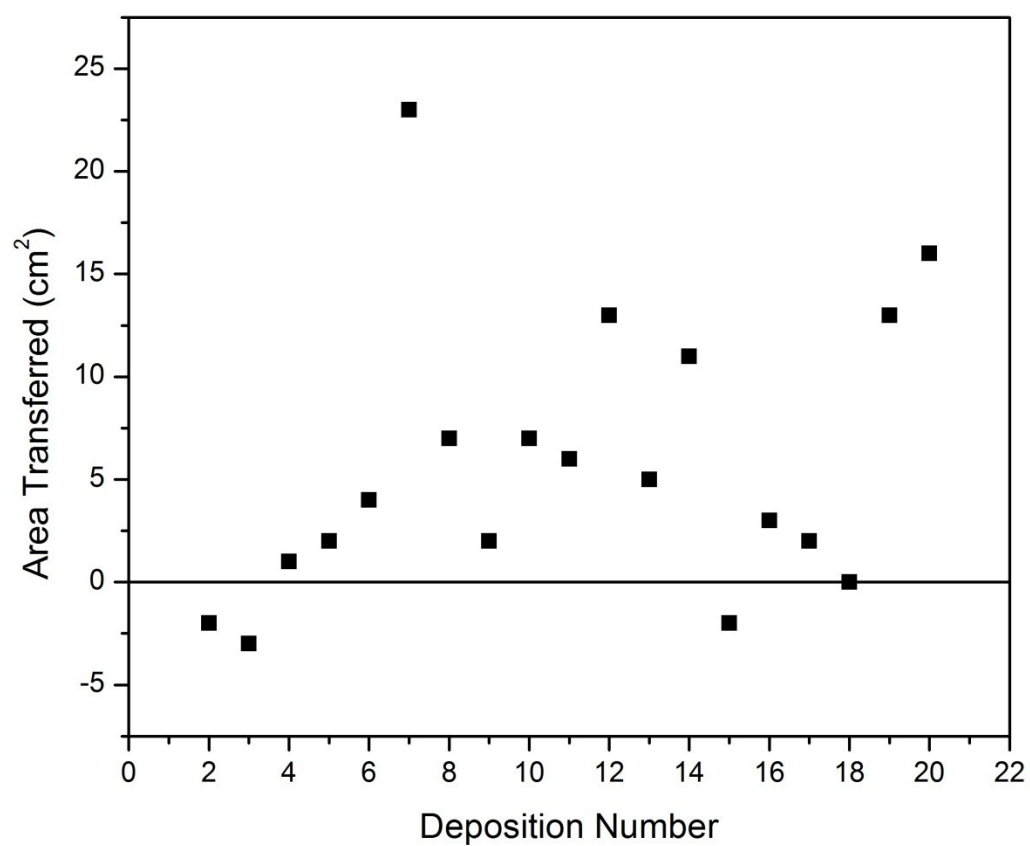
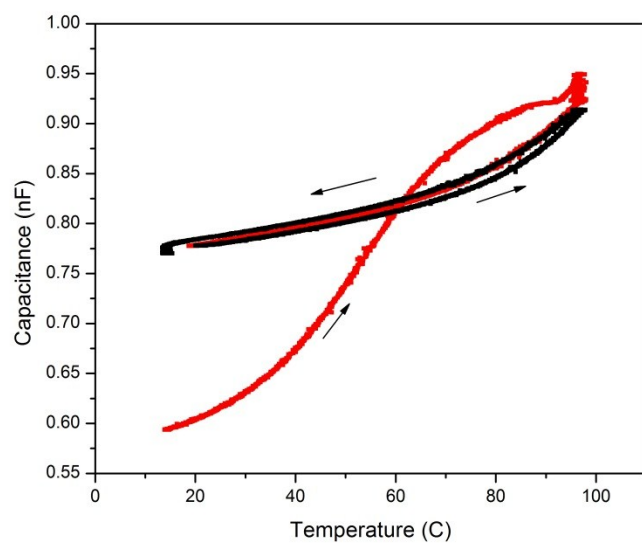


Figure 3-8. Area transfer for iodine oligomers at 10 mN/m pressure to a 6 cm<sup>2</sup> substrate.

A



B

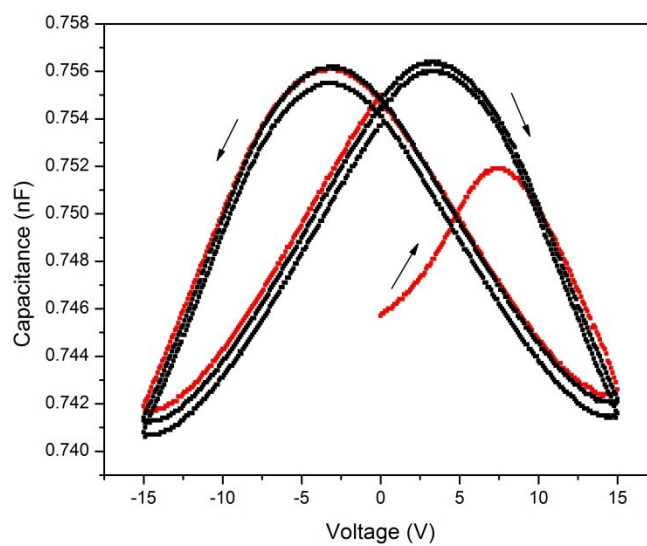


Figure 3-9. Dielectric results for an 18 unit VDF oligomer film compressed to a surface pressure of 10 mN/m. (A) Temperature dependence and (B) frequency dependence of the capacitance.

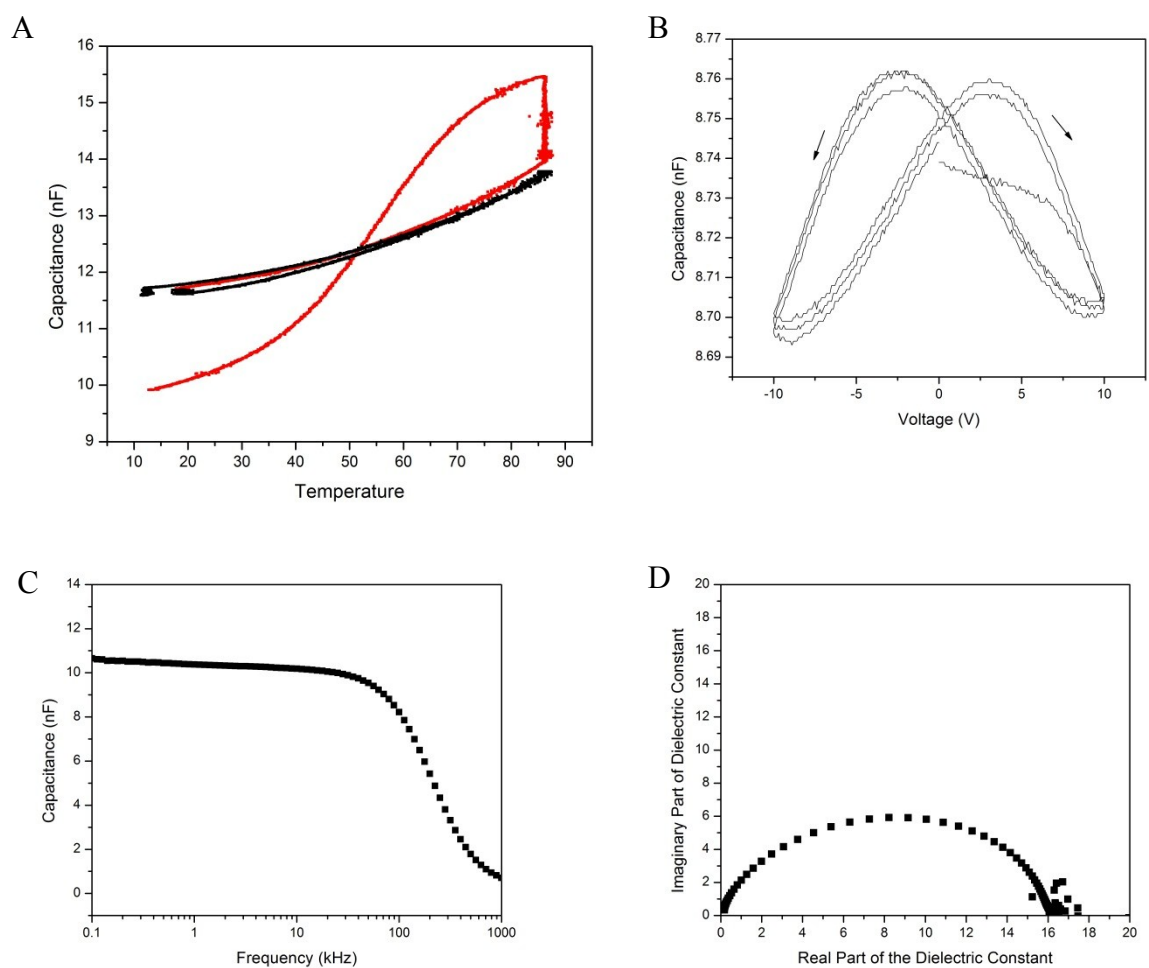


Figure 3-10. Dielectric results for another typical 18 unit VDF oligomer sample. The (A) temperature dependence, (B) voltage dependence, (C) frequency dependence, and (D) Cole-Cole plot for the sample.

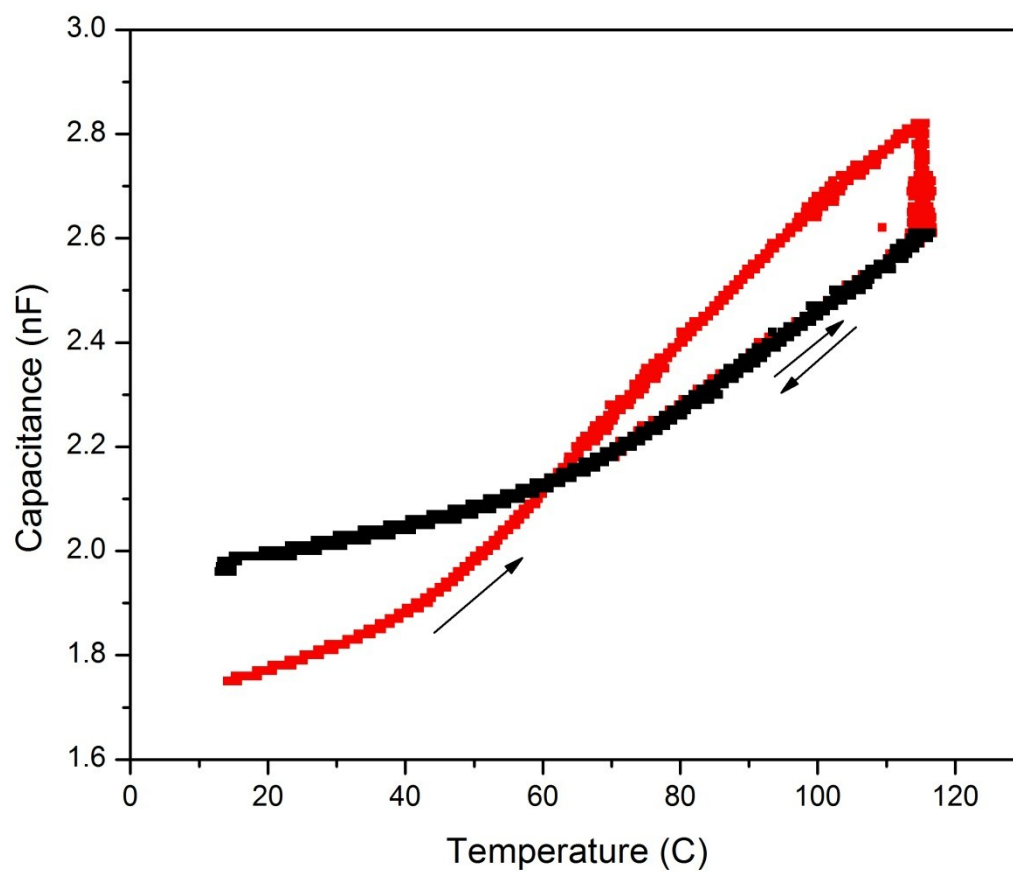


Figure 3-11. Temperature dependence for a 25 unit VDF oligomer.

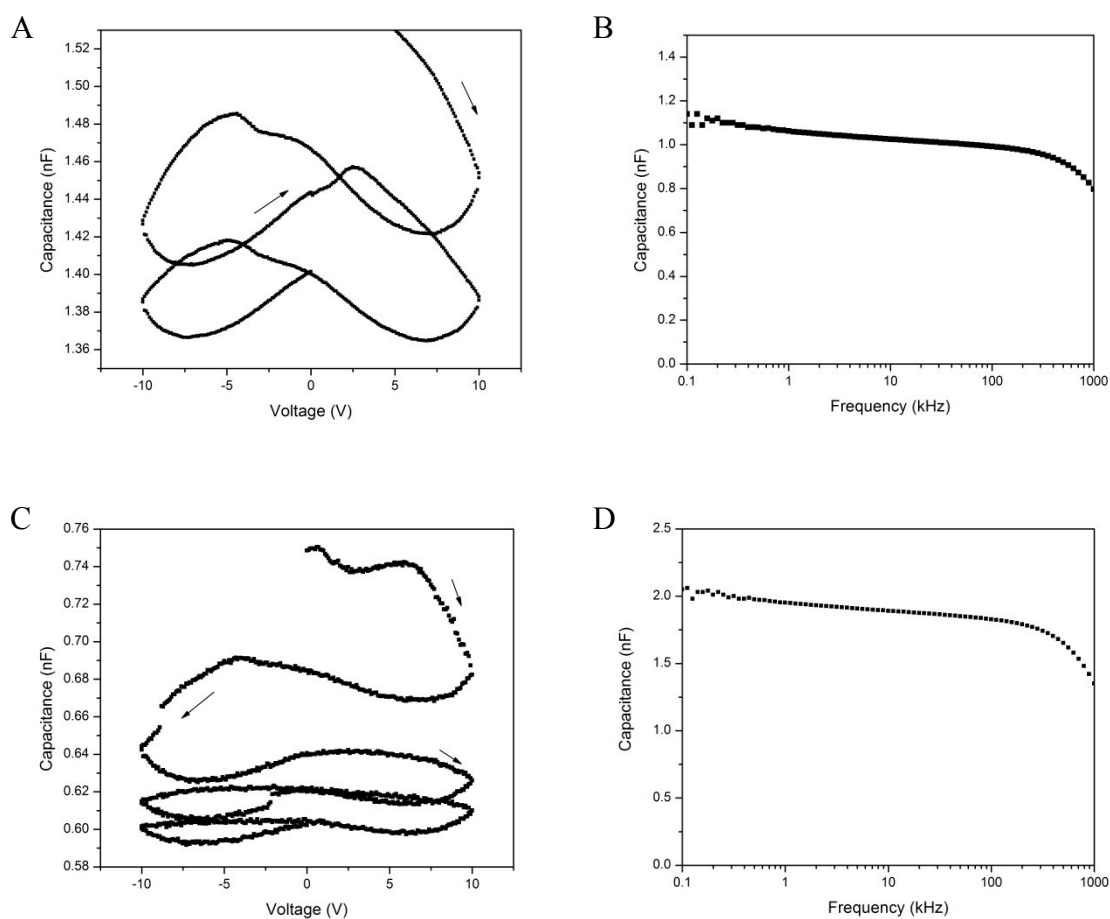


Figure 3-12. Typical samples with 25 units of VDF. (A) Voltage dependence and (B) Frequency dependence for films deposited at 20 mN/m. (C) Voltage dependence and (D) frequency dependence for films deposited at 25 mN/m.

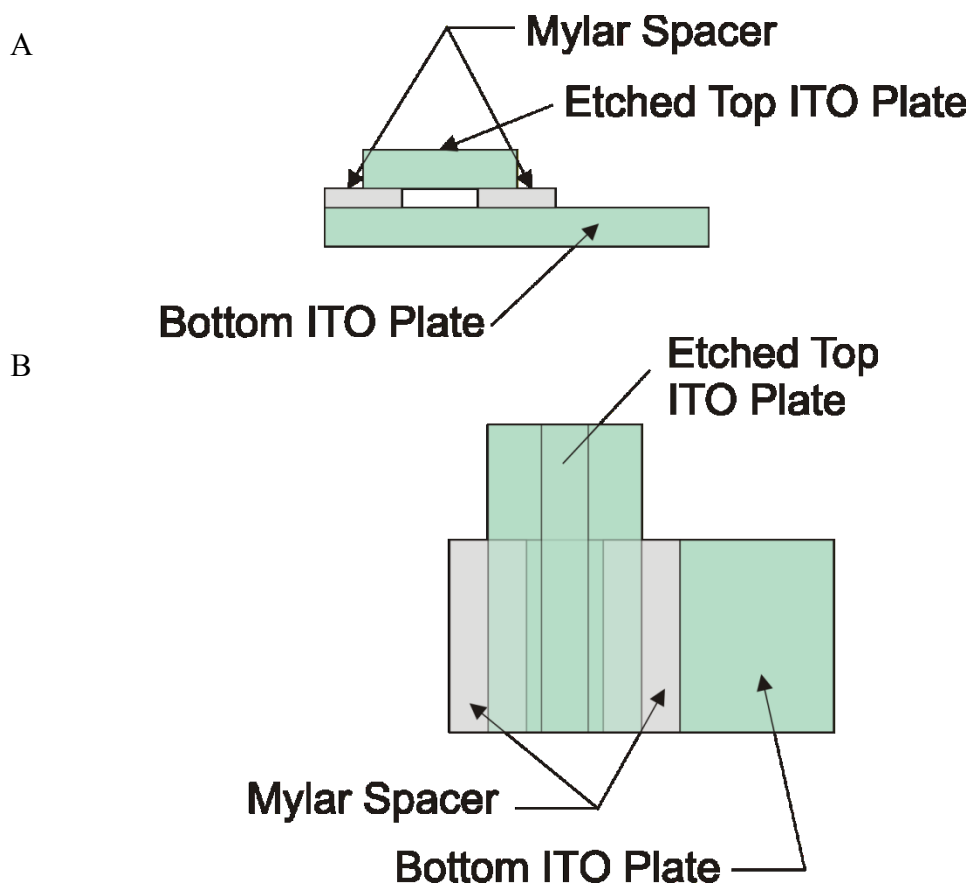


Figure 3-13. Sketch of capillary cell setup. (A) Side view of two ITO coated plates with a Mylar spacer. (B) The top view of a capillary cell where one plate had patterned electrodes.

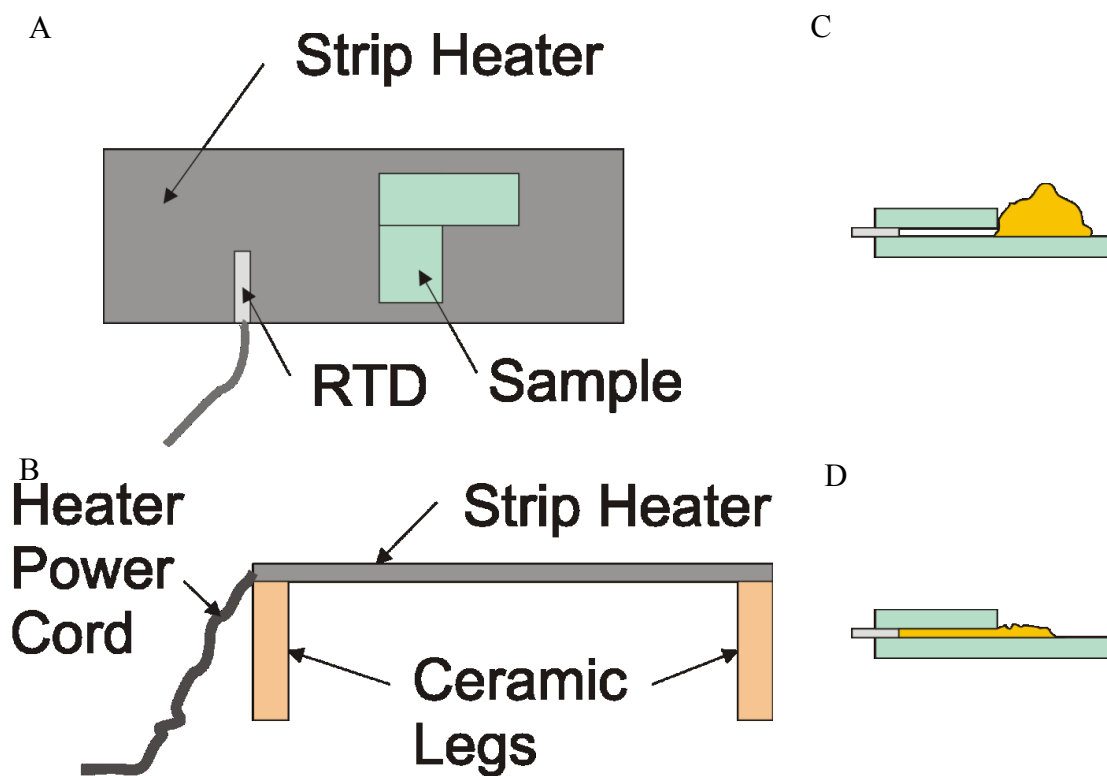


Figure 3-14. The oligomers were melted on a strip heater. (A) Top and (B) side view of the heater stage for heating the capillary cells. (C) The unmelted oligomer was placed at the opening of the capillary cell. (D) When the oligomer melted, capillary forces drew it into the cell.

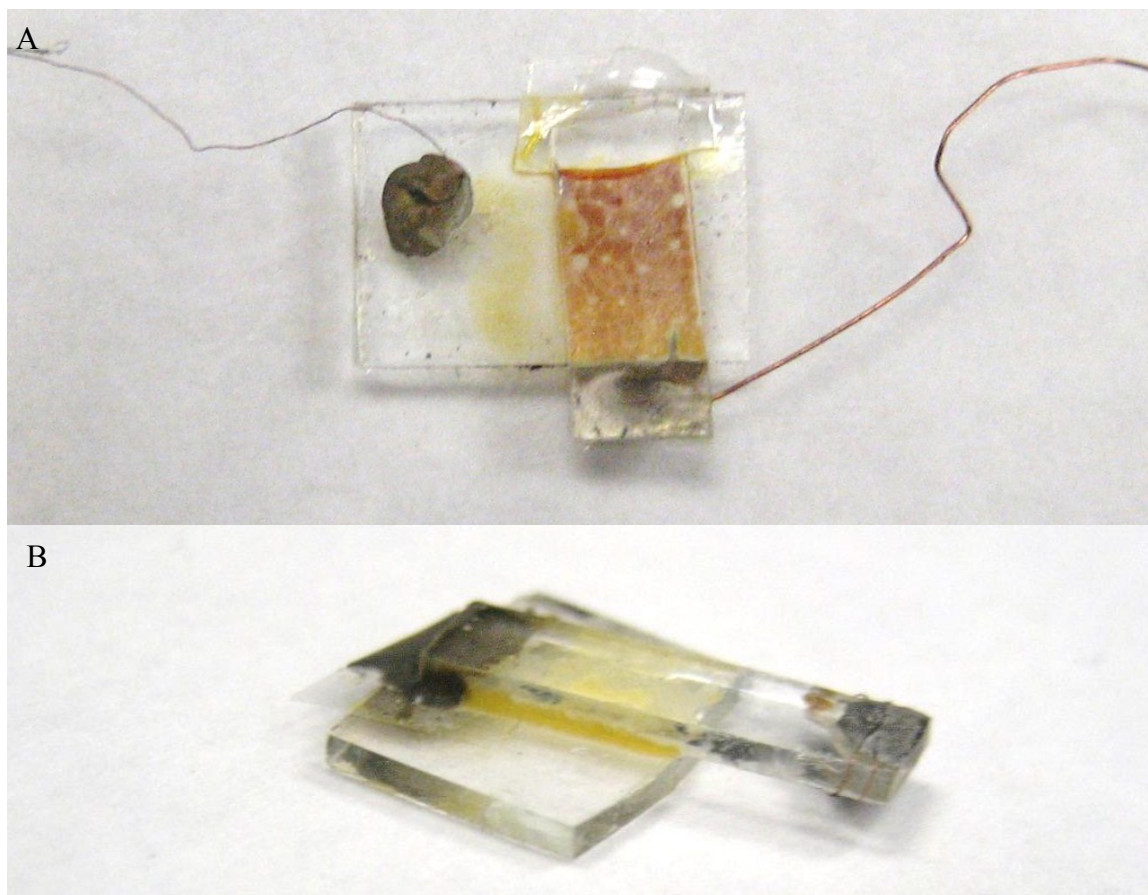
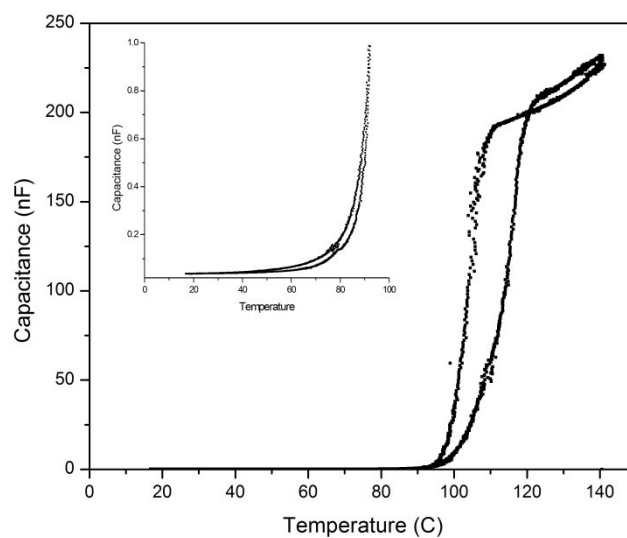


Figure 3-15. Pictures of capillary cells with oligomers between the two plates. (A) Top view and (B) side view of a filled cell.

A



B

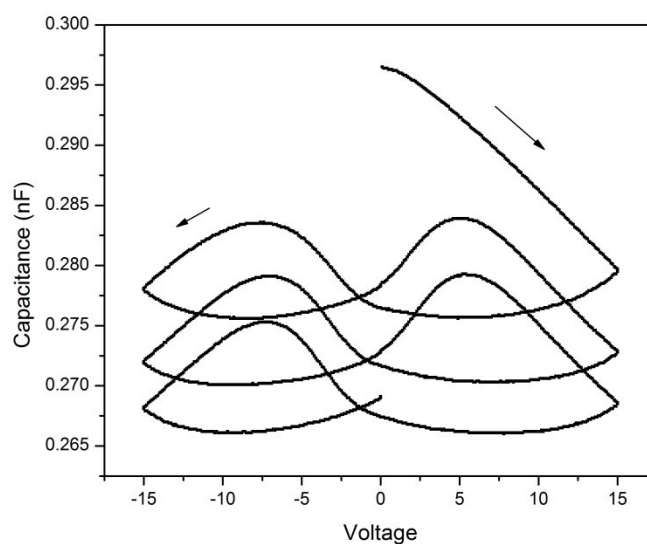


Figure 3-16. (A) Temperature results for a 12 unit VDF oligomer with a 12  $\mu\text{m}$  Mylar spacer. (B) Voltage dependence for a 6 unit VDF oligomer in a capillary cell with a 12  $\mu\text{m}$  Mylar spacer.

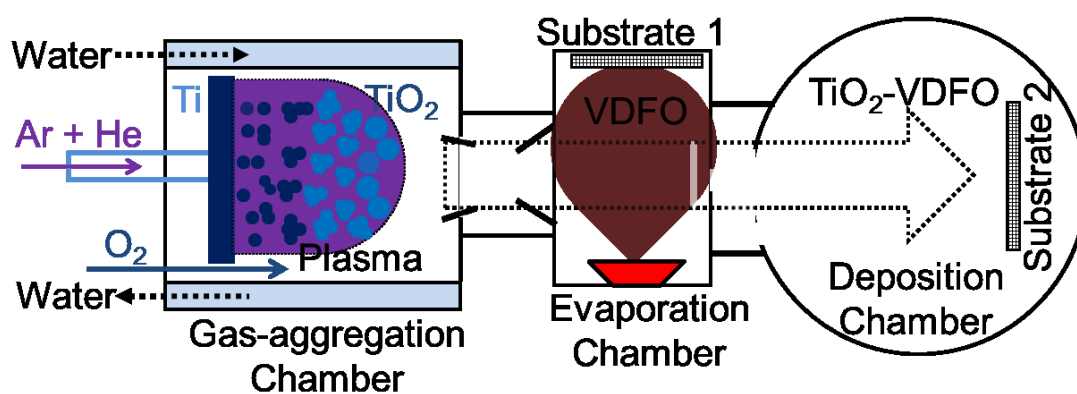
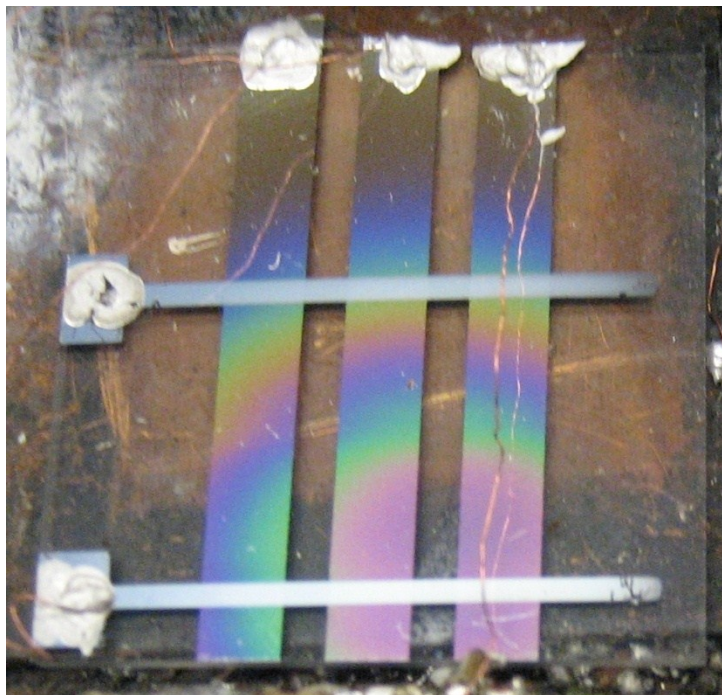


Figure 3-17. The cluster deposition system. Evaporated oligomer samples were made in the evaporation chamber with the substrate located at Substrate 1 location. Adapted from [13]. (Taken from *Balasubramanian, B., et al., Nanotechnology, 2011. 22 (405605)* with permission.)

A



B

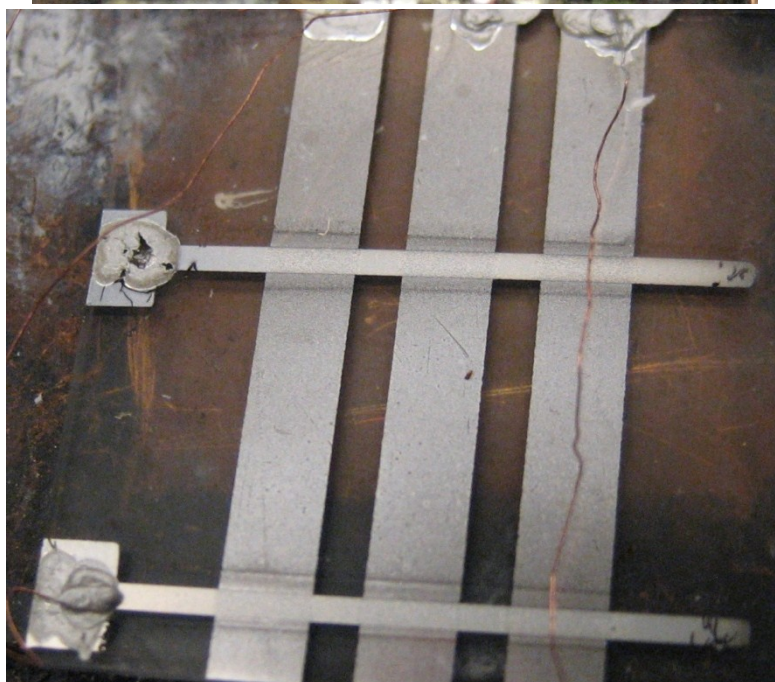


Figure 3-18. Evaporated film (A) before and (B) after annealing.

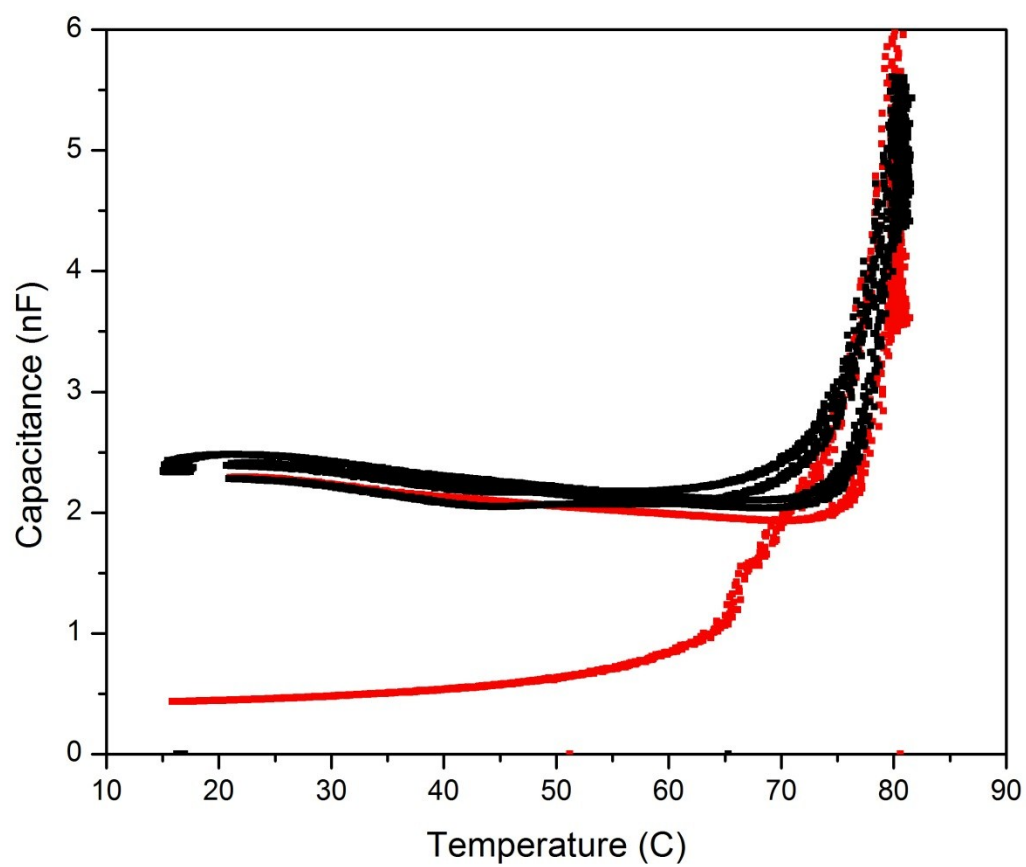
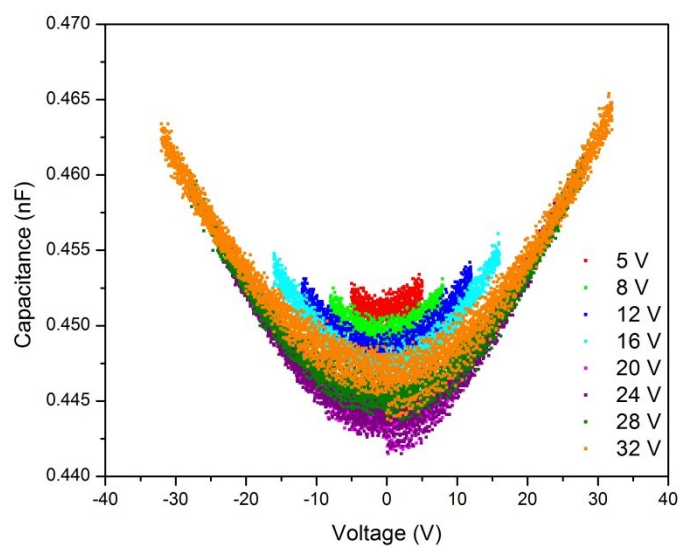


Figure 3-19. Temperature dependence of the capacitance for the evaporated oligomer film.

A



B

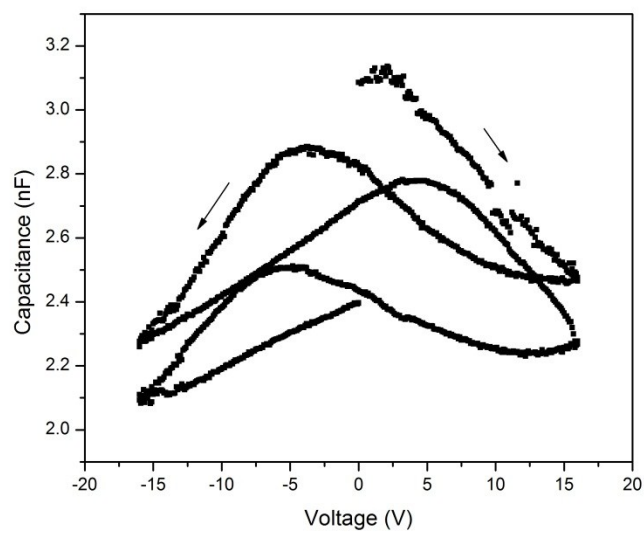


Figure 3-20. Voltage dependence of an evaporated film (A) before and (B) after annealing.

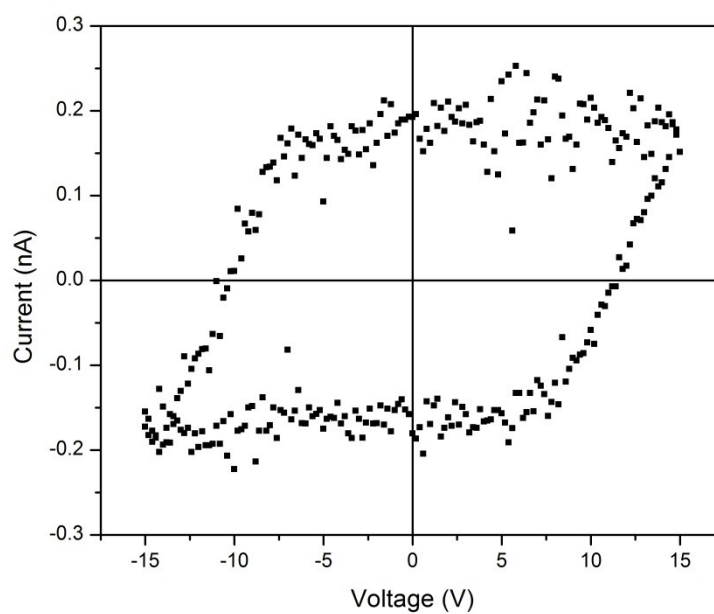


Figure 3-21. Pyroelectric hysteresis loop for the evaporated thin film after annealing.

## CHAPTER 4

### SELF-ASSEMBLED MONOLAYER THIN FILMS

#### 4.1 Introduction

A self-assembled monolayer (SAM) is a spontaneous structure one molecular layer thick. When a bare metal or metal oxide surface adsorbs organic material, the free energy of the interface between the metal and the surrounding environment is lowered [1]. When the surface layer of adsorbed organic materials organizes itself spontaneously into complex hierarchical structures from predesigned building blocks, this is called a self-assembly [2]. An example is the alkanethiol SAM on gold shown in Figure 4-1. The organic material used in a SAM typically consists of a head group which is functionalized to have an affinity to a particular substrate, such as a thiol attached to gold, and a tail. A common example of a tail is an alkane [3]. The end of the tail may have another functional group attached to it.

Self-assembled monolayers are formed from solution or by vapor deposition onto solid substrates such as metals, metal oxides, and semiconductors [1, 4, 5]. In some cases, SAM's can be formed on liquid metal surfaces, such as mercury [1]. The functional groups on a SAM must be tailored to the surface to which it should attach. Table 4-1 lists several common functional groups and some of the surface to which the functional group prefers to attach. One of the most commonly studied systems is the thiol functional group on metals such as gold or platinum [1, 6]. Several functional groups contain -OH attachments, such as hydroxyl, carboxylic acid and phosphonic acid, which attach to a wide range of metal oxides [1].

There are a variety of factors that affect the growth of the SAMs on substrates. Some of the conditions are the solvent, temperature, concentration, and the cleanness of the substrate. The choice of solvents will affect the kinetics of the interaction between the surface of the substrate and the solvent along with the interactions between the adsorbents and the solvent [1]. In some cases, the interactions between the surface of the substrate and solvent may decrease the growth of the SAM, especially if the solvent molecules must be displaced from the surface. It has been shown with alkanes that the use of a polar solvent decreases the defect rate compared to using nonpolar solvents [1].

Temperatures above room temperature help to improve the quality of the SAM by allowing surface contaminants and solvents to adsorb more easily. It also makes it easier to cross activation barriers to attach and reorganize on the substrate [1]. Figure 4-2 shows several mechanisms for film growth. At low temperature (A) the growth starts in a vapor phase, and then goes through a vapor-solid coexistence phase, then to a solid phase. At higher temperatures, the SAM has a laying down phase and a disorder phase as it nucleates into islands [6].

The concentration will affect how likely the molecules are to come into contact with the substrate. The concentration and immersion time are inversely related. A more concentrated solution will require less time to assemble into a film. While very dilute SAMS (less than 1  $\mu\text{M}$ ) do not tend to show the same properties as ones formed at higher concentrations [7, 8], most general physical properties were similar for films grown at higher concentrations ( $\sim 1\text{mM}$ ) for more than 12 to 18 hours [1]. As the immersion time increased, the surface coverage increased and the defect rate decreased [1].

There are many different potential applications for SAMs in sensors, protective layers, electronics and biotechnology. By customizing the tails, properties such as wetting, adhesion, and chemical resistance can be controlled [1, 9]. Some applications in biosystems for SAMs include the purification of complex media, drug immobilization for local drug delivery devices, and surface modifications for implants [10]. The SAMs can be customized to modify the surface for cell adhesion or to inhibit the growth of bacteria [10].

In electronics, SAMs have also found many applications. In solar cells, polypyridyl ruthenium molecules were attached to TiO<sub>2</sub> nanofilms as photosensitizers [10]. When grown on metallic substrates, SAMs can be used as electrochemical sensors for detecting, measuring or trapping molecular species [9, 10]. With the ability to modify substrates for improved compatibility between surfaces, the potential application for customizing SAMs is nearly endless.

## **4.2 Overview of Materials**

This project was started to answer several questions about the particle coatings in Chapter 5, such as how thick one layer of organic coating was and to verify that the oligomers were attached to the substrates. There were two organic materials used to coat barium titanate nanoparticles, octadecylphosphonic acid (ODPA) which has an alkane tail and VDF (vinylidene fluoride) oligomers with a phosphonic acid functional group. The ODPA is a well-studied SAM [11, 12] while the VDF oligomers are a new material.

#### 4.2.A Organic Materials

Both the VDF oligomer and ODPA, chosen for functionalizing the surface of barium titanate nanoparticles and for the SAM study, have a phosphonic acid or very closely related functional group (Figure 4-3A). Phosphonic acid attaches well to the surface of metals, oxides, and other materials with exposed metallic atoms [10, 13-15]. Glass and silicon dioxide are the two main exceptions to this, and silanes functional groups tend to attach more efficiently [10]. The phosphonic acid makes metal-oxygen-phosphorus (M-O-P) bonds between the substrate and the surface functionalizing material [10, 13, 16]. One advantage of phosphonic acid is that it is able to bind to the substrate with one, two, or all three of its oxygen (Figure 4-3). Since many of the other functional groups (Table 4-1) only contain one or two potential binding sites, the phosphonic acid attaches more securely with the additional M-O-P bond.

##### 4.2.A.a Octadecylphosphonic Acid

Octadecylphosphonic acid contains an alkane with an eighteen carbon backbone and a phosphonic acid functional group (Figure 4-4A). The carbon chain determines the intermolecular interactions and the orientation of molecules [17]. The functional group, phosphonic acid, attaches to a wide range of oxides such as aluminum oxide [4, 12, 14, 18], indium tin oxide [19], mica [12], titanium dioxide [15], zinc oxide [20]. This is a well-studied material and was used as a control system for gaining an understanding of how to make SAMs. The ODPA used in these studies was purchased from NanoAmor.

#### *4.2.A.b Poly(vinylidene fluoride) Oligomer*

Poly(vinylidene fluoride) [PVDF] and its copolymers have been of much interest due to the ferroelectric and other electroactive properties [21-25]. As nanoscience develops molecular electronics, there is a need to be able to control the organic materials with high precision. One way to do this is to reduce the polymer chain containing tens of thousands of VDF units ( $\text{CH}_2\text{CF}_2$ ) to oligomers with a few to several dozen units. Oligomers of VDF have been synthesized and demonstrated to be ferroelectric [21]. Oligomers for this study were synthesized with 6 to 25 VDF units and a phosphonic functional group [26].

#### *4.2.B Substrates for Self-Assembled Monolayers*

While barium titanate nanoparticles were used for the nanocomposite project, macroscopic substrates of barium titanate were not readily available. Instead, the initial studies were performed on native aluminum oxide grown on evaporated thin films deposited on silicon substrates. Later studies were performed on indium tin oxide and mica for smoother substrates. As shown in Figure 4-5A, the aluminum surface was granular with an average roughness of 2-3 nm. Later studies such as the time dependent study on the formation of SAMS was performed on mica. Mica substrates are atomically flat and single crystalline over large areas. This makes an ideal substrate for atomic force microscopy (AFM) and scanning force microscopy experiments [27]. Figure 4-5B shows an AFM image of a typical mica substrate. The mica substrate had an average roughness of less than 0.2 nm. Even substrates which cleave poorly were atomically flat over several square microns. Grain boundaries in substrates create defects in the SAM film, as

shown in Figure 4-6. Since the aluminum substrate was polycrystalline, the film was expected to have more defects than the films grown on mica substrates.

### 4.3 Procedure for Growing Self-Assembled Monolayers

Self-assembled monolayers were grown into thin films. The first substrate was aluminum oxide. Silicon wafers were cut into 2 cm<sup>2</sup> rectangles and cleaned with the procedure described in Chapter 2. Aluminum stripes were evaporated onto the silicon by thermal evaporation with a thickness of 100 nm and the native oxide layer was allowed to grow for at least 24 hours. Native oxide layers on aluminum are approximately 3 nm thick [18]. The second substrate used for SAMs was commercially prepared indium tin oxide (ITO) film on glass. The third substrate was mica. Mica substrates were cleaved with a razor blade to expose fresh surfaces for growing SAMs.

The procedure for growing a SAM is shown in Figure 4-7. The films were grown in 1 mM solutions. The alkane SAMs were made in ethanol and the VDF oligomers used acetone as the solvents. The SAMs were grown in a glass microscope staining jar which held the substrates upright allowing several films to be grown at once. When the substrates were ready to be submerged, they were first rinsed with either ethanol or acetone, depending on the film being grown, to remove any dust that had settled on the surface of the substrate. The substrates were then submerged into the solution and allowed to soak for the desired number of days as the films self-assembled. Early films used in the thickness studies grew for 3 days while the time dependent study films grew from 1 minute to 24 hours. After the film had time to adsorb to the surface, it was carefully removed with clean tweezers and any remnant surfactant was rinsed off. The alkane films were rinsed with ethanol, acetone and water and then allowed to dry. The

oligomer films were rinsed with acetone, isopropanol and water, and then allowed to dry. After the films dried, ellipsometry and atomic force microscopy (AFM) measurements were made on them.

#### **4.4 Octadecylphosphonic Acid Self-Assembled Monolayer Films**

##### *4.4.A Ellipsometry Thickness Measurements*

The thickness of the ODPA SAM was measured with ellipsometry. As shown in Figure 4-8, there was a slight decrease in delta when the substrate measurement (orange curve) was compared to the SAM measurements (blue) at three angles. This shift was typical for film only a few molecules thick. Since the film was so thin, the ellipsometer could not accurately calculate both the thickness and the index of refraction [28]. Therefore, the value of the index must be set. The thickness was calculated to be 2 nm for an index of refraction of 1.6 [29].

##### *4.4.B Atomic Force Microscopy Thickness Measurements*

Typical AFM results for an ODPA SAM grown on an aluminum oxide substrate are shown in Figure 4-9. The difficulty with the interpretation of this data was that the grains of aluminum were of a similar size as the islands of the SAM. The section analysis showed most clumps were about 4 nm tall, while the larger ones were 10-15 nm tall. The taller areas on the section analysis could have been caused by multilayers of the alkanes on the SAMS or by a larger grain of aluminum.

## 4.5 Vinylidene Fluoride Oligomer Self-Assembled Monolayer Measurements

### 4.5.A Ellipsometry Thickness Measurements of Vinylidene Fluoride Self-Assembled Monolayers

Ellipsometry results were measured for two samples, one with 8 units of VDF (Figure 4-10A) and one with 7 units of VDF (Figure 4-10B). The first sample had a very thin film on it, shown by the narrow space between the green substrate measurement and the blue film measurement. With an index of refraction of 1.4 [30], the thickness was calculated to be 0.8 nm. The second oligomer was thicker (Figure 4-10B). With the index set to 1.4, the calculated thickness twice as thick as the previous film, at 1.8 nm. Since both oligomers were nearly the same length, the films were expected to be a similar thickness. It could be that the second film was a bilayer instead of a single monolayer SAM.

### 4.5.B Time Dependent Atomic Force Microscopy Measurements

The time dependent film formation for VDF oligomers on mica are shown in Figure 4-11. Freshly cleaved mica was placed into a 1 mM solution of the oligomers in acetone for 1 minute, 2 minutes, 3 minutes, 5 minutes, 20 minutes, 1 hour, and 24 hours. At the end of the desired deposition time, the substrate was removed from the solution and rinsed well with acetone, isopropanol, and water. The amplitude and phase images for the series of samples are shown in Figure 4-11. Section analysis for each of the times is shown in Figure 4-12 to Figure 4-18.

At 1 minute, the substrate showed the growth of islands surrounded by bare substrate. The area not containing oligomer was visible in the darker regions of the phase

image in Figure 4-11A. The section analysis (Figure 4-12) showed island growth of 0.74 nm tall surrounded relatively flat regions. As the time increased to 2 minutes, there were more small islands present with less substrate visible in the phase image in Figure 4-11B. The section analysis also supported this observation (Figure 4-13). Many of the islands were narrower than the ones present at 1 minute and the space between the islands had decreased. This was similar to the low coverage regime in time dependent ODPa growth on mica where the growth was dominated by island nucleation [31].

At three minutes, there were two types of structures present. The first was the round islands visible in the amplitude image in Figure 4-11C. The second was the thin film between the islands visible in the phase image. In the phase image, the dark mica substrate was no longer visible between the islands. Instead, the space between the islands was very similar in color to the islands, signifying that the materials were of similar stiffness. The section analysis (Figure 4-14) showed the space between the islands was no longer flat as had been in the shorter time measurements. This could be an intermediate regime where nucleation has slowed down and island growth is starting [31] or an intermediate phase similar to the one shown in Figure 4-2B [6] where molecules were laying down between the islands.

By 5 minutes (Figure 4-11D and Figure 4-15), the film became denser as the islands grew. Previously, there were regions of substrate between the islands. At this deposition time, the islands dominated the space with dark regions visible in the phase image only in the area immediately surrounding the islands. This was further supported by the lowest minimums in the section analysis were right next to the islands (Figure

4-15. This was the regions where the islands started to aggregate together, similar to the ODPa SAMs [31].

By 20 minutes (Figure 4-11E), the islands had grown larger than in previous images and were starting to grow together. The sectional analysis (Figure 4-16) no longer showed distinct islands; rather the film was mostly at 0.4 nm above the substrate, with a few regions taller and shorter than this.

At 1 hour (Figure 4-11F), the islands had grown together and the phase image appears to be nearly continuous, although individual islands could still be distinguished from neighboring islands. By 24 hours (Figure 4-11C), the islands had grown together to the point of being indistinguishable from neighbors for the most part. The section analysis (Figure 4-17 and Figure 4-18) further supported the merger of the islands. Individual islands have most grown together, although there may still be regions where the film was not standing up all the way or where a second layer had started to form on top of the first. This would be the coalescence regime described for the alkane SAMS [31].

As the islands started to form on the mica substrates, the surface roughness increased during the 1 minute to 3 minute deposition times (Table 4-3). From 3 to 5 minutes, the roughness was the greatest, and then it started to decrease back to similar amount as the early deposition time. This would support the islands starting to nucleate, growing larger, and finally filling in most of the void spaces.

#### **4.6 Conclusion**

Self-assembled monolayers were grown with octadecylphosphonic acid and VDF oligomers on aluminum and mica substrates. The ODPA films had a thickness of 2 nm when measured by ellipsometry. The AFM measurements of the film thickness were around 4 nm, although it was very difficult to distinguish between the grains in the aluminum and the thickness of the SAM. The SAMs grown with VDF oligomers on aluminum oxide had a thickness between 0.8 nm and 1.8 nm when measured by ellipsometry. The two materials were of a similar length, so one sample may have been a bilayer instead of a monolayer. On mica, the VDF oligomers grew SAMs which started as isolated islands and grew together as a continuous film.

#### 4.7 References

1. Love, J.C., et al., *Self-Assembled Monolayers of Thiolates on Metals as a Form of Nanotechnology*. Chemical Reviews, 2005. 105(4): p. 1103-1170.
2. Schreiber, F., *Self-assembled monolayers: from 'simple' model systems to biofunctionalized interfaces*. Journal of Physics: Condensed Matter, 2004. 16(28): p. R881.
3. Ulman, A., *Formation and structure of self-assembled monolayers*. Chemical Reviews, 1996. 96(4): p. 1533-1554.
4. Hoque, E., et al., *Phosphonate self-assembled monolayers on aluminum surfaces*. The Journal of Chemical Physics, 2006. 124(17): p. 174710-6.
5. Adler-Abramovich, L., et al., *Self-assembled arrays of peptide nanotubes by vapour deposition*. Nat Nano, 2009. 4(12): p. 849-854.
6. Schwartz, D.K., *Mechanisms and kinetics of self-assembled monolayer formation*. Annual Review of Physical Chemistry, 2001. 52(1): p. 107-137.
7. Bain, C.D., et al., *Formation of monolayer films by the spontaneous assembly of organic thiols from solution onto gold*. Journal of the American Chemical Society, 1989. 111(1): p. 321-335.
8. Bensebaa, F., et al., *Kinetics of formation of long-chain n-alkanethiolate monolayers on polycrystalline gold*. Langmuir, 1997. 13(20): p. 5335-5340.
9. Gooding, J.J., et al., *Self-assembled monolayers into the 21st century: recent advances and applications*. Electroanalysis, 2003. 15(2): p. 81-96.
10. Queffelec, C., et al., *Surface Modification Using Phosphonic Acids and Esters*. Chemical Reviews, 2012. 112(7): p. 3777-3807.
11. Fontes, G., R. Moreira, and B. Neves, *Thermally induced stacking of octadecylphosphonic acid self-assembled bilayers*. Nanotechnology, 2004. 15(5): p. 682.
12. Nie, H.-Y., M.J. Walzak, and N.S. McIntyre, *Delivering Octadecylphosphonic Acid Self-Assembled Monolayers on a Si Wafer and Other Oxide Surfaces*. The Journal of Physical Chemistry B, 2006. 110(42): p. 21101-21108.
13. Mutin, P.H., G. Guerrero, and A. Vioux, *Hybrid materials from organophosphorus coupling molecules*. Journal of Materials Chemistry, 2005. 15(35-36): p. 3761-3768.

14. Hauffman, T., et al., *Study of the Self-Assembling of n-Octylphosphonic Acid Layers on Aluminum Oxide*. Langmuir, 2008. 24(23): p. 13450-13456.
15. Gawalt, E.S., et al., *Self-assembly and bonding of alkanephosphonic acids on the native oxide surface of titanium*. Langmuir, 2001. 17(19): p. 5736-5738.
16. Lushtinetz, R., et al., *Adsorption of phosphonic and ethylphosphonic acid on aluminum oxide surfaces*. Surface Science, 2008. 602(7): p. 1347-1359.
17. Lushtinetz, R., et al., *Self-assembled Monolayers of Alkylphosphonic Acids on Aluminum Oxide Surfaces – A Theoretical Study*. Zeitschrift für anorganische und allgemeine Chemie, 2010. 636(8): p. 1506-1512.
18. Koutsioubas, A.G., et al., *Formation of alkane-phosphonic acid self-assembled monolayers on alumina: an in situ SPR study*. Surface and Interface Analysis, 2009. 41(11): p. 897-903.
19. Chockalingam, M., et al., *Importance of the indium tin oxide substrate on the quality of self-assembled monolayers formed from organophosphonic acids*. Langmuir, 2011. 27(6): p. 2545-2552.
20. Zhang, B., et al., *Surface functionalization of zinc oxide by carboxyalkylphosphonic acid self-assembled monolayers*. Langmuir, 2010. 26(6): p. 4514-4522.
21. Noda, K., et al., *Remanent polarization of evaporated films of vinylidene fluoride oligomers*. Journal of applied physics, 2003. 93(5): p. 5.
22. Lovinger, A.J., *Ferroelectric Polymers*. Science, 1983. 220(4602): p. 1115-1121.
23. Koga, K. and H. Ohigashi, *Piezoelectricity and related properties of vinylidene fluoride and trifluoroethylene copolymers*. Journal of Applied Physics, 1986. 59(6): p. 2142-2150.
24. Bune, A.V., et al., *Two-dimensional ferroelectric films*. Nature, 1998. 391(6670): p. 874-877.
25. Zhang, Q., V. Bharti, and X. Zhao, *Giant electrostriction and relaxor ferroelectric behavior in electron-irradiated poly (vinylidene fluoride-trifluoroethylene) copolymer*. Science, 1998. 280(5372): p. 2101-2104.
26. Korlacki, R., et al., *Oligo (vinylidene fluoride) Langmuir-Blodgett films studied by spectroscopic ellipsometry and the density functional theory*. The Journal of Chemical Physics, 2008. 129: p. 064704.

27. Woodward, J.T., A. Ulman, and D.K. Schwartz, *Self-assembled monolayer growth of octadecylphosphonic acid on mica*. Langmuir, 1996. 12(15): p. 3626-3629.
28. J. A. Woollam Co, I., *Complete Ease Data Analysis Manual*. 2011, Lincoln, Ne.
29. Hauffman, T., et al., *In Situ Study of the Deposition of (Ultra)thin Organic Phosphonic Acid Layers on the Oxide of Aluminum*. Langmuir, 2012. 28(6): p. 3167-3173.
30. Bai, M., et al., *Determination of the optical dispersion in ferroelectric vinylidene fluoride (70%)/trifluoroethylene (30%) copolymer Langmuir–Blodgett films*. Journal of Applied Physics, 2004. 95(7): p. 3372-3377.
31. Doudevski, I. and D.K. Schwartz, *Concentration dependence of self-assembled monolayer island nucleation and growth*. Journal of the American Chemical Society, 2001. 123(28): p. 6867-6872.

## 4.8 Tables

Table 4-1. Common functional groups to attach to nanoparticles and substrates. Based on table from Love et al[1].

Ligand	Common Name	Substrates
RSH	Thiol	Au, Ag, Cu, ZnSe, Pt, Ni, Hg, CdSe, CdTe
ROH	Hydroxyl	Fe <sub>x</sub> O <sub>y</sub> , Si, Glass
RSiX <sub>3</sub> X=H, Cl, OR'	Silanes	HfO <sub>2</sub> , ITO, PtO, TiO <sub>2</sub>
RP(O)(OH) <sub>2</sub>	Phosphonic Acid	Al <sub>2</sub> O <sub>3</sub> , TiO <sub>2</sub> , Nb <sub>2</sub> O <sub>5</sub> , ITO, Mica, CdSe
RNH <sub>2</sub>	Amino	Mica, Stainless Steel, FeS <sub>2</sub> , CdSe
RCOOH	Carboxyl	ITO, Glass, Al <sub>2</sub> O <sub>3</sub> , TiO <sub>2</sub>

\*R is the tail of the surfactant and can be tailored to the desired properties for the coatings.

Table 4-2. Film thickness for VDF oligomer SAMs grown on aluminum oxide.

Sample Number	n=1.45 Thickness (nm)	n=1.60 Thickness (nm)
1	2.89	2.48
2	3.44	2.94
3	1.76	1.51
4	2.72	2.23
5	1.96	1.69

Table 4-3. AFM height and roughness for VDF oligomer SAMs at different deposition times.

Time	Height Measured (nm)	RMS Roughness (nm)
1 min.	0.740	0.230
2 min.	0.621	0.216
3 min.	1.25	0.448
5 min.	0.782	0.312
20 min.	0.469	0.191
1 hour	0.740	0.239
24 hours	0.621	0.216

## 4.9 Figures

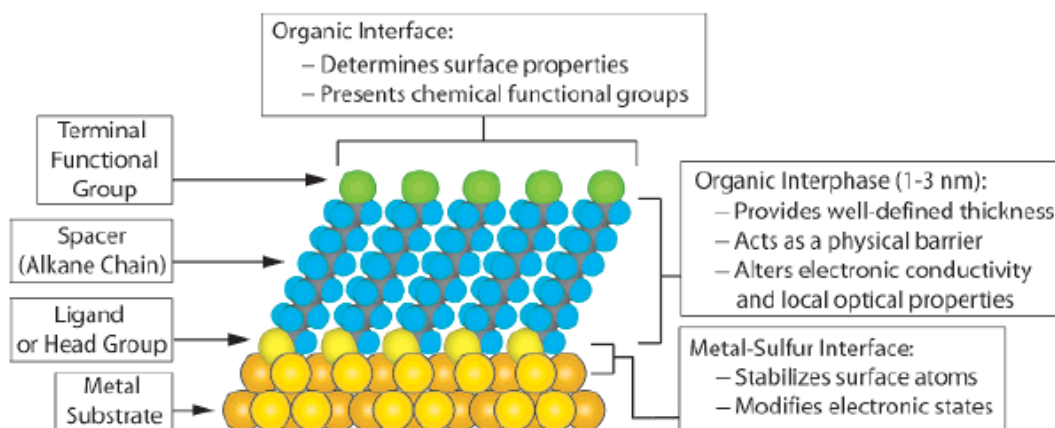


Figure 4-1. Parts of a Self-Assembled Monolayer. [1] Reprinted with permission from (Love, J.C., et al., *Chemical Reviews*, 2005. **105**: (1103).) Copyright (2005) American Chemical Society

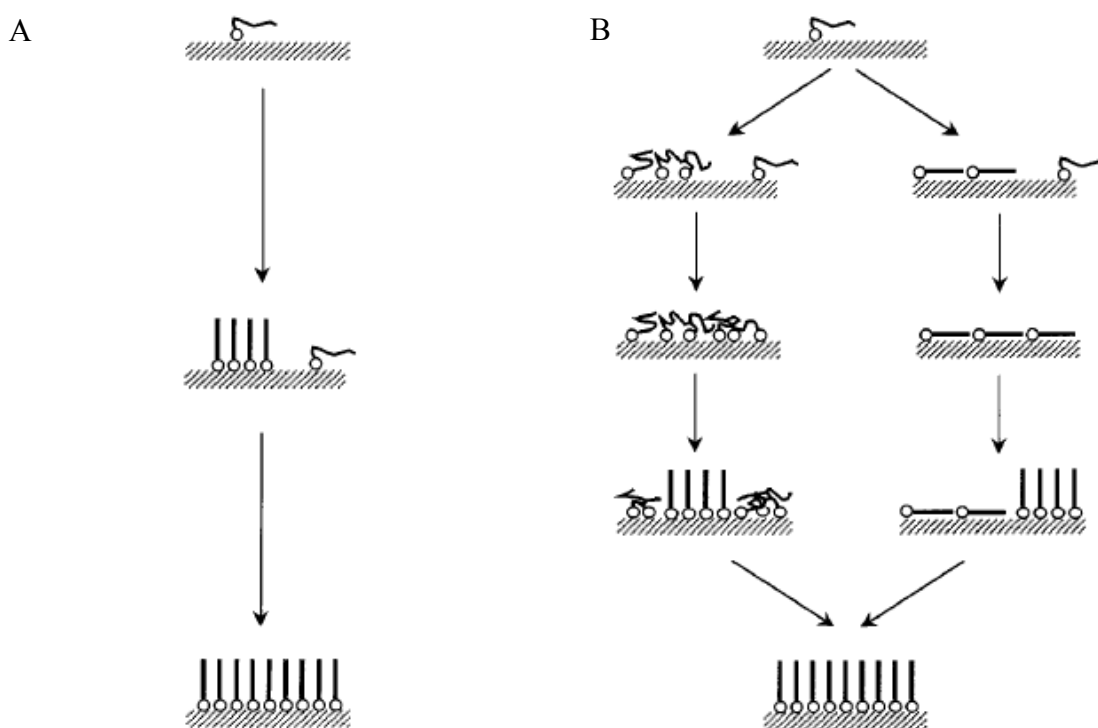


Figure 4-2. (A) At low temperatures, the SAM growth starts in the vapor phase. (B) At higher temperatures, the SAM has an additional laying down phase and a disordered phase as it grows into islands [6]. (Taken from Schwartz, D.K., *Annual Review of Physical Chemistry*, 2001. **52**. (107) with permission.)

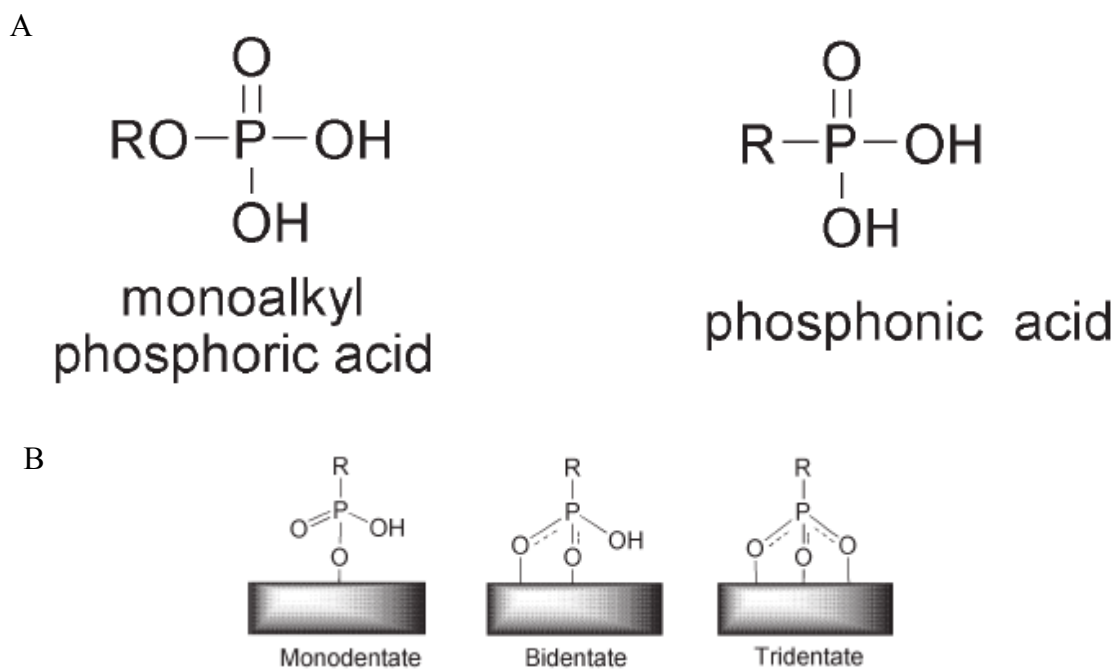
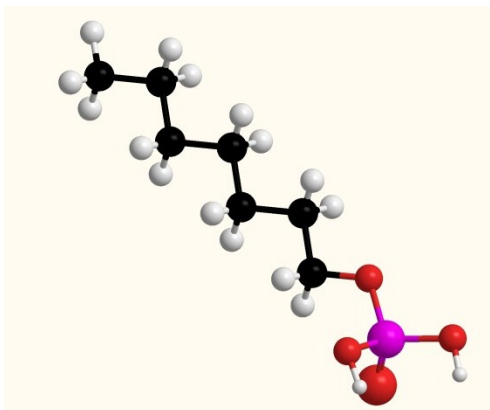


Figure 4-3. (A) Common functional groups containing phosphorus. (B) Phosphonic acid attachments onto oxide surfaces. Image from Mutin et al. [13] Phosphonic acid can attach to an oxide with one, two, or three of its oxygens. This allows for a stronger attachment than many of the other functional groups. (Taken from *Mutin, P.H., et al., Journal of Materials Chemistry, 2005. 15. (3761)* with permission.)

A



B

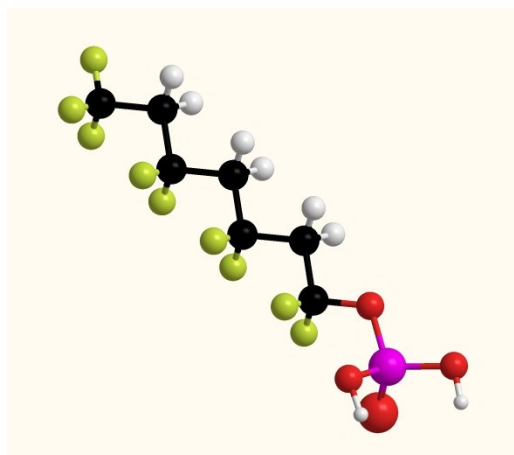


Figure 4-4. The dielectric tail used for coating the oxide nanoparticles. (A) Alkanes were the prototype material since they were commercially available. (B) VFDO was synthesized by our collaborators. R is the functional group, in this case phosphonic acid used to attach the surfactant to the particles.

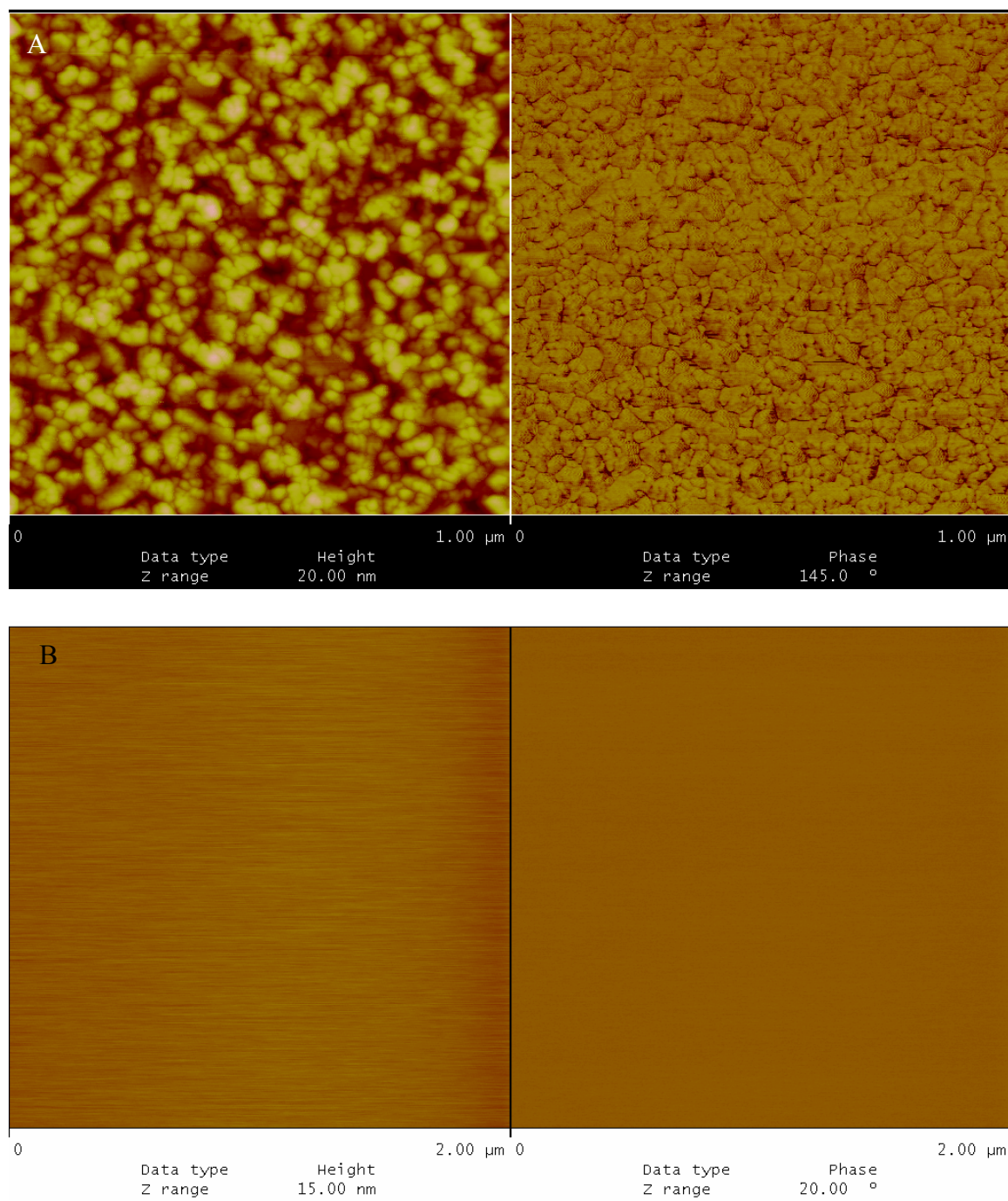


Figure 4-5. AFM of substrate surfaces, (A) Aluminum Oxide and (B) Mica. The left image is the amplitude and the right image is the phase.

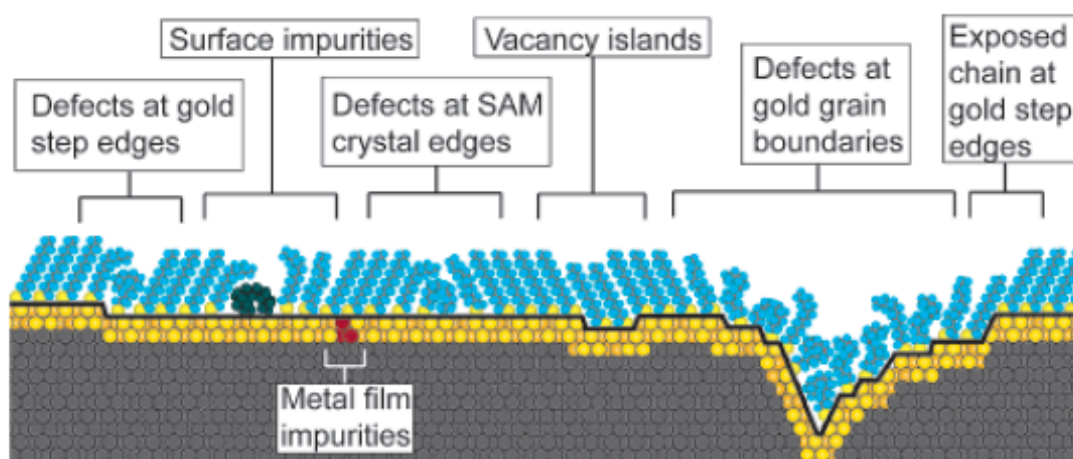
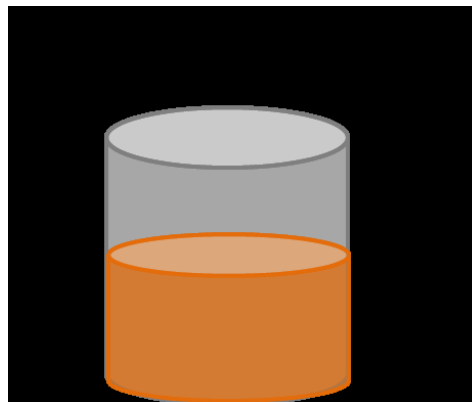


Figure 4-6. Schematic of some of the defects found in SAMs grown on polycrystalline surfaces. [1] (Love, J.C., et al., *Chemical Reviews*, 2005. **105**: (1103). Copyright (2005) American Chemical Society)

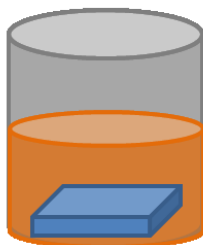
A

**1. Prepare a Substrate**

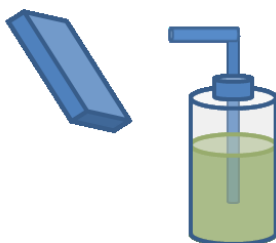
B



C

**3. Soak Substrate in the Solution**

D

**4. Rinse Surplus Surfactant Off Substrate**

E

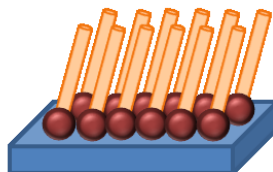
**5. Have a SAM**

Figure 4-7. Basic procedure for making a self-assembled monolayer. (A) Prepare a clean substrate of the desired surface. (B) Make a solution of 0.01 to 1 mM in a suitable solvent. (C) Submerge the substrate in the solution and allow it to soak for several days. (D) Rinse off the surplus surfactant. Any surfactant that has chemically attached to the substrate should stay on the substrate. (E) Allow the remaining solvent to evaporate. Then, the SAM is ready for use.

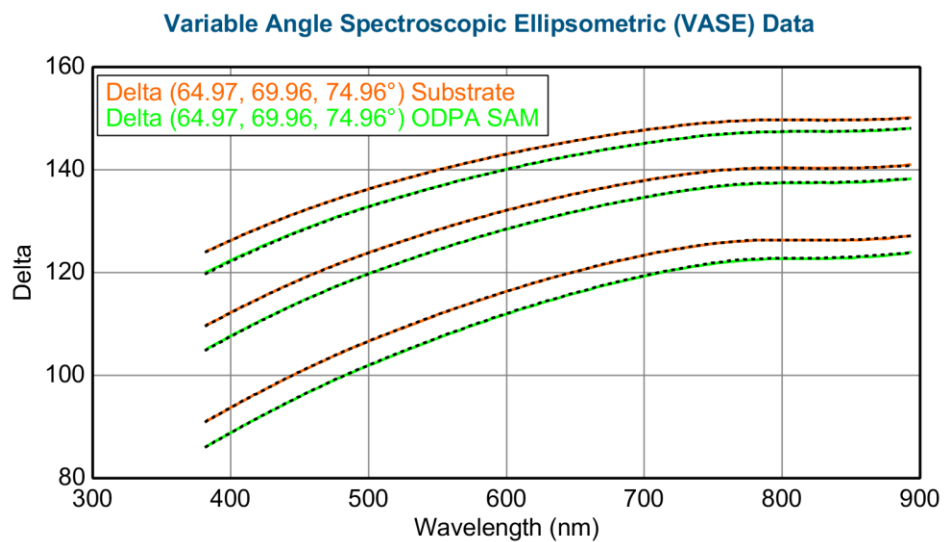


Figure 4-8. Ellipsometry measurements and fit for an ODPA film grown on aluminum dioxide substrate. The orange curve was the measurement of the substrate and the green curve was the measurement of the film. With an index of 1.6, the film was calculated to be 2 nm thick.

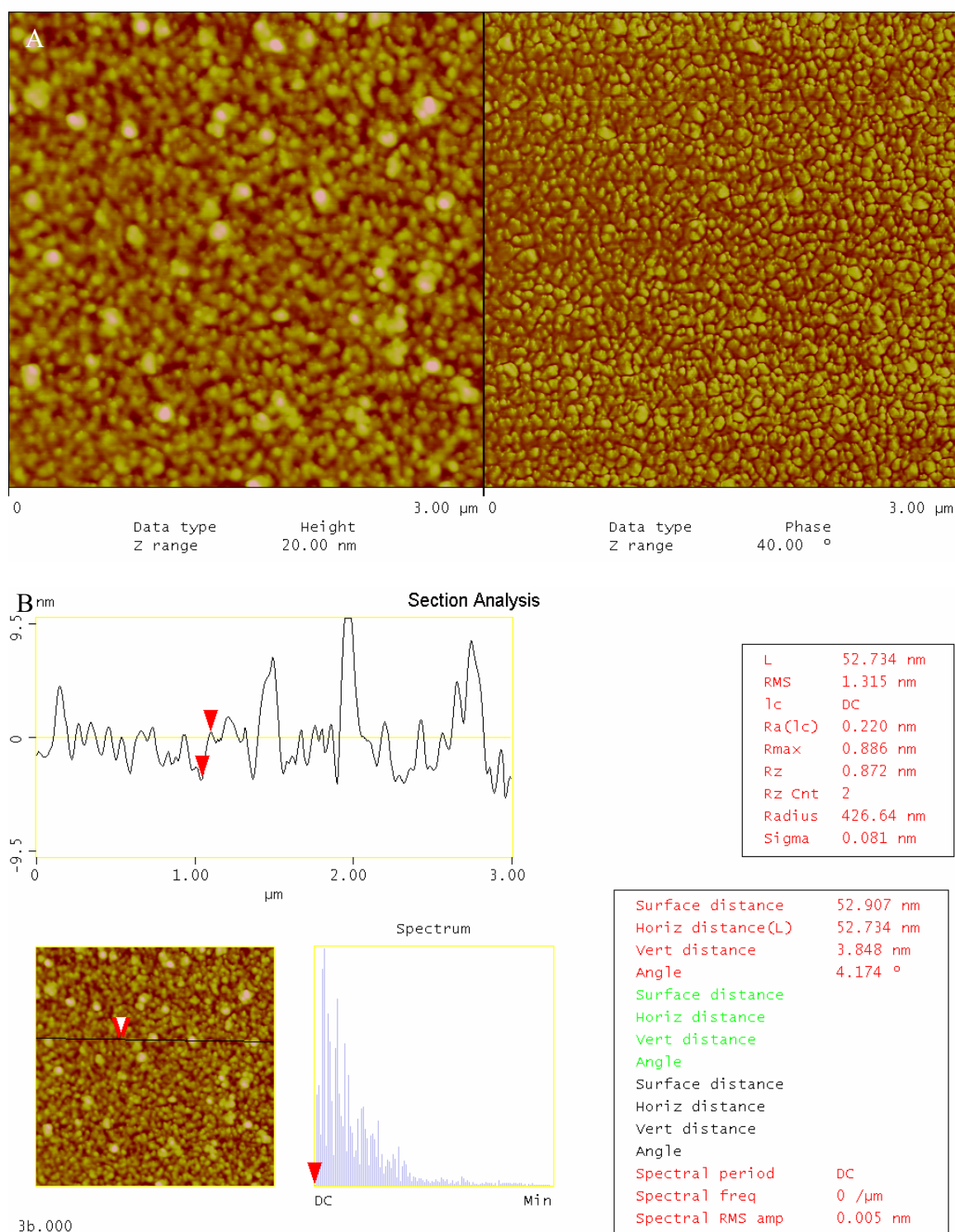


Figure 4-9. AFM measurement of an ODPA SAM grown on aluminum oxide. (A) Amplitude and phase images for the film. (B) Section analysis of the film. Most islands were 4 nm tall, although some were 10-15 nm in height.

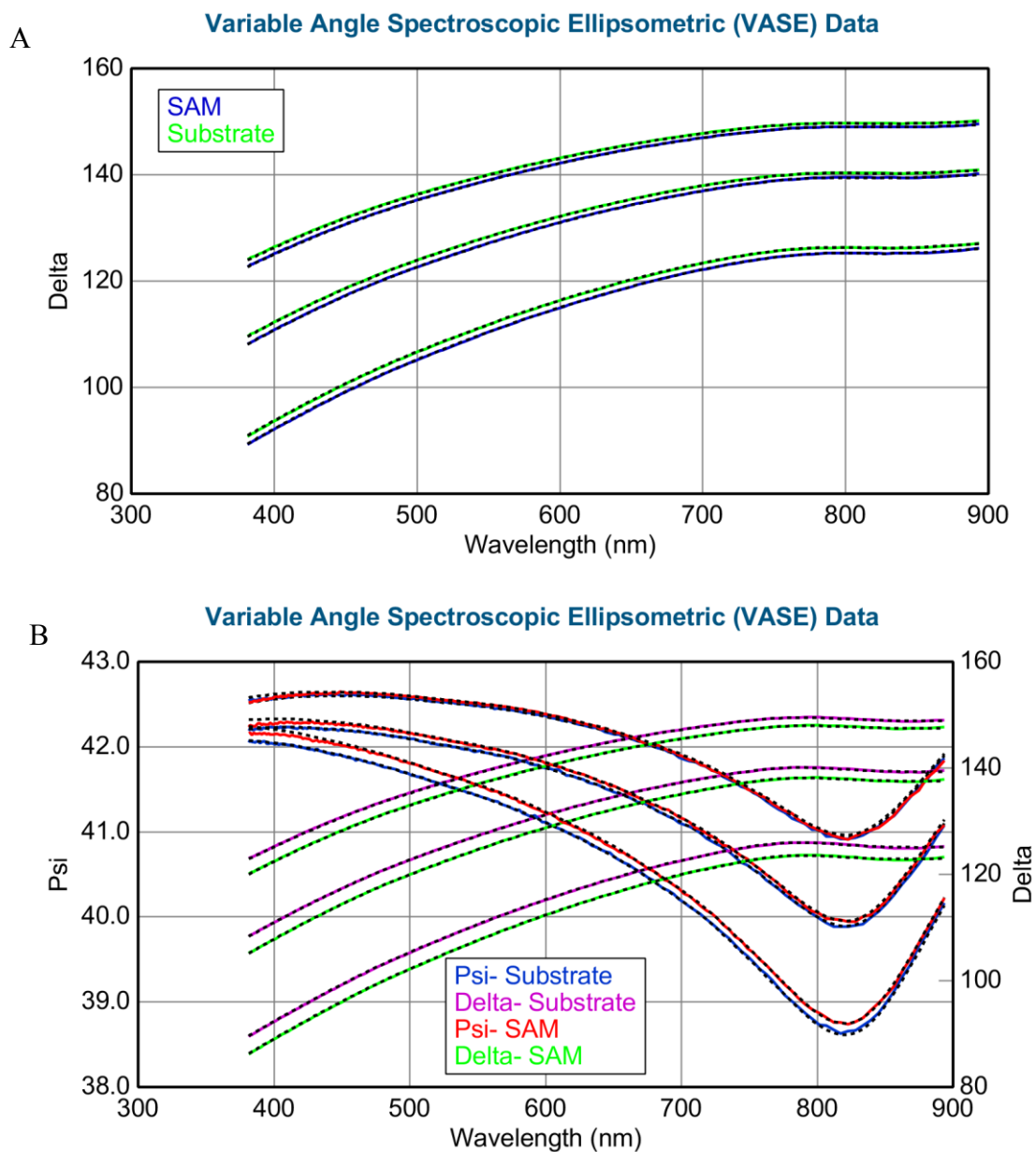


Figure 4-10. SAMs of VDF oligomers grown on aluminum oxide. (A) The film (8 units of VDF) was approximately 0.8 nm with an index of refraction of 1.4. (B) The film (7 units of VDF) was approximately 1.8 nm thick with an index of refraction of 1.4. Both films had good fits with the data, and the MSE values were between 0.75 and 0.85.

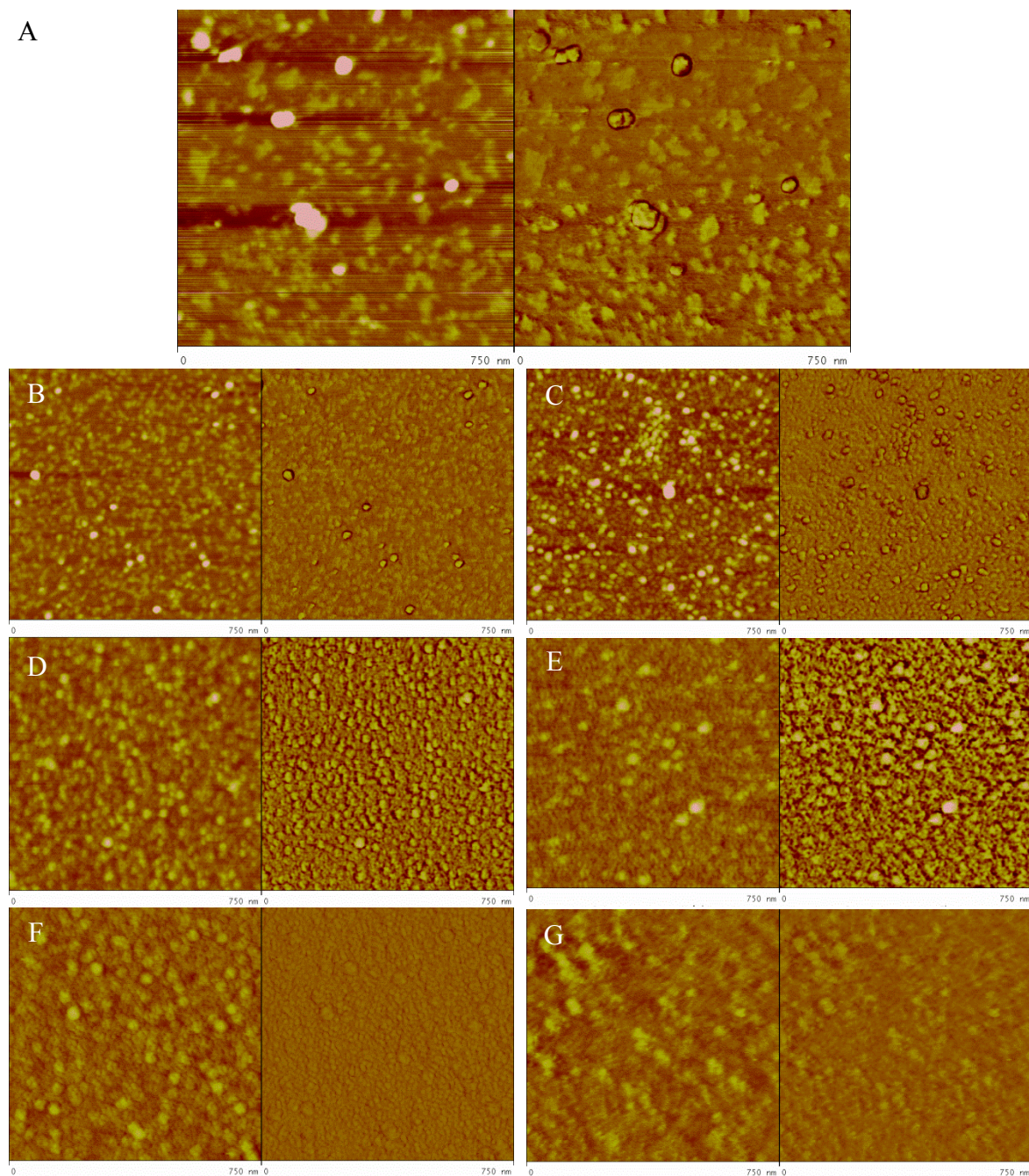


Figure 4-11. Time dependent growth of the VDF oligomer SAMs on mica. The left image is the amplitude and the right image is the phase. (A) 1 minute growth time. (B) 2 minutes growth time. (C) 3 minutes growth time. (D) 5 minutes growth time. (E) 20 minutes growth time. (F) 1 hour growth time. (G) 24 hours of growth time.

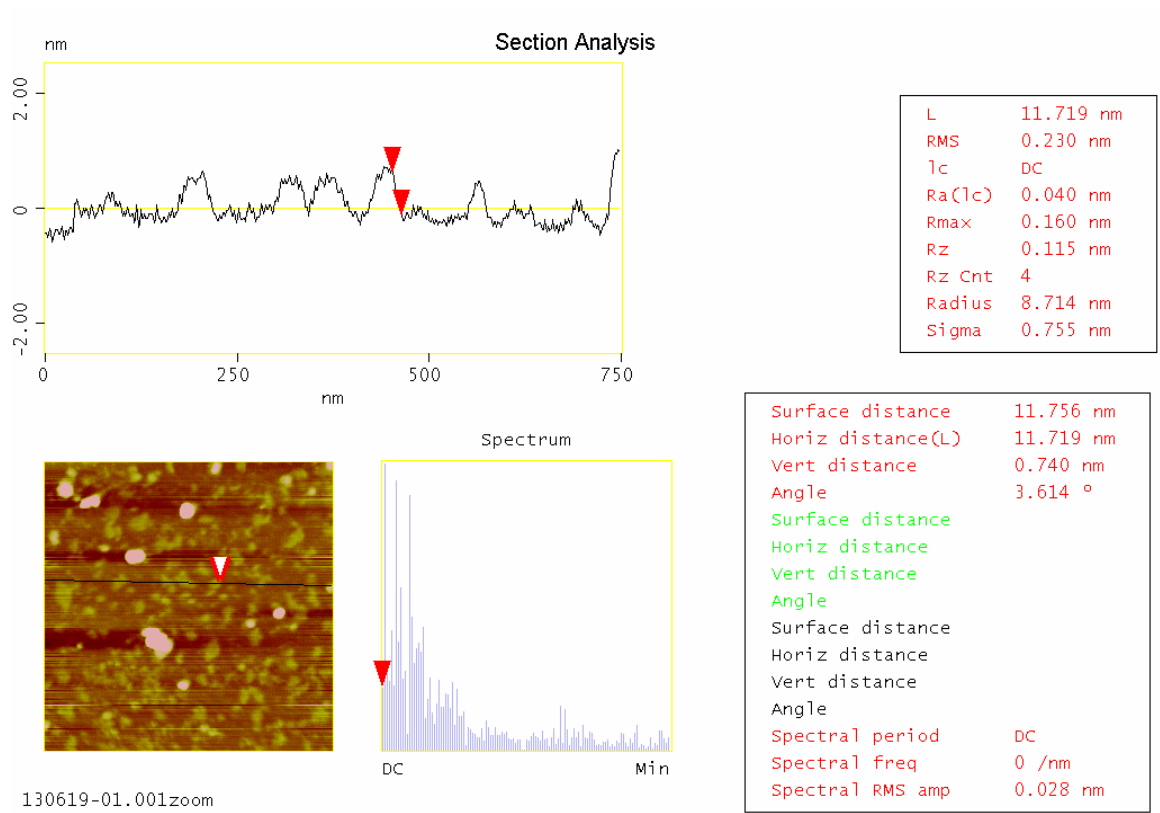


Figure 4-12. Section analysis for 1 minute deposition of the VDF oligomer SAM on mica.

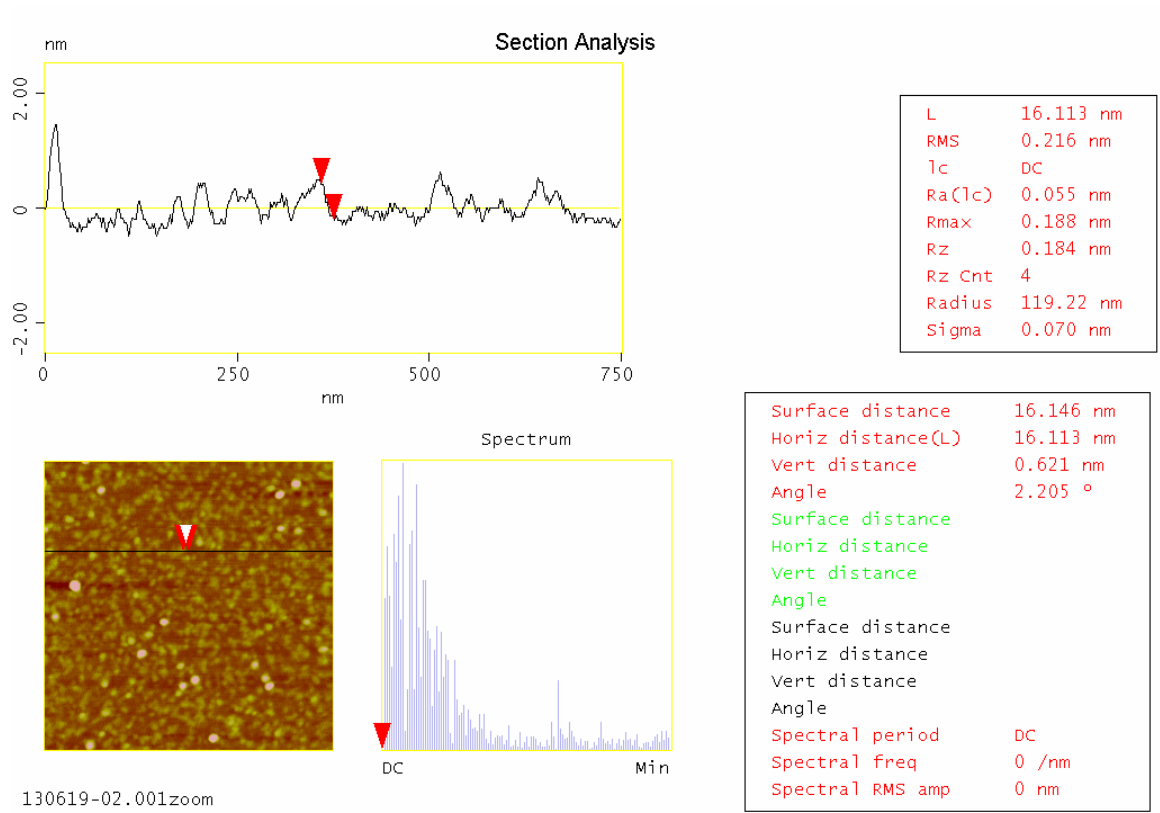


Figure 4-13. Section analysis for 2 minute deposition of the VDF oligomer SAM on mica.

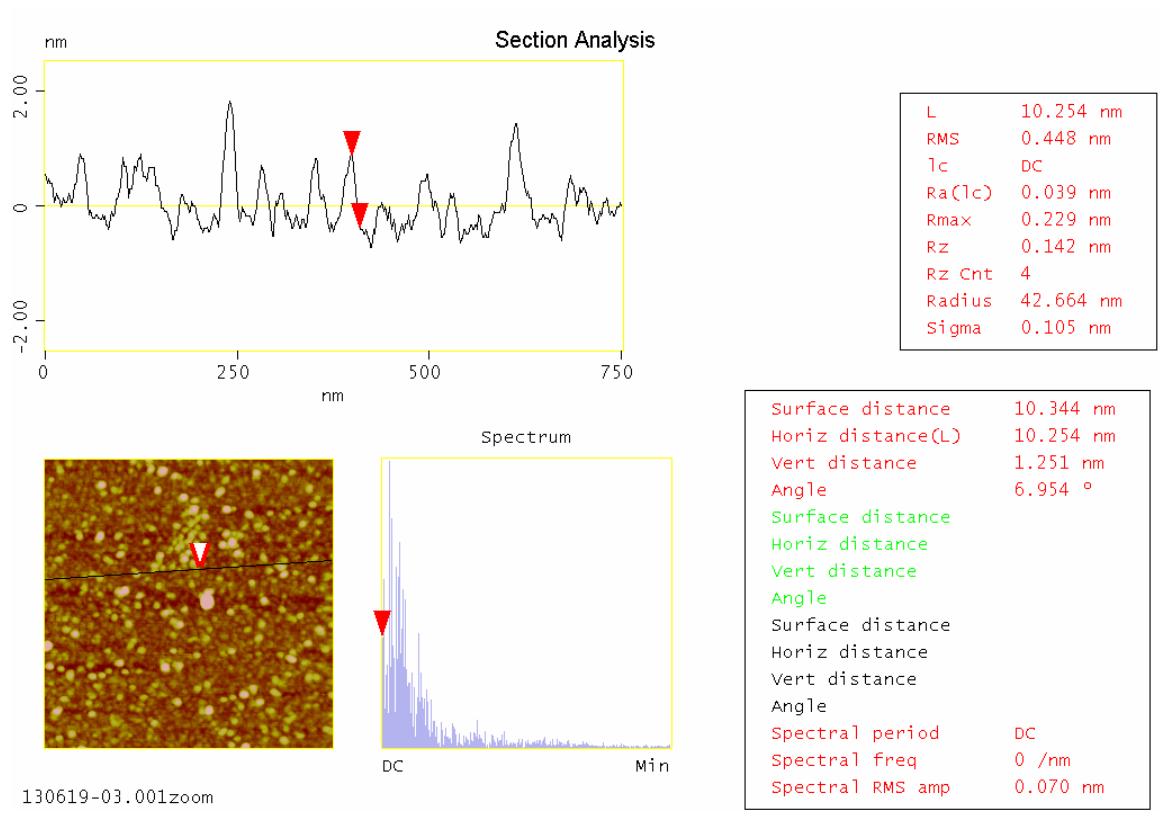


Figure 4-14. Section analysis for 3 minute deposition of the VDF oligomer SAM on mica.

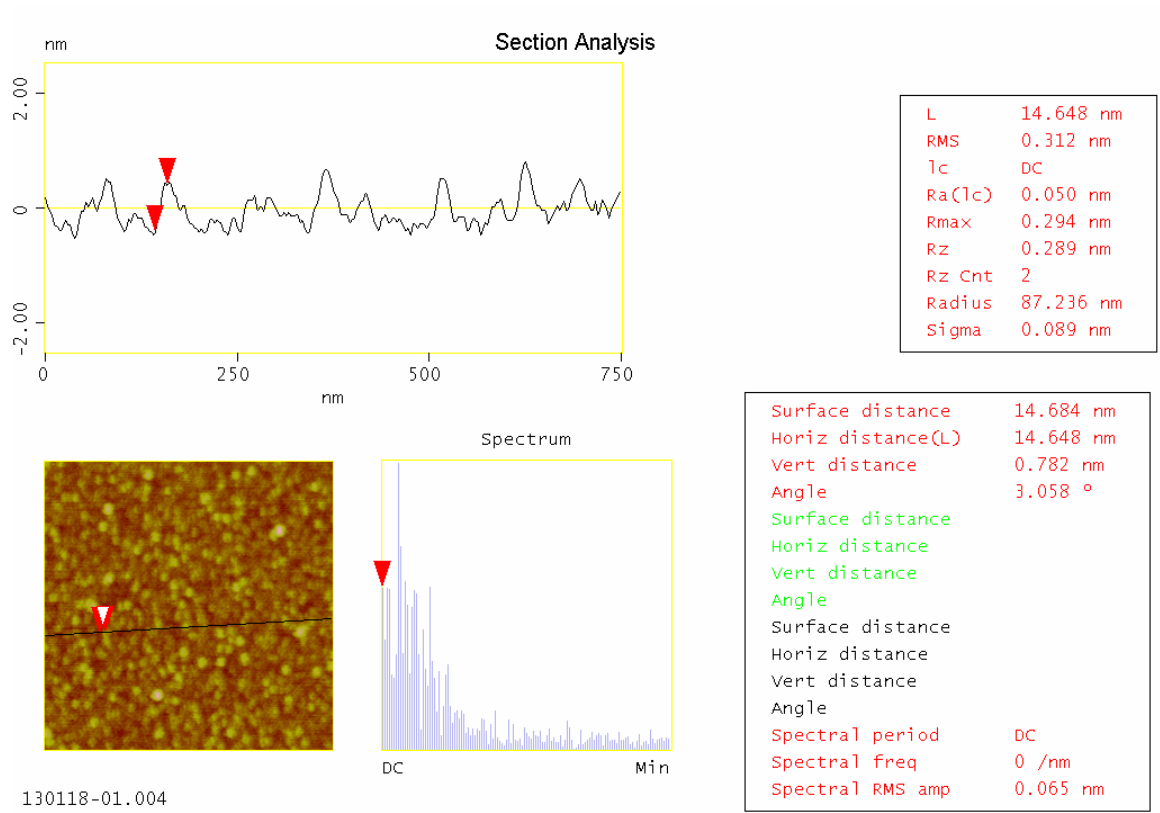


Figure 4-15. Section analysis for 5 minute deposition of the VDF oligomer SAM on mica.

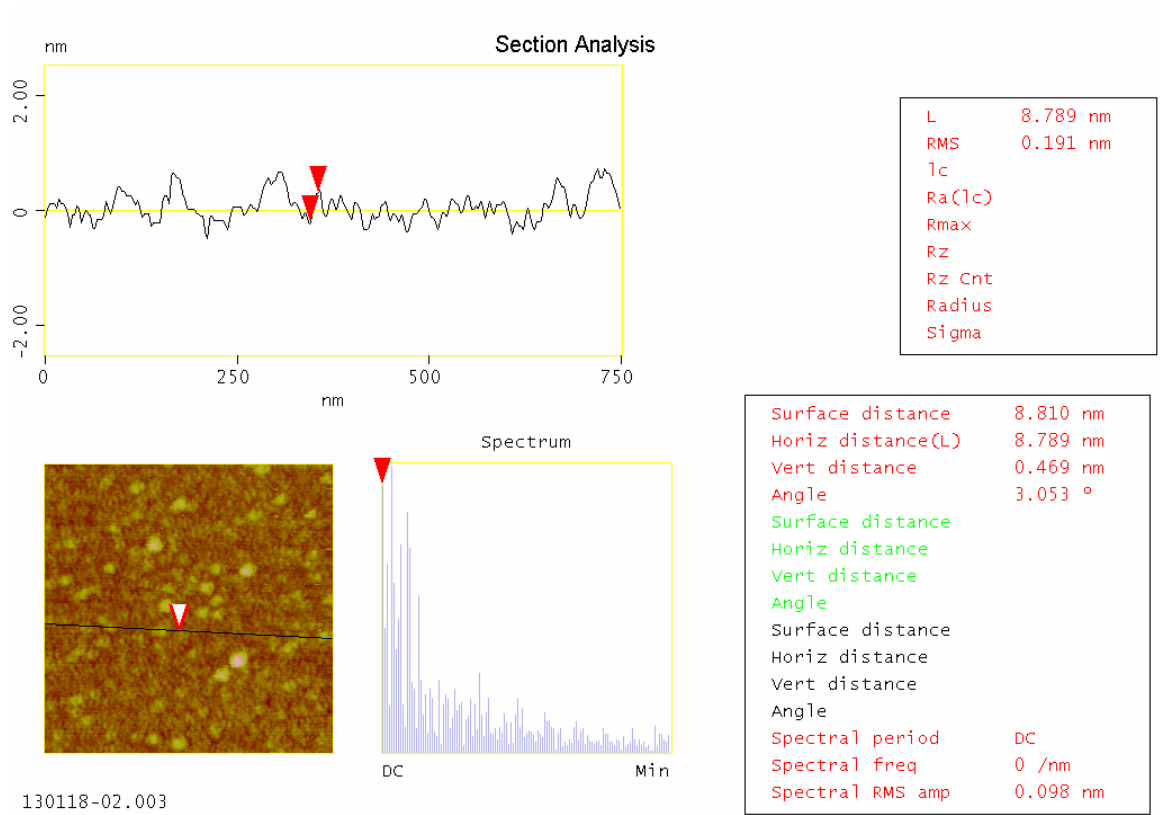


Figure 4-16. Section analysis for 20 minute deposition of the VDF oligomer SAM on mica.

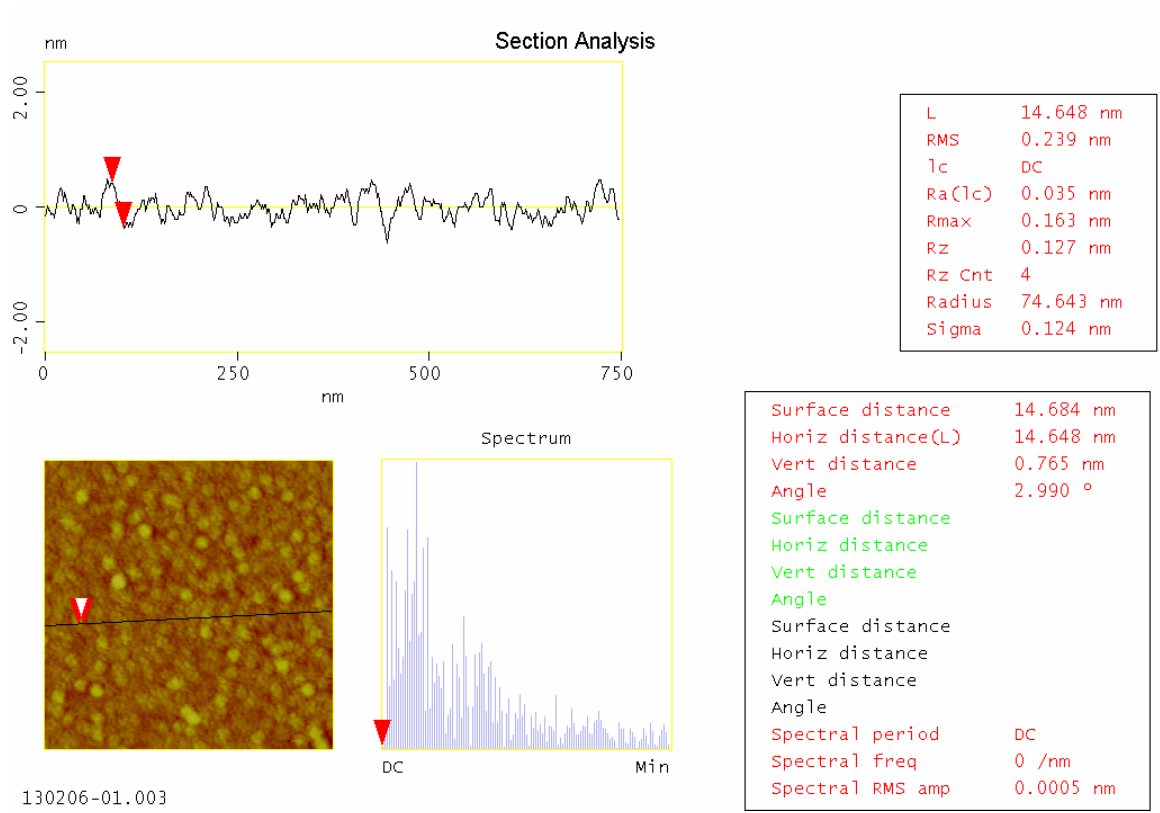


Figure 4-17. Section analysis for 1 hour deposition of the VDF oligomer SAM on mica.

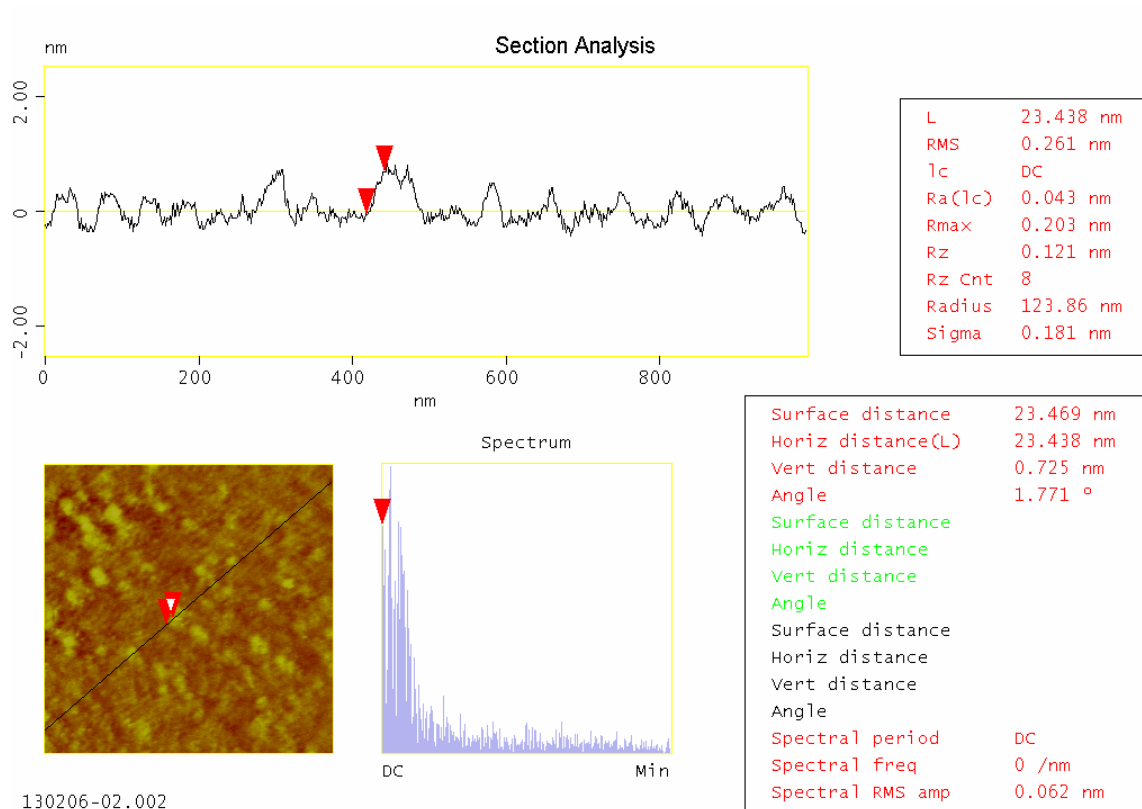


Figure 4-18. Section analysis for 24 hour deposition of the VDF oligomer SAM on mica.

## CHAPTER 5

### CHEMICAL COATING OF BARIUM TITANATE NANOPARTICLES

#### 5.1 Introduction

To achieve the goals of having high energy storage and high breakdown strength in capacitors, it is necessary to have good compatibility between all of the parts of the composite dielectric. One way to improve the surface boundaries between the particles and the surrounding matrix is to coat the particles with a compatible material similar to the matrix [1]. Since the matrix used in the composite samples was poly(vinylidene fluoride) (PVDF) copolymers and terpolymers, we coated the barium titanate nanoparticles with two materials, alkanes as a prototype system and VDF oligomers to match the matrix.

The particle coating procedure was essentially growing a self-assembled monolayer (SAM) onto the surface of the particles. For the alkane and VDF oligomer coatings, the same general procedure was used. The particles were first de-agglomerated and cleaned of any surface contaminants. Then, they were dispersed in a solvent with the coating materials and allowed to stir for several days. Finally, the coated particles were washed to remove the surplus surfactant.

Once the particles were coated, it was necessary to verify that the coatings were actually attached to the particles and the coating to particle ratios. This was accomplished through by variety of techniques. Thermal gravimetric analysis (TGA) measures the change in mass as temperature increased [2]. This allowed for the calculation of the mass ratios of the particles to coatings. Since our functional group and

the chains of the coatings were nuclear magnetic resonance (NMR) active elements, we used the NMR to verify that the coatings on the particles were the desired materials and to show that the functional end group signatures changed, signifying attachment to the particles [1-3]. Finally, we needed a way to measure how thick the coatings were on the particles. Initial attempts were made with the tunneling electron microscope (TEM). The difficulty with organic materials primarily consisting of carbon was the low contrast between the TEM grids and coatings. This left us always questioning if we were seeing the real coating or artifacts of the imaging. An alternative way to determine the coating thickness was to grow a self-assembled monolayer (SAM) on a flat substrate and then measure the thickness of the layer. The coating thickness was measured using ellipsometry and atomic force microscopy (AFM), and was a reasonable estimate for the coating thickness and density as long as the radius of curvature of the particles was not too small. The results of the SAM studies are discussed in Chapter 4.

## **5.2 Choice of Particles**

This project required small, high-dielectric constant nanoparticles to be dispersed throughout the dielectric layer. Oxides and other high dielectric constant materials with a bulk dielectric constant ranging from 100 to  $10^4$ , as shown in Table 5-1, were considered as nanoparticles for composite films. Many of the materials listed were commercially available. Syntheses of other particles have been announced in literature. These include barium titanate [4-7], potassium tantalate niobate [8, 9], strontium titanate [5, 10, 11], titanium dioxide [12], potassium tantalate [13], lead titanate [14, 15], lead zirconate [16, 17], lithium niobate [18, 19], manganese dioxide [20, 21], and potassium tantalate [22].

The ones that were not available could be in the future and would be worth considering for future studies. Due to size effects and synthesis techniques, nanoparticles may not always have the same dielectric constants as the bulk materials [23]. Since many of the particles were relatively new and had not been well studied, there was very little literature available about nanoparticle dielectric constants for many of the particles. Therefore, we based our decision on which nanoparticles to try on the bulk properties and the availability of the particles either commercially or through collaborators. The particle we chose to work with for coating with wet chemistry was barium titanate. It had a dielectric constant of 150 or higher in bulk. Due to the size effects and synthesis techniques, it was in the cubic phase when made into nanoparticles of less than 100 nm with a few exceptions [7, 24]. Barium titanate is convenient since it is commercially available as nanoparticles in sizes ranging from 15 nm to 100 nm from Sigma-Aldrich.

The size of the nanoparticles was verified using a field emission scanning electron microscopy (SEM). Figure 5-1 shows several SEM images of the uncoated particles. As can be seen, there was a small distribution of sizes. To determine the average size of the particles, the particles in the Figure 5-1B SEM image were measured with a ruler and color coded based on size, as shown in Figure 5-2. Using the scale bar on the image where 300 nm was 65 mm on the original printout, the particle sizes were broken into bins, each 10 nanometer wide. Each size was assigned a color. For example, the 50 nm wide particles were color coded green and the 60 nm particles were colored purple. After all of the visible particles were color coded, the particles of each color were counted up. The bins were then plotted on a histogram as shown in Figure 5-3. When the data was

fitted with a Gaussian curve, the peak was at 56 nanometers, representing the average size of the nanoparticles.

### 5.3 Choice of Coatings

Since the particles chosen are oxides, the functional group on the head of the coating needs to be able to attach to the surface of oxides. After considering the work done by the Perry group [1, 25], we chose to use phosphonic acid as the functional group for attaching ligands to the BTO nanoparticles. This acid was attractive because it had three potential binding sites to the surface of the oxide [26]. This increased the chance that the coatings would attach to the particle and stay attached throughout the sample preparation.

Phosphonic acid oligomers are commercially available with various types of tail groups for use in making self-assembled monolayers and as a surfactant from various vendors such as Sigma Aldrich and PlasmaChem. For this study, the tail groups should be a dielectric. The ideal tail group was the VDF oligomers (VDFO). This oligomer was chosen because it matched well with the matrix which was composed of PVDF copolymers or terpolymers. The drawback to this oligomer was that it had to be specially synthesized, limiting the availability. The control coatings were phosphonic acid alkanes. These were commercially available in a range of lengths from six to eighteen CH<sub>2</sub> units from PlasmaChem. The alkanes had a dielectric constant of approximately 2 and could be processed with similar coating techniques as the VDFO. Additionally, alkanes make ideal SAM's [27-34] which gave us a chance to test our verification techniques for the coatings by making SAMs, as discussed in Chapter 4.

## 5.4 Detailed Particle Coating Procedure

The coating procedure was divided into two parts. The first part was to clean and break up the nanoparticles, removing any surface contaminants and remnant surfactants. This step was the same for any of the surfactants used to coat the particles. The second part was to coat the particles, and this procedure changed slightly with the different types of surfactants. The two steps could be done immediately following each other, or the particles could be cleaned, dried, and stored under vacuum until they were needed for the second step [25, 35]. It was often convenient to scale up the cleaning step if there were plans to coat multiple batches of particles in the near future, using part of the cleaned particles right away and storing the rest of the particles. Although making larger batches required a few extra hours of sonification to de-agglomerate the particles and to disperse them in solution, it saved several days' time needed to clean another set of particles.

### 5.4.A *Cleaning the particle surface*

This procedure was designed to clean one gram of BTO nanoparticles with an average diameter of 56 nm. It could be rescaled to any convenient sized batch of particles. First, the cleaning solution was prepared by measuring 0.35 grams of ammonium chloride ( $\text{NH}_4\text{Cl}$ ) into a 50 ml flask. Then, 24 ml of ultrapure deionized water was added to the flask. The flask was covered with a parafilm sheet or a stopper and vortexed the ammonium chloride solution for approximately one minute. The BTO nanoparticles (1 gram) were measured in a weight boat or measuring paper and slowly poured into the 50 ml flask containing the ammonium chloride solution. The flask was covered with parafilm or a stopper to prevent the solution from splashing and the solution

was vortexed for approximately 60 seconds to start dispersing the particles into solution. Then, the solution was ultrasonicated for two to three days to de-agglomerate the particles using a Hielscher UP100H (100% power) or a Sonic Vibra-Cell (80% power) probe sonicator. Since the sonication process released a large amount of heat, it was important to use a water bath. As shown in the photos in Figure 5-5, the bath should consist of either 2 liters of room temperature water or 1 liter of ice water. The vial or flask with the particles was submerged most of the way into the water bath, so there was increased surface area between the flask and the ice bath to increase the heat transfer away from the particles. While the solution was sonicating, the solvent level was monitored for evaporation, and more solvent was added as needed to maintain a constant volume.

After the particles were well de-agglomerated, it was necessary to wash the ammonium chloride from the particles. The flask was removed from the sonicator, and the solution was poured into 50 ml Teflon centrifuge tubes. It was easier to centrifuge the particles if the tubes are not filled to the very top, so multiple tubes were used. Any remaining particles in the flask were rinsed into the centrifuge tubes with ultrapure water. The centrifuge required all of the tubes to have the same weight and an even number of tubes to keep the centrifuge balanced. Depending on how much solvent was used, it may be necessary to use an additional tube of solvent as a counter-balance inside of the centrifuge to keep the weight evenly distributed.

For the 56 nm in diameter particles, the solution was centrifuged for 20 minutes at room temperature and 5000 RPM. For the 15 nm particles, it was necessary to increase

the centrifuge speed to 8000-1000 rpm. At higher speeds, the centrifuge may start to heat up and refrigeration was used if this happened. Care had to be taken to keep from freezing the solutions, especially the counterweights that did not contain salts to lower the freezing points and often stayed in the centrifuge for longer periods of time. After centrifuging the particles, the water was carefully decanted, leaving the particles in the bottom of the tube. If the particles were not well pressed to the side, it was necessary to pipet out the last of the water using a glass pipet and small rubber bulb to prevent turbulence from disturbing the particles. Once the old water was removed, 25 ml of deionized water was added to the tubes and the particles were first vortexed and then sonicated back into solution. The centrifuging was repeated at least two more times. As the particles were re-dispersed into the solution, it was possible to start combining the particles solutions into fewer tubes, making it easier to dry and reducing particle loss. If the plan was to coat immediately, the particles were kept as a wet paste; otherwise they were dried in the vacuum oven over night at about 40°C. After drying, the particles were stored in an air-tight bottle for a few days or under vacuum for longer periods of time.

#### *5.4.B Coating Barium Titanate Nanoparticles with Alkane-Phosphonic Acids*

The barium titanate nanoparticles were coated with 10- and 18-carbon chain alkanes. The alkanes were chosen as a reference material to allow for the development of the procedures needed to coat the particles prior to having the VDF oligomers and to make reference samples. Due to difficulties with the synthesis methods for the oligomers, the alkane-coated particles were used in a majority of the capacitor samples discussed in Chapter 6 and 7.

To coat the particles, they were first be re-dispersed in a 95/5 ethanol/water mixture and the agglomerations broken up. The cleaned and dried particles were poured into a round-bottom flask or the particles from the cleaning step were rinsed with into the flask. The typical batch size to coat was 1.0 grams and all amounts listed in this section were for that size batch. In a flask, 25 ml of 95/5 ethanol/water was added and the solution was sonicated for several hours to disperse and de-agglomerate the particles. A water bath similar to the one in the cleaning step shown in Figure 5-5 was used to prevent the solution from heating up from heating up too much. This was more important in this step since the ethanol evaporated faster than the water. It was necessary to monitor the volume of the solution while sonicating and add more solvent as it evaporated.

While the particle solution was sonicating, the alkane surfactant solution was prepared by measuring 0.5 mmole of the alkane powders into a 10 ml vial. See Table 5-2 for the molecular weights of the each of the different alkanes. The amount of alkanes, in grams, needed to coat one gram of 56 nm in diameter particles was calculated by taking 0.005 times the molecular weight. When the particles were much small than 56 nm in diameter, the amount of surfactant needed to be scaled up for the increased surface area. To the alkanes, 3 ml of 95/5 ethanol/water was added and the solution was vortexed. Since this was a very concentrated solution, it was often necessary to use the bath sonicator to heat and sonicate the surfactant in addition to vortexing it to get it into solution. If the alkanes were not completely dissolved after heating and sonicating for a few minutes, a small amount of solvent was added until the surfactant was completely dissolved.

The particle solution was removed from the sonicator, and the surfactant solution was slowly added to the flask containing the nanoparticles. The solution was vortexed to mix it together, and then it was sonicated for another hour to disperse the surfactant throughout the particles solution. At the end of the hour, the solution was transferred to the hot plate with the magnetic stirrer. See Figure 5-6A for a sketch of the setup. The water bath was held at 60-70 degrees. To prevent pressure from building up inside of the flask and to prevent the solvent from evaporating, a water-cooled West Tube was used to condense the solvent back into the flask. The solution was stirred at a moderate speed for several days to ensure complete coating of the particles and to prevent the particles from settling out of solution onto the bottom of the flask.

Once the particles were coated, it was necessary to wash the excess surfactant from the particles. To wash the particles, the water bath was removed and the particles were allowed to slowly cool to room temperature while stirring. Once the particles were cooled, they were poured into Teflon centrifuge tubes. Particles sticking to the side of the flask were rinsed into the centrifuge tubes using the 95/5 ethanol/water solvent.

The solution was centrifuged for 25 minutes at 5000 RPM and at room temperature using a Sorvall RC-5B Refrigerated Superspeed Centrifuge. Then the liquid was decanted, leaving the particles behind in the bottom of the centrifuge tubes. For some batches, the solution from the first wash was collected in a vial or bottle and the surfactant was reclaimed. After decantation, 25 ml of pure ethanol (200 proof) was added to the particles. The solution was vortexed and sonicated until the particles completely suspended in solution. The centrifugation was repeated two more times using

200 proof ethanol to rinse the particles. After the final centrifuging, the liquid was poured off and the particles were dried in the vacuum oven at 40°C overnight. Once the particles were dry, they were scraped out of the centrifuge tube into a glass vial and stored for future use.

#### *5.4.C Coating Barium Titanate Nanoparticles with VDF Oligomer*

The procedure for coating the particles with VDF oligomers was very similar to the procedure for coating the particles with alkanes. The particles from the cleaning step were rinsed with acetone or 1.0 grams of the dried particles was measured into a round-bottom flask. A total of 25 ml of acetone was added to the flask and the solution was sonicated for several hours. The water bath, as shown in Figure 5-5, was used to keep the solution cool.

While the particle solutions were sonicating, the oligomer solution was prepared. Table 5-3 gives the molecular weights of some of the oligomers. Since there were many different variations of the VDF oligomers, there were too many combinations to list completely. There were a limited number of head and tail groups, though, so the total molecular weight could be found by adding the weight of the head and tail together. Once the total molecular weight had been found for the oligomer, the amount of material needed to coat a 56nm in diameter particle could be calculated by multiplying the molecular weight by 0.005 to get a 0.5 mmol solution.

Once the oligomers have been measured into a 10 ml vial, 3 ml of acetone was added and the solution was vortexed. As needed, the bath sonicator was used to help dissolve all of the oligomers into the solution. Since this was highly concentrated

solution, it was sometimes necessary to add a little more solvent to completely dissolve the oligomers.

The particle solution was removed from the sonicator and the oligomer solution was added to the round flask. The solution was vortexed to combine the oligomers and particles, and then sonicated for an hour to disperse the surfactant with the particles. At the end of the hour, the solution was transferred to the hot plate with the magnetic stirrer. Figure 5-6B shows a sketch of the setup. The solution was held at room temperature, so a stopper was used in the flask to prevent evaporation. For about a week, the solution was stirred at a moderate speed to ensure complete coating of the particles. The reaction was slow and without using any heat, so it required longer stirring time than the alkanes to improve the coverage of the particles.

Once the particles were coated, the excess surfactant was washed from the particles. The solution was poured into Teflon centrifuge tubes and any remaining particles stuck to the side of the flask were rinsed with acetone into the tubes. Depending on the size of the batch and the amount of rinsing needed, the solution may require several tubes for the initial centrifugation. Later, they could be poured together between centrifuge steps. The solution was centrifuged for 25 minutes at 7500 RPM and at room temperature. Then liquid was decanted, leaving the particles behind in the bottom of the centrifuge tubes. Since the oligomer was of limited supply, the solution from the first wash was collected and the oligomers were reclaimed by evaporating the solvent. Approximately 25 ml of acetone was added to the particles and sonicated for a minute or two, until the particles were in solution. The centrifuging was repeated two more times

using acetone to rinse the particles. For the final wash, isopropanol alcohol was used to rinse the particles. This removed any residue left from acetone. After the final centrifuging, the alcohol was poured off and the particles were dried in the vacuum oven at 40°C overnight. Once the particles are dry, they were scraped out of the centrifuge tube into a glass vial and stored under vacuum for future use.

## 5.5 Verification of Particle Coatings

Once the coating procedure was complete, it was necessary to ensure that the particles were actually coated and to obtain an estimate of the coating thicknesses. This was done with techniques that could help confirm that the coating was present, such as NMR, and to determine the relative ratios of the particles and coatings through TGA. Finally, the actual coating thickness was measured using TEM and by growing a self-assembled monolayer on an alternative substrate.

### 5.5.A Nuclear Magnetic Resonance of Particles and Coatings

Nuclear magnetic resonance (NMR) allows us to determine the relationships between spin  $\frac{1}{2}$  elements and their neighbors [2]. Since we are using hydrogen, fluorine, and phosphorus, which contain a nuclear spin of  $\frac{1}{2}$ , we can probe the structure of the material. The carbon backbone does not give us a signature in NMR unless we substitute the natural carbon 12 for carbon 13.

NMR was used to confirm a variety of properties. First it was used to verify the composition of the VDF oligomer and the presence of the phosphonic acid functional group. It was also used to obtain the average chain length. Finally, the NMR was used to

show if the particle coatings were present, attached to the particles, and that there was no large surplus of surfactant remaining in solution.

The structural part of the study was done with the VDF oligomer dissolved into deuterated acetone. 1D  $^1\text{H}$  NMR was used to examine the hydrogens along the backbone and the  $\text{CH}_2$  linkers between the tail and the phosphonic acid functional group, as shown in Figure 5-7. The integrated area of the peaks was used to determine the total number of hydrogen per molecule. The peaks between 2.8 and 4 ppm represent the  $\text{CH}_2$  groups. The peaks at 9.5 ppm were the OH groups and there was minimal evidence of benzene present at 7.5 ppm. It also allowed us to verify that the starter materials, such as benzene, were no longer contaminating the oligomers.

Fluorine NMR was able to confirm the presence of fluorine, verifying that the sample was predominantly VDF, and allowed us to calculate the average length of the VDF tail. The length of the tails was calculated by comparing the area of the  $\text{CF}_3$  peak to the area of the  $\text{CH}_2\text{CF}_2$  peak. Since we know that there was one  $\text{CF}_3$  group present in each oligomer, we could use the ratio of the areas to determine how many  $\text{CH}_2\text{CF}_2$  monomers were present in the material, as shown in Figure 5-8. Since the area of the  $\text{CF}_3$  peak was three, and the area of the  $\text{CF}_2$  peaks was almost 15, there was between 7 and 8 VDF units in each oligomer. This result was consistent with the hydrogen results.

The 1D phosphorus NMR spectrum shows that phosphorus was present in the solution, as shown in Figure 5-9. The final experiment to confirm the structure of the oligomers was using 2D  $^1\text{H}$ - $^{31}\text{P}$  Heteronuclear Multiple Bond Correlation (HMBC). HMBC looks at the interactions between hydrogen and phosphorus atoms that are two to

four bonds away from each other. This allowed us to determine if the phosphorus cluster was actually attached to the VDF chain as opposed to having the end group and the chains mixed together but not attached. The 2D  $^1\text{H}$ - $^{31}\text{P}$  HMBC spectrum indicates that the phosphate group was attached to the VDF oligomer since there were peaks present in the 2D spectrum, as shown in Figure 5-10. If the phosphorus was not attached to the VDF tail, there would be no peaks in the 2D spectrum.

Once we verified the structure of the oligomers and coated the particles, we needed to show that the coatings were present and attached to the particles. The normal way to run solution NMR was to dissolve everything in solution completely; similar to the structure verification part, since the NMR can only probe what is actually dissolved. As shown in Figure 5-11A, we used the normal solution method to analyze the pure oligomers where the oligomers were completely dissolved in the solution. Since we knew that the barium titanate nanoparticles were not soluble in acetone, we made a suspension of the coated particles. If the functional group of the surfactant was attached to the nanoparticles, as shown in Figure 5-11B, we should be able to see the signature of the tail group. The phosphonic acid that was attached to the nanoparticle would not be in solution and it should not show up in any of the scans. Instead, if we have the situation shown in Figure 5-11C, where the coatings were agglomerated around the particle but not physically attached or have a large amount of surfactant free in the solution, we should get a signal from both the hydrogens and fluorines in the tail and the phosphorus functional group since the phosphorus group is now in solution. The other possible scenario is that all of the surfactant washed away during the coating procedure, and in that case, we would have no signal related to the surfactant from any of the elements.

This data was collected on several different instruments due to issues with various machines being out of commission during the duration of the experiment. The instruments used for various parts were the 300 MHz, 400 MHz, and the 600 MHz NMR. The higher the frequency, the better the signal to noise is possible. A more detailed description of the procedure is described in Chapter 2.

#### *5.5.B Thermal Gravitational Analysis of Particles and Surfactants*

Thermal gravitational analysis (TGA) is a measurement of the change in mass as the temperature is ramped linearly. The typical ramp rate for the particles and surfactants was 5 degrees per minute from 25°C to 1000°C. Measurements were made on clean, bare particles; particles coated with surfactants; and the plain surfactants. It was important that the particles were dry from humidity before running TGA. Any moisture left in the particles showed up as a change in mass, so the materials were dried overnight in either the vacuum oven or the vacuum desiccator, then transported to the instrument in a portable desiccator. All measurements were made on a Perkin Elmer STA 6000 model instrument. A more detailed description of the procedure is discussed in Chapter 2.

The uncoated particles showed approximately a 5% change in mass over the range of 1000 °C, as shown in Figure 5-12. This mass loss could be caused by remaining moisture leaving the particles that was not removed before heating or by elements, such as oxygen, leaving the particles. The hypothesis was that the particles lost the same amount of mass during each TGA measurement, regardless of the coatings on the surface. The coatings were expected to be completely incinerated by high temperatures, so the remaining mass was solely the particles.

### 5.5.B.a Thermal Gravitational Analysis of Alkane Coated Nanoparticles

In comparison to the uncoated particles, the TGA of the octadecylphosphonic acid (ODPA) shows a sharp drop at 454 °C, as seen in Figure 5-13. This was from the alkanes decomposing. The coated particle data could be combined with the pure particle and alkane data to determine the coating efficiency. Figure 5-14 shows the coated particle data in blue with a 17% total change in mass. The large decrease in mass occurred at approximately the same temperature for the composite samples as the drop in the pure alkane curve, shown in red.

From the TGA plot, we get that there was a 3.47% decrease in mass due to the weight change in the particles and a 14.77% mass change due to the loss of the oligomers. This means that the remaining material should be pure BTO. Since the average particle size was known, we calculated the expected volume ratios of the alkanes and particles, and make a prediction about the coating thickness. Using the bulk density of each material, we get an experimental volume of 65% BTO and 35% alkane. If the alkanes had the bulk density of around the particle, then the coating thickness would be about 4 nanometers thick. Alternatively, it has been shown that the phosphonic alkanes can attach to the particle with several different configurations [31], as shown in Table 5-4. If there was a single layer of alkanes with the ideal spacing of each functional group, the weight percentage of the alkanes would be 3% and the shell would be about 2 nm thick. If there was a double layer or a bilayer, the mass of the coatings would be approximately 6% of the total mass. If there was a double bilayer, we would have a 4 nm

thick shell and approximately a 11% change in mass. This implies that the shell must be at least 4 nm thick, depending on the density of the alkane chains.

#### *5.5.B.b TGA of VDFO coated particles*

The same procedure was used to determine the coating thickness of the oligomer coated particles as the alkanes. Unlike the alkane curve shown in Figure 5-13, the VDF oligomer curves were not nearly as repeatable or clean. Figure 5-15 shows the TGA for two different batches of VDFO. The first batch of oligomer shows a start to the mass loss approximately 170 °C and a majority of the mass is lost around 275 °C. The second set of materials shows an earlier onset of mass loss, around 150 °C and a majority of it leaves around 245°C. These values were surprisingly low considering that the bulk PVDF has a decomposition temperature around 380 °C in air. Since both materials contain chains of  $\text{CH}_2\text{CF}_2$ , it is expected that both materials would have needed similar amounts of energy to decompose. The other surprising thing about this set of data is the differences in the shapes of the curves. Both samples were measured at the same heating rate, 5 degrees per minute. It was expected that two similar materials scanned at the same rate should have had similar shaped curves.

Also, it was puzzling why there was mass left at high temperatures. The alkanes dropped to zero mass after the material decomposed at 454 °C. The oligomers, though, still had 20-30% of the mass left. This additional mass not being completely incinerated at high temperatures made the analysis of the coated particles much more difficult to obtain accurate mass ratios for the particles and oligomers. As shown in Figure 5-16, the

total mass loss for the VDF oligomers was less than 1%. This implies that there was less than 1 monolayer covering the surfaces of the particles, as shown in Table 5-5.

### *5.5.C Transmission Electron Microscopy of Coated Nanoparticles*

Once the barium titanate nanoparticles were coated, it was desirable to directly measure the thickness of the coatings on the particles. One way to do this was by using a transmission electron microscope (TEM) to directly measure the shells around the particles. The particle solution was dripped onto a carbon coated copper grid and allowed to dry.

As shown in Figure 5-17, there were several rings surrounding the particles. Part of the difficulty with using TEM grids and analyzing the images was the carbon coated grids and the coatings on the particles were both carbon based. While the heavier elements in the particles gave good contrast with the grids, the coating thickness was harder to resolve and left to a bit more interpretation. It was believed that the inner ring around the particles was the coating and the outer ring was an artifact of the solvent. This would make the thickness of the particle coating when coated with octadecylphosphonic acid about 4 nm thick. This was twice the expected thickness based on the published results of self-assembled monolayers made of the same materials, but is in agreement with our TGA results and the AFM results in Chapter 4.

Since the TEM images of the alkane-coated barium titanate particles were difficult to interpret, we did not use this method to measure the coating thickness of the oligomer coated particles. Instead, we grew SAMs on flat substrates and measured the average film thicknesses using ellipsometry, which gave a thickness approximately 1 nm.

## 5.6 Solubility Testing

Once the particles were coated, we wanted to make suspensions of the particles. To do this, the solvent must be compatible with the coatings and would allow the particles to stay suspended in solution for several hours to a day or more. While longer would be ideal, they could be re-dispersed between uses over a longer time frame. In some cases, the solvent needed to be compatible with the matrix material, such as for the spin coated samples. In other cases, the solvent did not have to be compatible with the matrix or perhaps the matrix would not be soluble, such as the case of the multi-layer samples. The series of images in Figure 5-18-Figure 5-20 were of the alkane coated nanoparticles in a variety of solvents.

For the octadecylphosphonic acid coated particles, small amounts of the particles were tested in various polar and nonpolar organic solvents. In each case, 0.1 grams of the coated particles were added to 1.0 mL of the solvent. The mixture was vortexed briefly to get the particles into solution, and then sonicated in the bath sonicator for 10 minutes. The initial series of solvents was ethanol, chloroform, toluene, water, DMF, and hexane, as shown in Figure 5-18 and Figure 5-19. The second series of samples contained acetone, isopropanol, DMSO, and benzene, as shown in Figure 5-19 and Figure 5-20. Even though the alkanes were a nonpolar coating, the particles suspended better in some of the polar solvents. After a few minutes following the sonification, most of the particles in ethanol and hexane had started to settle on the bottom of the vial. The particles in water had a tendency to float on the surface and were difficult have stay

suspended in the solution. Within a few hours of being sonicated, most of the particles from the toluene and benzene had settled to the bottom of the vial from the suspension.

This left chloroform, DMF, DMSO, isopropanol, and acetone as the potential solvents to use with the particles. After sitting for a few days, all of the solutions showed settling, but the particles would re-disperse relatively easily with some sonicating. Of the five solvents that initially passed the suspension test, acetone (and butanone) and chloroform were the solvents most often used to make polymer samples. Initially, DMF and DMSO were used with the coated nanoparticles, but it was observed that the strong polar solvents would strip the coatings from the particles. When this would happen, there would be a layer of particles at the bottom of the vial and a layer of the alkane micelles at the top of the solvent. This tended to happen over a week or two, making it difficult to assure the particles were well coated for the duration of making one series of samples. Due to this issue, the solvent was changed to acetone instead of DMF, and then later to butanone to take advantage of the higher boiling point and the slightly higher viscosity. With acetone and butanone, the separation of the particles and the coating was not observed over the weeks to months that a solution was in use. When the particles were in chloroform, the solution would show discoloration (slight yellowing) of the solution after a few weeks. Since the chloroform solutions were used for LB and were very dilute, it was easier to make fresh solutions as needed whenever it started to show signs of discoloration or had been not used for a while.

## 5.7 Conclusions

We were able to coat barium titanate nanoparticles with phosphonic acid functionalized VDF oligomers and alkanes. The particle coatings were verified with TGA and NMR. Based on the TGA calculations, the average particle coating was 4 nm in thickness. This was much thicker than the ellipsometry measurements of the SAM films, which were approximately 1 nm thick. The difference in thickness could be from multilayers on the particles or unattached coatings surrounding the particles. After the particles were coated, we determined which solvents the coated nanoparticles were compatible.

## 5.8 References

1. Kim, P., et al., *Phosphonic Acid-Modified Barium Titanate Polymer Nanocomposites with High Permittivity and Dielectric Strength*. Advanced Materials, 2007. **19**(7): p. 1001-1005.
2. Skoog, D.A., F.J. Holler, and T.A. Nieman, *Principles of Instrumental Analysis*. 5 ed. 1998: Saunders College Publishing.
3. Vasavi, Y., et al., *Heteronuclear Multiple Bond Correlation Spectroscopy- An Overview*. International Journal of PharmTech Research, 2011. **3**(3): p. 1410-1422.
4. O'Brien, S., L. Brus, and C.B. Murray, *Synthesis of Monodisperse Nanoparticles of Barium Titanate: Toward a Generalized Strategy of Oxide Nanoparticle Synthesis*. Journal of the American Chemical Society, 2001. **123**(48): p. 12085-12086.
5. Urban, J.J., et al., *Synthesis of single-crystalline perovskite nanorods composed of barium titanate and strontium titanate*. Journal of the American Chemical Society, 2002. **124**(7): p. 1186-1187.
6. Yoon, S., et al., *Synthesis of Tetragonal Barium Titanate Nanoparticles Via Alkoxide-Hydroxide Sol-Precipitation: Effect of Water Addition*. Journal of the American Ceramic Society, 2007. **90**(1): p. 311-314.
7. Huang, L., et al., *Barium titanate nanocrystals and nanocrystal thin films: Synthesis, ferroelectricity, and dielectric properties*. Journal of Applied Physics, 2006. **100**(3): p. 034316-034316-10.
8. Wei, N., et al., *Synthesis and mechanism of ferroelectric potassium tantalate niobate nanoparticles by the solvothermal and hydrothermal processes*. Journal of the American Ceramic Society, 2007. **90**(5): p. 1434-1437.
9. Zheng, K.-y., et al., *KTa<sub>0.4</sub>Nb<sub>0.6</sub>O<sub>3</sub> nanoparticles synthesized through solvothermal method*. Frontiers of Physics in China, 2007. **2**(4): p. 436-439.
10. Mao, Y., S. Banerjee, and S.S. Wong, *Large-scale synthesis of single-crystalline perovskite nanostructures*. Journal of the American Chemical Society, 2003. **125**(51): p. 15718-15719.
11. Zhang, S., et al., *Formation mechanisms of SrTiO<sub>3</sub> nanoparticles under hydrothermal conditions*. Materials Science and Engineering: B, 2004. **110**(1): p. 11-17.

12. Hayashi, H. and K. Torii, *Hydrothermal synthesis of titania photocatalyst under subcritical and supercritical water conditions*. Journal of Materials Chemistry, 2002. **12**(12): p. 3671-3676.
13. Hayashi, H. and Y. Hakuta, *Hydrothermal epitaxy of KTaO<sub>3</sub> thin films under supercritical water conditions*. Journal of Materials Science, 2008. **43**(7): p. 2342-2347.
14. Cho, S.-B., et al., *Low temperature hydrothermal synthesis and formation mechanisms of lead titanate (PbTiO<sub>3</sub>) particles using tetramethylammonium hydroxide: thermodynamic modelling and experimental verification*. Journal of the European Ceramic Society, 2003. **23**(13): p. 2323-2335.
15. Hubert-Pfalzgraf, L.G., et al., *Solution routes to lead titanate: synthesis, molecular structure and reactivity of the Pb–Ti and Pb–Zr species formed between various lead oxide precursors and titanium or zirconium alkoxides. Molecular structure of Pb<sub>2</sub>Ti<sub>2</sub> (μ<sub>4</sub>-O)(OAc) 2 (OPri) 8 and of PbZr<sub>3</sub> (μ<sub>4</sub>-O)(OAc) 2 (OPri) 10*. J. Mater. Chem., 1997. **7**(5): p. 753-762.
16. Camargo, E.R., et al., *Wet-chemical route for the preparation of lead zirconate: An amorphous carbon- and halide-free precursor synthesized by the hydrogen peroxide based route*. Chemistry of Materials, 2001. **13**(11): p. 3943-3948.
17. Kong, L., et al., *Preparation and characterization of lead zirconate ceramics from high-energy ball milled powder*. Materials Letters, 2001. **49**(2): p. 96-101.
18. Wood, B.D., V. Mocanu, and B.D. Gates, *Solution-Phase Synthesis of Crystalline Lithium Niobate Nanostructures*. Advanced Materials, 2008. **20**(23): p. 4552-4556.
19. Aufray, M., et al., *New synthesis of nanosized niobium oxides and lithium niobate particles and their characterization by xps analysis*. Journal of nanoscience and nanotechnology, 2009. **9**(8): p. 4780.
20. Djerdj, I., et al., *Nonaqueous synthesis of manganese oxide nanoparticles, structural characterization, and magnetic properties*. The Journal of Physical Chemistry C, 2007. **111**(9): p. 3614-3623.
21. Shin, J., et al., *Hollow manganese oxide nanoparticles as multifunctional agents for magnetic resonance imaging and drug delivery*. Angewandte Chemie International Edition, 2009. **48**(2): p. 321-324.
22. Golovina, I.S., et al., *Dielectric Properties and Electron Paramagnetic Resonance of Nanocrystalline Potassium Tantalate*. Ferroelectrics, 2011. **416**(1): p. 133-138.

23. Huang, C. and Q. Zhang, *Enhanced Dielectric and Electromechanical Responses in High Dielectric Constant All-Polymer Percolative Composites*. Advanced Functional Materials, 2004. **14**(5): p. 501-506.
24. Bansal, V., et al., *Room-temperature biosynthesis of ferroelectric barium titanate nanoparticles*. Journal of the American Chemical Society, 2006. **128**(36): p. 11958-11963.
25. Kim, P., *Surface modification of nanoparticles for polymer/ceramic nanocomposites and their applications*, in *School of Chemistry and Biochemistry*. 2008, Georgia Institute of Technology.
26. Mutin, P.H., G. Guerrero, and A. Vioux, *Hybrid materials from organophosphorus coupling molecules*. Journal of Materials Chemistry, 2005. **15**(35-36): p. 3761-3768.
27. Hoque, E., et al., *Phosphonate self-assembled monolayers on aluminum surfaces*. The Journal of Chemical Physics, 2006. **124**(17): p. 174710-6.
28. Hauffman, T., et al., *Study of the Self-Assembling of n-Octylphosphonic Acid Layers on Aluminum Oxide*. Langmuir, 2008. **24**(23): p. 13450-13456.
29. Gao, W., et al., *Self-assembled monolayers of alkylphosphonic acids on metal oxides*. Langmuir, 1996. **12**(26): p. 6429-6435.
30. Allara, D.L. and R.G. Nuzzo, *Spontaneously organized molecular assemblies. 1. Formation, dynamics, and physical properties of n-alkanoic acids adsorbed from solution on an oxidized aluminum surface*. Langmuir, 1985. **1**(1): p. 45-52.
31. Spori, D.M., et al., *Influence of alkyl chain length on phosphate self-assembled monolayers*. Langmuir, 2007. **23**(15): p. 8053-8060.
32. Luschinetz, R., et al. *Infrared spectra of alkylphosphonic acid bound to aluminium surfaces*. in *Macromolecular Symposia*. 2007: Wiley Online Library.
33. Maxisch, M., et al., *Interface chemistry and molecular interactions of phosphonic acid self-assembled monolayers on oxyhydroxide-covered aluminum in humid environments*. Langmuir, 2011. **27**(10): p. 6042-6048.
34. Koutsioubas, A.G., et al., *Formation of alkane-phosphonic acid self-assembled monolayers on alumina: an in situ SPR study*. Surface and Interface Analysis, 2009. **41**(11): p. 897-903.
35. Perry, J., et al., *COATED METAL OXIDE NANOPARTICLES AND METHODS FOR PRODUCING SAME*. 2006, WO Patent 2,006,124,670.

36. *CRC Handbook of Chemistry and Physics*. 92 ed, ed. W.M. Haynes. 2011: Taylor and Francis Group, LLC.

## 5.9 Tables

Table 5-1. Table of high dielectric bulk materials. The bulk dielectric constants are from the CRC handbook [36] unless stated otherwise.

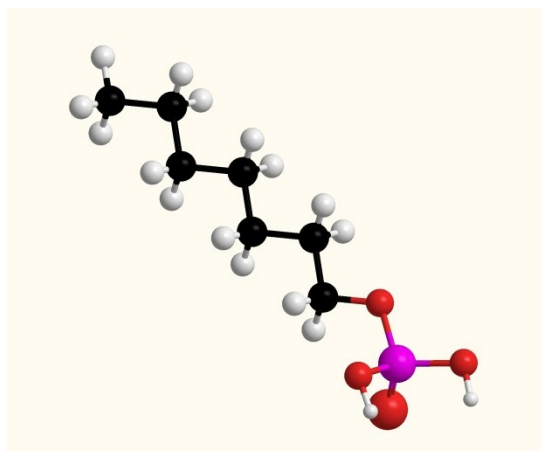
Name	Formula	$\kappa$
Antimonous Sulfide Iodide	SbSI	2000
Barium Sodium Niobate	Ba <sub>2</sub> NaNb <sub>5</sub> O <sub>15</sub>	235-250
Barium Titanate	BaTiO <sub>3</sub>	150-3600
Barium titanium Niobate	Ba <sub>6</sub> Ti <sub>2</sub> Nb <sub>8</sub> O <sub>30</sub>	190-220
Cadmium Pyroniobate	Cd <sub>2</sub> Nb <sub>2</sub> O <sub>7</sub>	500-580
Lead Manganese Niobate	Pb <sub>3</sub> MgNb <sub>2</sub> O <sub>9</sub>	10, 000
Lead Metatantala	PbTa <sub>2</sub> O <sub>6</sub>	150-450
Lead Niobate	PbNb <sub>2</sub> O <sub>6</sub>	180
Lead Titanate	PbTiO <sub>3</sub>	200
Lead Zirconate	PbZrO <sub>3</sub>	200
Lithium Niobate	LiNbO <sub>3</sub>	30-80
Manganese Dioxide	MnO <sub>2</sub>	$\sim 10^4$
Potassium Strontium Niobate	KSr <sub>2</sub> Nb <sub>5</sub> O <sub>15</sub>	800-1200
Potassium Tantalum Niobate (KTN)	KTaNbO <sub>3</sub>	34000
Potassium Tantalate	KTaO <sub>3</sub>	242
Rochelle Salt	NaK(C <sub>4</sub> H <sub>4</sub> O <sub>6</sub> ) 4H <sub>2</sub> O	170
Strontium titanate	SrTiO <sub>3</sub>	332
Titanium Dioxide	TiO <sub>2</sub>	86-170

Table 5-2. Table of molecular weights for the alkanes.

Name	Formula	Molecular Weight (g/mol)
N-Hexylphosphonic Acid	$C_6H_{15}O_3P$	166.16
N-Octylphosphonic Acid	$C_8H_{19}O_3P$	194.21
N-Decylphosphonic Acid	$C_{10}H_{23}O_3P$	222.66
N-Dodecylphosphonic Acid	$C_{12}H_{27}O_3P$	250.36
N-Tetradecylphosphonic Acid	$C_{14}H_{31}O_3P$	278.37
N-Hexadecylphosphonic Acid	$C_{16}H_{35}O_3P$	306.42
N-Octadecylphosphonic Acid	$C_{18}H_{39}O_3P$	334.47

Table 5-3. The oligomers have the form of X-R, where X is the tail group and R is the functional group. The molecular weights of the VDFO are calculated by adding the tail weight to the functional group weight.

Format: X-R



R

n units	Molecular weight
4	292
6	453
8	581
10	709
12	837
14	965
16	1093
18	1221
20	1349
22	1433
25	1601

Functional Group	Molecular Weight
P(O)(OH) <sub>2</sub>	81
OP(O)(OH) <sub>2</sub>	97
(CH <sub>2</sub> ) <sub>3</sub> P(O)(OH) <sub>2</sub>	123
(CH <sub>2</sub> ) <sub>3</sub> OP(O)(OH) <sub>2</sub>	139

Table 5-4. Relative mass calculations for the VDF oligomers and BTO nanoparticles.


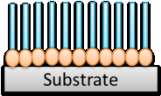
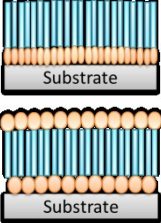
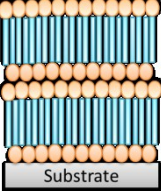
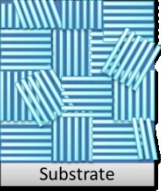

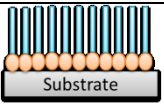
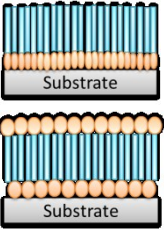
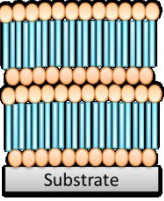
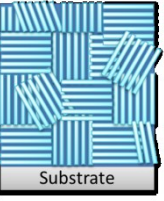
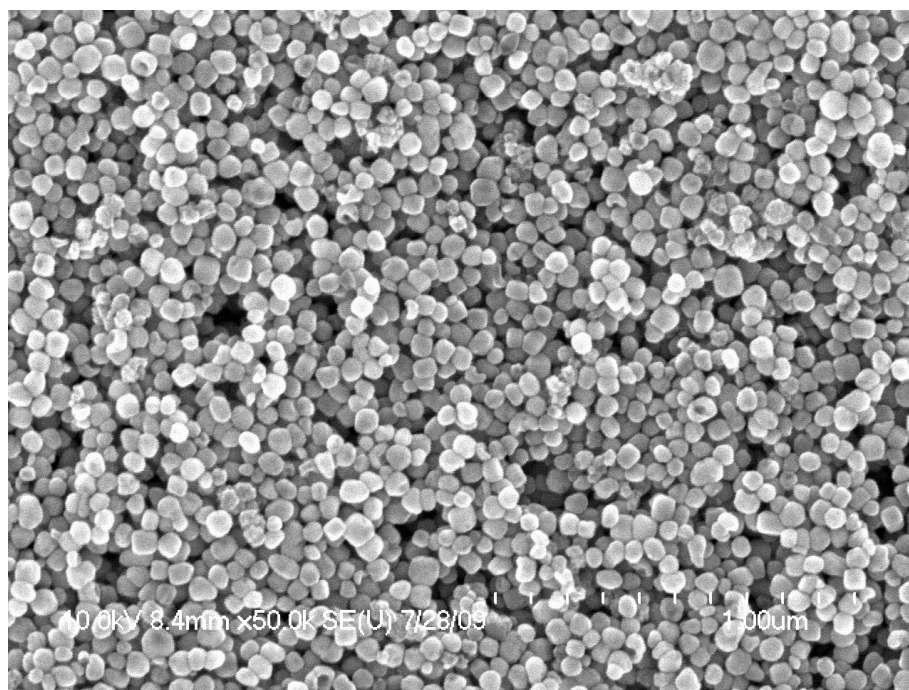
Packing Condition	Sketch of Coating	Particle Mass	Coating Mass	Total Mass	% Mass of Particle	% Mass of Coating	Approximate Thickness
No Coating		$9.062 \times 10^{-16} \text{ g}$	0 g	$9.062 \times 10^{-16} \text{ g}$	100 %	0%	0 nm
Single layer with ideal spacing		$9.062 \times 10^{-16} \text{ g}$	$3.04 \times 10^{-17} \text{ g}$	$9.366 \times 10^{-16} \text{ g}$	96.75%	3.25%	2 nm
Double Single layer or bilayer		$9.062 \times 10^{-16} \text{ g}$	$6.08 \times 10^{-17} \text{ g}$	$9.67 \times 10^{-16} \text{ g}$	93.71%	6.29%	2 nm
Double Bilayer		$9.062 \times 10^{-16} \text{ g}$	$1.216 \times 10^{-16} \text{ g}$	$10.284 \times 10^{-16} \text{ g}$	88.12%	11.82%	4 nm
Original Calculations with Bulk Density		$9.062 \times 10^{-16} \text{ g}$	$1.263 \times 10^{-16} \text{ g}$	$10.325 \times 10^{-16} \text{ g}$	87.76%	12.22%	4 nm

Table 5-5. Relative mass calculations for VDFO and BTO nanoparticles. Note that the bulk calculation has less oligomer than the double bilayer.

Packing Condition	Sketch of Coating	Particle Mass	Coating Mass	Total Mass	% Mass of Particle	% Mass of Coating	Approximate Thickness
No Coating		$9.062 \times 10^{-16} \text{ g}$	0 g	$9.062 \times 10^{-16} \text{ g}$	100 %	0%	0 nm
Single layer with ideal spacing		$9.062 \times 10^{-16} \text{ g}$	$5.38 \times 10^{-17} \text{ g}$	$9.600 \times 10^{-16} \text{ g}$	94.40%	5.6%	2.5 nm
Double Single layer or bilayer		$9.062 \times 10^{-16} \text{ g}$	$1.076 \times 10^{-16} \text{ g}$	$10.138 \times 10^{-16} \text{ g}$	89.39%	16.61%	2.5 nm
Double Bilayer		$9.062 \times 10^{-16} \text{ g}$	$2.152 \times 10^{-16} \text{ g}$	$11.214 \times 10^{-16} \text{ g}$	80.81%	19.19%	5 nm
Original Calculations with Bulk Density		$9.062 \times 10^{-16} \text{ g}$	$1.411 \times 10^{-16} \text{ g}$	$10.473 \times 10^{-16} \text{ g}$	86.52%	13.47%	5 nm

## 5.10 Figures

A



B

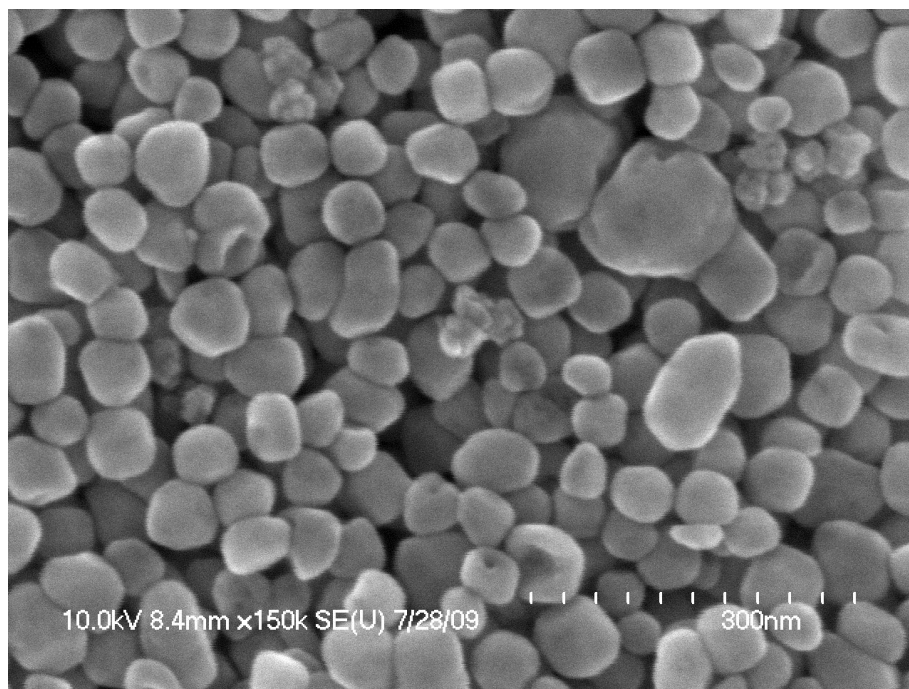


Figure 5-1. SEM images of deagglomerated BTO nanoparticles. (A) A sample at 50k magnification showing that the particles are mostly the same size. ( B) The same sample at 150k magnification. This image was used in Figure 5-2 to determine the size distribution of the particles.

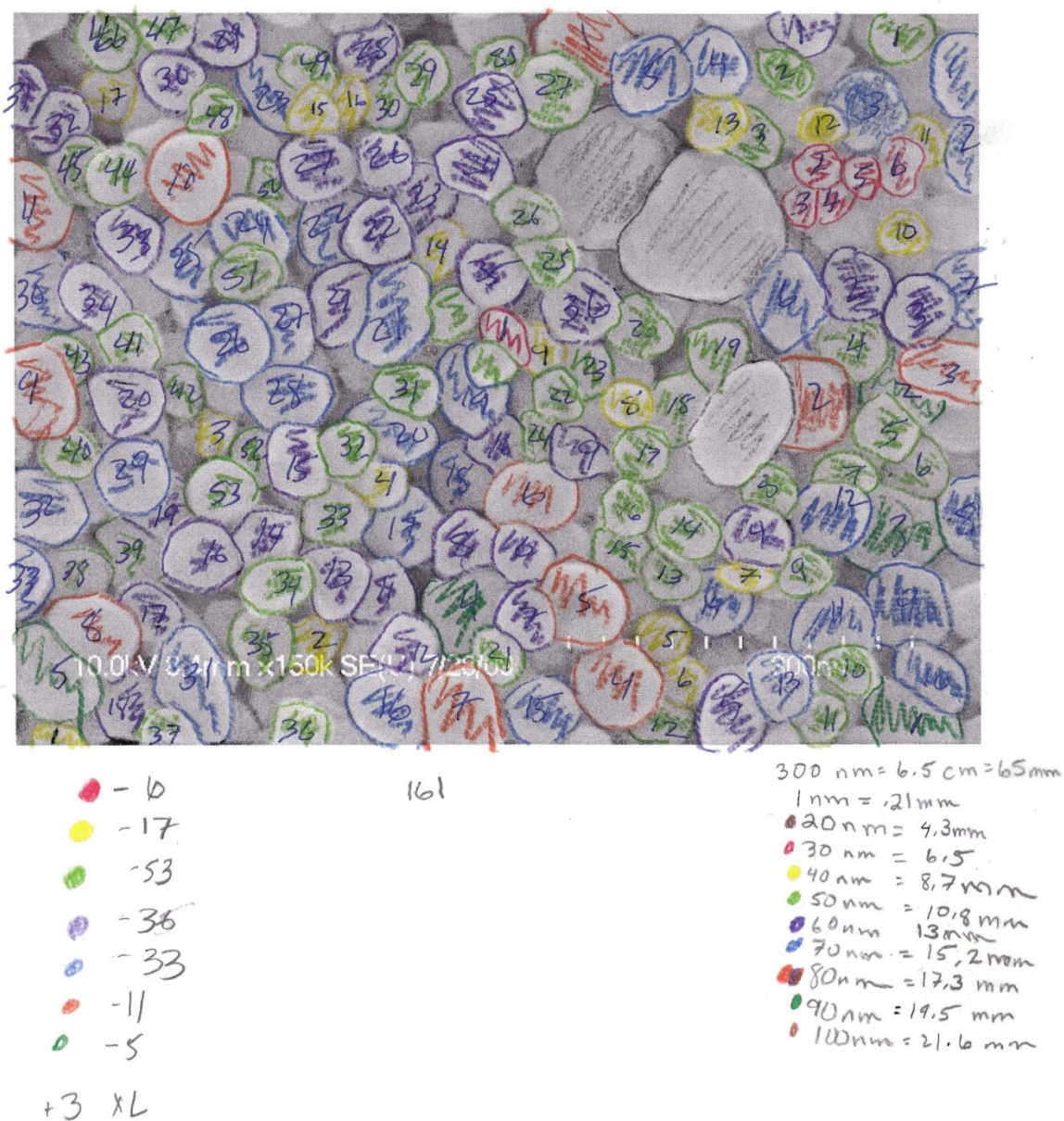


Figure 5-2. Size distribution of the particles was determined by measuring each particle in the image and using the scale based on  $300 \text{ nm} = 65 \text{ mm}$ , the particles were assigned to a color-coded bin size. After all of the particles were color-coded, the number of particles of each color was counted and the size distribution was plotted in Figure 5-3

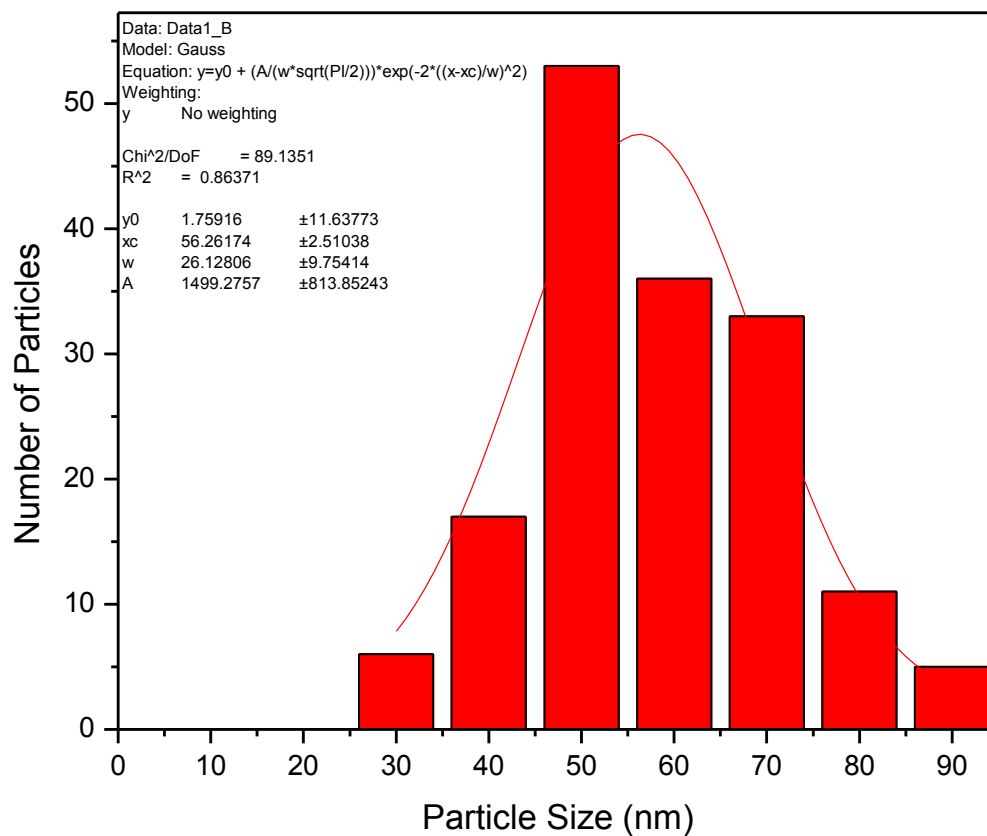


Figure 5-3. Distribution of sizes of barium titanate nanoparticles in Figure 5-2. The histogram was fitted with a Gaussian curve. The average particle size was 56 nm with a half width of 13 nm.

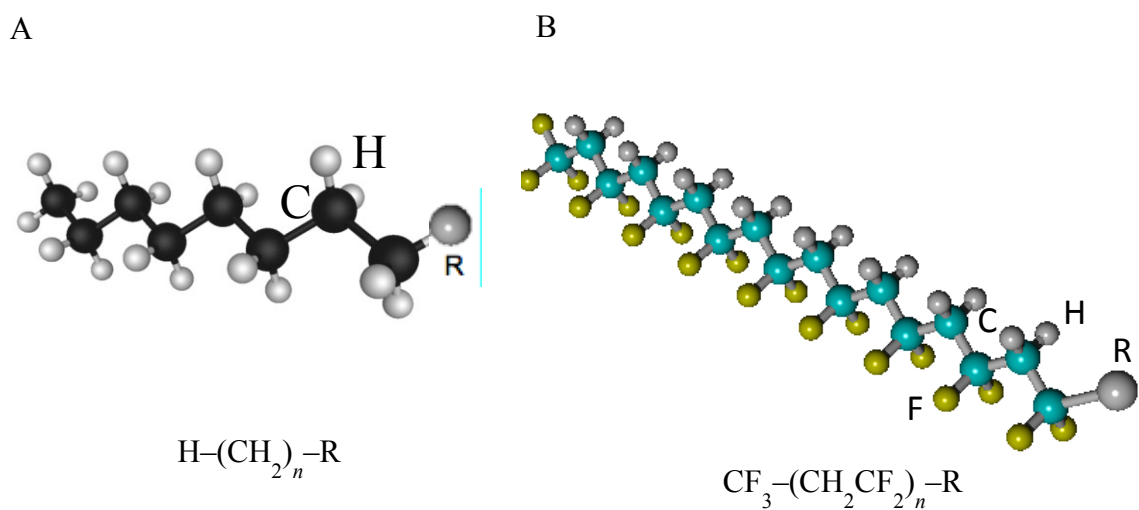


Figure 5-4. The dielectric tail used for coating the oxide nanoparticles. (A) Alkanes were the prototype material since they were commercially available. (B) VDFO was synthesized by our collaborators. R is the functional group, in this case phosphonic acid used to attach the surfactant to the particles.

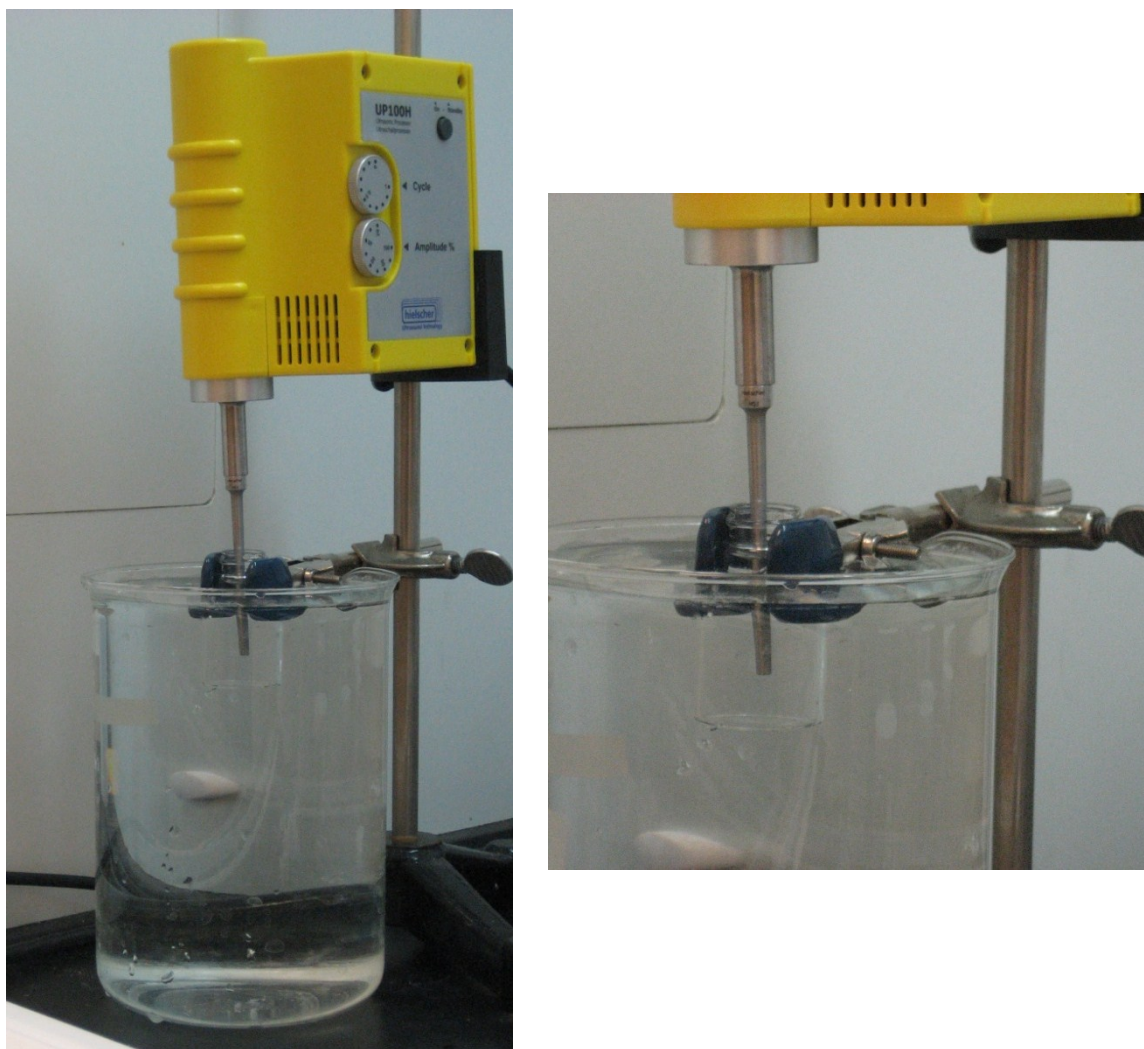


Figure 5-5. Water bath setup for sonicating nanoparticles. It is important to use a large enough bath so the heat can be effectively transferred away from the solution. In this case, a 2L beaker was used with room temperature water. A smaller bath could also be used, if it was filled with ice.

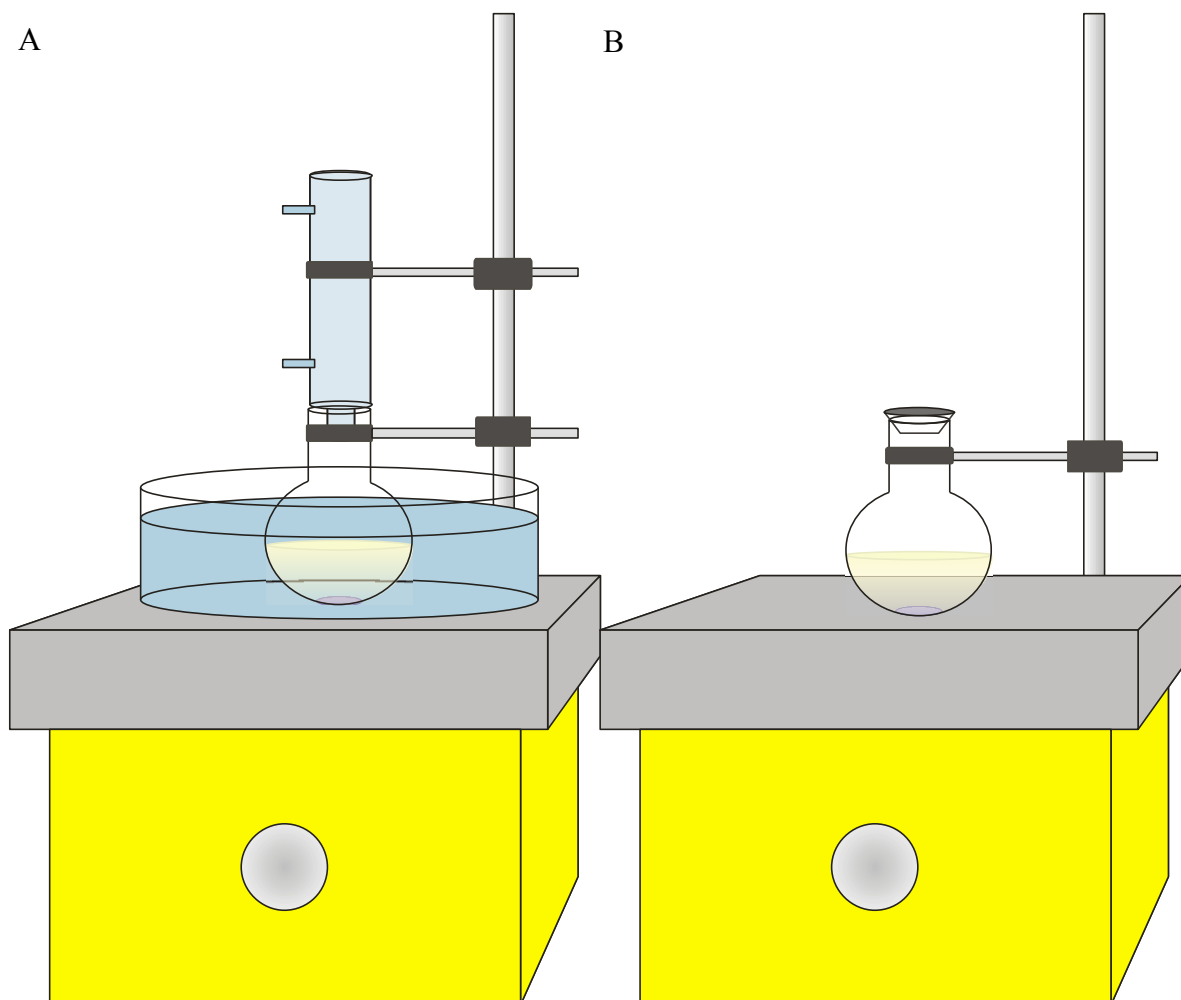


Figure 5-6. Sketch of the stirrer for coating the particles with (A) alkanes and (B) oligomers. When coating with alkanes, the temperature of the solution was raised to about 65°C. The oligomers were stirred at room temperature.

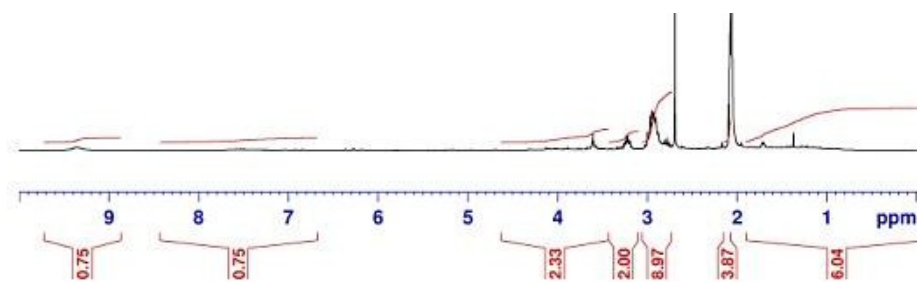


Figure 5-7. 1D  $^1\text{H}$  NMR spectrum of VDF oligomers in deuterated acetone.

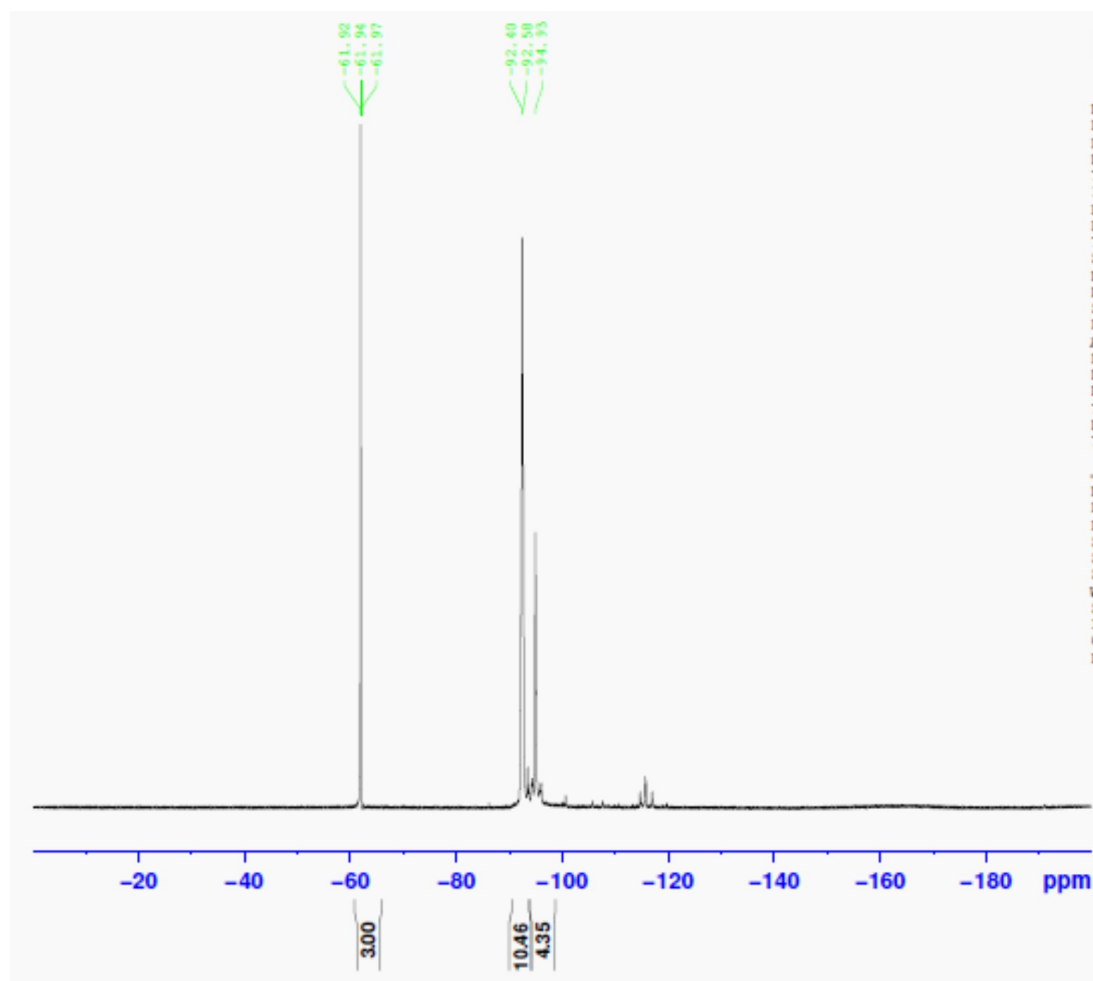


Figure 5-8. 1D  $^{19}\text{F}$  NMR spectrum of VDF oligomers in deuterated acetone.

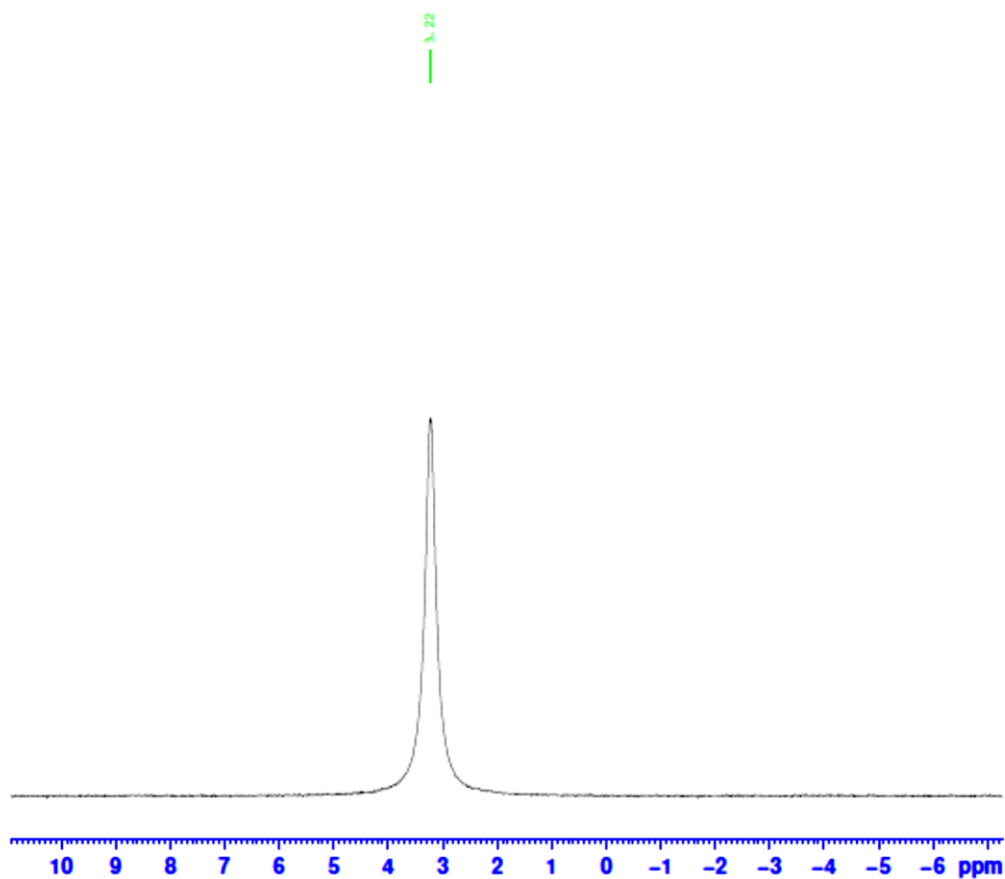


Figure 5-9. 1D  $^{31}\text{P}$  NMR spectrum of VDF oligomers in deuterated acetone.

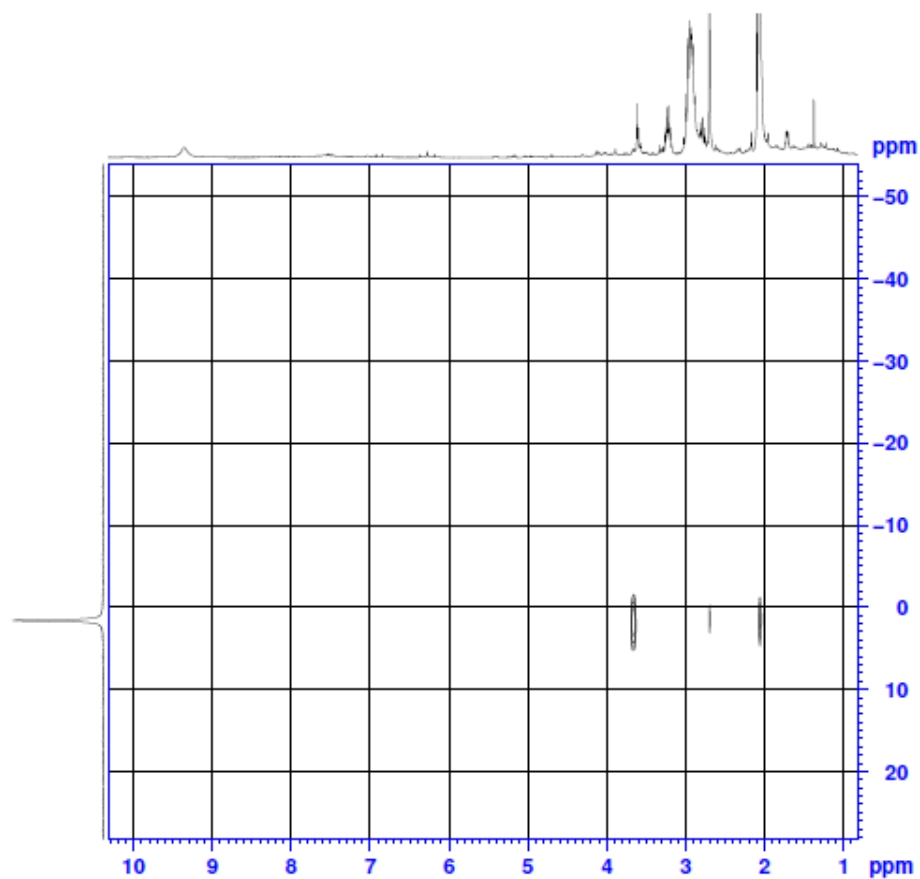


Figure 5-10. 2D HMBC NMR spectrum of VDF oligomers in deuterated acetone.

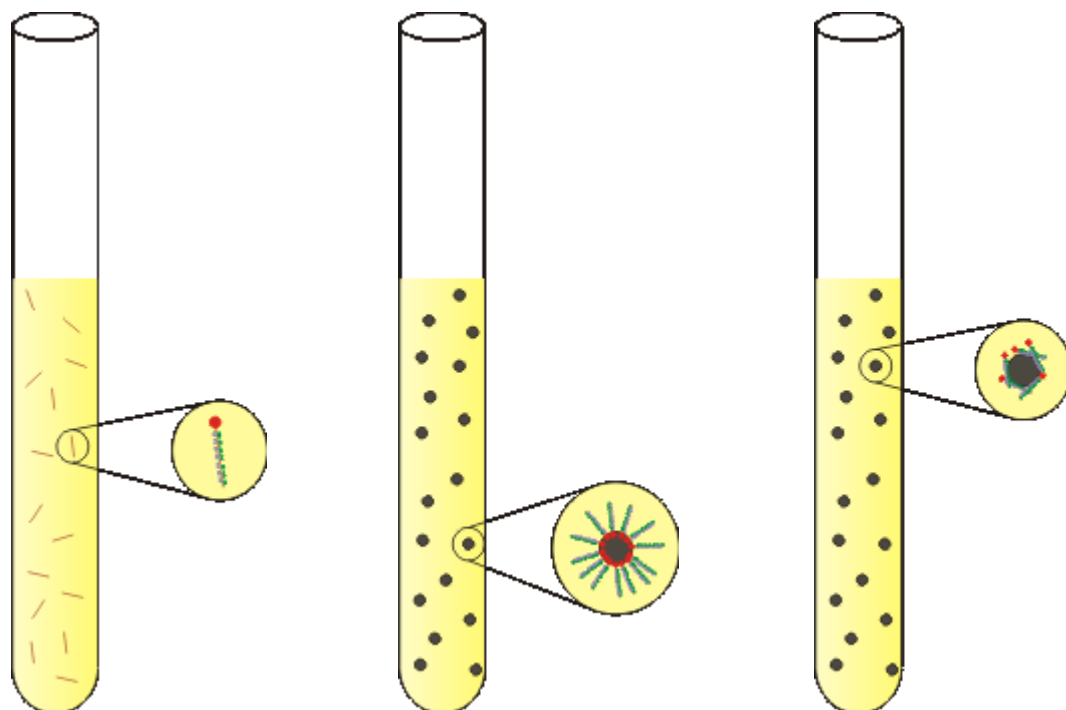


Figure 5-11. Various configurations of oligomers used in the NMR studies. (A) In this case, we used liquid NMR to determine if the functional group was physically attached to the particles. (B) Since the particles are not in solution, anything directly attached to them will not give off a signal. In comparison, the tails are in solution, and we will pick up a NMR Signal from them. (C) If the oligomers were physically surrounding the particles as in Figure C, the head groups would also be in solution. By not seeing a phosphorus signal in the NMR data, we can infer that there were no free phosphorus or very few that are not attached to the particle. We were able to determine that the oligomers and alkanes were present by looking for the NMR signatures of the tail groups and not seeing a phosphorus signal.

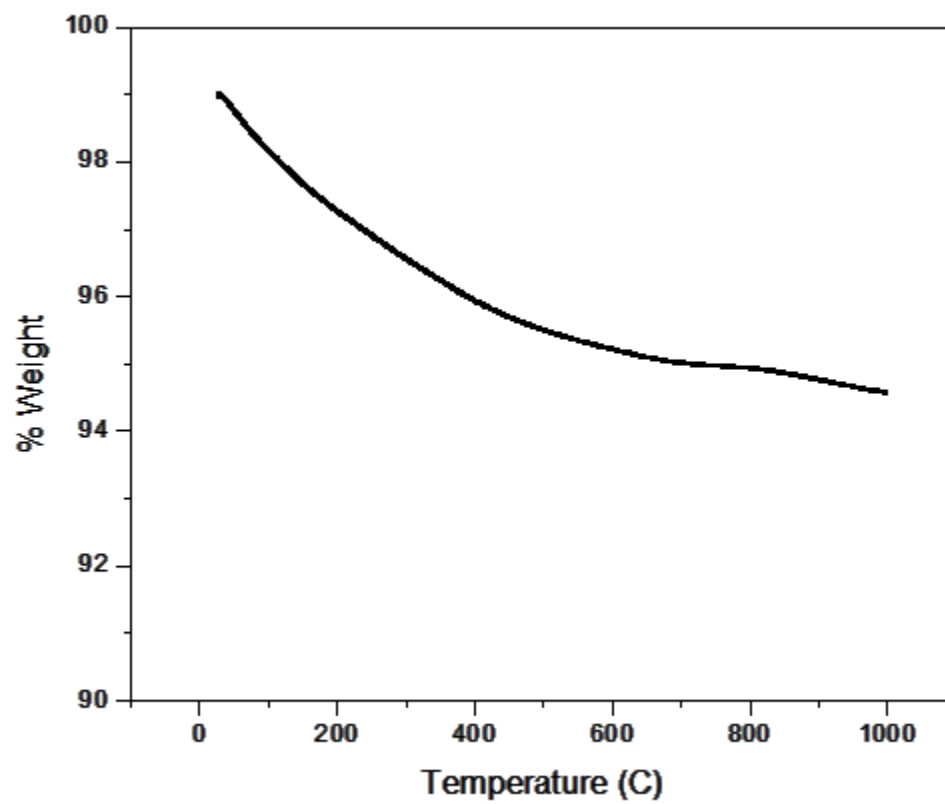


Figure 5-12. TGA of cleaned and dried BTO nanoparticles. The change in the weight is likely caused by moisture leaving the particles.

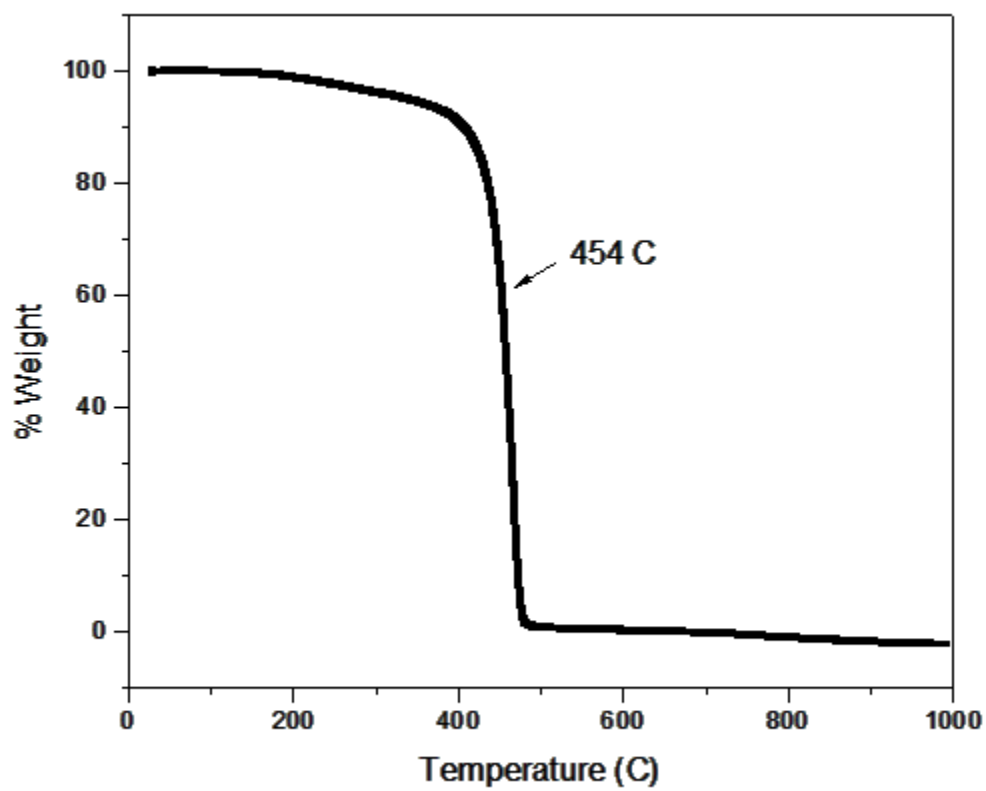


Figure 5-13. TGA of octadecyl phosphonic acid ( $C_{18}H_{37}P(O)(OH)_2$ ). The sharp drop at 454°C is from the thermal decomposition of the alkanes.

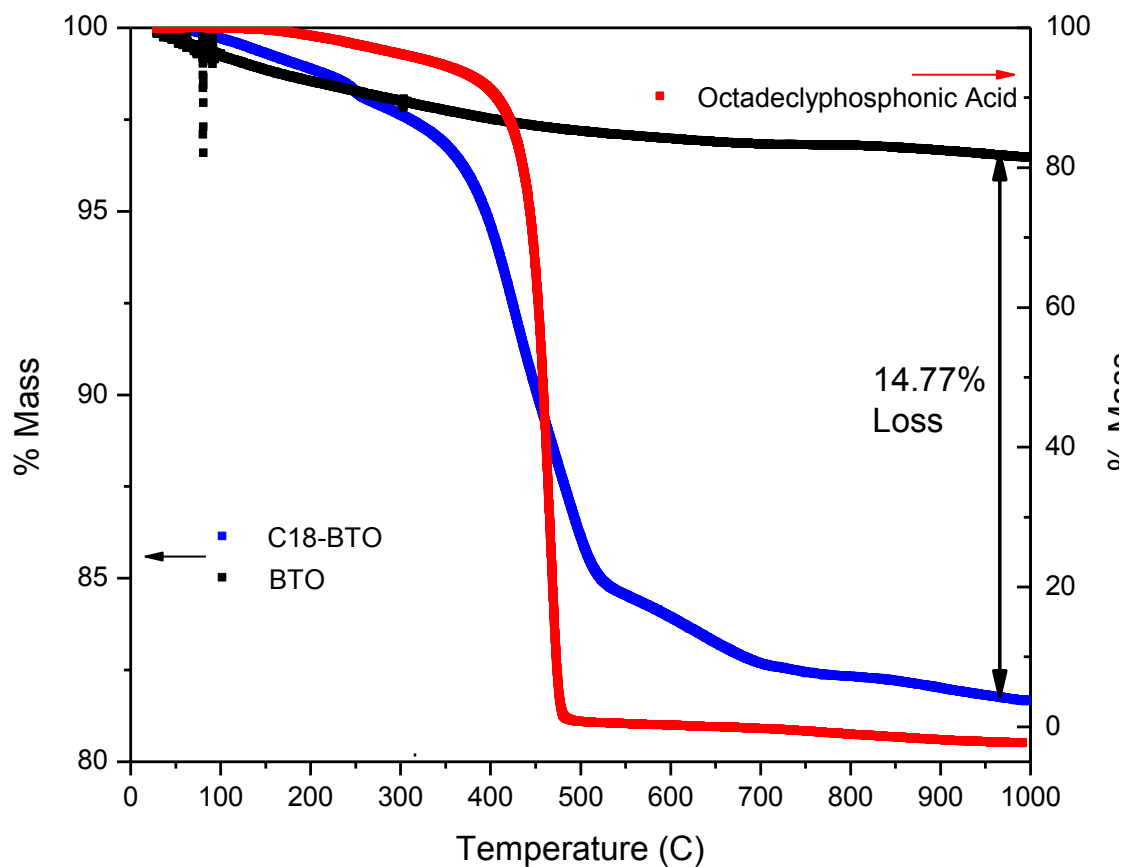


Figure 5-14. The TGA curve of the coated particles is shown in blue. The decrease in mass corresponds well with the decrease shown in the TGA curve of the pure alkanes, shown in red. There is a total mass reduction of about 17% at 1000 °C. 3.47% of this change is from the particles losing weight when they dry. The remainder of the loss belongs to the loss of the coatings on the particles. In this case, the coating account for about 14.8% of the mass. The remainder of the mass belongs to the particles.

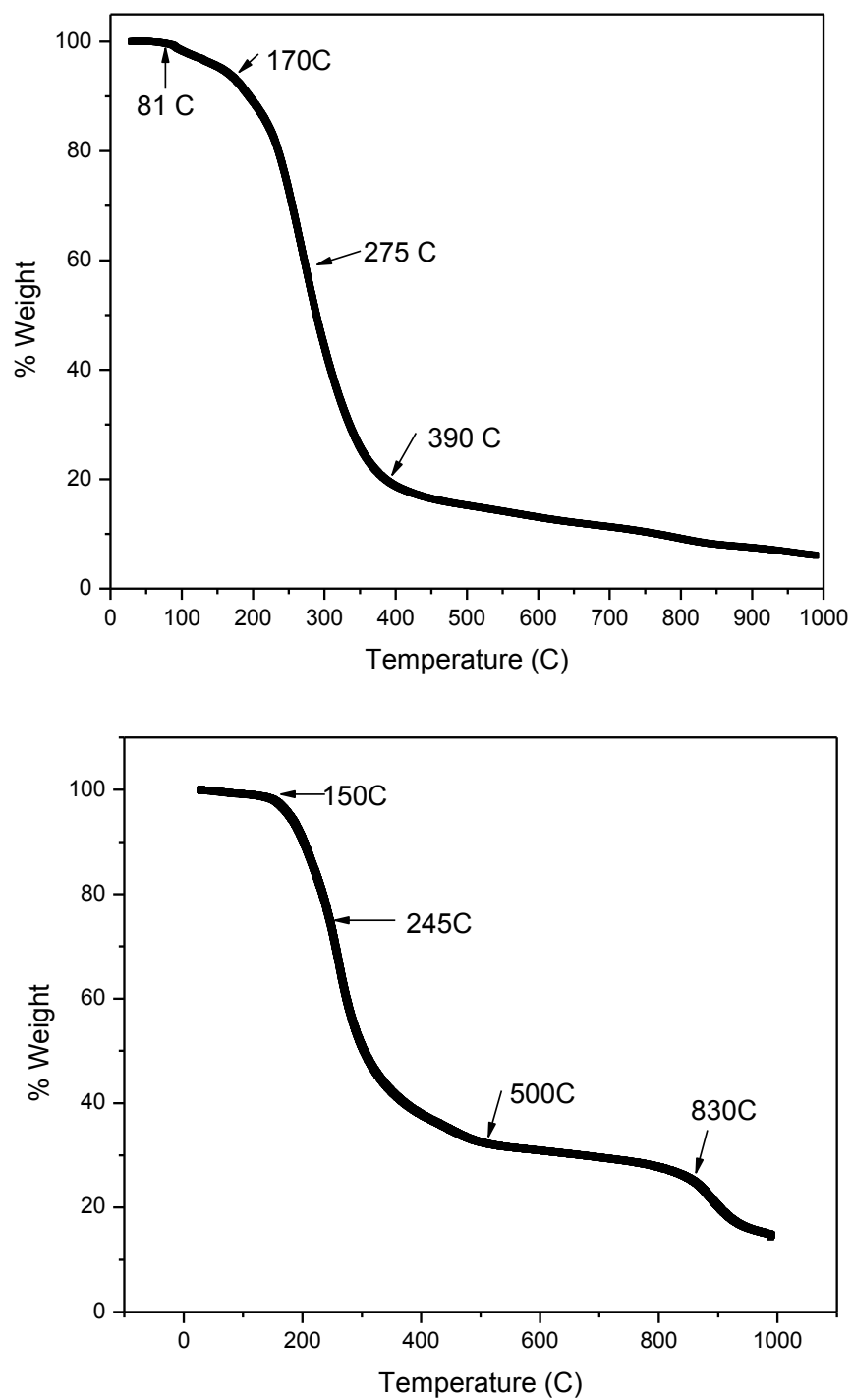


Figure 5-15. TGA of several VDF oligomers. Decomposition temperature is lower than expected when compared to bulk PVDF which is around 380C in air.

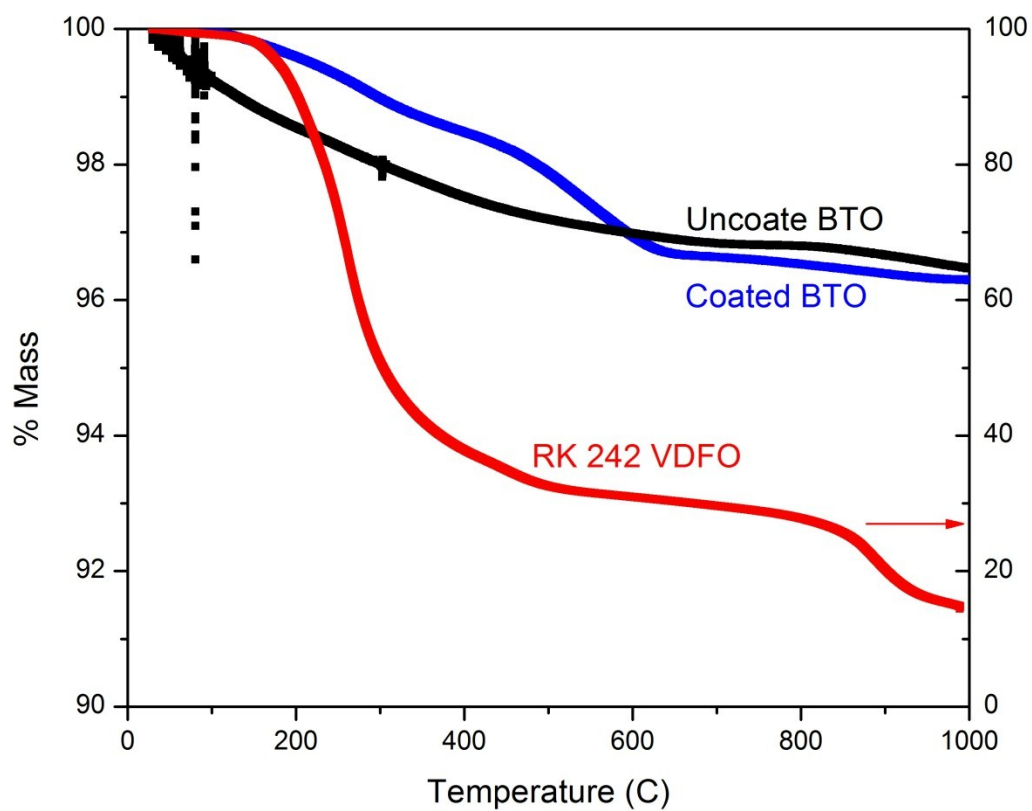


Figure 5-16. TGA of oligomer coated nanoparticles (blue) compared to TGA data of uncoated particles (black) and pure oligomers (red).

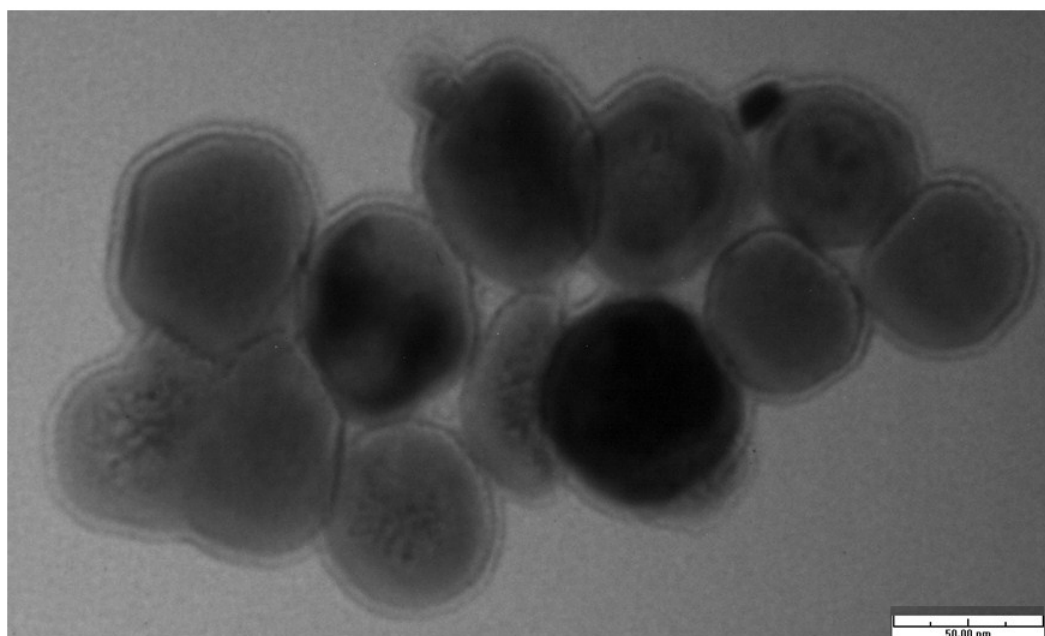


Figure 5-17. TEM image of Alkane coated nanoparticles.

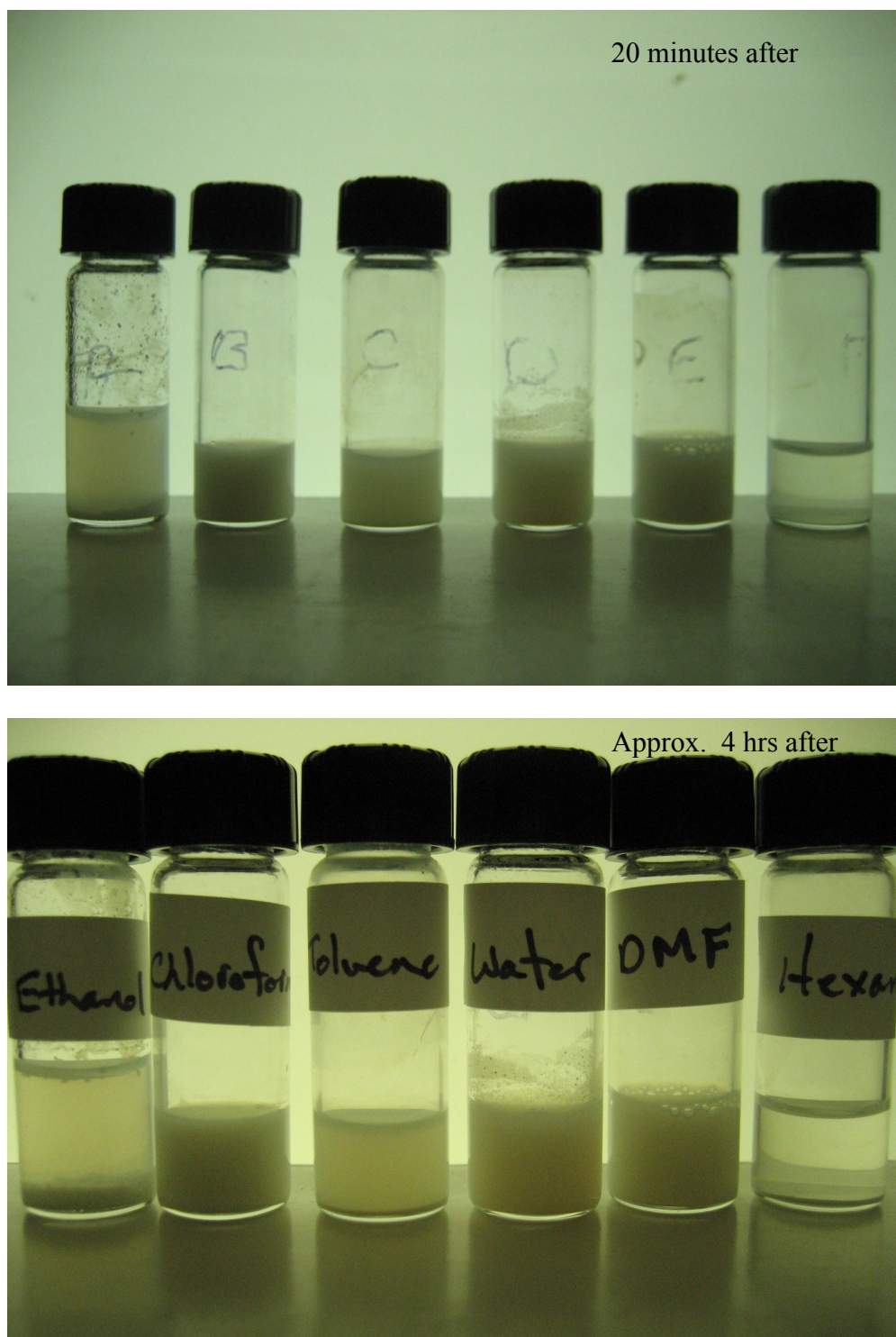


Figure 5-18. Solvent testing of the dodecylphosphonic acid coated BTO nanoparticles in various solvents. A small amount of the coated particles was added to a milliliter of various solvents and monitored over a few days to see which solvents allowed the particles to stay suspended the best.

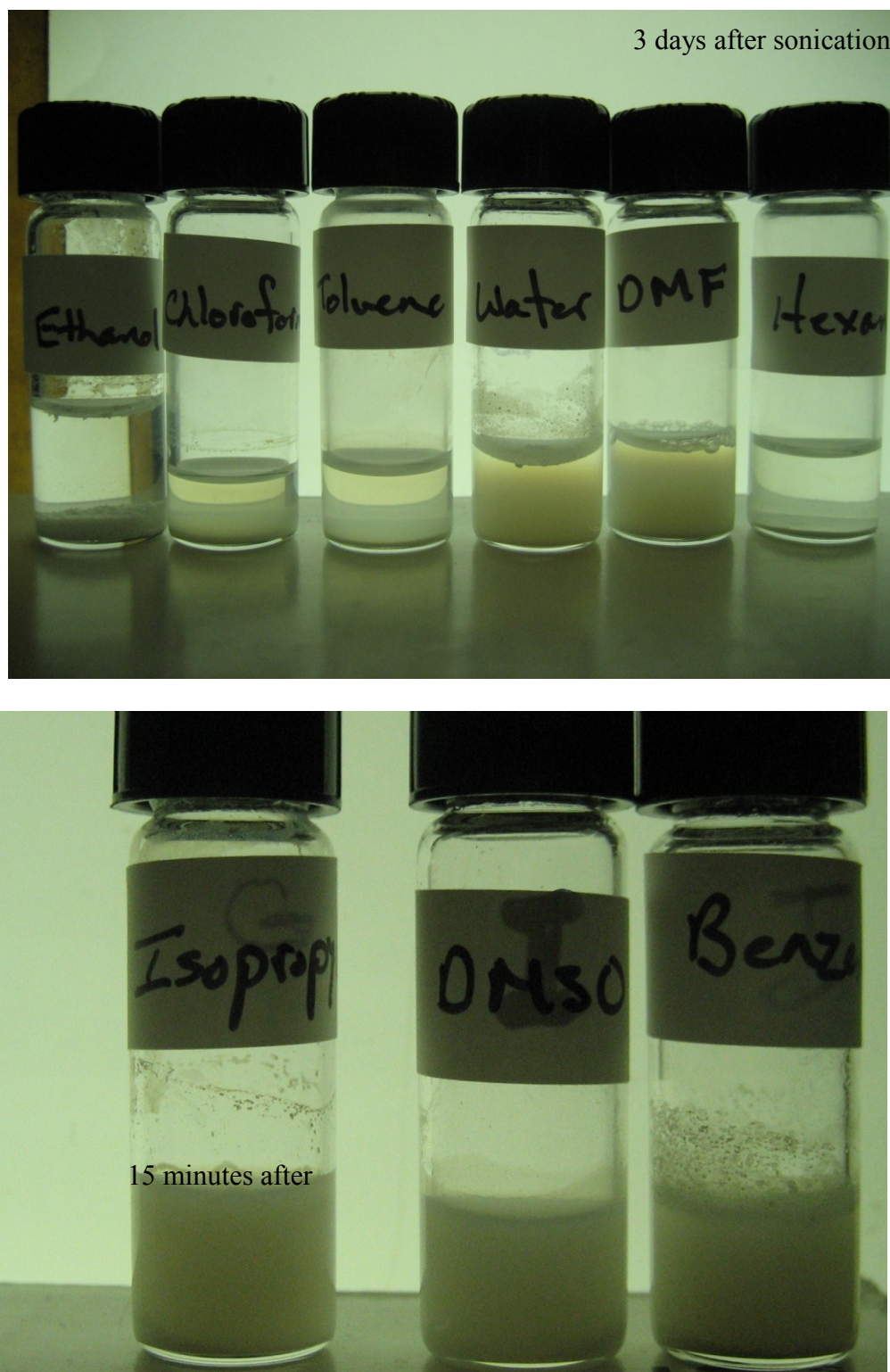


Figure 5-19. Solvent testing of the dodecylphosphonic acid coated BTO nanoparticles in various solvents. After several days, the particles had settled from all of the solvents.

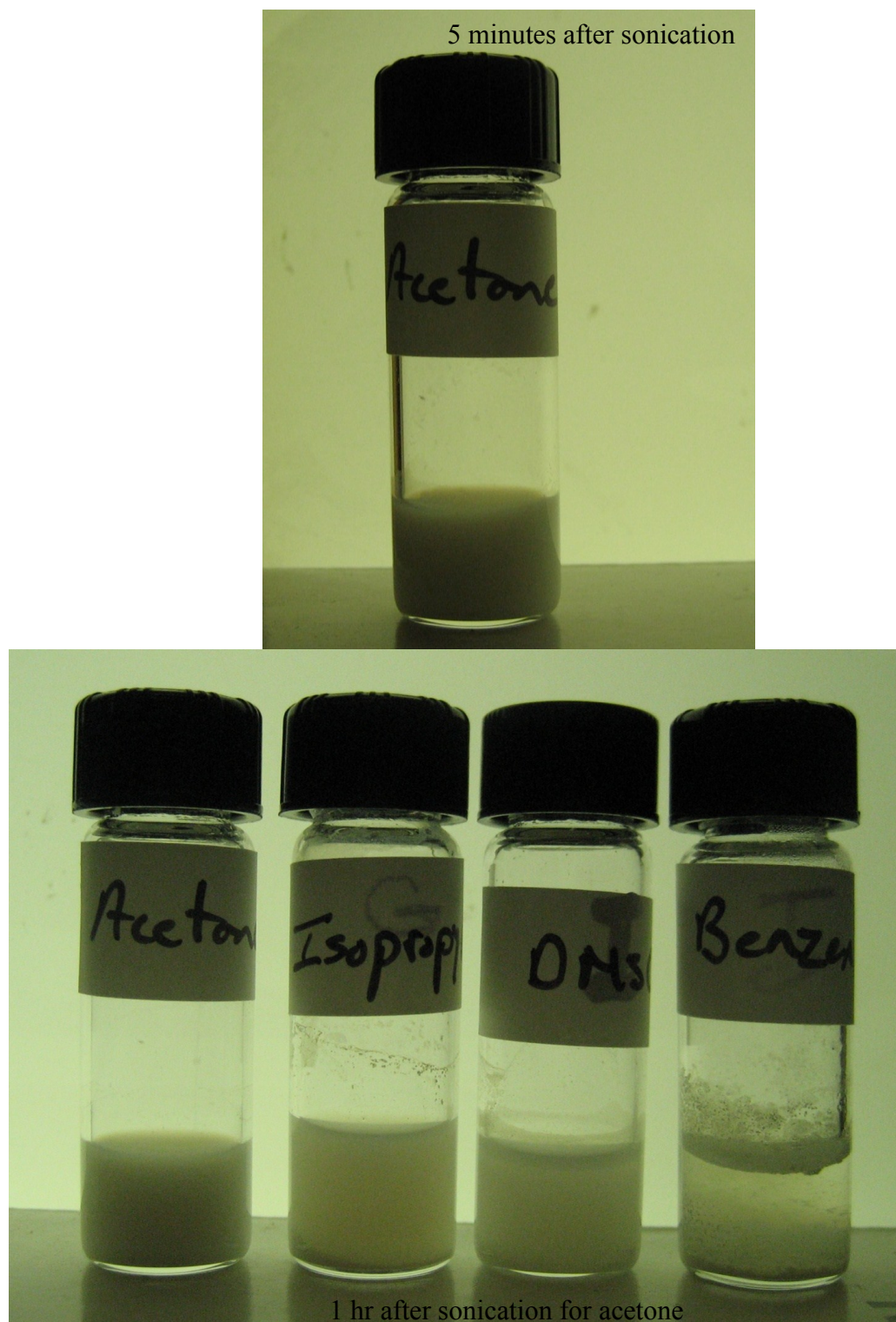


Figure 5-20. Solvent testing of the dodecylphosphonic acid coated BTO nanoparticles in various solvents.

## CHAPTER 6

### CONSTRUCTION AND STRUCTURAL MEASUREMENTS OF NANOCOMPOSITE DIELECTRIC MATERIALS

#### 6.1. Introduction to overall project

Samples were constructed for the energy storage project with the goal of having high breakdown strength and high dielectric constant simultaneously in a sample [1, 2]. With this goal in mind, several types of samples were constructed. All samples were composites consisting of nanoparticles and an organic material as a coating, matrix, or both. In most cases, the particles were coated with an organic layer to prevent agglomeration of the particles, to increase the breakdown strength, and to prevent percolation of the particles through the sample [3-5]. Samples were made with three different fabrication techniques as summarized in Figure 6-1.

The first method, discussed in Section 6.2, was to spin-coat mixtures of polymer and particles, as shown in Figure 6-1A and B. For this method, a variety of copolymers and terpolymers of polyvinylidene fluoride (PVDF) were used as the matrix. In the original series of samples, uncoated barium titanate (BTO) nanoparticles were dispersed into the matrix. Later, the particles were coated with either functionalized alkanes or VDF oligomers. The concentrations of particles to matrix ranged from all coated particles to pure matrix materials.

A second method of making the dielectric layers used the same particles and polymers as in the previous method, but used Langmuir-Blodgett deposition instead of spin coating to form the films, as shown in Figure 6-1C and discussed further in Section

6.3. With this method, there were alternating layers of polymer and particles. This method was developed with concept of having thin polymer sheets to prevent percolation of particles between the top and bottom electrodes.

The third method of sample preparation, as discussed in Section 6.4, was to create titanium dioxide nanoparticles by sputtering clusters of atoms in a vacuum system, and then coating the particles with either paraffin or VDFO shells while still in the vacuum chamber, as shown in Figure 6-1D [6, 7]. The particles were directly deposited onto substrates to make capacitors without an additional matrix.

The sample characterizations discussed in this chapter are related to sample thickness, surface morphology, and composition. This was done through a variety of techniques including scanning electron microscopy (SEM), X-ray diffraction (XRD), atomic force microscopy (AFM), and ellipsometry. For most of these techniques, the measurement theory and basic procedure is discussed in Chapter 2, while the few techniques unique to this chapter are discussed in Section 6.4.B. The following chapter will discuss the dielectric aspects of the samples discussed in this chapter.

## **6.2. Spin-coated Nanocomposite Films**

Spin-coated samples were made by mixing particles with a polymer matrix in an appropriate solvent. This type of sample was ideal since the ratio of particle to matrix was easy to control in solution. The assumption was that the ratio of particles to polymer stayed the same upon spin coating, although there could have been preferential spin off due to mass differences.

### *6.2.A. Solutions for making samples*

The solutions for the spin-coated samples started as two separate solutions. The first solution was a polymer solution made to the desired concentration, typically between 1-5% by weight. The ratio was adjusted to produce films that were approximately 100 to 150 nm thick, and was altered to fit the properties of different polymers and solvents. Solvents had to be selected to match to both the spin-coating conditions and to be compatible with all of the parts of the dielectric. For example, DMF was a very good solvent for spin-coating the copolymer, but it was polar enough to strip the alkane coatings off of the particles. This resulted in a layer of particles at the bottom of the vial and a layer of alkanes on the surface of the solution.

The initial solutions to be prepared were the polymer solution and the particle solution. Making the particle solution separately had several advantages. The first was that it allowed time for all of the particles to be well sonicated before individual concentrations were made; reducing the overall processing time needed to prepare each individual solution in a series. The particle solutions were sonicated for 2-3 days to ensure that agglomerations of particles were fragmented and the particles were well dispersed, as was verified by SEM imaging. Then when mixed with the polymer solution, the composite solution was sonicated another 12-18 hours initially and again 2-6 hours before each use. The second advantage of making a stock solution of nanoparticles was that it allowed the particles to be used more efficiently. It was often desirable to make composite solutions of 3-5 mL in total quantity. To make a solution that was 1% polymer by weight, and to have the particles be 20% of the polymer weight meant the

amount of particles needed per solution would have been on the order of micrograms. Since the balance measured down to hundredths of a milligram, it was easier to make 10-20 mL of stock solution, and then divide this solution between a series of samples using a micropipette. An example of ratios of solutions is shown in Table 6-1. This was a typical set of 2 mL solutions ranging from 20% to 80% particle to polymer concentrations at 1% by volume total concentration.

Once the stock solutions had been prepared at the desired concentrations, they were sonicated to disperse the particles and polymer with a probe sonicator. Two probe sonicators were used. The first was a Hielscher UP100H sonicator with a 3 mm probe (Sonotrode MS3) operated at 100% power. The second sonicator was a Sonic Vibra-Cell with a 3 mm probe at 60% power. The second sonicator was operated at lower power since it was more powerful than the Hielscher sonicator and heated the solution too much at full power, causing the solvent to evaporate quickly.

### *6.2.B. Sample Construction for Spin-coated Films*

#### *6.2.B.a. Uncoated Barium Titanate in Copolymer P(VDF-TrFe)*

The initial series of samples were uncoated BTO nanoparticles, first in a 75/25 P(VDF-TrFe) copolymer matrix and then in a 65/35 P(VDF-TrFe) matrix. The polymer choice was dependent on the availability of materials since spin-coating required a larger quantity of materials per sample than LB films. The concentration of particles ranged from 15 to 40% particles by weight ratio to the polymer, as shown in Table 6-2. The volume ratios were calculated from the density of the polymer and particles, and the weight ratios of the two materials. The distribution of values in the table came from

refinement in the solution-making techniques over time. This series of samples was made before we had the probe style sonicator, so the bath sonicator was used to attempt to de-agglomerate the nanoparticle clumps. The bath sonicator did not have as much power as the probe style did for breaking up clumps of particles, resulting in larger agglomerates of particles in the sample.

The solutions were made with either DMF or butanone. The polymer solution had an initial concentration of 1-5% by weight for the polymer to solvent ratio. The particles were then added at a ratio over the range of 15-40% by weight of the polymer. The samples were then spin-coated with 15-22 drops using a glass pipet and rubber 2 mL bulb at 400 RPM and then spun at 1500 RPM for the remainder of the 180 seconds. The substrates were glass slides with aluminum electrodes, prepared as described in Chapter 2.

*6.2.B.b. Octadecylphosphonic Acid Coated Barium Titanate Nanoparticles in 50/50 P(VDF-TrFe) Matrix*

The composites for the second series of spin-coated samples consisted of BTO nanoparticles coated with octadecylphosphonic acid (ODPA) in a 50/50 P(VDF-TrFe) matrix. The coating and verification procedure for the nanoparticles was discussed in the previous chapter. Once the coatings had been verified, composite samples were designed. The sample compositions ranged from pure coated particles to pure matrix, in 20% intervals by weight. Table 6-3 shows a range of sample compositions designed for capacitor studies. These samples were spin-coated with 15-18 drops at 400 revolutions per minute (RPM) and then the velocity was increased to 1000 RMP for the remainder of

the 180 seconds. The temperature of the spin-coating chamber was elevated to 35-40 °C to improve the sample quality.

*6.2.B.c. Octadecylphosphonic Acid Coated Barium Titanate Nanoparticles in a Terpolymer Spin-coated Matrix*

The third type of spin-coated composite samples that was made used a VDF terpolymer consisting of P(VDF-TrFe-CFE) (56/36.5/7.5) from Kunshan Hisense Electronics Company. The terpolymer was selected for its relaxor properties, which should enhance the amount of energy stored in the capacitor over the ferroelectric matrix by reducing hysteresis losses [3], as shown in Figure 6-2. The polymer concentration in the solvent was 1% by volume to produce samples in the range of 100-150 nm for pure polymer samples. Alkanes with two chain lengths were used to coat the BTO nanoparticles. The first were the ODPA alkanes, which were used in the previous study, with a backbone length of 18 carbons and the second were decylphosphonic acid (DPA) alkanes with a backbone length of 10 carbons. One of the desired goals of this part of the study was to see if the coating length affected the dielectric properties, which will be discussed in the next chapter. There were also two sizes of particles to be considered. The first was 56 nm in diameter and the second was 15 nm in diameter.

The particle concentration in the terpolymer matrix ranged from pure coated particles to pure matrix. Particle concentrations were incremented at 20% by weight ratios. Table 6-4 shows the calculated volume ratio of barium titanate particles for a given weight ratio of coated particles to the matrix. Each series of samples had the volume ratio of particles and coating to polymer matrix increase by 20%. In the table, the

two left-hand columns are the volume ratios of coated particles and matrix. The other columns are the percentage of volume occupied by the BTO. When the longer ODPA coatings were used with small particles most of the volume was in the shell coating, resulting in a low concentration of particles, even in the case of no polymer matrix.

#### *6.2.B.d. Vinylidene Fluoride Oligomer Coated Barium Titanate Nanoparticles in a Polyvinylidene Fluoride Terpolymer*

The final study was to examine the effect of coating the particles with VDFO instead of alkanes. This was an advantageous mixture since the particle coatings should have been more compatible with the matrix. There were unforeseen difficulties with the coating procedure, so this study was not carried out fully.

#### *6.2.C. Analyzing Film Properties of Spin-Coated Samples*

There were several characteristics investigated for the dielectric samples made by spin-coating. Scanning electron microscopy (SEM), as discussed in Chapter 2, was used to examine the surface morphology. X-ray diffraction (XRD) was able to compare the ratios of crystalline materials in the composite samples to verify that there was an increase in particle concentration in the sample as the particle concentration was increased in the solution. The third set of studies was the thickness measurements made by ellipsometry. In the cases of the high particle concentration samples, the samples were too rough and opaque to use ellipsometry, so profilometry was used instead.

*6.2.C.a. Surface Morphology of Spin-coated Samples imaged with Scanning Electron Microscopy*

The scanning electron microscope allowed us to observe the features on the surface of the dielectric layer. Figure 6-3 shows a typical series of samples ranging from 13% by volume of 65 nm in diameter BTO nanoparticles to 54% by volume of 65 nm in diameter BTO nanoparticles coated with ODPA in 50/50 P(VDF-TrFe). The first image shows a few particles near the surface of the film, and more appear to be below a layer of polymer. Figure 6-3B shows a higher concentration of particles, increasing to about 27% by volume. In this figure, a large number of particles were visible below a layer of polymer. At 40% particle concentration by volume, more particles were seen on the surface of the film. By the time the film reaches 54% BTO by volume, large clusters of particles were observed in the sample. Some clustering of particles was expected due to the difference in polarity between the particle coatings and the polymer matrix. Another sample of 54% by volume ODPA coated BTO in 50/50 copolymer was shown in Figure 6-4. This sample showed the segregation of particles and polymer more clearly than the sample in Figure 6-3. It appears that there was space around the particles where the polymer had contracted. This may have occurred upon drying when the film contracted and pulled away from the particles or it could have been caused by the electron beam heating the sample and causing the polymer to contract. Polymer samples tended to be very fragile, and were easily melted or vaporized if exposed to the electron beam at too high of a power or for too long of a time.

### *6.2.C.b. Cross-Sectional Scanning Electron Microscopy of Spin-coated Samples*

One of the ways to examine the internal structure of the films was to examine the cross section of the sample with a SEM. This measurement was made using the field emission scanning electron microscope (Hitachi S4700 FE-SEM) and a vertical sample holder. The sample holder, shown in Figure 6-5A, had a spring clamp that held the sample in place between two flat pieces of metal. One of the drawbacks to this setup was that the surface of the sample to be imaged had to be close to parallel to the surface of the holder, and the sample itself could not be more than a millimeter taller than the holder, due to height restrictions in the SEM. Later this chapter, in Section 6.3.C.d, an alternative technique was used to capture cross-sectional information for the multilayer samples.

Figure 6-5B is a sketch of the composition of the sample shown in Figure 6-5C. One of the difficulties with the SEM was that it has a narrow focal range, and samples tended to have a slightly beveled edge when they were fractured. In Figure 6-5C, the polymer layer was in sharp focus. The white layer below the polymer was the aluminum electrode. Beneath that was the silicon substrate with a layer of oxide visible between the silicon and the aluminum. While individual particles were not visible in the image, the surface roughness was of the same size scale as the particles and the particles were likely the source of the roughness.

Due to complications with high concentration polymer samples melting and contracting when exposed to the electron beam, it was difficult to obtain thickness measurements with the SEM. In later studies, a top electrode was added to the sample,

keeping the film more rigid and allowing the heat to escape the local area, reducing the amount of distortion in the film.

#### *6.2.C.c. X-Ray Diffraction of Composite Spin-Coated Samples*

X-ray diffraction (XRD) measurements were made on composite samples consisting of aluminum-coated silicon with a native oxide. The aluminum was approximately 25 nm thick, and the silicon oxide was 2-3 nm thick. The spin-coated composite film consisted of ODPA-coated BTO in a 50/50 P(VDF-TrFe) copolymer matrix. The volume of particles in each sample ranged from pure copolymer to all coated particles. Since the coated particles consisted of a shell surrounding the particles, the particle only samples did not contain 100% BTO, rather had a maximum of 67% by volume.

Characterization measurements made for the samples before and after annealing. Figure 6-6 shows the XRD results for a series of samples ranging from 6% to 40% BTO nanoparticle concentration, before annealing. As the particle concentration increased, the polymer peak located at approximately  $19^\circ$  decreased in intensity until it was no longer visible in the 40% BTO sample's results. At the same time, the peaks from BTO particles increased in intensity with expected concentration. This verified the expectation that there was a higher particle to polymer ratio in the samples as the particle to polymer ratio was increased in the solutions.

Figure 6-7 shows the relative ratios of area of the polymer and particle peaks from Figure 6-6. At 6% BTO by volume, the peak area was primarily polymer, although there was enough particles present to be able to resolve the particle peaks. At 24% BTO

concentration, the area of the polymer and particle peaks was nearly equal. By 40% BTO by volume, the area of the peaks was over 88% barium titanate even though there should have been 60% polymer by volume. This could imply that either there was less polymer present in the samples than we expected or that a large amount of the polymer was not crystalline and did not contribute to the polymer XRD peaks. Annealing the polymer film has shown to increase the crystallinity of pure polymer films by as much as 12 times [8]. Annealing the particles was not expected to change the area of the BTO peaks, since the particles were expected to be in the cubic phase due to size effects from being smaller than 115 nm in diameter [9]. In some samples, there may have been slight shifting of the particles as the polymer softened with annealing, and this may have resulted in a change in orientation of the particles with respect to the substrate surface.

#### *6.2.C.d. Thickness Measurements of Spin-Coated Composite Films*

For most samples, ellipsometry was used to determine the thickness of composite samples. The psi and delta values measured at three or seven angles, depending on the instrument, were fit using the Cauchy model to determine the film thicknesses and index of refraction. Most samples were around 100 nm thick. Some of the highest particle concentration samples were no longer a transparent film, so they were not suitable for ellipsometry. The thickness of these samples was measured using an optical profilometer.

### **6.3. Langmuir-Blodgett Capacitor Samples**

One major source of electrical breakdown in composite samples was caused by the low breakdown strength particles percolating from one electrode to the other, as

shown in the sketch in Figure 6-8A. This could be prevented by creating interrupts with high-breakdown-strength materials along the path of the breakdown, as shown in the alternating layer sample in Figure 6-8B [10]. By using thin layers of polymer, one can create high particle concentration films. Even in more realistic samples, such as the one in Figure 6-8C, the layers of polymer will prevent the particles from making a path of particles between the electrodes.

There are several challenges for making this type of sample. The first was to characterize the Langmuir-Blodgett layers made of the terpolymer and nanoparticles individually. Since we had not studied either previously, we had questions such as the thickness of a typical terpolymer layer upon transfer and if nanoparticles could actually be made into a Langmuir layer on the trough. Once the components of the capacitor were understood, composite samples were constructed for both dielectric and non-dielectric measurements.

#### *6.3.A. Langmuir-Blodgett Layers of Terpolymer*

The first of the materials used to make composite samples consisted of Langmuir-Blodgett layers of relaxor terpolymer, P(VDF-TrFe-CFE) (56/36.5/7.5). While some previous work had been done by other research groups, this was our first experience with it [11-13]. Preliminary results showed a promising material in terms of breakdown strength and dielectric constant.

### 6.3.A.a. Making Langmuir-Blodgett Layers

Langmuir films were made using solutions containing 0.01% by weight terpolymer in dimethylformamide (DMF). This solvent was chosen instead of DMSO since it was the solvent reported by other research groups in the literature, and we wanted to be able to compare our results to those reports [11]. The polymer solution was loaded onto the surface of the trough using the glass microscope slide ramp method, as described in Chapter 2. Using a digital pipet, 1500  $\mu\text{L}$  of solution was loaded onto the trough and the solvent was allowed to disperse into the water and air for about an hour. The surface pressure of the trough was 0 mN/m when the trough was filled with ultra-pure water, and, immediately after loading, the pressure was 2 mN/m. After waiting an hour for the Langmuir layer to reach equilibrium on the trough, the pre-compression pressure was 1 mN/m. As shown in Figure 6-9, there was a low-pressure horizontal region upon compression from 625  $\text{cm}^2$  to 550  $\text{cm}^2$ . At that point, the pressure started to climb steadily. At 175  $\text{cm}^2$ , the pressure-area curve had a sharp increase in slope. The film was compressed to a surface area pressure of 18 mN/m with no signs of collapse on the trough. The area of the film on the trough at that point was 87  $\text{cm}^2$ , which was the minimum area the barriers could enclose, while the barrier speed was 20  $\text{cm}^2/\text{min}$  during compression. Figure 6-10 shows the deposition cycles after the trough was cleaned and reloaded with 0.01% by weight terpolymer solution with the same technique as the previous isotherm. The trough was allowed to stabilize for 55 minutes while the barriers were fully open. The pre-compression surface pressure was 0.8 mN/m. Since a pressure increase of 5 mN/m was desired, the typical deposition pressure for making PVDF films [11, 14], the pressure was set to 5.8 mN/m for deposition.

Figure 6-10A and B compare the compression and deposition cycles between our work and work done by Wang et al. In both cases, films were made with 0.01% terpolymer by weight in DMF, and samples were deposited using the horizontal Schaefer method at 5 mN/m surface pressure [11]. The compression curve shown in Figure 6-10A had a more gradual increase in the slope compared to the data from the Wang group which stayed mostly horizontal until the sharp increase in pressure around  $230 \text{ cm}^2$ . Figure 6-10C shows a close-up of the first 35 deposition cycles distributed between eight substrates. The first 5 ML deposited onto a substrate were observed to have more water droplets on them than the later layers. It was also observed that the glass tended to be wetter than the electrodes, suggesting a preferential adhesion of the polymer film to the electrodes over the glass. The area of the film used was  $83 \text{ cm}^2$ , which would be a 49% transfer ratio to the substrates.

#### *6.3.A.b. Thickness Measurements of a Terpolymer Monolayer*

The next question of interest was how thick each monolayer of the LB film was on average. A series of samples were deposited on glass coated with a large aluminum pad covering most of the substrate. The aluminum pad provided a reflective surface for ellipsometry, and was large enough that the focusing microprobes were not needed for measurements. The films ranged in thickness from 5 ML to 59 ML, and were annealed at  $110^\circ \text{C}$  for three hours. The thickness of the films was measured using a J.A. Woollam Co. VASE Ellipsometer. More details about ellipsometry are discussed in Chapter 2. Since the measurements were made without the microprobes, a larger area, approximately  $1 \text{ cm}^2$ , was measured each time. The data was fit to a Cauchy model with

an aluminum substrate. The uncertainty in thickness came from the uncertainty in the index of refraction for the fits. The thinnest samples had an index in the range of 1.2-1.3 while the thicker samples had an index in the range of 1.3-1.4. This created an uncertainty in the thickness in the range of 10-15%. The data shown in Table 6-5 is for the fixed index of 1.3. Figure 6-11 shows the plot of the sample thickness as a function of the number of monolayers deposited on a substrate. The data had a slope of 2.03 nm, which was the thickness of the average monolayer. This value was thinner than the films obtained by Wang, who measured a monolayer to be 2.82 nm [11].

#### *6.3.A.c. Terpolymer Capacitor Samples*

A series of pure terpolymer films (no nanoparticles) were constructed to use as a standard to compare with the composite films. The samples were constructed with the standard parallel plate capacitor configuration described in Chapter 2. The samples ranged in thickness from 10 to 35 ML. The thickness of the dielectric layers was 2.03 nm per layer, as determined in the previous section.

#### *6.3.B. Langmuir-Blodgett Layers of Particles*

The second material in the composite samples were the layers of nanoparticles residing between the polymer layers. The particles were barium titanate (BTO), with an average diameter of 65 nanometers. The particles were coated with phosphonic acid functionalized alkanes or VDF oligomers. The coating of the particles is discussed in detail in Chapter 5. Most of the results in this section are over on the octadecylphosphonic acid (ODPA) coated particles. The VDF oligomer coated particle samples are discussed in Section 6.3.B.g.

### *6.3.B.a. Langmuir Layers of Octadecylphosphonic Acid-Coated Barium Titanate Nanoparticles*

Langmuir films were made with 0.05% by volume solutions with ODPA coated BTO nanoparticles in chloroform. Chloroform was chosen since it was a common solvent used in Langmuir nanoparticle films for particles coated with hydrophobic alkane tails [15-17].

#### *6.3.B.a.i. Deposition of Langmuir Layer on Water and Isotherms of Particle Films*

The particle solution was dispersed on the surface of the trough using a Hamilton 250  $\mu\text{L}$  syringe and a wide diameter flat-tip needle. Microdrops of solution were placed directly onto the surface of the water. Depending on the loading efficiency, 500-750  $\mu\text{L}$  of solution was typically used. Once the solution was dispersed on the surface, the solvent was allowed approximately one hour to evaporate before the film was compressed. Figure 6-12 shows a pressure-area curve for the 65 nm BTO coated in ODPA. The area of the trough was decreased to the minimum space of 90  $\text{cm}^2$ . By 54  $\text{mN/m}$ , the film was visible on the surface of the water and had a plastic appearance. The isotherm does not show evidence of large scale buckling or collapse of the film, although there may be a little buckling occurring at the slope change at 46  $\text{mN/m}$ .

At lower pressures, the expansion and compression of the film was mostly reversible. Figure 6-13 shows a 3 cycle isotherm of ODPA coated BTO nanoparticles. The first cycle in red was compressed at the rate of 100  $\text{cm}^2/\text{min}$ . The next two cycles shown in blue and black were compressed at the rate of 20  $\text{cm}^2/\text{min}$ . The cycles were set to have a minimum area of 200  $\text{cm}^2$  and a maximum area of 650  $\text{cm}^2$ . A small amount of

area was lost between the first two cycles. At 15 mN/m surface pressure, the initial cycle was compressed to 280 cm<sup>2</sup> of area and the second cycle had 245 cm<sup>2</sup> area upon compression. The second and third cycles were nearly identical to each other.

#### *6.3.B.a.ii. Nanoparticle Film Deposition onto Substrates*

Both vertical and horizontal deposition methods, as discussed in Chapter 2, were attempted to create particle thin films. The z-type vertical deposition creates bilayers of the particles with each time it is dipped into the trough. The horizontal Schaefer method creates a monolayer each time a layer is deposited. To allow the number of z-type layers to be compared to samples made with the Schaefer deposition technique, each bilayer was counted as two ML. Based on SEM measurements of single depositions, the layer deposited by Schaefer deposition was mostly a single layer and the layer deposited by z-type deposition was a multilayer where particles stuck to the substrate. Figure 6-14 shows the deposition curve for a series of samples being deposited at 10 mN/m. The inset was for the first few depositions. In most cases, the horizontal depositions showed a larger surface area loss than the vertical depositions. It was likely that some of the particles came off of the substrates while submerged in the water during vertical deposition based off of the poor surface coverage. The advantage of the particles coated with a hydrophobic alkane was that it was less likely that the particles sink into the water after the initial deposition phase.

For samples that were made with the vertical method, surface wetting had decreased by the 4<sup>th</sup> or 5<sup>th</sup> deposition, indicating that the surface of the substrate was covered with a hydrophobic material. One concern with the z type deposition was that

the later layers were causing very little change in the trough area, possibly signifying low transfer ratios or that the particles were re-depositing themselves on the surface of the water.

The second method used to make samples was the Schaefer method. There was a significant amount of water on the substrate for the first five ML, although the electrodes showed less wetting than with the vertical depositions even during the first few layers. This may signify preferential attachment of the particles to the electrodes. By 10 ML, the substrates were no longer showing any signs of wetting.

#### *6.3.B.b. Scanning Electron Microscopy of Multilayer Thin Films*

Closer examination of the surface morphology was performed by SEM on a series of samples deposited at a surface pressure of 7 mN/m using both horizontal Schaefer method and vertical z-type deposition. The images in Figure 6-15 were taken with a FESEM. Samples consisting of 5 transfers were deposited onto a silicon substrate. Figure 6-15A shows the sample made with the Schaefer method. This sample contained a fragmented film of particles which covered areas on the scale of a micron and smaller patches where there were no particles present. Figure 6-15B shows a sample with z-type depositions. Since each z-type deposition deposits a bilayer, it should have twice as many particles present if each layer made a film. The samples made with this deposition method had very irregular coverage. Large sections of the sample contained no evidence of nanoparticles. In the areas with particles, the film appeared to contain multiple layers, as expected with a sample with 5 bilayers.

### 6.3.B.c. Ellipsometry

Thickness measurements were made on several of the samples deposited at 10 mN/m and 7 mN/m, using the J.A. Woollam Co. VASE Ellipsometer. The samples were made using the Schaefer deposition technique on aluminum-coated silicon and aluminum-coated glass substrates. The data was fit as a Cauchy layer on a 3 nm aluminum oxide layer, which sat upon a 40 nm aluminum film and on a 1 mm glass substrate. Previous experience had shown that there was no change in film thickness results if a glass or a silicon substrate was used, as long as the aluminum layer was thick enough.

Table 6-6 shows the ellipsometry results for a series of samples deposited at 7 and 10 mN/m ranging in thickness from 10 to 40 ML. Several trends were observed in the fitted data. For samples with the same number of monolayers, the first observation was that the samples deposited at higher pressures show a higher index of refraction. This would be expected if the particles were more closely packed at 10 mN/m compared to 7 mN/m, and there was less air space between particles since the index of refraction for air is 1 and barium titanate is 2.45 at 546 nm wavelength [18].

Another trend was related to sample thickness. For 20 mL samples, increasing the pressure from 7 mN/m to 10 mN/m caused the sample thickness to increase. When the number of monolayers was doubled, the sample thickness did not double. For example, at 10 mN/m increasing the number of layers from 10 ML to 20 ML increased the average thickness by 1.6 times and going from 10 mL to 40 ML increased the thickness by 2.1 times the thickness of the 10 ML sample.

There were several possible explanations for these results. The first was that the film became denser with each monolayer being deposited, but not necessarily much thicker if the particles were mostly filling in the void spaces. This would support the increase in the index of refraction, as bulk BTO has an index of 2.44 [18]. The particle film's index was much lower, indicating that there were a large number of voids in the sample. The other alternative is that the index does not depend on the number of layers. Based on the results of the next section, we concluded that the first explanation was more likely.

#### *6.3.B.d. Particle Coverage of a Langmuir-Blodgett Layer*

Knowing the nanoparticle coverage area on a substrate was desirable. By using the SEM images of 1 ML films deposited at 7 mN/m and 10 mN/m, the average particle coverage per layer was calculated for each deposition pressure, as shown in Figure 6-16 and Figure 6-17. The software package Gwyddion was used to calculate the area masked in each image, and these values were compared to the overall area of the figures. For each sample, a low magnification image was used to calculate the percentage of area covered by nanoparticles. Then a high magnification image was used to calculate how much percent area the particles were covering within a single clump of particles.

The 10 mN/m low magnification image was collected at 2.00k magnification and had a sample area of  $3.02 \mu\text{m}^2$ , as shown in Figure 6-16A. When the particle clumps were masked, they had an area of  $0.988 \mu\text{m}^2$  (Figure 6-16B). This gave the particle coverage to be 33% of the total space. Then, a single cluster of particles (Figure 6-16C and D) had an area of  $1.304 \mu\text{m}^2$  and the area of the particles within the cluster (Figure 6-16E) was  $0.745 \mu\text{m}^2$ . This means that the particles covered 57% within each cluster.

This gives a total particle coverage of 19% (33% x 57%). For a 20 ML sample with 100% coverage of 65 nm in diameter particles, the expected thickness would be 1300 nm. A particle layer density of 19% gave an average thickness of 247 nm. Samples measured with ellipsometry gave a thickness in the range of 273-326 nm, as shown in Table 6-6. This was a reasonable approximation since it was within the thickness of one nanoparticle with a diameter of 65 nm.

The same set of calculations was repeated for the samples deposited at 7 mN/m, as shown in Figure 6-17. The low magnification image (Figure 6-17A and B) captured at 5.00k magnification had a total area of  $476.3 \mu\text{m}^2$  and the particles covered  $98.7 \mu\text{m}^2$  of the image space. This meant that the particles covered 21% particle of the sample area. The high resolution images in Figure 6-17C-E (magnification of 50k) showed a particle density of 55%. This means that the total particle coverage was 12% (21% x 55%). For a 20 ML sample with 100% coverage, the thickness would be 1300 nm of particles with a height of 65 nm. 12% of this thickness gave a theoretical thickness of 156 nm. Actual samples ranged in thickness from 220-240 nm, which was thicker than the estimate. When one examines the thickness of the 40 ML samples, the values were in much better agreement. The expected thickness would be 312 nm, which was within one particle thickness of the thickness measured by the ellipsometer of 260-276 nm.

#### *6.3.B.e. Pressure Dependent SEM Study on Langmuir-Blodgett Nanoparticle Films*

After analyzing the data of the samples at 7 mN/m and 10 mN/m, it was desirable to know what happened to the particle layers as they were deposited at higher pressures. Figure 6-18 shows a pressure-area isotherm for a series of samples deposited over a range

of pressures from 9 mN/m to 33 mN/m. A SEM was used to examine the film qualities for samples ranging from 7 mN/m to 21 mN/m. The 7 mN/m sample and the 10 mN/m sample were deposited onto substrates prior to making the samples in data shown in Figure 6-18. The later samples were made by slowly increasing the surface pressure on the trough and depositing one monolayer films at each set pressure. Due to the limited availability of the FESEM, only selected samples over a range of pressures were analyzed for coverage and film quality.

For each sample, a low magnification image, recorded at 5000 magnification, was shown. A higher magnification image was also shown for each sample, containing more details of the particle arraignment. For most samples, the higher magnification image of the sample was recorded at 80k magnification, although in a few cases, a 40k or 50k magnification image was shown when no high-quality 80k magnification images were available.

At the deposition pressure of 7mN/m, the films were sparse clumps with a diameter of a few microns as shown in Figure 6-19A. The higher magnification image shown in Figure 6-19B showed loosely clustered particles. There was more void space between individual particles at this pressure than was seen in images at higher pressures. When the surface pressure was increased to 10 mN/m, the particle clusters appeared to merge and grow, as shown in Figure 6-19C. The higher magnification image collected at 50k magnification (Figure 6-19D) showed that there was still space between particles, but the density was starting to increase, as was shown in the analysis in the previous section.

By the time the pressure had increased to 12 mN/m, which was point C on the pressure-area isotherm in Figure 6-18, the clumps of particles were mostly circular in shape and had started arranging themselves in a superstructure, as shown in Figure 6-19E. Circular clusters with diameters of 1  $\mu\text{m}$  to 3  $\mu\text{m}$  had started packing closer together, with large areas surrounding the groups of clusters where no particles were visible. It was unclear if the particles did not transfer from the surface of the trough in this area, or if there was another material such as alkanes that were no longer attached to the nanoparticles filling the void spaces. It was unlikely that there was open water or the pressure would not have held constant. The higher magnification image (Figure 6-19F) showed the individual clumps of particles starting to pack tightly. While most clumps were circular in shape, there were still particle clumps that appear oblong shaped or single particles in spaces between clusters of particles.

At 15 mN/m, point D on the plot in Figure 6-18, the overall film appearance has started to densify. The low magnification image in Figure 6-20A showed a film that had dense regions over large sections of the film. The higher magnification film, shown in Figure 6-20B, was collected at 40k magnification. In both the high and low magnification images, the edges of some of the clusters appear to curl upwards slightly, as if some of the film did not stick to the substrate during the transfer from the trough.

When the pressure was increased to 18 mN/m, point E on the pressure-area isotherm, the film appears to be a sheet of particles with some sort of a filler material, perhaps ODPa that was no longer attached to the nanoparticles. The low magnification image shows several interesting features in Figure 6-20C. The first was the large void

spaces at the top and bottom right corners and in the space on the center of the left side. The edges of this sheet appeared to have been torn from the neighboring particles, leaving behind a jagged edge. The second feature was the appearance of buckling of the film in the lower left corner. This was the first pressure where there was any evidence of the film starting to collapse. It was difficult to determine if the wrinkles in the film occurred on the trough or were caused by the tear in the film. A closer examination of the buckled area of the film shows that it was formed of nanoparticles, and not the primarily a polymer film. The particles are packed tightly together and stay together as a film even when not laying on the substrate.

The final set of films to be analyzed with the FESEM was made at 21 mN/m, shown at point F on the pressure-area isotherm. The low magnification image shown in Figure 6-20E, showed circular clusters of particles spread across most of the image. The 80k magnification image shown in Figure 6-20F was captured along the edge of a tear region. The figure has two clusters of particles, and between the two clusters is a film. While this is the only sample showing direct evidence of a material between the clusters, the other samples must have had a material present to maintain the surface pressure between clusters and to encourage the cluster to minimize their edges, forming circular clusters. If the spacing between clusters at higher pressures was due to incomplete transfer, the edges would have resembled the tear regions instead of being smooth and flat.

### *6.3.B.f. Capacitor Samples of ODPa Coated BTO*

Capacitor samples were made with ODPa-coated barium titanate nanoparticles. The samples were made on a glass substrate, with aluminum electrodes, as described in Chapter 2. The dielectric layer consisted of multiple monolayers of nanoparticles deposited at 7 mN/m or 10 mN/m. The film thicknesses ranged from 10 monolayers to 40 monolayers. The thinnest samples were difficult to obtain dielectric measurements from due to the samples having electrical shorts. Samples containing 20 or 40 monolayers were more reliable and robust for repeated electrical measurements.

### *6.3.B.g. LB Layers of VDFO Coated BTO*

Langmuir layers were made with barium titanate nanoparticles coated with phosphonic acid functionalized VDF oligomers. Unfortunately, there were synthesis difficulties, and the samples that were believed to be coated with VDF from TGA evidence were later shown not to have any oligomers attached due to missing functional groups. Samples made with these particles are discussed in the chapter, but should be treated as a layer of VDF oligomers mixed with particles rather than particles coated with an electroactive material.

### *6.3.C. Composite Capacitor Samples*

#### *6.3.C.a. Trough Setup of Langmuir-Blodgett Layers*

Once the Langmuir film properties and the thin film samples of VDF terpolymer and coated nanoparticles had been examined, the films were combined to make multilayer composite samples. The samples were made on a double-well Nima Langmuir

trough. A fixed barrier divided the trough into two parts, and the moveable barriers on each side were controlled individually to maintain the proper surface pressure, as shown in Figure 6-21. The section containing the terpolymer was compressed to 5 mN/m and the particle film section was compressed to 10 mN/m. One of the drawbacks to using the trough divided into two parts was that the usable area was much smaller than when using the full trough and each side must be reloaded after depositing approximately 20 ML onto one square inch substrates. The advantage of using the divided trough was that two materials could be deposited in alternating layers, as shown in Figure 6-21D, without having to clean and reload the trough between each type of layer.

#### *6.3.C.b. Design of Sample Structures*

The composite samples were constructed by alternating layers of polymer and particles. A layer of polymer was deposited directly onto the bottom electrode to ensure a high quality thin film on a smooth surface to reduce the chance of electrical shorts, as shown in Figure 6-21B. On the polymer film, layers of nanoparticles were deposited, as shown in Figure 6-21C. Then more layers of polymer and particles were added to the sample to build up the dielectric layer, as shown in Figure 6-21D. Since the polymer layers were approximately 2 nm thick per layer, and the particles had a diameter of 65 nm, the polymer layers did not increase the volume fraction greatly, while providing separation between rows of particles in the direction of the electric field. The polymer layer should increase the electrical breakdown strength of the samples and help reduce the probability of avalanches occurring in the sample [19]. The samples made for electrical study then had a top electrode deposited on top of the final layer of polymer.

The composite samples were made with symmetric construction. A simple sample consisting of polymer-particles-polymer is shown in the sketch in Figure 6-22A. The number of layers of polymer and particles were adjusted to the desired composition. Experience has shown that five monolayers were the minimum layers of polymer needed for reliable samples. Since each layer of particles covered approximately 21% of the surface area at 10 mN/m, a sample with 5 ML of particles would have 100% coverage in the ideal situation. In reality, the particles will overlap and make larger clusters, so most of the time, the number of particle layers was kept to three or less.

More complex samples were made by adding additional layers of particles and polymer, as the example sketch shows in Figure 6-22B. The number of depositions within a layer and the total number of layers could be tailored to nearly any particle concentration.

### *6.3.C.c. Surface Morphology of Particles on Terpolymer Films*

In the capacitor samples, the particles were deposited onto layers of polymer instead of a bare substrate. Therefore, it was desirable to determine how well the particles transferred from the trough when deposited onto polymer films. The surface of the film consisting of a single deposition of ODPA coated BTO on a terpolymer film was imaged with a FESEM, as shown in Figure 6-23.

The first image, Figure 6-23A, is a low magnification image of the sample, and shows the wide scale coverage of the particles on the surface. While most of the surface has particles distributed across it, there were regions that appeared absent of particles in

areas of a few thousand square micrometers. On this size scale, it appears that several multilayers of particles would create a continuous layer of particles within the capacitor.

Figure 6-23B is a 10k magnification of the film, where the individual particles were visible. Over large sections of the film, the particles have formed small clusters with open space on all sides of them. In other regions of the film, such as the one shown in Figure 6-23, the particles were arranged into a film with mostly continuous clusters covering several square microns. This image also shows evidence of the particles forming multilayers in some locations. Previous samples with multilayers formed on the trough had a hill-like appearance. In contrast, this film mostly had multilayers near the edges of the particle clusters. Based on the irregular edges, it was suspected that the multilayers formed when the film tore during the transfer of the film from the trough to the substrate.

Figure 6-23D is a 50k magnification image of a cluster of particles. In this image, the particles have started to pack together. It was difficult to tell if the particles were an isolated cluster or if it was a partial transfer from a larger film. The size was a typical size for a single cluster, but the edges were not as round as isolated clusters tend to be. Therefore, it was suspected that at least part of the cluster had separated during the transfer from the trough. Further studies of the surface of the trough would be able to reveal more the transfer properties.

#### *6.3.C.d. Cross-Section Samples*

Once the samples were made, it was desirable to learn about the distribution of the particles within the sample by examining the cross section. Two methods were used

to attempt to obtain insight into the films. The first method was to break the sample into pieces and to image the fractured edge of the film with a SEM. The second was to use a focus ion beam to mill a pattern into the sample, and then view the patterned surface.

The first sample to be examined for cross-sectional analysis consisted of 20 monolayers of terpolymer, 3 layers of ODPA coated BTO, and capped with another 20 monolayers of terpolymer with a top and bottom aluminum electrode on a silicon substrate, as shown in Figure 6-24A. The silicon substrate was a narrow rectangle, approximately 1 cm by 4 cm in dimensions. The back surface of the silicon was scored in several places before the film was deposited, to allow the substrate to break smoothly after sample deposition was completed and to reduce the surface damage. The sample was broken into several pieces for cross sectional analysis and imaged using the FESEM and the vertical sample holder described in Figure 6-5A.

The image of the cross section is shown in Figure 6-24B. The top and bottom electrodes are clearly visible along with a layer of particles in the center of the image. The top and bottom layers of polymer may be the dark stripe above and below the particles, although the dark stripe was narrower than predicted. The polymer layers were expected to be about 40 nm each, which should have been easily resolvable at this resolution. It was possible that the film was stretched or distorted during the creation of the cross section or the effects of the electron beam made it thinner than expected.

The second method for imaging the cross section of the sample was to mill into the sample using a focus ion beam, and then rotated the substrate for imaging. This had

the advantage over breaking a sample since the polymer layer was not pulled apart and distorted over long ranges as it was when breaking the sample into two pieces.

A sample consisting of a silicon substrate, aluminum bottom electrode, a dielectric layer, and top electrode was fabricated for milling. The dielectric layer consisted of 20 monolayers of terpolymer, three layers of VDF oligomer coated BTO, and 20 more monolayers of terpolymer. The terpolymer layers were made thicker than was typical for composite samples so they would show up more easily with the SEM. The samples were milled with a FEI Strata 200xp Focus-Ion Beam Workstation. A 9 by 10  $\mu\text{m}$  area of the sample was milled to a maximum depth of 300  $\mu\text{m}$ . A sketch of the milling pattern is shown in Figure 6-25. The sample was etched with a 150 pA beam and the edge to be viewed with the FESEM was polished with a lower power beam. Figure 6-25A shows a sketch of the steps being cut into the sample, and Figure 6-25B shows a sketch of the cross section of the stepped layers. Since the thickness of the particle layer was not known, the depth of milling was chosen to be 300  $\mu\text{m}$  to ensure that the silicon layer was reached. In reality, this was much deeper than was needed. Figure 6-25C and D show how the sample was imaged by the FESEM. The sample was mounted on a 45° triangle wedge, and the sample stage was rotated 30° to bring the sample to a 75° angle with the horizontal surface, and the surface of the sample to a 75° angle with the electron beam.

Figure 6-26 shows the FESEM image of the sample. The first image, Figure 6-26A, was of the sample mounted horizontally in the instrument. The milled steps increased in depth from left to right. Figure 6-26B and C were of the sample rotated 75°

from the horizontal surface. Figure 6-26B was a 5k magnification image that has been rotated 90 degrees to have the same orientation as Figure 6-26A. The image in Figure 6-26C was taken at a medium magnification of 15.6k and shows the steps along with the cross section surface. At high magnification, Figure 6-26D, the various layers of the capacitor could be seen. Surprisingly, there was no evidence of any nanoparticles along the 9  $\mu\text{m}$  of the milled surface. Due to difficulties with the VDFO coated particles, it was possible that a large section of the film was mostly oligomers. The high magnification image shows a series of stripes representing the top electrode, polymer layer, the bottom electrode, and then the silicon substrate before losing the focus due to the slope of the substrate. While the FIB milled image did not reveal any particles in the composite sample, it did provide a demonstration of technique to be used for viewing cross sectional samples without distorting the sample by fracturing it into pieces.

### *6.3.C.e. Thickness of Multilayer Composite Films*

The thickness of the dielectric layer of the multilayer capacitor samples was measured with a JA Woollam Co. VASE Ellipsometer. The film thicknesses were measured on capacitor samples, next to the capacitor and over the bottom electrode to provide a reflective surface. The ellipsometer was equipped with microprobes which focused the light onto 1  $\text{mm}^2$  allowing only the reflected light from the film over the electrode was contributing to the measurement.

Table 6-7 displays the values for a variety of composite samples. In the composition column of the table, the terpolymer layers are listed in black, the ODPA coated BTO layers are listed in blue, and the VDFO coated BTO layers are listed in red.

The first two samples listed were pure terpolymer film, and the rest of the samples were multilayer samples similar to the one shown in the sketches in Figure 6-22.

From the previous ellipsometry study of terpolymer LB layers shown in Figure 6-11, the expected thickness of each monolayer of polymer was 2.03nm. Rather, the pure terpolymer films were much thinner than expected, with an average thickness per layer of 1.1-1.7 nm. The index of refraction from the fits, 1.4, was reasonable for a fluorinated polymer film and was the same index as was measured for 70:30 copolymer films [20].

The composite samples were also much thinner than predicted. The sample with three layers of particles should have had close to a complete layer of particles on the polymer film. For example, the expected thickness of a 10/3/10 dielectric layer was predicted to be 40 nm of polymer and 65 nm from the width of a particle, for a total film thickness of 105 nm. Instead, the films were about half the expected value, in the range of 50-65 nm. Similar trends were observed in the other composite films.

The ellipsometer measured the average film properties for the area that the light was incident onto the sample. One reason that the films could be thinner than expected was that the particle layers did not transfer well from the trough. As the low magnification image in Figure 6-23A showed, a single layer had nearly complete coverage on the size scale of millimeters and it seems unlikely that all of the samples had poor coverage when they were made on four separate occasions.

The other possible cause for all of the films to be thinner than expected would be if the fit of the index of refraction was off by a large amount. The index of refraction of PVDF was 1.42 and the index of BTO was 2.41. The fit for the index of refraction for

most of the samples was between 1.4 and 1.55, which was much closer to the index of the polymer. If the value of the fit was actually closer to the value of barium titanate (2.4) instead of the polymer (1.4) the thickness would scale close to the expected values from adding the contribution to thickness from each layer.

#### **6.4. Cluster Deposition Nanoparticle Capacitor Samples**

There were many challenges to solvent coating nanoparticles such as keeping the particles well dispersed and to prevent aggregation during the coating procedure and sample manufacturing. One alternative approach was investigated with the help of Dr. Balamurugan Balasubramanian from Dr. David Sellmyer's research group. Particles were made and coated in situ without ever coming in contact with solvents by creating cluster deposition particles.

Cluster deposited particles were a way to make monodispersed coated nanoparticles. First, since they were synthesized in a vacuum, there was no concern about solvent compatibility. This meant core-shell particles could be made with various layers that were polar and nonpolar without needing a suitable solvent. Also, by coating particles in situ, the particles were coated before they agglomerated into large clusters. An assortment of organic molecules, including paraffins and VDF oligomers, could be evaporated onto the surface of the particles. Additionally, traditional synthesis of many oxides involves high temperature annealing that was not compatible with organic coatings on the particles [21]. By sputtering the particles in the appropriate atmosphere, particles of the desired structure were created, in this case titanium dioxide. This allowed the growth of high dielectric strength particles coated in a high breakdown strength

material such as alkanes or a VDF oligomer [6, 7]. Also, by coating the particles and directly depositing onto substrates, it allowed for higher concentrations of particles than would have been possible by spin-coating a film with a matrix.

#### *6.4.A. Methods for Production of Particles by Sputtering in a Vacuum*

The methods are described in detail in references [6] and [7]. The process of sputtering and coating the particles occurred in a linear plasma condensation system, as shown in Figure 6-27. In this system, atomic metal vapor was created using a plasma sputtering process with a titanium target. The atomic molecules were condensed in a water cooled inert atmosphere of helium and argon, at a pressure of  $5 \times 10^{-1}$  torr. The titanium atoms lost energy in the collisions with the gas molecules to agglomerate into titanium nanoparticles. To create oxide nanoparticles such as titanium dioxide particles, oxygen was mixed into the inert atmosphere. Different flow rates of oxygen ranging from 6.7 to 80 SCCM were used to produce different compositions and stoichiometries.

Once the atoms have agglomerated into nanoparticles, they entered into the evaporation chamber for coating, as shown in the center part of Figure 6-27. In this chamber, a desired organic coating such as paraffin or VDF oligomer was heated to either evaporate or sublime onto the surface of the particles. The temperature of the paraffin determined the coating thickness on the nanoparticles. The higher the temperature, the thicker were the shells on the particles. A similar process was used for the oligomer coated particles.

After being coated with the organic shell, the particles passed into the deposition chamber. In this chamber, the particles were deposited onto a substrate for further

measurements. For dielectric measurements, a glass substrate with aluminum electrodes was used, while XRD and microscopy measurements used either TEM grids or silicon substrates. The capacitor samples were made with the standard parallel plate construction discussed in Chapter 2. The substrates were microscope slide glass cut into one inch squares. The aluminum top and bottom electrodes were typically 1 or 3 mm wide and approximately 25-50 nm thick. The dielectric layer consisting of nanoparticles was deposited upon the bottom electrodes, and then the top electrodes were evaporated in place. Most substrates had six parallel plate capacitors on them. Each capacitor was then isolated from its neighbors by cutting the metal electrodes between sample spots.

#### *6.4.A.a. Uncoated Titanium Dioxide Particles*

The first series of samples to be studied were uncoated  $\text{TiO}_2$  nanoparticle samples. This was to allow for an understanding of how to make high quality, uniform particles and to understand the dielectric properties of such a sample. This also gave a base comparison for the dielectric studies to compare the coated nanoparticles.

##### *6.4.A.a.i. X-ray Diffraction of Uncoated Titanium Dioxide Nanoparticles*

The XRD results [6] of the  $\text{TiO}_x$  particles are shown in Figure 6-28. By varying the rate of flow for the oxygen, Ti, TiO, and  $\text{TiO}_2$  nanoparticles were created, as shown Figure 6-28A. With no oxygen flowing into the chamber, pure titanium nanoparticles were created. At low flow rates of less than 25 SCCM, TiO nanoparticles formed. By further increasing the flow rate of the oxygen to more than 40 SCCM,  $\text{TiO}_2$  nanoparticles in the rutile and anatase phases were created. By increasing the flow rate from 40 SCCM to 80 SCCM, the particles were nearly all in the anatase phase.

Figure 6-28B shows how the particle phase of the  $\text{TiO}_2$  particles were controlled with the flow rate of oxygen, measured in standard cubic centimeters per minute (SCCM). At 40 SCCM, there were nearly equal ratios of anatase and rutile particles based on the area of the respective peaks. As the flow rate increased, so did the ratio of anatase particles. By 70 SCCM, the rutile peak located between  $27^\circ$  and  $28^\circ$  had mostly disappeared.

#### *6.4.A.a.ii. Transmission Electron Microscopy Results of Uncoated Titanium Dioxide Nanoparticles*

The particle size distribution was measured with a transmission electron microscope [6]. As shown in Figure 6-29A and B, the uncoated  $\text{TiO}$  nanoparticles had a small size distribution with the average particle size of about 17.6 nm, with  $\sigma/d = 0.6$ . The ratio  $\sigma/d$  shows how narrow the particle sizes are distributed. Once the oxygen was introduced into the chamber, the average particle size decreased to about 13.4 nm with a  $\sigma/d = 0.08$ , as shown in Figure 6-29C and D. The  $\text{TiO}_2$  particles were hypothesized to be smaller than the pure titanium nanoparticles due to the higher collision rates with the oxygen molecules and the oxidation process itself, causing the atoms to lose energy faster and reach an equilibrium state sooner. As seen in the inset of Figure 6-29C, the nanoparticles were spherical in shape with smooth edges.

#### *6.4.A.b. Paraffin Coated Titanium Dioxide Nanoparticles*

Titanium dioxide nanoparticles were coated with a shell of paraffin to increase the breakdown strength of the dielectric and to reduce particle agglomeration. The particles

were formed using the same method as the uncoated particles with organic material being evaporated onto the particles in the evaporation chamber, as shown in Figure 6-27. For the particles coated in paraffin, the paraffin, with a melting point of 70-80 °C, was resistively heated in a steel crucible at temperatures between 60-165 °C.

#### *6.4.A.b.i. Coating Thickness of Paraffin Coated Nanoparticles*

The particle coating thicknesses depended on the temperature of the organic materials being deposited [6]. In the case of the paraffin coatings, at low temperatures, no visible coating could be seen as shown in Figure 6-30A. Once the paraffin was melted, the evaporation rate increased rapidly. The rate of evaporation was measured by placing a quartz crystal monitor above the crucible of the melted organic, inside of the chamber. The assumption was made that the rate did not change with the amount of material in the crucible, which was not the case when evaporating metal with a wire basket. At low temperatures, the evaporation rate of the paraffin was slow, at 1 Å/s. As the temperature increases, so did the evaporation rate. At 110 °C, the evaporation rate was at 1.2 Å/s, and by 160 °C, the rate was up to 1.8 Å/s.

The evaporation rate did not give a direct measurement of the shell thickness on the particles, since the particles pass perpendicular through the cloud and were tumbling as they pass through. The rate did allow for an approximation of the ratio of coatings relative to other thicknesses to be made. One additional assumption that must be made about the coating thicknesses was that all of the particles were traveling at similar velocities through the cloud of organics, and that the density of the cloud was similar for each particle.

The only way to obtain the particle coating thickness was to measure it directly. Typical samples were deposited onto TEM grids for measurement by transmission electron microscopy (TEM). As shown in Figure 6-30B, the coatings were visible under high magnification. The dark centers in the figure were the dense particles and the shells were the lighter colored rings. The inset was a high resolution image of the coated nanoparticles, more clearly showing the shell-core structure. Based on the TEM images, the shells evaporated at 110 °C had a thickness of 2 nm and the shells evaporated at 165 °C had a thickness of 3.5 nm.

#### *6.4.A.b.ii. X-ray Diffraction of Paraffin Coated Nanoparticles*

Another way to verify the coatings on the nanoparticles was to use x-ray diffraction [6]. Figure 6-31 shows a series of samples where the paraffin was evaporated over a range of temperatures from 60 °C to 165 °C. All of the samples showed the anatase peak around 25° and the rutile peak around 28.5°, although the ratio of the peaks changed from sample to sample.

The paraffin peaks were present in samples that had an evaporation rate higher than 110 °C, signifying a thick enough crystalline layer to produce an XRD peak. As shown in Figure 6-31B, there were no peaks from paraffin at 60 °C. By 110 °C, the (110) peak was present around 21°. The (200) peak was not significant until the temperature was increased to 165 °C.

#### *6.4.A.b.iii. Volume Ratios of Coated Titanium Dioxide Nanoparticles*

The volume ratio of coated titanium dioxide nanoparticles was calculated for the two measured shell coatings. This would allow the determination of the expected amount of each material in a capacitor with respect to each other, but it did not account for the volume of air in each sample. Calculating the volume of air was much more difficult since the particle shells were soft and easily deformed to fill spaces between the hard spheres or the particles could stick together in ways that would create missing particles and have voids that spanned a volume much larger than the ideal maximum packing for spheres of 74% [22].

If the particles were assumed to be a sphere, as supported by the TEM image in Figure 6-29C, a 17.7 nm diameter particle would have the volume of  $2903 \text{ nm}^3$ . When a 2 nm shell was added to a particle, the total volume of the particle-shell system was  $5350 \text{ nm}^3$ . This gave the volume of the coatings to be  $2447 \text{ nm}^3$ . This meant that the maximum particle concentration in a sample was 54% of the volume and the coating would account for a maximum of 46% of the volume. When the coating thickness increased to 3.5 nm, the total volume of the particle-shell system increased to  $7890 \text{ nm}^3$ . This meant that the volume of the shell was  $4987 \text{ nm}^3$ . In this case, a maximum of 37% of the volume was particles and 63% of the volume was coating. Even if the coatings deformed upon impact with the substrate, the total amount of material would stay constant, and the paraffin would still account for 1.7 times the volume as the particles.

#### *6.4.A.c. VDF Oligomer Coated Titanium Dioxide Nanoparticles*

The structure of the oligomer coated titanium dioxide nanoparticles was very similar to the structure of the paraffin coated nanoparticles [7]. For this series of samples, titanium dioxide nanoparticles were coated with VDF oligomer purchased from Kunshan Hisense. The oligomers were an average of 17 VDF units long with an iodine end group. The VDF oligomers have the advantage over the paraffin coatings since they have a higher dielectric constant and breakdown strength [2, 23].

##### *6.4.A.c.i. Titanium Dioxide Particle Properties for the Particles to be Coated in VDFO*

The titanium dioxide cores were formed using the sputtering system shown in Figure 6-27. In this case, the composition of anatase and rutile phases was regulated with the DC power,  $P_{DC}$ , while holding the gas flow at a constant 50 SCCM [7]. As shown in Figure 6-32, the particles deposited at 120 W, curve (i), were primarily in the anatase phase. When the  $P_{DC}$  was increased to 150 W, curve (ii), there was a mixture of anatase and rutile phases. By 200 W, curve (iii), the sample was mostly rutile. The particles created with this technique are shown in the SEM image in Figure 6-32B. While the particles are still spherical, the distribution of sizes was larger,  $\sigma/d = 0.15$ . The average particle size was 14.4 nm, as shown in Figure 6-32C.

##### *6.4.A.c.ii. X-Ray Diffraction of VDFO Coated Titanium Dioxide Nanoparticles*

The titanium dioxide nanoparticles were coated as they passed through a vapor of evaporated oligomers [7], as shown in the evaporation chamber of Figure 6-27. The oligomers were evaporated over a range of temperatures up to 300 °C. Figure 6-33A

shows the XRD results of the titanium dioxide nanoparticles coated with VDF oligomer evaporated at 200 °C and 300 °C, along with the uncoated particles, curve (i). The particles coated with an evaporation temperature of 200 °C were shown in curve (ii). There was no evidence of the ferroelectric  $\beta$  phase in this set of data. The paraelectric  $\alpha$  phase was present around 18° with a broad peak. In comparison, the particles coated at 300 °C, shown in curve (iii), have both a sharp  $\beta$  phase peak around 19° and the broad  $\alpha$  phase peak at 18°. Figure 6-33B shows a close up of the region with the VDF peaks and the rutile titanium dioxide peak located near 27°. When the particles were coated with oligomers, the rutile peak remained narrow, signifying a surface pacification on the surface of the particles.

#### *6.4.A.c.iii. Volume Ratio Estimations of Particles to Coatings*

Unfortunately, no VDF oligomer-coated particle samples were deposited onto TEM grids for direct measurements of the particle-shell radii to determine the particle to oligomer volume ratios for the different coating conditions. Instead, the volume ratios of the particles to oligomers were estimated two ways. The first was to use the Reitveld fit [7] of the XRD data in Figure 6-33B, which gave the weight ratios from the fits. The second method was to measure the diameter of the particle-shell system from SEM images and to use the particle size from the Figure 6-32 to determine the ratios of VDFO to TiO<sub>2</sub>.

As reported [7], the weight ratios of polymer to particles was calculated using the x-ray diffraction in Figure 6-33B. It was determined that the sample prepared at 200 °C was 95 ± 2.3% titanium dioxide by weight and 5 ± 2.8% VDF oligomer by weight. At the

evaporation temperature of 300 °C, the ratio was  $60 \pm 4.3\%$  particles by weight and  $40 \pm 7.5\%$  VDF oligomer by weight. By using these values and the density of bulk titanium dioxide and PVDF (the bulk density of VDF oligomers was not available), the volume ratios were calculated from the mass ratios.

For the 200 °C evaporation sample, the 95% weight of the titanium dioxide nanoparticles was 89% of the volume of the particle-shell system. The 5% of the weight from the VDF oligomers accounted for 11% of the volume. For the samples evaporated at 300 °C, the 60% of the total weight belonging to the nanoparticles was 39% of the volume. The 40% of the weight from the oligomers was 61% of the volume. The problem with this measurement was that only the crystalline material was measured. This means that most of the  $\text{TiO}_2$  was accounted for, but most of the VDF oligomer maybe missing. Any material that was amorphous did not contribute to the diffraction peak. Also, these samples were not annealed before being measured, and it has been shown that annealing samples increases the area of XRD peaks by 5 to 12 times [8]. As an estimate, if the volume of the polymer was actually 5 times the measured amount, the volume percentages would be 11% particles and 89% VDF oligomer.

The second method used to determine the volume ratio of particles to VDF oligomer was performed with the FESEM images taken of a sample coated at 300 °C. The diameter of thirty-five nanoparticles whose edges could be determined from the image was measured and the data was plotted on a histogram, as shown in Figure 6-35. The particles in the sample show a range of coating thicknesses with the particle-shell size ranging from 34 to 55 nm. This size calculation made the assumption that the

coating size did not change due to exposure to the electron beam. A Gaussian curve was fitted to the data to determine the particles size distribution. The coated particles had an average diameter of 53 nm and the average diameter of the uncoated particles was 14.4 nm from Figure 6-32. This gave a particle volume of  $1563 \text{ nm}^3$  and the total particle-shell volume of  $77,952 \text{ nm}^3$ . This means that the average shell occupied  $76,389 \text{ nm}^3$  per particle. This implied that 2.0% of the volume was occupied by the particles and 98.0% of the volume was VDF oligomers. There were several potential sources of errors with this analysis. The first was the nanoparticles were assumed to stay the same size each time samples were made. The second was that the electron beam did not distort the shell size. If the beam slightly melted the surface of the shell and caused it to flatten out, the particles would appear slightly larger than they actually were. If the beam heated the sample enough to vaporize the oligomers, the shells would appear smaller. Both behaviors have been observed in similar samples, and it is difficult to state if either happened in this case without observing the behavior of the sample was first exposed to the electron beam.

These two methods gave an upper and lower limit to the volume ratios of the particles used to make the capacitor samples. From XRD, the maximum particle concentration would be 39% of the volume. This value was probably an over-estimate. From SEM, a value of 2% of the volume was calculated for the particles, which is probably a more realistic value compared to the XRD calculated volume [7].

#### *6.4.B. Measurement Methods for Determining Sample Thicknesses*

One of the major difficulties was determining the thickness of the dielectric layer. Often the center of the sample area where the stream of particles was deposited was thicker than the edges of the sample. This meant a method was needed to determine the thickness of each capacitor spot on the sample. Three methods were used to do this. The first was to use the optical visible interference pattern on the sample. This method was an easy way to get a quick estimate of the thickness, but had the drawback that one must know where the initial band ( $m=1$ ) is located to have the correct determination of the thickness. The second method used was ellipsometry. This method used a series of angles of incidence and wavelengths to calculate the index of refraction and sample thickness, and gave a more accurate sample thickness if the index of refraction could be determined. Ellipsometry is discussed in more detail in Chapter 2. For some of the thickest samples, the thickness of the dielectric layer was measured using profilometry.

##### *6.4.B.a. Optical Interference*

The thickness of the dielectric layer was determined by photographing the samples that showed clear interference patterns, such as the one shown in Figure 6-36. Optical thickness measurements used a white light source such as the overhead lights or sunlight, a digital camera, and the sample. The first challenge was to obtain a photograph of the sample where the bands are distinct enough in the image to be able to easily count them. For many samples, it was necessary to adjust the photo contrast to make the bands more distinct.

This method is based on the principle of thin film interference [24, 25]. For constructive interference to occur, the change in path length,  $\Delta$ , must meet the following condition:

$$\Delta = m\lambda, \quad \text{Equation 6-1}$$

where  $m$  is the index number, and  $\lambda$  is the wavelength of light. Constructive interference occurs when light reflects at the interfaces. For two materials as shown in Figure 6-37, if the index of the first material,  $n_1$ , is greater than the index of the second material,  $n_2$ , then the shift is zero. If  $n_1$  is less than  $n_2$ , then the shift,  $\Delta a$ , is

$$\Delta a = \frac{\lambda}{2}. \quad \text{Equation 6-2}$$

If  $\Delta b$  is the path the light traveled in the dielectric material, then

$$\Delta b = 2t \quad \text{Equation 6-3}$$

if  $n_2 > n_3$ , and

$$\Delta b = 2t + \lambda/2 \quad \text{Equation 6-4}$$

if  $n_2 < n_3$ .

The total change in path length is the change in path length between the light in air and the light in the sample. Since the bottom electrode is metal, then the condition in

$\Delta b = 2t$  Equation 6-3 is met. The change in path length would then be

$$\Delta = \Delta b - \Delta a, \quad \text{Equation 6-5}$$

where  $\Delta b = 2t + \lambda/2$  and  $\Delta a = \lambda/2$ . Since the change in path length,  $\Delta$ , must be an integer number of wavelengths,  $\Delta$  is given by

$$\Delta = 2t + \lambda/2 - \lambda/2 = m\lambda. \quad \text{Equation 6-6}$$

Solving this for the sample thickness,  $t$ , we get

$$t = \frac{m\lambda}{2}. \quad \text{Equation 6-7}$$

The wavelength,  $\lambda$ , in the above equation is the wavelength of light in the dielectric layer, in this case titanium dioxide. Since the wavelength of light in the material is related to light in a vacuum with the following equation,

$$\lambda_2 = \lambda_{VAC}/n_2. \quad \text{Equation 6-8}$$

Substituting Equation 6-8 into Equation 6-7 for the sample thickness, the thickness of the dielectric layer is given by

$$t = \frac{\lambda_{VAC}}{2n_2}m. \quad \text{Equation 6-9}$$

While this method gave decent estimates of thickness for samples when the location of the initial  $m=1$  band was located, it did not work as well for samples where it was unclear where the  $m=1$  band was found. For samples that were more uniform and have fewer bands located on the substrate, it was especially difficult to estimate where the  $m=1$  band was located or if they were even located on the substrate. Ellipsometry was used for the thinner samples and to obtain the verification that we had the correct index of  $m$ .

### **6.4.C. Capacitor Sample Properties**

#### *6.4.C.a. Uncoated Titanium Dioxide Particles*

##### *6.4.C.a.i. Scanning Electron Microscopy of the Surface of the Film*

A FESEM was used to image the surface of uncoated titanium dioxide nanoparticle films deposited onto a silicon substrate. A typical example was shown in Figure 6-38. This sample's image was collected using a 5kV electron beam with 80.0k magnification. The particles appear have a diameter around 50 nm, compared to the expected size of 13nm as shown in Figure 6-29. Also, the image showed that many of the particles were agglomerated to their neighbors in clusters ranging from a few particles to several hundred nanometers in diameter. One of the goals of coating the particles with an organic shell was to reduce the amount of agglomeration that occurred relative to the uncoated particles.

##### *6.4.C.a.ii. Cross-sectional Scanning Electron Microscope Imaging of Uncoated Titanium Dioxide Nanoparticle Thin Films*

Capacitor samples were made for cross sectional analysis. Onto a silicon substrate, 25 nm of aluminum was deposited for the bottom electrode. Then, approximately 1  $\mu\text{m}$  of particles was deposited over the aluminum and the particles were capped with approximately 50 nm of aluminum, as shown in Figure 6-39A. The sample was fractured into two pieces and mounted for cross sectional analysis, as described in Chapter 2. The top electrode was distinguishable from the dielectric layer as the grains of aluminum were larger than the nanoparticles and irregularly shaped. In contrast, the bottom electrode was a smooth layer of metal with no obvious granular features. The

dielectric layer between the two electrodes consisted of spherical nanoparticles of a similar size as the ones shown in the TEM images.

Figure 6-39B shows a high magnification image of the uncoated nanoparticle sample shown in Figure 6-39A. The sample was imaged with 15 kV beam at 130k magnification. In this image, the particles linked together making chain-like structures in the sample. These structures then came together to form the thin film, leaving voids between the chains of particles. The void space caused a number of difficulties in determining the sample thickness (due to altering the index of refraction) and in making electrical measurements (from having a low breakdown strength).

#### *6.4.C.a.iii. Sample Thickness Measurements of Uncoated Titanium Dioxide Nanoparticle Films*

The film thicknesses for uncoated titanium dioxide nanoparticle samples were determined using the optical interference patterns. A typical sample is shown in Figure 6-36. This sample was made with a layer of titanium dioxide nanoparticles deposited onto aluminum electrodes. The thickness calculations for the red bands of the sample shown in Figure 6-36 are listed in Table 6-8 for each of the  $m$  values. For this sample, the index of refraction used for the calculations was the index of titanium dioxide, 2.4. This index would have been larger than the actual index, since we know there was a fraction of the sample with air voids, as shown in Figure 6-39. This would have caused the thickness estimate to be thinner than the real sample. This estimate was still closer to the actual value than the previously predicted sample thickness of less than 100 nm. When the thickness of the sample was plotted against the distance from the center of the

mound of particles, a Gaussian curve fits remarkably well, as shown in Figure 6-40. A Gaussian distribution for the spatial distribution of the particles was a reasonable estimate for the beam shape and helped support the thickness estimates.

A second sample of uncoated titanium dioxide nanoparticles is shown in Figure 6-41A. The capacitor being measured was the one located in the lower left corner of the image. Like the previous sample, this sample also shows a large distribution of thicknesses over the substrate. The only spot that was reliable enough for electrical measurements was the spot mentioned above, with a green interference band passing through the center of it. Since the wavelength increased as it goes from blue to red light, and there was a faint red band visible at the edge of the sample, the green band must have had an  $m$  value of at least two. Experience has shown that it was not likely to be off by more than one  $m$  value for bands that were as faint as the one in the image. By using 510 nm for the wavelength of green light, the approximate calculated sample thickness would be 213 nm. Similar calculations were carried out for other samples not shown here.

#### *6.4.C.b. Titanium Dioxide Nanoparticles with a Paraffin Shell as a Thin Film*

##### *6.4.C.b.i. Scanning Electron Microscopy Studies of the Surface of Paraffin Coated Titanium Dioxide Nanoparticle Thin Films*

The structure of the surface of the titanium dioxide nanoparticles coated with a paraffin shell is shown in Figure 6-42A[6]. The first image was measured using a field emission SEM with a beam power of 10.0 kV and 100k magnification. This image showed that the particles were still agglomerating with the coatings present. The particles may have clustered together before they were coated, and then the coating was

deposited on the surface of the clusters. (See the AFM results in Section 6.4.C.b.ii for further discussion of this.) The other possibility was that the thin shells did not have high enough contrast to be visible with the SEM.

*6.4.C.b.ii. Atomic Force Microscopy Studies of the Surface of Paraffin Coated Titanium Dioxide Nanoparticle Thin Films*

Atomic force microscopy measurements were made on the sample shown in Figure 6-42A to measure the coating thicknesses. The resulting AFM images were not as expected from such a sample. Instead of many small particles smaller than 20 nm in diameter, there were large particles surrounded by a soft coating, as shown in Figure 6-42B. The first image was of the amplitude of deflection of the AFM tip, showing the height profile of the sample. As expected, the surface of the sample was not smooth, and contained a distribution of heights with a Z value of 100 nm. The interesting results were in the second image, showing the phase data. As the stiffness of the material changed, it appears in the phase image as different colors. The bright centers were thought to be over the hard particles, while the darker surroundings were the soft paraffin coatings. If this interpretation of the data was correct, it would imply that there was very little air voids in the sample due to the particle shells deforming when they collided on the substrate and neighboring particles.

Figure 6-43 showed line scan analysis of the AFM image in Figure 6-42B over a region of bright centers and darker surroundings in the phase data. Figure 6-43A was of the bright centers, and showed that the centers were approximately 72 nm in diameter. Figure 6-43B was the analysis for the darker coatings, with a thickness of 76 nm. The

expected size of the nanoparticles was approximately 13 nm, as shown in Figure 6-29, with a paraffin shell of a few nanometers thick. There were no features visible in the shown images or at higher magnifications on that size scale. This would imply that it was likely that the particles agglomerated into clusters before they were coated and the heavier particles passed more slowly through the coating chamber, creating a thicker shell around the cluster of particles.

#### *6.4.C.b.iii. Sample thickness of Paraffin Coated Titanium Dioxide Nanoparticles*

The film thicknesses for the paraffin-coated titanium dioxide nanoparticles were determined using the optical method for a majority of the samples. Typical samples are shown in Figure 6-44 and Figure 6-45. The sample in Figure 6-44 had an evaporation temperature of 170 °C. This meant the coating on the particles was expected to be thicker than on the nanoparticles coated at lower temperatures. The capacitor that it was desirable to know the sample thickness for was located in the center of the sample. This means it was the red  $m=4$  band that was used to determine the sample thickness. The index of refraction was determined to have a value of 2.3 based on the volume ratios of the particles and coatings. The air voids were not considered in this calculation, so the value of the index of refraction may have been a little larger than the actual value, causing the film thickness to be a slight under estimate. For this sample, the thickness was estimated to be 565 nm.

A second sample shown in Figure 6-45 had the particles that were coated at 110 °C evaporation temperature. For this sample, the spot of interest was located in the upper left corner. There was a large distribution of thicknesses under the capacitor spot. As

shown in the sketch in Figure 6-45B, the thickness was calculated for the yellow  $m=2$  band and the blue  $m=3$  band. The index of refraction was calculated to be 2.3, based off of the original TEM images of the coated particles. The thinner part of the sample had an estimated thickness of 248 nm while the thicker part was 310 nm. This gave an average thickness for the sample of approximately 279 nm.

#### *6.4.C.c. Titanium Dioxide Nanoparticle with a VDFO Shell as a Thin Film*

##### *6.4.C.c.i. Scanning Electron Microscope Studies of the Surface of VDFO Coated Titanium Dioxide Nanoparticle Thin Films*

The surface morphology was imaged using a field emission SEM. There was a notable change in appearance of the early films such as the ones shown in Figure 6-46 and the later samples such as the one shown in Figure 6-47A. In the early samples, there was clear evidence of coated particles. On the surface of the sample, there are round clusters with an approximate diameter of 50 nm. TEM images had shown that the uncoated particles were approximately 14 nm in diameter. This would imply that particles coated with an evaporation temperature of 300 °C have a shell that was 18 nm thick.

In later samples, such as the one in Figure 6-47A, there was little evidence of the particles. The image shown was collected with a 10kV electron beam and 3k magnification. At this magnification, the sample had a fluffy, cloud-like appearance. As the magnification was increased, the sample vaporized almost immediately, the way that a sample that was pure polymer would sometimes behave if the beam was too energetic. Even when the beam was decreased in power to 5 kV, there was no evidence of particles

when the magnification was increased up to 130k. By that magnification, 15 nm particles should have been visible, so either the particle density was very low, or the particles were much smaller than expected and were not resolvable. The other possibility was that the particles were being removed from the surface of the sample when the polymer was distorted by the electron beam. While this could account for some loss of particles, it was unexpected that this would cause any particles from being visible if the initial concentration was very significant.

#### *6.4.C.c.ii. Atomic Force Microscopy Studies of the Surface of VDFO Coated Titanium Dioxide Nanoparticle Thin Films*

The atomic force microscopy measurements made on the sample shown in Figure 6-47A are shown in Figure 6-47B. The AFM measurements were made over a thicker region of the sample to ensure that the film was being measured and not the substrate. The first image was the height displacement and the second figure was the phase showing the relative stiffness of the surface. In contrast to the light and dark regions shown in the phase image of the sample in Figure 6-42, this sample did not show any evidence of particles over a large range of resolutions. Therefore, it must be concluded that the sample either has a very low particle concentration or that the particles are too small to be resolved with this measurement technique.

#### *6.4.C.c.iii. Sample Thickness of VDFO Coated Titanium Dioxide Nanoparticles*

In addition to the optical interference method used in previous sections, some of the VDFO coated titanium dioxide sample thicknesses were measured using ellipsometry as described in Chapter 2. Figure 6-48 shows the ellipsometry data for a typical sample.

Figure 6-48A and B were the psi data as a function of the wave number for two different locations on the substrate, spots B1 and A3 respectively. Figure 6-48C and D were the delta values as a function of wave number for the sample spots mentioned above. The data for all of the locations on the substrate was fit using the Cauchy model, and the sample thickness were given in the table in Figure 6-48F. The distribution of thicknesses was reasonable for a sample with the thickest region of film being under or to the left of electrode B.

## 6.5. Conclusion

Nanocomposite samples were made using three general techniques. The first two techniques consisted of barium titanate nanoparticles coated with either an alkane or VDFO containing a functionalized phosphonic acid head group. The particles were embedded in a VDF copolymer or terpolymer matrix. The composite films were constructed using either spin-coating or Langmuir-Blodgett deposition. These two methods produced relatively uniform films that ranged in thickness from seventy-five to several hundred nanometers. The advantage of these two techniques was that the particle to matrix volume ratio could easily be adjusted by altering the relative concentrations of particles and matrix during spin-coating, or the ratio of polymer to particle layers during the assemblage of the LB films. The disadvantage of the spin-coated films was that there was no way to control the placement of the particles within the films and to prevent the particles from creating low breakdown strength locations within the film. In contrast, the LB multilayer samples had the advantage of being able to control the location of the particles through the cross section of the film. Also, very high volume ratios of particles

to matrix could be achieved with these samples, although it came at the cost of increased thickness.

The third method for depositing thin composite films was to make and coat the particles while in vacuum and deposit them directly onto the substrate. This method had the advantage of not requiring a solvent for the coating process and any organic material that can be evaporated would be a candidate for coating particles. The disadvantage of this method of making samples was that it was difficult to make samples with uniform thicknesses, and the repeatability of measurements on samples was poor.

In the next chapter, the dielectric and energy density results will be discussed for the sample types made in this chapter. Basic characterization measurements such as the temperature and voltage dependence on capacitance will be discussed along with analysis of energy storage and breakdown strengths for a variety of sample types.

## 6.6. References

1. Li, J., L. Zhang, and S. Ducharme, *Electric energy density of dielectric nanocomposites*. APL, 2007. 90: p. 132901.
2. Dionne, G.F., J.F. Fitzgerald, and R.C. Aucoin, *Dielectric constants of paraffin-wax--TiO<sub>2</sub> mixtures*. Journal of Applied Physics, 1976. 47(4): p. 1708-1709.
3. Chu, B., et al., *A Dielectric Polymer with High Electric Energy Density and Fast Discharge Speed*. Science, 2006. 313(5785): p. 3.
4. Chu, B., et al., *Large enhancement in polarization response and energy density of poly(vinylidene fluoride-trifluoroethylene-chlorofluoroethylene) by interface effect in nanocomposites*. Applied Physics Letters, 2007. 91(12): p. 122909-3.
5. Kim, P., et al., *Phosphonic Acid-Modified Barium Titanate Polymer Nanocomposites with High Permittivity and Dielectric Strength*. Advanced Materials, 2007. 19(7): p. 1001-1005.
6. Balasubramanian, B., et al., *Synthesis of Monodisperse TiO<sub>2</sub>-Paraffin Core-Shell Nanoparticles for Improved Dielectric Properties*. ACS Nano, 2010. 4(4): p. 1893-1900.
7. Balasubramanian, B., et al., *Cluster synthesis of monodisperse rutile-TiO<sub>2</sub> nanoparticles and dielectric TiO<sub>2</sub>-vinylidene fluoride oligomer nanocomposites*. Nanotechnology, 2011. 22(40): p. 405605.
8. Kim, J., *Nanoscale investigation of polarization interaction and polarization switching in ferroelectric P(VDF-TrFE) copolymer samples*, in *Physics and Astronomy*. 2008, University of Nebraska: Lincoln. p. 179.
9. Zhong, W.L., et al., *Phenomenological study of the size effect on phase transitions in ferroelectric particles*. Physical Review B, 1994. 50(2): p. 698-703.
10. Wolak, M.A., et al., *Electromechanical Response of Multilayered Polymer Films for High Energy Density Capacitors*. MRS Online Proceedings Library, 2011. 1312: p. null-null.
11. Wang, J.L., et al., *The Optical Dispersion of Langmuir-Blodgett Terpolymer Films*. Ferroelectrics, 2010. 405(1): p. 120-125.
12. Bauer, F., E. Fousson, and Q.M. Zhang, *Recent advances in highly electrostrictive P(VDF-TrFE-CFE) terpolymers*. Dielectrics and Electrical Insulation, IEEE Transactions on, 2006. 13(5): p. 1149-1154.

13. Chu, B., et al., *Poly(Vinylidene Fluoride-Trifluoroethylene-Chlorofluoroethylene) Terpolymer as High-energy-density Capacitor Materials*. MRS Online Proceedings Library, 2005. 889: p. null-null.
14. Palto, S., et al., *Ferroelectric Langmuir-Blodgett films*. Ferroelectrics Letters Section, 1995. 19(3-4): p. 65-68.
15. Chitu, L., et al., *Modified Langmuir-Blodgett deposition of nanoparticles-measurement of 2D to 3D ordered arrays*. 2010.
16. Huang, S., et al., *Experimental conditions for a highly ordered monolayer of gold nanoparticles fabricated by the Langmuir-Blodgett method*. Journal of Vacuum Science & Technology B: Microelectronics and Nanometer Structures, 2001. 19(6): p. 2045-2049.
17. Yang, P. and F. Kim, *Langmuir-Blodgett Assembly of One-Dimensional Nanostructures*. ChemPhysChem, 2002. 3(6): p. 503-506.
18. Bass, M., et al., *Handbook of Optics*. 3rd ed. Vol. Volume IV: Optical Properties of Materials, Nonlinear Optics, Quantum Optics. 2009, New York: McGraw-Hill.
19. Wolak, M.A., et al., *Dielectric response of structured multilayered polymer films fabricated by forced assembly*. Applied Physics Letters, 2008. 92(11): p. 113301-3.
20. Bai, M., et al., *Determination of the optical dispersion in ferroelectric vinylidene fluoride (70%)/trifluoroethylene (30%) copolymer Langmuir-Blodgett films*. Journal of Applied Physics, 2004. 95(7): p. 3372-3377.
21. O'Brien, S., L. Brus, and C.B. Murray, *Synthesis of Monodisperse Nanoparticles of Barium Titanate: Toward a Generalized Strategy of Oxide Nanoparticle Synthesis*. Journal of the American Chemical Society, 2001. 123(48): p. 12085-12086.
22. Gauß, C.F., *Besprechung des Buchs von LA Seeber: Untersuchungen über die Eigenschaften der positiven ternären quadratischen Formen usw*. Göttingische Gelehrte Anzeigen, 1831. 2: p. 188-196.
23. Ducharme, S. and M. Jogad, *Dielectric properties of a ferroelectric copolymer Langmuir-Blodgett film*. Current Science, 2002. 83(4): p. 5.
24. Jenkins, F.A. and H.E. White, *Fundamental of Optics*. 4 ed. 1976: McGraw-Hill College.
25. Hecht, E., *Optics*. 4 ed. 2001: Addison-Wesley. 680.

## 6.7. Tables

Table 6-1. Example of stock solutions used to make a series of samples.

Particle Concentration*	Polymer Concentration*	Amount of Particle Solution	Amount of Polymer Solution
20%	80%	0.4 mL	1.6 mL
40%	60%	0.8 mL	1.2 mL
60%	40%	1.2 mL	0.8 mL
80%	20%	1.6 mL	0.4 mL

\* By volume for coated particle samples

Table 6-2. Sample configurations for uncoated, 65 nm diameter barium titanate particles in a copolymer matrix.

% Volume		% Weight	
% Particles	% Polymer	% Particles	% Polymer
4	96	13	87
5	95	15	85
6	94	17	83
7	93	20	80
9	91	25	75
11	89	30	70
16	84	40	60

Table 6-3. Concentration ratios for ODPA coated 56 nm BTO particles in VDF copolymer or terpolymer.

% Volume			% Weight	
Particle	Coating	Matrix	Particle & Coating	Matrix
67	33	0	100	0
40	20	40	80	20
24	12	64	60	40
14	6	80	40	60
6	2	91	20	80
0	0	100	0	100

Table 6-4. Volume percentages of barium titanate for different sample configurations.

% Volume Concentration		56 nm BTO Nanoparticle		15 nm BTO Nanoparticle	
Particles & Coating	Matrix	DPA-BTO (% of BTO)	ODPA-BTO (% of BTO)	DPA-BTO (% of BTO)	ODPA-BTO (% of BTO)
0	100	0	0	0	0
20	80	16.4	13.4	7.3	4.1
40	60	32.8	26.8	14.6	8.3
60	40	49.1	40.2	21.9	12.4
80	20	65.4	53.6	29.7	16.6
100	0	81.9	67.0	36.5	20.7

Table 6-5. Ellipsometry thickness measurements of terpolymer Langmuir Blodgett films

Number of ML	Thickness (nm)*
5	19-28
6	23-31
8	27-34
10	27-32
17	37-41
20	50
25	59-70
26	66-68
59	133-146

\* The uncertainty in the thickness comes from the uncertainty in the index of refraction in the fittings. The thinner samples had a lower index than the thicker samples.

Table 6-6. Ellipsometry results for ODPa coated BTO Langmuir-Blodgett films.

Number of Monolayers	Deposition Pressure (mN/m)	Thickness (nm)	Index of Refraction
10	10	187-209	1.30-1.34
20	7	190-210	1.32-1.38
20	7	224-244	1.37-1.38
20	10	273-316	1.42-1.43
20	10	322-326	1.38-1.39
40	7	260-276	1.38-1.43
40	10	402-427	1.49-1.55

Table 6-7. Ellipsometry results for composite samples.

Composition*	Thickness (nm)	Index of Refraction
10	17.2	1.4
35	54	1.4
10/1/10	50	1.32
10/3/10	50-65	1.58
20/3/20	90	1.51
20/1/20	58	1.45
5/3/5	52	1.49
5/3/5	45	1.52
10/3/5/3/10	57-92	1.7-2.35
10/3/1/2/1/2/1/3/10	152	1.74
20/3/20	71	1.43-1.44
10/3/10	54	1.36
5/3/5	>50	-

\***Black**- Terpolymer Layers

**Red**- VDFO Coated BTO Layers

**Blue**- ODPA Coated BTO Layers

Table 6-8. Estimated film thickness for constructive interference of red light.

m	t (nm)
1	135
2	270
3	406
4	542
5	677
6	812

## 6.8. Figures

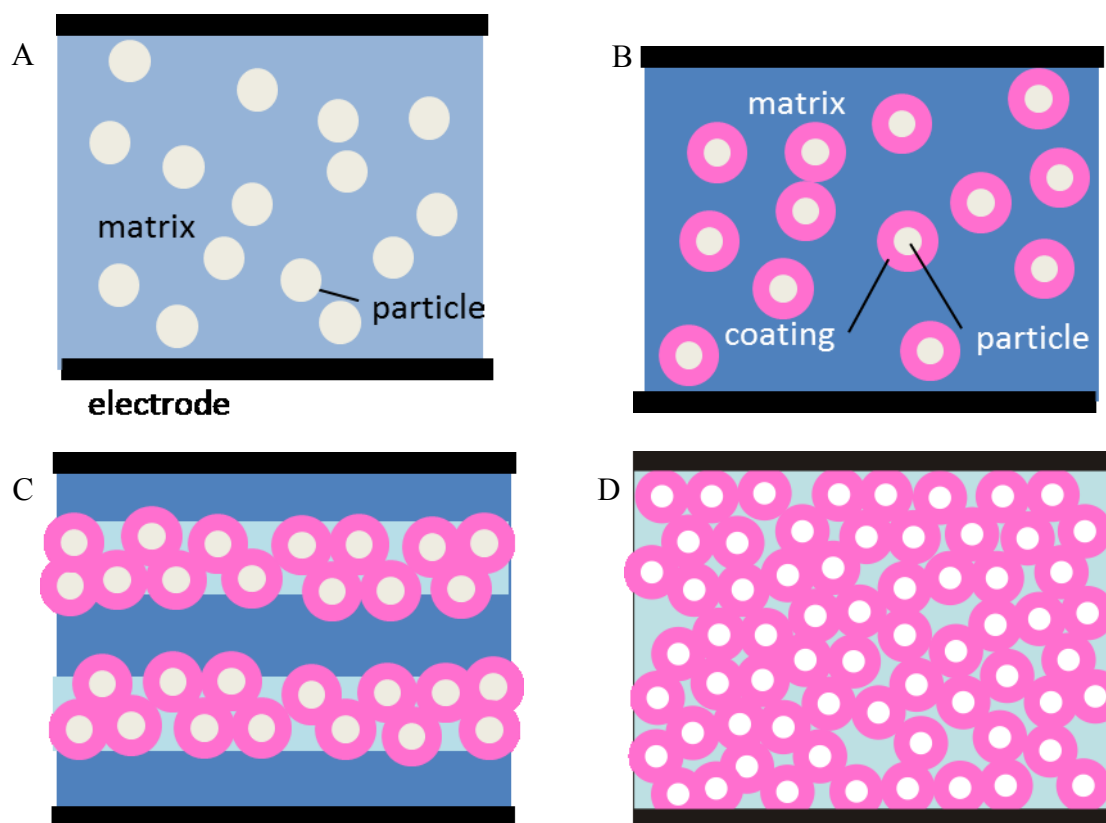


Figure 6-1. Sketches of different sample configuration used for the dielectric study. Composite samples were made by spin coating a polymer matrix and (A) uncoated nanoparticles or (B) particles coated with an organic shell. (C) With Langmuir-Blodgett deposition, particles and polymers were deposited in alternating layers. (D) Particles created by sputtering metal oxides were coated with an organic shell and deposited directly onto the substrate without a matrix.

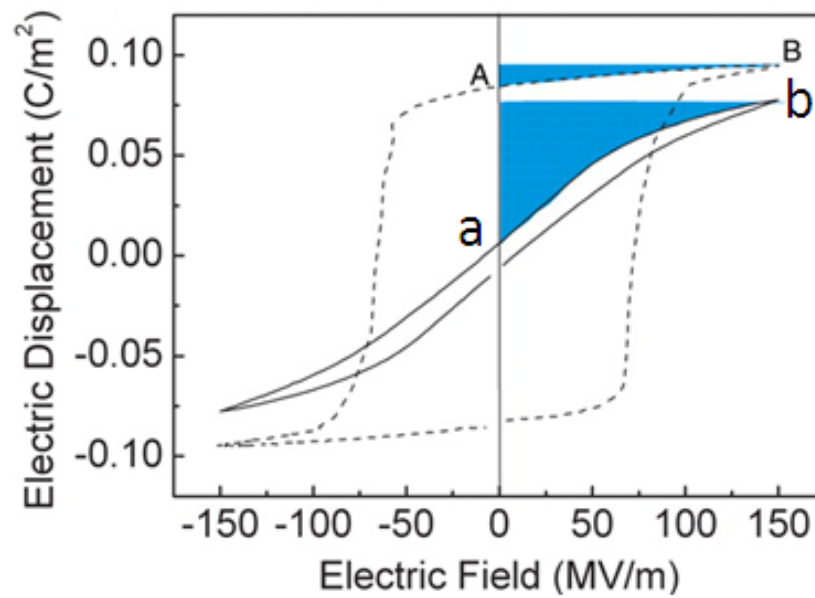


Figure 6-2. The discharged energy density of in capacitor is the blue shaded area. A ferroelectric loses a large amount of energy due to the permanent dipoles compared to the relaxor.[3] (Taken from *Chu, B., et al., Science, 2006. 313(3)* with permission.)

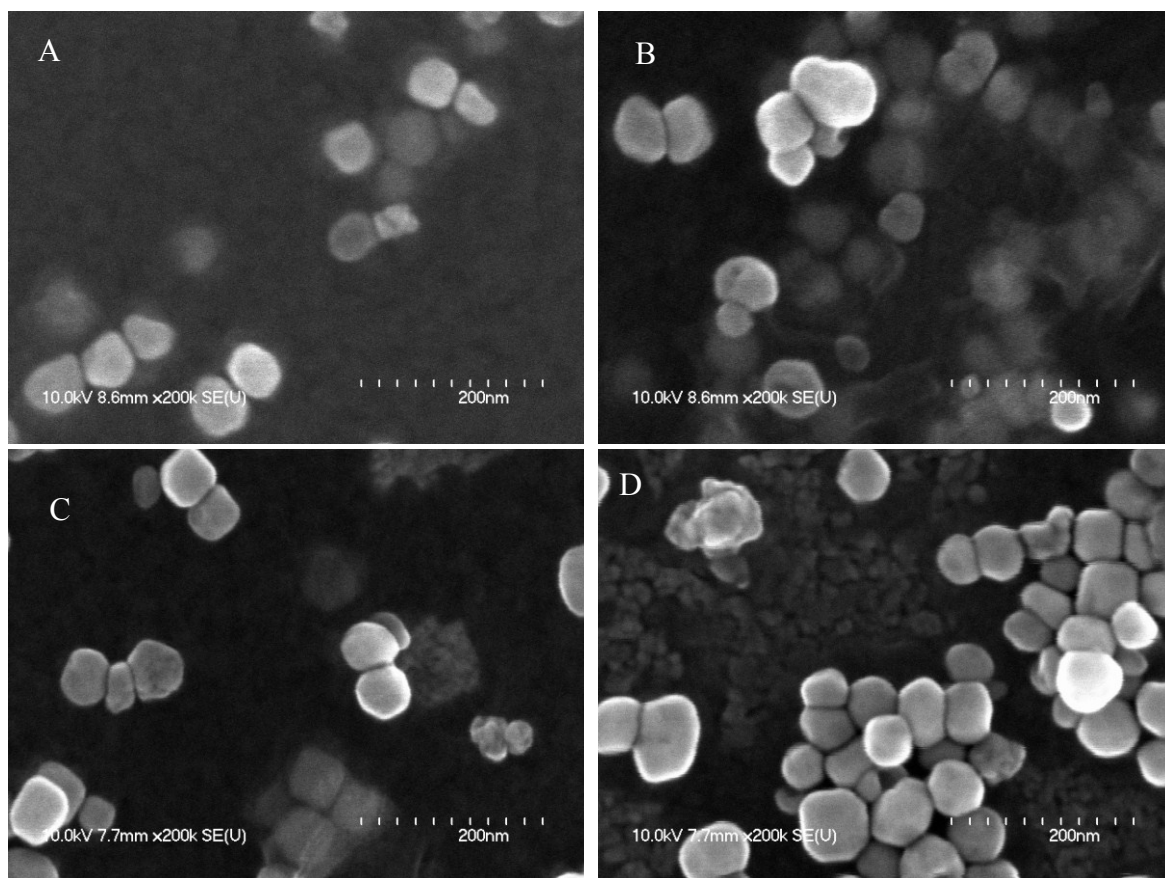


Figure 6-3. ODPA coated BTO nanoparticles were mixed with 50/50 copolymer and spincoated into thin films. (A) Six percent of the samples volume was occupied by BTO particles. At this concentration, the particles were well dispersed in the polymer film. (B) With 14% of volume occupied by BTO, the particles were distributed on the surface and embedded in the film. (C) When the concentration of particles was increased to 24% of the volume, more particles are starting to appear at the surface of the film. (D) At a higher particle concentration of 40% particles, the film had started to form aggregates of polymer and particles.

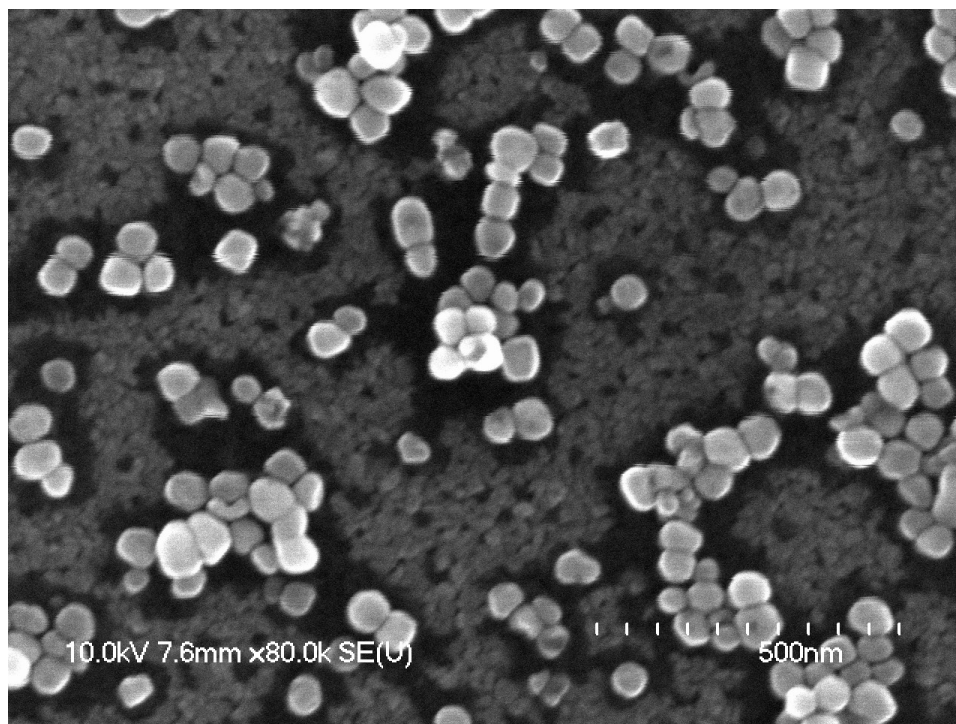


Figure 6-4. ODPA coated BTO in 50/50 P(VDF-TrFe) with a volume ratio of 40% particles. This sample showed the segregation of polymer and particles, along with the structure of the polymer film.

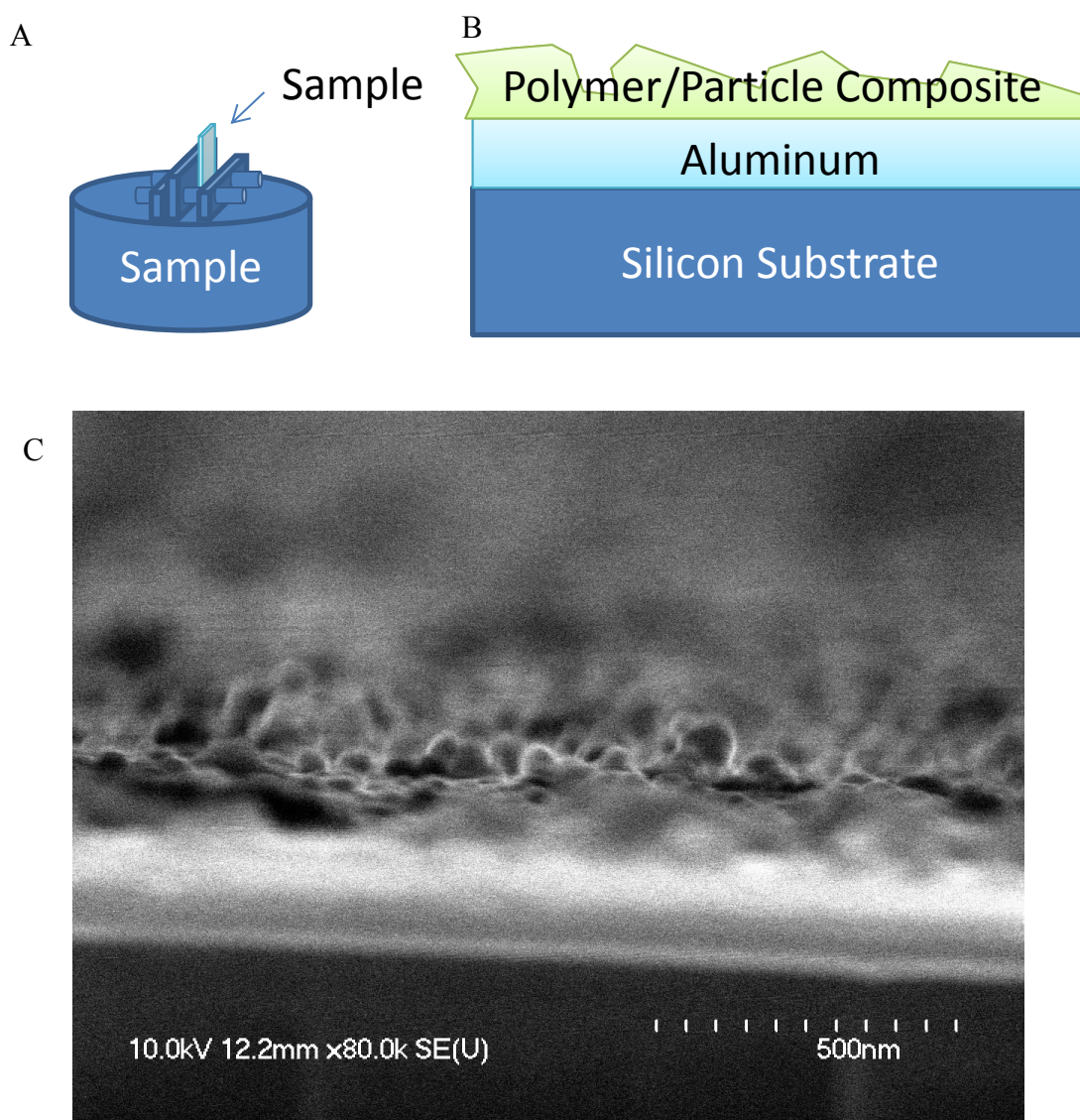


Figure 6-5. (A) Sketch of sample holder for imaging cross sectional samples. (B) Diagram of the composition of the composite sample used for imaging the cross section. (C) FESEM image of the cross section of a 14% by volume ODPA coated BTO sample in 50/50 copolymer. The dielectric layer was in focus.

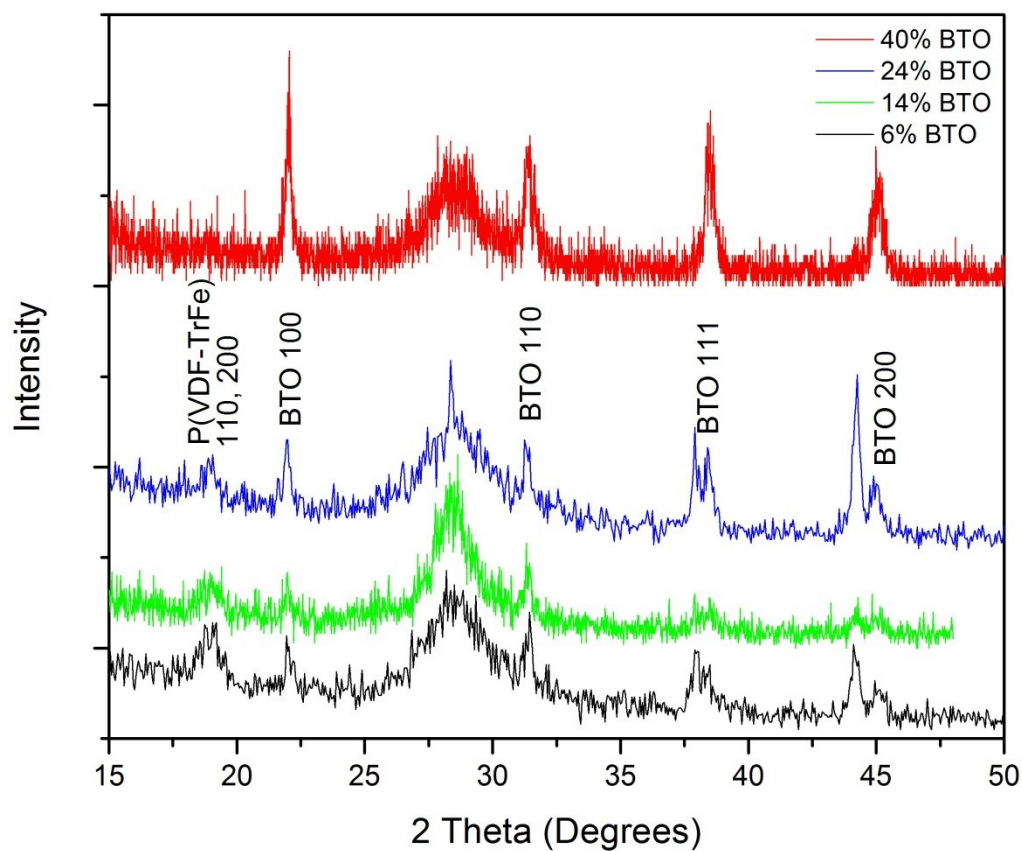


Figure 6-6. X-ray diffraction data for ODPA coated BTO in a 50/50 P(VDF-TrFe) matrix. As the volume concentration of particles increased, the BTO peaks increased while the polymer peak decreased.

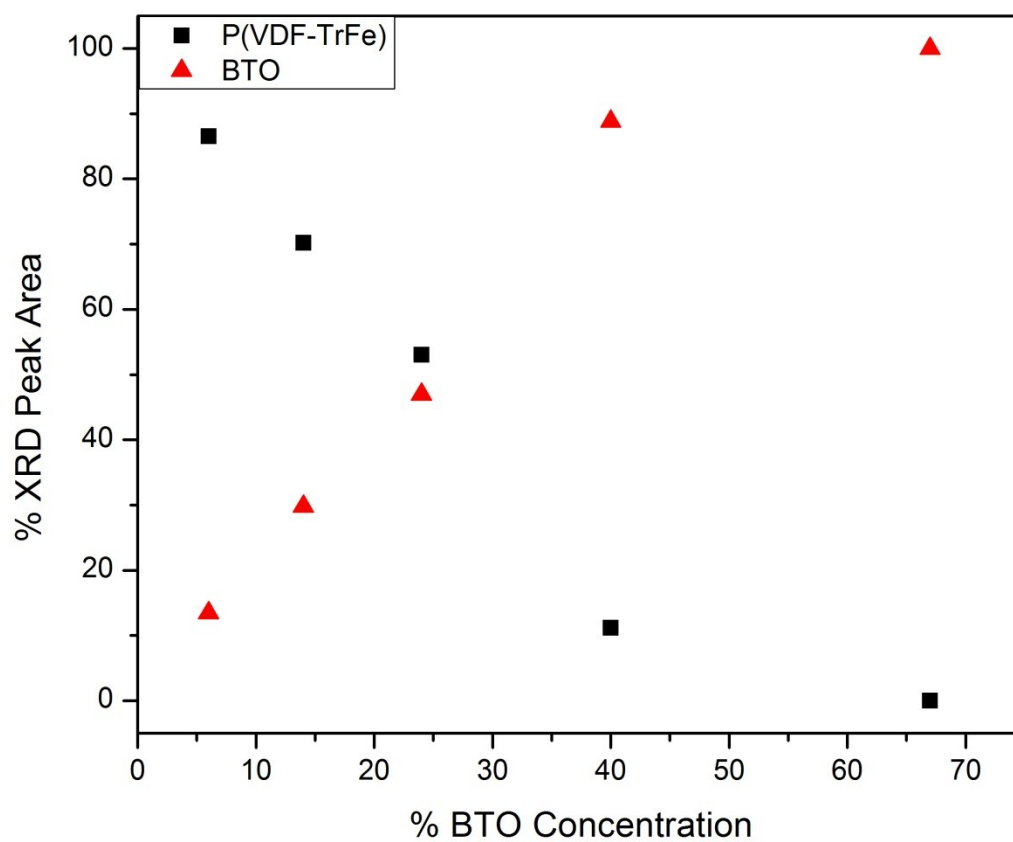


Figure 6-7. Ratio of polymer and particle peaks as a function of the BTO volume concentration in composite spin-coated films. As the concentration of particles increased, the polymer peak area decreased.

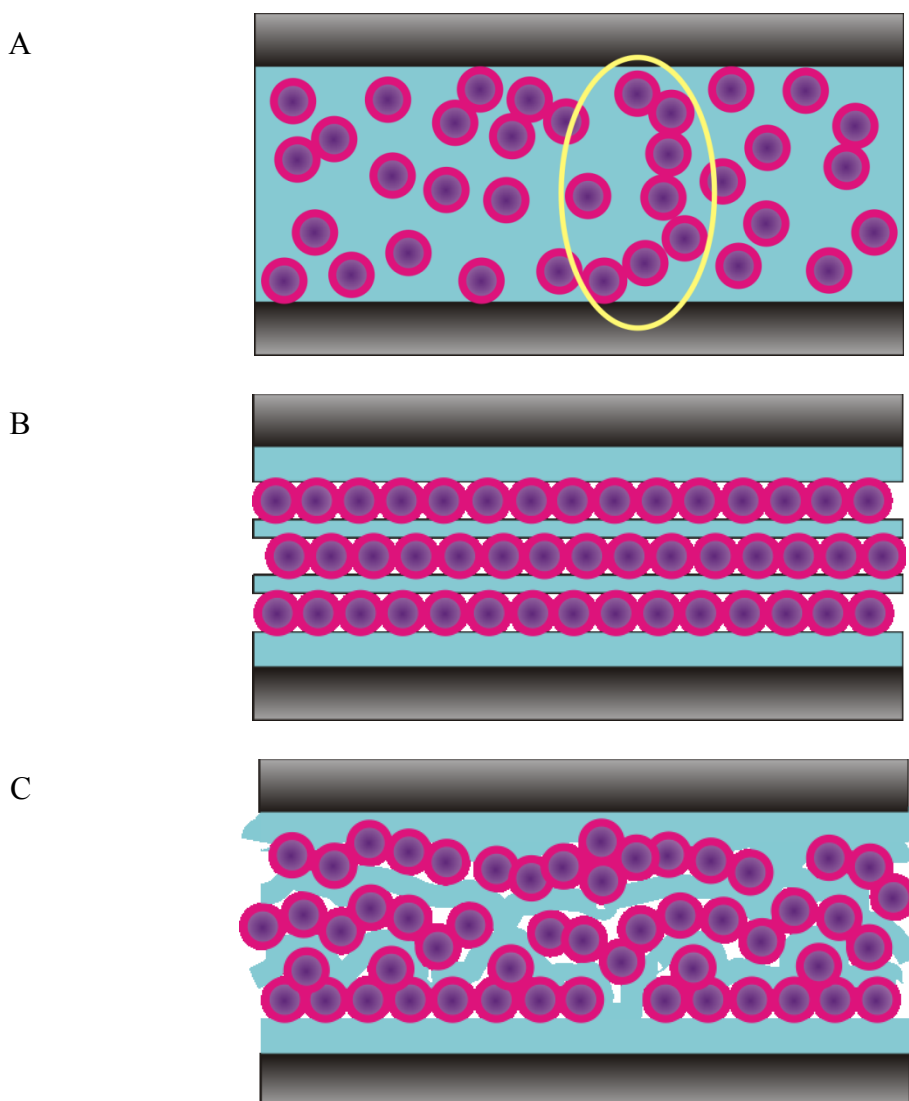


Figure 6-8. Breakdown path of percolated sample compared to the LB samples. (A) In a spin-coated sample, there was no control of where the particles were located in the sample. This means that the probability of having spots in the sample where the particles create a path of lower breakdown strength increased as the particle concentration increased. (B) In the ideal LB multilayer sample, particles and polymer made alternating rows. (C) Even in a less ideal and more realistic sample, there is still little chance for particles to create a path from one electrode through the sample to the other. Since the film is flexible, it can conform to irregularities in the particle layers. By capping each layer with a thin layer of particles, a much higher particle concentration can be created than with spin-coating.

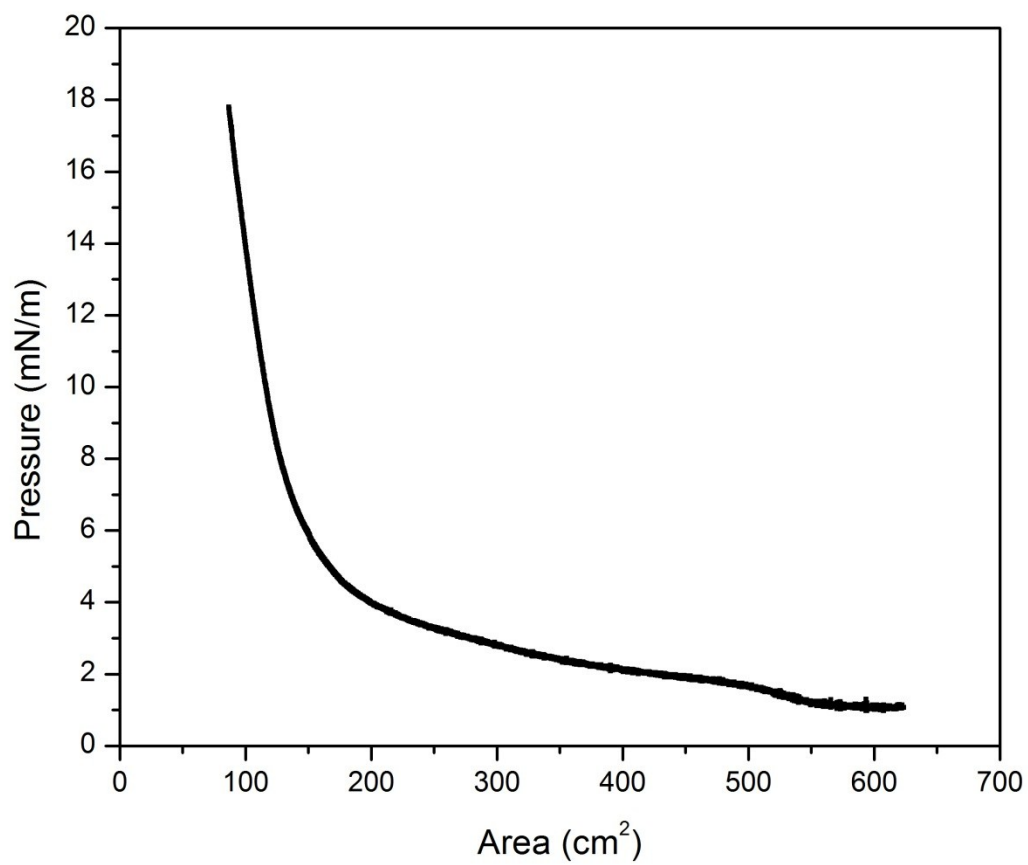


Figure 6-9. Pressure area isotherm for a pure terpolymer film showing no evidence of collapse up to 18 mN/m.

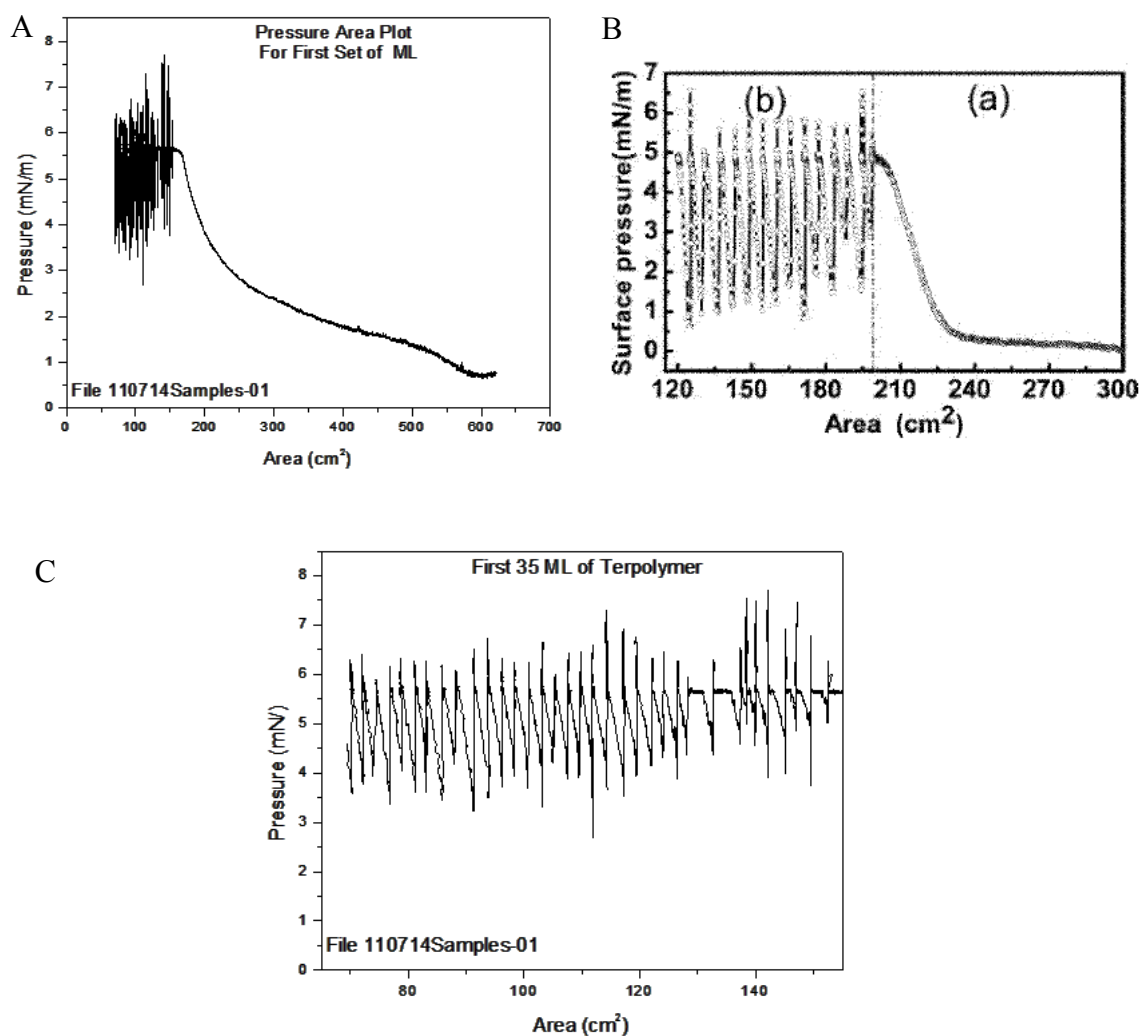


Figure 6-10. Deposition of terpolymer films at 5 mN/m using 0.01% by weight terpolymer in DMF. (A) Typical PA curve on our trough. (B) PA curve from Wang's Paper.[11] (Taken from *Wang, J.L., et al., Ferroelectrics, 2010. 405(120-125)* with permission.) (C) The first 35 ML's transferred onto 8 substrates from our trough. For each sample, the first 5 ML were typically wetter than the later layers. The sample coverage was about 49% on average for all layers transferred.

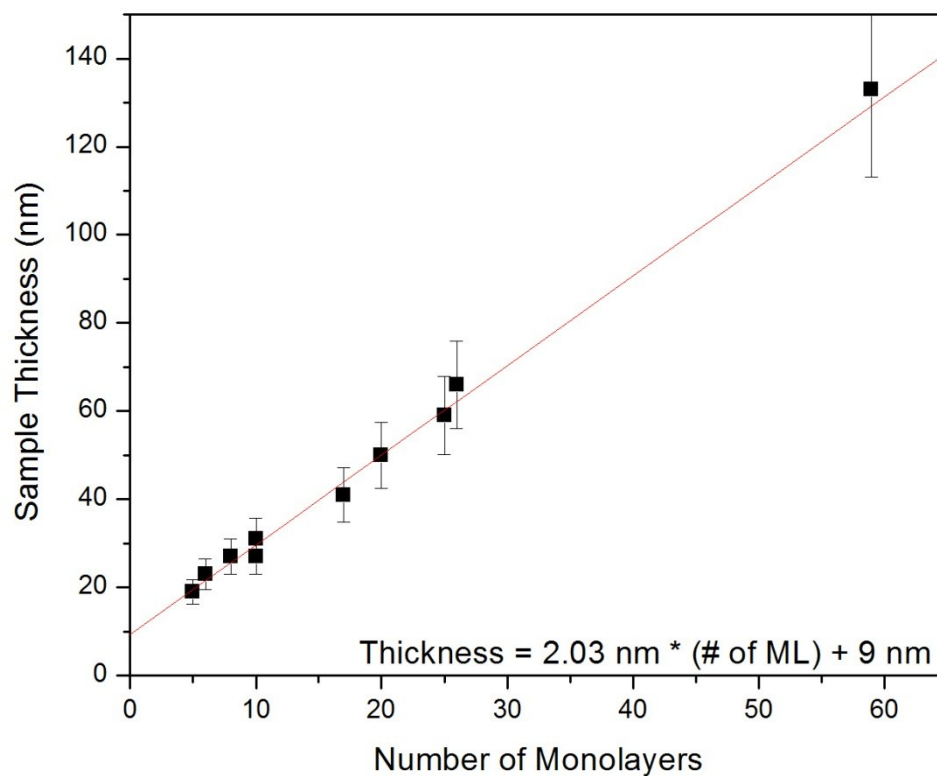


Figure 6-11. Thickness of the terpolymer Langmuir-Blodgett films deposited at 5 mN/m. The uncertainty in the thickness came from the uncertainty in the index of refraction in the fittings of the data from ellipsometry.

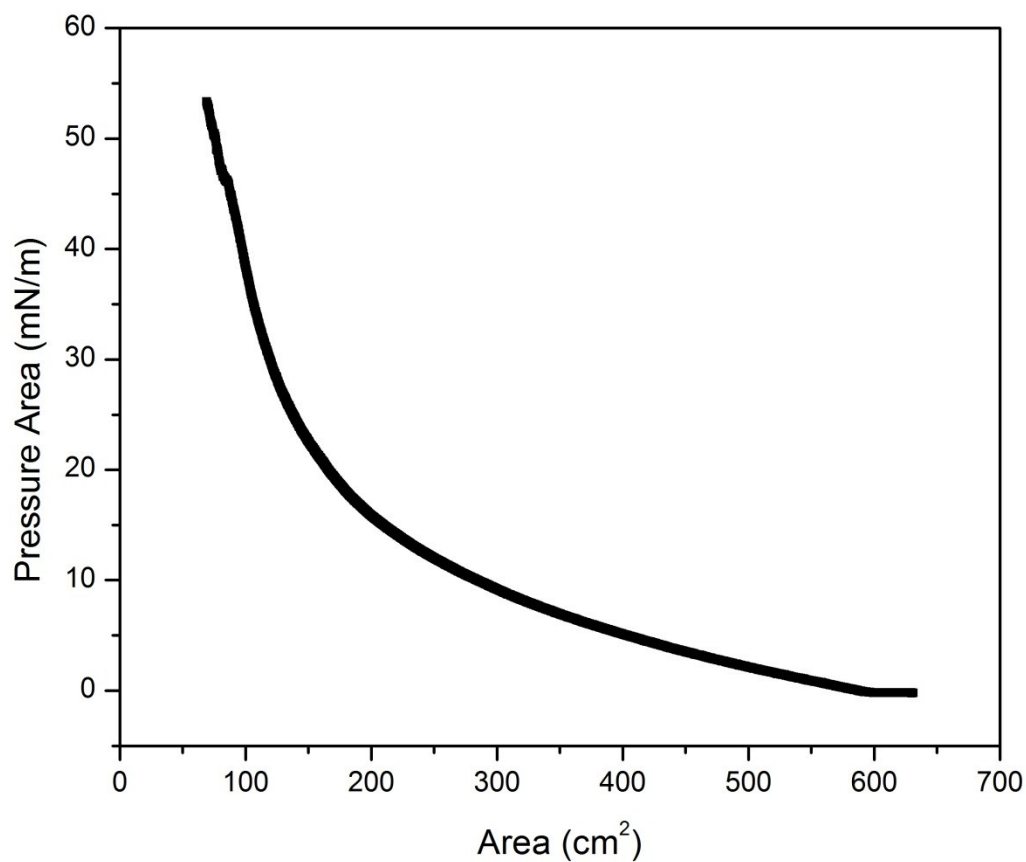


Figure 6-12. Pressure area curve for ODPa-coated BTO nanoparticles. The particles were compressed to the minimum area on the trough without any sign of major buckling or collapse, although minor collapse may have occurred at the slope change around 46 mN/m.

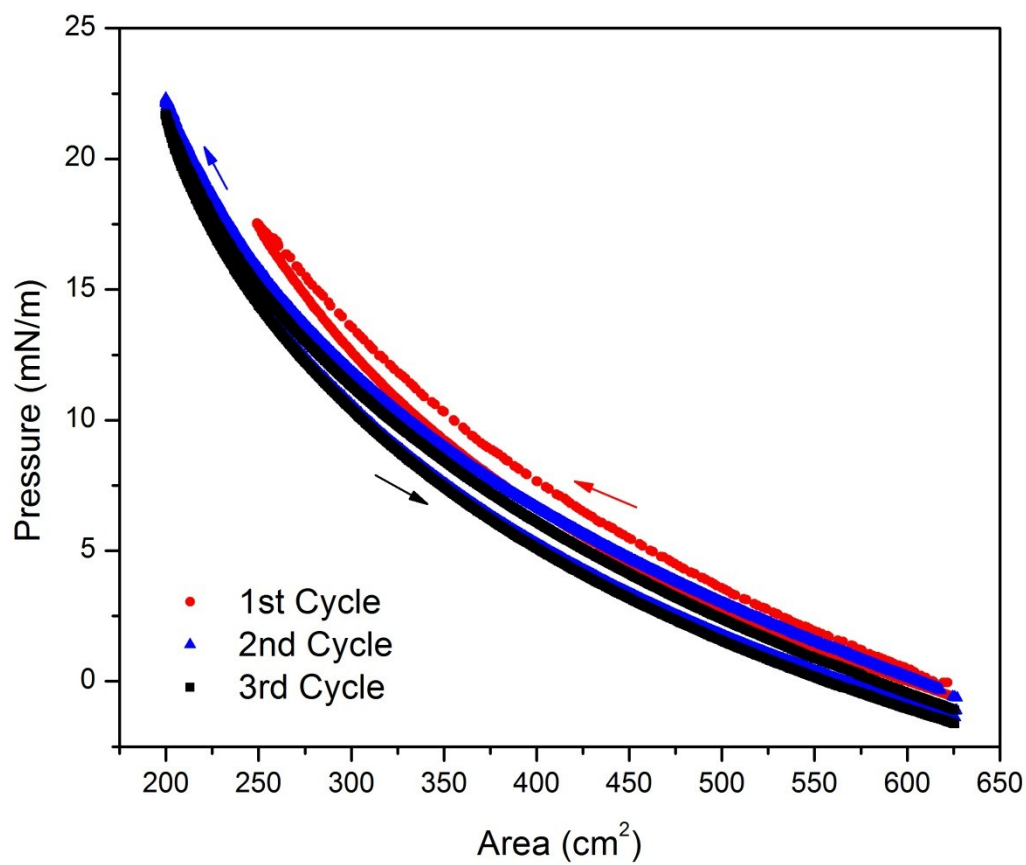


Figure 6-13. Three isotherm cycles for ODPA coated BTO nanoparticles. The particles behavior on the trough was nearly reversible up to pressures as high as 22 mN/m.

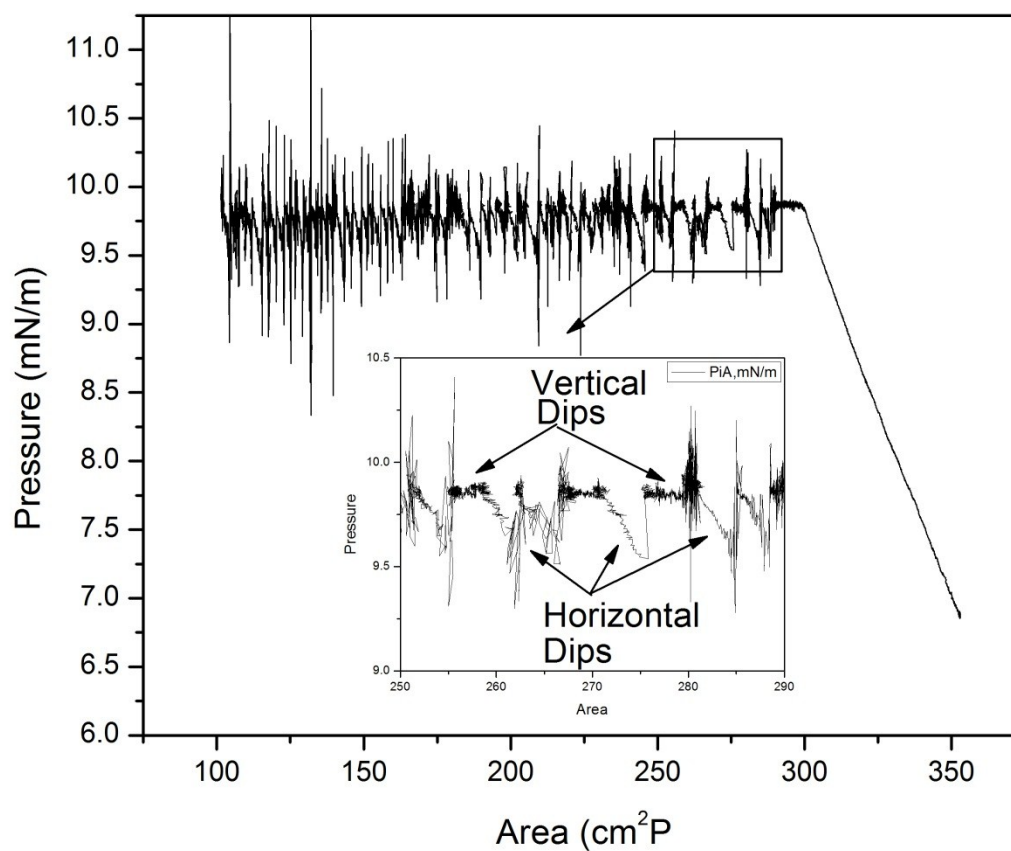


Figure 6-14. Deposition of ODPA coated BTO nanoparticle Langmuir-Blodgett layers onto substrates. The early cycles had a larger loss of area than the later cycles did. The inset shows the first few deposition cycles. The layers deposited with the horizontal method show a larger area loss per deposition than the cycles made with the vertical z-type deposition technique.

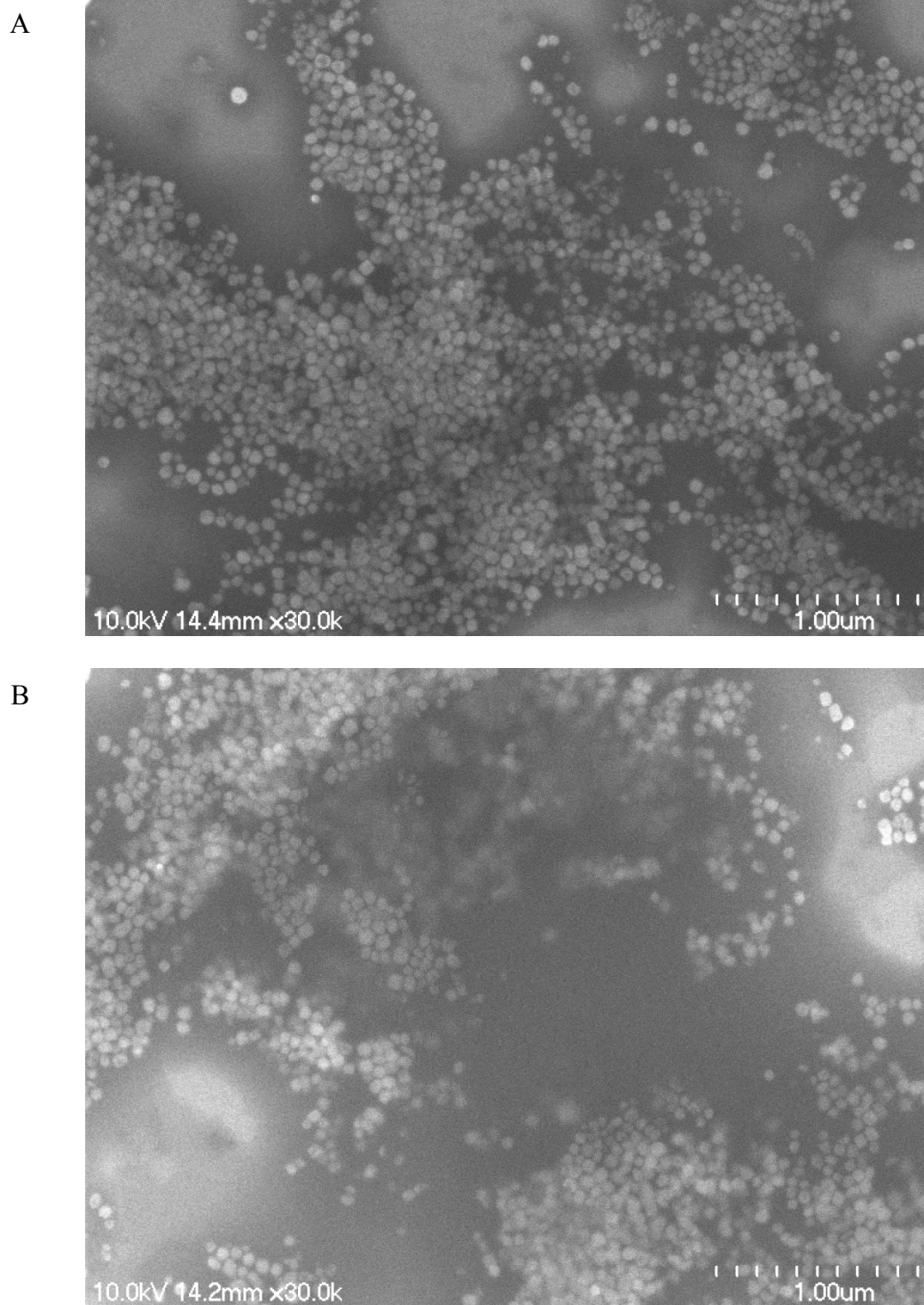


Figure 6-15. (A) Five monolayer of ODPA coated BTO nanoparticles deposited onto a silicon substrate using the Schaefer method of deposition at 7 mN/m. (B) Five bilayers of ODPA coated BTO nanoparticles deposited onto a silicon substrate using the Z-type deposition at 7 mN/m.

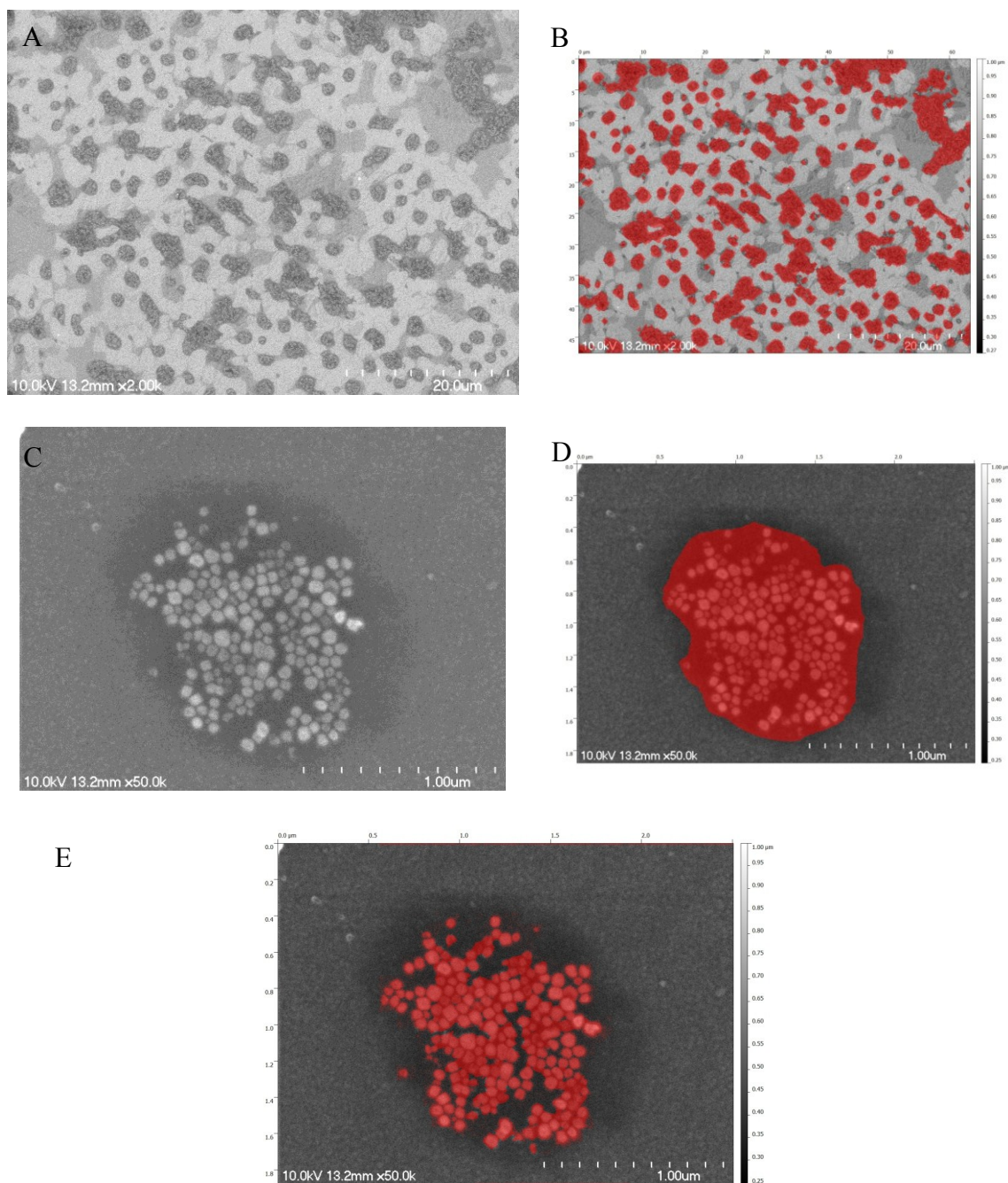


Figure 6-16. Particle coverage calculations for a sample deposited at 10 mN/m. (A) Low magnification image of sample. (B) The particles were masked off using the software Gyddion. The total area and masked area was measured. (C) The high magnification image of a typical cluster of particles. (D) The area of the cluster and (E) the area of the particles were measured using the masking procedure.

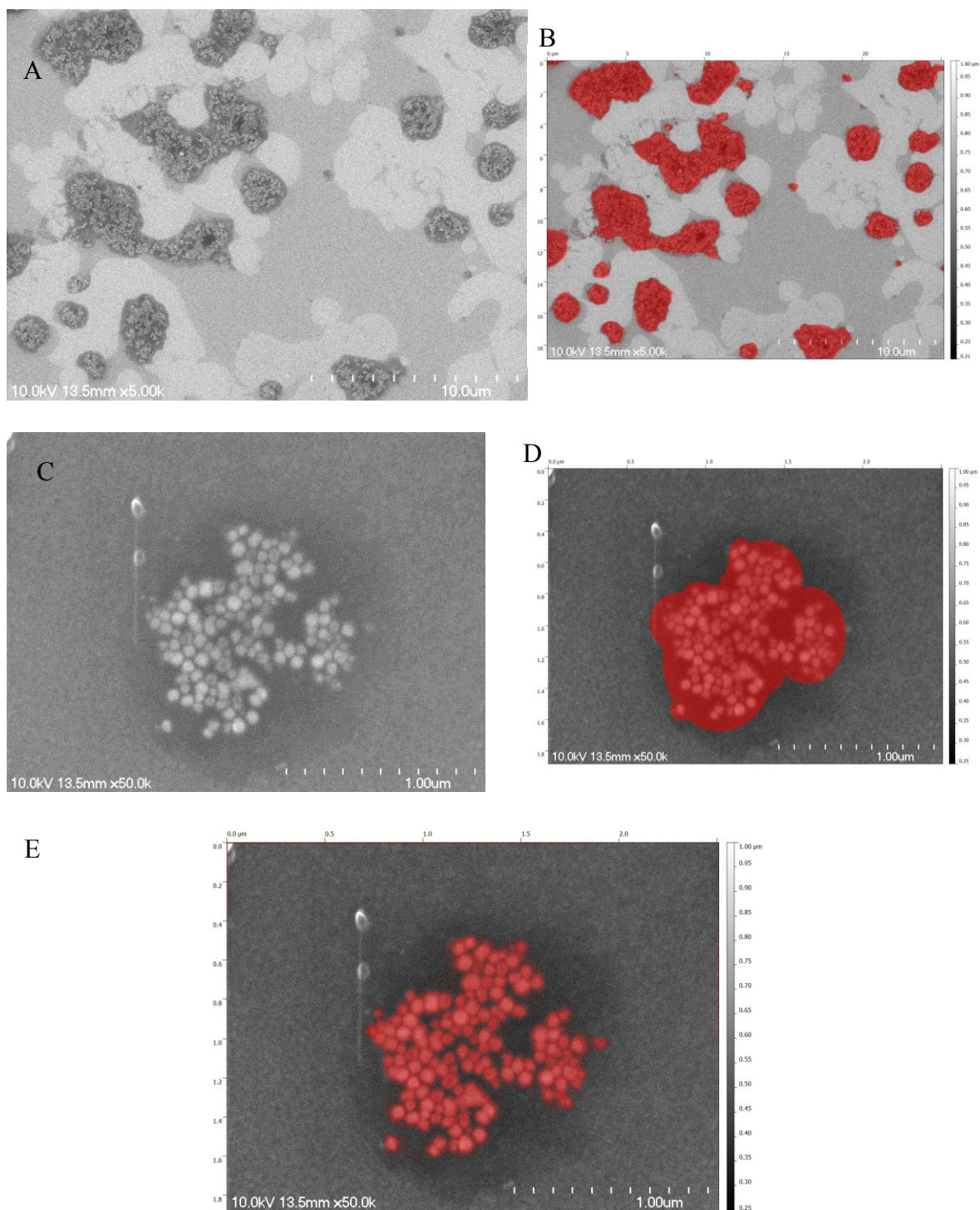


Figure 6-17. Particle coverage calculations for a sample deposited at 7 mN/m. (A) A low magnification image of sample showing clusters of particles. (B) The particle areas were masked off and measured using the software Gyddion. (C) A high magnification image of a typical cluster of particles. (D) The area of the cluster and (E) the area of the particles of particles within a cluster were measured using the software.

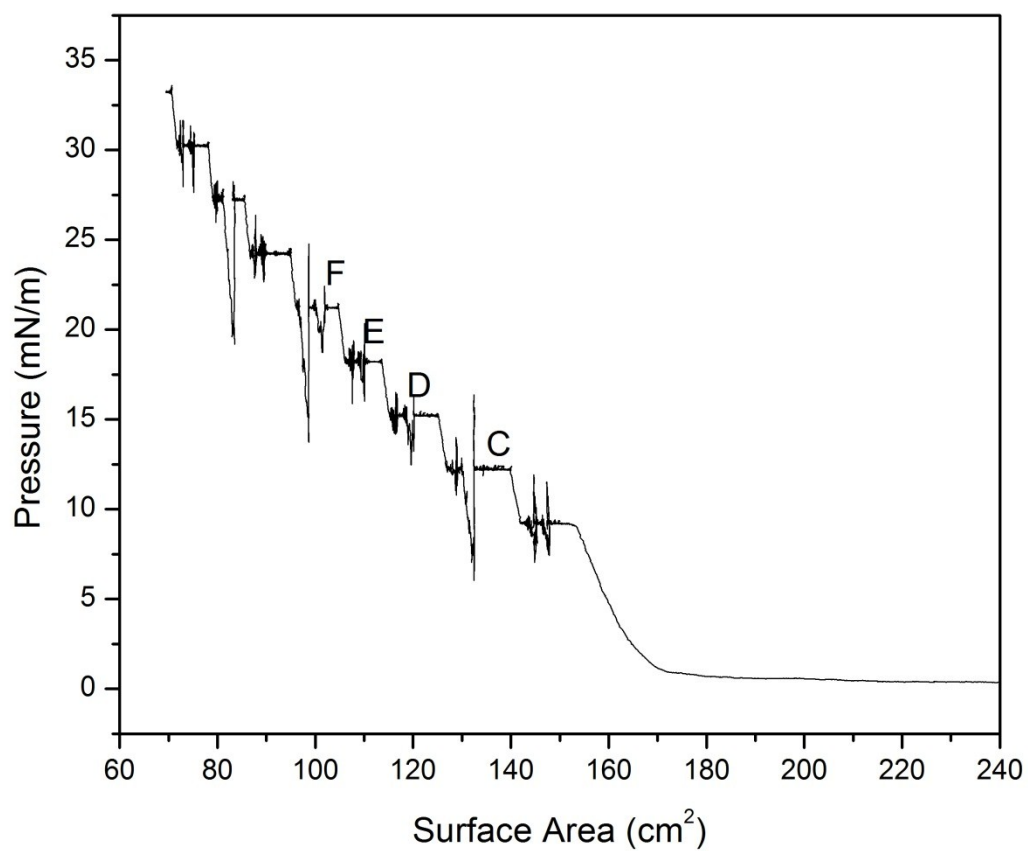


Figure 6-18. Pressure-Area Isotherm for ODPa coated BTO nanoparticles. Samples were made at each of the deposition points. SEM images of the samples are shown in Figure 6-19 and Figure 6-20.

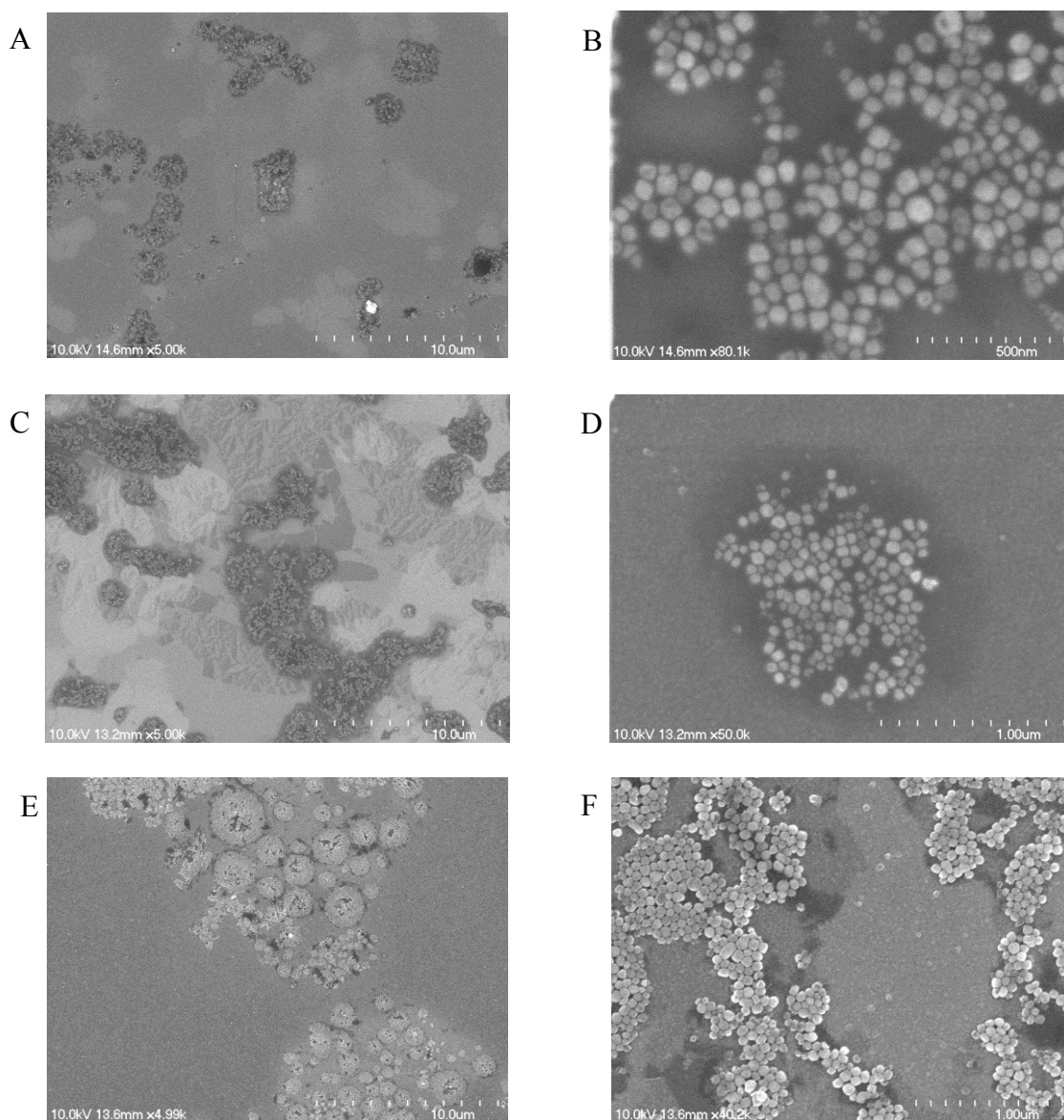


Figure 6-19. (A) Low magnification image of sample deposited at 7 mN/m. (B) High magnification image of sample deposited at 7 mN/m. (C) Low magnification image of sample deposited at 10 mN/m. (D) High magnification image deposited at 10 mN/m. (E) Low magnification image deposited at 12 mN/m. (F) High magnification image deposited at 12 mN/m.

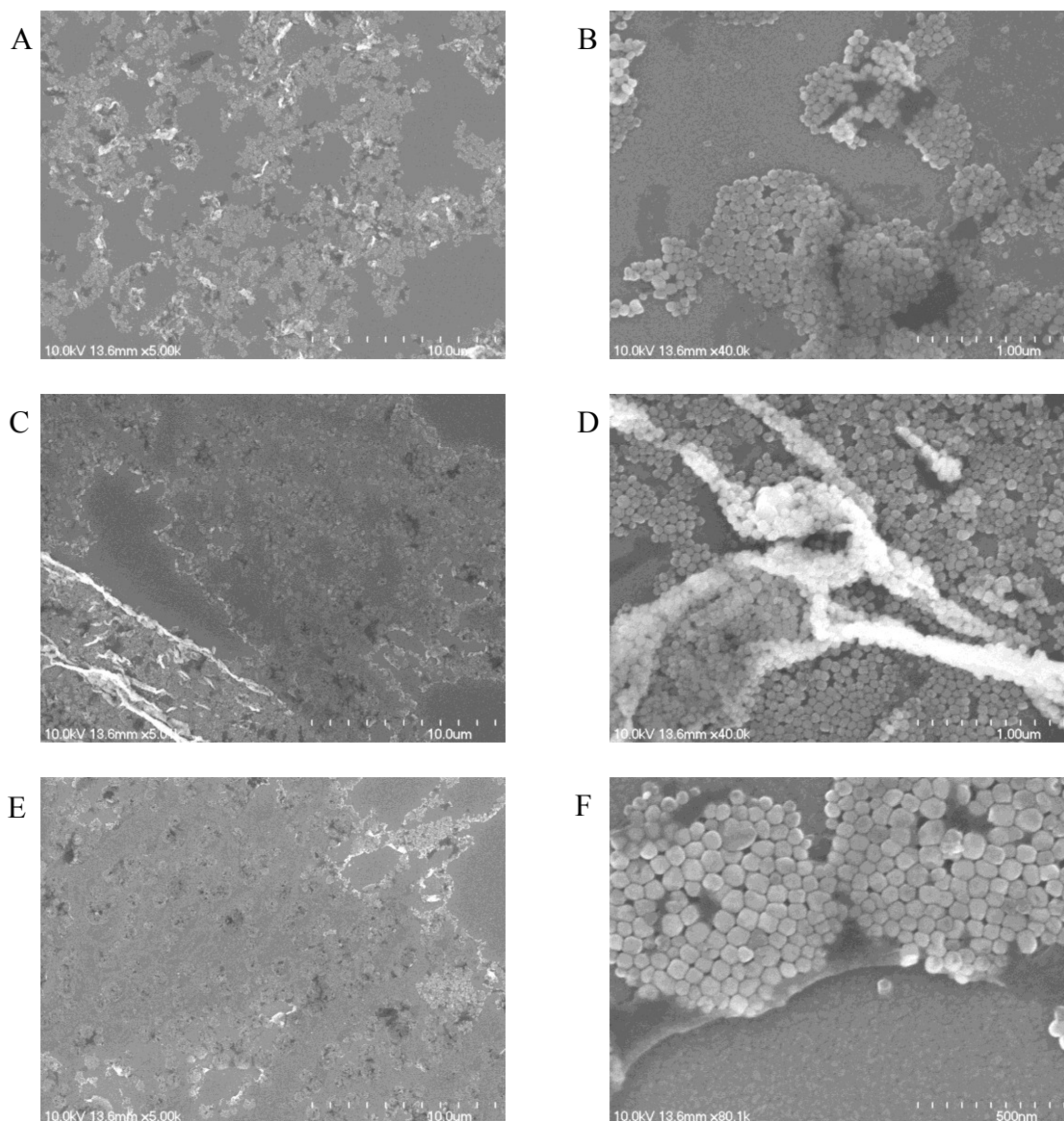


Figure 6-20. (A) Low magnification image of a sample deposited at 15 mN/m. (B) High magnification image of a sample deposited at 15 mN/m. (C) Low magnification image of a sample deposited at 18 mN/m. (D) High magnification image of a sample deposited at 18 mN/m. (E) Low magnification image of a sample deposited at 21 mN/m. (F) High magnification image of a sample deposited at 21 mN/m.

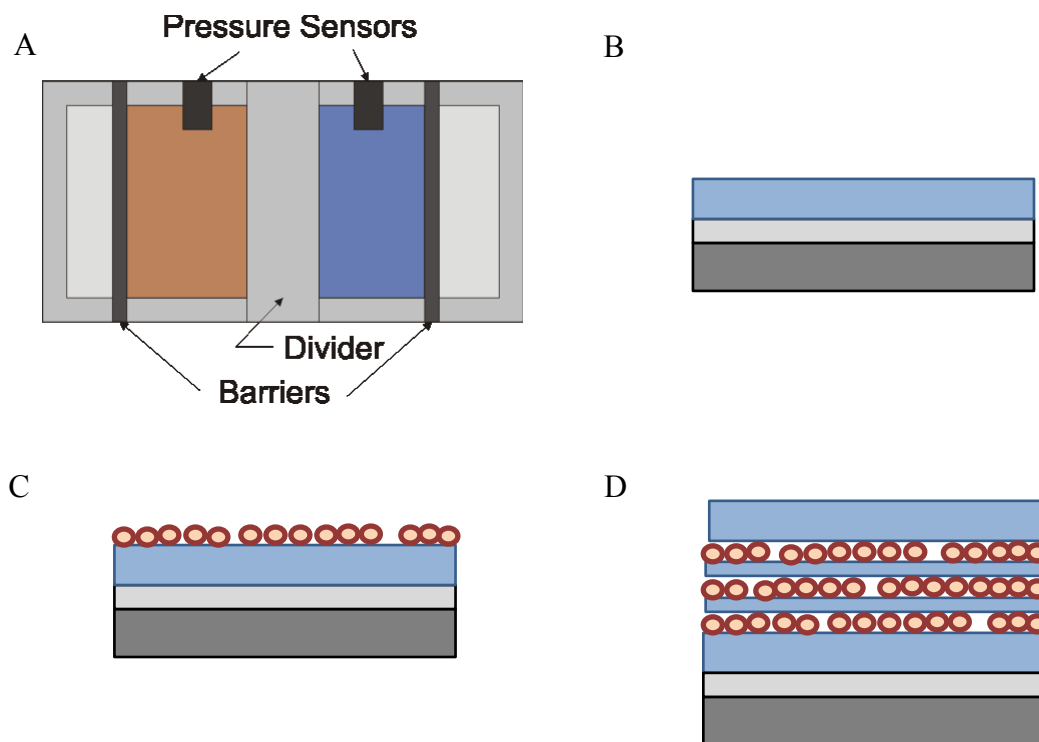


Figure 6-21. (A) Multilayer samples were made by dividing the trough into two parts. Each side of the trough had its own movable barrier and a surface pressure sensor. This allowed for deposition of two materials. (B) Multilayer capacitor samples started with 5 to 20 ML of polymer on a glass or silicon substrate with aluminum electrodes. (C) Particle Langmuir-Blodgett layers were deposited onto the initial polymer layers. (D) The sample was built up alternating layers of polymer and particles until the desired composition was constructed.

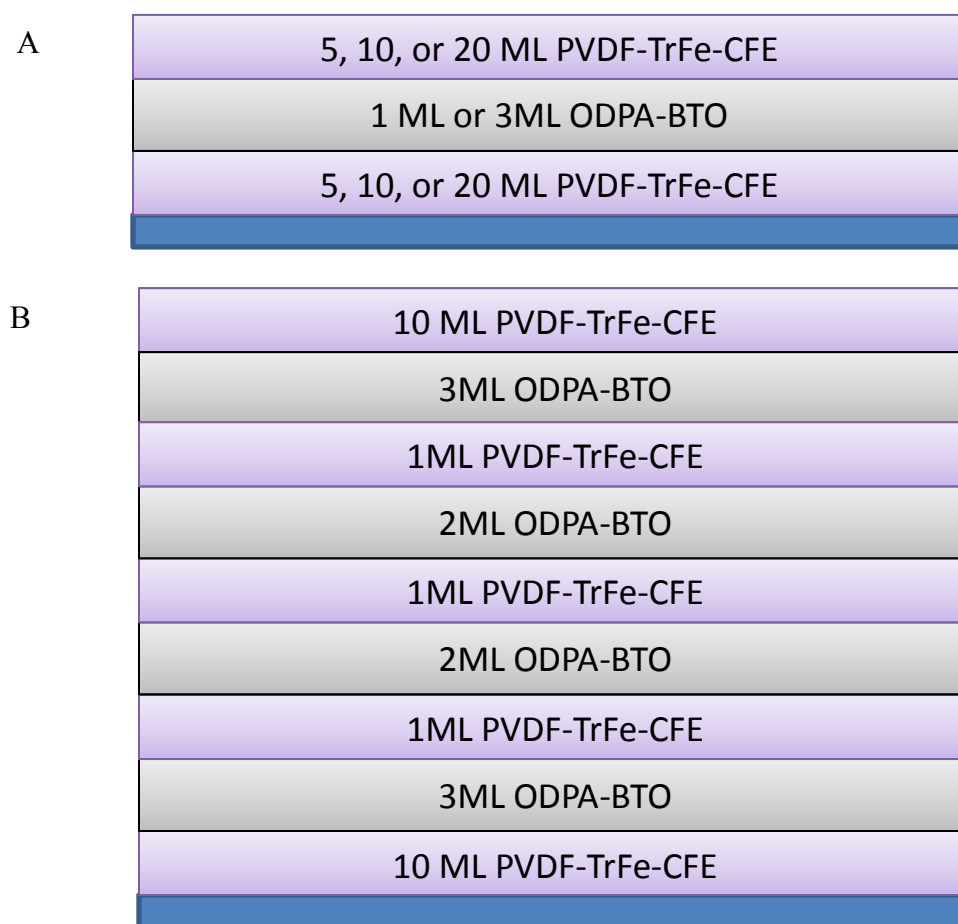


Figure 6-22. Samples were constructed by building multilayers of particles. Each ML of terpolymer was on average 2 nm thick. The nanoparticles had an average diameter of 65 nm, and 19% coverage for deposition at 10 mN/m. (A) The most common sample composition was 5, 10, or 20 ML of terpolymer, and then a few layers of particles, capped with another polymer layer. (B) More complex samples were made by making many layers of polymer and particles. This allowed for a higher volume concentration of particles.

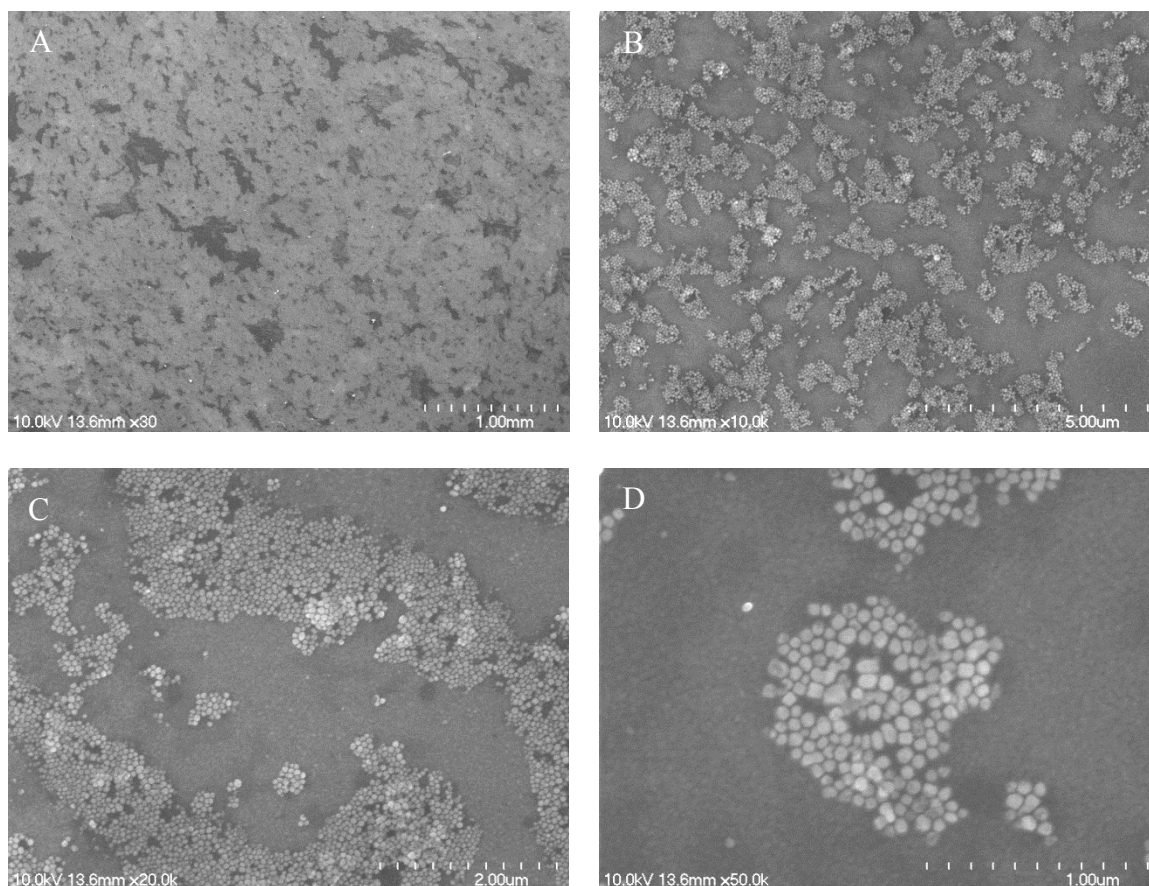


Figure 6-23. FESEM images of 1 ML of ODPA coated BTO on terpolymer films. (A) The particles had good adhesion over large sections of the film. While there are voids in the low magnification film, most of the sample was covered with particles. (B) At 10k magnification, there was some space between clusters of particles. (C) Most of the particles were in a single layer. Some particles were stacked on neighbors. (D) The high magnification 50k image showed that the particles were starting to pack together.

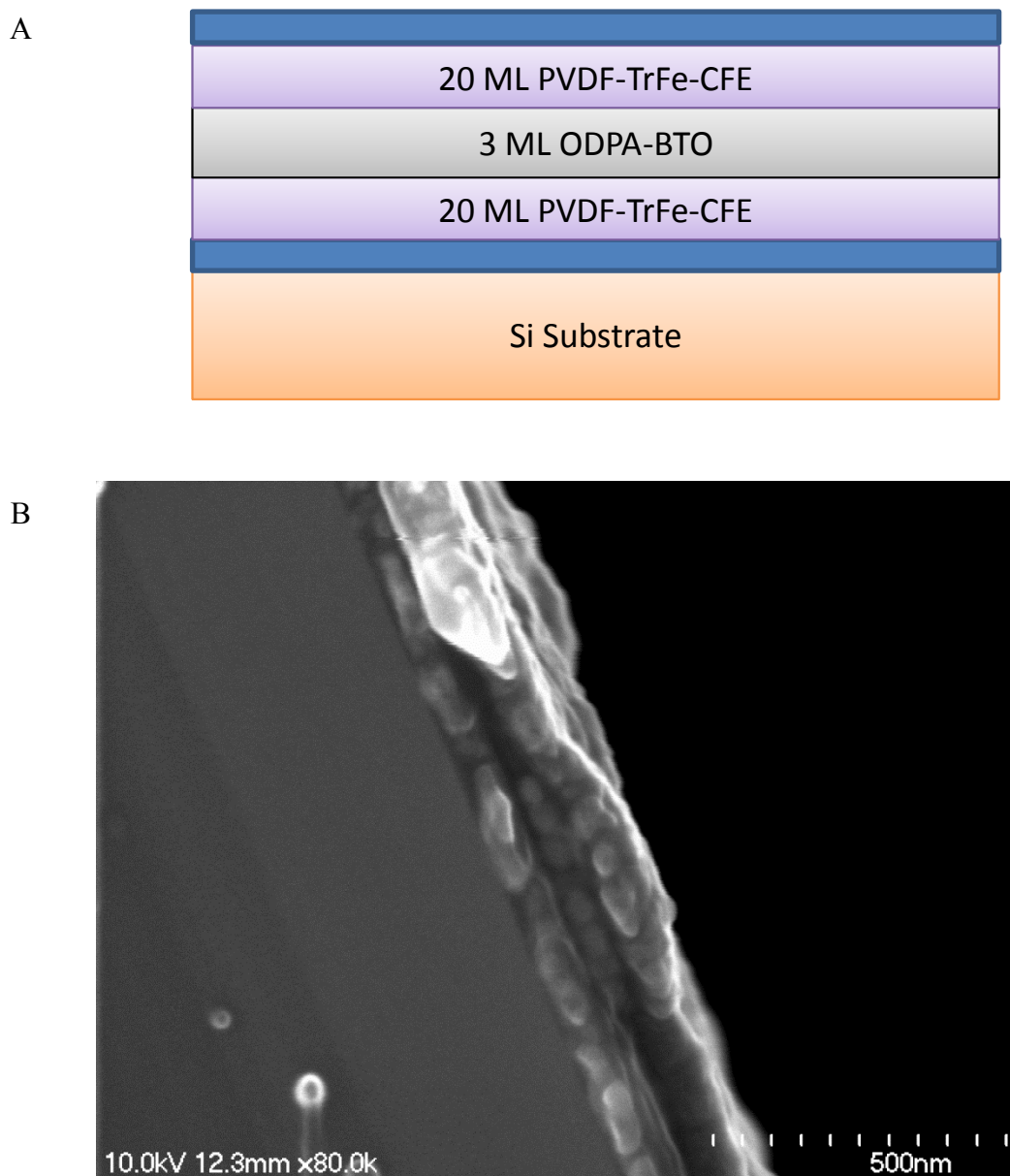


Figure 6-24. (A) Sketch of the multilayer sample used for cross sectional imaging. The sample consisted of a silicon substrate, aluminum bottom electrode, 20 ML of terpolymer, 3 ML of ODPA coated BTO, 20 ML of terpolymer, and aluminum top electrode. (B) FESEM image of the cross section of a composite sample. The polymer layers were not clearly visible and the sample contracted upon initial contact with the beam, signifying damage from the electron beam to the polymer.

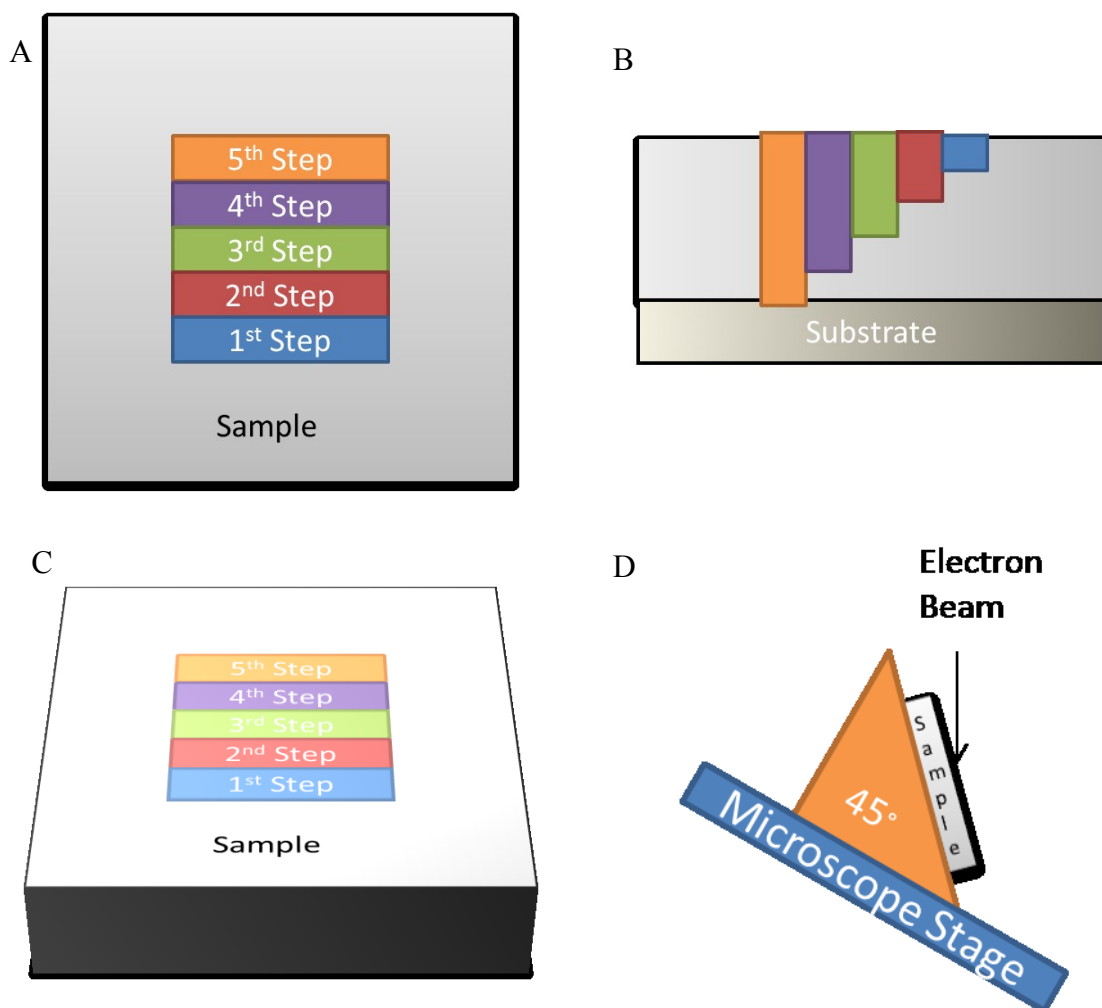


Figure 6-25. Sketches of the pattern milled by the FIB. (A) Each step was milled  $60\text{ }\mu\text{m}$  deeper than the previous step. (B) A cross section of the steps being milled into the sample. (C) The sample was rotated so the flat edge of the sample could be viewed. (D) The sample was mounted on a triangle wedge, and then the sample stage was rotated, so the surface to be imaged made a  $75^\circ$  angle with the electron beam.

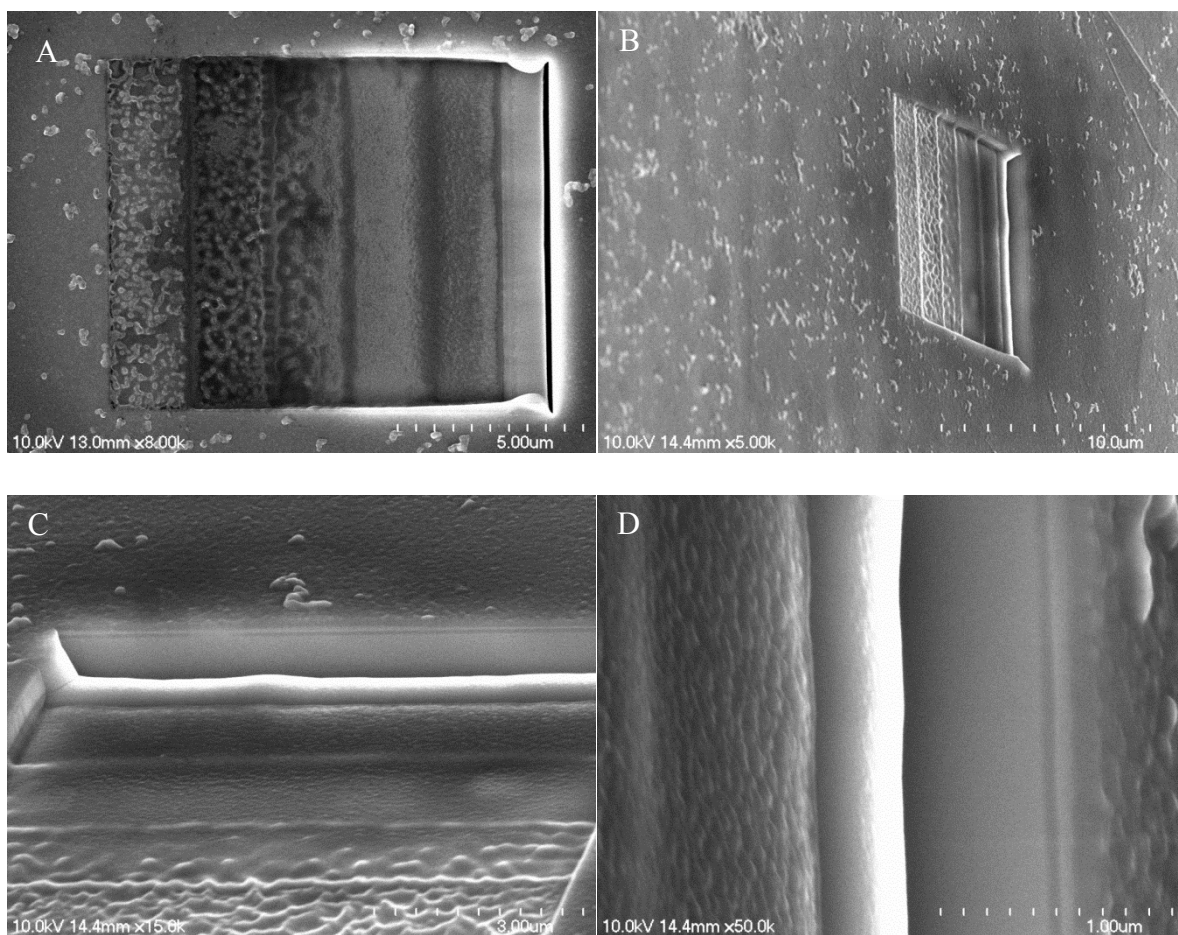


Figure 6-26. FESEM images of cross section composite sample milled using a FIB. (A) Horizontal view of the sample showing the steps cut into the sample. (B) Low magnification image of the sample tilted at 75°. (C) Medium magnification image showing the layers of the film. (D) High magnification image with no evidence that nanoparticles were present.

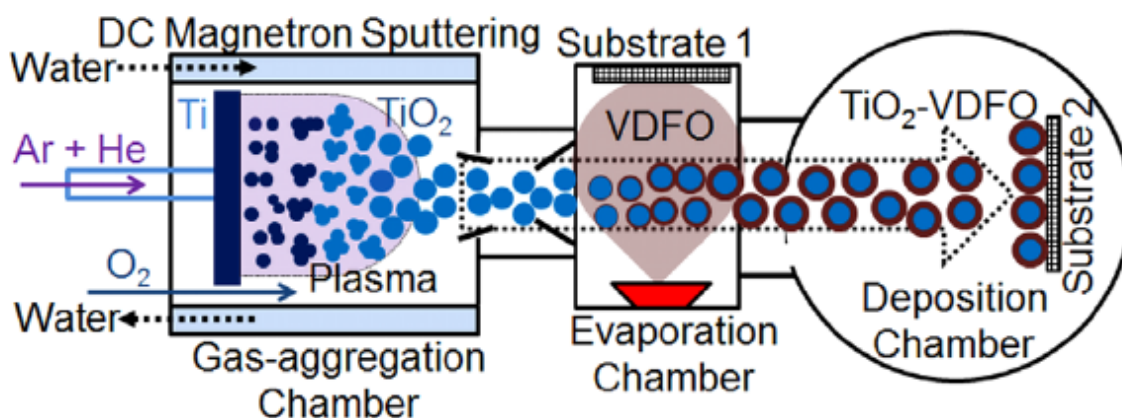


Figure 6-27. Schematic of plasma condensation chamber. By sputtering on a titanium target in a mixed atmosphere of oxygen and inert gases, nanoparticles were created. The particles then passed into the evaporation chamber where they were coated with an organic shell. Finally, the particles entered the deposition chamber where they were deposited onto a substrate. [7] (Taken from Balasubramanian, B., et al., *Nanotechnology*, 2011. 22 (405605) with permission.)

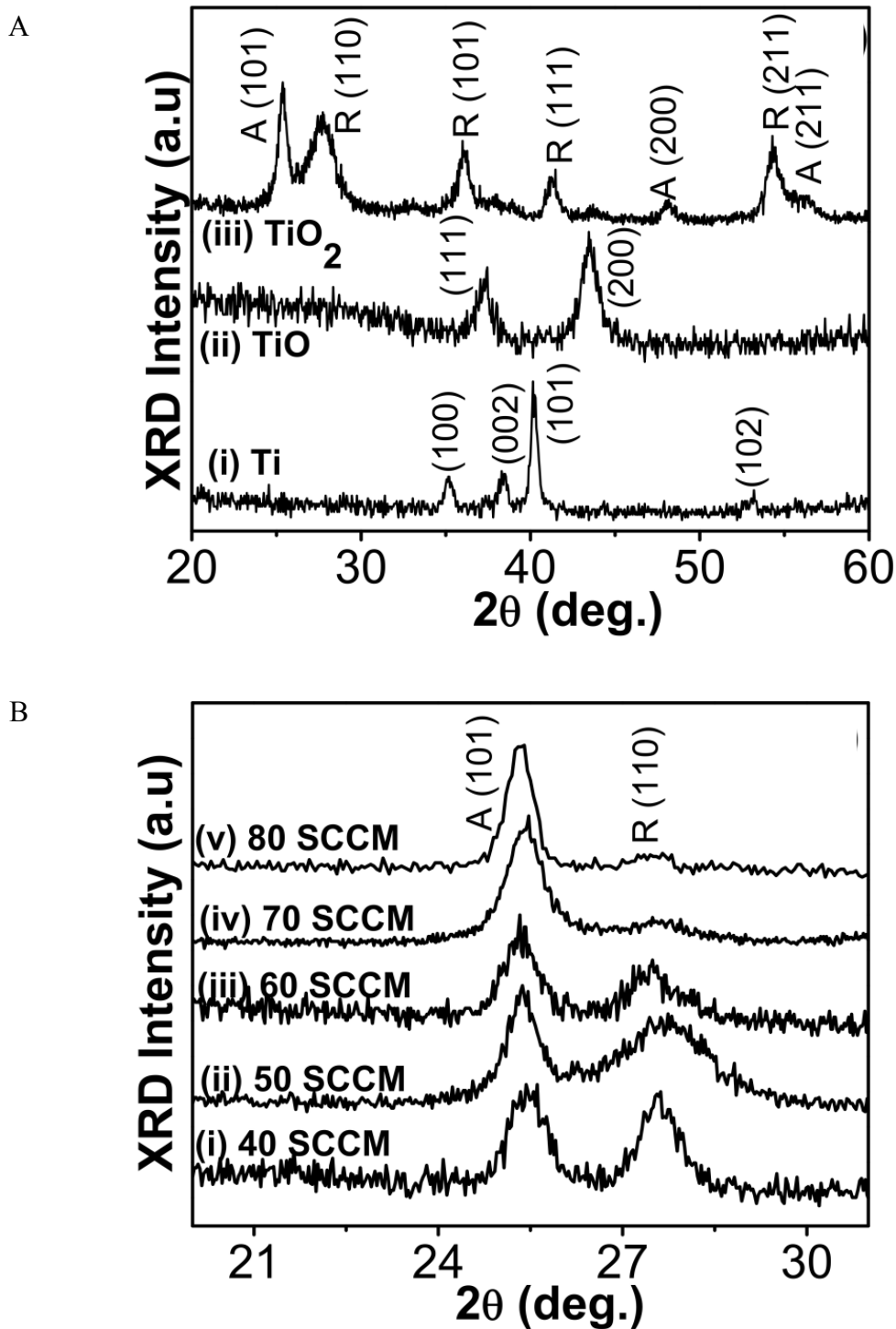


Figure 6-28. XRD results of uncoated Titanium oxide nanoparticles. (a) As the oxygen flow rate increased, the particles changed from Ti (curve i) to TiO (curve ii) to  $\text{TiO}_2$  (curve iii). (b) As the oxygen content increased, the nanoparticles went from a mixed rutile and anatase phase to a nearly pure anatase state [6]. (Taken from Balasubramanian, B., et al., *ACS Nano*, 2010. 4 (1893) with permission.)

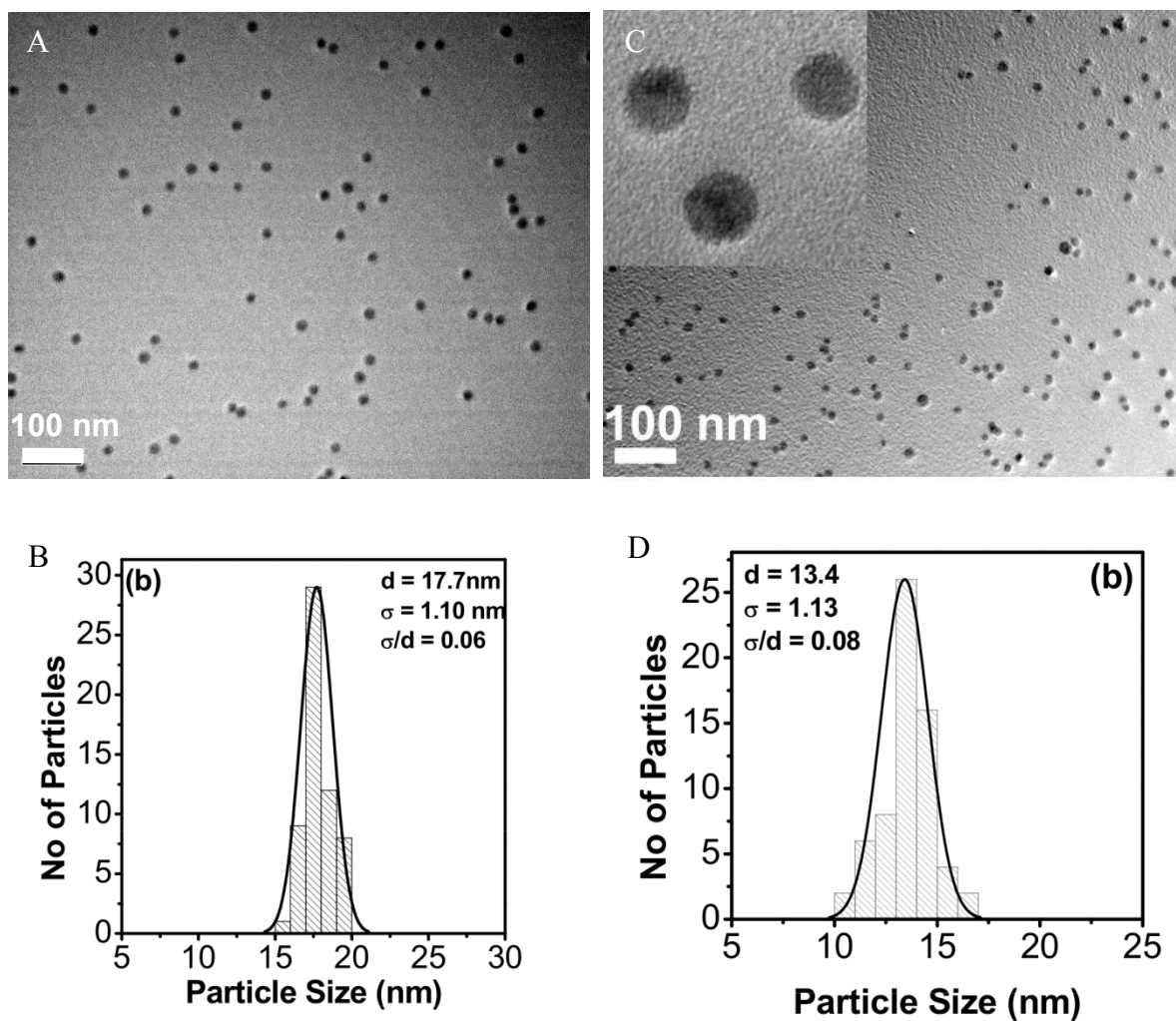
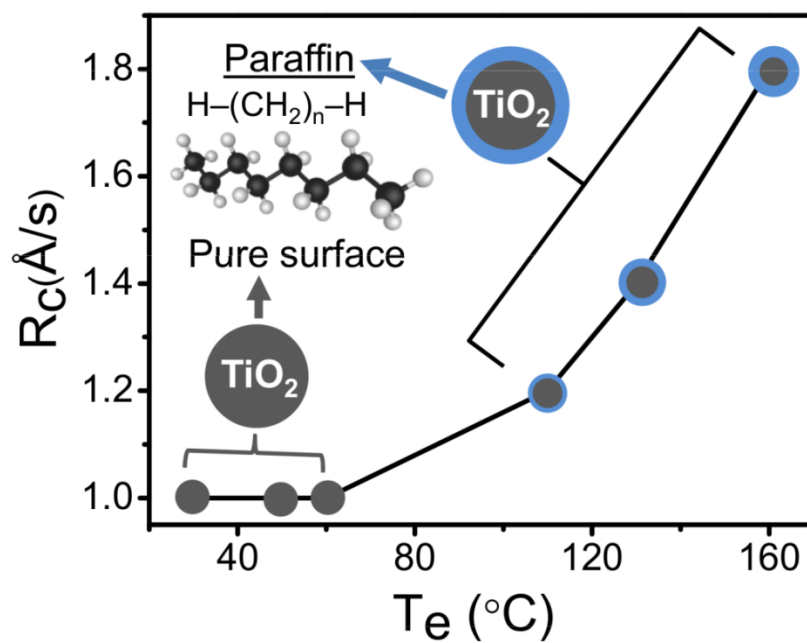


Figure 6-29. (A) TEM image of TiO nanoparticles (B) The particle size distribution histogram. The average particle size,  $d$ , is 17.7 nm with a standard deviation,  $\sigma$ , of 1.1 nm. (C) TEM image showing well dispersed of TiO<sub>2</sub> nanoparticles. The inset shows smooth, spherical particles. (D) The average size distribution is 13 nm with a narrow distribution of sizes [6]. (Taken from Balasubramanian, B., et al., *ACS Nano*, 2010. 4 (1893) with permission.)

A



B

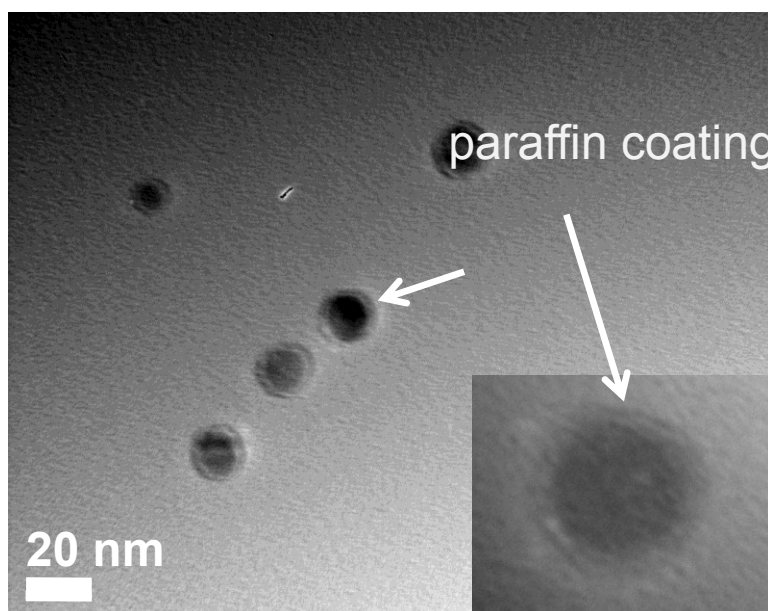
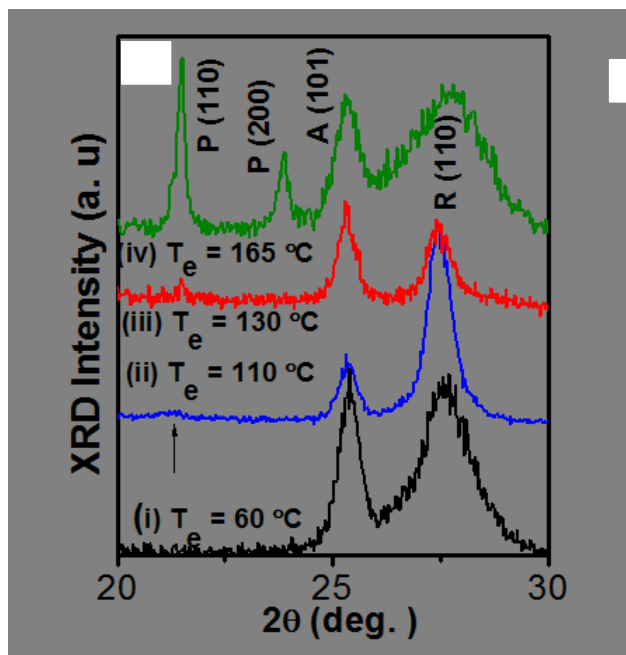


Figure 6-30. Evaporation rate organic shells (A) Coating rates for paraffin shell. (B) TEM of paraffin coated  $\text{TiO}_2$  nanoparticles. The coating is the thin ring surrounding the dark particle in the center [6]. (Taken from Balasubramanian, B., et al., *ACS Nano*, 2010. 4 (1893) with permission.)

A



B

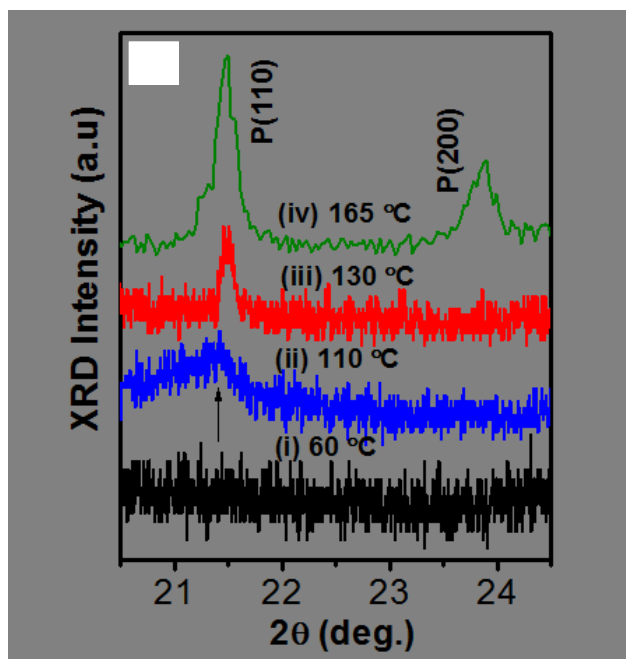


Figure 6-31. XRD of coated nanoparticles. (A) XRD results of TiO<sub>2</sub>-Paraffin coated nanoparticles prepared under different evaporation temperatures. At low temperature, there was no evidence of any paraffin coating. The paraffin peaks increased as the evaporation temperature increased. (B) A slow scan of the region where the paraffin peaks were expected. [6] (Taken from Balasubramanian, B., et al., *ACS Nano*, 2010. 4 (1893) with permission.)

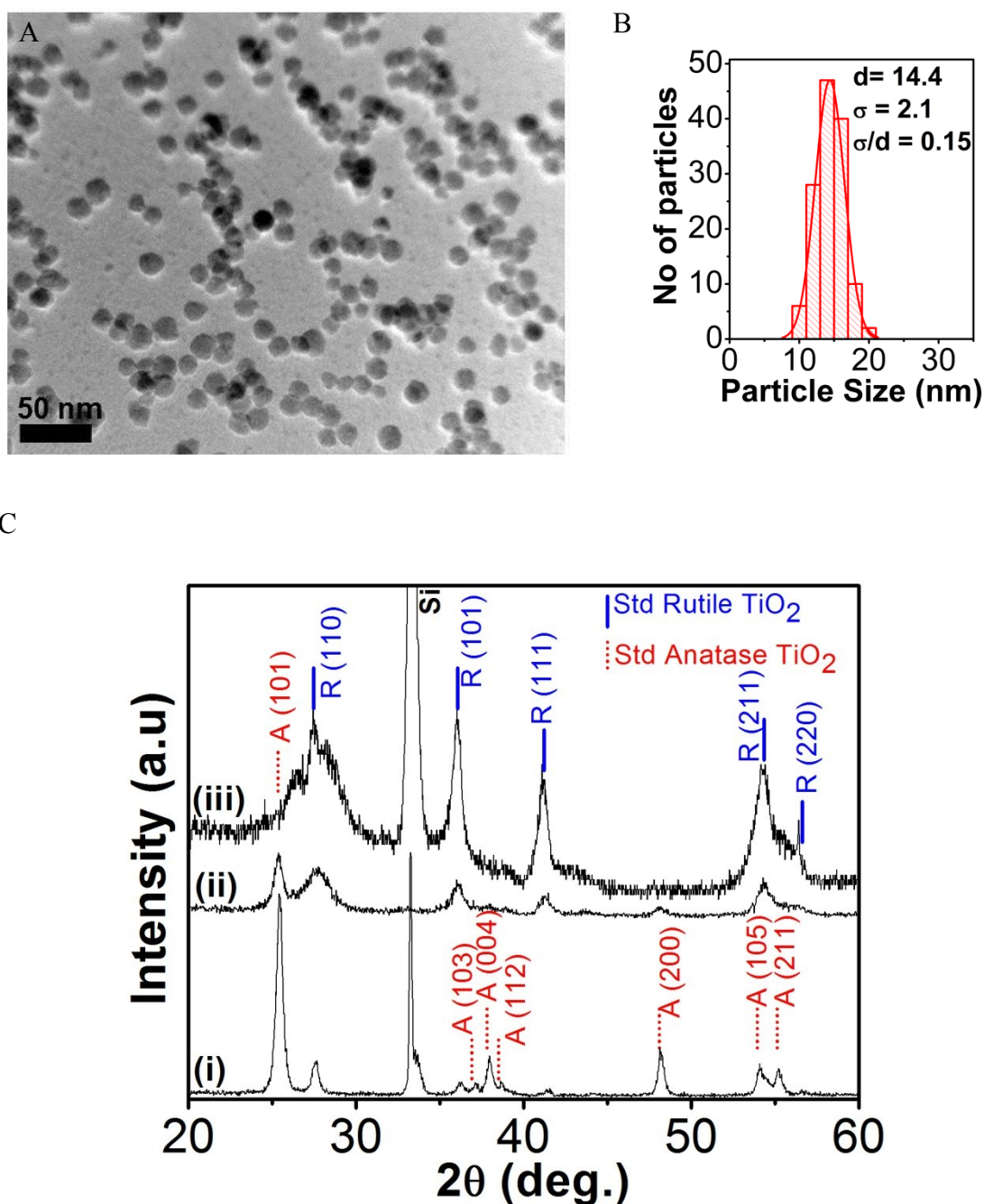


Figure 6-32. Uncoated titanium dioxide nanoparticles created with the process used for the VDFO coated particles. (A) SEM image of the uncoated particles. (B) The average particle size was 14.4 nm. (C) XRD data for particles made at different DC power. [7] (Taken from Balasubramanian, B., et al., *Nanotechnology*, 2011. 22 (405605) with permission.)

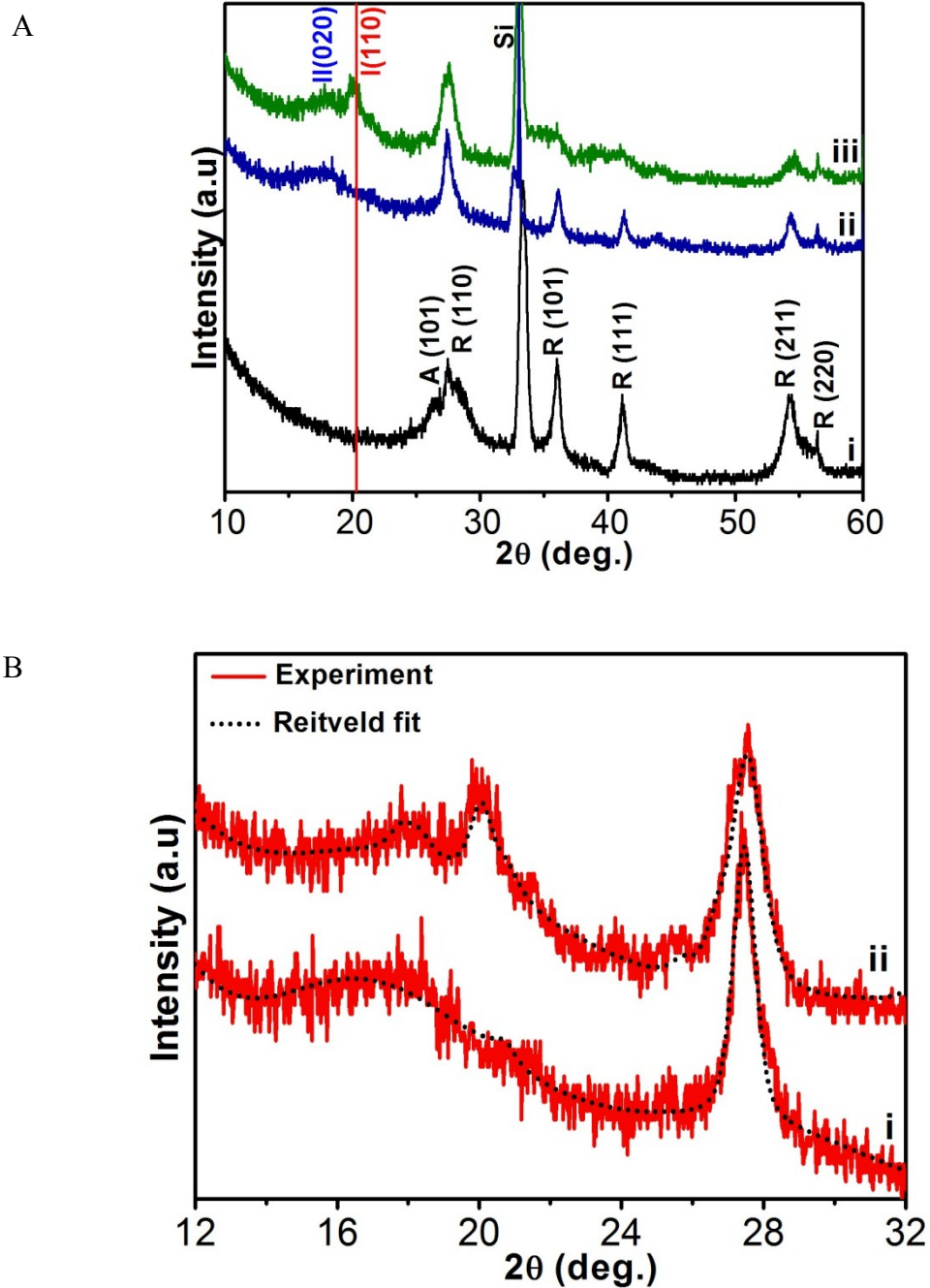


Figure 6-33. X-ray diffraction of VDFO coated titanium dioxide nanoparticle films. [7] (Taken from Balasubramanian, B., et al., *Nanotechnology*, 2011, **22** (405605) with permission.)

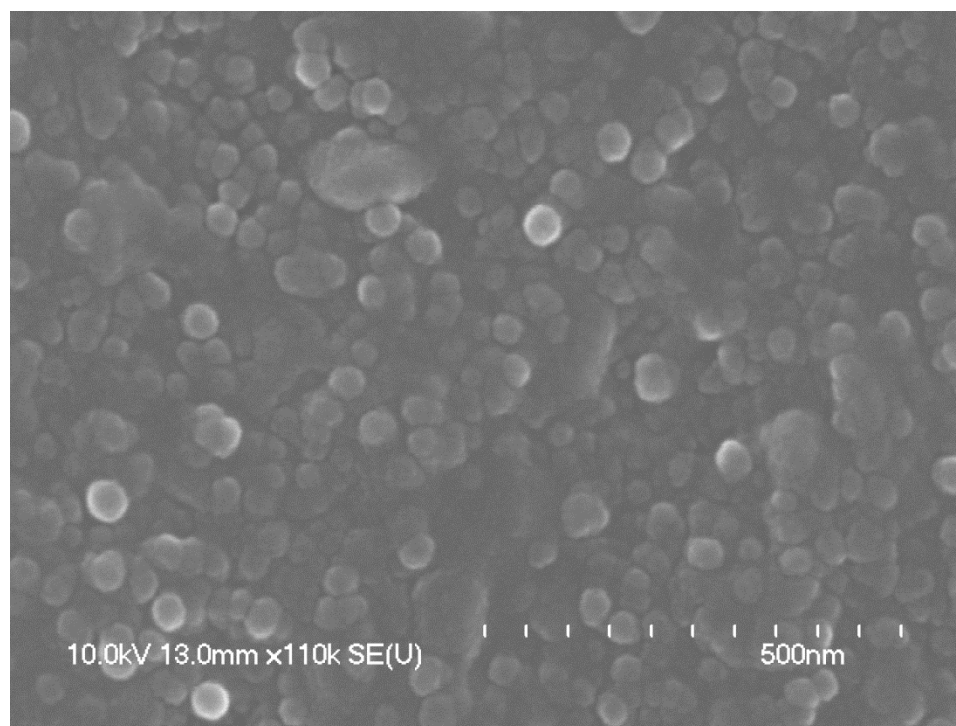


Figure 6-34. SEM image of VDFO coated Titanium Dioxide Particles.

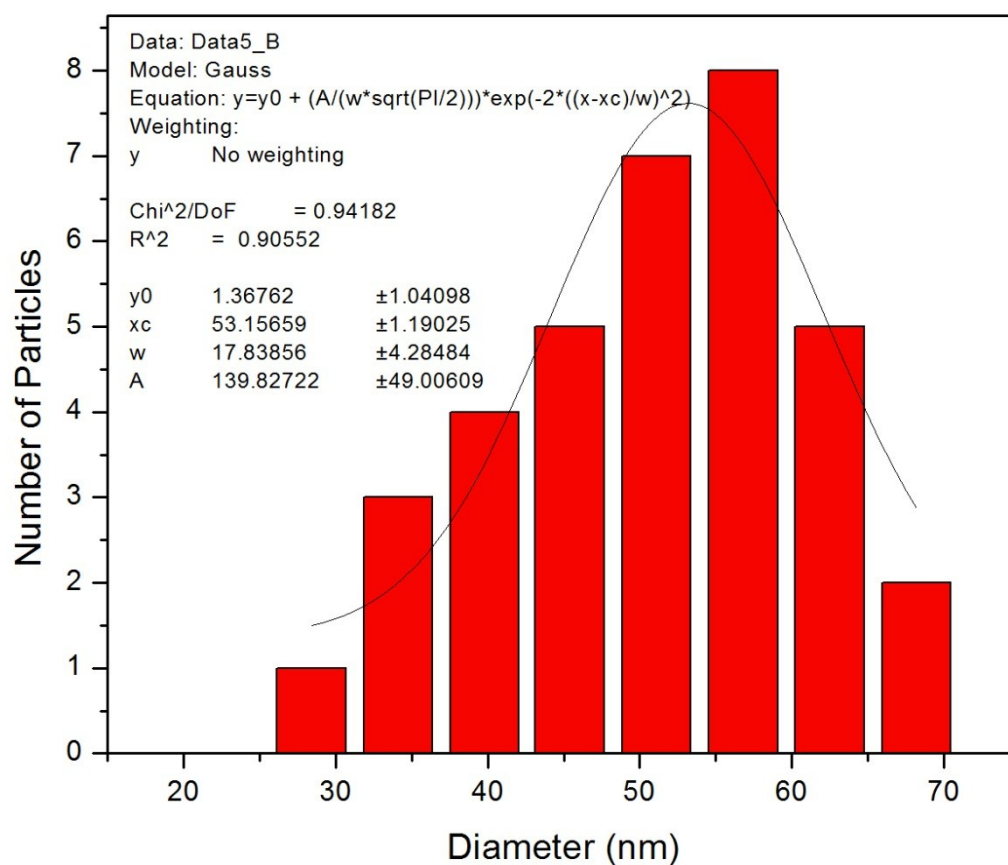


Figure 6-35. Histogram of the VDFO coated titanium dioxide nanoparticles measured from Figure 6-34. The particles had an average width of 53 nm, and the half width was 18 nm.

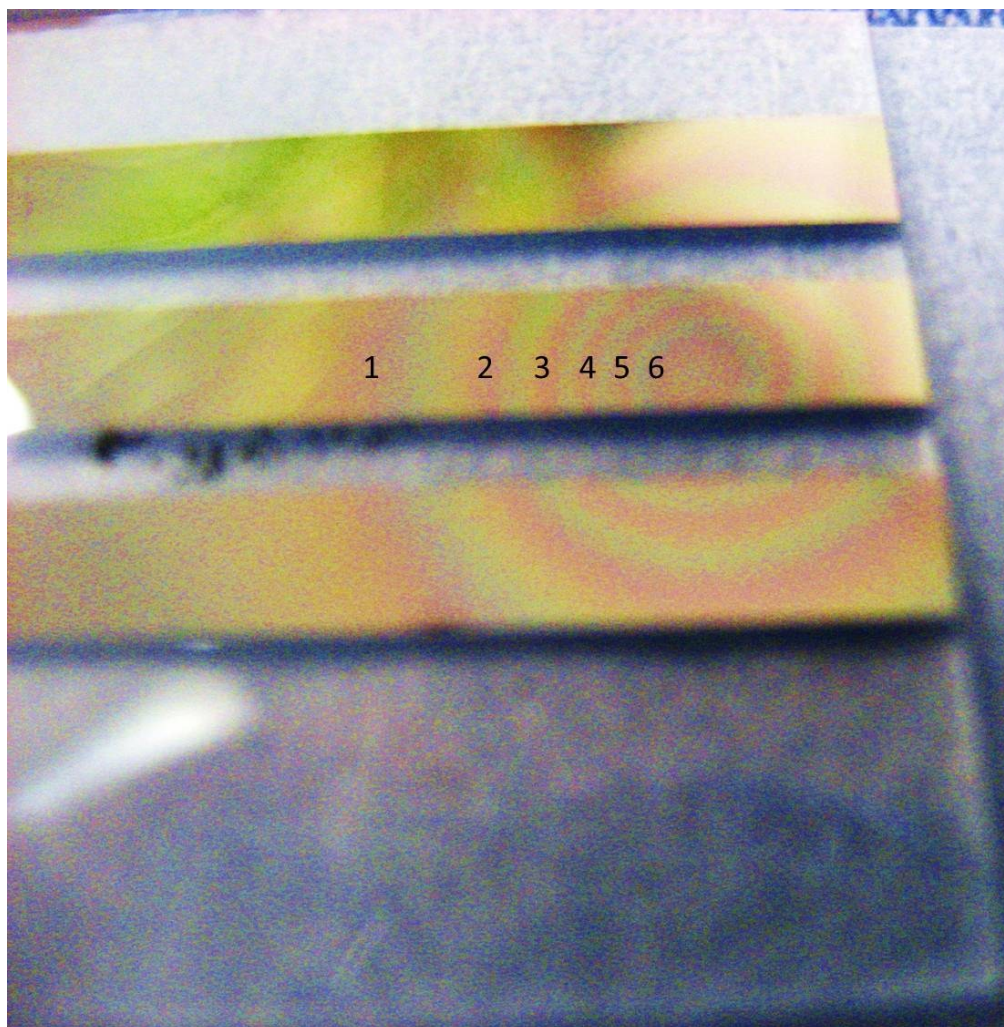


Figure 6-36. A typical sample with different thicknesses. The contrast of the photo was increased to make it easier to see each of the color bands. In this sample, six red bands can be clearly seen.

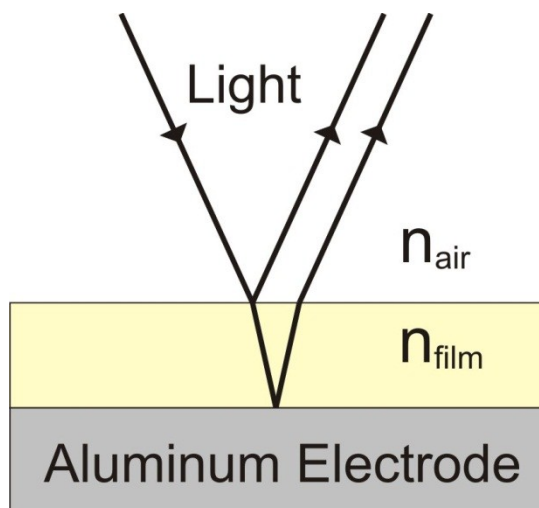


Figure 6-37. The light reflecting from the top and bottom surfaces of the film created interference patterns such as the ones shown in Figure 6-36.

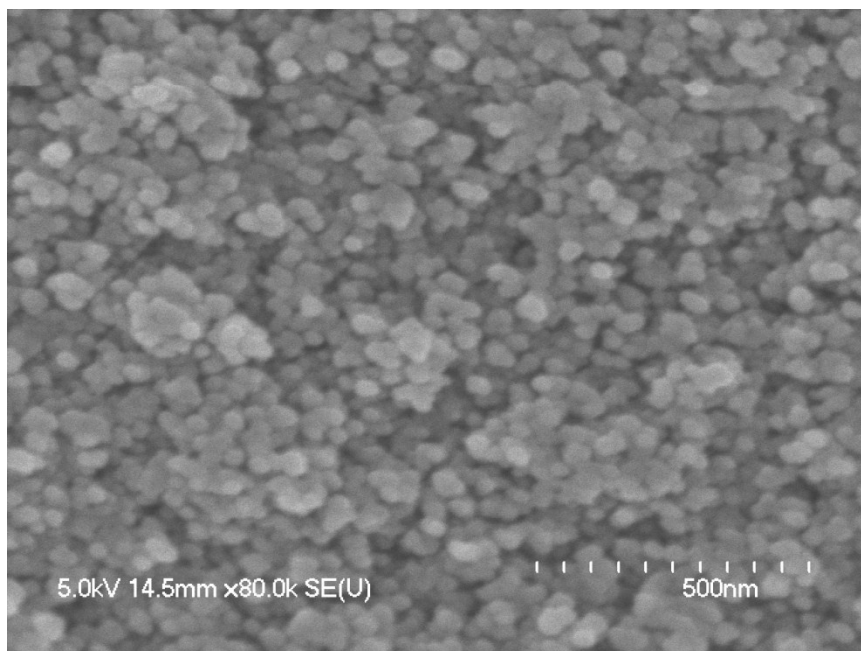


Figure 6-38. Scanning electron microscope image of an uncoated titanium dioxide nanoparticle film. [7] (Taken from *Balasubramanian, B., et al., Nanotechnology, 2011. 22 (405605)* with permission.)

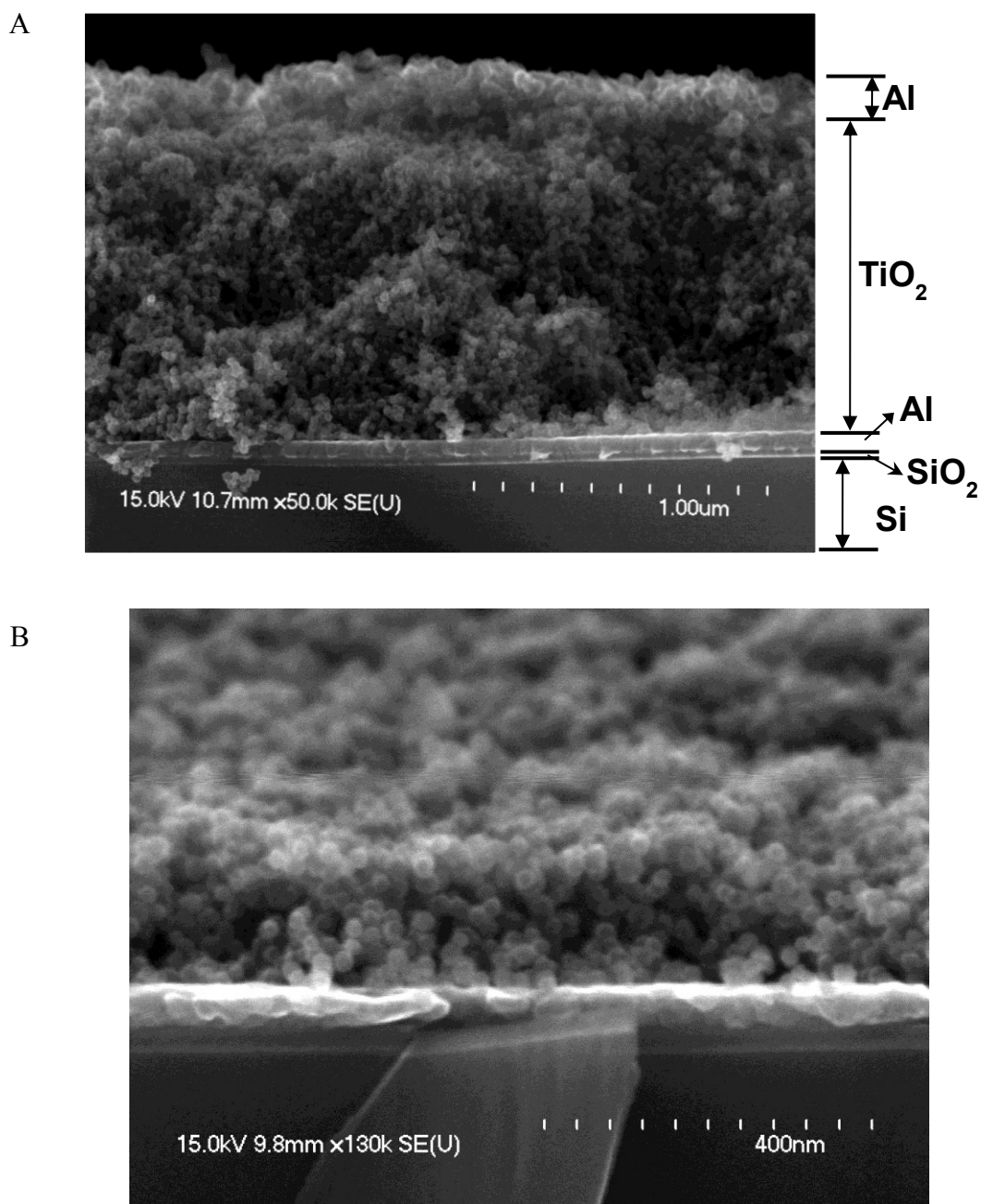


Figure 6-39. Cross sectional FESEM of a capacitor made on Si with TiO<sub>2</sub> nanoparticle. The dielectric layer was approx. 1  $\mu\text{m}$  thick, while the top electrodes were approx. 100 nm, the bottom electrodes were 60 nm, and it was on a thin SiO<sub>2</sub> covered Si substrate. (Taken from Balasubramanian, B., et al., *ACS Nano*, 2010. 4 (1893-1900) with permission.)

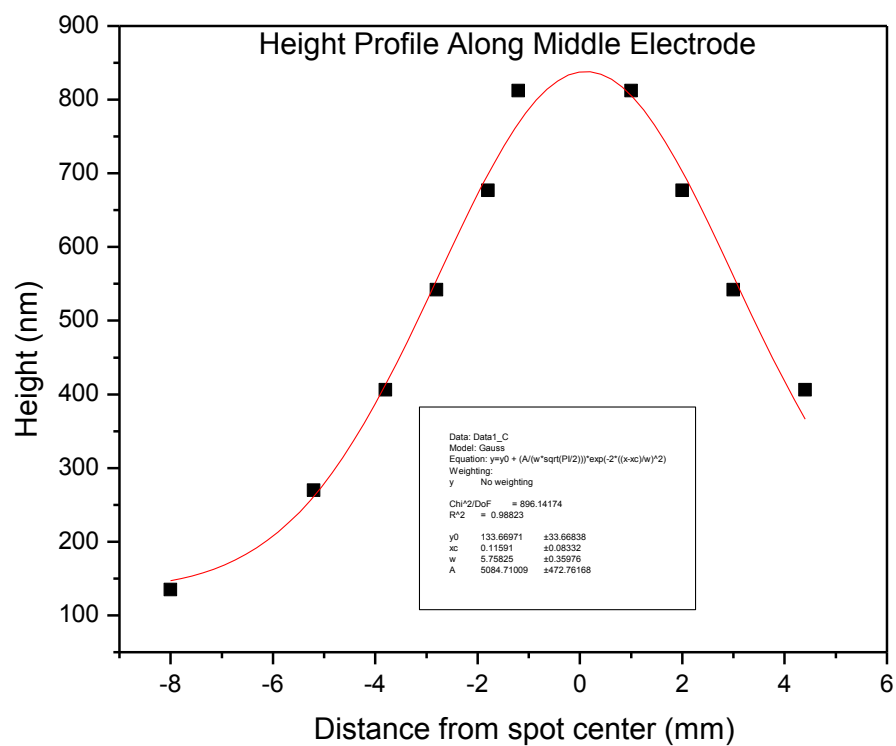
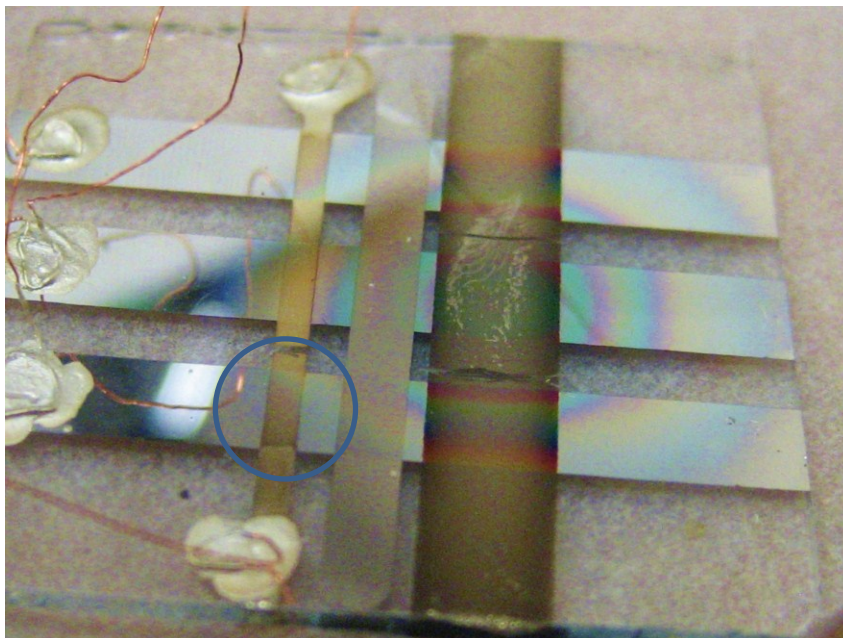


Figure 6-40. Plot of sample thickness with respect to distance from center of beam spot for the sample shown in Figure 6-36. The distribution of thickness fit a Gaussian distribution well.

A



B

Index of Refraction	2.4
m value	2
Color Band	Green
Wavelength	510 nm
Thickness (d)	213 nm

Figure 6-41. Thin film of uncoated titanium dioxide nanoparticles with a distribution of thicknesses over the sample. (A) The desired sample spot was the one in the lower left corner inside the circle with the faint green band. (B) Table of values used to calculate the sample thickness of 213 nm.

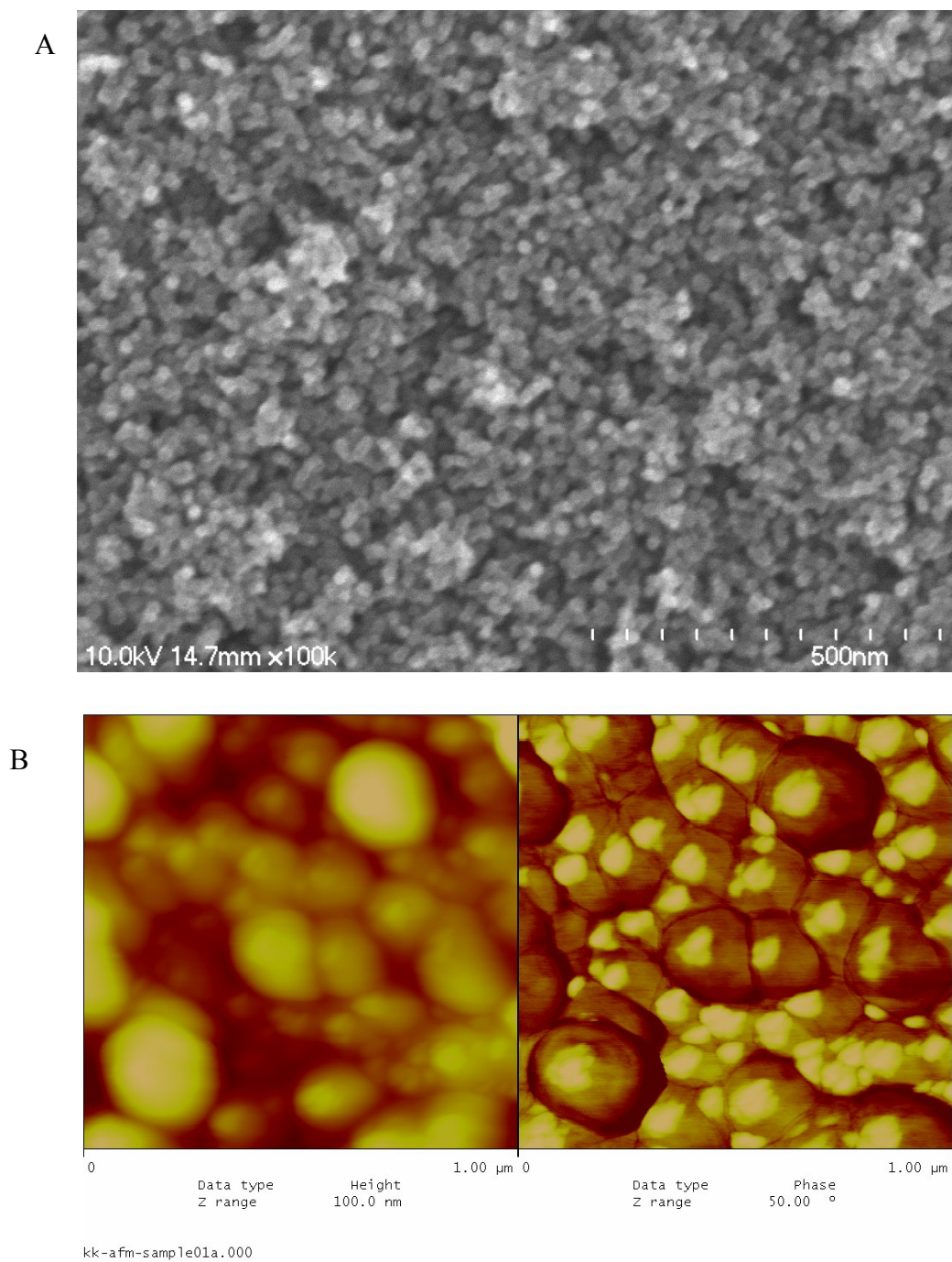


Figure 6-42. Two images from the same paraffin coated titanium dioxide nanoparticle thin film. (A) Scanning electron microscope image of the sample. (B) Atomic force microscopy images of the amplitude of deflection and the phase for the sample.

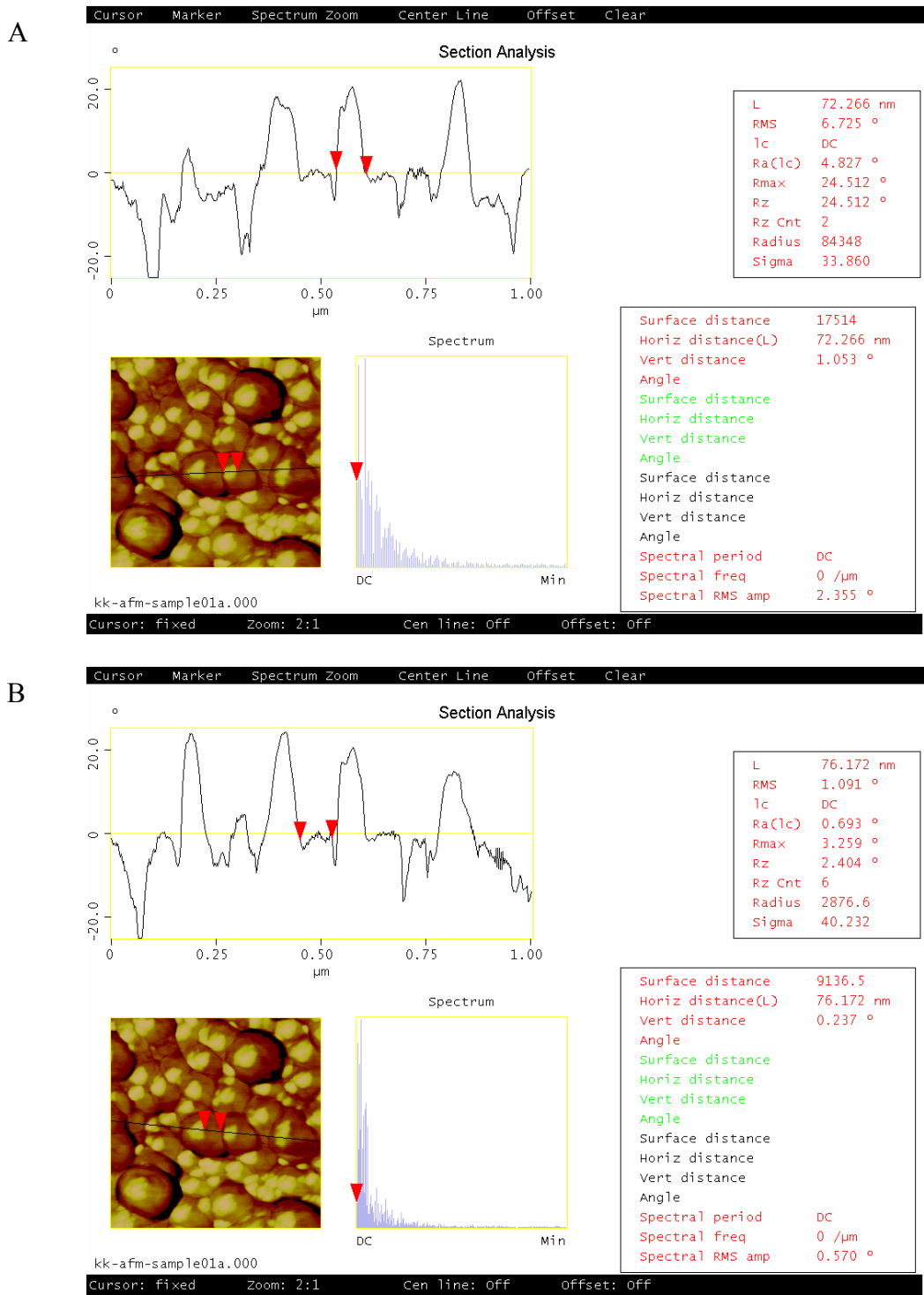
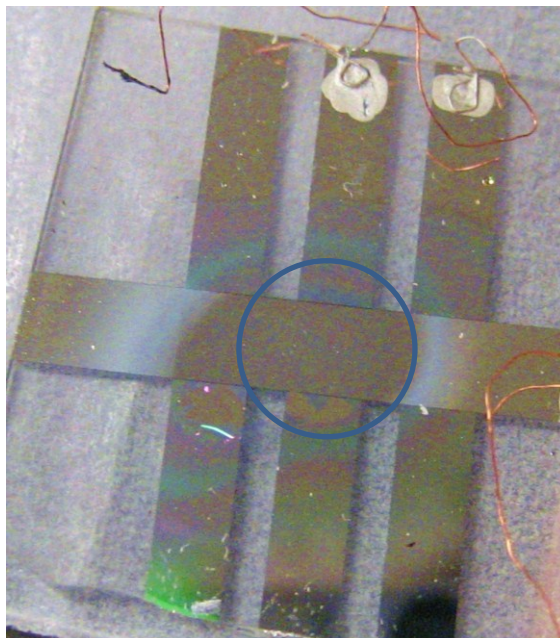


Figure 6-43. Section analysis for the paraffin coated titanium dioxide sample shown in Figure 6-42. (A) Line scan measuring the width of the bright center of a cluster. (B) Line scan measuring the darker soft region of a cluster.

A



B

Index of Refraction	2.3
m value	4
Color Band	Red
Wavelength	650 nm
Thickness (d)	565nm

Figure 6-44. A thin film of titanium dioxide nanoparticles with a paraffin shell deposited at 170°C. Index of refraction was the volume average of the coating and the particle.

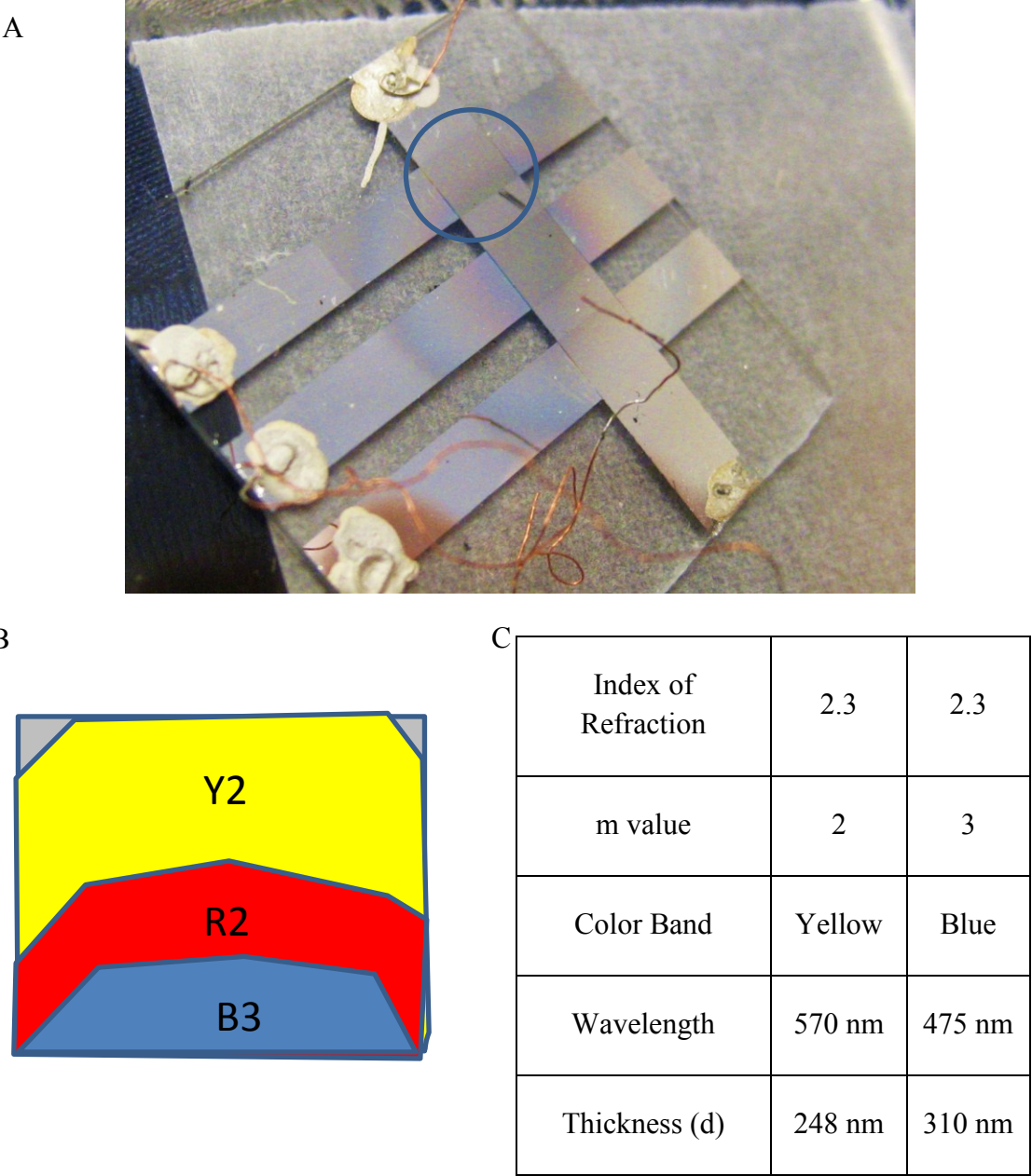


Figure 6-45. Thin film of titanium dioxide nanoparticles coated with a paraffin shell deposited at 110 °C. The index of refraction was a composite value based off of the volume ratios of paraffin and nanoparticles. The sample thickness for this sample ranged from 248 nm to 310 nm, with an average value of 279 nm.

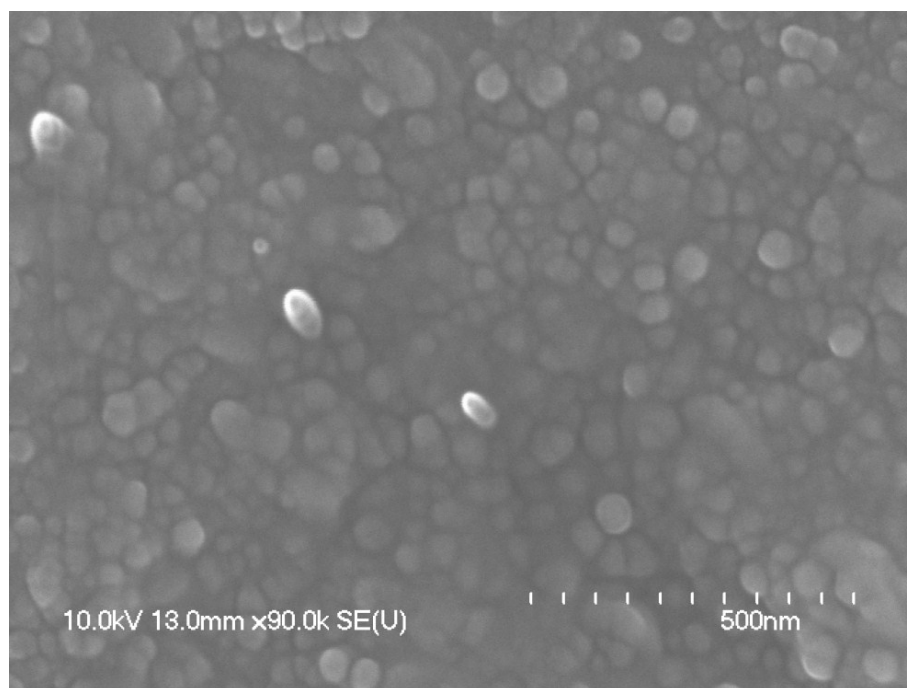


Figure 6-46. Scanning electron microscope image of a thin film consisting of VDFO coated titanium dioxide nanoparticles [7]. (Taken from *Balasubramanian, B., et al., Nanotechnology, 2011. 22 (405605)* with permission.)

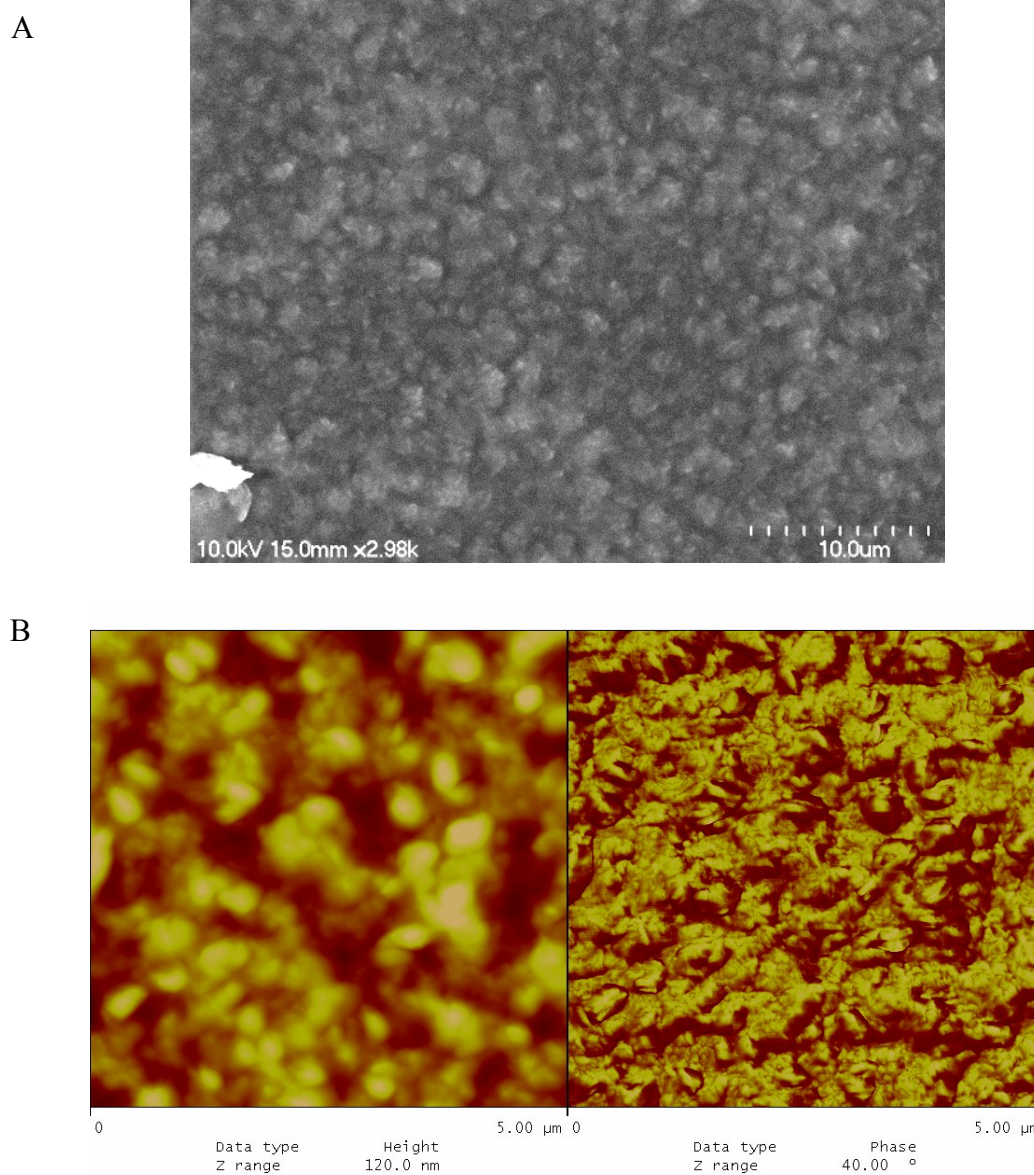


Figure 6-47. Titanium dioxide nanoparticles with a VFDO shell. (A) The SEM image shows a soft material, with no evidence of any particles. (B) The AFM also did not show any evidence of nanoparticles.

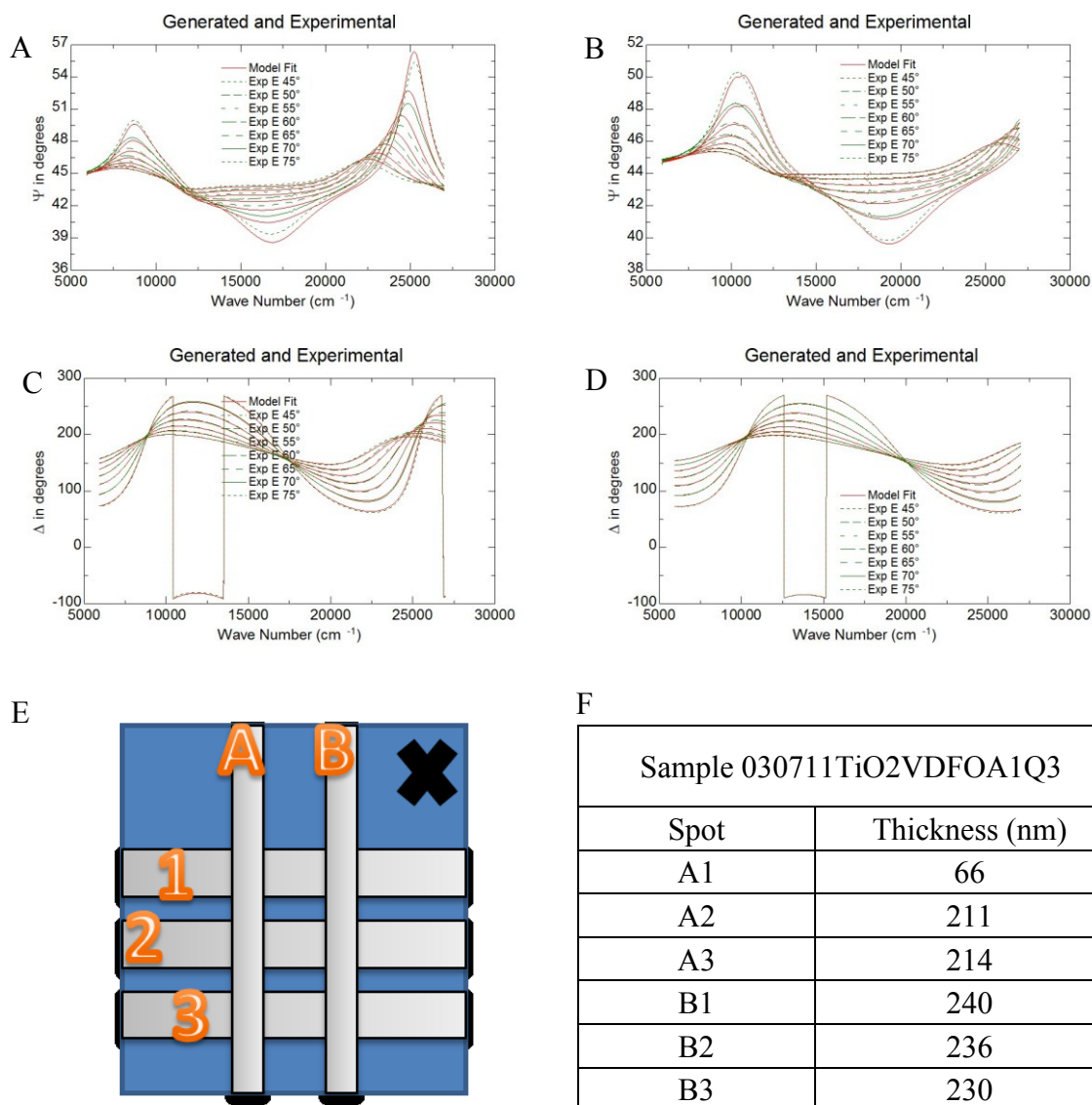


Figure 6-48. Psi and delta data for two sample spots on a sample of titanium dioxide with a VDFO shell. (A) The psi data and fits for spot B1. (B) The delta data and fits for spot B1. The sample thickness was 240 nm. (C) The psi data and fits for spot A3. (D) The delta data and fits for spot A3. The sample thickness was calculated to be 214 nm. (E) A sketch of the sample with each electrode labeled. (F) Table of thickness values for each spot on the sample.

## CHAPTER 7

### DIELECTRIC STUDIES OF COMPOSITE CAPACITORS

#### 7.1 Introduction

The previous chapter reported the construction and characteristic properties, such as thickness and morphology, that were measured for three basic sample constructions: spin-coated films, Langmuir-Blodgett (LB) films, and cluster deposition nanoparticle films. This chapter will continue with the characterization of the films by examining the dielectric and energy density properties of typical films from a variety of compositions. This includes measurements of the effect of temperature, frequency, and bias on the capacitance; and the energy density and efficiency for the film.

#### 7.2 Electrical Measurement Results for Nanocomposite Samples Fabricated by Spin-Coating

##### 7.2.A Uncoated Barium Titanate in Copolymer *P(VDF-TrFe)*

The first series of capacitor samples was made with poly(vinylidene fluoride trifluoroethylene) or *P(VDF-TrFe)* copolymers mixed with uncoated, 56 nm in diameter barium titanate nanoparticles. A 75:25 copolymer was used for the first series of samples, and then a 65:35 copolymer was used for later samples. The copolymer was dissolved in DMF or butanone at a 1-5% by weight concentration. The solution was spin-coated onto aluminum electrodes and fabricated into parallel plate capacitors. More detailed descriptions of the sample fabrication and characterization of the morphology and thickness are discussed in Chapter 6.

### *7.2.A.a. Dielectric Measurements*

Dielectric measurements are compared for two samples, the first was a pure 75:25 P(VDF-TrFe) with no nanoparticles and the other was made with the same polymer with the addition of 20% by weight of uncoated barium titanate nanoparticles, as shown in Figure 7-1. The first series of measurements probed the effect of temperature on the capacitance as shown in Figure 7-1A & B. The first figure shows a typical set of copolymer data with an increase in the dielectric constant at the phase transition between the ferroelectric and paraelectric phases on heating and cooling. The heating peak maximum occurs around 120 °C and the cooling peak maximum was at 78 °C. Interestingly, the addition of a small amount of nanoparticles made the cooling peak sharper in the case of the 20% barium titanate in a 75:25 copolymer compared to the pure films. Also the pure copolymer film had a 150 % increase in capacitance between 25 °C on cooling and a max peak height compared to a 190 % increase in capacitance for the sample with 20% BTO by weight. This was an unexpected result since later results with ODPa coated showed a decrease in cooling peak height and broadening of the peak.

The effect of applied voltage is shown in Figure 7-1C & D. Both samples show a switching voltage of 10 volts and the polarization was well saturated by 25 volts. While the nanoparticles affected the temperature dependence of the capacitance, there was little or no change in the “butterfly” curves beyond the typical sample to sample variation of a given composition of P(VDF-TrFe) copolymer.

### *7.2.B Octadecylphosphonic Acid Coated Barium Titanate in 50/50 P(VDF-TrFe) Copolymer Matrix*

The next series of capacitor samples was made with octadecylphosphonic acid coated barium titanate nanoparticles in a 50:50 P(VDF-TrFE) copolymer. The particle concentrations in the films ranged from pure particles to pure polymers. The samples were fabricated by spin-coating composite solutions onto a glass substrate with aluminum electrodes. Further details of fabricating samples and characterizing the thickness and morphology are discussed in Chapter 6.

#### *7.2.B.a. Dielectric Measurements*

The temperature dependence of the capacitance is shown in Figure 7-2 for a series of samples ranging from pure copolymer (Figure 7-2A) to 70% ODPA-coated barium titanate nanoparticles by volume (Figure 7-2E). In this series, there was little or no change in the peak shape at low concentrations of the nanoparticles (Figure 7-2A & B). The first graph shows the results for the pure 50:50 copolymer film. As the particle concentration increased to 14% by volume, the cooling and heating peaks became broader. In addition to the broadening of the dielectric peaks, there was a decrease in the temperature where the dielectric maximum occurred, as shown in Figure 7-2F. Both the heating and cooling peaks showed a shift to lower temperatures with the effect more pronounced in the cooling peaks as the maximum temperature was 62 °C for the pure film and 58 °C for the 65% by volume particle film.

The frequency dependence of the capacitance is shown in Figure 7-3 for a pure 50:50 P(VDF-TrFE) film and a film with 65% coated nanoparticles by volume. Both

samples showed low dielectric loss at low frequencies up to 10 kHz. At that frequency, the loss started to increase rapidly. The capacitance was mostly constant until it dropped quickly at 100 kHz. Figure 7-3C shows the dielectric constant at 1 kHz for the series of samples. As the particle concentration increased, so did the dielectric constant, approaching the bulk value of 50-300 for grain sized of several hundred nanometers [1].

#### *7.2.B.b. Energy Density Measurements*

The energy density for the series of samples of ODPA-coated barium titanate nanoparticles in a 50:50 copolymer is shown in Figure 7-4. The highest energy density was the blue curve of the pure polymer film. As the particle concentration increased from 0% to 40% by volume, the average energy density decreased to a minimum value. As the concentration increased past 40% to higher concentrations, the energy density also increased, with the sample containing 80% nanoparticles by volume having the highest density of any of the samples with particles. This was further explored by examining the energy efficiency. The two lowest particle concentration samples started with low efficiency at low applied voltages, but then increased around 2 volts applied. The highest concentration films of 60 and 80% particles started out with the highest efficiency for this series of samples, but started dropping to 20% at 4 volts. By 10 volts, all of the samples in this series were below 40% efficiency.

#### *7.2.C Langmuir-Blodgett Layers of Terpolymer*

Since the general properties of the spin-coated and LB samples for the (56/36.5/7.5) P(VDF-TrFe-CFE) terpolymer films were very similar, both film types are discussed in this section. The spin-coated sample was made with a 1% by volume of the

polymer solution in butanone. The LB film was fabricated with a 0.01 % by weight solution in DMF deposited onto the surface of the trough. The Langmuir layer was compressed to 5 mN/m and 35 mL were transferred to the substrate. Further discussion of the sample fabrication and analysis of the film thickness and morphology is discussed in Chapter 6.

#### *7.2.C.a. Dielectric Measurements*

The temperature dependence of the capacitance is shown in Figure 7-5A for a LB film and Figure 7-5B for a spin-coated film. While the LB film has a dielectric peak that was sharper than the spin-coated peak, the temperature where the maximum dielectric constant occurred,  $T_m$ , was the same for both samples at 46 °C. The value of  $T_m$  is a function of the composition of terpolymer [2] and the frequency of measurement [3, 4]. Using the thickness of 2 nm per layer, as determined in Chapter 6 by ellipsometry, this gave a dielectric constant of 48 for the LB film at  $T_m$ .

The frequency dependence of the capacitance is shown in Figure 7-5C for a 35 ML Langmuir-Blodgett film measured at room temperature. The dielectric loss was low from 100 Hz to 100 kHz. A final dielectric measurement made on the Langmuir-Blodgett film is shown in Figure 7-5D. The dependence of the dielectric constant on the electric field is shown for a 35 ML film. The terpolymer had a very different shape compared to the copolymer “butterfly” curves shown in Figure 7-1C. This supports the expectation of little to no net permanent polarization in the terpolymer films [5, 6].

### *7.2.C.b. Energy Density Measurements*

The energy density measurements for a spin-coated terpolymer film are shown in Figure 7-6. The absolute energy for the film (Figure 7-6A) showed an increase in energy density with applied voltage. Once the voltage on the sample exceeded 10 volts, the increase in the energy density was nearly linear. The energy efficiency was between 80 and 90% for all voltages above 5 volts (Figure 7-6B). At low voltages, the film may not have been saturated or pinhole defects may have been present causing the sample to leak charge. It was likely that the defects may have burned out when the efficiency dropped to 50% for one set of measurements and then returned to a higher efficiency. The results of this sample were comparable to those previously announced in literature [7, 8] and provide a basis for an expectation of a well performing matrix for future studies.

### *7.2.D Octadecylphosphonic Acid Coated Barium Titanate in Terpolymer Matrix*

This series of samples consisted of two different diameter barium titanate nanoparticles, 56 and 15 nm in diameter, coated with one of two phosphonic acid functionalized alkanes, decylphosphonic acid and octadecylphosphonic acid, in a PVDF terpolymer matrix at concentrations from pure polymer to pure particles, increasing in amount by 20% volume of the particle-coating system. The thin film solutions were spin-coated onto glass substrates with aluminum electrodes. The sample compositions and morphologies are discussed in more detail in Chapter 6.

### *7.2.D.a. Dielectric Measurements*

The dielectric results for the larger 56 nm in diameter barium titanate nanoparticles coated with ODPa are shown in Figure 7-7. Two data sets, the lowest particle concentrations of 13.4% barium titanate by volume and the highest particle concentration of 54% barium titanate by volume, were compared. A common feature of all the high nanoparticle concentration films was that the films had to be made very thick or else there were too many defects and they shorted almost immediately upon application of an electric field. Even with thick samples, the reliability was poor, with less than half of the capacitors usable.

Figure 7-7A & B compare the temperature dependence of the low and high concentration of barium titanate particle samples. As the concentration of particles increased, the temperature of the max dielectric peak shifted to a lower temperature. The dielectric loss also stayed low for the higher particle concentrations sample, just starting to increase at 1000 kHz instead of increasing at 100 kHz as was typical in most of the polymer samples.

### *7.2.D.b. Energy Density Measurements*

Temperature-dependent energy density results are shown in Figure 7-8. Since the hysteresis of the polarization of a relaxor film was temperature dependent [9], it was expected to see an improved energy density as the temperature decreased and the net permanent polarization decreased. This is what was shown in Figure 7-8. The pure terpolymer film (Figure 7-8A) showed a 38% increase in energy as the temperature increased from 0 °C to 20 °C. By 40 °C, any remnant polarization had mostly

disappeared since the energy density was relatively constant at higher temperatures for a given applied voltage. Similar trends were seen in the data with nanoparticles. As the temperature increases, so does the energy until 40 °C, and then each further cycle showed little or no change in the stored energy.

#### *7.2.E Spin-Coated Octadecylphosphonic Acid Coated Nanoparticles with No Matrix*

The coated particles without a matrix were the highest concentration particle samples made for these studies. The same particles as in the previous section were spin-coated onto a glass substrate with aluminum electrodes. These samples were very thick, and had a capacitance of a few picofarads. This made it very difficult to resolve which properties were the capacitors and which were a feature of the cables or stage. Thinner samples tended to be too leaky to make measurements successfully.

### **7.3 Electrical Measurement Results for Nanocomposite Samples Fabricated by Langmuir-Blodgett Deposition**

#### *7.3.A Langmuir-Blodgett Layers of Particles*

Langmuir-Blodgett films were made with ODPA-coated barium titanate nanoparticles. Particles were suspended in chloroform and deposited onto the surface of the Langmuir trough. The particle film was compressed to 7mN/m and then 20 mL were transferred to the substrate by Schaefer deposition. More details about the particle Langmuir layers and the thin films are discussed in Chapter 6.

### *7.3.A.a. Dielectric Measurements of Langmuir-Blodgett Particle Films*

The temperature dependence of the capacitance of a coated nanoparticle film was fairly flat to and without many features (Figure 7-9A). There was a slight increase in capacitance during the sample annealing, shown in red, which remained for future cycles. This may have been caused by the particle coatings softening and the film becoming slightly more dense and thinner. Either a decrease in total thickness or an increase in the dielectric constant due to having air voids would result in an increase in the capacitance. The other interesting thing was the shape of the curve. The LB sample has a convex shape compared to the spin-coated sample with the same particles, which was concave. It was possible that the LB film may have a higher concentration of unattached alkanes due to being very hydrophobic and being likely to float on the surface of the trough where as some of the particles may sink to the bottom if they were not well covered with the alkanes. The frequency data (Figure 7-9B) shows a very flat constant capacitance until 100 kHz, although the dielectric loss has a minimum at 1kHz and increases linearly when plotted on a log-log scale.

### *7.3.A.b. Energy Density Measurements*

The LB nanoparticle samples showed an increase in energy density with applied field until 8-9 MV/m (Figure 7-10A). At that field, the density started to drop, likely from damage to the film. The energy efficiency was not nearly as impressive, as the efficiency started to decrease at 2 to 4 MV/m (Figure 7-10B).

### *7.3.B Multilayer Composite Capacitor Samples*

Composite LB samples were made by alternating layers of polymer and coated nanoparticles, as shown in Figure 7-11A. The terpolymer layers were 5-20 mL thick, while the particle layers contained 3-5 depositions of particles. The particles were coated with ODPA or VDF oligomers. More details about the sample construction and morphology are described in Chapter 6.

#### *7.3.B.a. Dielectric Measurements*

The dielectric results are shown for a typical sample of 20 ML terpolymer, 3 depositions of ODPA-coated barium titanate, and 20 more ML terpolymer. Similar to the pure terpolymer temperature dependence curve (Figure 7-5A), the composite film showed an increase in capacitance upon annealing (Figure 7-11B) with a  $T_m$  of 49 °C. With this sample, it appeared that the temperature dependence was primarily dictated by the terpolymer layers. Figure 7-11C compares the frequency dependence of the capacitance of a sample with ODPA-coated barium titanate to one with VDF oligomer-coated barium titanate sample. While both samples showed low dielectric loss from 100 Hz to 100 kHz, the sample with the VDF oligomer-coated particles showed a 25% increase in the dielectric constant, increasing from 15.6 in the ODPA-coated particle sample to 19.8 in the VDF-coated particle sample.

#### *7.3.B.b. Energy Density Measurements*

Unfortunately the increase in the dielectric constant of the VDF oligomer coated nanoparticle samples did not result in a higher energy density compared to the ODPA-

coated barium titanate. Rather, the two films performed nearly identically (Figure 7-12). The efficiency of both samples was also very similar. The multilayer composite films showed high energy density similar to the pure terpolymer films. Figure 7-13 shows results for a variety of composites ranging from 5 mL layers of terpolymer up to the 20 mL layers discussed previously. While all samples performed similarly, the two samples with 5-3-5 structure showed higher efficiency than the other samples in the 20-80 MV/m range. At higher electric fields, the efficiencies of all the samples started to decrease to zero.

## **7.4 Electrical Measurement Results for Nanocomposite Samples Fabricated by Cluster Deposition**

### *7.4.A Uncoated Titanium Dioxide Particles*

The samples in this section were constructed with uncoated titanium dioxide particles made by cluster deposition. The particles were deposited directly into the substrate as described in Chapter 6 [10, 11]. The particles had an average diameter of 18 nm. Since there was no matrix in the sample, the samples tended to be very fragile and often burned out at low voltages making it difficult to obtain electrical measurements.

#### *7.4.A.a. Dielectric Measurements*

Dielectric measurements are shown in Figure 7-14. The first measurement shown in Figure 7-14A is the temperature dependence of the capacitance. The decrease in capacitance was not expected for the pure particle samples, especially at 70 °C. A titanium dioxide film would need temperatures of 300 °C or higher to change the crystallinity [12]. Instead, the slow increase in capacitance followed by the sharp drop

which did not return on further temperature cycles was suspected to be caused by moisture in the sample. The effects of water vapor on capacitance are further discussed in Chapter 8.

The effect of frequency on capacitance for the uncoated titanium dioxide nanoparticles after annealing is shown in Figure 7-14B. The dielectric loss was low from 500 Hz-100 kHz. The capacitance decreased by 20% over that frequency range, although it did not start to drop rapidly until the frequency was greater than 100 kHz and the dielectric loss was increasing greatly.

#### *7.4.B Paraffin Coated Particles*

The cluster deposition titanium dioxide nanoparticles were coated with paraffin by evaporating a shell onto the particles while still in the vacuum system [10]. This created particles with an organic shell without the use of solvents. The particles used in capacitor samples were coated with paraffin evaporated at two temperatures, 110 °C and 170 °C. This resulted in two different thicknesses of shells, 2nm and 3.5 nm respectively. The particles and sample structures and morphologies are discussed in Chapter 6.

##### *7.4.B.a. Dielectric Measurements*

Capacitor samples were fabricated with titanium dioxide nanoparticles coated at 110 °C and 170 °C. The effect of frequency on the dielectric constant and loss were measured for both type of samples, as shown in Figure 7-15A. These samples tended to be leaky and it was difficult to obtain high quality measurements. The D value was at 0.1 or greater over the entire range of frequencies measured with a minimum at 200 kHz. Most

high quality samples had a D value of less than 0.1 over a majority of the range 100 Hz to 100 kHz. The high dielectric constant from 100 Hz to 1kHz was likely an artifact of a leaky sample.

The sample with the 3.5 nm paraffin shells shown in Figure 7-15B had a lower dielectric loss, but also had a lower dielectric constant. This was typical of the paraffin-coated nanoparticle samples. The samples with high quality measurements had shells that were thick and the overall samples were at least several hundred nanometers thick.

#### *7.4.C Oligomer Coated Particles*

Titanium dioxide particles were coated with VDF oligomer by evaporation [11]. The coated particles were deposited directly onto the substrate without using organic solvent or a matrix polymer. Sample thickness and characterization of the morphology is described in detail in Chapter 6.

##### *7.4.C.a. Dielectric Measurements*

The results of the dielectric measurements were not very consistent from sample to sample. Figure 7-16 shows two typical series of samples. As can be seen in the temperature dependence data shown in Figure 7-16A & B, the shape of the dielectric capacitance curves was very different. Both samples show three temperature cycles, with the first one shown in red. The sample in Figure 7-16A showed no sign of hysteresis after the first cycle. The second sample (Figure 7-16B) showed some hysteresis, similar to the shape of the copolymer temperature dependence (Figure 7-1), only shift to much lower temperatures by 50 °C or more. It was unlikely that the dielectric maxima were

caused by an outside factor such as humidity, since humidity shows the largest effect on the first cycle unless a high amount of moisture was added to the chamber during the data collection. Also, there was no reason to expect the titanium dioxide to produce hysteresis over that temperature range, as shown in Figure 7-16A. Therefore, the likely cause of the hysteresis was the oligomer as evidence of polarization had been found in evaporated films using the same oligomers. The results of the evaporated films are discussed in Chapter 3.

The dielectric loss for both samples was also not very similar. The first sample (Figure 7-16C) showed low loss from 100 Hz to 100 kHz. The second sample (Figure 7-16D) showed low loss from 1kHz to 700kHz. The high loss at low frequency caused the increase in capacitance at low frequency.

#### *7.4.C.b. Energy Density Measurements*

The energy density results for the samples used in Figure 7-16 are shown in Figure 7-17. The first sample (Figure 7-17A) had a lower energy density at a given field compared to the second sample (Figure 7-17B). For example, at 50 MV/m, the first sample had a density of 0.1 J/cc while the second sample had a density of 0.15 J/cc. The energy efficiency also showed different trends. The first sample showed a decrease in efficiency with applied field until it reached a value of 80% (Figure 7-17C). The second sample increased in energy density at low electric fields (Figure 7-17D) as was seen in some of the other high polymer composition samples. Once the field reached 20 MV/m, the efficiency stabilized at 90% efficiency of the range of fields measured.

## 7.5 Conclusions

Samples were made using three techniques: spin-coating, Langmuir-Blodgett deposition, and cluster deposition, as a way to increase the energy density in dielectrics. While spin-coated films with copolymer matrix performed poorly due to the energy lost to the dipoles, the terpolymer films had efficiency over 80%. The addition of ODPA-coated barium titanate nanoparticles did not significantly improve the energy density over the pure terpolymer, though.

The Langmuir-Blodgett multilayer samples showed promise with the use of the VDFO-coated barium titanate nanoparticle multilayer samples. At low particle concentration, the addition of the VDFO oligomer coatings increased the dielectric constant by 25% over the alkane coated particles. Also, the samples with the largest particle to terpolymer volume ratios had slightly better energy efficiency performance. Further experimentation on this type of samples would be promising as the particle to polymer ratio continues to increase with more layers of polymer and particles.

The cluster deposition samples were unreliable and the sample to sample repeatability was low. Measurements were only able to be made on samples that were much thicker than the spin-coated or LB films, and the particle coatings had several nanometers thick to prevent the sample from burning out. In theory, the concept was nice since it did not require solvents to coat the particles. In practice, reliable measurements were hard to obtain and samples that were supposed to be of the same composition did not behave the same way.

## 7.6 References

1. Frey, M., et al., *The role of interfaces on an apparent grain size effect on the dielectric properties for ferroelectric barium titanate ceramics*. *Ferroelectrics*, 1998. **206**(1): p. 337-353.
2. Bao, H.-M., et al., *Phase Transitions and Ferroelectric Relaxor Behavior in P(VDF-TrFE-CFE) Terpolymers*. *Macromolecules*, 2007. **40**(7): p. 2371-2379.
3. Shrout, T.R. and J. Fielding, Jr. *Relaxor ferroelectric materials*. in *Ultrasonics Symposium, 1990. Proceedings., IEEE 1990*. 1990.
4. Lang, S.B., et al., *Normal ferroelectric to ferroelectric relaxor conversion in fluorinated polymers and the relaxor dynamics*, in *Frontiers of Ferroelectricity*. 2007, Springer US. p. 271-280.
5. Samara, G.A., *The relaxational properties of compositionally disordered ABO<sub>3</sub> perovskites*. *Journal of Physics: Condensed Matter*, 2003. **15**(9): p. R367.
6. Bauer, F., E. Fousson, and Q.M. Zhang, *Recent advances in highly electrostrictive P(VDF-TrFE-CFE) terpolymers*. *Dielectrics and Electrical Insulation, IEEE Transactions on*, 2006. **13**(5): p. 1149-1154.
7. Chu, B., et al., *A Dielectric Polymer with High Electric Energy Density and Fast Discharge Speed*. *Science*, 2006. **313**(5785): p. 3.
8. Chu, B., et al., *Relaxor ferroelectric poly(vinylidene fluoride-trifluoroethylene-chlorofluoroethylene) terpolymer for high energy density storage capacitors*. *Dielectrics and Electrical Insulation, IEEE Transactions on*, 2006. **13**(5): p. 1162-1169.
9. Cross, L.E., *Relaxor ferroelectrics*. *Ferroelectrics*, 1987. **76**(1): p. 241-267.
10. Balasubramanian, B., et al., *Synthesis of Monodisperse TiO<sub>2</sub>-Paraffin Core-Shell Nanoparticles for Improved Dielectric Properties*. *ACS Nano*, 2010. **4**(4): p. 1893-1900.
11. Balasubramanian, B., et al., *Cluster synthesis of monodisperse rutile-TiO<sub>2</sub> nanoparticles and dielectric TiO<sub>2</sub>-vinylidene fluoride oligomer nanocomposites*. *Nanotechnology*, 2011. **22**(40): p. 405605.
12. Fitzgibbons, E., K. Sladek, and W. Hartwig, *TiO<sub>2</sub> film properties as a function of processing temperature*. *Journal of The Electrochemical Society*, 1972. **119**(6): p. 735-739.

## 7.7 Figures

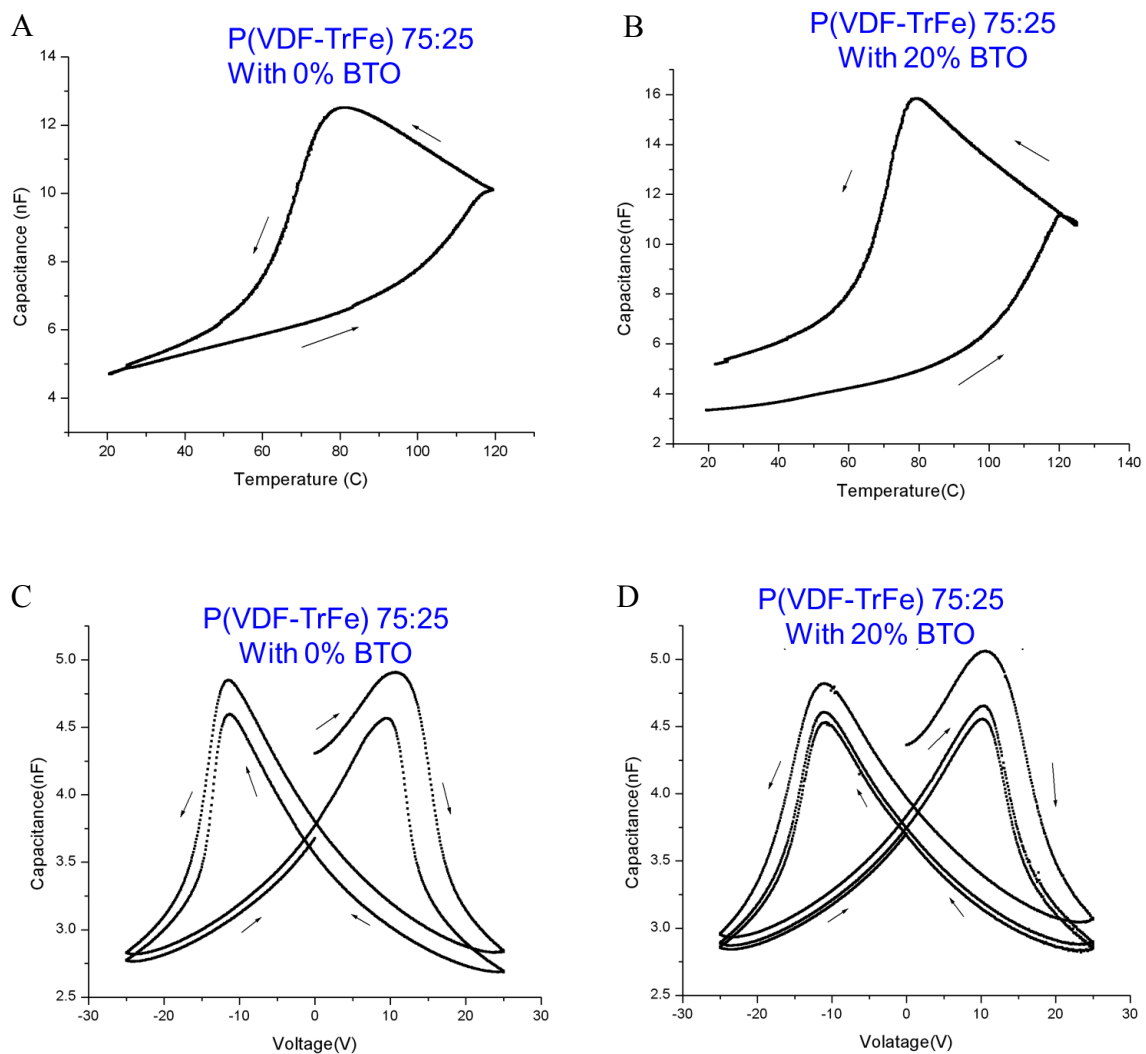


Figure 7-1. Pure P(VDF-TrFE) 75:25 film and composite film with uncoated barium titanate nanoparticles spincoated as a thin film. (A) Temperature dependence of the capacitance of a pure copolymer film. (B) Temperature dependence of the capacitance for a composite film. (C) Voltage dependence on the capacitance for a pure copolymer film. (D) Voltage dependence on the capacitance for a composite film.

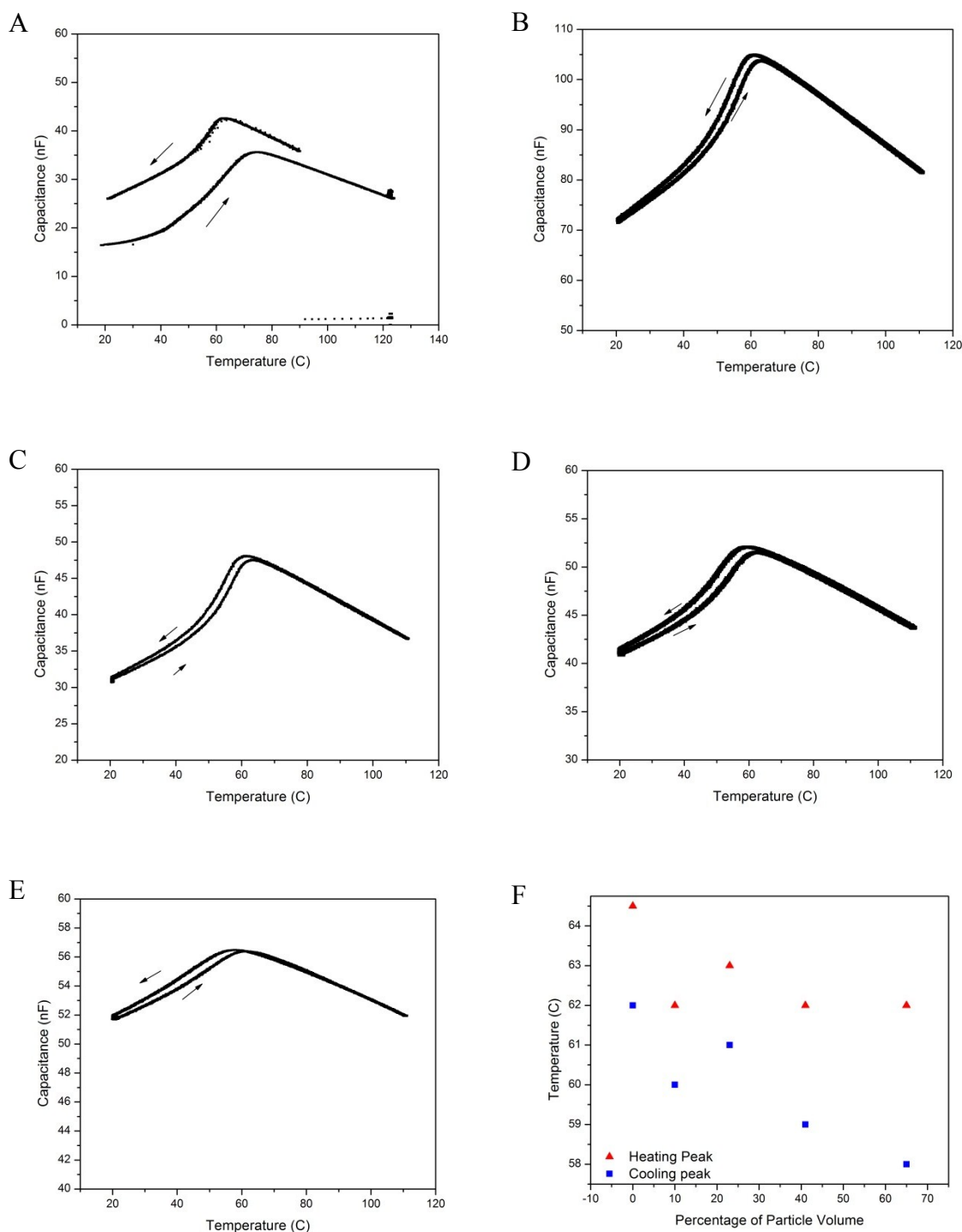


Figure 7-2. Temperature dependence of the capacitance for samples with (A) 0%, (B) 6%, (C) 14%, (D) 24%, and (E) 40% by volume of ODPA-coated BTO nanoparticles in a 50:50 P(VDF-TrFe). (F) Peak location of the heating and cooling peaks for the series of data in the Figure 7-2 A-E.

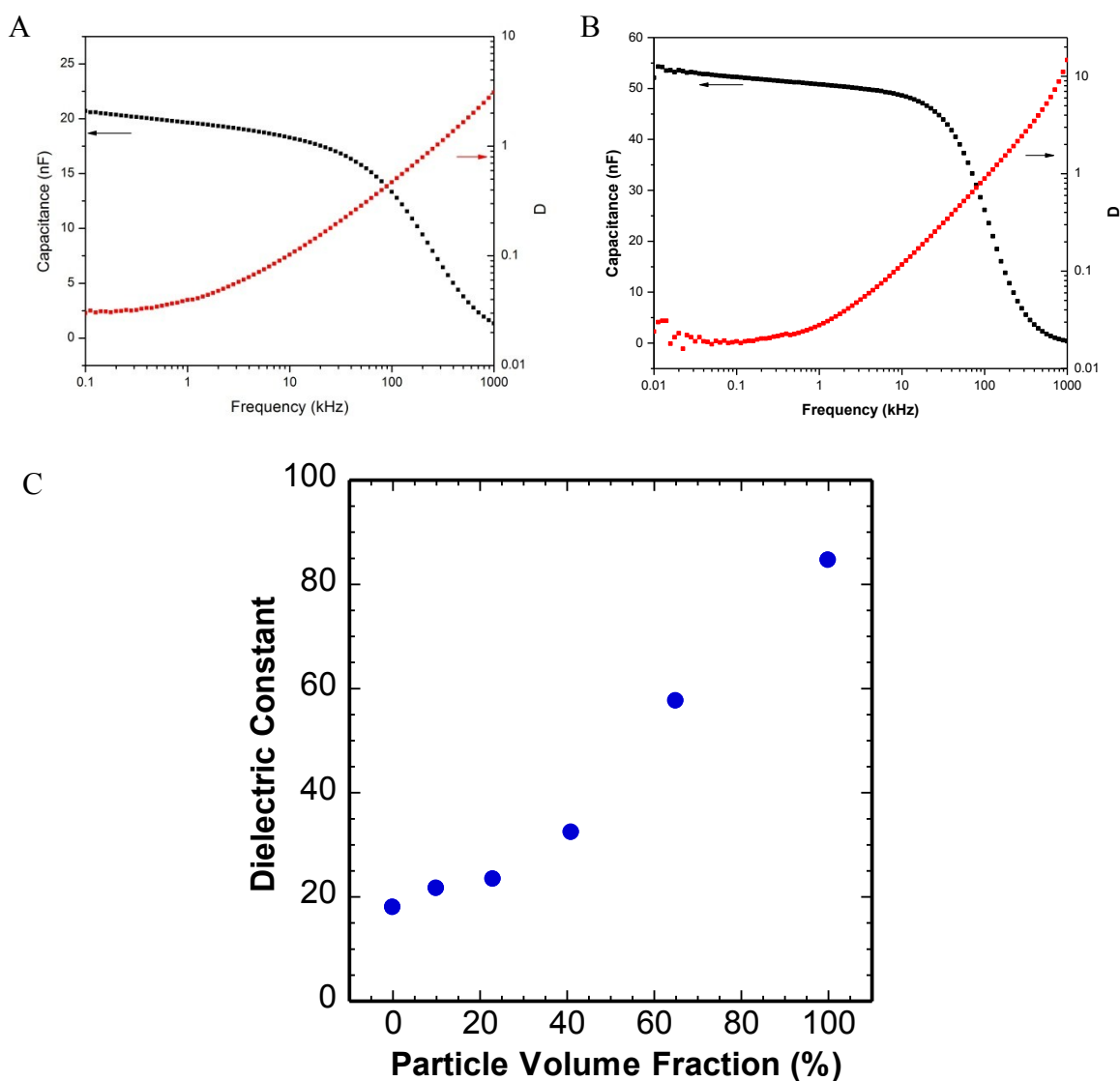


Figure 7-3. Comparison of the frequency dependence of the capacitance for a (A) pure 50:50 P(VDF-TrFe) copolymer film and (B) a copolymer film with a 65% by volume ODPA-coated barium titanate nanoparticles. (C) The dielectric constant increased as the concentration of nanoparticles increased.

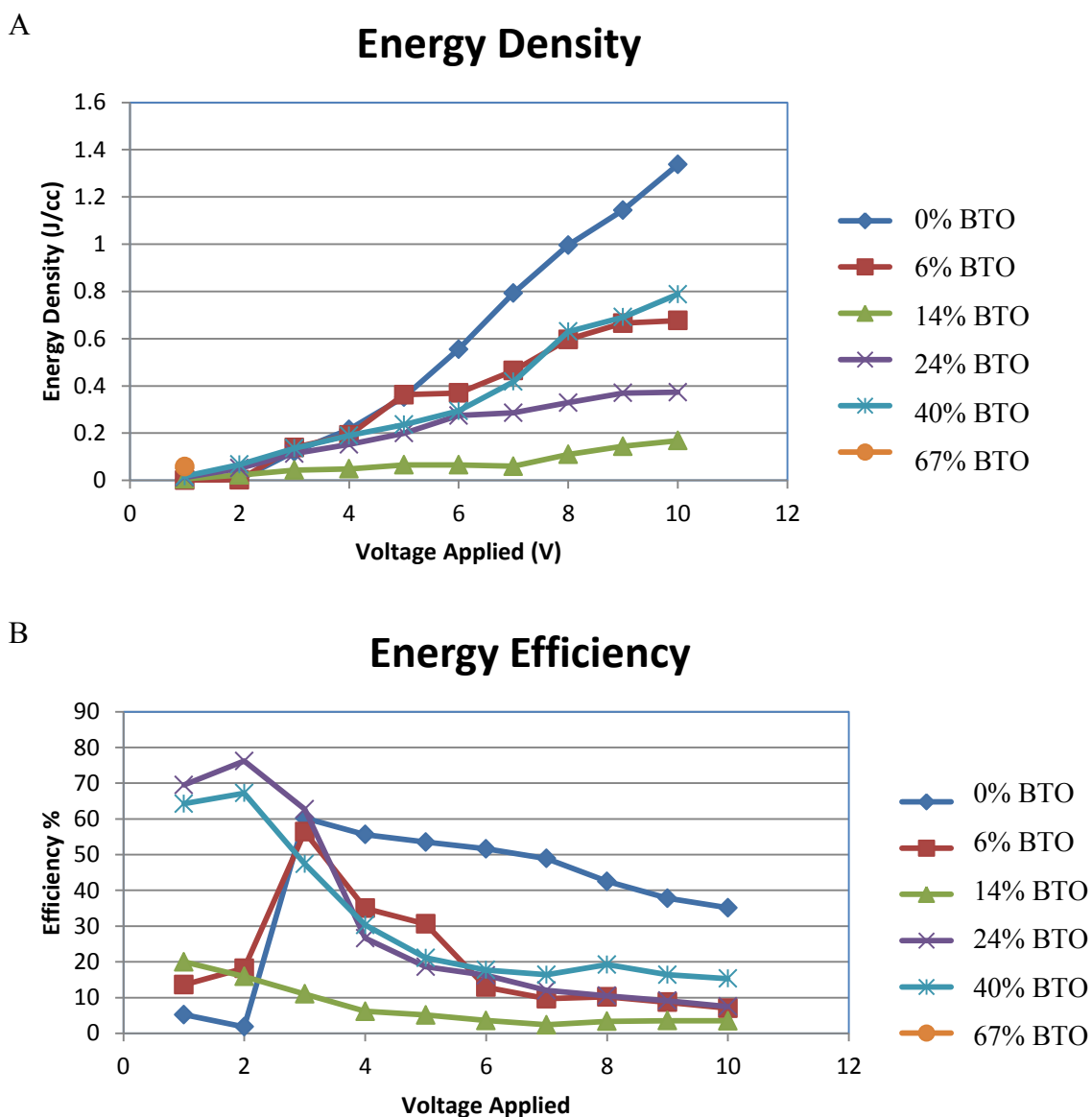


Figure 7-4. Energy results for ODPA coated BTO nanoparticles in 50/50 P(VDF-TrFE) matrix series. (A) Energy density results for the series of samples. (B) Energy efficiency results for the series of samples.

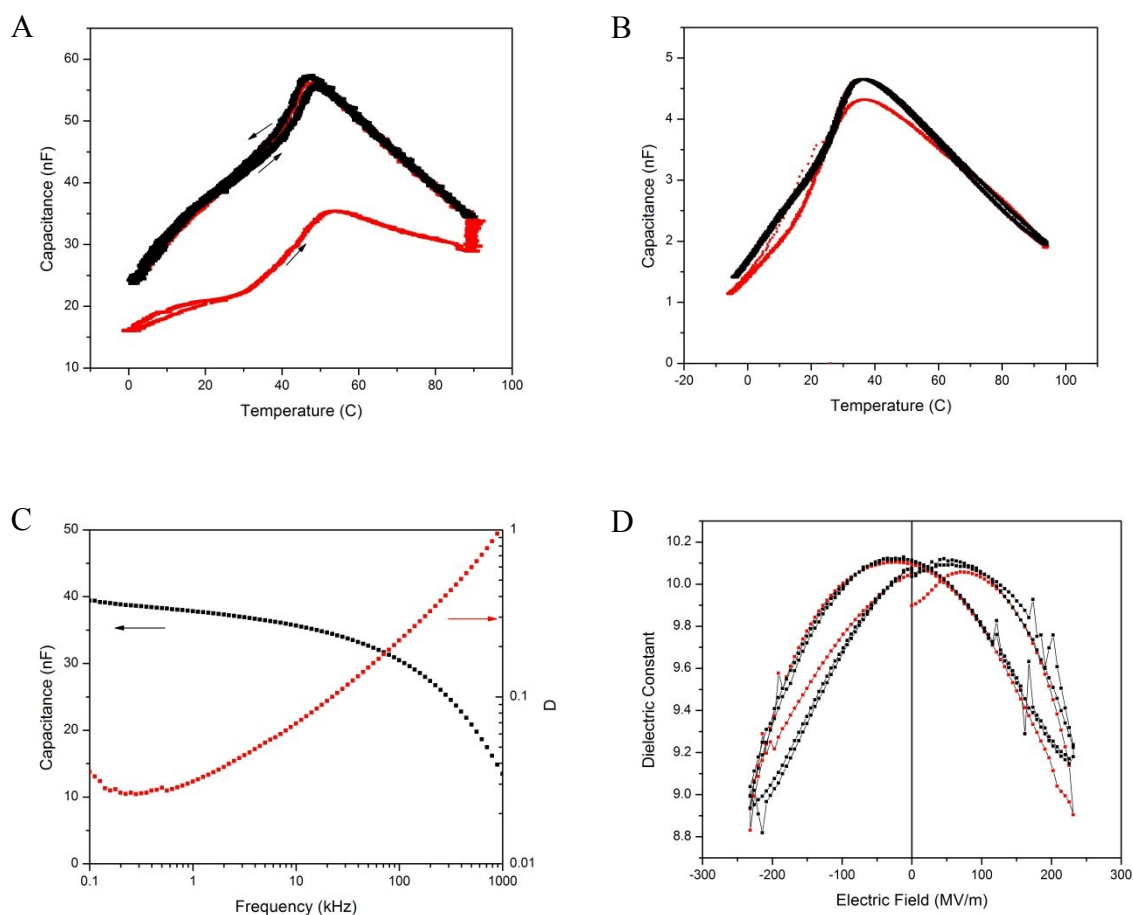
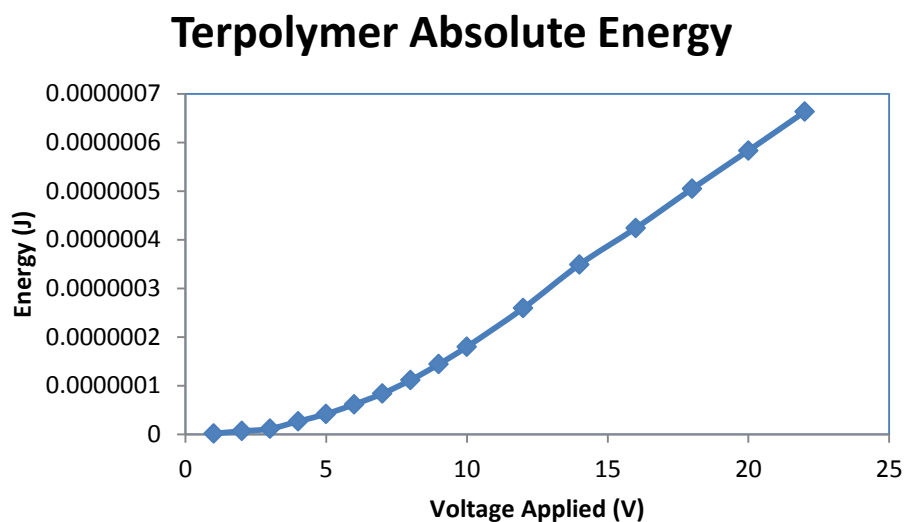


Figure 7-5. Terpolymer dielectric results for LB and spin-coated films. (A) The annealing cycle plus two more temperature cycles for a 35 mL sample. (B) The annealing cycle plus two more temperature cycles for a spin-coated terpolymer film. (C) Frequency dependency of the capacitance for a LB terpolymer film. (D) "Butterfly" curve for a 35 mL terpolymer sample.

A



B

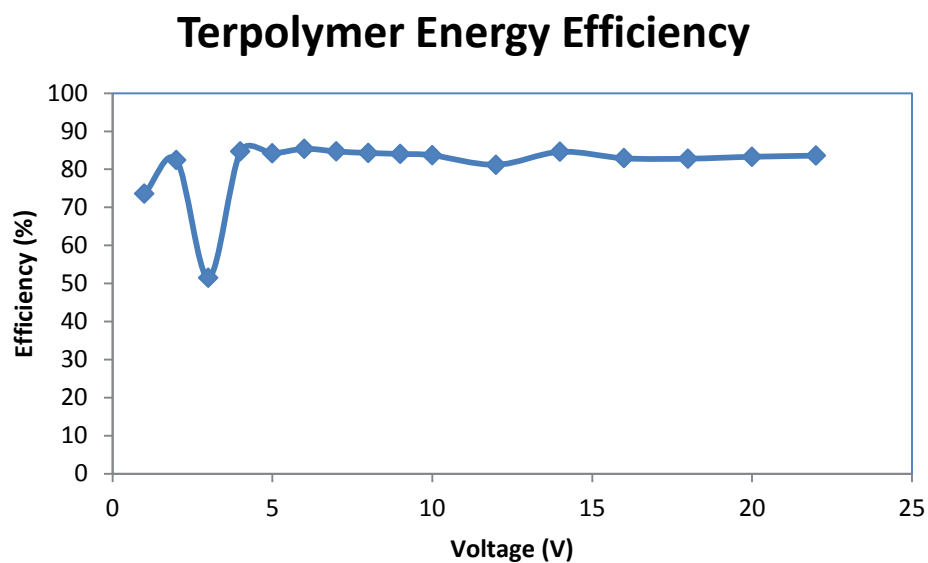


Figure 7-6. (A) Absolute energy density for a terpolymer film. (B) Energy efficiency for a pure terpolymer film.

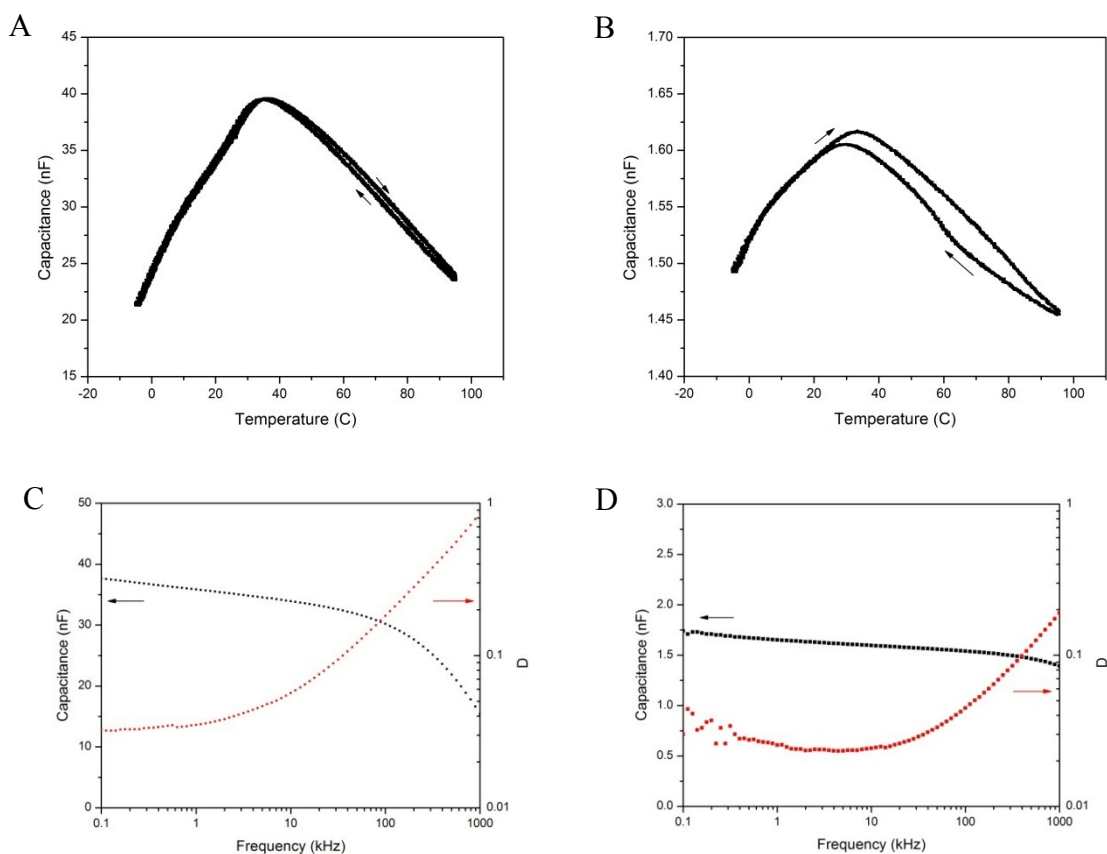
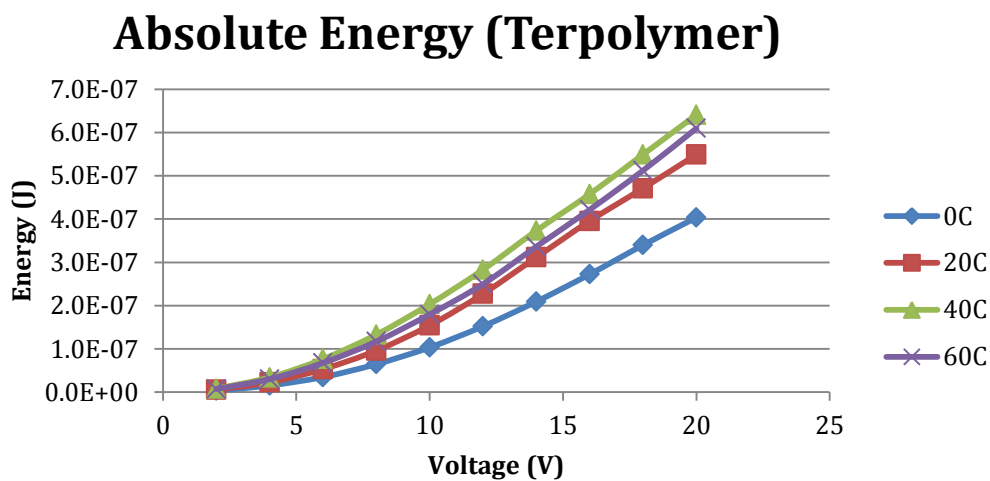
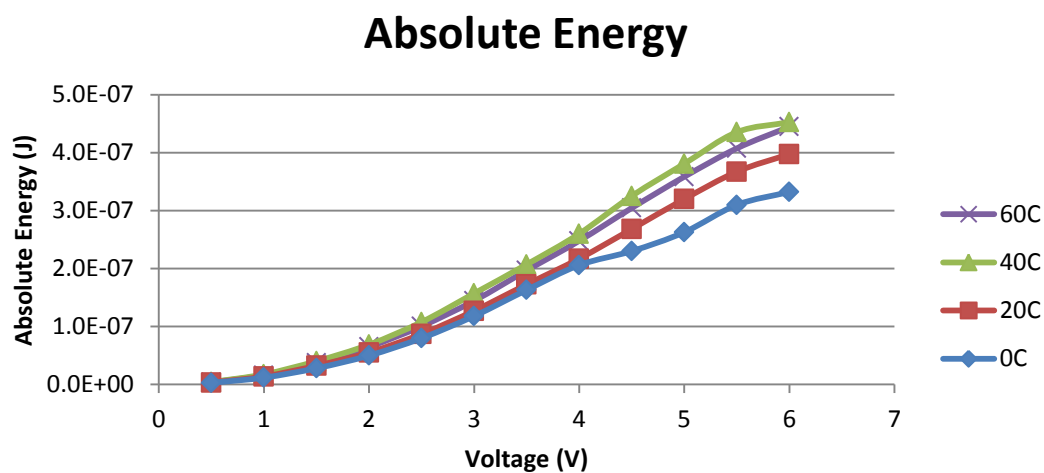


Figure 7-7. Dielectric results for octadecylphosphonic acid coated barium titanate in a PVDF terpolymer. (A) Temperature dependence on capacitance for a sample with 13% BTO. (B) Temperature dependence on capacitance for a sample with 54% BTO. (C) Frequency dependence on capacitance for a sample with 13% BTO. (D) Frequency dependence on capacitance for a sample with 54% BTO.

A



B



C

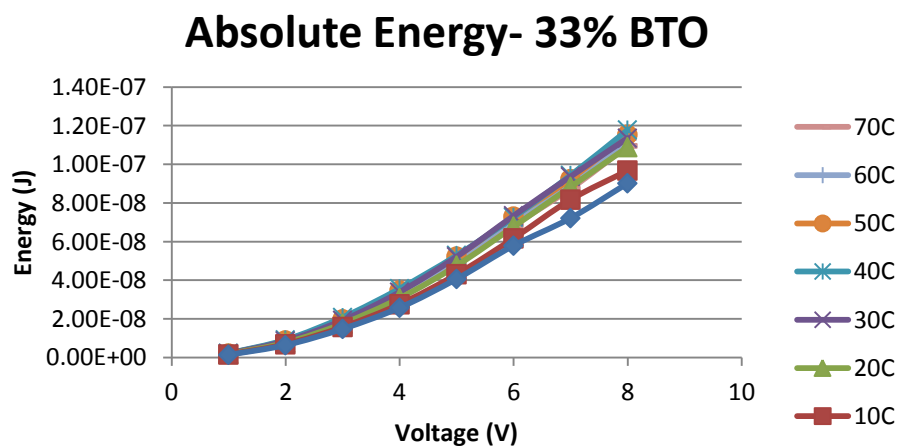
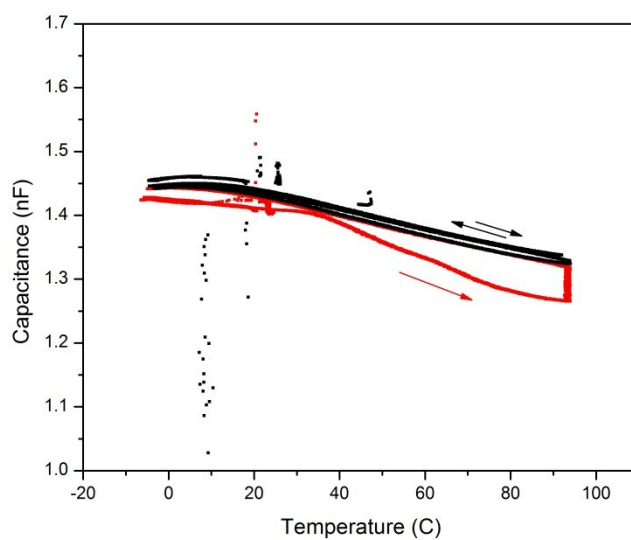


Figure 7-8. Energy for terpolymer composite samples as a function of temperature, including (A) pure terpolymer, (B) 13% BTO composite, and (C) 33% BTO composite films.

A



B

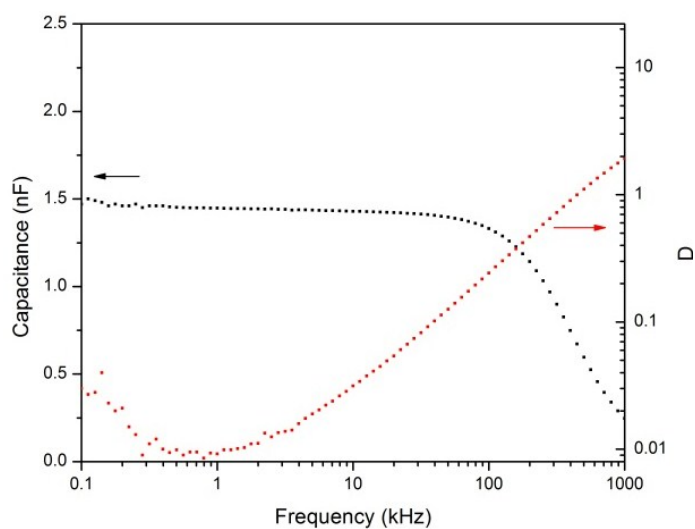
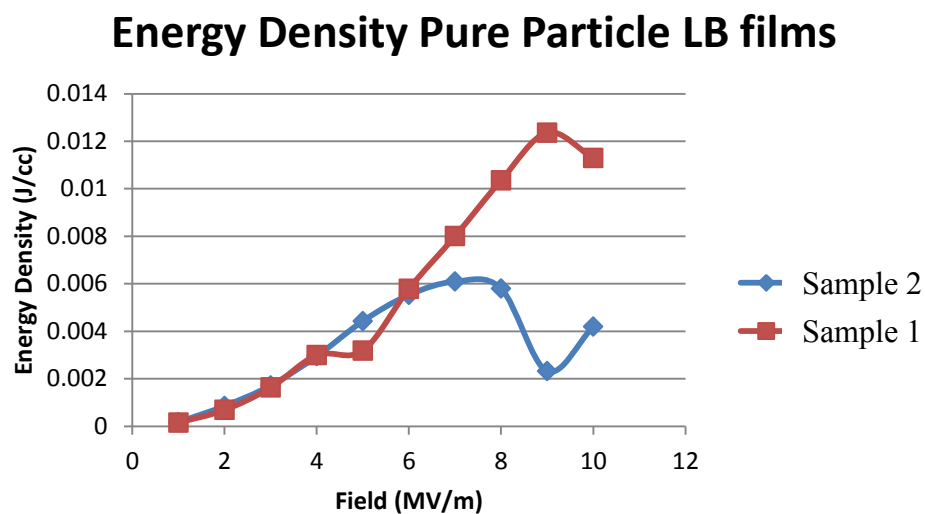


Figure 7-9. Dielectric data for LB films made of ODPA-coated BTO. (A) Temperature dependence of the capacitance and (B) frequency dependence of the capacitance for a film containing only coated nanoparticles, with no terpolymer layers.

A



B

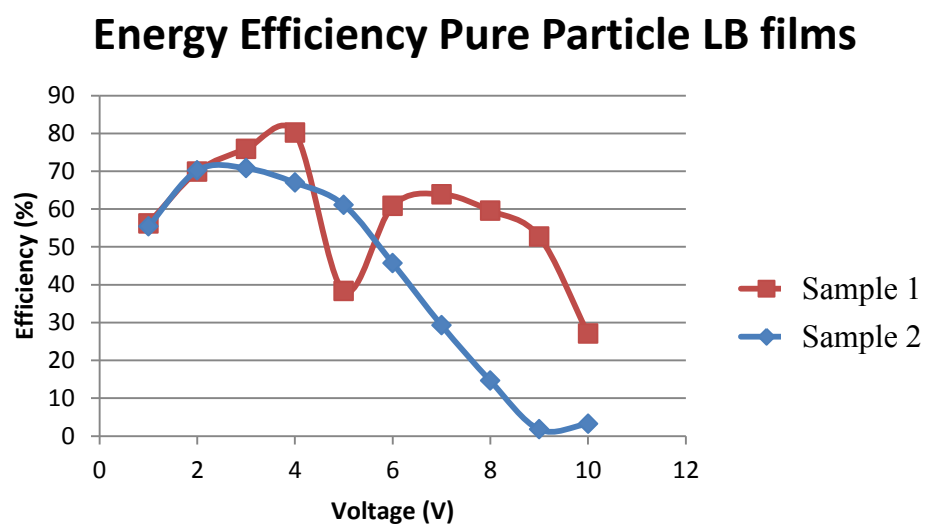


Figure 7-10. Energy density results for a LB film constructed with 20 depositions of ODPA-coated BTO nanoparticles. (A) Energy density for two typical samples. (B) Energy efficiency for two typical samples.

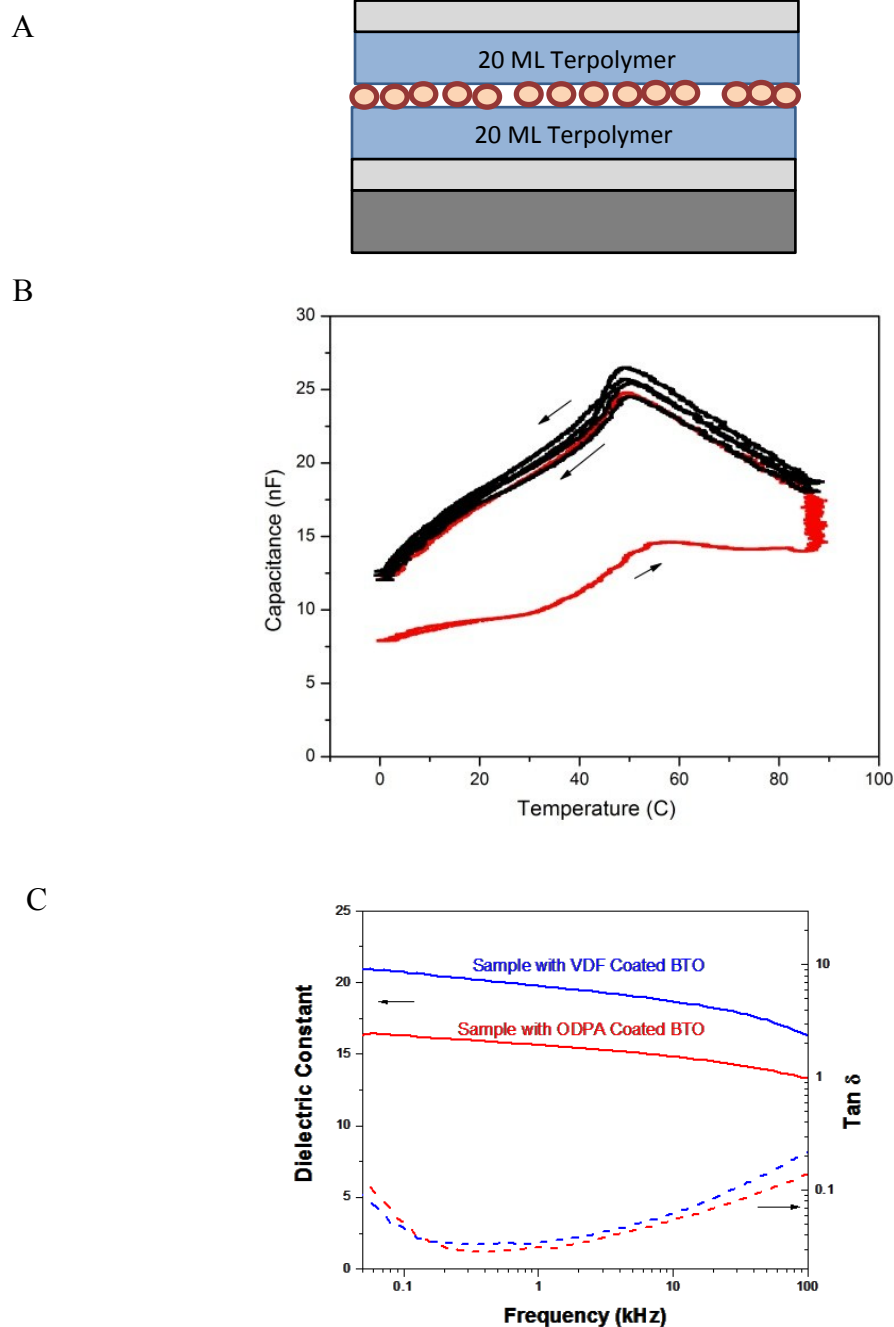


Figure 7-11. Multilayer composite films. (A) Sketch of a typical sample with two layers of polymer and a layer of particles. (B) Temperature dependence of a sample with 20 ML of terpolymer, 3 layers of ODPA-coated BTO nanoparticles, and 20 more ML of terpolymer. (C) Comparison of a sample with VDF oligomer coated particle film with an ODPA-coated particle film. Both samples had 20 ML of terpolymer above and below the 3 particle layers.

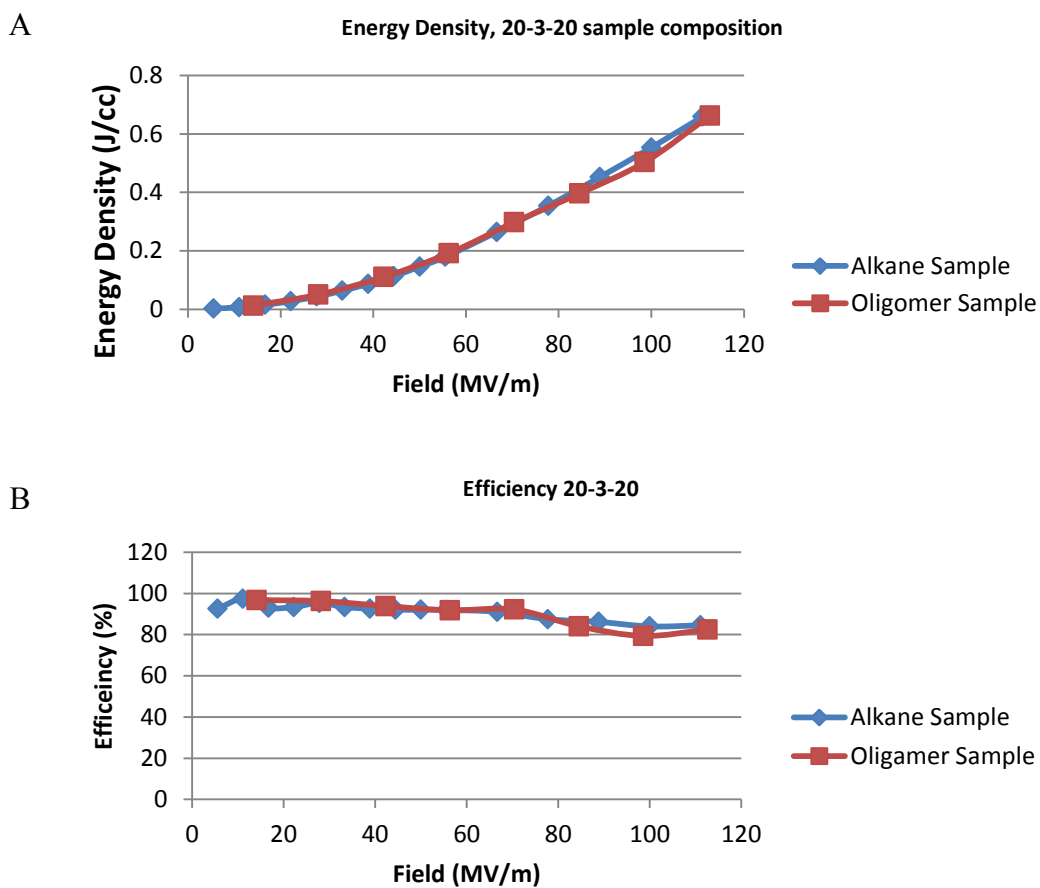
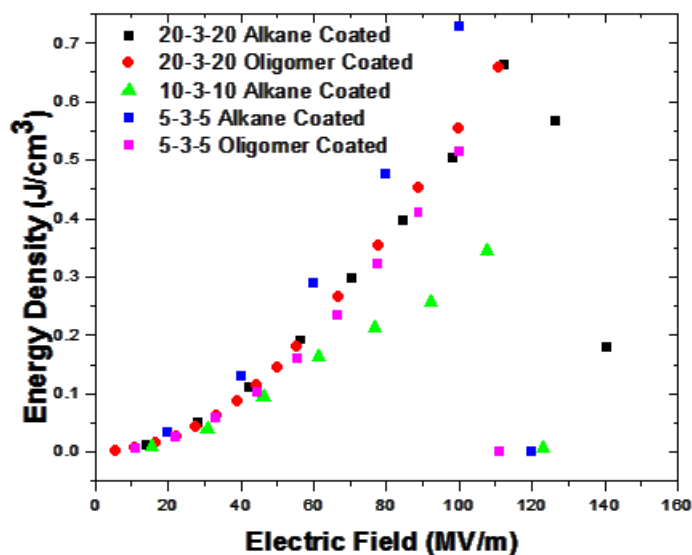


Figure 7-12. Comparison of energy results for samples made with 3 layers of ODPA-coated particles and VDF oligomer coated particles. (A) Energy density comparison for the two films. (B) Energy efficiency for the two films.

A



B

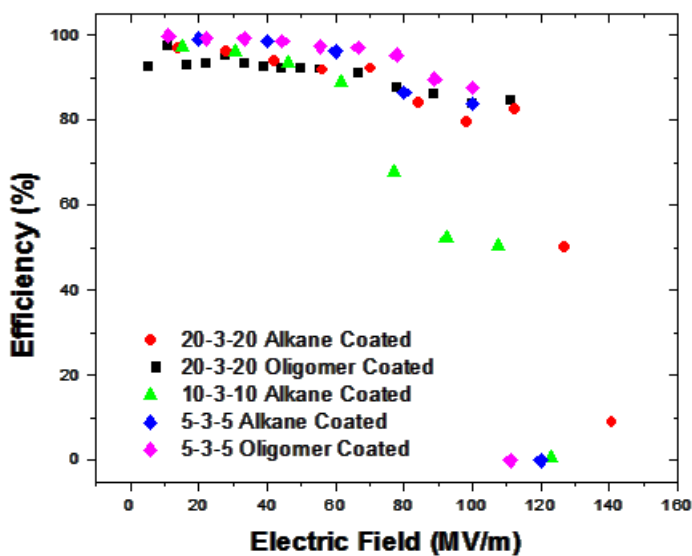
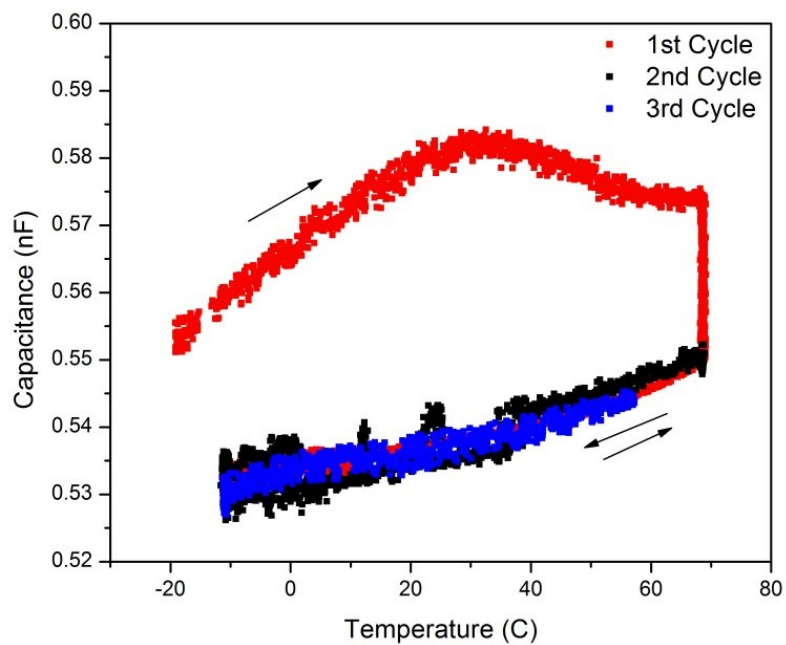


Figure 7-13. Comparison for the series of multilayer samples, of configuration A/B/A where A is the number of terpolymer layers and B is the number of particle layers. (A) Energy density for the multilayer films. (B) Energy efficiency for the multilayer films.

A



B

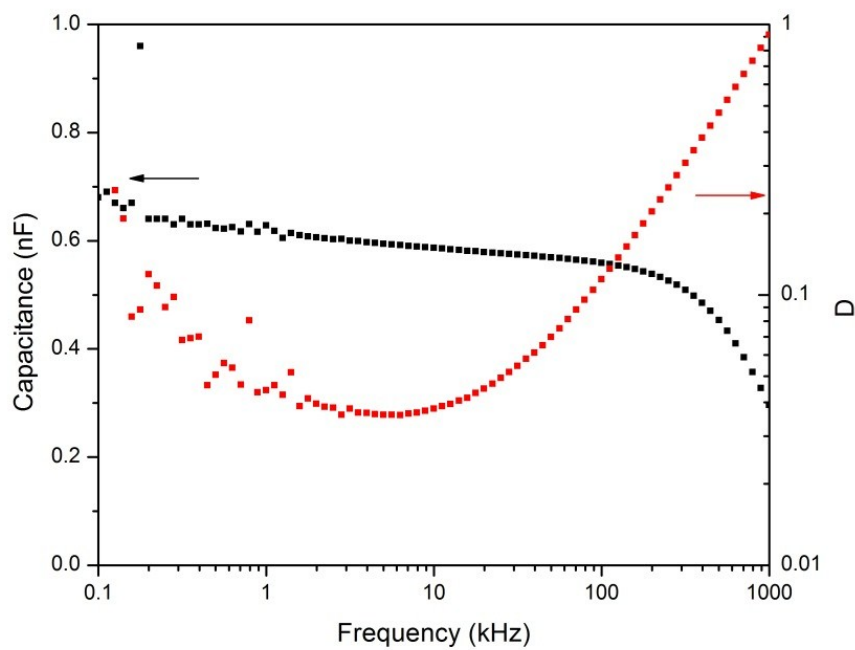
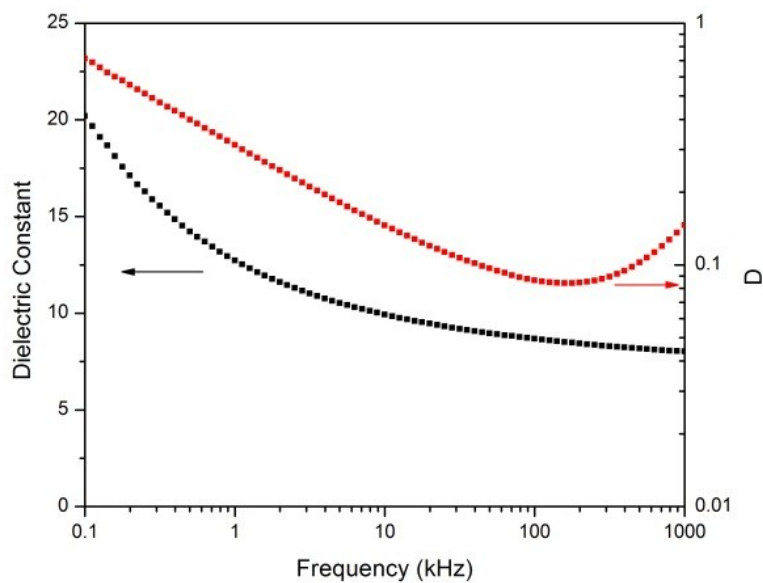


Figure 7-14. Dielectric results for uncoated titanium dioxide particle samples made by cluster deposition. (A) Temperature dependency of the capacitance for three temperature cycles. (B) Frequency dependence of the capacitance.

A



B

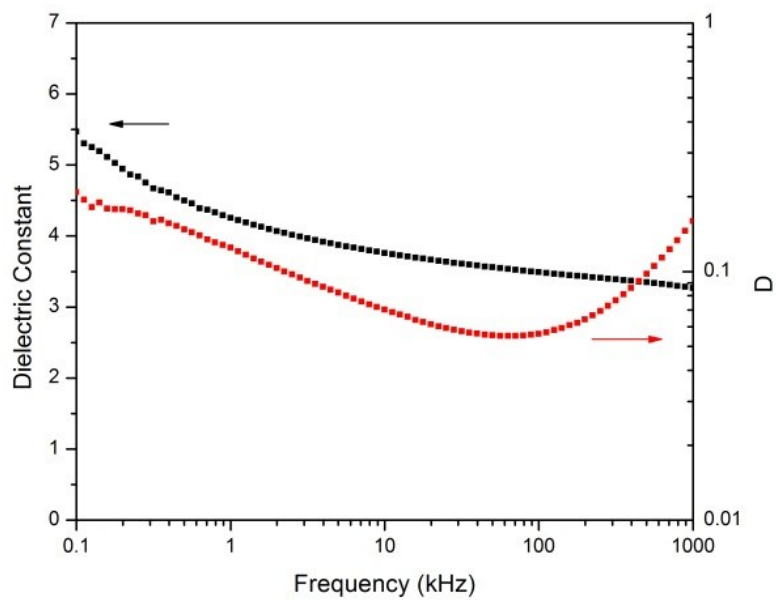


Figure 7-15. Frequency dependence for titanium dioxide nanoparticles coated in paraffin at (A) 110 °C and (B) 170 °C with the cluster deposition system.

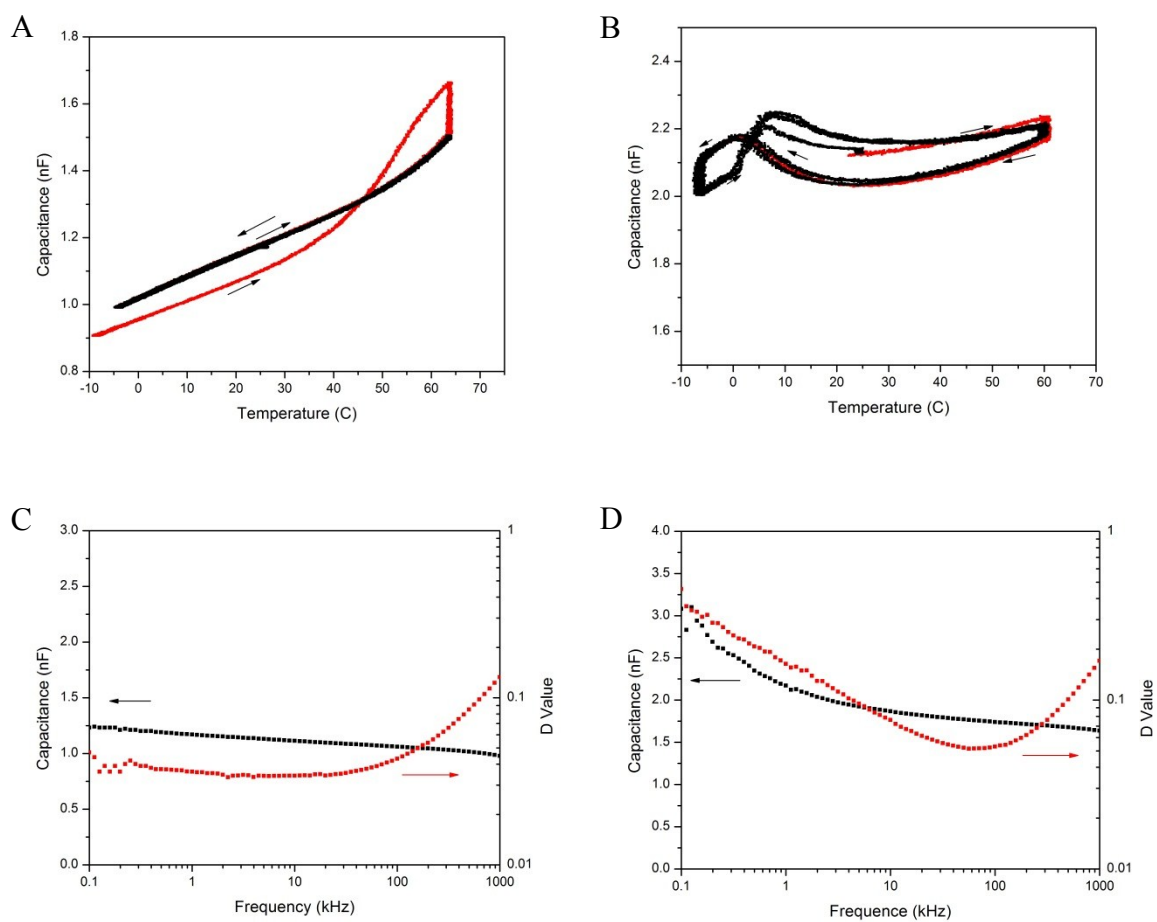


Figure 7-16. Comparison of two films of VDF oligomer coated titanium dioxide nanoparticles. The temperature dependence results are shown for (A) Sample 1 and (B) Sample 2. The frequency dependence on the capacitance for (C) Sample 1 and (D) Sample 2. The two samples were supposed to be of the same composition.

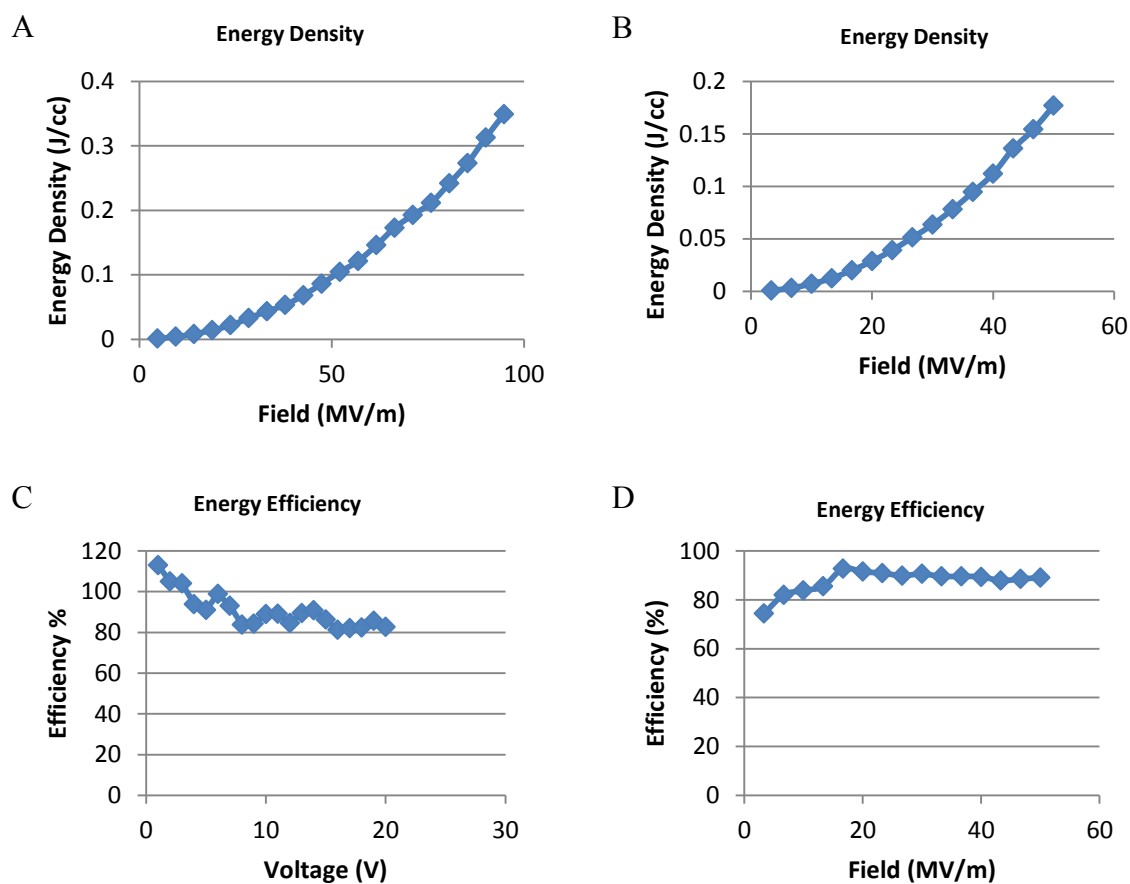


Figure 7-17. Energy measurements for VDF oligomer coated titanium dioxide nanoparticles. The energy densities are compared for (A) Sample 1 and (B) Sample 2. The energy efficiency for (C) Sample 1 and (D) Sample 2 also show a different trend for the same type of sample.

## CHAPTER 8

### THE EFFECTS OF HUMIDITY ON THE DIELECTRIC AND FERROELECTRIC PROPERTIES OF PVDF

#### 8.1 Introduction

Having an understanding of how humidity affects the ferroelectric and dielectric properties is important because the applied uses for the material will occur in the real world where there is an atmosphere containing water vapor, in locations such as Nebraska summer days and on ships at sea. It is important to know how changing environments will affect the PVDF film properties when used in a memory or FET[1-3], an actuator[4, 5], a transducer[6], force sensor[7], a solar cell[8, 9], a humidity sensor, or a capacitor[10, 11]. There have been multiple studies where carried out under vacuum or in an inert atmosphere such as nitrogen gas. However, water vapor was not a contributing factor in these studies. Therefore, it is important to see how the introduction of humidity could affect the ferroelectric and dielectric properties.

The investigation into the effects of humidity started as an investigation into the dielectric anomaly found around 30° C upon heating in poly(vinylidene fluoride-trifluoroethylene) Langmuir-Blodget films. Earlier studies had originally attributed the anomaly to a first order ferroelectric transition [12], as shown in Figure 8-1. When a film is heated in ambient laboratory air, a peak representing a dielectric anomaly occurs in the capacitance versus temperature graph between 0 and 30 degrees Celsius. However, the peak is no longer present when the experiment is repeated in a dry nitrogen atmosphere [13]. Also, the peak does not appear when the sample is heated in a vacuum.

This implied that there was something in the air that was responsible for the change in dielectric properties. The most likely candidate was water vapor.

Very little work has been done on the effect of humidity on dielectric and ferroelectric thin films prior to our investigation. In this investigation, a series of experiments were performed to probe the effect of humidity on thin ferroelectric films. This included basic measurements on how the humidity entered and exited the samples, and where it went when it was inside of films. By examining both the XRD and dielectric desorption studies, it was observed that the humidity went into the crystal lattice and did not leave quickly. Also, variations in the dielectric constant was observed as a function of temperature at constant humidity and how it changed when the temperature was held constant and the humidity level was ramped. Lastly, it was examined the how the polarization was affected through capacitance-voltage sweeps and pyroelectric hysteresis loops at various humidity levels. The results of these experiments are presented in this chapter.

## **8.2 Sample Preparation**

All of the samples used in this series of experiments were made with a standard configuration, as shown in Chapter 2. The samples were made on one inch square pieces of glass cut from microscope slides. Aluminum electrodes were deposited vapor deposition (50 nm thick) on the glass substrates to allow for the study of the dielectric properties. The films were then deposited onto the glass substrate by Langmuir-Blodgett deposition [14] as described in Chapter 2, Section 2.2.B. All of the samples for this series of experiment are made of 70:30 P(VDF-TrFe) copolymer with the exception of

the sample used for the x-ray diffraction study, which was 80:20 copolymer. The samples for dielectric studies then had a top electrode deposited on them to complete the parallel plate capacitor. The samples were then annealed at 130 °C for one hour. For the constant temperature studies, non-equilibrium temperature studies, voltage sweeps and pyroelectric signal studies, the samples ranged in thickness from five monolayers to 30 monolayers. For the desorption studies, all of the samples were 5 monolayers thick. The desorption study samples were kept thin so the entire sample would act like the top surface layers whereas the samples that had voltages applied to them had to be thick enough to not break down quickly.

Once the samples were made, electrical connections had to be attached to the samples. This was done with several different methods using thin copper wires which were attached to the electrodes and soldered to the sample holder. See Chapter 2, Section 2.2.E.c for more details. For the early studies, leads were attached to the sample with a colloidal silver paint. Since the humidity caused the paint to delaminate from the electrodes, the leads were soldered to the sample with indium metal in later studies, as shown in Chapter 2, Figure 2-8. Indium has a low melting point of 157°C [15], so it was possible to attach the leads without transferring too much heat to the sample and damaging it.

### **8.3 Experimental Setup**

The sample measurements were made in a specially designed chamber for the humidity experiments. The chamber is larger than the traditional stages since it was necessary to allow for the atmosphere to reach equilibrium at the sample. The chamber

was milled from a copper block and had multiple connections for gas lines and electrical inputs, as shown in the sketch and photograph of the chamber Figure 8-2. The copper lid had two holes to allow the humidity sensor and laser light to enter the chamber for the pyroelectric measurements. The dry nitrogen gas and the humidified nitrogen gas entered from the side of the chamber and mixed to reach the desired humidity level. On the opposite side of the chamber, there was an additional uncovered gas port to allow the gas to escape and to prevent the buildup of pressure in the chamber. There was no evidence of room moisture reentering the chamber as the dry gas flowed into the chamber.

The temperature was controlled by Mylar heaters (Minco model HK 5163 R78.4L12A), thermoelectric solid state coolers (Custom Thermoelectric model 07111-5L31-06CL), and a water cooling system. The heaters were controlled by a feedback loop using a platinum resistive temperature device (RTD) and controlled by an Omega CN 2041 temperature controller. The RTD was embedded into the base of the sample chamber, just below the sample. This allowed for control of the temperature of the stage at  $\pm 1^{\circ}\text{C}$  when there was no gas flowing. When gas was flowing into the chamber, the temperature controller was within a few degrees of the set point, depending on the gas temperature and flow rate. When the gas temperature was at a similar temperature as the chamber set point, the temperature fluctuations were similar to the case of no gas flowing. When the stage was raised to a high temperature or decreased to a low temperature, there could be an offset from the set point as large as five to 10 degrees Celsius. A thermocouple measured the sample temperature inside of the chamber.

To allow for electrical connections, the stage had a pair of BNC connectors on the outside of the sample stage connecting to a pair of soldering pins on the inside. The

copper wires attached to the sample were soldered to the pins and the outside connections were attached to various measurement apparatus using BNC cables. When a 4 wire connection was needed, BNC “T” connectors were used at the sample box to convert the two wire connection into a 4 wire connection.

The production and control of the humid nitrogen air entering the chamber was a two part process, each with its own feedback loop. The first part was a feedback loop that regulated the ratios of dry and moist air entering into the chamber. The second feedback loop in the setup controlled the temperature of the gas and water entering into the sample stage, as shown in Figure 8-3 .

The first feedback loop which regulated the flow of gas into the sample chamber consisted of a polymer humidity sensor (HYCAL Sensing Products, Model HIH-3206-C), a pair of normally closed valves (Omega PV101-5V), and a logic controller (CN4420 Series Temperature/Process Controller). The humidity sensor output a voltage proportional to the humidity in the chamber. This voltage was passed into the humidity controller and to the A to D board where it was recorded by the computer. Since the controller was designed for a single valve, and it was observed that the gas flow rates fluctuated too much with just one valve, the voltage output meant for the single valve was fed into the A to D board at the computer. The computer then calculated how much voltage should go to both valves so the flow rate of air would be nearly constant. Each of the valves was connected to one of the ultra-high purity nitrogen gas lines entering the chamber. One of the gas lines went directly to the sample chamber; the other went through a humidity producing chamber, shown in Figure 8-4.

The humidity production chamber was responsible for the production of the moist air that entered the chamber. One of the challenges with flowing air into the chamber was to prevent the sample temperature from fluctuating too much. This meant that the incoming air needed to be fairly close to the same temperature as the rest of the chamber to prevent condensation and temperature dependent artifacts. To do this, two variations of the humidity setup were used. The basic humidity production chamber was a one liter flask approximately half full of deionized water, as shown Figure 8-5. Two pieces of plastic tubing ran through a rubber stopper and into the flask. One piece of tubing went into the water and produced a current of moist air. The second piece of tubing was above the water line and took the moist air to the sample chamber. There was also an RTD coated in waterproof sealant submerged in the water that fed back to an Omega CN9000A temperature controller with a programmable set point.

For experiments above room temperature, a hot plate was regulated by the temperature controller and the water was set slightly above the temperature of the chamber. This allowed the carrier air flow to pick up a relatively high amount of humidity. For the highest temperature trials, tape heaters were attached to the copper gas lines to help keep the gas from cooling and condensing. Finally, foam insulation was wrapped around the tubing to help it maintain its temperature.

The challenge for the experiments below room temperature was to prevent the gas from greatly increasing the temperature of the sample. An ice bath was used to cool the gas and water flask, as shown in Figure 8-4B. The outer container was a 5 gallon bucket with several holes cut into the lid to allow the gas lines and wires to enter. The flask sat

in a smaller plastic bucket, about 6 inches in diameter. There was a ceramic tile and a blanket heater (Brisk Heat model SRL 06061) in the bottom of the smaller bucket. The ceramic tile served as a thermal insulator to reduce the amount of heat flowing into the ice bath from the blanket. The heating blanket was used to raise the temperature of the water in the flask above the temperature of the ice bath. The flask sat directly on top of the heater blanket. This setup allowed us to control the temperature of the humid gas entering the chamber. The dry air line passed through a series of copper tubing coils in the ice water bath. This was especially important on summer afternoons when the sun would directly hit the gas tanks and heat them up.

### *8.3.A Temperature Dependence of the Capacitance at Low, Medium and High Humidity Levels*

The first property we examined was the temperature dependence of the capacitance. In this study, the humidity was held relatively constant while the temperature was increased and decreased at a constant rate. The relative humidity (RH) levels were either low from the dry nitrogen gas (close to 0%), medium from the ambient air (approximately 40% RH), or high when humidity was introduced into the sample chamber (up to 93% RH).

The temperature was controlled with a feedback loop system described in the previous section. The controller was programmed to linearly increase the temperature at the rate of 1°C per minute, to soak for a designated amount of time, and then decrease linearly in temperature at the rate of 1°C per minute. For the low and medium humidity scans, the sample was cooled from room temperature to -15°C and then heated to 40°C or

70°C, depending on the run. It was then cooled back to -15°C before returning to room temperature. In the low humidity case, dry nitrogen air was flowing into the chamber the entire run. In the medium humidity case, ambient air was used and no gas beyond the normal atmospheric conditions was entering the chamber.

For the high humidity trial, the scan started at 15°C due to concerns about condensation if taken below freezing. The sample was heated to 60°C and then cooled back to 15°C. For this experiment, a primitive version of the humidity production system described earlier was used. It consisted of the flask and gas tubing. This gave us a high humidity level. The HP 4192A Impedance analyzer was used to measure the capacitance. Both the capacitance and the temperature were recorded by a computer using Labview, version 6.1.

### *8.3.B Dependence of Capacitance on Relative Humidity at a Constant Temperature*

The next set of measurements was performed with the temperature held constant while the humidity was linearly increased and decreased at the rate of 1% RH per minute. As with the previous experiment, the humidity levels are controlled with the dual valve system that mixes dry air with humid air to maintain the desired level of humidity in the chamber. The capacitance for this experiment was measured with the HP 3192A impedance analyzer.

### *8.3.C Enthalpy and Activation Energy of Humidity in PVDF*

The capacitor was first heated at the rate of 1°C per minute in a dry nitrogen atmosphere to 80°C and then cooled to the desired temperature at the rate of 1°C per

minute. The desired temperature was held constant for the remainder of the run. This experiment was run over a large range of temperatures from 5°C to 80°C at 5 degree intervals.

Humidity was introduced into the chamber at the rate of 0.4% RH per minute, until it reached 80%, and this level was maintained for 20 minutes. The humidity was turned off and nitrogen gas was then used to flush the chamber. The capacitance of the sample was measured with a Quadtech 1689M Digibridge. The drying curves were analyzed in an attempt to calculate the enthalpy and the activation energy of the vapor leaving the films.

#### *8.3.D Dependence of Capacitance on Applied Bias at a Constant Relative Humidity*

It was desirable to learn about the ferroelectric switching properties of the materials. The voltage was increased until the polarization was saturated and then linearly returned to zero volts. This was then repeated for the negative bias. This type of measurement in this chapter was made with a different technique due to the unavailability of the HP Impedance Analyzer and since the Quad Tech Digibridge did not have a built in bias sweep capabilities. See Figure 8-5 for a sketch of the setup. The voltage was applied to the sample using the SRS DS345 programmable function generator. When voltages larger than the voltage that the function generator could output were needed, a voltage amplifier was used. The voltage is applied to an Agilent 160656 external bias adaptor which allows the Quadtech to measure the capacitance of the sample while protecting it from the applied voltage. The voltage applied to the sample was a triangle wave and it swept through the voltages at a sweep rate of 40 seconds per volt. This value was picked

because it was similar to the rate that the voltage is increased for the HP impedance meter with a triangle step wave and it worked well with the rate that the QuadTech's computer could collect data. Using the same humidity control setup described previously in this chapter, the humidity was set at 10% intervals for the voltage scans ranging from 0 to 80% relative humidity. The temperature was held at 40°C.

### *8.3.E The Effect of Relative Humidity on the Pyroelectric Hysteresis of PVDF*

Another method to examine the effect of water molecules on the polarization properties of the films is to look at the hysteresis in the pyroelectric response, which is proportional to the electric polarization in the sample. This was done using the Chynoweth method [16-20] for measuring the pyroelectric current. For this measurement, the sample was rapidly heated and cooled using a laser, and the current produced was measured by a lock-in amplifier. For this series of experiments, the entire experiment was controlled by a Labview Virtual Instrument. More details on the experimental setup and theory of the measurement are discussed in Chapter 2.

For this study, two capacitor samples made by Langmuir Blodgett technique were constructed with 70/30 PVDF-TrFe were studied. The first was 30 monolayers and the second was 15 monolayers. For all of the pyroelectric measurements, the sample environments were first carefully controlled. The sample was first heated to 80°C and then cooled to 40°C under dry nitrogen gas to remove any moisture that was in the sample. Once the sample temperature was reached, humid nitrogen air was introduced into the chamber until the desired humidity level was reached.

## 8.4 Results

### *8.4.A Temperature Dependence of the Capacitance at Low, Medium, and High Humidity Levels*

The dielectric response to the change in temperature largely depends on the environment in the chamber. When the surrounding environment is heated or cooled, the relative humidity within the chamber changes. Since these experiments did not have the system built to control the humidity precisely throughout the run, the humidity fluctuated based on the environment inside and outside of the sample chamber. This means two similar runs may have different shaped peaks due to subtle changes in the environment. Figure 8-6 shows two typical results.

For Figure 8-6A, the sample was heated in ambient air and dry nitrogen gas. The black curve is the temperature scan in dry nitrogen gas. The red curve was the temperature scan performed in atmospheric conditions. The curve made in air starts at 20 °C and decreases to -15 °C. As the moisture condenses in the sample, the capacitance value reaches a constant value. This is due to the decrease in dielectric constant expected from cooling a sample and the increase in the dielectric constant from the water entering the polymer crystal lattice [21]. As the temperature crosses zero, the water freezes and the capacitance starts to decrease more quickly. The formation of ice would cause the dielectric contribution from the water molecules to increase from a value of about 73 to over 100 [15, 22]. This would also decrease the slope of the capacitance curve with respect to temperature, even after the dielectric contribution from the polymer should have started dropping sharply in a dry film.

On heating, broad peaks in the range of 15-30°C appeared in the dielectric data when the water started to melt. As the water evaporated from the sample, the capacitance quickly decreased until it reached nearly the same value as the black curve. The black curve was the dry nitrogen gas curve. The dry gas had very low moisture content, less than 0.001% by volume, so the chamber contained little moisture. The black curve contains no large peaks.

Figure 8-6B is a different set of temperature dependent sweeps. The setup for this one was more preliminary. Instead of using the polymer humidity sensor, an environmental sensor was placed into a large beaker and the air flowed through the beaker on its way to the sample chamber. The humidity level was measured at room temperature, showing an upper limit on the amount of moisture that entered the chamber.

The temperature sweep made in dry nitrogen gas was linear, showing no hysteresis due to water or a transition in the film. This was important because if the secondary phase transition was present in the thin film, it should show a feature in this set of data. The ambient air data showed broad peaks starting around 20 °C. It is not as pronounced as the peaks in Figure 8-6A, most likely due to less moisture in the air at the time of the run. The amount of moisture in the ambient air was dependent on the lab conditions, such as humid summer days compared to dry winter days. Also the humidity levels fluctuated depending if it was raining outside or if the air conditioning was running.

The high humidity run was made at higher temperatures to prevent large amounts of condensation from depositing on the sample or flooding the chamber. There was a

broad heating peak that covers the similar ranges as the ambient air peaks in Figure 8-6A, from about 0 °C to 45 °C. When the sample was cooled, the peak starts around 30 °C, sooner than the ambient air cooling peaks in either plot. This is likely due to the air in the high humidity case reaching saturation (100% relative humidity) sooner than the ambient air, and condensing on the sample at a higher temperature.

#### *8.4.B Dependence of Capacitance on Relative Humidity at a Constant Temperature*

When the temperature was held constant and the humidity increased, the capacitance increased linearly with increased RH. There was no noticeable hysteresis in the films, as shown in Figure 8-7. This was observed for temperatures from 10 °C to 60 °C. The increase in the capacitance had the following linear form,

$$C = C_0 + a[RH] \quad \text{Equation 8-1}$$

where  $C$  was the capacitance,  $C_0$  was the capacitance at 0% relative humidity,  $a$  was a constant, and  $[RH]$  was the relative humidity level.

The added humidity caused the capacitance to increase by 1 pF per 1% relative humidity at 40C. The volume percentage of water in the film can be estimated for 80% relative humidity at this temperature. The dielectric contribution from water was approximately 73 at this temperature [15, 22], so the calculated percent volume is 0.046% for a 20 layer film. This calculation was made with the assumption that the film does not swell during the adsorption of water. Later studies [21], showed that the film could swell as much as 10% when submerged in water. To measure the change in thickness caused by exposure to 80% RH, a separate experiment such as interferometry should be performed. Also, the

DC conductance of the sample follows the same trend as the capacitance, indicating the water vapor is in the bulk of the film, not just the electrode or the surface of the film. If the water was only on the surface of the film or between the electrodes and the film, the overall conductance would not increase, as this would be the same situation as having a thicker electrode. Since the overall value increased, this supports the water being distributed through the film. The change in capacitance for non-equilibrium and equilibrium conditions can be attributed to a change in dielectric constant due to water vapor entering the film.

#### *8.4.C X-ray Defraction of Swelled Films*

The results of Jacobson et al. [21] showed that the presence of water caused the crystal lattice to expand. A 100 ML 80:20 sample was deposited onto a  $1\text{ cm}^2$  Si (111) substrate. The crystal lattice properties were measured with a RigakuD/Max-B  $\theta$ -2 $\theta$  xray diffractometer after the sample had been freshly annealed, after 50 hours of contact to water, 120 hours of contact, 240 hours of contact, and then after the sample was annealed at the end. As seen in Figure 8-8A, the dry PVDF film has a peak at 20 degrees [14]. The  $\langle 110 \rangle$  lattice spacing was measured for a film that has been freshly annealed, 50 hours of contact, 120 hours of contact, and 240 hours of contact. As water vapor is exposed to the sample, the polymer swells due to water entering the bulk crystal lattice. The initial dry film has a peak from 4.35 to 4.45 Å. When it is exposed to water for long periods of time, the lattice expands to 4.55 Å. This is an increase of 0.2 to 0.8 Å after exposure to water and an increase of about 4%. By annealing the sample for 3 hours at 110°C, the original spacing is recovered, as shown in Figure 8-8B. This demonstrates

that the water is slowly entering the bulk of the crystal and expanding the crystal lattice. At least some of the water is interstitial and the change in the crystal lattice is reversible.

#### *8.4.D Enthalpy and Activation Energy of Humidity in PVDF*

Since some of the water is interstitial in the crystal lattice and not solely on the surface of the films or in the amorphous regions, we wanted to know how quickly the water leaves the film and to determine what was the activation energy for the water to leave the films. In order to study this phenomenon, samples were exposed to water vapor and then dried out. The decay of the capacitance curve was analyzed in an attempt to determine the time constants for the water leaving the film.

Langmuir-Blodgett samples with 20 ML thicknesses were placed into the sample chamber. The chamber was first heated to 80°C at the rate of 1°C per minute in a dry nitrogen atmosphere to bake the chamber and sample dry, as shown in Figure 8-9A. Then, the sample was cooled to 20 °C. This was to give all of the runs the same initial condition. An example of the humidity and capacitance data is shown in Figure 8-9 through Figure 8-12. The sample was held at zero percent relative humidity while the temperature was increased to the final set point, as shown between points 1 and 2 in Figure 8-9A. After point 2, the temperature was held constant for the remainder of the run, in this case, 80 °C. The humidity was then introduced into the chamber at the rate of 1% per minute. The capacitance follows the same trend as the humidity, as shown in the close up of the humidity loading phase in Figure 8-9B. In Figure 8-9A, at point 3, the humidity is held at a constant 60% RH for one hour. At the end of this hour, the moist air was turned off and dry gas is flushed into the chamber, as marked at point 4 in Figure

8-9A. At this point, the humidity and capacitance drop quickly, and after about 45 seconds, the chamber is nearly dry. See Figure 8-10, where the first 45 seconds of data are shown in red. After the initial flush of the sample box, the humidity sensor would read a constant, small value. Since the first 45 seconds were not in equilibrium, this data was excluded from the analysis of the activation energy.

The decay curves are fit using Origin's least squares data fitting algorithm, as shown in Figure 8-11A. This data was fit using the model for two exponential decays, in the following form:

$$y = y_0 + A_1 e^{-x/t_1} + A_2 e^{-x/t_2} \quad \text{Equation 8-2}$$

Where  $t_1$  and  $t_2$  were time constants,  $A_1$  and  $A_2$  were constants of proportionality, and  $y_0$  was the background capacitance.

Once the double-exponential model is fit to the data, the background capacitance fitted by the  $y_0$  term in the capacitance was subtracted from the data, as shown in Figure 8-11B. The natural log of the data was then taken and it was plotted versus time. See Figure 8-12. The linear portion of the natural log plots are related to the time constants by the following discussion.

A generic exponential decay has the form of  $y = e^{-\beta t}$ . When the natural log of both sides was taken, we get  $\ln(y) = -\beta t$ . We also know that the time constant  $\tau = 1/\beta$ . Our data that has been plotted has the form of  $\ln(y) = Bt$ . This means that  $B = -\beta$  and  $\tau = 1/-B$ . The example data shown in Figure 8-12B showed two linear sections of data. The first linear section of data was the short time constant while the

second linear region is the long time constant. The example data had a slope for the short time constant shown in Figure 8-12A of  $1.58 \times 10^{-3} \text{ s}^{-1}$ . This gave us a short time constant of 633 seconds. The slope for the long time constant was  $-5.10 \times 10^{-5} \text{ s}^{-1}$  which means the time constant was 19608 seconds. It was predicted that the two time constants,  $t_1$  and  $t_2$ , correspond to the humidity leaving the sample surface or chamber, and to the humidity leaving the bulk of the sample. This procedure was repeated for multiple runs over a range of temperatures from  $10^\circ$  to  $80^\circ\text{C}$  in 5 degree intervals.

There are two scenarios that we should consider for the way the water interacts with the films. The first is where the water vapor bonds to the polymer creating a new system. The second scenario was where the water enters the lattice, filling in spaces between the polymer, but does not bond.

In the first scenario, we should have to break the bond energies for the water to leave the film. In this case, the initial drop was caused by the humidity leaving the chamber, and the tail was caused by the water vapor leaving the film. The time constant should be longer for lower temperatures and decrease as the temperature increases, producing a negative slope when the time constants were plotted versus the temperature.

In the second scenario, the water inserts itself into the lattice, causing a strain on the polymer. Since there is no bonding occurring between the polymer and the water, the time constant should be the same as the water from the surface with no additional energy required. For this situation, the time constant versus temperature plot would have no slope or obvious trends.

When the time constants were plotted versus temperature, there is no evident temperature dependence, as shown in Figure 8-13. When the data is fitted with a line, there is a slight downward trend, but the uncertainty in the fit is of the same value of the fit itself. This means that the activation energy would be small, with an average long time constant of  $220 \pm 55$  min and the average short time constant of  $9.2 \pm 3.0$  min. We hypothesized that the short time constant depends on the water leaving chamber and the long time constant is related to the water leaving the sample. Due to an inability to control the environment around the sample well enough, there was a large fluctuation in the time constants measured with this method.

The other paper to study the desorption times was done by Martin, et al. [23] They measured the desorption by a different method than our study. The sample was held at 100% RH and a 1 volt bias source was applied to the sample, as shown in Figure 8-14. The resulting transient current was then measured with an electrometer. The water was removed by decreasing the pressure, causing it to evaporate. The current was recorded with respect to time, and when the value reached the same value as the pre-high humidity conditions, the sample was declared dry. The authors proposed a time constant of about 100 seconds for the desorption of the water from the film. This is the same time scale as our short time constant. By examining the inset in Figure 8-14A, there appears to be a decrease in the current data over the long tail. I suspect this data maybe showing the same effect as our long time constant. Further examination of their data may also show the same long time constant.

#### *8.4.E Dependence of Capacitance on Applied Bias at a Constant Relative Humidity*

Voltage scans were made on samples while monitoring the effect on the dielectric properties. For this study, a 30 ML sample was held at various humidity levels ranging from 0% to 80% relative humidity. For all of the runs, the temperature was held constant at 40 °C. The voltage was applied using the function generator, which means that the run did not always start at zero volts; rather it started wherever the function generator was in the cycle. Each humidity set point for the CV ran between 2 and 17 cycles. For most humidity levels, each of the cycles were similar to the previous cycle and very little decay was observed, as shown in Figure 8-15 and Figure 8-16.

At low relative humidity levels, up to 40% RH, there is no significant change in the capacitance with the increase in humidity. Near 50% RH, there was a significant additional drop in the capacitance, most likely from degradation caused by cycling of the sample. As the humidity levels continue to increase, the capacitance levels continue to drop. In the final CV, the sample was returned to 0% RH, and the capacitance decreased by about 20% compared to the original 0% RH scan, indicating some degradation in the sample.

In addition to the change in capacitance values, one also sees a change in the switching peak positions with changes in humidity levels, as shown in Figure 8-17. At low humidity levels, the coercive voltage decreases by about 30%. This would imply that the polarization switches more readily. Once the sample has reached a moderate level of humidity, around 40-50%, the coercive voltage starts to increase. This is in agreement with the pyroelectric results in the next section. At higher humidity levels, the peak

position continues to shift outward accompanied by a qualitative change in the shape of the curves. The peaks are no longer rounded curves, but are rather flat, followed by a steep drop. This could imply that the sample no longer switches over a small range of voltages. Rather the entire sample becomes more difficult to switch and there is a range of coercive voltages depending on the damage in the sample. It could also imply that the water dipoles are screening some of the voltage from PVDF dipoles. Even after drying out the sample, the switching peak position stays at a higher voltage than it was initially, showing that there was irreversible changes in the sample.

Another interesting trend in the data was the shift in the voltage bias, where the capacitance crossed itself. Figure 8-18 shows this trend over a range of relative humidities. At low humidity levels, the offset is at its highest, both on the original cycle and on the final cycle at 0% RH after the 80% RH cycle. Unlike many of the other properties such as the peak switching voltage shown in Figure 8-17 and the capacitance at the crossing point shown in Figure 8-19, the bias returned to a similar value as the initial offset. As the humidity level increased, the bias offset decreased from around 0.3 V to 0.05 V. This would imply that the water vapor inside of the film screened the source of the offset. If the offset is caused by slightly asymmetric electrodes creating a potential, as is often seen in films of this type, the water entering the films maybe causing the electrodes to appear the same for the sample, screening the potential difference.

Another characteristic of the series of CV curves shown in Figure 8-15 and Figure 8-16 was the capacitance at the crossing point. As shown in Figure 8-19, the capacitance is relatively constant from 0% RH to 40% RH, in the range of 1.30 to 1.35 nF. Above

40% RH, the capacitance starts to decrease with increased humidity. The capacitance does not return to its original value when the film is brought back to 0% RH after being cycled at 80% RH. This further supports the hypothesis that the samples start to become permanently damaged at approximately 40-50% RH. This damage appears to be caused by the combination of humidity and voltage. At low RH, the sample was cycled many times at  $\pm 15\text{V}$  with little evidence of decay, with a change of less than 1.5%. At 30% RH, the sample was being cycled to  $\pm 12\text{ V}$  with no signs of further damage, but at 50% RH, significant decay is starting to show up over many cycles. The decrease in capacitance was around 6% at higher humidity levels. When the sample was dried out at zero RH, there was a 22% drop in the crossing point capacitance compared to the original value at zero RH.

#### *8.4.F The Effect of Relative Humidity on the Pyroelectric Hysteresis of PVDF*

There were two samples used for the polarization hysteresis measurements at various humidity levels. The first sample was a 30 ML sample and the second was a 15 ML film. The 30 ML sample was recorded at 20% RH intervals from 20% RH up to 80% RH. The series of hysteresis loops consisting of pyroelectric current versus applied voltage was then plotted, as shown in Figure 8-20. The 20% RH scan had an initial saturated pyroelectric current of  $\pm 0.8\text{ nA}$ . The coercive voltage for the 20% RH was between 6.5 and 7.4 volts for increasing voltages and between -5.4 and -5.7 volts for decreasing voltages. As the humidity increased, the saturated pyroelectric current decreased and the switching voltage increased. At 80% RH, the saturated pyro current was down to 0.36 nA for the positive side and 0.5 nA for the negative side. In addition to

the nearly 50% decrease in the pyro current, there is a downward shift in the pyroelectric loop creating an asymmetry.

The pyroelectric hysteresis loops from the 15 ML sample (Figure 8-21) tell a slightly different story. For this sample, the 0% RH was the first measurement made and then the 80% RH set of measurements were made. After this set of data, the sample was irreversibly damaged and the following cycles display very little hysteresis. As with the previous sample, there was a decrease in the saturated pyroelectric current when the humidity was increased from 0% to 80%. The 0% RH was around 0.3 nA and the 80% RH was around 0.15 nA, representing the same 50% decrease. In the second sample, the coercive voltage did not increase as much as it shifted to more positive values by about one volt.

Both sets of data showed some of the same trends. First, there was a decrease in the amplitude of the remnant polarization, which is the polarization value at zero bias. Figure 8-22 is a plot of the amplitude of the polarization from the 30 ML sample. The amplitude decreases with increased humidity levels and cycling. Since the amplitude decreases from the first to the second cycle at a given humidity level, there is probably either damage being done to the sample, or there are regions of the sample that are either becoming amorphous or are being pinned and not switching easily. Since the current is proportional to the net polarization, one cannot differentiate between the two mechanisms based off of a decrease in polarization current.

Figure 8-23 shows the vertical shift of the center of the hysteresis loops. The initial cycle was well centered. By the fourth cycle, the midpoint had shifted down

almost 0.1 nA. As the humidity level continued to increase, the shift decreased and then stabilized around -0.06 nA. Unfortunately, this sample was burned out before the zero percent RH measurements could be made. The asymmetry in the sample would imply that there was more polarization when it was poled downward as compared to being poled upward. This could mean that part of the sample was pinned in a downward polarization, especially at the middle humidity levels.

There was also an increase in the switching voltage with increase in humidity levels, as shown in Figure 8-24. The increase was predominately from increase in humidity levels and not from cycling, which implies that the increased humidity levels made the sample harder to switch. If part of the sample was being pinned due to an increase in water vapor in the film, the film would have needed a higher voltage to reverse polarizations. This is supported by the increase of 1.5 volts over the increase in humidity to switch the sample to the downward polarization compared to the increase of 3.5 volts to switch the sample to an upward polarization. As in the previous figure, it appears the sample is more easily switched to negative polarization than to positive polarization.

The Martin paper looked at the effect of humidity on the polarization of the films [23]. They made their measurements with the Saur-Tower hysteresis loops instead of pyroelectric hysteresis loops. The Saur-Tower method measures the polarization charge,  $P$ , as a function of  $E$ . This method will pick up all charges measured including space charge, charge injection, relaxation charge in addition to the desired ferroelectric polarization charge. The authors find that the polarization charge increase as the humidity is increased. We found that the polarization from the hysteresis curves

decreased as the humidity increased. The authors' conclusion was that they could not determine the true ferroelectric behavior from their measurements. These two sets of measurements are difficult to compare as there are a variety of other sources that can contribute to the signal besides the ferroelectric polarization, for the case of the Saur-Tower loops.

## 8.5 Conclusions

As the water vapor entered the film, it resided in the crystal lattice and affected all of our measurements. Based on dielectric measurements, the amount of water in the film at 80% relative humidity was 0.046%. Even with 50 nm aluminum electrodes, the vapor could quickly enter the film, although it was slower to leave, with a long time constant of five to six hours.

Another consequence of high humidity was that the films become more fragile. They tended to show irreversible damage after being cycled at high humidity levels and voltages. In addition, the polarization became more difficult to switch while showing a decrease in the net polarization. Based on the XRD results, the change to the crystal lattice appeared to be reversible and there was no significant change to the film during the constant temperature, increasing humidity data experiments. If humidity alone caused the damage, we should have seen hysteresis in this set of data. Instead, we see evidence of damage when there is both high humidity and moderate voltages. At lower humidity levels (40% RH and lower), the effects of the humidity appear to be reversible, even under higher electric fields.

## 8.6 References

1. Lee, G.G. and B.E. Park, *Fabrication and Characterization of a MFIS-FET with a PVDF-TrFE/ZrO<sub>2</sub>/Si Structure*. Journal of the Korean Physical Society, 2010. **56**(5): p. 1484-1487.
2. Kang, S.J., et al., *Printable Ferroelectric PVDF/PMMA Blend Films with Ultralow Roughness for Low Voltage Non-Volatile Polymer Memories*. Advanced Functional Materials, 2009. **19**: p. 2812-2818.
3. Park, Y.J., et al., *Non-volatile memory characteristics of epitaxially grown PVDF-TrFE thin films and their printed micropattern application*. Current Applied Physics, 2011. **11**(2, Supplement): p. e30-e34.
4. Lee, Y.-S., S.J. Elliott, and P. Gardonio. *Distributed four-layer PVDF actuator/sensor arrangement for the control of beam motion*. 2001. Newport Beach, CA, USA: SPIE.
5. Xu, J., et al. *Design and microfabrication of a PVDF acoustic sensor*. 2009. San Diego, CA, USA: SPIE.
6. Fourie, D., *Shoe-Mounted PVDF Piezoelectric Transducer for Energy Harvest*. Massachusetts Institute of Technology Undergraduate Research Journal, 2010. **19**.
7. Wang, Y.R., et al., *A flexible piezoelectric force sensor on PVDF fabrics*. Smart Materials and Structures, 2011. **20**: p. 045009.
8. Priya, A.R.S., et al., *High-Performance Quasi-Solid-State Dye-Sensitized Solar Cell Based on an Electrospun PVdF-HFP Membrane Electrolyte*. Langmuir, 2008. **24**(17): p. 9816-9819.
9. Han, H.W., et al., *A Hybrid Poly(ethylene oxide)/ Poly(vinylidene fluoride)/TiO<sub>2</sub> Nanoparticle Solid-State Redox Electrolyte for Dye-Sensitized Nanocrystalline Solar Cells*. Advanced Functional Materials, 2005. **15**(12): p. 1940-1944.
10. Guan, F., et al., *Fast discharge speed in poly(vinylidene fluoride) graft copolymer dielectric films achieved by confined ferroelectricity*. Applied Physics Letters, 2009. **94**(5): p. 052907-3.
11. Zhang, Z. and T.C.M. Chung, *The Structure-Property Relationship of Poly(vinylidene difluoride)-Based Polymers with Energy Storage and Loss under Applied Electric Fields*. Macromolecules, 2007. **40**(26): p. 9391-9397.

12. Bune, A.V., et al., *Two-dimensional ferroelectric films*. Nature, 1998. **391**(6670): p. 874-877.
13. Kraemer, K.L., et al., *The Effects of Humidity on the Dielectric Response in Ferroelectric Polymers Made by Langmuir-Blodgett Deposition*. Ferroelectrics Letters Section, 2005. **32**(3-4): p. 85-89.
14. Ducharme, S., S.P. Palto, and V.M. Fridkin, *Ferroelectric Polymer Langmuir-Blodgett Films*, in *Handbook of Thin Film Materials*, H.S. Nalwa, Editor. 2002, Academic Press: San Diego.
15. *CRC Handbook of Chemistry and Physics*. 92 ed, ed. W.M. Haynes. 2011: Taylor and Francis Group, LLC.
16. Chynoweth, A.G., *Dynamic Method for Measuring the Pyroelectric Effect with Special Reference to Barium Titanate*. Journal of Applied Physics, 1956. **27**(1): p. 78-84.
17. Bune, A.V., et al., *Piezoelectric and pyroelectric properties of ferroelectric Langmuir--Blodgett polymer films*. Journal of Applied Physics, 1999. **85**(11): p. 7869-7873.
18. Bune, A., et al., *Novel switching phenomena in ferroelectric Langmuir--Blodgett films*. Applied Physics Letters, 1995. **67**(26): p. 3975-3977.
19. Ducharme, S., et al., *Ultrathin ferroelectric polymer films*. Ferroelectrics, 1997. **202**(1): p. 29-37.
20. Sorokin, A.V., V.M. Fridkin, and S. Ducharme, *Pyroelectric study of polarization switching in Langmuir-Blodgett films of poly(vinylidene fluoride trifluoroethylene)*. Journal of Applied Physics, 2005. **98**(4): p. 044107-10.
21. Jacobson, P.A., et al., *Water absorption and dielectric changes in crystalline poly(vinylidene fluoride-trifluoroethylene) copolymer films*. Applied Physics Letters, 2004. **84**(1): p. 88-90.
22. Aragonés, J.L., L.G. MacDowell, and C. Vega, *Dielectric Constant of Ices and Water: A Lesson about Water Interactions*. The Journal of Physical Chemistry A, 2010. **115**(23): p. 5745-5758.
23. Martin, B., G. Vizard, and H. Kliem, *Influence of the relative humidity on the properties of ferroelectric poly(vinylidene fluoride-trifluoroethylene)*. Journal of Applied Physics, 2009. **105**(8): p. 084114-7.

## 8.7 Figures

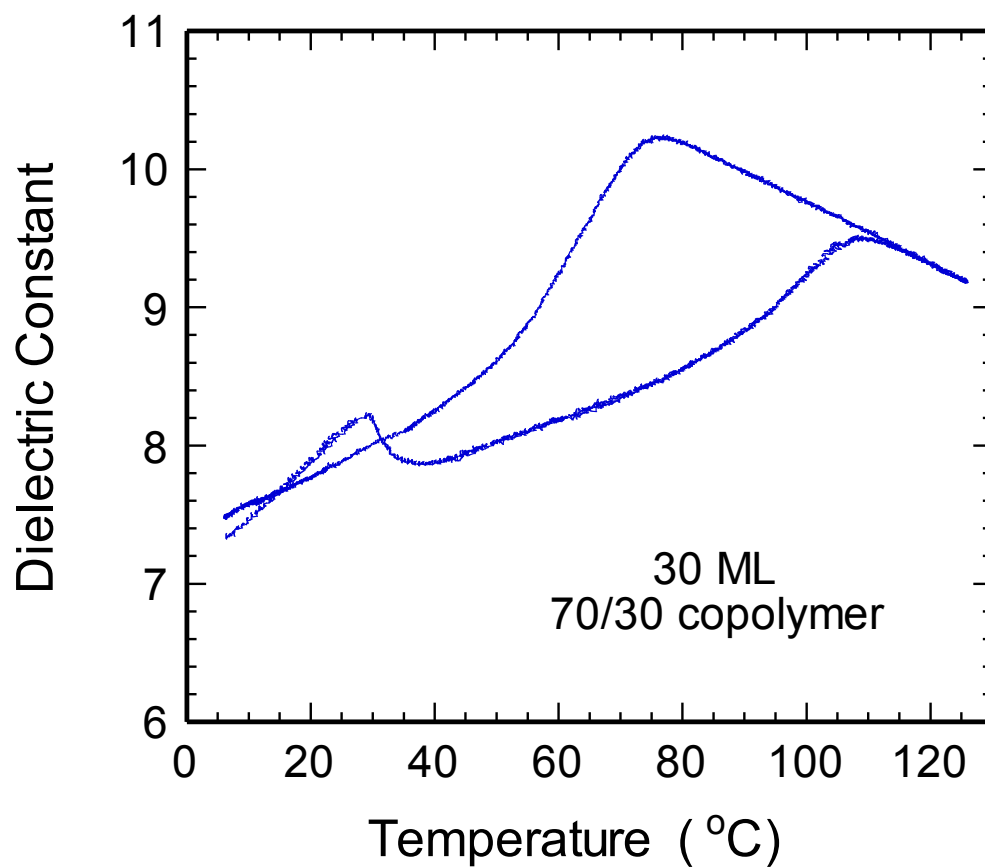
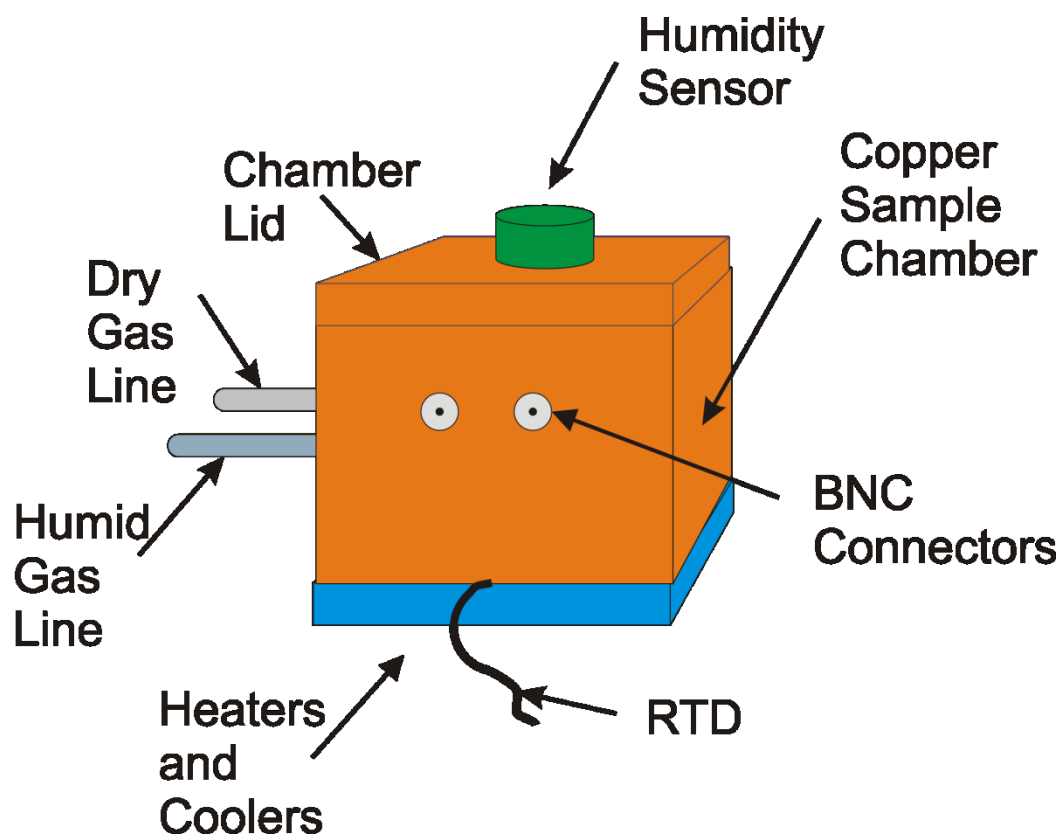
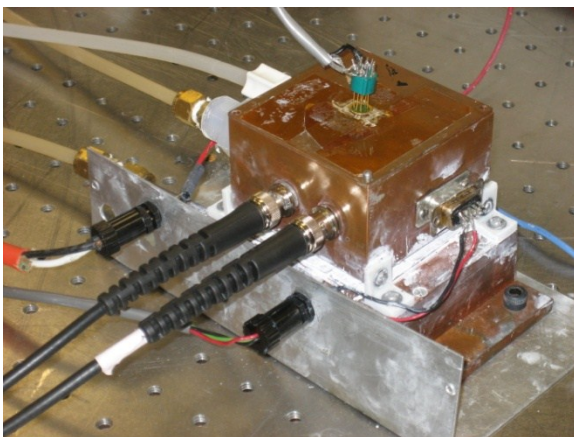


Figure 8-1. Typical temperatures scan of a PVDF copolymer thin film. The peak at 35° was originally attributed to the secondary phase transition seen in XRD data [12]. It was the further investigation of this peak that led to this project.

A



B



C

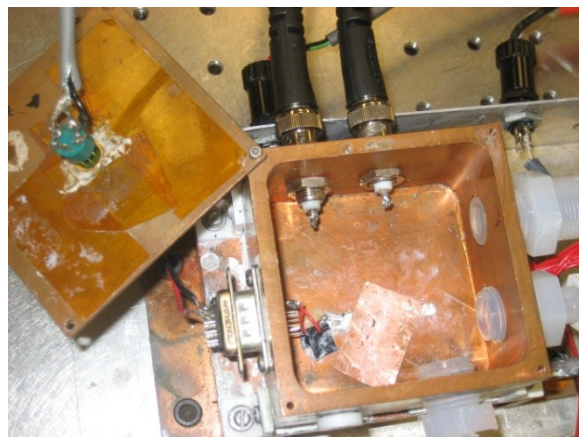


Figure 8-2. Sketch and photos of the humidity sample chamber. (A) Moist air was brought into the side of the chamber and the level was monitored by the humidity sensor in the top of the box. (B) Photo of the chamber with the sensor in the top of the lid. (C) Photo of the inside of the chamber. The sample wires are soldered onto the pins inside of the chamber.

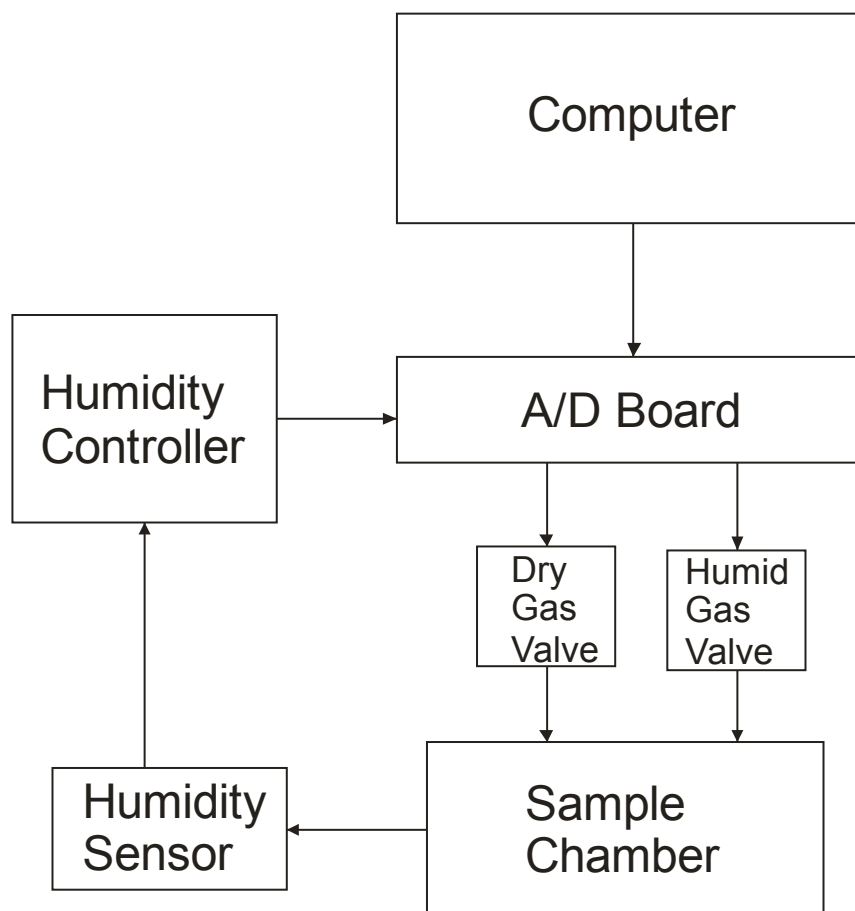


Figure 8-3. Sketch of the feedback loop to control the humidity levels in the chamber. The humidity sensor would measure the humidity and the controller would determine if the level was too high or too low. The controller would output a voltage which was passed to the analog in on the computer, and it would determine which of the two gas valves needed to be opened or closed to reach the desired humidity level.

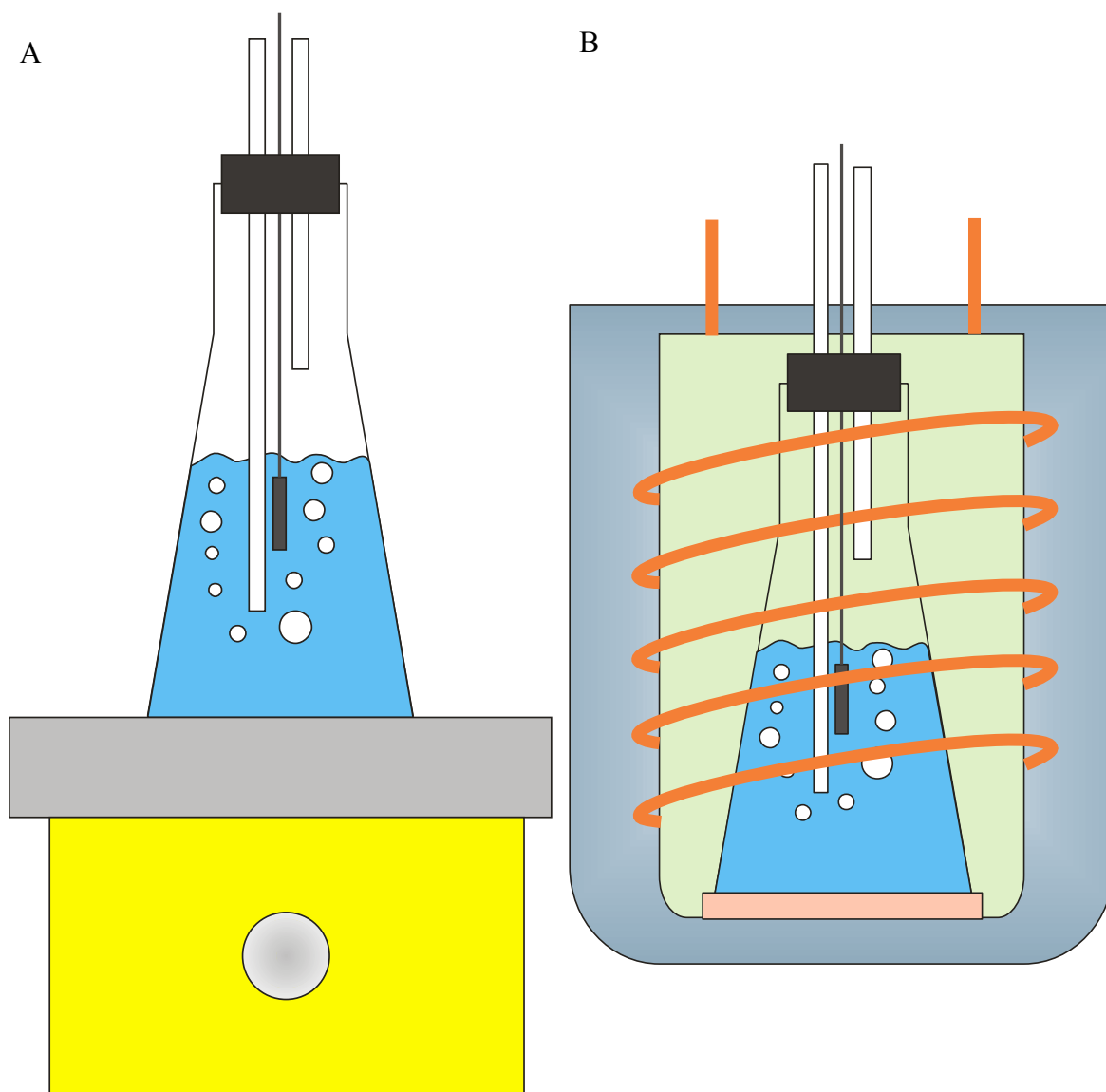


Figure 8-4. The humidity production chambers. (A) When the sample chamber was at or above room temperature, the water used to produce humidity was warmed to a few degrees higher than the sample chamber with the use of a hotplate connected to a temperature controller. The dry nitrogen gas was bubbled into the chamber to force the moist air into the sample chamber. (B) When the sample chamber was cooled below room temperature, it was necessary to cool the water used to produce humidity. This was to prevent condensation in the chamber. The flask sat on a blanket heater in a small bucket that was sitting in an ice bath. The dry gas line ran through the copper tubing that was submerged in the ice bath, so it would not heat the sample chamber.

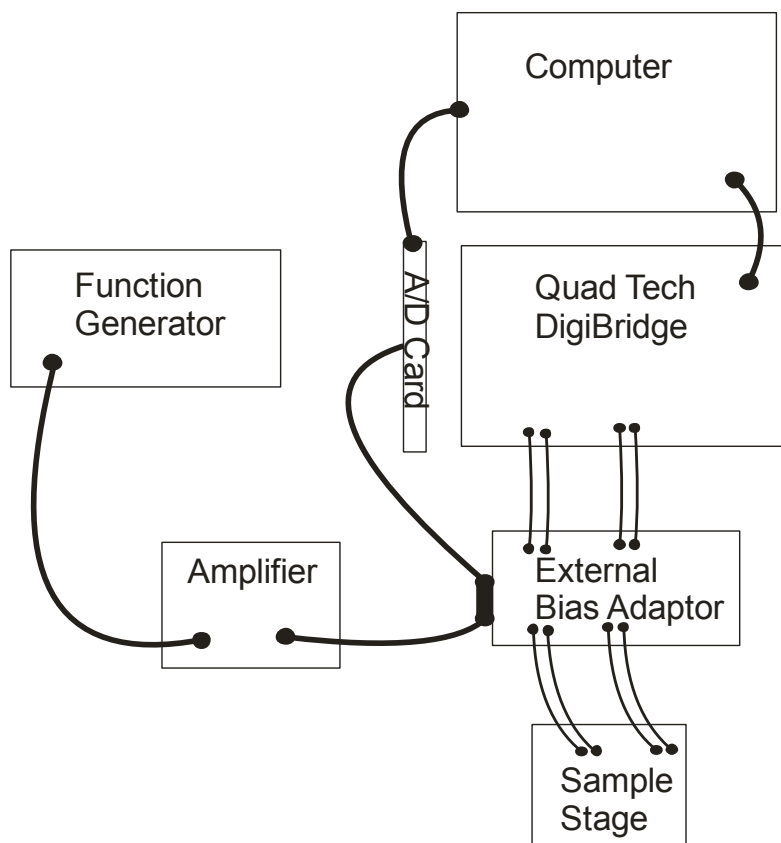


Figure 8-5. Sketch of setup for using the function generator to provide the voltage sweep for a capacitance versus voltage sweep with the Quadtech DigiBridge. The voltage sweep was provided by a function generator while the capacitance was measured with the digibridge.

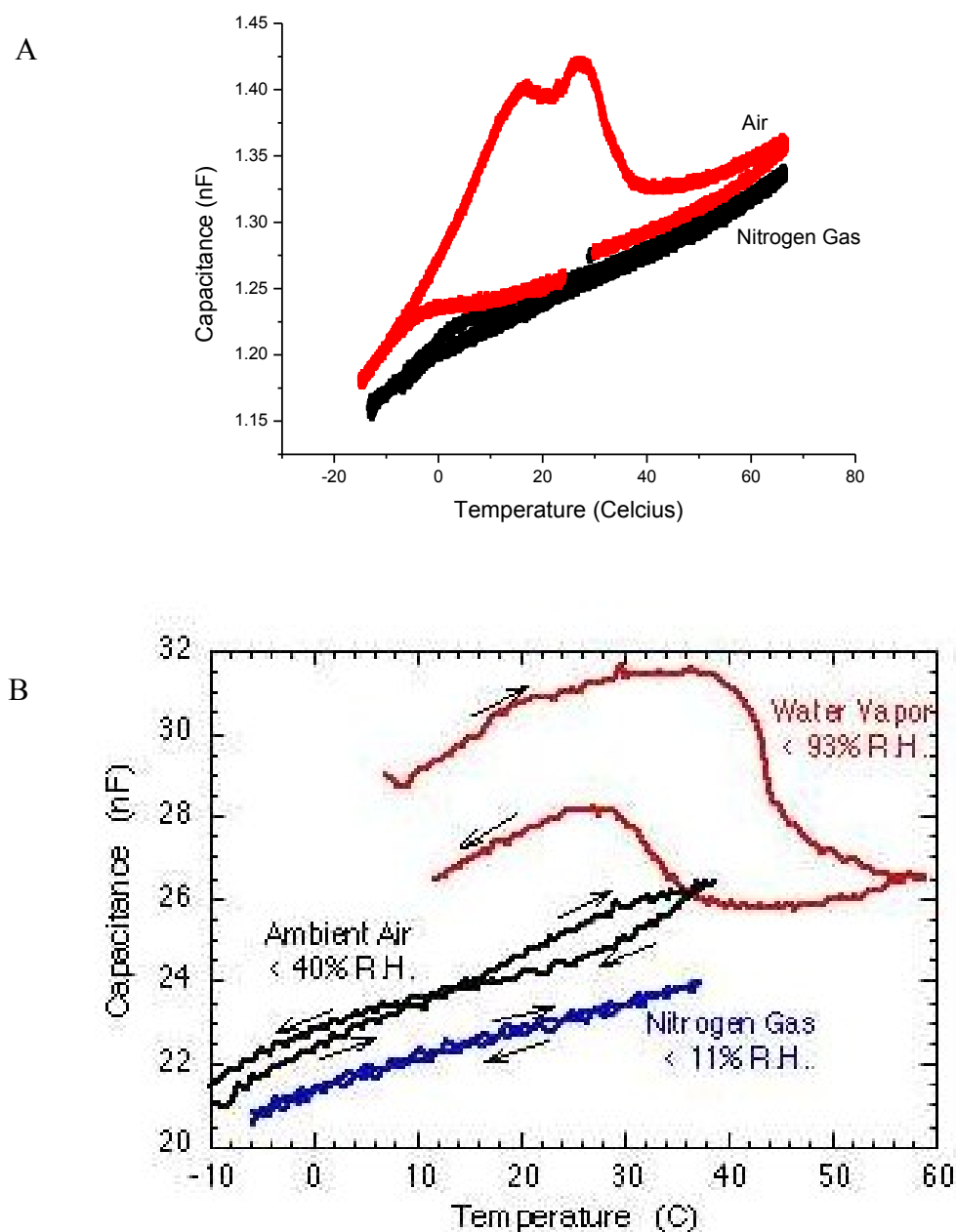


Figure 8-6. Peaks in the temperature data caused by the humidity. The shape and location of the peak is dependent on the conditions in the chamber. (A) The red curve shows the bumps in the curve from the humidity on heating and cooling. When the same experiment is reproduced in a dry nitrogen atmosphere, the bumps have nearly disappeared due to there being little or no condensation present (black curve). (B) This series of runs was one of the original sets of data demonstrating the effect of humidity on the thin films. The setup was primitive with very little control of the flow rates and a large environmental humidity sensor to monitor the humidity levels. The data is divided into three groups with low, medium, and high humidity levels.

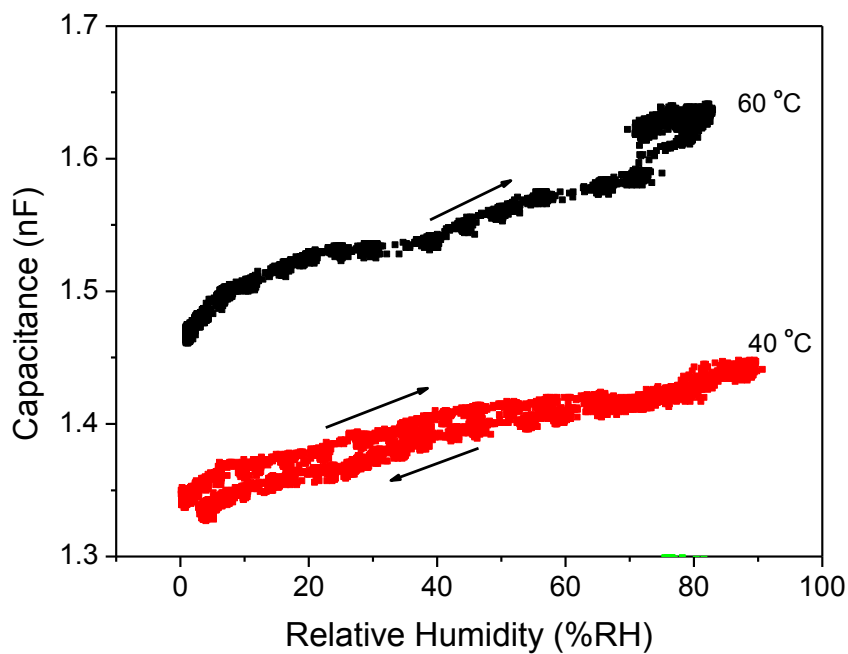


Figure 8-7. Ramping of the humidity while holding the sample at a constant temperature. The increase in the capacitance is nearly linear with very little hysteresis. At 80% relative humidity, there is 0.046% water volume in the sample based on dielectric calculations, assuming a constant thickness.

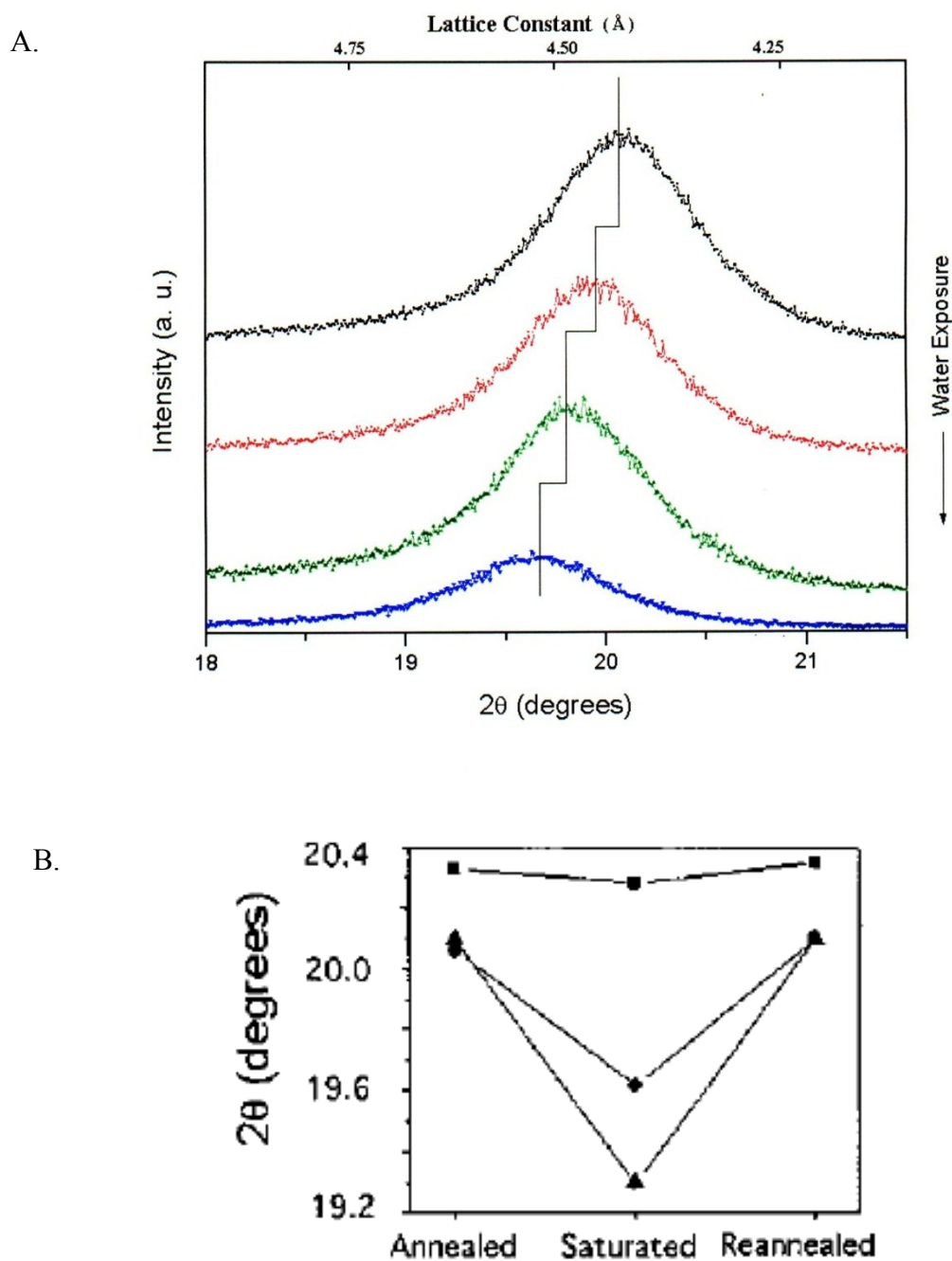


Figure 8-8. XRD results showing that the water vapor is in the crystal lattice causing the crystal spacing to increase [21]. (A) As the concentration of water increases, the  $2\theta$  XRD peak shifts to smaller angles. (B) The lattice spacing increase when it is saturated, but when it is re-annealed, it returns to its original spacing. [21] (Taken from Jacobson, P.A., et al., *Applied Physics Letters*, 2004. **84** (88) with permission.)

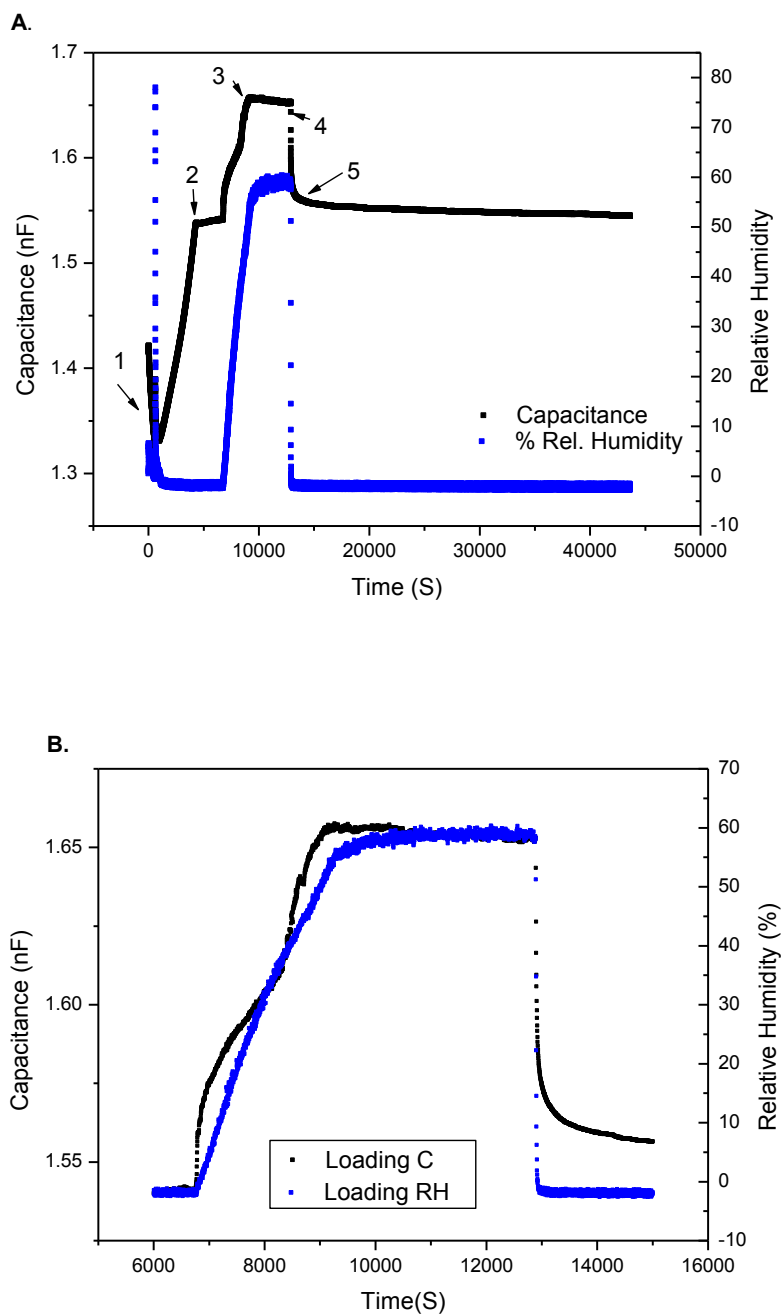


Figure 8-9. A. A typical capacitance (black) and humidity (blue) plot. Some of the important events that occur in the data are 1. Drying out sample so there is no initial humidity present. 2. Heat the sample to the desired temperature. For this run, the sample was heated to 80°C. 3. Load the humidity to 60%. 4. Turn on the dry nitrogen gas and flush the chamber. 5. The drying tail that is later analyzed to determine the time constants. (B) Loading the humidity into the chamber. The capacitance follows the same trend as the humidity.

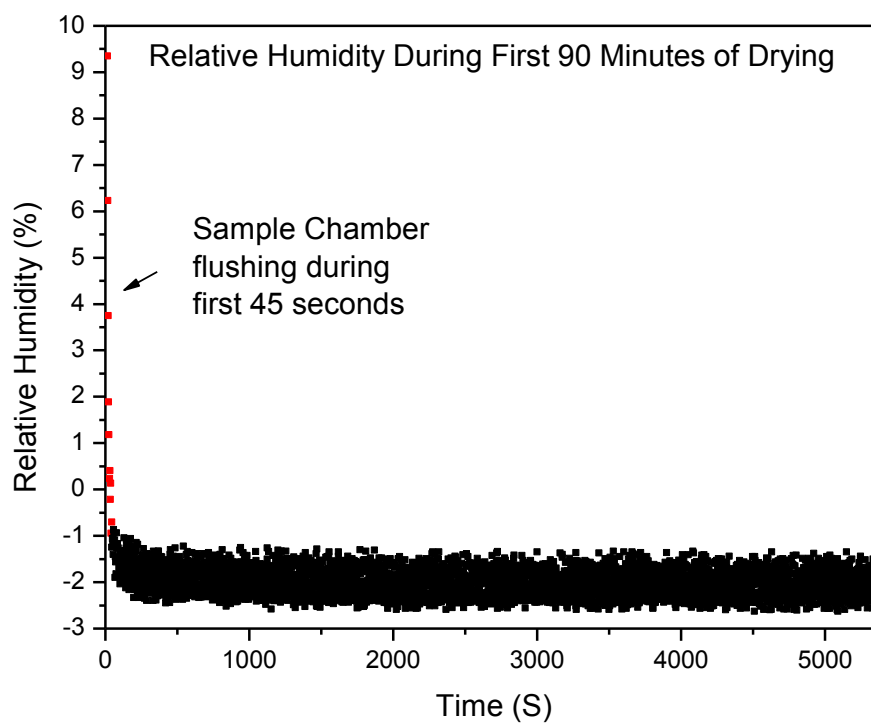


Figure 8-10. The chamber takes about 45 seconds to flush out the humidity. After that, the humidity level stays nearly constant.

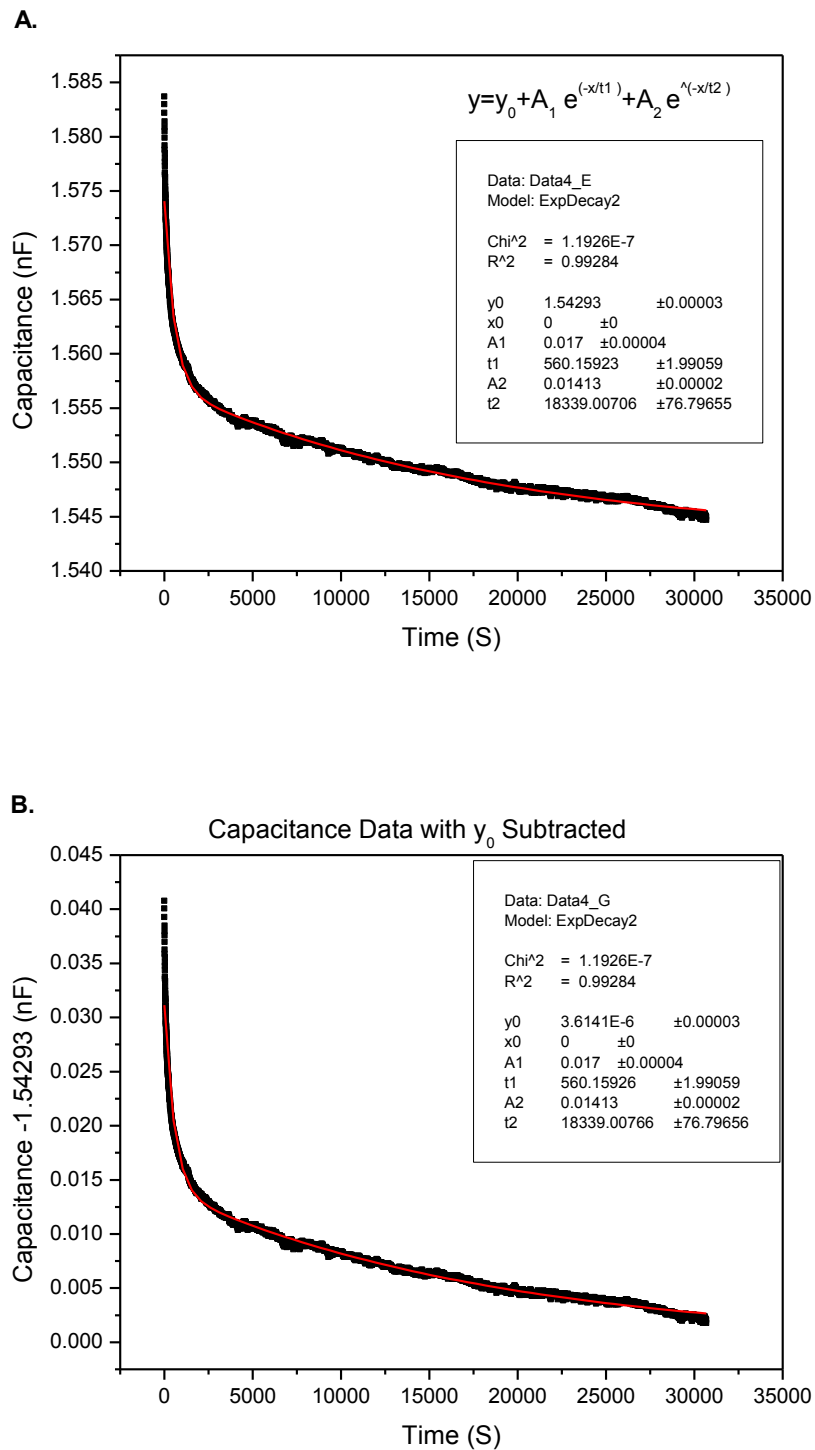


Figure 8-11. An example of typical drying curves. (A) The curve is fit with a two term exponential decay. (B) The  $y_0$  term from part A is subtracted from the data. This will allow us to linearize the data in Figure 8-12.

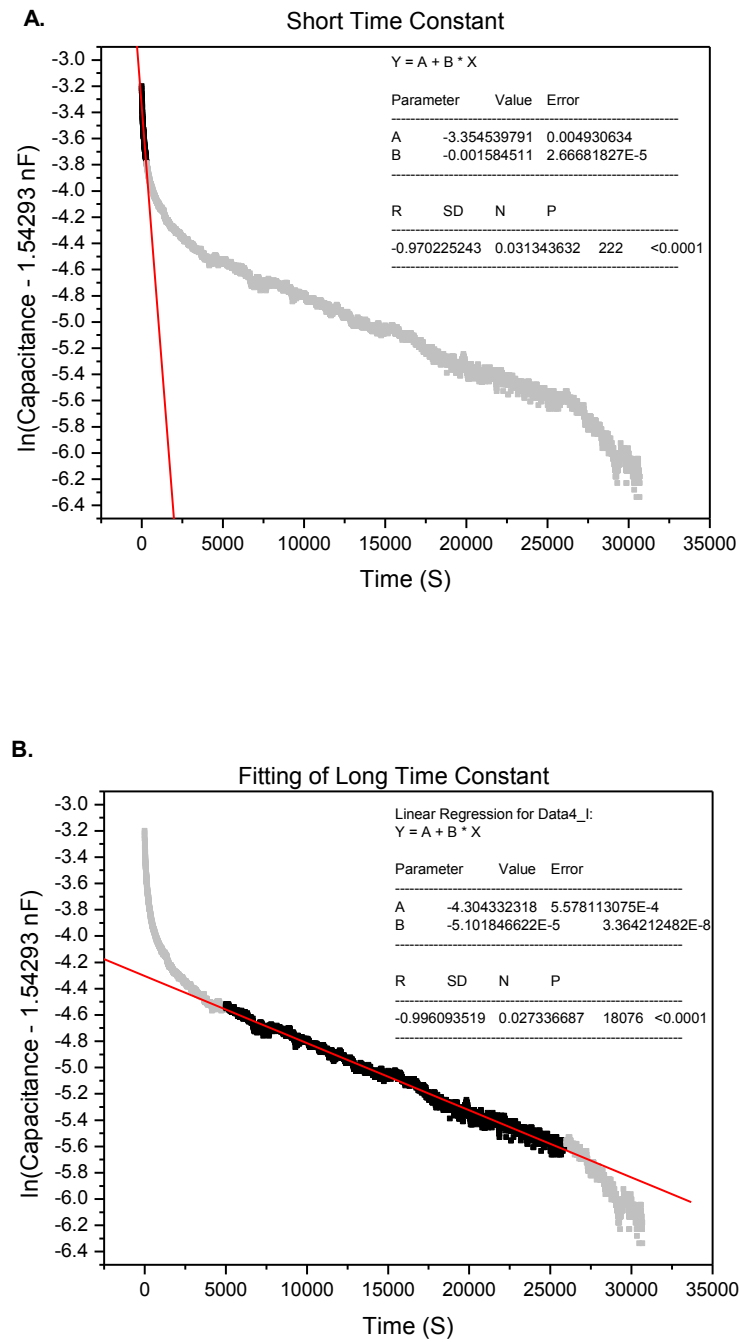


Figure 8-12. The natural log of the capacitance of the data in Figure 8-11. By fitting each linear portion of the data, the time constants can be determined. The time constants are the negative inverse of the slope. (A) The short time constant is found in the first linear section of each plot. (B) The long time constant is the straight section in the middle of the data.

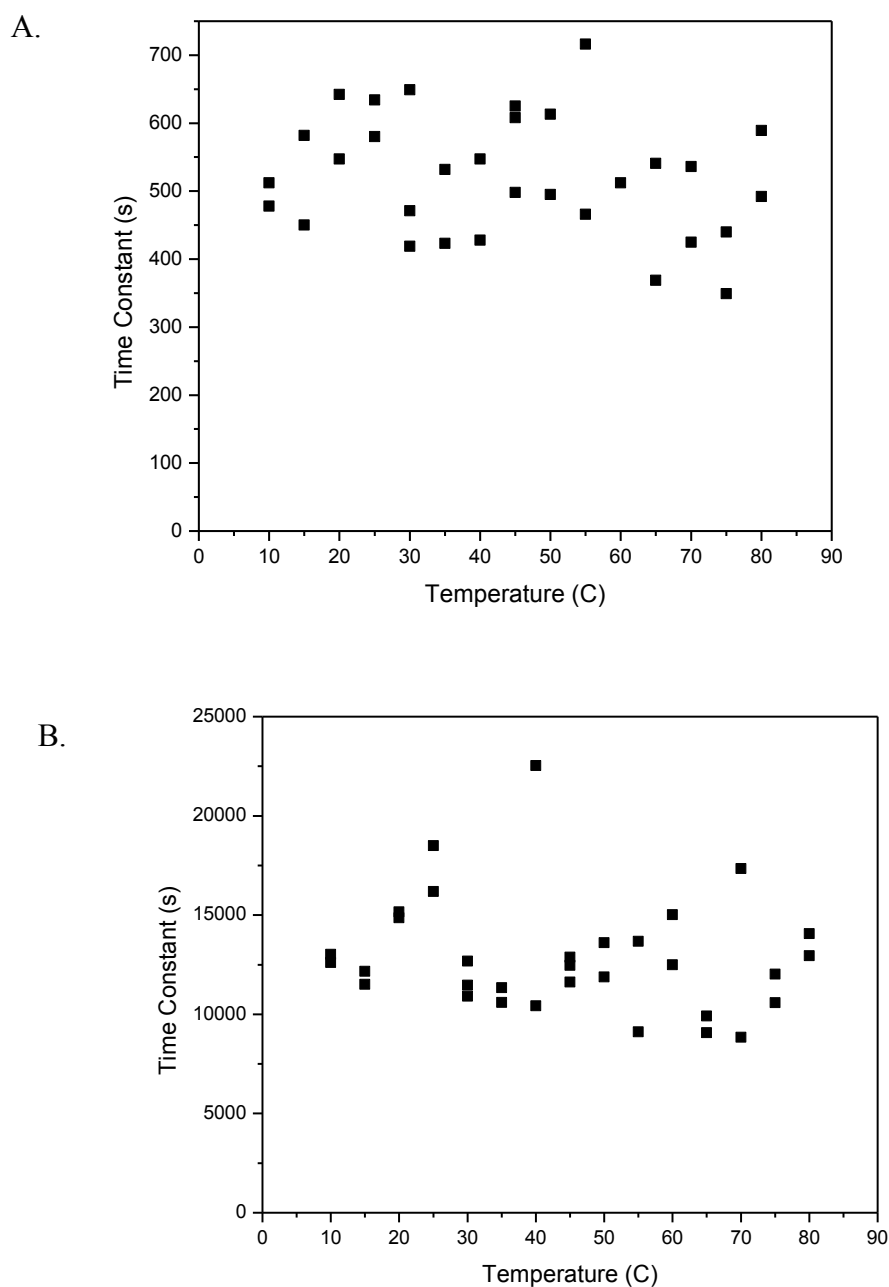


Figure 8-13. (A) Short time constant plot. This time constant is believed to represent the time it takes the chamber to completely flush out and for the water to leave the surface of the sample. (B) The long time constant plot. This is believed to be the time it takes for the water to leave the bulk of the sample. The lack of a downward trend in the data means there is very little temperature dependence.

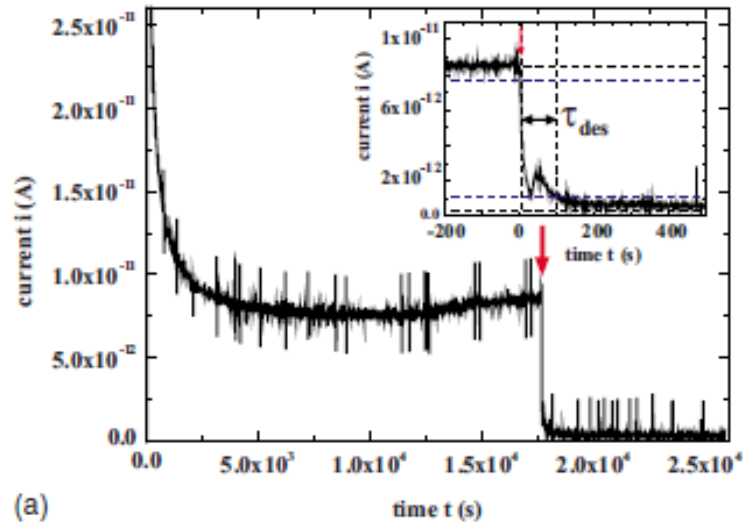


Figure 8-14. Martin's, et al,[23] measurements of the desorption properties of a 50 ML film. The transient behavior of the current with the rapid change in humidity from near 100% to 0%. The desorption time,  $\tau_{\text{des}}$ , is marked by the red arrow and is around 100 seconds. (Taken from *Martin, B., et al., Journal of Applied Physics*, 2009. **105**(084114) with permission.)

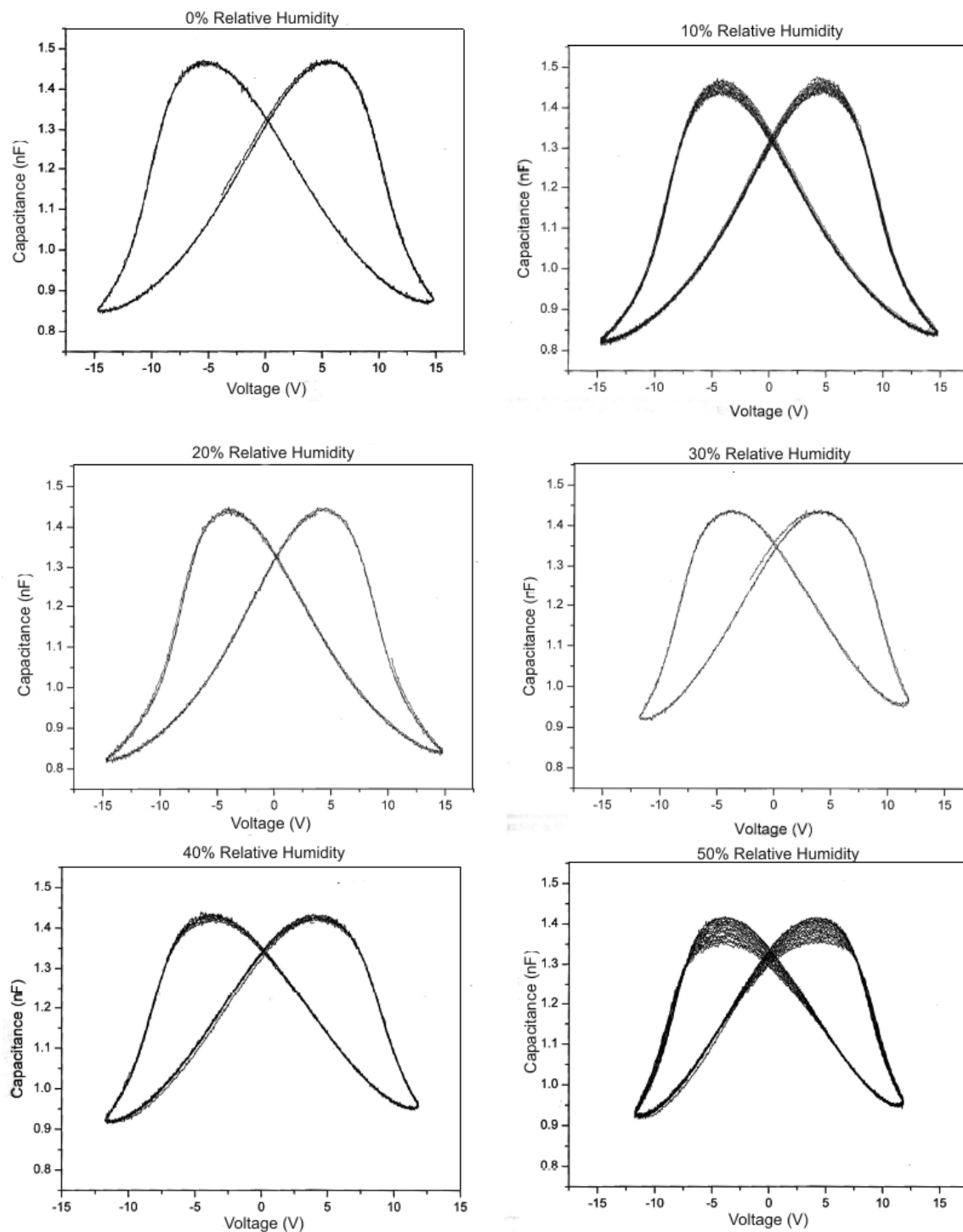


Figure 8-15. Capacitance vs voltage curves over the range of humidity levels from 0% relative humidity to 80% relative humidity. The data is continued in Figure 8-16.

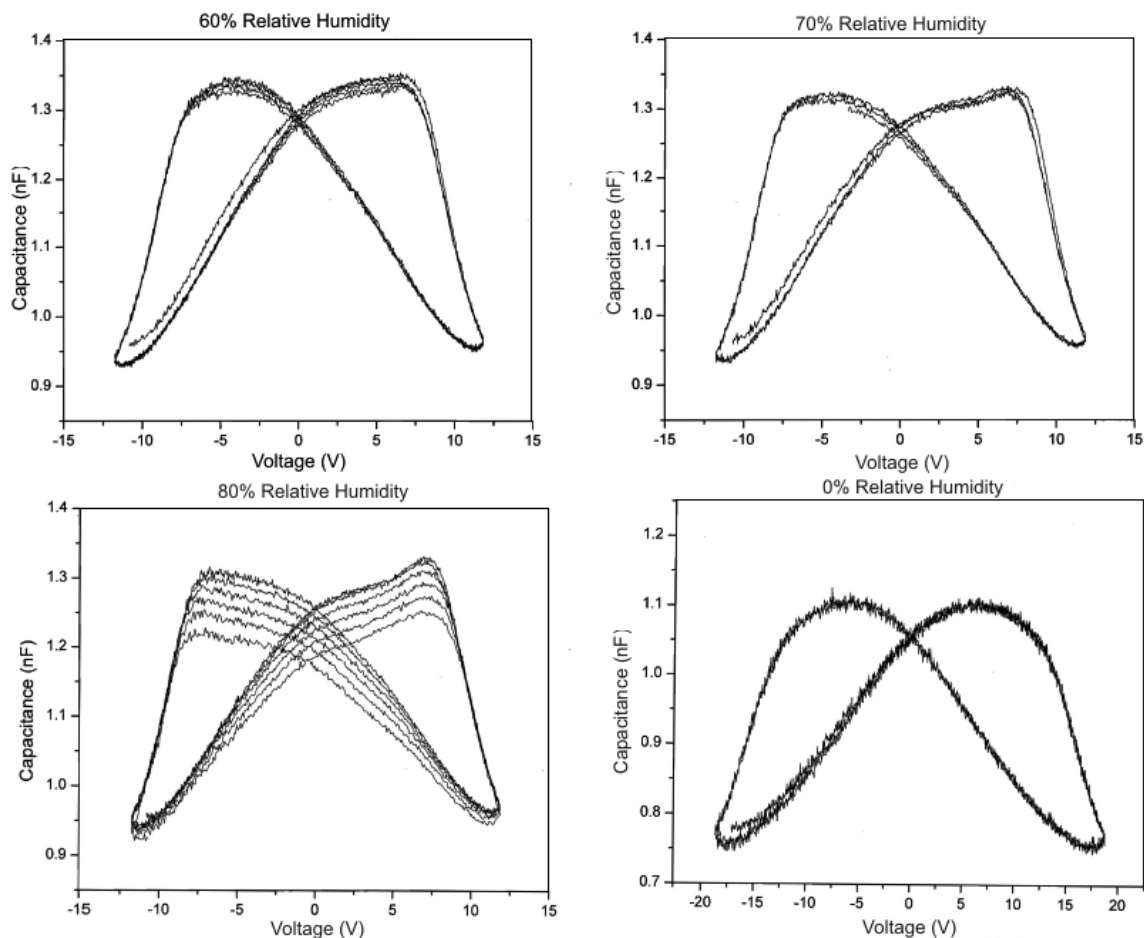


Figure 8-16. Continuation of the humidity data from from Figure 8-15. At higher humidity levels, the overall capacitance decreases while the peak shifts to much larger voltages. At lower humidity levels, the switching peak moves to smaller voltages.

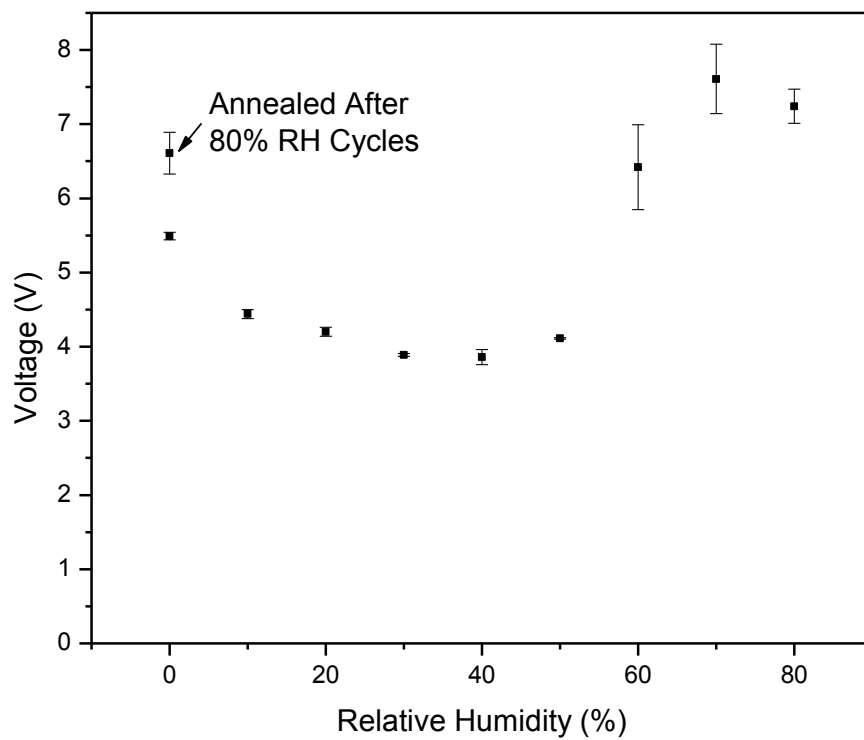


Figure 8-17. Peak switching voltages of samples under humidity. The largest uncertainty in the peak positions is due to the broadening and flattening of the peaks.

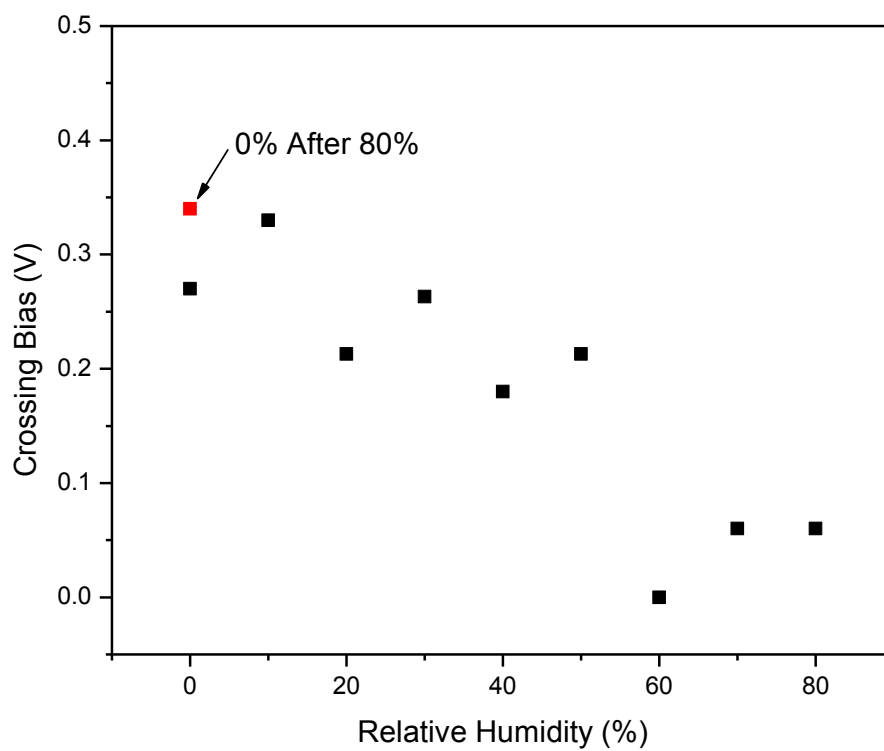


Figure 8-18. Offset of Bias at point where the increasing capacitance crosses itself. There was a shift to smaller and more negative bias at the crossing point in the capacitance data as the humidity was increased.

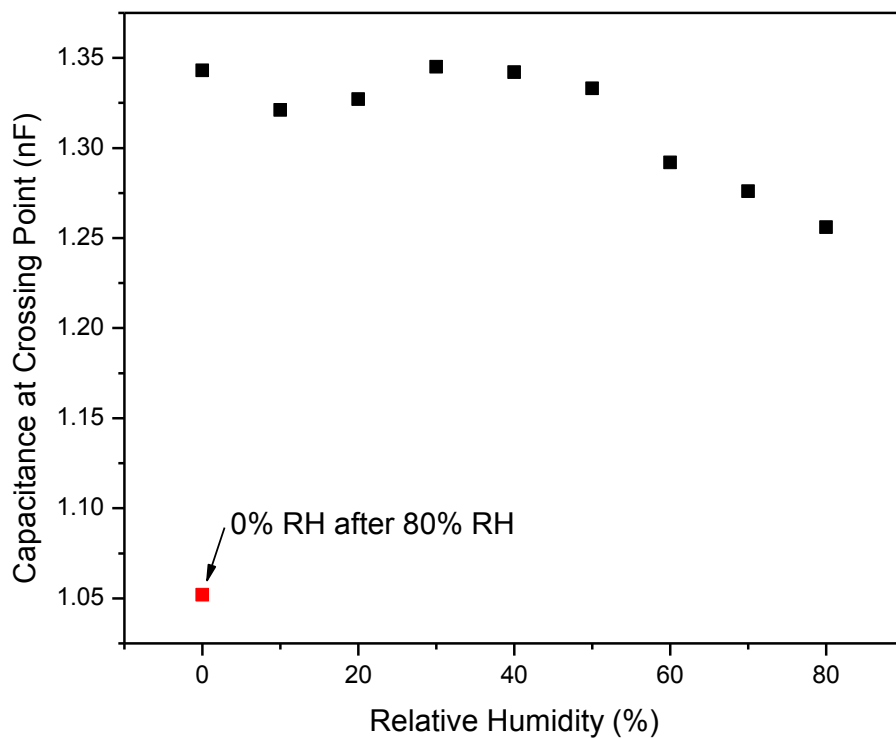


Figure 8-19. The overall capacitance measured at the point where the increasing capacitance of the butterfly loops cross each other. The capacitance remains relatively constant until it reaches 40%, and then it starts to decrease.

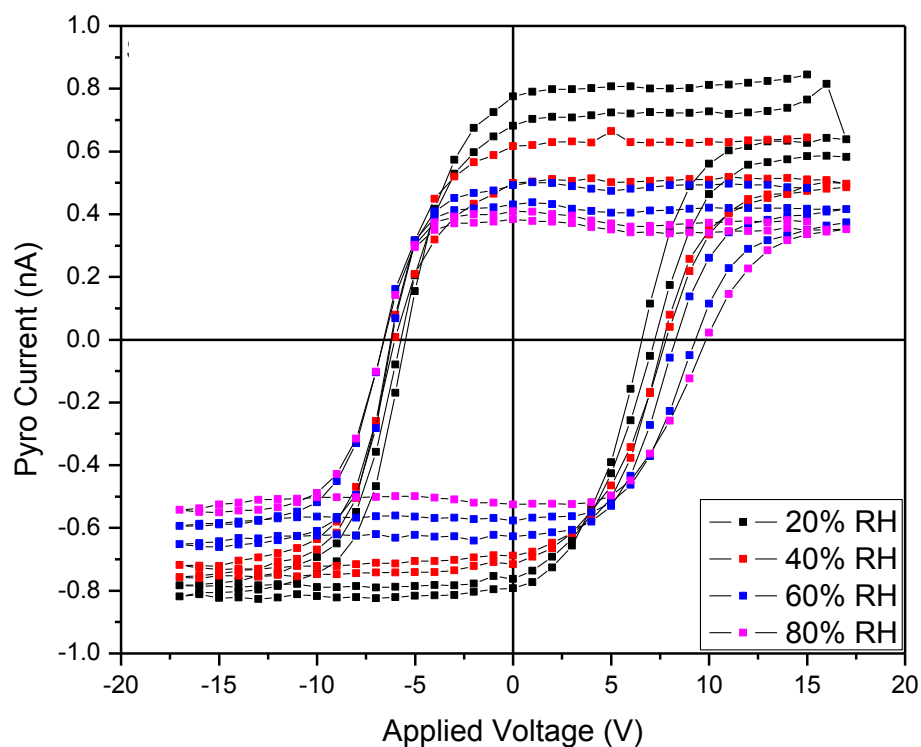


Figure 8-20. Pyroelectric scans of a 30 ML sample over range of humidity levels from 20% to 80% relative humidity. As the humidity level increases, the coercive voltage increases, the saturated pyroelectric current decreases, and the loop is no longer symmetric. See Figure 8-22, Figure 8-23, and Figure 8-24 for further analysis of this data.

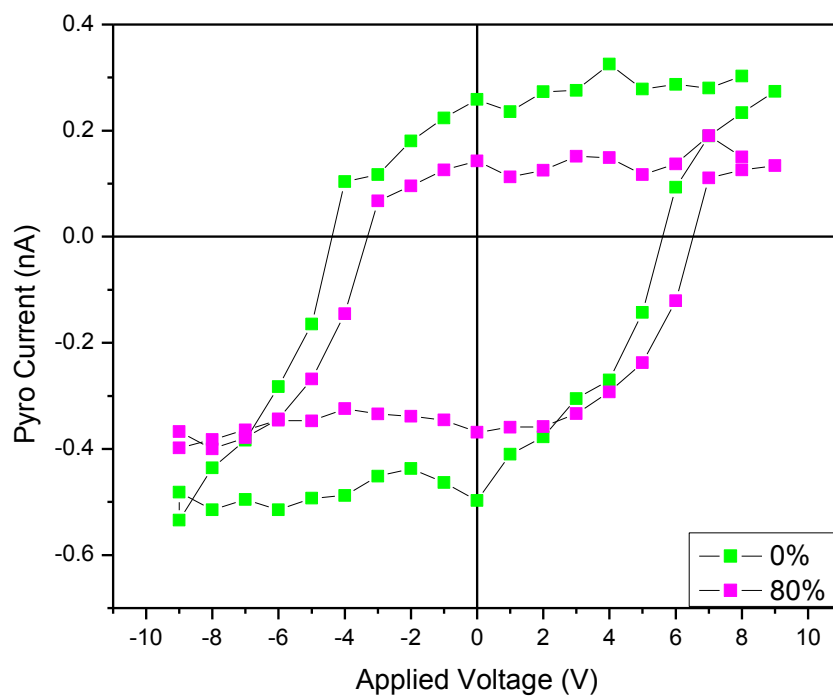


Figure 8-21. For this spot, the 0% RH cycle was ran first, followed by the 80% RH cycle. After the 80% RH cycle, the sample had irreversible damage done to it, and the following runs showed no hysteresis.

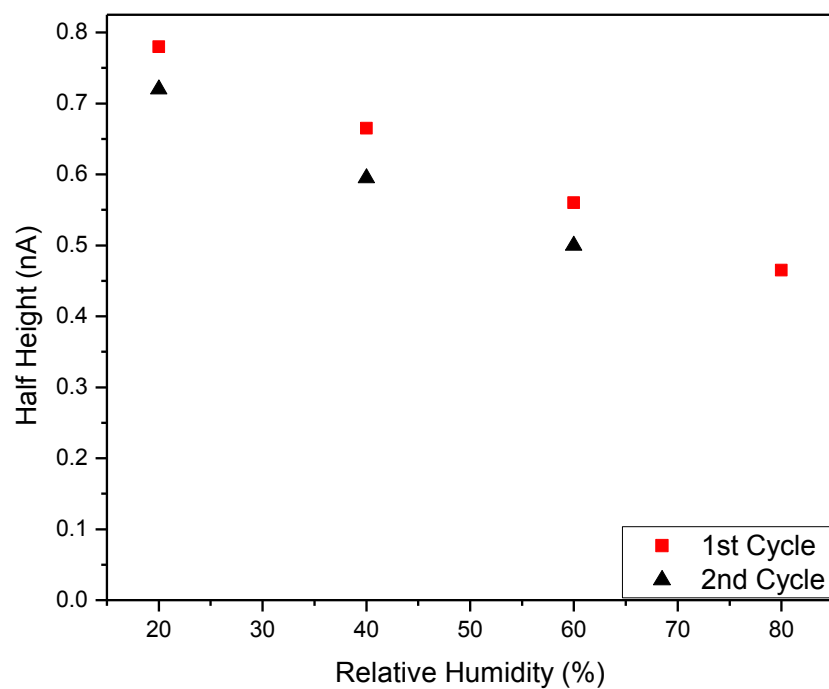


Figure 8-22. The half-height remnant polarization for the data shown in Figure 8-20. With the increase in humidity and cycling, there is a decrease in the remnant polarization.

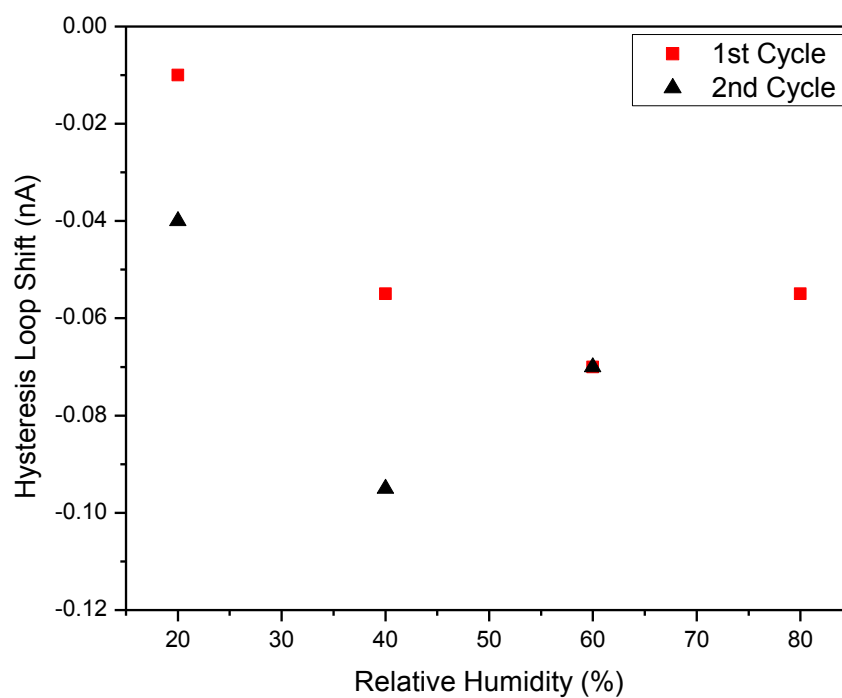


Figure 8-23. The vertical shift of the middle of the data shown in Figure 8-20. Overall, the data shifts downward as the humidity level increases. At 80% RH, the shift of the midpoint was less than at lower levels of humidity.

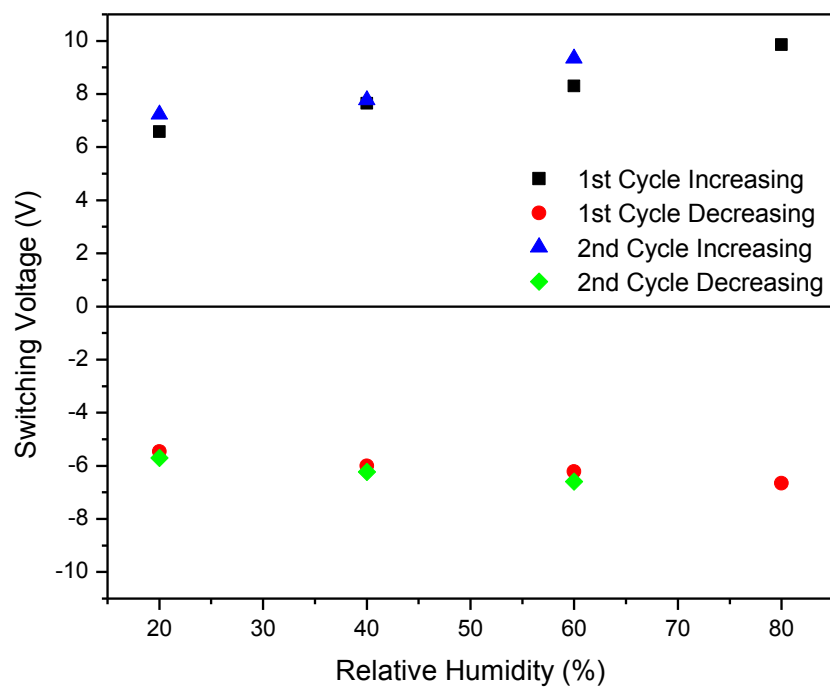


Figure 8-24. The cohesive voltage for the series of runs in Figure 8-20. Each humidity level was cycled twice, except for the 80% relative humidity. There was very little change from cycle to cycle at a given humidity level, but there was an increase with humidity levels.

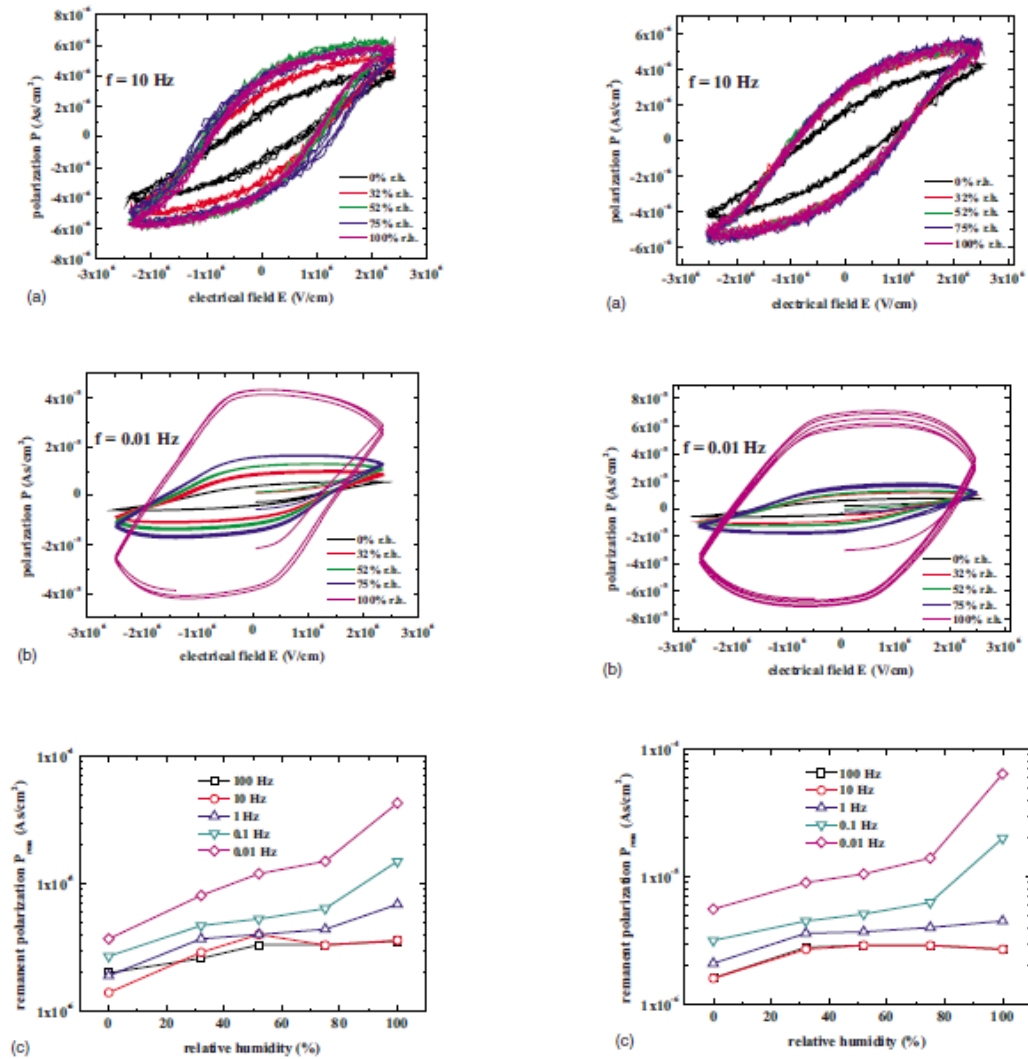


Figure 8-25. The figures in the first column are for a 50 ML sample [23]. The figures in the second column are for a 30 ML sample. (Taken from *Martin, B., et al., Journal of Applied Physics*, 2009. **105**(084114) with permission.)